BULGARIAN CHEMICAL COMMUNICATIONS

Journal of the Chemical Institutes
of the Bulgarian Academy of Sciences
and of the Union of Chemists in Bulgari

This special issue of the Bulgarian Chemical Communications contains selected papers of the conference **"Advances in Polymer Materials'** being organized during April 25-26, 2023 (APM-2023) at Department of Chemistry, G.B. Pant University of Agriculture & Technology, Pantnagar. The conference was sponsored by Defense Research Development Organization (DRDO), Ministry of Defense India.APM-2023 was conducted by the Department of Chemistry, College of Basic Sciences & Humanities, G.B. Pant University of Agriculture & Technology (GBPUAT), Pantnagar, Uttarakhand, India. The conference was conducted under the Patronage of Dr. Manmohan Singh Chauhan, the Vice Chancellor, GBPUAT, Pantnagar, India. The conference was presided over as Chief Guest by Dr. Mayank Dwivedi, Director, Defense Materials and Stores Research and Development Establishment, DRDO, Kanpur, UP India.

The theme of conference "Shaping Future by Combining Knowledge & Innovations in Polymer Materials" has been crafted to explore the viable ways to rectify the technological challenges associated with development and applications of polymer materials across the world. APM-2023 was fortunate to have around two hundred delegates including keynote speakers, oral and poster presenters from India and abroad to share their experience and perspectives to achieve the smart and leading solutions in development and execution of polymer materials through their cutting age innovations. Conference intended to bring together the scientists, engineers and practitioners from cross disciplines of sciences & technology and discussed the academic aspects of polymer science and technology for sustainable development of society and industries across the world.

We gratefully thank the Editorial Board of the Bulgarian Chemical Communications for the opportunity to disseminate a part of the papers reported at the conference to the audience of the journal.

<u>EDITORS</u>
Sameena Mehtab, MGH Zaidi
Department of Chemistry College of Basic Sciences & Humanities G. B. Pant University of Agriculture & Technology Pantnagar (Uttarakhand), India
Pushpendra Kumar
Department of Physics, Manipal University Jaipur, Jaipur-303007, Rajasthan, India

Sameena Mehtab   **Pushpendra Kumar**   **MGH Zaidi**

Effect of calcination on nickel-doped calcium hydroxide nanoparticles

Akash[1], R. Singhal[2], M. G. H. Zaidi[3], S. Rawal[4], A. K. Mukhopadhyay[4], P. Kumar[1]*

[1]Department of Physics, Manipal University Jaipur, Jaipur-303007, Rajasthan, India
[2]Department of Physics, Malaviya National Institute of Technology, Jaipur-302017, India
[3]Department of Chemistry, College of Basic Science and Humanities, G.B Pant University of Agriculture and Technology, Uttarakhand, 263145, India
[4]Department of Physics, Sharda School of Basic Sciences and Research, Sharda University, Greater Noida 201310, Uttar Pradesh, India

In this study, we have synthesized calcium hydroxide (CH) and nickel (Ni)-doped calcium hydroxide nanoparticles (NPs), through the inexpensive chemical precipitation route. The nickel-doped CHNPs were then calcined at 500 °C for 3 hours. The produced samples were characterized by X-ray diffraction (XRD), scanning electron microscopy (SEM), energy dispersive X-ray (EDX), Fourier transform infrared spectroscopy (FTIR), and UV-visible spectroscopy techniques to investigate the changes in structural, morphological and optical parameters. The XRD study showed the phase formation of $Ca(OH)_2$, $Ni\text{-}Ca(OH)_2$, and $CaCO_3$. The $Ca(OH)_2$ nanoparticles were transformed into $CaCO_3$ NPs due to the high-temperature carbonation reaction. It was also found that the crystallite size is decreasing from 62.32 nm to 40 nm. The FESEM pictures expose the prepared samples' morphology and particle size. The UV-Vis spectra showed a blue shift in the absorbance band. The band gap energy of all prepared samples, plotted by Tauc's plot, showed a concomitant change with crystallite size.

Keywords: Calcium hydroxide, Calcium carbonate, Doping, Chemical synthesis.

INTRODUCTION

Due to its many commercial uses, calcium hydroxide $(Ca(OH)_2)$, a semiconductor with a wide band gap [1], has become one of the most promising hydroxide materials in the fields of food packaging [2], wastewater treatment [3], and construction [4]. The material has many uses in different categories, which involve dental cement [5], energy storage [6], cultural heritage conservation [7], antimicrobial activity [8], dye removal [9], and Portland cement production [10]. It is a fascinating semiconductor material because of its eco-friendliness and low cost when compared to other nanohydroxide materials. Nature makes it inevitable for humans to use materials in their daily lives, and there is a constant need for novel materials for a variety of uses, including solar cells, energy storage devices, magnetic materials, biosensors, dye degradation effects, and other applications [11]. As a result, for the preparation of nanostructured powders with a variety of compositions, sizes, and morphologies, improvements in powder processing procedures are required. For this instant, various categories of nanoparticles can be utilized to synthesize new materials. Due to their potential qualities and uses in optoelectronics, electronics, sensing, medicine, and catalysis, transition metals like Ni, Co, and Fe are of particular interest among the several categories of nanoparticles (NPs) [12, 13].

Recent studies have shown that after doping of such transition metals like Ni in ZnO nanoparticles the optical, structural, and morphological properties can be controlled and demonstrated effective biosensor applications and promising outcomes in the medical field [14]. Magnesium oxide and co-existing cobalt oxide agents have attracted considerable interest as the manufactured products retain an enormous surface area and band gap bowing. Thus, the obtained products may be crucial for photocatalysis [15]. Zinc oxide doped with transition elements (Ni and Cu) created by the chemical co-precipitation method demonstrates a blue shift in peak wavelength from undoped ZnO to doped ZnO in the PL spectra and a shift from lower to higher wavelength in the UV-Vis spectra [16]. Because of the differing electronic shell structure and comparable size of Ni^{2+} (0.069 nm) and Zn^{2+} (0.074 nm), it is anticipated that the doping of nickel in ZnO will change its absorbance, photocatalytic, and other physical or chemical assets. Research on Ni-doped ZnO nanostructures using spray pyrolysis, precipitation, and sputtering has also been described [17, 18].

This paper first reports the synthesis of Ni-doped CHNPs using the inexpensive co-precipitation

---

* To whom all correspondence should be sent:
E-mail: pushpendra.kumar@jaipur.manipal.edu

method. Then, the Ni-doped $Ca(OH)_2$ was calcined for 3h at 500 °C in air. This research sought to understand how calcination affected nickel-doped $Ca(OH)_2$ nanoparticles. The change in structural, morphological, and optical features of the primed nanoparticles was examined by various characterization methods including XRD, FTIR, FESEM, and UV-VIS. In this research report, the outcomes that were achieved are thoroughly addressed.

EXPERIMENTAL

Materials

All the chemicals, containing sodium hydroxide (NaOH), calcium nitrate hexahydrate $(Ca(NO_3)_2.6H_2O)$, and nickel nitrate hexahydrate $(Ni(NO_3)_2.6H_2O)$, obtained from Merck (India), were used as received. All the samples were prepared using deionized water throughout the experiment.

Method

In this experiment, calcium hydroxide and Ni-doped calcium hydroxide samples were prepared using the co-precipitation route. To create calcium hydroxide (sample A), $Ca(NO_3)_2.6H_2O$ and NaOH solution were prepared in distilled water. The precipitator sodium hydroxide (0.6 M, 200 ml) was dropwise added into the solution of calcium nitrate hexahydrate (0.6 M, 200 ml) while utilizing magnetic stirring at 1200 rpm solution, at room temperature. Following the completion of the reaction, the white precipitate was filtered from the remaining $NaNO_3$ using Whatman 40 filter paper (GE Healthcare UK Limited, UK), that had been created during the synthesis. The white precipitate was dried at 60 °C for 2 hours. The synthesis of Ni-doped $Ca(OH)_2$ was also completed by the precipitation method. Firstly, (1-x) atom% $Ca(NO_3)_2.6H_2O$ and x atom% $Ni(NO_3)_2.6H_2O$ solution (where x = 0.10) were made in 200 ml distilled water. The calcium nitrate hexahydrate (0.6 M, 200 ml) solution was then mixed into nickel nitrate hexahydrate (0.6 M, 200 ml) on a magnetic stirrer under continuous mixing. In addition, NaOH aqueous solution (0.6 M, 200 ml) was made of deionized water and then mixed dropwise into the aforesaid solution while utilizing magnetic stirring at 1200 rpm. The entire process was held at normal temperature. Following an hour of applying the precipitator NaOH, the precipitate was acquired and filtered using Whatman 40 filter paper. The $NaNO_3$ residue was also removed by repeated washing with deionized water. Finally, the Ni-$Ca(OH)_2$ precipitate was dried at 60°C for 2 hours in the air. The final product was denoted as sample B. Finally, Ni-doped

6

$Ca(OH)_2$ (sample B) was calcined at 500 °C for 3 hours in the air, and assigned as sample C.

Characterization techniques

An X-ray diffractometer (Rigaku Miniflex-II, Japan) was used to characterize the phases of the product samples. It used a diffractometer with wavelength Cu K_α = 0.15406 nm, an angle range of 10-80°, and a step size of 0.02°. The FESEM (JEOL JSM-7610FPlus) with an EDX spectrometer connected was used for the microstructural analysis and elemental composition. The functional group information of all the dry samples was gathered with an FTIR spectrometer (KBr, Bruker Alpha, USA). The data were recorded over the 500–4000 cm^{-1} wavenumber. (UV-vis) absorbance spectra were obtained on a UV-Vis spectrometer (Shimadzu UV–NIR 2600, Japan) over the wavelength range of 190–800 nm. Using Tauc's Fig., the optical band gap values were computed.

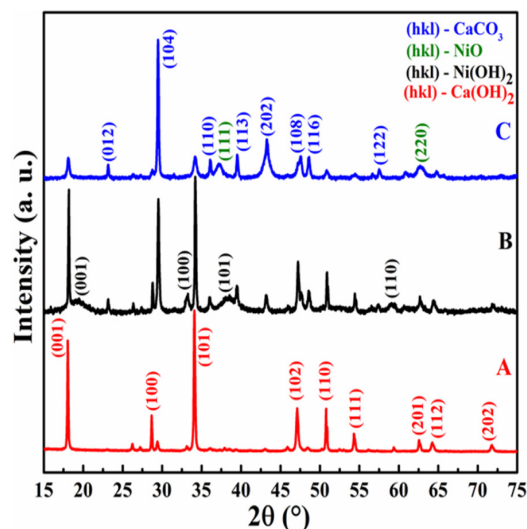## RESULTS AND DISCUSSION

Structural study

Fig. 1. X-ray diffraction pattern of samples A, B, and C.

The crystal structure of all prepared samples was studied by XRD analysis. In Fig. 1 (A-C), the XRD patterns of synthesized samples A, B, and C are shown. The $Ca(OH)_2$ phase seen in the XRD pattern shows typical diffraction peaks corresponding to (001), (100), (101), (102), (110), (111), (201), (112), and (202) appearing at 2θ values of, for instance, 18.04°, 28.67°, 34.09°, 47.12°, 50.80°, 54.35°, 62.60°, 64.26°, and 72.10° in turn. These data disclosed the hexagonal structure of calcium hydroxide nanoparticles with space group (P-3m1, No. 164) and had a good match with standard data, (PDF Card No. 00-004-0733) [19].
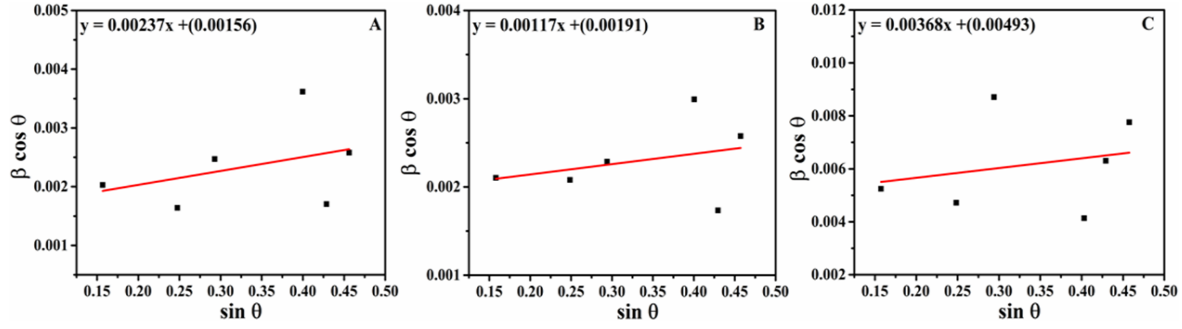
Fig. 2. Williamson–Hall plots of samples A, B, and C.

Furthermore, additional diffraction peaks corresponding to (001), (100), (101), and (110) on pattern B follow at the 2θ values of e.g., about 19.43°, 33.12°, 38.08°, and 59.13° in turn. It matches the published standard values with excellent precision (space group: P3m1, JCPDS card 742075) to the crystal phase of β-Ni(OH)$_2$ [20]. The XRD pattern shows the successful doping of the nickel atom into the CHNP structure. Numerous peaks conforming to the planes (012), (104), (110), (113), (202), (108), (116), and (122) appear respectively at 2θ values of, for instance, 23.11°, 29.44°, 36.12°, 39.54°, 43.30°, 47.50°, 48.61°, and 57.59° which are observed in the XRD pattern of sample C. The present pattern bouts with the standard rhombohedral calcite (CaCO$_3$) phase (space group No: 167, JCPDS card 00-005-0586) as the main phase and two minor peaks related to (111) and (220) at 2θ values of about 37.22° and 62.72°confirm the NiO phase [21, 22]. The calcite and NiO phases are induced due to the calcination process of nickel-doped calcium hydroxide nanoparticles. The result shows that the produced samples are polycrystalline in nature. Debye-Scherrer (D-S) formula is used to determine the average crystallite size using X-ray diffraction line broadening:

$$\delta = K\lambda / \beta \cos\theta \qquad (1)$$

where δ stands for the crystallite size; K is the Scherrer constant valued to be 0.9; λ is the X-ray wavelength (Cu K$_\alpha$, 1.54056 Å,); θ is the diffraction angle of the peak; and β is full-width at half-maxima (FWHM) (in radian) [23]. The crystallite size for samples A, B, and C is 62.32 nm, 56.75 nm, and 40.00 nm, respectively. The crystallite size as well as if the (D-S) methodology provides the correct trend of the nanocrystallite size data were confirmed using the Williamson-Hall method [24]. The equation below was used for the same:

$$\beta \cos\theta = \frac{k\lambda}{\delta_{W-H}} + 4\varepsilon\sin\theta \qquad (2)$$

where β is the FWHM. Moreover, k has a constant value of ~0.9 [19]. Here λ denotes the wavelength, which is 1.506 Å. For samples A, B, and C, the quantity (cos) as a function of (sin) was then linearly fitted. The sizes of the crystallites (W-H) were estimated for each sample using the intercepts on the Y-axes of the linear interpolations of the corresponding fitted lines. The proper W-H plots for samples A, B, and C are depicted in Figs. 2(a), (b), and (c), respectively. Using the equation below, the dislocation density (ρ$_d$) of the prepared samples was determined:

$$\rho_d = \frac{1}{\delta^2} \qquad (3)$$

According to calculations, CH sample A has a dislocation density of~ (2.5 ×10^{14} m^{-2}). Whereas, for the Ni-CHNPs sample B it increased to ~ (3.1 × 10^{14} m^{-2}), and for CaCO$_3$ sample C the value also increased to ~ (6.2 × 10^{14} m^{-2}). A smaller crystallite size suggests a greater surface-to-volume ratio. The dislocation network in the smaller crystallites is prevalent with a higher surface-to-volume ratio. So, more dislocations per unit area are raised in this case, accommodating the reduced crystallite size [25]. Table 1 summarizes the crystallite size with both δ$_{D-S}$; and δ$_{W-H}$ data with the dislocation density and band gap energy. The prepared samples A, B, and C have crystallite sizes in the following order: A > B > C, for both δ$_{D-S}$; and δ$_{W-H}$ values. The crystallite size is decreasing because the dopant ion will substitute itself into the structure of Ca(OH)$_2$ as the dopant's ionic radius is smaller than that of the host material; if the ionic radius is bigger, the ions will be embedded *via* an interstitial process. The interstitial process causes a disruption in the structure, resulting in a positive charge around the crystal or the formation of an oxygen vacancy [26]. Since the ionic radius of Ni^{2+} (83 pm) is smaller than that of Ca^{2+} (114 pm), the drop in crystallite size is most likely the result of the deformation process caused by Ni atom replacement into the CHNP structure. The main root cause of the decrease in crystallite size was the distortion of the host lattice of Ca(OH)$_2$ caused by the hosted ions Ni^{2+}, which decreased nucleation and slowed the growth of Ca(OH)$_2$ nanoparticles.

Table 1. Crystallite size, dislocation density, and bandgap of samples A, B, and C.

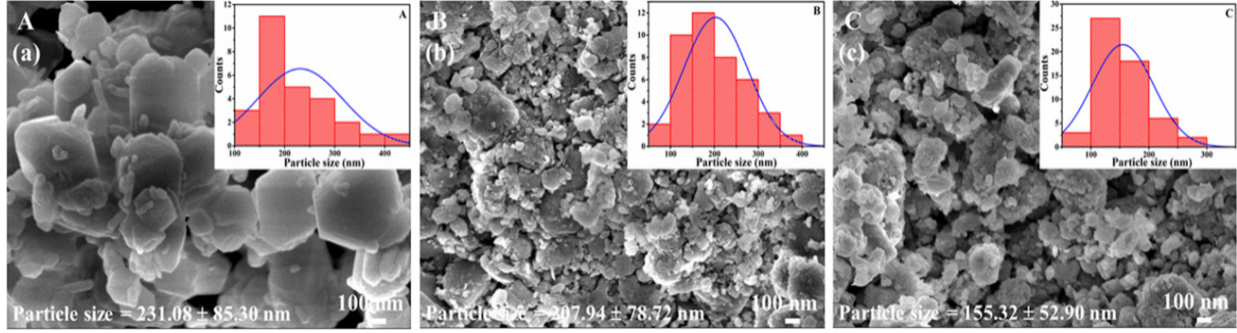| Sample	Crystallite size, δ_{D-S} (nm)	Crystallite size, δ_{W-H} (nm)	Dislocation density, ρ_d (m^{-2})	Bandgap (eV)
A	62.32	88.88	$2.5 * 10^{14}$	4.83
B	56.75	72.59	$3.1 * 10^{14}$	5.55
C	40.00	28.12	$6.2 * 10^{14}$	5.64

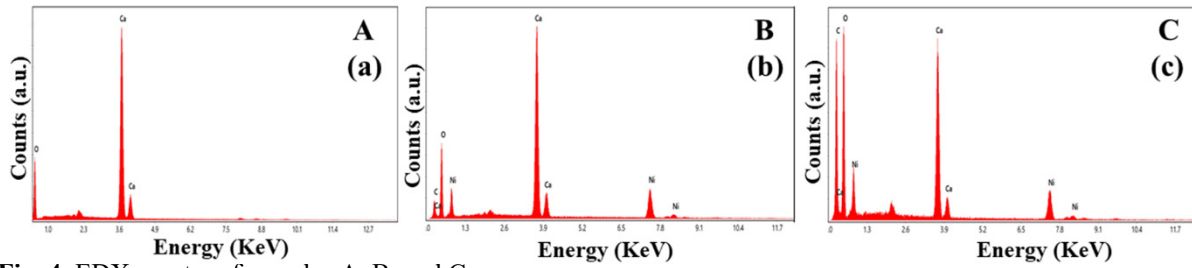**Fig. 3.** FESEM photomicrographs of samples A, B, and C.

Fig. 4. EDX spectra of samples A, B, and C.

After the calcination, particle size generally increases due to aggregation. But if the annealing temperature is improper (higher than the crystallization temperature or close to the melting point) then the material bonds will be disrupted, the order through the focused material will be increased and the crystallite size will consequently decrease.

FESEM study

The morphological study of the prepared samples A, B, and C was done by FESEM analysis. Fig. 3 shows the FESEM photomicrograph along with the corresponding EDX spectra of the prepared samples. From the study, the calcium hydroxide NPs (sample A) form nearly hexagonal-like structures (Fig. 3(a)) with a good contrast whereas the Ni-doped CHNPs and CaCO$_3$ have an irregular shape (Fig. 3(b), 3(c)) with more agglomerated particles. When related to calcium hydroxide sample A, the particles in both samples B and C have uneven size and shape.

The aggregation happens due to the highly active surface of the nanocrystallite. The average agglomerate size was 231.08 nm (Fig. *3*a*),* 207.94 nm (Fig. 3b), and 155.32 nm (Fig. 3c) for samples A, B, and C, respectively. The average agglomerate size was decreasing with the crystallite size. The insets of the corresponding FESEM pictures display the histograms for the distribution of agglomeration size. Fig. 4 displays the EDX spectra of all the generated samples. The EDX spectra of sample A approve the existence of Ca and O in CHNPs, which confirms the creation of calcium hydroxide as a main phase. Furthermore, the EDX spectrum of sample B is exposed in Fig. 4(b), confirming the considerable presence of Ni in addition to Ca and O. The presence of Ni validates the nickel doping in calcium hydroxide NPs, which matches XRD data well. Similar to this, in Fig. 4 (c), the EDX spectrum shows that sample C also contains a major amount of carbon in addition to Ca, O, and Ni. The occurrence of carbon in the EDX spectra supports the creation of the calcite phase. All the findings agree well with the XRD data.

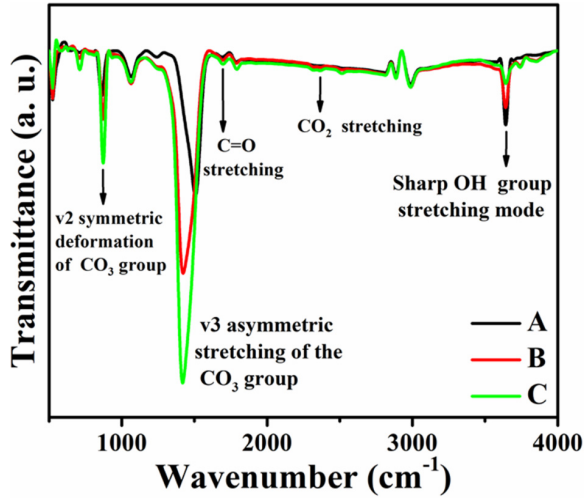The FTIR spectra of all prepared samples A, B, and C are presented in Fig. 5.

Fig. 5. FTIR spectra of samples A, B, and C.

The information was collected over a wavenumber range from 500 to 4000 cm⁻¹. The data has a good match with earlier published data [19, 21, 23]. FTIR shows an absorption band near ~ 3642 cm⁻¹, which is credited to the existence of the stretching mode of –OH groups in all samples. The absorption band of –OH groups is lowest in sample C, which can be due to the calcination of sample B at a high temperature. The large absorption band near ~1511 cm⁻¹ in sample A is attributed to the v_3 asymmetric stretching of CO_3 groups, which is shifted to the lower absorption band near ~1421 cm⁻¹ in sample B. This change can be due to the nickel doping in CHNPs. Furthermore, a broad and intense peak at ~1421 cm⁻¹ indicated the calcite phase in sample C. The C=O stretching mode was also thought to be responsible for the modest absorption bands that were found at around 2400 cm⁻¹ in the ranges of every sample. All prepared samples exhibit the v_2 symmetric distortion of the CO_3 group peak at the wave number of 860 cm⁻¹. The change in v_2 symmetric distortion of the CO_3 group peak can also

be seen in both samples B and C. As a result, these data also support the findings of the XRD studies.

UV-Vis spectroscopic analysis

The UV-Vis absorbance spectra were used to examine the optical characteristics of the prepared samples. The UV-Vis spectrum is presented in Fig. 6 as a function of wavelength.
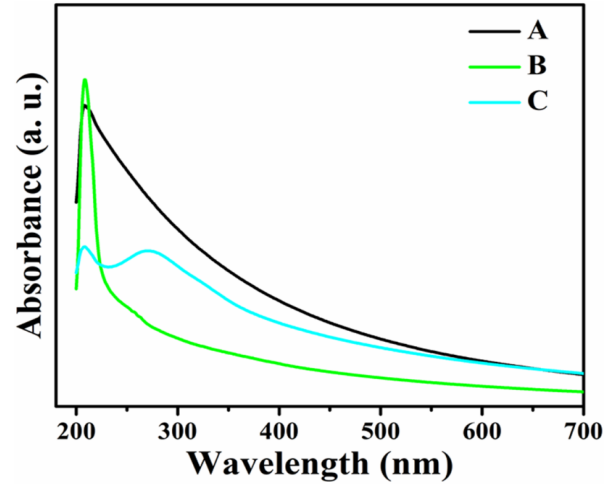

Fig. 6. Absorbance spectra of samples A, B, and C.

The sample absorbance can be affected by the band gap, surface roughness, impurity centers, and the quantum confinement effect [27, 28]. For CHNPs, Ni-CHNPs, and $CaCO_3$ NPs, the absorbance peaks originate at 256 nm, 223, and 219 nm, revealing a blue shift in absorbance. The band gap energy of the prepared samples was estimated by Tauc's plot as given below [29].

$$\alpha h\upsilon = A(h\upsilon - Eg)^{\frac{1}{2}} \qquad (4)$$

where n (=1/2 for a direct band gap) is a constant, α is the optical absorption coefficient. The straight portion of the curve between "$h\upsilon$" and $(\alpha h\upsilon)^2$ was extrapolated to determine band gap energy. Samples A, B, and C have band gap values of 4.83, 5.55, and 5.64 eV in order. Tauc's plot for the energy band gap is shown in Fig. 7. Hence, the optical band gap generally increases with the decrease in nanocrystallite size (Fig. 8), as expected.
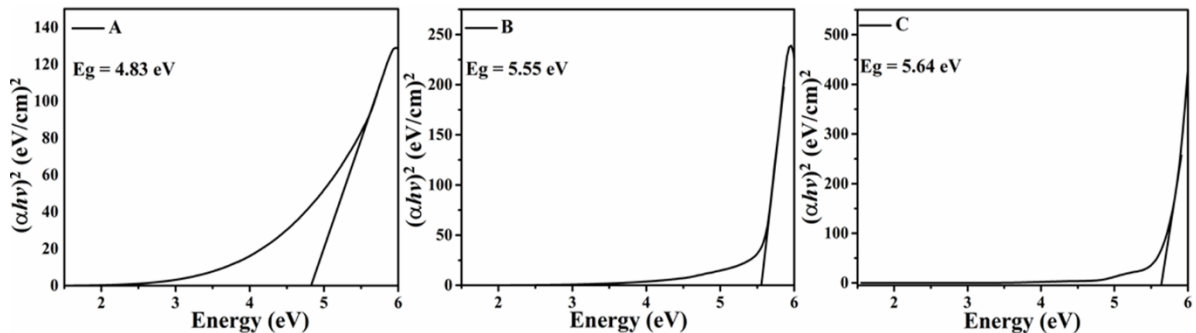

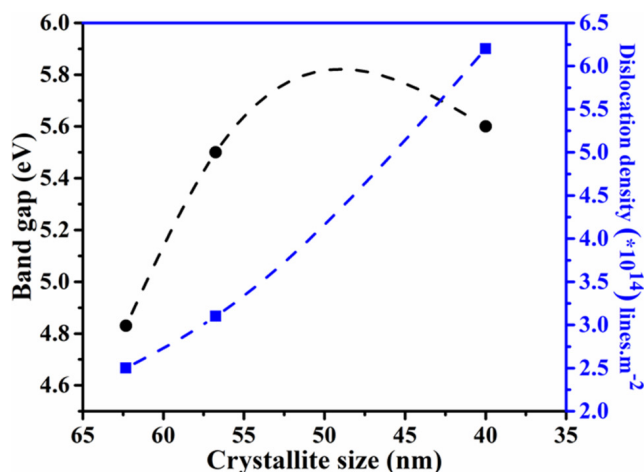**Fig. 7.** Tauc's plots of samples A, B, and C.

9

Fig. 8. Alteration in band gap and dislocation density with respect to crystallite sizes.

In general, the band gap energies could differ depending on the size of the nanoparticles. Since the ionic radius of Ni^{2+} (83 pm) is smaller than that of Ca^{2+} (114 pm), it was feasible for doping transition ions to occur, which resulted in a decreased lattice size in the samples. These findings indicate that Ni^{2+} transition metal ions have been successfully integrated into $Ca(OH)_2$ nanoparticles by replacing Ca^{2+} sites in the lattice. Additionally, when the average crystallite size decreased, the nanoparticles in use had higher band gap energies. The samples' smaller particle sizes caused the restricted dimension to shrink.

Further, the Fermi level in nominally doped semiconductors is situated between the conduction band and valence band. For the degenerate doping in semiconductors, the Burstein-Moss shift occurs because the conduction band edge density of states is exceeded by the electron carrier concentration. As the doping level is increased in n-type semiconductors, conduction band states are populated by electrons, increasing the energy of the Fermi level. The Fermi level of a degenerate level of doping is located inside the conduction band. Transmission/reflection spectroscopy is a tool that can be used to measure the actual band gap of a semiconductor. In a degenerate semiconductor, all the states below the Fermi level are occupied states, hence an electron from the top of the valence band can only be excited into the conduction band above the Fermi level (which is currently in the conduction band). In these occupied states, excitation is prohibited by Pauli's exclusion principle. Hence, we see a wider apparent bandgap [30].

CONCLUSION

In summary, calcium hydroxide and Ni-doped calcium hydroxide NPs were successfully produced through a precipitation process. The Ni-doped calcium hydroxide NPs were then calcined at 500°C temperature for three hours. The XRD data proved the phase formation of $Ca(OH)_2$, Ni-$Ca(OH)_2$, and that heating caused the calcite phase to develop. The nanocrystallite sizes of $Ca(OH)_2$, Ni-$Ca(OH)_2$, and $CaCO_3$ NPs were 62.32 nm, 56.75 nm, and 40.00 nm, in turn. The EDX data reinforced the existence of Ca, Ni, and C in the prepared NPs samples. The UV-Vis spectroscopy showed the energy band gap to be 4.83 eV, 5.55 eV, and 5.64 eV. The enhancement in the band gap may be attributed to the decrease in crystallite size.

REFERENCES

1. A. Samanta, D. K. Chanda, P. S. Das, J. Ghosh, A. K. Mukhopadhyay, A. Dey, *J. Am. Ceram. Soc.,* **99** (3), 787 (2016).
2. H. G. Lee, C. H. Cho, H. Kim, S. R. Yoo, *Food Packag. Shelf Life*, **26,** 100558 (2020).
3. Harish, Pushpendra Kumar, A. G. Chakinala, R. Singhal, R. P. Joshi, A. K. Mukhopadhyay*, Chem. Select*, **7**, e202200393 (2022).
4. P. A. Basto, V. E. de Lima, A. A. de Melo Neto, *Constr. Build Mater.,* **325**, 126767 (2022)
5. A. Zamanian, M. Yasaei, M. Ghaffari, M. Mozafari, *Ceram. Int.,* **39**, 9525 (2013).
6. C. Huang, M. Xu, X. Huai, *Chem. Eng. Sci.,* **206,** 518 (2019).
7. V. E. García-Vera, A. J. Tenza-Abril, A. M. Solakb, M. Lanzón, *Appl. Surf. Sci.,* **504,** 144195 (2020).

8. Harish, P. Kumar, S. Kumari, M. Debnath, A. Salim, R. Singhal, R. P. Joshi, A. K. Mukhopadhyay, *J. Mater. Sci.*, **57**, 8241(2022).

9. S. Pai, M. S. Kini, G. Rangasamy, R. Selvaraj, *Chemosphere,* **313**, 137476 (2023).

10. M. Kumar, S. K. Singh, N. P. Singh, *Thermochim. Acta*, **548**, 27 (2012).

11. G. Jayanthi, P. Kayalvizhi, *IJARIIT*, **7**(5), V7I5-1187 (2021).

12. E. I. Naik, H.S. B. Naik, M.S.Sarvajith, E. Pradeepa, *Inorg. Chem. Commun.* **130**, 108678 (2021).

13. M. M. Obeid, S. J. Edrees, M. M. Shukur, *Superlattices Microstruct.* (2018), doi: 10.1016/j.spmi.2018.08.015

14. S. H.Basri, M. A. M.Sarjidan, W. H. Abd Majid, *Adv. Mat. Res.,* **895**, 250 (2014).

15. M. M. Obeid, S. J. Edrees, M. M. Shukur, *Superlattices Microstruct.* (2018). doi: 10.1016/j.spmi.2018.08.015.

16. J. Chauhan, N. Shrivastav, A. Dugaya, D. Pandey, *J. Nanomed. Nanotechnol.,* **8**, 429 (2017).

17. K. Raja, P.S. Ramesh, D. Geetha, *Spectrochim. Acta,* **120**, 19 (2014).

18. N. Goswami, A. Sahai. *Mater. Res. Bull.,***48**, 346 (2013).

19. Akash, Harish, V. Kumar, R. K. Mishra, J. S. Gwag, R. Singhal, A. K. Mukhopadhyay, P. Kumar, *Luminescence*, **38**, 1297 (2023).

20. B. Shruthi, V. B. Raju, B. J. Madhu, *Spectrochim. Acta A Mol. Biomol.* Spectrosc., **135**, 683 (2015).

21. J. Kumari, Harish, Akash, A. Pandey, P. Kumar, M. K. Singh, A. Singh, M. S. Shishodia, R. P. Joshi, A. K. Mukhopadhyay, *Chemistry Select*, **7**(24), e202200416, (2022).

22. Z. Wei, H. Qiaoc, H. Yanga, C. Zhanga, X. Yan, *J. Alloys Compd.,* **479,** 855 (2009).

23. Akash, Harish, J. Kumari, A. K. Mukhopadhyay, P. Kumar, *Chem. Select*, **7**, e202200417 (2022).

24. Harish, P. Kumar, Akash, J. Kumari, L. Kumar, A. Salim, R. Singhal, A. K. Mukhopadhyay, R. P. Joshi, *Mater. Today Proc.,* **60**(1), 153 (2022).

25. A. Muiruri, M. Maringa, W. du Preez, *Mater.*, **13**(23), 5355 (2020).

26. D. Cahyaningsih, A. Taufik, R. Saleh, *J. Phys. Conf. Ser.,***1442,** 012017 (2020).

27. Harish, P. Kumar, V. Kumar, R. K. Mishra, J. S. Gwag, M. K. Singh, R. Singhal, and A. K. Mukhopadhyay, *Ceramic Int.*, **48**, 35771 (2022).

28. P. Kumar, P. Lemmens, *RSC Advance,* **5**, 91134 (2015).

29. Akash, Harish, V. S. Chouhan, R. Singhal, A. K. Mukhopadhyay, P. Kumar, *NanoWorld J.*, **8**(S1), S69 (2022).

30. C. Karthikeyan, L. Arun, A. S. Haja Hameed, K. Gopinath, L. Umaralikahan, G. Vijayaprasath, P. Malathi, *J. Mater. Sci. Mater. Electron,* **30**, 8097 (2019).

Spectroscopic studies on the interaction of BSA and anisaldehyde

A. Singh[1,2*], D. K. Sinha[3], K. K. Thakur[2]

[1]*M. J. P. Rohilkhand University, Bareilly, UP, India*
[2]*Chandigarh University, Gharuan Punjab, 140301, India*
[3] *K G K College, Moradabad, UP, India*

The flavouring molecule anisaldehyde (AA) is present in anise and is regarded as one of the most important flavouring chemicals in the world. Numerous yeast and mould strains have been found to be resistant to p-anisaldehyde. In this research paper, we investigated the bovine serum albumin (BSA) binding profile using both experimental and computational techniques, because the interaction with serum albumins may be essential in determining their pharmacological characteristics. The structural alteration of the BSA upon the addition of AA was investigated, as well as the binding parameters and method of binding. Results from UV-vis spectroscopy and fluorescence quenching studies suggested that AA and BSA can form a ground state complex. Meanwhile, thermodynamic characteristics (negative ΔH^0 and ΔS^0 values) showed that the formation of the AA-BSA complex is primarily influenced by hydrophobic interactions and hydrogen bond forces. AA appreciably alters the 2° structure of BSA, according to circular dichroism synchronised fluorescence spectra.

Keywords: Anisaldehyde, BSA, Interaction, Fluorescence, UV

INTRODUCTION

Due to the wide range of medicinal applications and absence of undesirable side effects, natural chemicals and their derivatives are the potential molecules for drug discovery. These natural compounds offer a wide range of therapeutic benefits because of their distinct chemical and structural composition [1, 2]. Many organic compounds have antioxidant and anti-cancer properties and are exploited in the creation of novel medications [3, 4]. Polyphenols, which are present in many different foods and beverages, including tea, coffee, nuts, vegetables, and fruits, are substances that occur naturally and are primarily being studied [5-7].

Anisaldehyde (AA), is a naturally occurring phenolic compound and one of the most common flavouring substances in the world [8]. It is a perennial herb with a long history of cultivation in South Asia, particularly India, and the Mediterranean region. The compound is present in several plant species like anise, cumin, fennel and garlic. Anisaldehyde, also known as anisic aldehyde, is an organic molecule composed of a benzene ring that has a methoxy and aldehyde group substituted on it. According to earlier research, p-anisaldehyde has antifungal properties that make it effective against a variety of yeast and mould strains in lab media, fruit purees, and fruit juices [9, 10]. Additionally, it has been claimed that anise fruit extracts provide therapeutic benefits for a number of ailments, including gynaecological and neurological diseases. Especially in paediatrics, the oil is used as a carminative and expectorant, in syrups, flavouring and spice. It is also used as a raw material for the synthesis of drugs such as amoxicillin.

The bio-distribution of endogenous and exogenous substances is predominantly carried out by serum albumins, which are the utmost prevalent proteins in blood plasma [11]. Drug-protein binding studies are important for figuring out a drug's biological effects because they can offer important details about a drug's pharmacological and pharmacodynamic therapeutic effects. Knowing the precise position of the drug binding site on a protein can help us better recognize how a drug is distributed throughout the body and how it interacts with other medications [12]. Bovine serum albumin (BSA), is a well-known protein with 76% similarity to human serum albumin (HSA). The binding capability of anisaldehyde with skin proteins is therefore investigated using BSA as a model protein. Two drug-binding sites, subdomain IIA (Sudlow I) and subdomain IIIA, are found in hydrophobic pockets in the BSA's single-chain globular protein structure, which comprises 583 amino acids (Sudlow II). There are two tryptophan residues nearby subdomains IA and IIA, Trp 134 in and Trp212. Utilizing multiple spectroscopic methods including UV-Vis absorption, steady-state fluorescence, synchronous

---

fluorescence, FTIR, and circular dichroism (CD), the current research examines the structural and thermodynamic characteristics of anisaldehyde binding to BSA. Through the use of molecular docking, the binding interactions within the binding pockets were demonstrated.

EXPERIMENTAL

Starting materials

Bovine serum albumin (BSA) devoid of essential fatty acids was purchased from Sigma-Aldrich Bangalore, India. Anisic aldehyde was received as a gift by Nishant Aromas, Mumbai (Maharashtra). We bought warfarin and ibuprofen from Tokyo Chemical Industry (TCI) Co., Ltd. The other reagents and chemicals utilized in the study were of analytical grade and didn't need any extra purification. Doubly distilled water was utilised during the studies.

Spectrophotometric titration

On a UV-1900iUV spectrophotometer (Shimadzu, Japan) with an 1-cm quartz cell, absorption spectra of AA binding to BSA were captured while scanning from 200 to 800 nm. UV-Vis titrations were conducted by gradually adding anisaldehyde (0-32 μM) to BSA (10 μM) in a phosphate buffer solution of pH 7.4. The solvent absorption was deducted from the spectra of BSA and BSA-AA complex absorptions in order to remove interference.

Measurements of fluorescence quenching by titration

Fluorescence spectra were captured using an RF-6000 spectrofluorometer, Shimadzu Scientific Instruments, Japan at excitation wavelength of 295 nm and an emission wavelength of 300–450 nm @ 240 nm/min, while keeping the excitation and emission slit width at 5.0 nm. In titration studies, AA concentrations ranged from 0.25 μM to 4.5 μM at three distinct temperatures of 303 K, 308 K, and 313 K that were regulated *via* a water bath. For the site marker assays, the AA and BSA interaction was conducted with equimolar concentrations of the site markers.

Measurements based on circular dichroism

In order to validate the outcomes of spectra, CD was applied. The BSA and anisaldehyde were mixed in molar ratios of 1:0, 1:1, and 1:5. After every addition, the solution was thoroughly shaken, and incubated for 2.0 min at ambient temperature, and its CD was detected in the 200–300 nm range at 1.0 nm band width. A minimum of three scans @ 50.0 nm/min were used to average the spectra. Baseline corrections were made to all CD spectra using blank solutions.

Docking of molecules

The Lamarckian genetic algorithm was considered to execute the molecular docking using Autodock 4.2 [16–18]. From the Brookhaven Protein Data Bank and PubChem, respectively, we were able to retrieve the structures of BSA and AA. The complete protein was chosen for docking with all polar hydrogen atoms. BSA was given responsibility for the Kollman allegations in part. The protein was configured to be stiff, and docking does not take solvent molecules into account. The minimal binding free energy conformation of the MC-AA complex was displayed using molecular graphics, as well as analyses performed with UCSF Chimera and Ligplot+ v2.2.

RESULTS AND DISCUSSION

Absorption measurements by UV-vis spectrometry

It is an effective method to explore the development of protein-drug complexes [13, 14]. The microenvironment around the chromophores has an impact on the protein spectrum [15]. Figures depict how AA has an impact on the spectra of BSA. A discernible strong absorption peak can be seen at 277 nm, as revealed in Fig.1(a). The figure displays that peak intensity increases with slight red shifting as AA concentrations rise, supporting the interaction between AA and BSA.

Fluorescence quenching of BSA induced by anisaldyde

The fluorescence quenching approach has been extensively used to explore the binding constant, the number of binding sites, and thermodynamic factors [16, 17]. In essence, variations in the intensity of protein fluorescence are picked up at the wavelength of maximal emission. TheAA-BSA complex, as depicted in Fig.1(b), is created when AA is added to the BSA solution. With rising AA concentrations, BSA fluorescence emission is quenched. Figure 1 demonstrates that the Trp residue [18] is primarily responsible for the fluorescence peak in BSA at about 335.0 nm. Regular quenching of BSA fluorescence was seen with the addition of anisaldehyde on a continuous basis. On additions of anisaldehyde (0.0625×10^{-3} M) to BSA (10×10^{-6} M) quenched the fluorescence at 335 nm by 70% at a molar ratio of 0.45 ([anisaldehyde]/[BSA]). The red shift of the fluorescence maxima from 335 nm to 340 nm was related to the quenching of BSA's fluorescence. These results showed that BSA and AA clearly interacted.
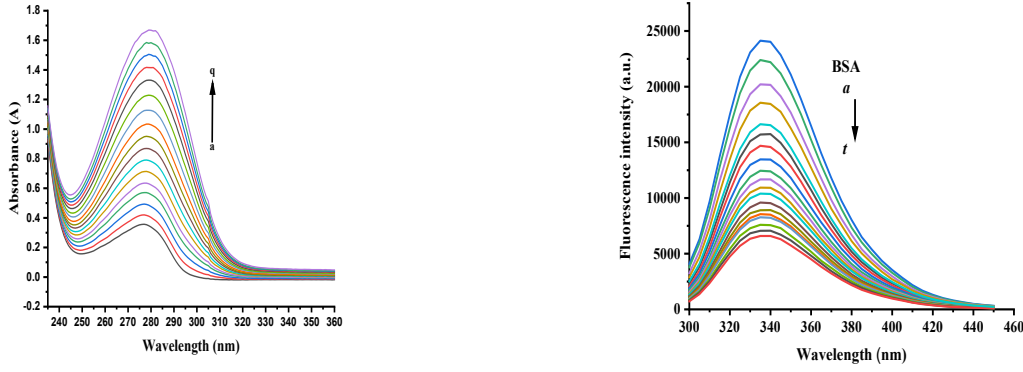
Figure 1. (a) UV-visible spectra at 298 K and pH 7.4 of BSA (C_{BSA} = 10μM)) and AA (C_{AA} = (0-32 μM); (b) Fluorescence quenching of BSA
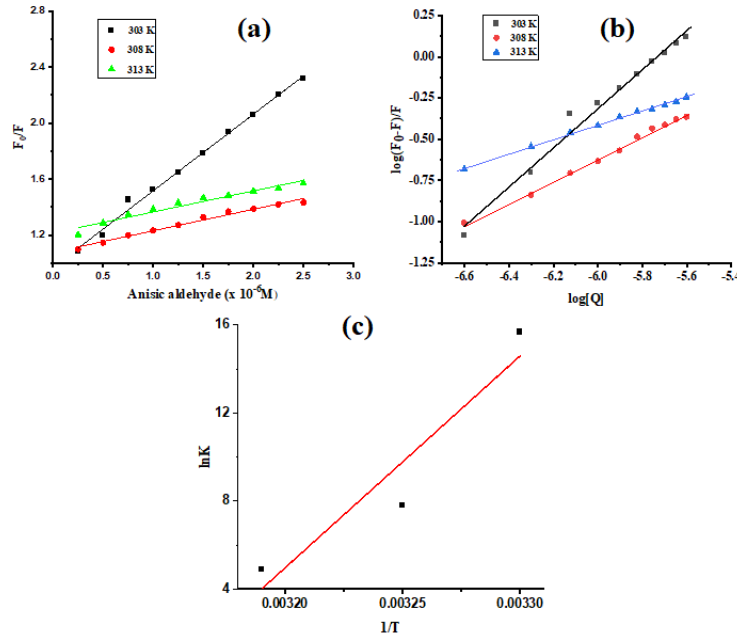

Figure 2. (a) Stern-Volmer graphs for the BSA-AA system at several temperatures; (b) Graph of log (Fo-F)/F *vs* log[Q] at three different temperatures; (c) Plot for Van't Hoff equation

The Stern-Volmer equation might be used to define the concentration-dependent Fl quenching under these circumstances [16, 19, 20]. The binding properties at numerous temperatures were investigated according to the following relation:

$$\frac{F_0}{F} = 1 + K_{sv}[Q] \quad (1)$$

Fluorescence levels of BSA before and after bonding with AA expressed as F_o and F respectively. [Q] is the concentration of the quencher, and K_{SV} is the Stern-Volmer constant. The K_{SV} was determined using the figure shown in Fig.2(a) of Eq. (1). One of three processes, including dynamic, static, or a mix of the two, can be used to control fluorescence quenching, but because each procedure is temperature-dependent, its underlying principles differ. It is projected that when temperatures rise, the

quenching constants in the dynamic quenching process will also rise, leading to high diffusion coefficients. The quenching constant value for static quenching might, however, drop as a result of a loss in complex stability brought on by increasing temperatures. The quenching rate constant (kq) values demonstrate complex development was calculated according to the following equation:

$$k_q = \frac{K_{sv}}{\tau_0} \quad (2)$$

Thus, for a biomacromolecule, 10^{-8} s is the average lifetime of the fluorophore in the excited state, and kq is the bimolecular quenching rate constant [21, 22]. Stern-Volmer graphs for AA quenching of BSA fluorescence are revealed in Figure 4 at various temperature settings, while the K_{SV} and kq values are listed in Table 1.

Table 1. AA-BSA interaction characteristics at various temperatures

T(K)	Ksv (Lmol^{-1})	Kq (Lmol^{-1})	Kb (Lmol^{-1})	n	ΔH^0 (kJ/mol^{-1})	ΔG^0 (kJ/mol^{-1})	ΔS^0 (kJ/mol^{-1})
303	5.47×10^5	5.47×10^{13}	6.4×10^6	1.18	-800.50	-1564.06	-2.52
308	1.53×10^5	1.53×10^{13}	2.54×10^4	0.67		-1576.16	
313	1.50×10^5	1.50×10^{13}	1.43×10^3	0.42		-1589.26	

According to this study, the quenching rate constant kq has a magnitude of 10^{13}. Moreover, the bimolecular quenching rate constant's value was revealed to be greater than 2×10^{10} L mol^{-1} s^{-1}, indicating a static quenching of the interaction between AA and BSA [22–24].

Binding sites and binding constant estimation

Both were calculated by applying what is known as the Modified Stern-Volmer equation:

$$\log \frac{F_0 - F}{F} = \log K_b + n \log[Q] \tag{3}$$

where K_b and n are the binding constant and number of binding sites, respectively [25, 26]. The intercept and slope of Fig. 2(b) correspondingly give the log K_b and n values. Table 1 displays the outcomes acquired under various temperature conditions. It was discovered that BSA and AA bind almost 1:1, and that the binding constant drops as temperature rises.

Calculation of the thermodynamic variables.

Hydrophobic, electrostatic, and van der Waals forces are the three primary forces involved in binding drugs and proteins. Enthalpy change (ΔH^0) and entropy change (ΔS^0), two thermodynamic quantities, define the forces that hold the process together. Subramanian and Ross looked at the connection between changes in binding forces and thermodynamic parameter values [27]. Hydrophobic forces predominate when $\Delta H^0 > 0$ and $\Delta S^0 > 0$, whereas van der Waals forces and hydrogen bonding predominate when $\Delta H^0 < 0$ and $\Delta S^0 < 0$. When $\Delta H^0 < 0$ and $\Delta S^0 > 0$, electrostatic forces are regarded as the dominant forces. Van't Hoff equation can be utilised to calculate ΔH^0 and ΔS^0 at the occurrence of small temperature differences [27, 28].

$$\ln K = -\frac{\Delta H^0}{RT} + \frac{\Delta S^0}{R} \tag{4}$$

where K_b is the binding constant at temperature T and R is the gas constant.

Plotting ln K against 1/T results in a straight line. The resulting slope denotes the change in enthalpy (ΔH^0), whereas the intercept denotes the change in entropy (ΔS^0) (Fig. 2(c)). The free energy change (ΔG^0) can be calculated using the equation below:

$$\Delta G^0 = \Delta H^0 - T\Delta S^0 \tag{5}$$

Table 1 shows that the negative entropy change (ΔS^0) and the negative free energy change (ΔG^0) indicate that the AA-BSA complex spontaneously bound. The van der Waals forces and hydrogen bonding are the key driving force behind this process. The negative enthalpy change (ΔH^0) values indicates that the reaction is exothermic.
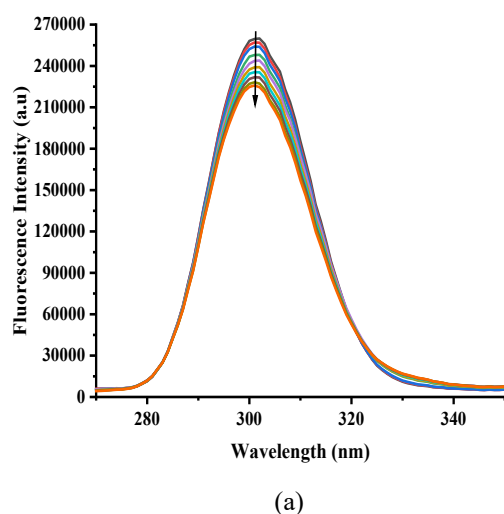
Synchronous fluorescence spectra of BSA

The benefits of the synchronous spectrofluorimetric technique are numerous and include spectral simplicity, sensitivity, spectral bandwidth, as well as restraining and avoiding different disturbing effects [29]. To explore the protein's microenvironment, it is extremely helpful to achieve the emission wavelength shift. By using synchronous fluorescence spectra at wavelength intervals ($\Delta\lambda$) of 60 nm and 15 nm, respectively, it is possible to identify the Trp and Tyr residues in BSA. It is also revealed in the synchronous BSA fluorescence spectra at $\Delta\lambda=15$nm and $\Delta\lambda= 60$ nm in Fig.3(a) and (b), respectively. In Fig. 3(b), at $\Delta\lambda=60$ nm, it was observed that the emission range maxima persisted unchanged, whereas at $\Delta\lambda= 15$ nm, a slight blue shift was seen as demonstrated in Fig. 3(a). Tyrosine residues were seen to have their surrounding polarity attenuated, indicating that this process took place in a hydrophobic environment. The observed spectrum change therefore suggests that BSA's conformation after interaction with AA [30].
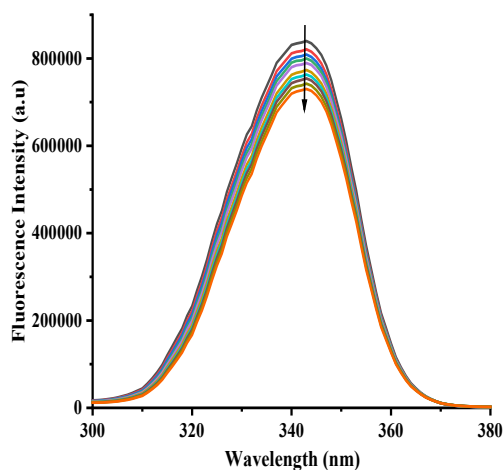
Analysis of the displacement of the site marker

BSA is made up of three domains: I, II, and III, each of which is further broken down into two subdomains, A and B. The AA binding site in BSA was identified by a review of site marker measurements. Warfarin, Ibuprofen and haemin were chosen as competitive probes for sites I, II, and III, respectively [29–31]. The Stern-Volmer equation was used to calculate the binding parameters as a result of the three site markers' effects on the AA-BSA interaction (Fig. 4). The

binding of anisaldehyde and BSA was altered by the three competing reagents to varying degrees, as evidenced by the data in Table 2. It demonstrates that adding ibuprofen, warfarin and haemin significantly reduced the binding constant values of AA with BSA, indicating that these drugs may be able to displace the AA. In conclusion, these findings showed that AA binds to BSA at all three sites I, II and III. As seen from the table the better binding would be at the site I, as the binding constant was reduced to a greater extent, which is in good agreement with the findings of the molecular docking approach.
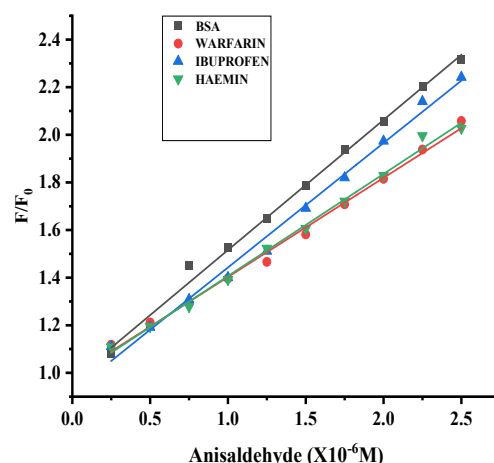

Figure 4. Pre- and post-marker addition Stern-Volmer plots for BSA quenching by AA.

Table 2. Stern-Volmer quenching constants for the AA-BSA interaction in the presence of site markers.

Site Marker	Ksv (Lmol^{-1})	R^2	Standard Error
BSA+AA	5.47×10^5	0.99726	0.01434
BSA+AA+ WAR	4.17×10^5	0.99728	0.01089
BSA+AA+ IBU	5.23×10^5	0.99577	0.01707
BSA+AA+ HAEM	4.29×10^5	0.99738	0.01101

Circular dichroism studies

When globular proteins bind tiny ligands, circular dichroism is the preferred method for observing conformational changes and modifications in secondary structures. Using CD, the changes in BSA's confirmation after binding to anisaldehyde will be assessed in this section.The intermolecular forces necessary to maintain the secondary and tertiary structures are impacted by the binding of ligands to globular proteins; if these forces are harmed, the proteins' conformational states are altered. When a ligand binds to a protein, it alters the protein's structural conformation, and these changes in CD spectra are indicative of these structural changes [34]. The far UV CD spectra of free BSA and BSA-AA are displayed in Fig. 5. The image makes it clear that the CD spectra are just slightly changing. Natural BSA exhibits peaks at 209 nm and 220 nm, demonstrating that it is a protein with a high content of α-helices. In the presence of AA, there was a decrease in the secondary structure of BSA as evident from the decrease in two minima at 209 and 220 nm that are characteristic of α -helix.
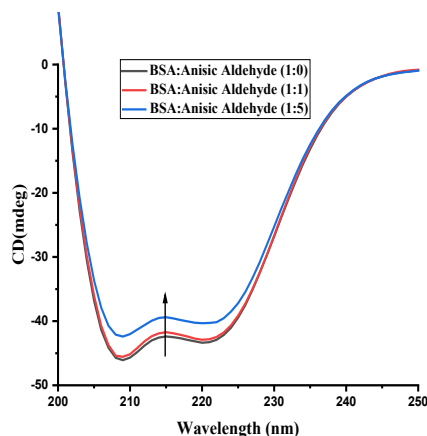

(a)

(b)

Figure 3. Synchronous fluorescence spectra of BSA (10 μM) at (a)Δλ 15 nm; (b) Δλ60 nm

Figure 5. CD Spectra of BSA-AA

Molecular docking

Molecular docking is a practical simulation procedure for assessing the nature of drug-protein binding. It served as a means of validating the information discovered during the experimental study regarding the interactions and binding affinities of AA at its binding site in BSA. Findings from this method confirm earlier investigations of the site marker displacement, i.e., the binding of AA with BSA at site I of subdomain IIA (Fig.6 (a) and (b)). After binding with BSA, the configuration of AA was observed, giving a binding energy of -5.2kcal mol^{-1}. This AAligandis found in the active site residues Arg 256, Arg 217, Ile289, Ser 286 and Ala 290 (Fig. 6(c)). Also, the results of molecular docking suggested that hydrogen bonding and hydrophobic forces dominated the contact, which was in line with our thermodynamic analysis.
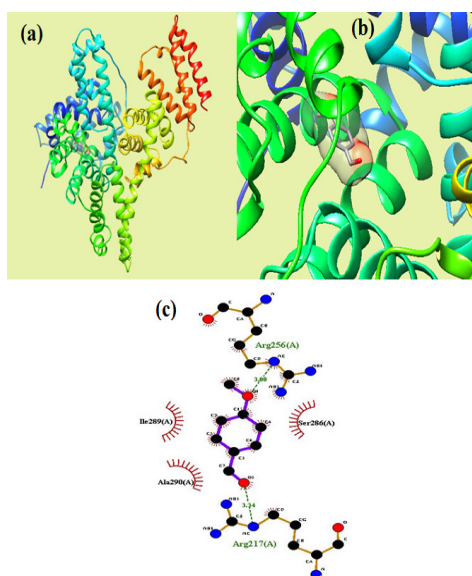

Figure 6 (a) AA docked in BSA; b) BSA and AA active site residues. The ribbon structure is used to illustrate the BSA. c) Hydrogen bonding and hydrophobic interactions in the AA interaction model at site I of BSA

CONCLUSION

With the aid of multi-spectroscopic and molecular docking techniques, the suggested work establishes the calculation of the AA-BSA binding under physiological circumstances. A variety of strategies have been used to perform extensive research. The binding of AA-BSA was discovered to be static quenching. Fluorescence spectroscopy data analysis was used to identify several binding factors. From the calculated n values it was depicted that AA and BSA bind in 1:1 ratio. The calculated thermodynamic parameter values for ΔH^0, ΔS^0 and ΔG^0 revealed that hydrophobic interactions and hydrogen bonding dominated other intermolecular forces in the interaction between AA and BSA.AA-BSA binding takes place at site I in subdomain IIA in accordance with the site marker technique that was confirmed by molecular docking experiments also. This study offers helpful information for a better comprehension of the pharmacokinetic behaviour of AA. The information in this study may contribute to a better understanding of the molecular processes underlying the negative side effects of AA, enhancing both its pharmacological and therapeutic efficacy. The findings supported the strong connection between AA and BSA as well as the simplicity of conveyance and removal, offering suggestions for additional research and study.

REFERENCES

1. P. Khan, S. Rahman, A. Queen, S. Manzoor, F. Naz, G. M. Hasan, S. Luqman, J. Kim, A. Islam, F. Ahmad, M. I. Hassan, *Sci Rep.,***7**, (2017).
2. G. I. Hernández-Bolio, J. A. Ruiz-Vargas, L. M. Peña-Rodríguez, *J. Nat. Prod.* (2019).
3. A. R. Guerra, M. F. Duarte, I. F. Duarte, *J. Agric. Food Chem.,* **66**, 10663 (2018).
4. H. N. Lv, S. Wang, K. W. Zeng, J. Li, X. Y. Guo, D. Ferreira, J. K. Zjawiony, P. F. Tu, Y. Jiang, *J. Nat. Prod*., **78**, 279 (2015).
5. G. R. Beecher*, Occurrence and Intake,* 1 (2003).
6. A. R. Guerra, M. F. Duarte, F. Duarte, *J. Agric . Food Chem*., **66**, 10663 (2018).
7. S. Zhao, C. H. Park, X. Li, Y. B. Kim, J. Yang, G. B. Sung, N. il Park, S. Kim, S. U. Park, *J. Agric. Food Chem.,* **63**, 8622 (2015).
8. S. Alban, G. Franz, R. Hänsel, W. Schier, O. Sticher, E. Spieß, E. Steinegger, *Pharmakognosie – Phytopharmazie,* Springer Berlin Heidelberg, 2013.
9. L. Yu, N. Guo, Y. Yang, X. Wu, R. Meng, J. Fan, F. Ge, X. Wang, J. Liu, X. Deng, *J. Ind. Microbiol. Biotechnol.*, **37**, 313 (2010).
10. S. Shreaz, R. Bhatia, N. Khan, S. Imran Ahmad, S. Muralidhar, S. F. Basir, N. Manzoor, L. A. Khan, *Microb. Pathog*., **51**, 277 (2011).
11. S. Khatun, Riyazuddeen, F. A. Qais, *J. Mol. Liq*., **299**, (2020).

12. Z. D. Zhivkova, V. N. Russeva, Analgesics · antiphlogistics antirheumatic drugs thermodynamic characterization of the binding process of sulindac to human serum albumin (2003).
13. N. Aggarwal, S Mehtab**,** S Maji, *Asian J. Chem.,* 29 (9), 2069 (2017).
14. S. M. S. Abdullah, S. Fatma, G. Rabbani, J. M. Ashraf, *J. Mol. Struct*.**, 1127**, 283 (2017).
15. J. A. Molina-Bolívar, F. Galisteo-González, C. Carnero Ruiz, M. Medina-Ó Donnell, A. Parra, *J. Lumin.,***156**, 141 (2014).
16. J. R. Lakowicz, Principles of Fluorescence Spectroscopy, 1 (2006).
17. G. Mocz, J. A. Ross, *Methods Mol. Biol.,***1008**, 169 (2013).
18. V. D. Suryawanshi, L. S. Walekar, A. H. Gore, P. V. Anbhule, G. B. Kolekar, *J. Pharm. Anal*.,**6**, 56 (2016).
19. B. L. Wang, D. Q. Pan, K. L. Zhou, Y. Y. Lou, J. H. Shi, *Spectrochim. Acta A Mol. Biomol Spectrosc*., **212**, 15 (2019).
20. S. Mehtab, H. Parmar, T.I. Siddiqi, A.S. Roy, Asian J. Res. Chem. **8** (2), 99 (2015).
21. Y. J. Hu, Y. Ou-Yang, C. M. Dai, Y. Liu, X. H. Xiao, *Mol. Biol. Rep.,* **37**, 3827 (2010).
22. E. Cobbina**,** S. Mehtab, I. Correia, G. Gonçalves, I. Tomaz, I. Cavaco, *J. Mexi. Chem. Soc.*, **57** (3), 180 (2013).
23. Y. J. Hu, Y. Liu, R. M. Zhao, J. X. Dong, S. S. Qu, *J. Photochem. Photobiol. A Chem.,***179**, 324 (2006).
24. F. Macii, T. Biver, *J. Inorg. Biochem.,***216**, (2021).
25. D. Yang, A. Singh, H. Wu, R. Kroe-Barrett, *Anal. Biochem.*, **508**, 78 (2016).
26. R. N. El Gammal, H. Elmansi, A. A. El-Emam, F. Belal, M. E. A. Hammouda, *Sci Rep***., 12**, (2022).
27. P. D. Ross, S. Subramanian, *Biochemistry,* **20**, 3096 (1981).
28. M. Otagiri, *Drug Metab. Pharmacokinet.,* **20**, 309 (2005).
29. A. S. Abdelhameed, A. M. Alanazi, A. H. Bakheit, H. W. Darwish, H. A. Ghabbour, I. A. Darwish, *Spectrochim. Acta A Mol. Biomol. Spectrosc.,***171**, 174 (2017).
30. S. K. Pawar, S. Jaldappagari, *J. Pharm. Anal.,.***9**, 274 (2019).
31. G. Sudlow, D. Birkett, D. Wade, *Mol. Pharmacol.,* (1976).
32. X. X. Cheng, Y. Lui, B. Zhou, X. H. Xiao, Y. Liu, *Spectrochim. Acta A Mol. Biomol. Spectrosc.,***72**, 922 (2009).
33. Y. Z. Zhang, J. Dai, X. Xiang, W. W. Li, Y. Liu, *Mol. Biol. Rep.,* **37**, 1541 (2010).
34. A. Radha, A. Singh, L. Sharma, K. K. Thakur, in: Mater. Today Proc*.,* Elsevier Ltd, 2021.

Fabrication of polymethyl methacrylate reinforced wood lumbers for outdoor environment

M.Aziz[1], K. Varshney[1], S. Mahtab[*], M. Arif [2], T.I. Siddiqui[3], M.G.H. Zaidi[1**]

[1]Department of Chemistry,[2]Department of Mechanical Engineering,
G.B. Pant University of Agriculture & Technology Pantnagar, Uttarakhand 263145, India
[3]Department of Chemistry, Sir Syed Faculty of science, Mohammad Ali Jauhar University, Rampur 244901, India

Polymethyl methacrylate (PMMA) reinforced wood lumbers (PWLs) with improved mechanical properties, thermal stability and resistance against degrading environment were fabricated and investigated for their feasibility under outdoor environment. The process of fabrication of PWLs was executed through swelling of mango wood lumbers (MWLs) into a polymerizing composition in methanol followed by thermal curing n anaerobic environment. A representative procedure of fabrication of PWLs involves swelling of MWLs into a polymerizing composition involving 2, 2-azobisisobutyronitrile (1.0% w/v) and methyl methacrylate in methanol (20 and 40%, v/v) for 24h followed by curing at $75\pm1°C$ for additional 6h. This has afforded the PWLs with PMMA loading (wt %) up to 25 wt%. The reinforcement of PMMA into PWLs was reveled through UV, visible, Fourier transform infrared spectra and atomic force microscopy. Diverse analytical procedures revealed the formation of PWLs with improved thermal stability, mechanical properties, resistance against moisture, chemicals and biodegradation. The study reveals a feasible method for producing PWLs for potential use as a high-performance construction material that may sustain outdoor environment.

Keywords: Polymethyl methacrylate, reinforcement, mango wood lumbers, fabrication, performance evaluation

INTRODUCTION

Wood has drawn a great deal of attention since the dawn of civilization as a renewable material for construction of building components, furniture, transport, tools and weapons [1-4]. Commercially, wood has been considered as lumber or timber particles, compressed and plies boards over decades leading to circular economy [2]. This is despite the fact that the construction industry relies on concrete and alloys as substitute possibilities [1]. Preservation of wood through biocides and their polymer-assisted modification has been of great academic and industrial interest over decades due to affordable cost of manufacture and ease of operations [2-4]. Leo H. Arthur Baekeland from North America, credited as inventor of polymer reinforced wood materials, called wood plastic composites by the early 20th century. This has been accomplished during his exploratory attempt to combine wood flour with phenolic resins.The process was based on Italian extrusion technology in which wood floors were extruded at equal weight of thermoplastic materials to afford the products that have been deployed as floorings for ships and panels for automobiles [5].

Mango wood tree (*Mangifera Indica*) is a hard wood with dense grains and is primary grown for its fruit in the tropical Asian regions and other parts of Oceania. Mango tree produces a soft wood with sufficient strength for construction of furniture and building components. Mango wood suffers from periodic expansions and contractions under humid environment and is prone to dehydration in sun, heat and dry outdoor conditions [6, 7].

PMMA as such and in combination of copolymers has been employed as reinforcement for modification of a series of low-grade woods [8-10]. However, to the best of the literature survey, no reports are available on development of PWLs through reinforcing PMMA into MWLs and their onward investigation for outdoor applications sustained outdoor applications.

In order to have an insight into the scope of mango wood as a sustainable construction material for outdoor environment, investigations are still persistent to improve their mechanical properties, dimensional stability, resistance against chemicals, moisture, and microorganisms. The current study aims to develop a facile method of fabrication of PWLs through reactive reinforcement of polymethyl methacrylate (PMMA) into MWLs for possible outdoor applications. PWLs with selected PMMA loading were investigated for mechanical properties, thermal stability, resistance against solvents, water, chemicals and biodegradation in presence of a decay fungus *Gleophyllum Striatum* (brown rot).

---

* To whom all correspondence should be sent:
E-mail: smiitr@gmail.com, mgh_zaidi@yahoo.com

EXPERIMENTAL

Starting materials

MMA and AIBN were procured from Ms Sigma Aldrich. Rest of the chemicals and solvents were locally purchased (purity > 99% and used without further purification) . Inhibitor content of MMA was removed through extraction in aqueous sodium hydroxide solution (10%), followed by washing with distilled water. Fraction of MMA collected at $101\pm1^{\circ}C/10mm$ Hg (density 0.98 g/cc) was used for polymerization reactions [8].

Mango wood (*Mangifera Indica*) was arranged from nearby forest area and seasoned under relative humidity of 40% at $27\pm 1^{\circ}C$ for 3 months. The oil and wax components of seasoned wood were leached through submerging into toluene: methanol mixture (1:1, v/v) over 36h.Leached wood (density, 0.56 g/cc) was fabricated as per recommendations of IS 1708 66 for mechanical testing [5].

Fabrication of PWLs

A series of PWLs was fabricated through slight modification in traditional Bethel process, conducted in a custom designed stainless-steel chamber with provision of an evacuator and volume regulated hoper. The fabricated MWLs (IS 1708 66) were evacuated at $50\pm1^{\circ}C400$ mmHg over 24h, thereafter submerged into a composition of MMA in methanol (20 to 60 %, v/v) supplemented with AIBN (5 wt %) at $30\pm1^{\circ}C$ for 24h.The treated MWLs were placed in a furnace maintained in anaerobic environment through circulation of carbon dioxide @ 0.1 mL/min and cured at $60\pm1^{\circ}C$ for additional 12h to afford the PWLs. The loading of PMMA into PWLS was quantified through differential weighing procedure. PMMA was also synthesized under identical reaction conditions to serve as control for spectral measurements [11].

Characterization

UV spectra were recorded on a Genesis10 Thermospectronic spectrophotometer. The stock solutions (0.025M) of MMA and AIBN were prepared in dichloromethane and used for scanning of their UV spectra. Clear solutions of MWLs and PWLs were separately prepared through ultrasonic treatment of their suspensions (1.0 wt %) of saw dust in dichloromethane at 500W over 1 min followed by filtration. The FTIR spectra were recorded on a Bruker Alpha-2 spectrophotometer in KBr. AFM images were recorded over NTEGRA Prima AFM in tapping mode using ultra sharp Si cantilevers having force constant of 48 N/m at room temperature. Compressive test was conducted on ENKAY-UT-40 Universal Testing Machine of capacity of 40 tons and a precision of 80 kg. Impact tests were conducted at a domestically developed swinging pendulum machine. Simultaneous TG-DTA-DTG was conducted on a Stanton Red-Croft model STA-781@ $10^{\circ}C/min$ up to $500^{\circ}C$ with reference to alumina in a nitrogen flow of (@ 50 mL/min). Effect of PMMA reinforcement on lignin content, moisture content and solubility of PWLs in water, NaOH (1%), methanol/benzene, and ether were investigated with reference to MWLs according to standard procedures (Table 1).

Biodegradation

Biodegradation of PWLs (mesh size 60) was investigated at $25^{\circ}C$ for 10 days under the invasion of a decay fungus *Gleophyllum Striatum (*brown rot) through food poison technique in minimal salt media (MSM) with reference to streptomycin according to early reported procedure [12]. The inhibition of fungal growth by PWLs was compared with solvents, wood flour, MMA, PMMA and AIBN. The MSM consisting of $Na_2HPO_4\cdot2H_2O$, KH_2PO_4, $MgSO_4$, $NH_4Fe (CH_3COO)_3$, and $Ca (NO_3)_2\cdot4H_2O$ was inoculated with fungus pellets and incubated at $30\pm1^{\circ}C$. The culture collected at different times was centrifuged and their supernatants were analyzed for protein, reducing sugar content and enzyme activities. A mixture containing Na_2CO_3 (2.0%), NaOH (0.1N, 50mL), $CuSO_4$ (0.5g), sodium potassium tartrate (1.0%, 5mL), and Folin Ciocalteu reagent (0.50 mL) was incubated at $25\pm1^{\circ}C$ for 30 min and measured at a wavelength of 660 nm. Standard curve was drawn using bovine serum albumin (0.5 mL, 20-200 mg/mL). Protein and reducing sugar contents were estimated (mg/mL) with reference to incubation time. CMCase assay [5,8] was made in citrate buffer (pH 4.8, 0.05M) supplemented with carboxymethyl cellulose (2%). The pre-incubated enzyme (0.5 mL) was mixed with the substrate (0.5 mL) and incubated at $50\pm1^{\circ}C$ for 30 minutes. The xylanase assay was made through monitoring the liberated reducing sugar from oat spelled xylem. A reaction mixture comprising enzyme (0.9mL) supplemented with birch xylem (0.1mL) was incubated at $50\pm1^{\circ}C$ for 10 minutes. The reducing sugar was liberated within 10 min and onward estimated at 540 nm with reference to xylose as positive control. FPase assay was made in presence of enzyme (0.5 mL), citrate buffer (pH 4.8, 1.0 mL,0.05M) and Whatman filter paper (No.1, 1×6 cm = 50 ± 0.025 mg) under incubation at $50\pm1^{\circ}C$ for 60 min [5, 8].
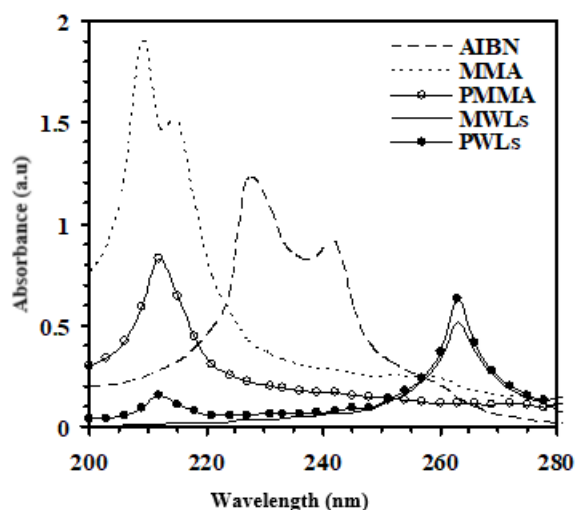
RESULTS AND DISCUSSION

Spectra

Figure 1. UV spectra

Formation of PWLs was ascertained through UV (Figure1), FTIR spectra (Figure2) and AFM (Figure3). AIBN [13], MMA [9] and PMMA [9] reveal characteristic wavelength maxima (λ_{max}, nm) at 227,245 [13],209 [9], and 212 [R], respectively. Red shift in λ_{max} of MMA from 209 to 212 nm reveals the n-π transition of the carbonyl linkage within the ester group [9]. MWLs reveal characteristic λ_{max} corresponding to lignin at 263 nm [14]. The pair of λ_{max} common to PMMA (212) and lignin (263) reveals the formation of PWLs [9, 13-14].
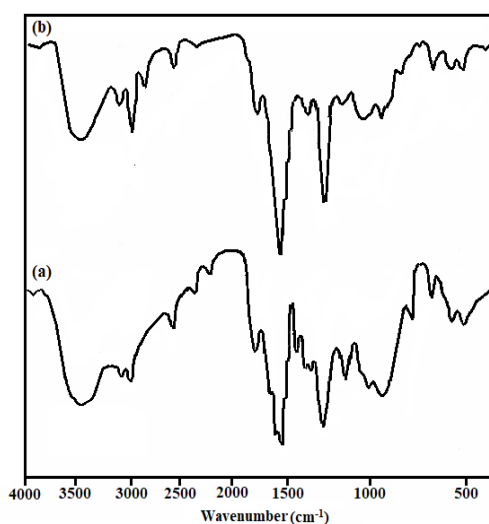

Figure 2. FTIR spectra of the saw dust of MWLs (a) and PWLs (b)

Figure 2 reveals the comparative FTIR spectra of the flours derived from MWLs and PWLs. Both MWLs and PWLs exhibit common wave numbers (cm^{-1}) corresponding to stretching vibrations of –OH (3371.5), C-H (2939.5), C=O (1738.7), bending

vibrations of CH_2 (1460.2), and skeletal vibrations corresponding to C-C and C-O (1245.2 cm^{-1}). MWLs and PWLs display lignin-related absorptions at 1594.9 cm^{-1} and 1508.1, respectively. The reinforcement of PMMA has rendered a shift in wave number corresponding to lignin at 1592.7 cm^{-1}, eliminating the absorption at 1508 cm^{-1} in MWLs. In both MWLs and PWLs the wave numbers at 1629.5 and 1364.0 attribute to the bending mode of absorbed water and stretching vibrations of –CH_3. Due to PMMA reinforcement, the C-O-C pyranose ring skeletal vibration associated with hemicelluloses, observed at 1053.6 cm^{-1} in MWLS was shifted to 1143.7 cm^{-1} in PWLs [14, 15].

Microstructure

Absorbance of PWLs was measured through AFM (Figure 3). (bottom). The AFM topo graphs of MWLs (bottom) and respective nano-indentation images (top) are presented at 10 μm scale. The bright and dark zones in AFM represent the cellular domains of the wood. AFM and respective nanoindentations reveal characteristic cellular morphology with occasional knots and voids into MWLs (Figure 3a). AFM of PWLs and the corresponding nanoindentations reveal the absence of knots and voids with random prominence of PMMA phase into the voids of MWLs (Figure 3b).

Thermal stability

Figure 4 illustrates the effect of PMMA loading on the thermal stability of PWLs in terms of TG(a), DTA(b), and DTG(c). MWLs have shown TG onset at 210^{0}C leaving 88.70 % Wr. Reinforcement of PMMA (15 wt %) has increased the TG onset for PWL-I to 240 ^{0}C leaving 90.70 %Wr. Further increase in PMMA loading to 35 wt% has raised the TG onset of PWL-II to 320 ^{0}C with a marginal reduction in the %Wr to 86.22. Prior to TG onset temperature the residual weight loss associated with MWLs and respective PWLs attributes to their moisture content. In the present investigation the moisture content based on TG was in close agreement with (ASTM D1037 72a 79) (Table 1). MWLs have shown 6wt% moisture content. Increase in loading of PMMA has gradually reduced the moisture content of PWLs-I and PWL-II to 3.02 and 1.5 wt%, respectively [9].

TG reveals a two-step thermal decomposition by MWLs and respective PWLs. With PMMA loading the first step decomposition range for PWLs was shifted to higher temperatures. For instance, PWL-I and PWL-II have shown their respective first step decomposition temperatures ranging from 210 to 320^{0}C and 320-372 ^{0}C leaving 55 to 54.5%Wr.

Accordingly, the second step decomposition for MWLs appeared in the range of 343-450^{0}C leaving 2wt% of char residue. PWL-1 has shown second step decomposition in the higher range of 372 to 450^{0}C leaving 3.75% of char residue. The second step decomposition of PWL-II appeared in the range of390 to 480 ^{0}C leaving 2wt% of char residue (Figure3a).
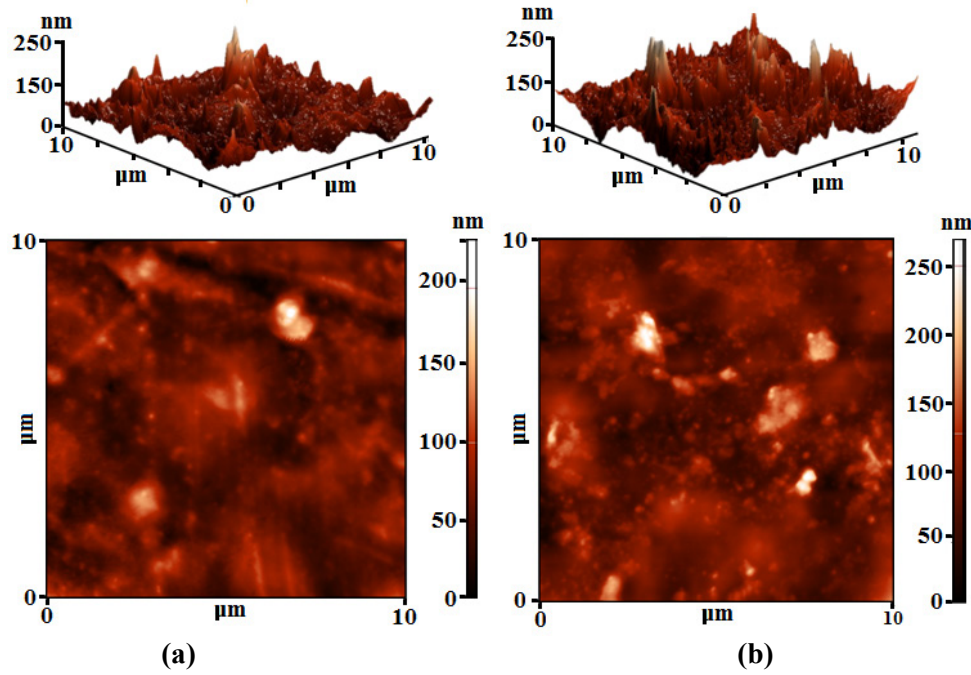

(a)

(b)

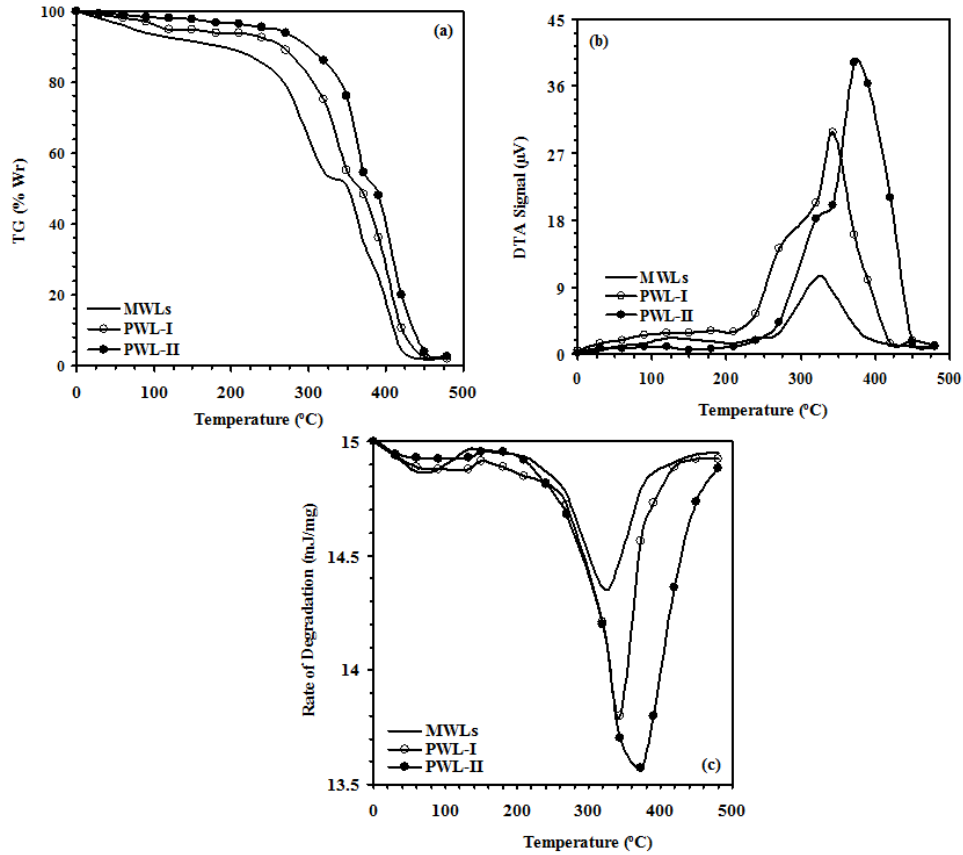**Figure 3.**AFM topographs of MWLs (a) and PWL-II (b)

Figure 4. Effect of PMMA loading on thermal stability of PWLs

In order to have further insight into the effect of PMMA loading on thermal stability of PWLs, their respective DTA and DTG were investigated. With PMMA loading, the peak temperatures corresponding to DTA and DTG gradually increased with simultaneous reduction in the rate of degradation of PWLs. With PMMA loading, the DTA and DTG peak temperatures of PWLs were found in ascending order ranging from 320 to 372 ^{0}C (Figure4b). This was followed by simultaneous reduction in their thermal degradation (mg/min) ranging from 14.36 to 13.49 (Figure 4c). Thermal data revealed that thermal stability of PWLs increased with quantitative loading of PMMA [8, 9].

Mechanical properties

Mechanical properties of PWLs were found in increasing order with PMMA loading (Table1). MWLs have rendered 16.56 Nm of Charpy impact. With PMMA loading, the Charpy impact of PWLs gradually increased to 18.96 Nm, Similarly, the Izod impact for MWLs (8.85 Nm) increased to 13.57 Nm for PWLs-II. The compressive strength ($\times 10^7$, N/m^2) of MWLs was 3.23 that marginally increased to 4.36 for PWL-II. The experimental data pertaining to mechanical properties in association with findings through AFM revealed modification in dimensional stability of PWLs due to grafting of PMMA into the cell walls of MWLs [9,17].

Biodegradation

Figure 5a demonstrates the production of protein and reducing sugar release (mg/mL) by MWLs and respective PWLs in presence of *Gleophyllum Striatum as* a model test fungus under incubation as a function of incubation time (h). MMA and AIBN each at 250 ppm showed100% and 38% respective inhibitions in the growth of *Gleophyllum Striatum as* a model test fungus under incubation over 10 days [5].

PMMA and MWLs at $\leq$ 50 ppm showed remarkable fungal growth under incubation within 12 days. Whereas, under the similar experimental conditions no fungal growth was noticed over PWLs till 12 h. Production of protein (mg/mL) was initiated (0.14) in presence of MWLs and PWL-I at 12h of incubation and reached the maximum level (0.31) at 96h of incubation. However, PWL-II rendered a remarkable reduction in the production of protein from 0.09 to 0.16 in 12h.
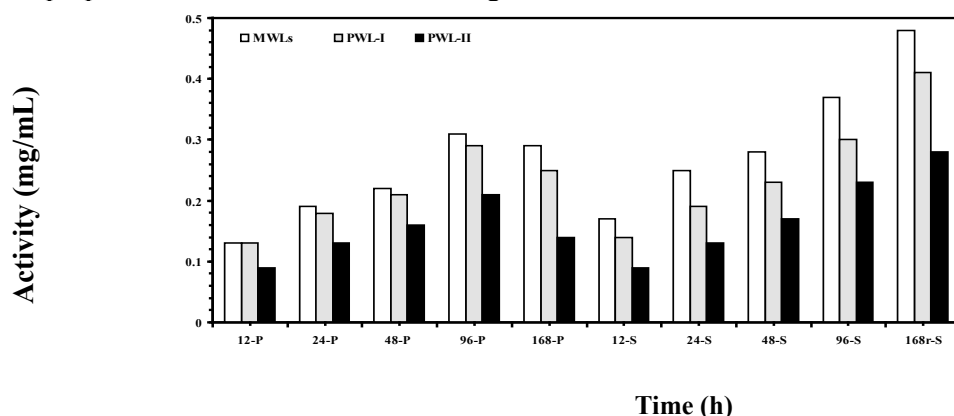

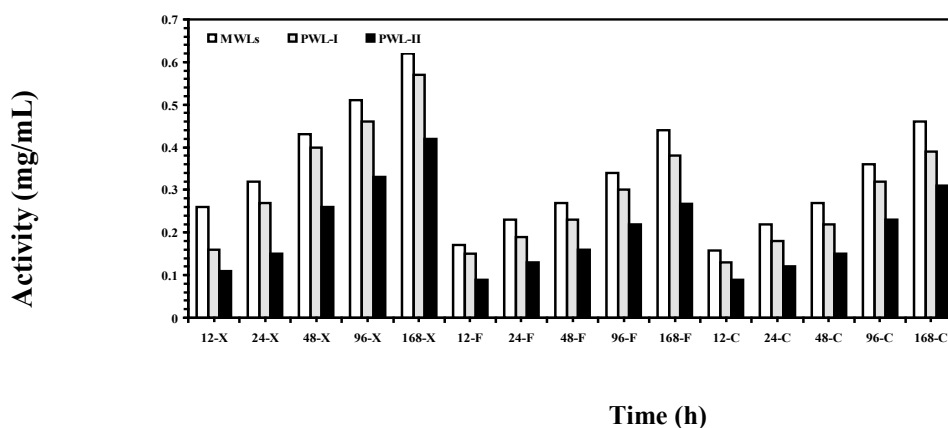**Figure 5a.** Effect of PMMA loading on protein and reducing sugar activity of PWLs

Figure 5b. Effect of PMMA loading on enzyme activity of PWLs

Table 1. Effect of PMMA reinforcement on physical characteristics of PWLs

Properties	MWLs	PWLs	
		PWL-I	PWL-II
[MMA] (v/v% in methanol)	0.00	20.00	40.00
PMMA Loading (%)	0.00	15.00	25.00
Charpy impact (Nm)[A]	16.56	17.71	18.96
Izod impact (Nm)[B]	8.85	11.65	13.57
Compression strength (n/ M^2)[C]	3.23	4.43	4.36
Moisture content (%)[D] ASTM D1037 72a 79	7.12	3.90	2.05
Lignin content (%)[E] ASTM D 1106-56	34.14	28.00	14.12
Solubility in NaOH (1%)[D]	21.11	20.50	18.35
Solubility in methanol/benzene[D]	84.80	80.12	74.36
Solubility in ether[D]	93.80	92.70	90.50
Solubility in hot water[D]	37.50	11.28	8.32
Solubility in cold water[D]	18.80	9.63	5.95

A:10 × 10 × 55 mm with V notch at the center with 2 mm depth and 45º included angle;
B: 10 × 10 × 75 mm with V notch at 28 mm with 2 mm depth and 45º included angle;
C: 50 × 50 × 75 mm;
D: ASTM D 1109 56 72.

The decline in production of protein after 96 h attributes to the utilization of available substrate in the medium by fungus. The reducing sugar content of MWLs reached maximum after 168h of incubation. PWLs-II showed reduction in reducing sugar content by 46.56% up to 24 h, followed by 25.22% for PWL-I and PWL-II. Such increase in the production of reducing sugar attributes to the availability of substrate for *Gleophyllum Striatum.*

MWLs and respective PWLs rendered a collective progress in Cellulolytic (FPase, CMCase) and xylanolytic enzymes production, that reached a maximum after 168 h of incubation in presence of *Gleophyllum Striatum.* PWLs rendered a remarkable reduction in enzyme activity due to PMMA loading. Relatively, MWLs rendered higher production of Xylanase (IU/mL) over cellulytic (IU/mL) enzyme in comparison to PWLs. In presence of MWLs, Xylanase enzyme activity (0.22) was initiated after 12 h of incubation and reached maximum (0.62) at 168h. PWLs-II rendered a reduction (50.80%) in the Xylanase activity within 24 h [5,9].

Figure 5b demonstrates the enzyme activity (IU/mL) by MWLs and respective PWLs in presence of *Gleophyllum Striatum* under incubation as a function of incubation time (h). FPase activity (0.15) was started after 12h of incubation and reached maximum (0.44) at 168 h of incubation in PWLs. The sequential reduction (45.6%) in the FPase activity was noticed for PWLs-II followed by PWLs at 12h. CMCase activity (0.16) started after 12 h of incubation and reached maximum (0.47) at 168 h for MWLs. PMMA loading reduced the CMCase activity for PWL-II (43.69%) followed by PWL-I

(39.25%) in 12h of incubation in presence of the test fungus. The reduction in production of protein, reducing sugar contents in coherence with enzyme activities attributes to resistance of PWLs towards biodegradation due to restricted transport of moisture across their cell walls due to the loading of PMMA [5,9,18].

Solubility behavior

Treatment of thermosetting [5, 8-10] and thermoplastic polymers [19] with wood substrates offers an amicable way to achieve the biocomposites with improve resistance against water and organic media. The present study demonstrates the impact of PMMA reinforcement on solubility behavior of PWLs in water, alkaline solutions and organic solvents. The solubility of PWLs in various solvating media has been gradually reduced with their PMMA content [8]. PWLs has rendered decreasing order of their solubility over MWLs in alcohol benzene mixture, followed by hexane, hot water, aqueous sodium hydroxide (1%), and cold water. The low solubility of PWLs in the alcohol benzene mixture attributes to the loss of waxes, fats, resins, and oil contents associated with MWLs [5]. The reduction in solubility in a sodium hydroxide (1%) solution attributes to the qualitative reduction in the fraction of lignin content with quantitative reinforcement of PMMA into PWLs [9,20]. (Table 1).

CONCLUSION

Polymethyl methacrylate (PMMA)-reinforced mango wood lumbers (MWLs) with improved mechanical properties, thermal stability, resistance to chemicals, solvents, and biodegradation were fabricated and designated as PWLs. Progressive loading of PMMA led to enhancement in mechanical characteristics, encompassing impact strength and compressive strength. The biodegradation studies through monitoring the changes in protein and reducing sugar contents (mg/mL), as well as cellulolytic *(FPase, CMCase)* and *xylanolytic* enzyme activities (IU/mL) at various incubation times up to 168 hours unveiled the significant resistance of PWLs to the *Gleophyllum Striatum* decay fungus. The study yielded valuable insights into the potential of PWLs as high-performance construction materials for future outdoor applications.

REFERENCES

1. Y. Ding, Z. Pang, K Lan, Y. Yao, G. Panzarasa, L.Xu, M. Lo Ricco, D. R. Rammer, J. Y. Zhu, M. Hu,X .Pan, T .Li, I. Burgert ,Liangbing Hu, *Chem. Rev*., **123**,1843 (2023).
2. L. Kristak, R. Reh, I. Kubovsky, *Polymers* (Basel), **15**, 1409 (2023).
3. M. J. Spear, S. F. Curling, A. Imitrou, G. A. Ormondroyd, *Coatings*,**11**, 327 (2021).
4. Y. Dong, K. Wang, J .Li, S. Zhang, S. Q. Shi, *ACS Sust. Chem. Eng*, **8**, 3532 (2020).
5. S. Mahtab, S. Masroor, N. Siddiqui, M. G. H. Zaidi, *Mater. Today: Proc*., **26**, 1831(2020).
6. A. Vedrtnam, S. Kumar, S. Chaturvedi, *Composite (B) ;Eng.* **176**, 107282 (2019).
7. M. Mandis, H. Amarasekara, R. Jayasinghe, R. U. Halwatura, *Conf. Proce. Int. Comf. Innovat. Emerg. Tech.*, **81**, 76 (2021).
8. M.Kumar, P.L. Sah, M.G.H.Zaidi, A.Srivastav. *Adv. Mater. Res*., **214**, 392 (2011).
9. B. Kumar, M. G. H. Zaidi, S. Rathore, A. K. Rai, I. S. Thakur, P. L. Sah. *Instrum. Sci. Tech*., **34**, 67 (2006).
10. T. K. Joshi, M.G.H.Zaidi, P.L. Sah, S. Alam, *Polym. Int*.,**53**, 198 (2005).
11. M. G. Aguayo, C. Oviedo, L. Reyes, J. Navarrete, L. Gomez, H. Torres, G. Gavino, E. Trollund, *Forests*, **12**,1606 (2021).
12. 12.C. A. Abbas, W. L. Bao, K. E. Beery, P. Corrington, C. Cruz, L. Loveless, M. Sparks, K. Trei, *Manual Ind. Microbiol. Biotechnol*., **23**, 621 (2010).
13. Z. Liu, G. Zhang, W.Lu, Y. Huang, J.Zhang, T. Chen. *Polym. Chem*., **6**, 6129(2015).
14. O. Y. Abdelaziz, P. Hulteberg. *Waste Biomass Valor.*,**8**, 859(2017).
15. X.F.Sun, R.C.Sun, J. Tomkinson, M.S. Baird. *Polym. Degrad. Stab.*,**83** ,47(2004).
16. M. A. Vidal, M. Frey, T. Keplinger. *J. Struct. Biol.* **211**, 107532 (2020).
17. Y. Dong, M. Altgen, M. Makela, L. Rautkari, M. Hughes, J. Li, S. Zhang. *Holzforschung,* **74**, 967 (2020).
18. E. Rebecca, R. M. Rowell. *Holzforschung*, **55**, 358 (2001).
19. M.Arif, S.Mehtab, A. Misra, M. G. H. Zaidi. *Mater. Today: Proc*., **47**, 4210 (2021).
20. P. Baishya, M. Mandal, P. Gogoi, T. K .Maji. *Nanocompos. Sci. Fund*., **7**, 433 (2017).

Breaking down the plastics paradox: polymer degrading microorganisms

D. Gupta*, G. Modi

RNB Global University, Ganganagar Road, Bikaner, Rajasthan, India-334601

Plastic's unique qualities, which make it appealing for daily usage, also endanger the sustainability of the global community. The main benefit of plastics is that they are sturdy, long-lasting, and non-reactive. As a result, the production of plastic garbage has exponentially increased, but due to its non-biodegradable nature, a threat to the environment is now identified on a global scale. The existing abiotic ways of getting rid of these wastes (incineration, landfilling, and recycling) are extremely expensive, unsustainable, and burdensome to the environment. In light of this, current attention has been drawn more to the possibilities for biological systems to break down plastics made from synthetic materials. A number of polymer-degrading microorganisms have been identified in various sources like garbage, mines, dumping yards, and other extreme environments. The microbial enzymes and their mode of action are also being investigated, in view to developing a recombinant microbial strain or enzyme for a sustainable approach to getting rid of plastic. The present review aims at studying all these efforts and draw a meaningful conclusion for breaking down the plastic paradox.

Keywords: Polymer, Biodegradation, Microorganisms, Microbial enzymes, Sustainability.

INTRODUCTION

One of the most pressing environmental issues today is the buildup of plastic garbage leading to 'White Pollution', which globally affects all living forms, natural ecosystems, and the economy. Plastics are man-made polymers with an enormous number of applications. Due to their pliability, endurance, and ability to withstand erosion, plastics are excellent materials for a variety of applications. Forty percent of the over 400 Mt of plastics manufactured are utilized in single-use applications, producing a sizable quantity of trash. The environmental harm is caused by the buildup of garbage made of polystyrene, polyethylene, polypropylene, polyvinyl chloride, polyurethane, and polyethylene terephthalate. The molecular structures of major polymers are presented in Fig. 1. There is a lot of study being done on their potential for degradation through biotic and abiotic processes. The majority of current waste management practices include abiotic processes like: recycling, burning for energy recovery, and buildup in landfills, causing more harm to the environment [1].

Moreover, the worldwide ecology and the health of living things are negatively impacted by the increasing amount of micro-nano plastics in the natural ecosystem. Through trophic transfer, ingestion, and inhalation, micro-nano plastics penetrate the agroecosystem, flora, fauna, and human body, causing blood vessel obstruction, infertility, and aberrant behaviors [2]. Therefore, using a cutting-edge method to remove micro-nano plastics from the natural environment becomes essential. In light of this issue, it is essential to find alternatives that are environmentally responsible options, like biodegradation instead of conventional dumping. Microbial remediation is viewed as a greener solution among the several micro-nano plastics remediation techniques now in use [3]. In order to build an efficient and sustainable approach to managing plastic trash, an eco-friendly strategy is required. This approach takes advantage of the potential of various microbial species to degrade these polymers [4].

Polymer-degrading microorganisms

Polymer-degrading microorganisms are a group of microbes that have the ability to break down various types of polymers, such as plastics and synthetic materials, into simpler compounds. These microorganisms play a crucial role in the natural biodegradation of polymers, helping to reduce environmental pollution caused by plastic waste [5]. There are several types of polymer-degrading microorganisms, including bacteria, fungi, and some types of algae. They possess specific enzymes that can target and cleave the chemical bonds present in polymers, breaking them down into smaller molecules that are potential sources of energy and nutrients for the microorganism [6].

It is important to fully comprehend how these microbes work to lessen the amount of plastic in the environment. Microorganisms can decompose a polymer either aerobically or anaerobically.

---

* To whom all correspondence should be sent:
E-mail: dipaligupta771@gmail.com

Microorganisms may utilize these polymers as a source of energy by releasing some extracellular enzymes. Numerous enzymes, including PETase, cutinases, hydrolases, and bacteriophilic enzymes thought to be involved in the breakdown of plastics, have been identified from bacteria. The first and crucial step is the adherence of microbes to the surface of the polymer. There are anchor peptides on the surface of these enzymes that work in the linking of enzymes with the polymer [7]. Enzymes catalyze the bioremediation process and convert large polymers into small inorganic molecules that can be utilized by microbes as a source of carbon and energy [8].

Studies that focus on the structural study of relevant enzymes and the reaction pathways to achieve desired outcomes have been carried out to optimize efficient enzymatic conditions for the breakdown of plastics. It is important to choose an appropriate microbe for plastic degradation that targets various types of polymers. Additionally, they can aid in the creation of better enzymes to handle the problems associated with plastic waste [9].

Assessment of bioremediation

In a study conducted on microbial degradation of polymers, it was observed that the anaerobic incubation of polymers with some bacterial strains resulted in structural changes in the raw and deteriorated polymers. It has been analyzed through the use of Fourier-transform infrared spectroscopy (FTIR), thermo-gravimetric analysis (TGA), X-ray diffraction (XRD), and contact angle research. The polymer-degrading bacteria *Brevundimonas* and *Sphingobacterium* served as catalysts for the succeeding aerobic treatment's stimulation of the PBAT/PLA polymers' breakdown by thermophilic anaerobic degradation. Under thermophilic circumstances, the physical breakdown of the PBAT/PLA polymer was noticed [10].

Apitius *et al*. (2019), immobilized polymer-degrading enzymes producing microorganisms to effectively reduce long-lasting plastics. In order to specifically adhere entire cells to the surface of polymers, polymer-binding peptides were used as adhesion promoters. To increase the binding strength of peptides that bind to polymers, guided development of such peptides for *Escherichia coli* surface display scanning method was designed. By immobilizing entire cells on polymer beads, the cell surface screening technique enabled the enrichment of better binding peptides from a culture broth. It is possible to employ this method of cell display screening to improve adhesion peptides in order to direct and immobilise organisms to polymer surfaces (like PP) and to break down certain types of plastic

in a targeted manner [11]. Ji *et al*. (2023) developed a procedure for locating and creating anchor peptides that were specially designed to act as non-catalytic binding sites for synthetic polymers. In order to increase the effectiveness of biocatalytic plastic recycling processes, the found anchor peptides have the potential to attach to plastic-degrading enzymes [12].

The fracturing stimulation process revealed challenges related to the effectiveness of the oxidative breaker when addressing oil and gas reservoirs marked by low permeability and temperature. This circumstance resulted in the accumulation of polymer blockages and subsequent decreases in production rates. To tackle this issue, researchers conducted a microbial-assisted experiment aimed at eradicating the polymer-caused congestion within fractures, with the goal of augmenting oil yields. The findings confirmed the viability of alleviating polymer blockages within these reservoirs by utilizing native microorganisms. Additionally, these findings carried noteworthy implications, as they laid the foundation for a crucial approach in enhancing oil recovery [13]. Scanning electron microscopy, Fourier transform infrared spectroscopy, and contact angle measurements were applied to determine the degree of microplastics' biodegradation in deeper strata than river [14]. Grivalský *et al*. (2018) revealed that nonisothermal chemiluminescence, which examines the polymer surface's momentary oxidation state, is a good tool to observe the biodegradation dynamics on polymeric film, while Ecoflex agar is able to choose advantageous bacteria that can break down polymers [15].

Polymer-degrading bacteria and their sources

Plastics are naturally broken down by enzymatic, aerobic, or anaerobic biodegradation due to the bacterial and fungus communities that live in garbage or abandoned plastics. Through a variety of approaches, bacteria, and fungi having the capacity to degrade polymers are identified. *Arthrobacter sp., Bacillus* sp*., Rhodococcus* sp*., Microbacterium* sp*., Phanerochaete* sp*., Pseudomonas* sp*., Staphylococcus* sp*.,* and other particular bacterial and fungal species specifically break down polymers at the appropriate rate and duration. In addition to improving agricultural crop productivity and surface and subsurface water quality, polymer decomposition by microbes modifies soil properties, ecology, ecosystem, and characteristics. It reduces the release of polymers from the industry and limits contamination in the soil layer. It will eventually aid in maintaining the ecosystem and natural resources [16].

Polymer biodegrading microorganisms have been identified from a broad range of habitats, including polluted soil, water bodies (such as rivers, lakes, and oceans), compost heaps, waste disposal sites, wastewater (WW) streams, municipal sludge, municipal solid waste (MSW), plastic dump yards, and even from the guts of certain organisms like insects and worms [17].

Water bodies

Microplastics are generated in various environments by physical and chemical disruption processes that break down plastic debris. Since microplastics may be transported anywhere in the globe by wind or ocean currents, they can even travel to the most distant parts of our planet. As a result, they are found in practically every habitat. Interest in the field of microbial ecology has increased with the discovery that this special substrate can facilitate microbial spread. On the growth, movement, persistence, and ecology of microorganisms, microplastics have synergistic effects [18, 19]. In a study conducted by Kumar *et al*., epiphytic bacteria associated with five different marine macroalgae (*Sargassum, Ulva, Padina, Dictyota*, and *Pterocladia* sp.), that were obtained from India's central west coast, were examined for their cultivable diversity and polymer-degrading ability. Using 16S rRNA gene sequence analysis, 238 bacteria were identified and subjected to degrading polymer (cellulose, pectin, xylan, and starch) activities. Out of the 360 total strains that were isolated, purified, and conserved, xylanase activity made up 61.3% of the polymer hydrolysis potential, whereas amylase, cellulase, and pectinase activity made up 59.7%, 58.8%, and 52.2% of the total, respectively [20].

Bacteria and fungi isolated from the marine environment have been used to biodegrade synthetic polymers made from discarded plastic bottles. By using characterization techniques including weight loss, FTIR, SEM, and XRD, the deteriorated polymer films were thoroughly assessed. According to the findings, in a period of 6 weeks, the polymers from waste samples from plastic bottles degraded by 35% when treated with bacterial strains and by 22% when treated with fungal strains. Different criteria were used to analyze the data, including temperature, pH, and inoculum dose concentration [21]. Longitudinal gradients of river sediments were examined and the microplastics and associated microbial populations were discovered by Niu *et al.* in 2021. The average quantity of microplastics increased from the upper levels to the lower levels of sediment, where smaller microplastic particles predominated. Microplastics deteriorated faster in

28

deeper layers, according to contact angle measurements, scanning electron microscopy, and Fourier transform infrared spectroscopy-attenuated total reflectance research [13].

Wastelands/ garbage soil

Polymer-degrading and thermophilic bacteria, *Acidicaldus* and *Granulicella*, were identified by Kohler *et al.* from a copper slag deposit. *Povalibacter*, a less prevalent but intriguing bacterium that breaks down polymers, was also discovered in soil specimens taken from the collection of pre-industrial mines. A single sample of industrial mining waste has been chosen for 16S rRNA analysis and identification. The findings demonstrated the presence of soil bacterial communities in soil samples from historic copper mine sites, which may provide a prospective source for microorganisms with important metabolic properties [22].

From waste soil, Patil (2018) identified four bacterial species and two fungus species. *Pseudomonas putida, Bacillus amylolyticus, Pseudomonas fluorescence* and *Bacillus firmus* were recognized as bacterial species. In a 30-day examination of the effectiveness of *Bacillus sp*. separated from waste dirt on the degradation of commercially available plastic carrying cases made of low-density polyethylene (LDPE) in shaker culture, it was shown that the bacteria reduced the plastic by up to 32%. [23]. Applying a polymer film-based examination method, PLA-degrading bacteria were collected from digester sludge, and the isolates were later identified as *Bacillus sp*. MYK2 and *Pseudomonas sp*. MYK1 by 16S rRNA analysis. An agar plate with a PLA film on it was infected with the associated biofilm during sludge addition on PLA granules, which were carried out by serially transferring a subculture into a new medium for 40 days. With the help of 3D optical microscopy, it was confirmed that isolates physically deteriorated the PLA sheet [24].

Chronically, plastic dump sites rich in LDPE may be used as a crucial resource of polymer degrading bacteria. Using biochemical tests and gram-staining techniques, the bacteria that break down polythene at soil waste sites were found. The decomposition using mineral salt media (MSM) in bags made of polythene using a weight determination technique beneath laboratory circumstances (inside the lab) was used for 30 days and demonstrated to be effective by *Klebsiella pneumonia, Pseudomonas aeruginosa, Micrococcus* sp, *Bacillus* sp.*, Arthobacter* sp.*,* and *Pseudomonas* sp. The weight loss method, FTIR, and SEM were used to measure

the decomposition of polythene in separate studies [25-28].

Potential bacterial strains identified from waste disposal sites in Uttaranchal, India, as well as others from specially created dirt beds included maleic anhydride, glucose, and minute particles of plastic. Based on their capacity for using high- and low-density polyethylenes (HDPE/LDPE) as a major carbon source, isolates were screened. The degradation of consortium-treated HDPE was confirmed by simultaneous thermogravimetric-differential thermogravimetric-differential thermal analysis (TG-DTG-DTA) and Fourier transform infrared spectroscopy (FTIR), which showed that it was significantly worse than that of LDPE and considerably worse than that of untreated samples [29-31]. LDPE biodegradation effectiveness of possible microbial consortia for polymer degradation was evaluated in relation to the effects of a pair of nanoparticles, specifically superparamagnetic iron oxide nanoparticles (SPION), nano barium titanate (NBT), fullerene-60. Using Fourier transform infrared spectroscopy (FTIR), thermogravimetric-differential thermo gravimetric-differential thermal analysis (TG-DTG-DTA), scanning electron micrographs (SEM) and other methods, it was demonstrated that LDPE degrades in many steps when exposed to nanoparticles. The study emphasized the importance of interactions between bacteria and nanoparticles, which had a significant impact on the biodegradation processes [32, 33].

The progressive response of various bacterial consortia made up of *Pseudomonas sp.* strains Rb10, Rb11, *Bacillus* sp. strain Rb18 and *Ps.* sp*.,* Rb13, *Lysinibacillus* sp. strain Rb1, and *Ps.* sp. was tested for degradation of PET, PHB, cellophane-like polymers. When these composites were treated with a bacterial consortium, significant alterations in the link strength, external morphology, and conductivity be situated discovered. Once compared to copolymer, these alterations in mixes were far more pronounced. The prospective isolates not only survived, but the variety of the bacteria increased significantly throughout the course of the whole incubation period [34-38]. There are reports on thermophilic, alkaliphilic, halophilic, and psychrophilic bacteria's biodegradation of typically manufactured plastics in both natural and laboratory environments. The majority of the information addresses two key issues: the degradation of different artificial polymers is expected to be facilitated by extremophilic microorganisms and their enzymes, and any potential effects can

extremophiles have on emerging technology for combating pollution [39].

An efficient method for selecting microbes adapted to degrading polyethylene (PE) and polypropylene (PP) was established and size of the polymer breakdown by separated populations of bacteria from wasteland was evaluated. The isolates included seven bacterial strains with PE degradation potential (three *Priestia megaterium, Enterobacter ludwigii, Klebsiella pneumoniae, Chryseobacterium* sp. *Ps. fluorescens*), seven varieties of fungi with PE degradation potential (two *Lecanicillium* spp., *Trichoderma* sp. and four *Fusarium* spp.,), seven different bacterium strains (two *Enterobacter* spp. and five *Serratia marcescens*) and six different fungal varieties (*Penicillium* spp*., Fusarium* spp*.,* and four *Aspergillus* spp*.,*) had the ability to break down PP. Analysis using scanning electron microscopy (SEM) demonstrated that a biofilm was present [40].

Genes coding the intracellular lipases LIP1 and LIP2, which are produced by the bacteria *Pseudomonas chlororaphis* PA23 were identified. Following incubation with LIP1 and LIP2, Gel permeation chromatography (GPC) examination revealed a reduction within the polymers' molecular mass. The polymer-degrading activity of the enzymes was also seen in polymers based on petroleum including polyethylene succinate (PES) and poly (-caprolactone) (PCL) [41]. From Chinese forest soil, Gram-negative, short rod-like strain that is capable of degrading different polymers was found. According to the examination of the 16S rRNA gene sequence, this particular strain had 99.3% higher similarity rates with *P.alcaliphila* NBRC 102411T, 99.2% with *P. mendocina* NBRC 14162T, and 99.0% with *P. oleovorans* NBRC 13583T [42].

Acinetobacter sp*., Escherichia coli*, and *Brevibacillus* sp*.* were isolated from industrial effluent and employed independently to track the breakdown of five synthetic polymers that are not biodegradable. All three strains have a greater than 75% degradation rate for the aforementioned polymers [43]. In landfills, *Bacillus megaterium* and *B. cereus* were isolated and tested for their capacity to break down polycarbonate (PC) polymers. By looking at the growing trajectory, clean area development, amylase & lipase creation, AFM, and FTIR, it was possible to assess the isolates' capacity for biodegradation. It was discovered that isolates had highly promising PC biodegradation abilities [44].

PET is a polymer that is widely utilized in plastic items, and its build up in the environment has raised

concerns throughout the world. A significant amount of PET-containing plastic materials due to an accretion in the atmosphere being a non-degradable contaminant, is posing serious threats to the survival of numerous endangered species and so endangering the ecosystem and biodiversity. A bacterium known as *Ideonella sakaiensis* has drawn notice for its unusual capacity to degrade and consume a kind of plastic known as polyethylene terephthalate (PET). A group of scientists from Japan's Kyoto Institute of Technology found this bacterium in 2016. It was given the name "*Ideonella sakaiensis*" since it was identified from soil samples taken at Sakai City PET bottle recycling facility. Debris made of polyethylene terephthalate (PET) are extremely durable and hence pose a long-term environmental burden. However, existing recycling initiatives are still not sustainable. A potential fix is two newly identified bacterial enzymes that selectively break down PET. First, PET is transformed hooked on mono-(2-hydroxyethyl) terephthalate (MHET) by *Ideonella sakaiensis*PETase, a consensus /-hydrolase fold enzyme with a well-characterized structural fold [45-59].

It was demonstrated that MHETase serves as exo-PETase by hydrolyzing the created PET pentamer based on structural studies and biochemical investigations. The experiments further showed that MHETase possesses hydrolysis activity against the PET film produced by termini, illustrative of the enzyme's exo-PETase activity. An MHETaseR411K/S416A/F424I variant with increased BHET activity was engineered, showing improved PET film degrading activity [60, 61].

Other sources

Tachibana *et al.* studied the microbiota of washed-rind cheeses from Japan and identified a bacterium similar to a marine inhabitant; *Alcanivorax dieselolei*, from one of the cheeses Muchuri. It is crucial to look into the microorganisms in fermented foods' capacity to hydrolyze polymers since the usage of biodegradable polymers for food packaging is growing in popularity [62].

The Greater wax moth gut microbiota was investigated using a culture-dependent methodology. In the GWM gut, nine bacterial and one microalgal species were identified by 16S-rDNA sequencing. They degrade low-density polyethylene, 2-methyl phenanthrene, and polycyclic aromatic hydrocarbons [63].

Role of fungi in polymer degradation

Marine fungi may also exhibit a significant role in the decomposition of complex organic matter in the ocean. An advanced research has shown that certain marine fungi, such as *Zalerion maritimum*, have the capacity to break down polyethylene [64]. As their sole supply of carbon, certain fungal strains use these plastic polymers to create environmentally benign carbon compounds. It has been discovered that a number of fungi may effectively and successfully break down a variety of plastic polymers. The following processes make up the biodegradation mechanism: biodeterioration, fragmentation, assimilation, and mineralization [65].

Fungi play a pivotal role in the biodegradation of polymers, as evidenced by their secretion of various enzymes including cutinase, lipase, proteases, and lignocellulolytic enzymes. They can also effectively break down plastics when exposed to specific pro-oxidant ions. Through enzymatic oxidation or hydrolysis, high molecular mass polymers undergo fragmentation into lower molecular mass polymers, leading to the introduction of functional groups that enhance polymer hydrophilicity. The quality of plastics begins to deteriorate within a short span. Specific well-known fungal species demonstrate efficient plastic breakdown, aiding in the degradation process by colonizing plastic materials. Combining photodegradation and thermo-oxidative processes with biodegradation, as suggested by multiple studies, accelerates the disintegration of plastic materials [66, 67].

Based on the literature that is currently accessible, a list of all the fungi that have been identified as degrading plastic, and remarks were made regarding the main fungal groups. In addition, 395 strains were used to analyze the evolutionary relationships of the fungus responsible for decomposing plastic. It was confirmed that polymer-decomposing fungi are found in eleven classes in the fungal phyla Ascomycota. The majority of plastic degraders in the kingdom of fungi are members of the Eurotiomycetes [68].

Although lignocellulose developed by plants is resistant to deterioration, fungi eventually learned to use it as a source of food. It may be helpful to consider the methods used to examine lignocellulose breakdown, including advanced microscopy, genomic, and post-genomic investigations (such as gene expression analysis). Based on known limits on biological lignocellulose breakdown, such as the necessity of physiochemical pretreatments for biofuel generation, potential limitations on biological plastic degradation might be expected. Although lignocellulose and plastics share many

characteristics, such as being mixtures of hydrophobic polymers with amorphous and crystalline regions and needing hydrolases and oxidoreductases to break them down, plastics differ significantly from lignocellulose in that they lack hydrolyzable C-C or C-O bonds, which gives them a higher degree of recalcitrance. Thus, the breakdown of lignocellulose by fungi can help to understand the degradation mechanism of fungi [69].

A study conducted in the vicinity of Lake Zurich in Switzerland unveiled a diverse array of fungal species thriving within the accumulated waste. Among these fungi, four saprotrophic species— namely *Cladosporium cladosporioides, Penicillium griseofulvum, Xepiculopsis graminea*, as well as a single plant pathogenic species, *Leptosphaeria* sp., exhibited the ability to degrade polyurethane. A number of different fungi that didn't grow on plastic waste were also examined. Of them, only two litter-saprotrophic fungi that can break down polyurethane were *Agaricus bisporus* and *Marasmius oreades* [70]. In a screening process, researchers utilized thirty fungal strains that had been isolated from terrestrial environments in Korea. Their objective was to assess the degradation potential of polymers such as polylactic acid (PLA) and polycaprolactone (PCL). This assessment involved observing the formation of a distinct clear zone around fungal colonies on agar plates that contained emulsified PLA or PCL. Five of them showed promising biodegradation outcomes. These were identified as *Apiotrichum porosum, Fusicolla acetilerea, Talaromyces pinophilus, Purpureocillium lilacinum,* and *Penicillium samsonianum* [71]. The printed circuit board, or PCB, is a crucial component of electronic waste. PCB is a secondary metal reservoir because of its abundant metallic content, which includes base, valuable, and poisonous metals. To safeguard the environment and preserve natural resources, PCB recycling is essential. *Aspergillus* species were used to try to bioleach certain metals from desktop PCB, The capacity of *Aspergillus niger* to produce organic acids helped in the bioleaching, which led to its selection. *Aspergillus nomius* was reported to degrade LDPE [72-74].

Role of algae in polymer degradation

Polyethylene (PE), a polymeric material produced from the basic building block ethene (C2H4), frequently obstructs sewer pipelines, agricultural land, rivers, canals, and oceans. Recently, it has been demonstrated that various algae can colonize PE surfaces using polymeric carbon and are widely accessible and relatively simple to separate. Using this group of organisms to biodegrade PE will probably help achieve a number of environmental objectives, including reducing carbon emissions and bioprospecting for products with added value. The ability to degrade PE was discovered in algae including *Anabaena spiroides, Navicula pupula, Oscillatoria subbrevis, Phormidium lucidum, Scenedesmus dimorphus* [75, 76].

In the era of plastic pollution, plants have been written off as a system that is unaffected by micro and nanoplastics, however, recent research shed light on how plastics interact with plants and explains how using plants' capacity to take up plastic particles can help get rid of plastics from water and soil systems. Due to their small size, microplastics often cannot be absorbed by plant root systems; nevertheless, some investigations suggest they may penetrate through stomata into the plant tissue while nanoparticles have been reported to travel from plant roots through the xylem to higher plant sections. However, through enzyme-facilitated breakdown processes, algae can be employed to break down polymers suspended in the water bodies [77].

Recombinant microorganisms for polymer biodegradation

Due to its intricate chemical composition, polystyrene is regarded as being both highly resistant to breakdown and non-biodegradable. The suspected enzymes that break down polystyrene come from a white-rot fungus that can break down the material. Eight *T. reesei* strains were successfully created, and the enzyme activity of the culture supernatants was checked. Several polymers had their ability to degrade tested, and gas chromatography-mass spectrometry and high-performance liquid chromatography were used to find degradation products. Although biodegradation was not observed with these recombinant strains, it was a stepping stone for further research [78].

Recently, a potential PETase-like enzyme called *Ideonella sakaiensis*PETase (IsPETase) has been discovered for entirely depolymerizing this polymer into its constituent parts. Three changes in the IsPETase active site were identified to increase its PET-degrading activity, based on the structure of cutinases and lipases being similar to the IsPETase 3D structure. The S238Y mutant which is close to the catalytic triad, had a 3.3-fold higher degrading activity than the wild-type enzyme. It's significant to note that this structural alteration boosted the enzyme's ability to degrade highly crystallized (around 31%) PET, which is used in commercial soft drink bottles. Additionally, a microscopic examination revealed that IsPETase works better under mechanical stress on the substrate surface.

These findings signify a significant step forward in the pursuit of a comprehensive and sustained degradation of PET contamination [79].

Insufficient soluble expression level of *Ideonellasakaiensis*PET hydrolase (IsPETase) prevents its efficient use in the biodegradation of PET. A variety of approaches were used to methodically investigate the IsPETaseMut, an active mutant of IsPETase ever discovered, expressed itself in *E. coli.* The higher product formation caused by NusA-IsPETaseMut PET decomposition over two weeks is more likely to be a result of the latter two catalytic qualities of the enzyme when combined. By combining the two mutations, IsPETaseS121E/D186H/S242T/N246D variant was created. Contrary to IsPETaseWT, which lost activity within a day at 37 °C, the quadruple version kept PET degradation activity going for 20 days. As a result, the activity was 58 times higher than it was for IsPETaseWT [80, 81]. To aid in a better understanding of the involvement of microorganisms, genes, enzymes, and biodegradation pathways in plastic mineralization, a thorough appraisal of the biotechnological and molecular development in plastic biodegradation is required [82]. Environmental safety is a prime concern for scientists globally. Through the use of living organisms, such as bacteria, fungi, and plants, bioremediation processes can efficiently break down and remove various contaminants from soil, water, and air. Nowadays research is also focusing on the development of alternative materials of nonbiodegradable polymers. Recently, biocarbon (BC) has come to be recognized as a sustainable filler for polymer nanocomposites made from biomass. The in-question nanocomposites have prospective uses in energy storage, heat-resistant coatings, and electrical conductivity [82]. Through value addition, pea peel waste has been effectively used to create biodegradable film. The latter showed good surface thickness, water solubility, and tensile strength. Therefore, a biodegradable film may replace synthetic plastic with the benefits of recovering energy, and contributing to a sustainable environment and development [83].

CONCLUSION

In conclusion, bioremediation is a strong and effective strategy for protecting the environment and eradicating pollution. A sustainable method, bioremediation, uses natural processes to break down contaminants. It decreases the need for dangerous chemicals and the production of extra trash. Bioremediation frequently turns out to be more affordable than conventional clean up techniques. It may be used for a variety of environmental cleaning operations since it uses fewer resources and can be scaled up. Numerous contaminants, including hydrocarbons, heavy metals, pesticides, and other dangerous compounds, can be treated *via* bioremediation. Due to its versatility, different forms of pollutants may be addressed in specialized ways. Table 1 summarizes some of the polymer-degrading microorganisms isolated from different sources, and the types of polymers they are degrading.

In addition to removing contaminants, bioremediation can enhance ecosystems' general health. The regenerated habitat may thrive with increasing biodiversity when natural microorganisms are used. Bioremediation helps to improve public health, lower exposure to dangerous compounds, and avert potential long-term health problems by removing contaminants from polluted locations. By helping to comply with legal requirements and international obligations to reduce pollution, bioremediation is in line with the concepts of sustainable development and environmental conservation.

Challenges

However, significant obstacles still stand in the way of the practical use of bioremediation. The particular circumstances that each contaminated site provides might determine how effective bioremediation is. For best outcomes, specific procedures and thorough site analyses are required. It may take persistence for bioremediation to be effective because it is sometimes a lengthy process. To get the intended result in some situations, additional methods or long-term monitoring may be required. It is essential that the public be made aware of and comprehend the advantages and safety of bioremediation. To increase confidence in this environmentally beneficial method, clear communication and education are required.

In spite of these difficulties, bioremediation is nevertheless a useful tool for the effort to create a cleaner and healthier environment. We can maximize the potential of bioremediation by continuously developing research, using technical advancements, and encouraging cooperation between researchers, policymakers, and communities.

Table 1. A list of polymer-degrading microorganisms.

Microorganisms	Source	Polymer	Ref.
Bacteria			
BrevundimonasSphingobacterium		Polylactide (PLA), Poly (butylene adipate-co-terephthalate) (PBAT)	[10]
Bacillus sp., Rhodococcus sp., Pseudomonas sp., Staphylococcus sp., Arthrobacter sp., Microbacterium sp., Phanerochaetesp	Plastic dumping yard	Polypropylene (PP), Low-density and linear low-density polyethylene (LDPE, LLDPE), Polyvinyl chloride (PVC), High-density polyethylene (HDPE), Polystyrene (PS), Expandable PS (EPS), Polyethylene terephthalate (PET)	[16], [19]
Acidicaldus,Granulicella, Povalibacter	Copper Slag Deposit	Polyvinyl alcohol	[22]
Bacillus amylolyticus, Bacillus firmus, Pseudomonas putida, Pseudomonas fluorescence	Garbage soil	Low-density polyethylene	[23]
Pseudomonas sp., Bacillus sp.	Digester Sludge	PLA	[24]
Klebsiella pneumonia, Pseudomonas aeruginosa, Micrococcus sp, Bacillus sp., Arthobacter sp., Pseudomonas sp.	Plastic dumpsites	Low-density polyethylene (LDPE)	[25], [26], [27], [28]
Pseudomonas sp., Bacillus sp.Lysinibacillus sp.	Culture	PET, PHB, Cellophane	
Priestia megaterium strains, Klebsiella pneumoniae, Pseudomonas fluorescens, Enterobacter ludwigii, Chryseobacterium sp. Fusarium spp., two *Lecanicillium spp., Trichoderma*	Wasteland	Polyethylene (PE)	[40]
Serratia marcescen sEnterobacter spp.) Aspergillus spp. ,Fusarium oxysporum, Penicillium granulatum	Wasteland	Polypropylene (PP)	[40]
Pseudomonas chlororaphis, Pseudomonas alcaliphila, Pseudomonas mendocina, Pseudomonas oleovorans	Forest Soil	Polyhydroxyalkanoates (PHAs), polylactic acid (PLA), and Para-nitrophenyl (pNP) alkanoates, Poly (-caprolactone) (PCL) Polyethylene succinate (PES)	[41], [42]
Acinetobacter sp., Escherichia coli, Brevibacillus sp.	Industrial Effluent	Maleic acid propane-1, 2 diol glycerol co-polyester, Maleic acid phthalic acid propane-1, 2 diol glycerol co-polyester, Maleic acid phthalic acid butan-1	[43]
Bacillus cereus, Bacillus megaterium	Landfills	Polycarbonate (PC)	[44]
Ideonellasakaiensis	Soil from Sakai City	Polyethylene terephthalate (PET).	
Alcanivoraxdieselolei	Washed rind cheese	Poly(3-hydroxybutyrate) (P(3HB))	[62]
Bacillus circulans, Enterococcus faecalis, Microbacteriumzaea, ExiguobacteriumaestuariiAgrobacterium sp., Sphingomonaspseudosanguinis, Sphingobiumyanoikuyae Acinetobacter radioresistens	Greater wax moth gut	Low-density polyethylene, 2-methyl phenanthrene, Polycyclic aromatic hydrocarbons	[63]
Fungi			
Aspergillus nidulans, A. flavus, A. glaucus, A. oryzae, A. nomius, Penicillium griseofulvum, Bjerkanderaadusta,	Marine plasisphere	Plastics	[66], [67]

|			
Phanerochaetechrysosporium, Cladosporium cladosporioides, Pleurotus abalones, P. ostreatus, P.eryngii, Agaricus bisporus			
Ascomycota, Mucoromycota		Plastics	[68]
Cladosporium cladosporioides, Xepiculopsisgraminea, Penicillium griseofulvumLeptosphaeria sp Agaricus bisporusMarasmiusoreades	Plastic waste	Polyurethane	[70]
Apiotrichumporosum, Fusicollaacetilerea, Talaromycespinophilus, Purpureocilliumlilacinum, Penicillium samsonianum	Terrestrial settings in Korea	Polymers polylactic acid (PLA), Polycaprolactone (PCL)	[71]
Aspergillus nomius	Culture	Low-density polyethylene (LDPE)	[74]
Algae			
Sargassum, Ulva, Padina, Dictyota, and Pterocladia sp.	Water bodies	Cellulose, Pectin, Xylan, Starch	[20]
Phormidium lucidum, Oscillatoria subbrevis, Scenedesmus dimorphus, Anabaena spiroides, Navicula pupula	Culture	Polyethylene (PE)	[75], [76]
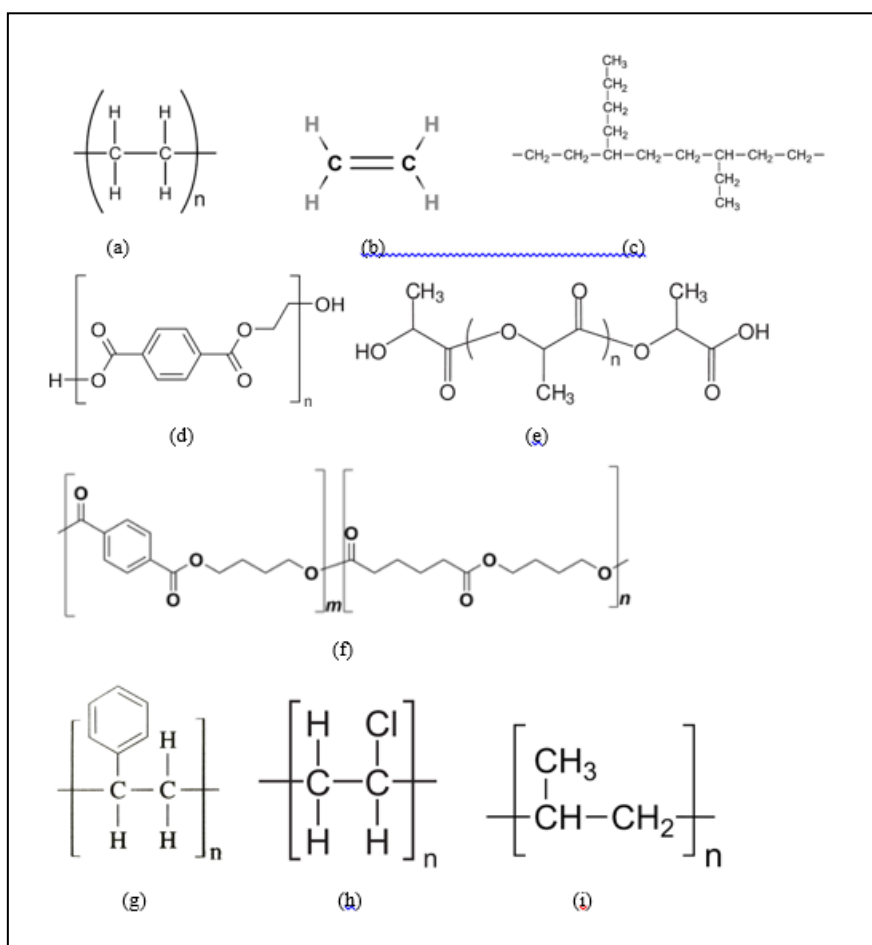
Fig. 1. Molecular structures of few polymers polluting the planet. a) Polyethylene (PE), b) Low-density polyethylene (LDPE), c) High-density polyethylene (HDPE), d) Polyethylene terephthalate (PET), e) Polylactide (PLA), f) Poly (butylene adipate-co-terephthalate) (PBAT), g) Polyurethane, h) Polyvinyl chloride) i) Polypropylene (PP)

REFERENCES

1. J. A. Verschoor, H. Kusumawardhani, A.F. Ram, J. H. de Winde, *Front. Microbiol.*, **13**, 821629 (2022).

2. N. Bostan, N. Ilyas, N. Akhtar, S. Mehmood, R.U. Saman, R.Z. Sayyed, S. Pandiaraj, *Env. Res.*, 116523 (2023).

3. Y. Zhou, M. Kumar, S. Sarsaiya, R. Sirohi, S. K. Awasthi, R. Sindhu, M. K. Awasthi, *Sci. Total Environ.,* 802, (2022).

4. S.S. Ali, T. Elsamahy, E. Koutra, M. Kornaros, M. El-Sheekh, E. A. Abdelkarim, J. *Sci. Total Environment*, **771,** 144719 (2021).

5. A. Amobonye, R. Bhagwat, S. Singh, S. Pillai, *Sci. Total Env.*, **759**, 143536 (2021).

6. N. Delangiz, S. Aliyar, N. Pashapoor, K. Nobaharan, B. A. Lajayer, S. Rodríguez-Couto, *Chemosph.*, **294**, 133709 (2022).

7. Y. Ji, Lu, Y. H. Puetz, U. Schwaneberg, *Methods in Enz.,* **648,** 271 (2021).

8. A. Elahi, D. A. Bukhari, S. Shamim, A. Rehman, *J. of King Saud Uni.-Sci.*, **33**(6), 101538. (2021).

9. Z. Cai, M. Li, Z. Zhu, X. Wang, Y. Huang, T. Li, M. Yan, *Microorg.*, **11**(7), 1661 (2023).

10. W. Peng, Z. Wang, Y. Shu, F. Lü, H. Zhang, L. Shao, P. He, *Biores.Tech.*, **343**, 126079 (2022).

11. L. Apitius, K. Rübsam, C. Jakesch, F. Jakob, U. Schwaneberg, *Biotch Bioeng.*, **116**(8), 1856 (2019).

12. Y. Ji, Y. Lu, H. Puetz, U. Schwaneberg, *Methods in Enz.,* **648,** 271 (2021).

13. L. Niu, Y.Li, Y. Li, Q. Hu, C. Wang, J. Hu, H. Zhang, *Water Res.*, **188,** 116449 (2021).

14. Q. A. Da, G. L. Lei, C. J. Yao, X. H. Qu, C. C. Chu, *Int. Field Explor. Devel.Conf.* 141 (2021).

15. T. Grivalský, J. Rychlý, L. Rychlá, M. Bučková, L. Kraková, A. Puškárová, D. Pangallo, *J. of Polym. Env.*, **26**, 680 (2018).

16. A. Sharma, V A. Nampoothiri Devadas, P. P. Nair, C. Manpoong, B. D. Kartha, *Curr.Green Chem.*, **9**(1), 3 (2022).

17. A. P. Asiandu, A. Wahyudi, S. W. Sari, *J. of Env. Treat.Tech.*, **9**(1), 148 (2021).

18. S. Dey, A. K. Rout, B. K. Behera, K. Ghosh, *Env. Microb.*, **17**(1), 1 (2022).

19. I. Wojnowska-Baryła, K. Bernat, M. Zaborowska, *Int. J. of Env. Res. and Pub.Health*, **19**(20), 13223 (2022).

20. P. Kumar, A. Verma, S. S. Sundharam, A. K. Ojha, S. Krishnamurthi, *Microorg.*, **10**(12), 2513 (2022)

21. R. Sarkhel, S. Sengupta, P. Das, A. Bhowal, *J. of Polymer Res.*, **27,** 1(2020).

22. J. M. Köhler, N. Beetz, P. M. Günther, F. Möller, J. Cao, *Microorg.*, **9**(7), 1422 (2021).

23. R. C. Patil, *J. Env. Sci.*, **6**(4), 33 (2018).

24. N. ISLAM, J. O. Geonwoong, J. U. N. G. Sokhee, *Proceeding KSBB Spring Meeting and Int. Symposium* 2023.

25. M. Yadav, S. Manderia, S. Singh, M. Deva, *Nature Env. Poll. Tech.*, **21**(1) (2022).

26. R. Naaz, W.A. Siddiqi, *Polym.Biomater. Bioeng.*, **87** (2022).

27. P. Satheeshkumar, M. Gopal, *Int. J. Mech.Eng.*, **6,** 981 (2021)

28. M., Wróbel, S. Szymańska, T. Kowalkowski, K. Hrynkiewicz, *Microbiol. Res.*, **267**, 127251 (2023).

29. A. Satlewal, R. Soni, M.G.H. Zaidi, Y. Shouche, R. J. Goel,*J. of Microb. Biotech.*, **18**(3), 477 (2008).

30. A. Kapri, M. G. H. Zaidi, A. Satlewal, R. Goel, *Int. Biodet.Biod..*, **64**(3), 238 (2010).

31. R., Soni, A. Kapri, M. G. H. Zaidi, R. Goel, *J.Biol. Biotech.,* **20**(6), 1032 (2010).

32. A. Kapri, M. G. H. Zaidi, R Goel, R. *J. of Microb. Biotech.*, **20**(6), 1032 (2010)

33. A. Sah, A. Kapri, M. G. H. Zaidi, H. Negi, R. Goel, *J. of Microbio. Biotech.***20**(5), 908 (2010).

34. S. Raghuwanshi, M. G. H. Zaidi, S. Kumar, R. Goel, *J. of Polym. Env.*, **26**, 2661 (2018).

35. P. Debbarma, D. C. Suyal, M. G. H. Zaidi, A. Yadav, Y. Shouche, R. Goel, *Res.Sq.*, (2022).

36. R. Goel, P. Jayal, H. Negi, P. R. Saravanan, & M. G. H. Zaidi, *Int. J. of Env. Waste Manag.*, **13**(4), 348 (2014).

37. S. Raghuwanshi, T. Agarwal, A. Yadav, M. G. H. Zaidi, Y. Shouche, R. Goel,*Chem. Ecol.*, **32**(6), 583 (2016).

38. P. Debbarma, S. Raghuwanshi, J. Singh, D. C. Suyal, M. G. H. Zaidi, R. Goel, *3Biotech***7** (178), 1 (2017).

39. N. Atanasova, S. Stoitsova, T. Paunova-Krasteva, M. Kambourova, *Int. J. Mol.Sci.*, **22**(11), 5610 (2021).

40. N. Mohanan, C. H. Wong, N. Budisa, D. B. Levin, *Front. Bioeng. Biotechnology.*, **10**, 854298 (2022).

41. N. Mohanan, C. H. Wong, N. Budisa, D. B. Levin, *Int. J. of Molecular Sci*, **24**(5), 450 (2023).

42. S. Zhou, Y. Wang, H. Xia, D., Liu, S. Chen, F. Li, *Int. J. of Systematic and Evolutionary Microbiology*, **70**(5), 3049 (2020).

43. S. Akther, G. K. Paul, S. Mahmud, M. S. Hossain, M. A. Saleh, S. Zaman, M S. Uddin, *Adv. Biotechnology Exp. Ther*, **5,** 487 (2022).

44. M. Arefian, A. Tahmourespour, M. Zia, *Archives of Env. Protection*, **46**(1), 14 (2020).

45. G. J. Palm, L. Reisky, D. Böttcher, H. Müller, E. A. Michels, M. C. Walczak, G. Weber, *Nature Communications,* **10**(1), 1717 (2019).

46. R. P. Magalhães, H. S. Fernandes, S. F. Sousa, *Catalysis Science and Technology*, **12**(11), 3474 (2022).

47. S. I. Hachisuka, T. Nishii, S. Yoshida, *Applied and Env.Microbiology*, **87**(18), (2021).

48. M. H. Weiland, *Mechanistic Enzymology: Bridging Structure and Function.* Bridging Structure and Function 161 (2020).

49. J. S. Poulsen, J. L. Nielsen, *J. of Proteomics*, **279**, 104888 (2023).

50. H. F. Son, I. J. Cho, S. Joo, H., Seo, H. Y. Sagong, S. Y. Choi, K. J. Kim, *ACS Catalysis*, **9**(4), 3519 (2019).

51. B. Alfieri, M. Alfieri, M. Kelly, S. Kilcoyne, L. Poprik, A. Sanyal, J. Pousont, *FASEB*, 36 (2022).

52. C. Liu, C. Shi, S. Zhu, R. Wei, C. C. Yin, *Biochemical and Biophysical Research Commu.*, **508**(1), 289 (2019).

53. W. Maity, S. Maity, S. Bera, A. Roy, *Applied Biochemistry and Biotechnology*, **193**, 2699 (2021).
54. Q. Yin, S. You, J. Zhang, W. Qi, R. Su, *Bioresource Technology*, **364**, 128026 (2022).
55. S. Yoshida, K. Hiraga, I. Taniguchi, K. Oda, *Methods in Enzymology*, **648**, 187 (2021).
56. H. Seo, S. Kim, H. F. Son, H. Y. Sagong, S. Joo, K. J. Kim, *Biochemical and Biophysical Research Commun.*, **508**(1), 250 (2019).
57. Y. Joho, V. Vongsouthi, M. A. Spence, J. Ton, C. Gomez, L. L. Tan, A. Ardevol, *Biochemistry*, **62**(2), 437 (2022).
58. S. Feng, Y. Yue, M. Zheng, Y. Li, Q. Zhang, W. Wang, *ACS Sustainable Chemistry and Eng.*, **9**(29), 9823 (2021).
59. H. Y. Sagong, H. F. Son, H. Seo, H. Hong, D. Lee, K. J. Kim, *J. of Hazardous Materials*, **416**, 126075 (2021).
60. H. Y. Sagong, H. Seo, T. Kim, H. F. Son, S. Joo, S. H. Lee, K. J. Kim, *ACS Catalysis*, **10**(8), 4805 (2020).
61. I. Karunatillaka, L. Jaroszewski, A. Godzik, *Proteins*, **90**(2), 504 (2022)
62. Y. Tachibana, K. Kageyama, M. Suzuki, H. Koshigumo, H. Takeno, Y. Tachibana, K.I. Kasuya, *Polymer Degradation and Stability*, 160, 264 (2019).
63. S. S. Saikia, B. K. Borah, G. Baruah, Rokozeno, M. K. Deka, *Folia Microbiologica*, **67**,133 (2022).
64. E. Zeghal, A. Vaksmaa, H. Vielfaure, T. Boekhout, H. Niemann, *Frontiers in Marine Science*, **8,** 738877 (2021).
65. S. Varshney, V. Gupta, A. N. Yadav, R. K. Rahi, D. K. Neelam, *J. of Applied Biology and Biot.*, **11**(3), 61 (2023).
66. M. Srikanth, T. S. R. S. Sandeep, K. Sucharitha, S. Godi, *Biores. Bioprocessing*, **9**(1), 42 (2022).
67. Y. Du, X. Liu, X. Dong, Z. Yin, *Comput. Struct.Biotech.*, **20,** 975 (2022).
68. A. H. Ekanayaka, S. Tibpromma, D. Dai, R. Xu, N. Suwannarach, S. L. Stephenson, S. C. Karunarathna, *J. of Fungi*, **8**(8), 772 (2022).
69. P. Daly, F. Cai, C.P. Kubicek, S. Jiang, M. Grujic, M.J. Rahimi, I. S. Druzhinina, *Biotechnology Advances*, **50**, 107770 (2021).
70. I. Brunner, M. Fischer, J. Rüthi, B. Stierli, B. Frey, *PLOS ONE*, **13**(8) (2018).
71. S. K. Lee, L. N. Ten, K. Das, Y. H. You, H. Y. H. Y. *Mycobiology*, **49**(3), 285 (2021).
72. A. Trivedi, S. Hait, *Energy, Environment, and Sustainability, Springer*, 271 (2020).
73. M. Osman, S. M. Satti, A. Luqman, F. Hasan, Z. Shah, A. A. Shah, *J. of Polymers and the Env.*, **26,** 301 (2018).
74. E. Munir, R. S. M. Harefa, N. Priyani, D. Suryanto, *Earth and Env.Sco., IOP Conf. Ser.* **126** (1) 012145, (2018).
75. P. Sarmah, J. Rout, *Advances in Cyanobacterial Biology*, 333 (2020).
76. W. Y. Chia, D. Y. Y. Tang, K. S. Khoo, A. N. K. Lup, K. W. Chew, *Env. Sci. and Ecotechnology*, **4,** 100065 (2020).
77. E. Karalija, M. Carbó, A. Coppi, I. Colzi, M. Dainelli, M. Gašparović, F. Martinelli, *J. Hazard. Mater.***438**, 129450 (2022).
78. D. C. La Grange, I. S. Pretorius, M. Claeyssens, W. H. Van Zyl, *Applied and Env. Microbiology*, **67**(12), 5512 (2001).
79. M. E. Sevilla, M. D. Garcia, Y. Perez-Castillo, V. Armijos-Jaramillo, S. Casado, K. Vizuete, L. Cerda-Mejía, *Polymers*, **15**(7), 1779 (2023).
80. L. Aer, Q. Jiang, I. Gul, Z. Qi, J. Feng, L. Tang, *Env. Research*, **212**, 113472 (2022).
81. H. F. Son, S. Joo, H. Seo, H. Y. Sagong, S. H. Lee, H. Hong, K. J. Kim, *Enzyme and Microbial Tech.*, **141,** 109656 (2020).
82. A. Priya, K. Dutta, A. Daverey, *J. of Chemical Tech. & Biotech.*, **97**(2), 381 (2022).
83. L. Liu, M. Xu, Y. Ye, B. Zhang, *Science of the Total Env.*, **806,** 151312 (2022).
84. R. Saleheen, M. G. H. Zaidi, S. Mehtab, K. Singhal, *Renewable Energy for Sust.Growth Ass.*, **305** (2022).
85. D. V. Upasana, M. G. H. Zaidi, A. K. Shukla, *Pharm. Innov.***11**(6), 2396 (2022).

Comparative study on the electrochemical performance of PPY/GO binary and PPY-GO/ZnO ternary nanocomposites

G. Singh, Nisha, A. Kumar, H. Mudila*

Department of Chemistry, Lovely Professional University, Phagwara, Punjab-144411, India

PPY/GO binary nanocomposites (PGs) and PPY-GO/ZnO ternary nanocomposites (PGZs) as electrode material were synthesized *via* the *ex-situ* method. The PGs, prepared by varying the proportions of GO (%w/w) in PPY, were characterized by FTIR, XRD, TGA, and electrochemical measurements. The PGs were analyzed by cyclic voltammetry (CV) for their electrochemical performance. The binary composite (PG5) having the highest specific capacitance (Cs=391.3 F/g) value was preferred for the preparation of ternary composites, i.e., PGZs with ZnO in different ratios (%w/w) by the *ex-situ* method. The highest specific capacitance of 352.1 F/g was obtained for PGZ-1 at 1 mV/s which is lower than for its binary counterpart (PG5) but was higher than those of ZnO, PPY, and GO. The incorporation of GO has enhanced the electrochemical performance of PGs, however, the encapsulation of ZnO in PG was found to decrease the electrochemical response of PGZs. The result suggested this to occur due to the disorder caused in the PPY chains by ZnO.

Keywords: Conducting polymer; Composites; Capacitance; Graphene oxide; Transition metal oxide, Clean energy.

INTRODUCTION

Conventional energy sources are largely employed to encounter the need for the energy required in various aspects of life. The use of these energy sources at a tremendous rate is the major contributor to climate changes such as air pollution, global warming, etc. [1]. To overcome these issues there is a great need to develop energy techniques that are readily available and environmentally friendly. Among the various energy sources, electrochemical supercapacitors are considered the potent candidates widely used in power inventors, electrochemical actuators, power supplies, etc. The mechanism of charge storage in supercapacitors is based on (a) electrochemical double-layer capacitors (EDLC) or (b) fast and reversible redox reactions that take place on the interface of electrodes and electrolytes (pseudo capacitors) [1, 2]. Various types of electroactive material, *viz*., carbonaceous material, conducting polymers (CPs), and transition metal oxides (TMOs) are employed as the electrode material in supercapacitors. CPs are appropriate as an electrode because of their high porosity, storage ability, and reversibility but they lack cyclic stability and slow charging-discharging rate. These drawbacks can be improved by entering structural changes in CPs by hybridizing them with other electroactive materials [2-4]. CPs with carbonaceous material like graphene oxide (GO) show a synergetic effect and produce an electrode with high capacitance behavior [5].

TMOs having pseudo capacitive behavior act as a filler between the CPs and carbonaceous material that may improve the electrolyte-electrode interaction resulting in the fast diffusion of ions and hence improving the capacitive behavior of the electrode material [3, 6]. However, some studies show a decrease in performance with the addition of TMO in the matrix [4]. Nowadays a variety of CPs (polypyrrole, polyaniline, etc.) are hybridized with carbonaceous material (GO, rGO, etc.), and TMOs (ZnO, V_2O_5, and others) to form ternary composites used in supercapacitors for the storage of the electrochemical energy [7, 8]. This work presents the fabrication of PPY/GO binary nanocomposites (PGs) and PPY-GO/ZnO ternary nanocomposites (PGZs). The as-fabricated PGs and PGZs were further studied for their electrochemical performance by cyclic voltammetry (CV).

MATERIALS AND METHODS

Materials

Monomer pyrrole (PY, >99%, Spectrochem), graphite powder, potassium permanganate ($KMnO_4$), sulfuric acid (H_2SO_4), hydrogen peroxide (H_2O_2), and hydrochloric acid (HCl) were acquired from Loba Chemie. Ferric chloride ($FeCl_3$), and PVDF (polyvinylidene fluoride) were from Sigma Aldrich, N- cetyl -N, N, N- trimethyl ammonium bromide (CTAB), and ascorbic acid were obtained from S D Fine Chem. Ltd.

---

* To whom all correspondence should be sent:
E-mail: harismudila@gmail.com

Preparation of polypyrrole (PPY) and graphene oxide (GO)

Polypyrrole (PPY) was prepared by the chemical oxidative polymerization method mentioned by Mudila *et al. 2013* which involves the use of pyrrole monomer, CTAB surfactant solution, and freshly prepared oxidant solution of $FeCl_3$ [7]. The preparation of GO was carried out by the modified Hummers method as mentioned by Song *et al. 2014* [9].

Preparation of polypyrrole/graphene oxide (PG) binary composites

The preparation of PPY/GO composite in different ratios (wt %, in mg) was carried out by the *ex-situ* method. Requisite amounts of PPY and GO were taken in ethanol (Table 1) followed by mechanical mixing through sonication for 30 minutes to acquire homogeneity. The resultant mixture was then dried in an oven at 60°C.

Table 1. Corresponding ratio, amount, and names of PPY and GO composites

Material	Ratio					
	1: ¼	1: 1/2	1: 3/4	1: 1	1: 2	1: 3
PPY (mg)	100	100	100	100	100	100
GO (mg)	25	50	75	100	200	300
Composite Name (PG)	PG1	PG2	PG3	PG4	PG5	PG6

Preparation of PPY-GO/ZnO (PGZ) ternary composite

Like the method followed for preparation of PGs, the PGZ was prepared (Table 2) with requisite amounts of PPY/GO and ZnO.

Table 2. Corresponding ratio, amount, and codes of PG (PPY-GO) and ZnO composites

Material	Ratio					
	1: 1/4	1: ½	1: 3/4	1: 1	1: 2	1: 3
PPY/GO (mg)	100	100	100	100	100	100
ZnO (mg)	25	50	75	100	200	300
Compos ite name (PGZ)	PGZ 1	PGZ 2	PGZ 3	PGZ 4	PGZ 5	PGZ 6

Preparation of the working electrodes

Electroactive material (0.05 g), and graphite (0.005 g) were mixed with the binder solution (PVDF in NMP, 5 g/dL), followed by ultra-sonication for 30 minutes and then applied on 1 cm^2 area of stainless steel (304-SS) sheet which was allowed to dry in a vacuum oven for 2 hours at 100°C. This SS sheet with a mass thickness of ~0.01 g on its surface functions as a working electrode [1, 9].

RESULTS AND DISCUSSION

FTIR Spectra

FTIR spectra of the samples were recorded in the range of 400-4000 cm^{-1} (Fig. 1 (a-e)). In the FTIR spectra of PPY the bands at 1631, 1543, and 1415 cm^{-1} are due to stretching of C=N, C=C, and C-N bonds. A broad band at 3300-3500 cm^{-1} is due to stretching of N-H bond. The bands at 1039 cm^{-1}, 1300 cm^{-1} and 884 cm^{-1} are due to in-plane and out-of-plane deformation of C-H, C-N and C-H bonds. (Fig. 1a) [10, 11]. In the case of GO, the band at 3272 cm^{-1} corresponds to O-H stretching. The vibrations at 1714 and 1585 cm^{-1} are due to the carbonyl (C=O) and aromatic C=C bonds, respectively. The bands due to stretching of epoxy (C-O-C) and alkoxy (C-O) take place at 1225 and 1045 cm^{-1} (Fig. 1b) [9]. In the FTIR spectrum of PG (Fig. 1c), the peak due to C=O stretching appears at 1705 cm^{-1} which has been shifted towards the lower wavenumber as compared to the same peak of GO. This shifting of the C=O peak may be due to interaction (H-bonding) between the carbonyl (C=O) group of GO and the N-H group of PPY. The bands at 2979 and 1038 cm^{-1} are due to stretching of O-H and epoxy (C-O-C) bonds of GO. The peaks at 1558 and 1210 cm^{-1} are ascribed to the C=C and C-N stretching of the PPY ring confirming the presence of PPY in PG composites [12, 13].

FTIR spectra of ZnO (Fig. 1d) show the vibrational mode of ZnO at 560 cm^{-1} [14]. The FTIR spectra of the PGZ composite (Fig. 1e) reflect the characteristic peaks of its individual components with some shifting in peak positions and peak intensities. The peak at 1708 cm^{-1} is due to C=O stretching. The shifting of the C=O peak in the case of PGZ may be due to interaction between the carbonyl (C=O) group of GO and the N-H group of PPY. The bands at 3126 and 1059 cm^{-1} are due to stretching vibrations of O-H and epoxy (C-O-C) bonds of GO. The absorption bands at 1562 and 1130 cm^{-1} are ascribed to the C=C and C-N stretching of the PPY ring which further confirms the presence of PPY in PGZ composites. The absorption band at 896 cm^{-1} due to ZnO in PGZ suggests the presence of ZnO in composite material [3, 12-14].
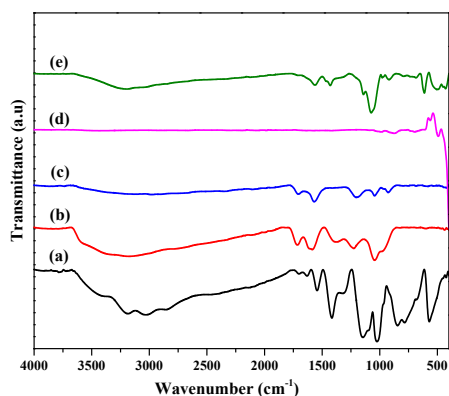
Fig. 1. FT-IR of (a) PPY, (b) GO and (c) PG (d) ZnO (e) PGZ

XRD spectra

The XRD spectra of graphite, PPY, GO, and PG are shown in Fig. 2 (a-f). The XRD spectra of PPY show a broad peak at $2\theta=27.52°$ with interplanar spacing (d spacing) of 0.33 nm suggesting its amorphous nature (Fig. 2b) [4, 10]. The XRD pattern of graphite shows a sharp and intense peak at $2\theta=26.38°$ with spacing (d=0.35 nm) indicating well-defined ordered arrangements of graphite layers (Fig. 2a). GO shows a peak at $2\theta = 10.91°$ with d spacing 0.85 nm (Fig. 2c). The increase in the gallery spacing in case of GO as compared to graphite is ascribed to the encapsulation of oxygen moieties between the carbon layers of GO [7, 15]. The spectra of PG composites show two peaks at $2\theta = 11.89^0$ due to GO and $2\theta = 23.53°$ due to PPY (Fig. 2d). These peaks signify the integration of GO layers over PPY amorphous nature of composites. [7, 12, 16]. In the XRD spectra of ZnO (Fig. 2e) the peaks at 31°, 34°,36°, 47°, 56°, 63° and 72° signify its crystal behavior. In the XRD spectra of PGZ, Fig. 2f, the peaks of PPY and GO are shifted and the intensity of the peaks increases with the increase of ZnO content suggesting an interaction between the three components in the composite material, which enhances the electrochemical stability of the ternary composite. [15, 17-19]

Thermal analysis

TGA curves of PPY, GO, PG, and PGZ are shown in Fig. 3 (a-e) below. Initially the weight loss at a temperature < 100 °C is due to the removal of moisture content in the prepared samples. In case of PPY the weight loss starts at TG onset of 207 °C with residual weight (W_r %) of 79.22. The weight loss of PPY continuously increases as the temperature rises and it ends at a TG offset of 595 °C indicating the volatilization of PPY (Fig. 3a). In case of GO the weight loss takes place at TG onset 187 °C with W_r % of 76.26 and ends at TG offset of 340 °C. This loss is mainly due to the removal of oxygen functionalities from the surface of GO (Fig. 3b). [8, 12]. In PG the weight loss at 150-170 °C is probably due to the removal of oxygen-containing moieties. The major weight loss in PG after 230 °C arises due to the degradation of PPY from the composite (Fig. 3c). [8, 20]. In the TGA curve of ZnO, the weight loss is due to the removal of moisture content (Fig. 3d) [14]. In case of PGZ, Fig. 3e, the weight loss at TG onset 212 °C and 348 °C is due to the removal of oxygen-containing functional groups and the degradation of the polymer chain from the surface of the composite material. The interaction between PPY and GO functionalities along with the barrier effects of ZnO imparts additional stability to the PGZ in comparison to PPY and GO [14, 21]
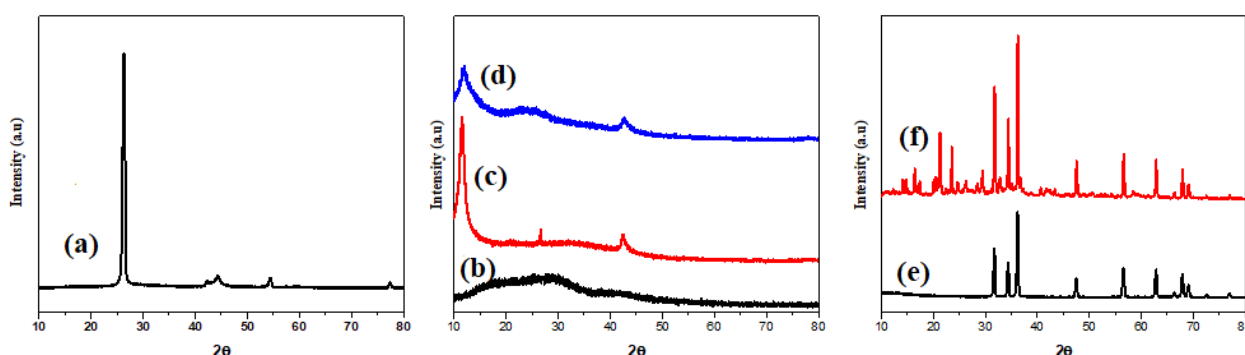

Fig. 2. XRD of (a) graphite (b) PPY, (c) GO (d) PG5 (e) ZnO (f) PGZ1
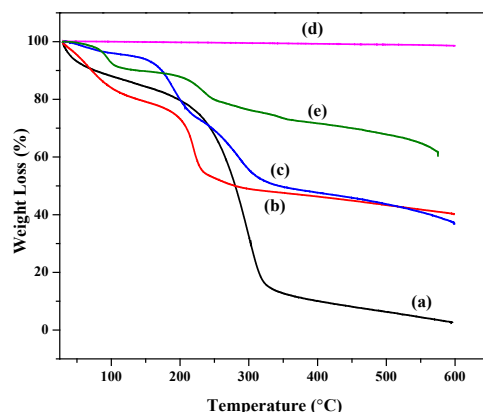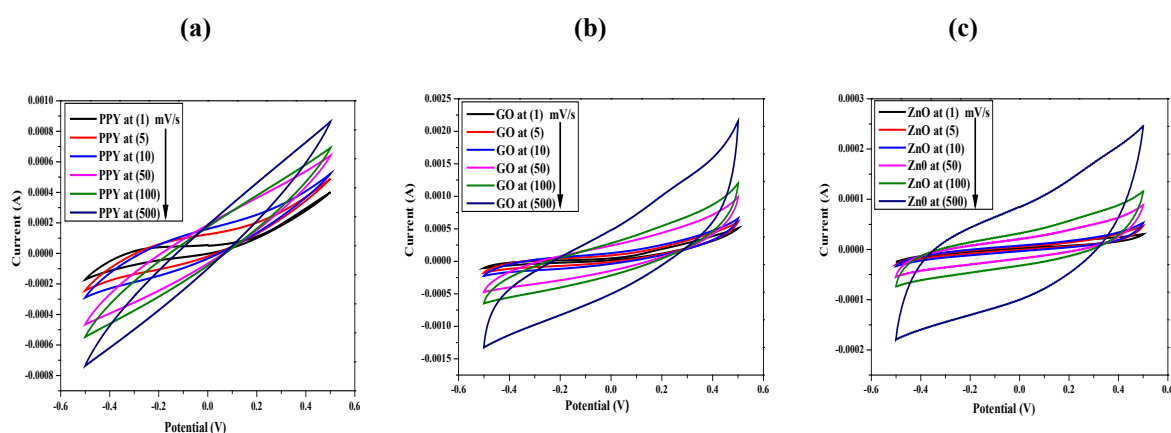
Fig. 3. TGA of (a) PPY (b) GO (c) PG5 (d) ZnO (e) PGZ1

(a) **(b)** **(c)**

Fig. 4. CV curves of (a) PPY (b) GO (c) ZnO at different scans.

Table 3. Cs values of PPY, GO and ZnO at different scans

Scan mV/s	Cs Values		
	PPY	GO	ZnO
1	102.2	233.0	69.2
5	43.9	121.9	28.1
10	27.6	53.3	11.3
50	16.1	26.1	4.5
100	4.1	8.4	2.2
500	2.0	4.3	1.3

Electrochemical measurement of PPY, GO, and ZnO

ZnO, an *n*-type semiconductor, was found to have much lower Cs as compared to PPY and GO. This may be attributed to the bandgap of ZnO which has been reported to be higher (3.2 eV) as compared to PPY (3.0 eV) and GO (2.2 eV). This higher bandgap of ZnO probably reduces the chances of movement of an electron from the valence to the conduction band. Also, the chances of agglomeration in the case of ZnO can reduce the probability of higher Cs by reducing the surface area (Table 3). [22-23].

Electrochemical measurements

The CV curves of PPY, GO, ZnO, PGs, and PGZs were recorded within the potential window of -0.5 to 0.5V at different scan rates in 1 M KOH electrolytic solution as mentioned earlier [6, 12].

A regular increase in the peak current values with scan rates within the potential window for individual components i.e., PPY, GO, and ZnO, was observed [7]. The low Cs value of PPY is due to its compact structure which does not allow the diffusion of counter-ion readily into its internal matrix. GO gives higher Cs due to increased surface area, porous structure, and large interlayer gaps which makes the

diffusion more feasible as compared to the PPY chains [12, 22].

Electrochemical measurement of PGs

The Cs value of PGs increases with an increase in the amount (%w/w) of GO up to a certain limit and then decreases with the addition of GO in the composite material at all scans (Fig. 5a). This decrease may be due to the assemblage of GO layers with PPY on further addition of GO that results in the decrease of the active surface area of the composite and increase in the resistance that hindered the diffusion of ions on its surface. Therefore, the right amount of GO is necessary for composite material for the effective interaction between PPY and GO which facilitates the transport of ions and decreases the resistance to the movement of ions during the charging/discharging process [24].

The Cs values of different PGs at different %w/w of GO are shown in Table 3 with the highest Cs value for PG5 (Fig. 4b). The Cs value of PG5 is higher than those of PPY, and GO which is because the introduction of GO into the PPY matrix increases the surface area and porosity of the composite material allowing the fast diffusion of counter-ions on its surface, and enhancing its electrochemical behavior [12, 22]. The slope, as well as the area of the CV curve of PGs is higher compared to PPY and GO suggesting the lower resistance< fast ion diffusion rate and good capacitance behavior in the composite material [6].
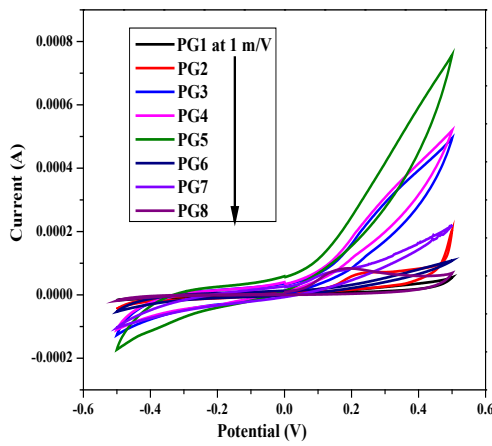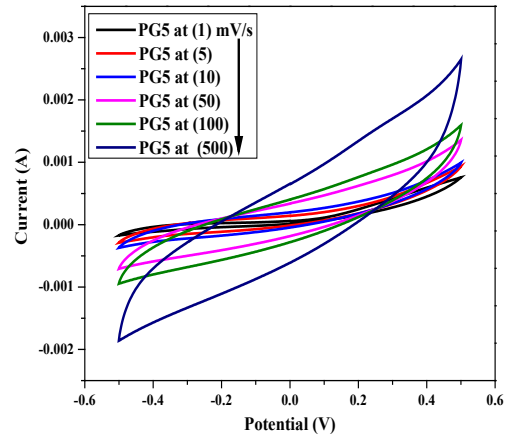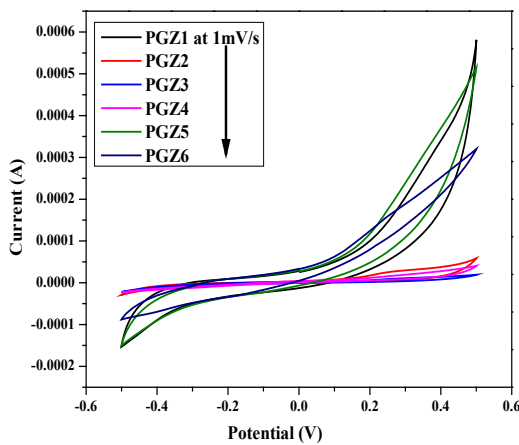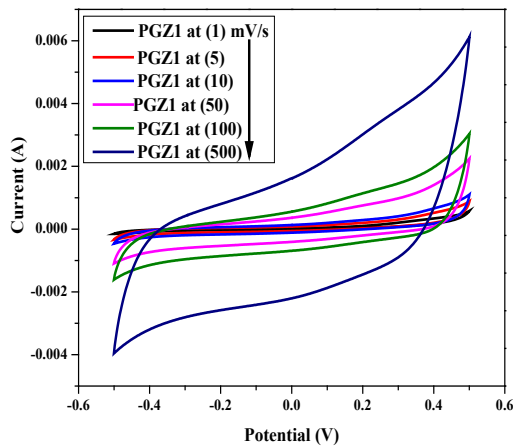

(a)   (b)

Fig. 5. CV curves of (a) PG with different %w/w of GO at 1 mV/S (b) PG5 at different scans.

(a)   (b)

Fig. 6. CV curves of (a) PGZ with different %w/w of ZnO at 1 mV/S (b) PGZ1 at different scans.

41

Table 4. Cs values of PGs at different scans

Scan mV/s	Cs values (F/g)							
	PG1	PG2	PG3	PG4	PG5	PG6	PG7	PG8
1	245.8	264.5	295.1	330.1	391.3	311.5	276.9	241.4
5	78.2	87.2	95.1	120.3	137.6	101.6	89.3	76.3
10	52.2	65.2	69.6	83.1	98.1	71.0	69.1	51.1
50	23.9	29.4	33.1	35.1	42.3	32.3	23.4	24.2
100	6.5	10.3	12.0	13.4	27.2	9.6	9.3	6.5
500	4.1	6.4	7.1	8.5	10.0	6.8	7.1	3.9

Table 5. Cs values of PGZs at different scans

Scan rate mV/s	Cs values (F/g)					
	PGZ1	PGZ2	PGZ3	PGZ4	PGZ5	PGZ6
1	352.1	256.5	182.4	47.5	26.3	18.9
5	137.5	121.3	59.9	16.3	10.5	13.5
10	94.5	89.3	38.1	12.6	8.6	7.4
50	39.0	32.3	13.5	8.2	4.4	4.2
100	25.1	21.1	8.3	7.3	3.6	3.1
500	9.4	9.1	3.4	3.8	2.7	2.2

Electrochemical measurement of PGZs

The Cs values of PGZ (Table 3) increase with an increase in the amount of ZnO up to a certain limit and then decrease with further addition of ZnO in the PG composite at a particular scan (Fig. 6a). This decrease may be due to the blockage of the porous surface of PG composite that results in the decrease of the active surface area of the ternary composite and an increase in the resistance that hinders the diffusion of ions on its surface. Thus, a requisite amount of ZnO is necessary for a composite material that decreases the internal resistance and enhances the electrochemical performance of the composite material [24].

The specific capacitance of PPY, GO, PGs, and PGZs decreases as the scan rate increases within a potential window, as shown in Fig. **7.** High Cs value at a low scan rate is due to the fact that electrolyte ions have enough time to attach to the surface of the material resulting in their strong interaction with the active sites of the electrode material and hence, enhancing its capacitive behavior. At higher scan rates the rate of diffusion of ions in the electrolyte is fast but the number of ions on the active sites of the electrode decreases resulting in a decrease in their Cs values**.** The oxidation and reduction peaks due to the internal resistance of the electrode are shifted towards positive and negative potential, respectively, with an increase in scan rate [2, 6].
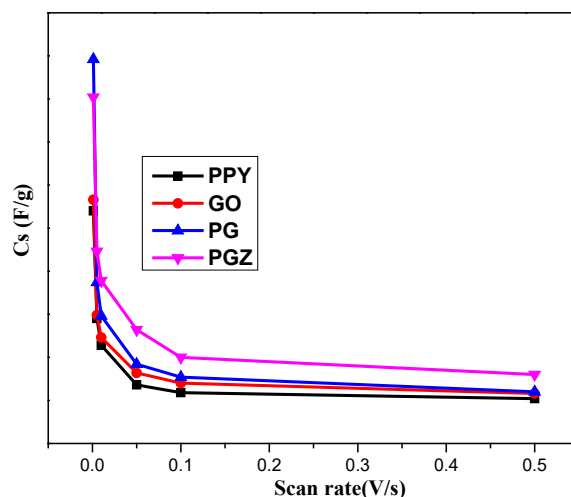
Fig. 7. Effect of scan rate on Cs value of PPY. GO, PG and PGZ

It is significant to note that the Cs of respective PGZs are lower as compared to the Cs of PGs. This relative decrease in the Cs in the case of PGZs may be attributed to the presence of ZnO which itself has a lower Cs due to the presence of a larger bandgap. The presence of ZnO in the matrix of PG brings undesired disorder in the PPY chain thus generating a large polaron bandgap as compared to the PG [4]. Further, it was also observed that with the increase in the amount of ZnO in the matrix of PG (specifically PG5) the Cs were found to get considerably lower (Table 5, Fig. 7).

CONCLUSIONS

A series of nanocomposites were fabricated by mixing PPY and GO (PGs) and PGs and ZnO (PGZs) in certain ratios. The obtained nanocomposites and individual materials were studied for their electrochemical behavior. CV of all the electroactive materials was taken for the earlier purpose, the CV results show that the PG5 was having the highest Cs (391.3 F/g) within all the PGs and individual components. With the addition of ZnO in PGZs, the Cs were found to decrease as compared to the parent PG5, possibly due to a large bandgap and low C_s of ZnO. Additionally, it was proposed that the ZnO may have generated disorder in the PPY chains again effectively reducing the Cs of PGZs. Out of all PGZs, PGZ1 was found to have the highest Cs (352.1 F/g) which continues to decrease with increasing ZnO in the PG matrix.

Conflicts of interest: The authors declared no conflicts of interest.

REFERENCES

1. A. Singh A. Chandra, *J. Appl. Electrochem,* **43**(8), 773 (2013).
2. P. Asen, S. Shahrokhian, A. Irajizad, *Int. J. Hydrog. Energy.,* **42**(33), 21073 (2017)
3. A. Pruna, Q. Shao, M. Kamruzzaman, J. A Zapien, A. Ruotolo, *Electrochim. Acta*. **187**, 517 (2016).
4. S. Dey A. K. Kar, *J. Sol-Gel Sci. Technol.,* **102**, 679 (2021).
5. J. Guerrero-Contreras, F. Caballero-Briones. *Mater. Chem. Phys*, **153**, 209 (2015).
6. W. K. Chee, H. N. Lim, I. Harrison, K. F Chong, Z., Ng, C. H. Zainal, N. M. Huang, *Electrochim. Acta,* **157**, 88 (2015).
7. H. Mudila, M. G. H. Zaidi, S. Rana, V. Joshi, S. Alam. *Int. J. Anal. Chem.* **4**(3), 139 (2013).
8. H. Mudila, V. Joshi, S. Rana, M. G. H. Zaidi, S. Alam, *Carbon Lett.* **15**(3), 171 (2014).
9. J. Song, X. Wang, C. T. Chang. *J. Nanomater.,* **2014,** 1. (2014)
10. A. Bisht, R. Sati, K. Singhal, S. Mehtab, M.G.H. Zaidi, *Advances in Solar Power Generation and Energy Harvesting,* 127 (2020)
11. R. Rikhari, B. Saklani, A. Bisht, S. Mehtab, M.G.H, Zaidi, *Sens. Lett.,* **17**, 511 (2019)
12. S. Konwer, R., Boruah, S. K. Dolui. *J. Electron. Mater.,* **40**(11), 2248 (2011).
13. S. Kulandaivalu, N. Suhaimi, Y. Sulaiman, *Sci. Rep.,* **9**(1) (2019).
14. A. Batool, F. Kanwal, M. Imran, T. Jamil, S. A. Siddiqi, *Synth. Met.,* **161** (23-24), 2753 (2012).
15. F. Yin, J., Ren, Y. Zhang, T. Tan, Z. Chen. *Nanoscale Res. Lett.,* **13**(1). (2018).
16. L. Li, K. Xia, L. Li, S. Shang, Q. Guo, G. Yan.*J. Nanopart. Res,* **14**(6) (2012).
17. A. Mostafaei, F. Nasirpouri, *Prog. Org. Coat.,* **77**(1), 146 (2014).
18. N. I. T. Ramli, S. A. Rashid, M. S. Mamat, Y. Sulaiman, S. A. Zobir, S. Krishna. *Electrochim. Acta,* **228**, 259 (2017).
19. P. Patil, G. Gaikwad, D. R. Patil, J. Naik, *Bull. Mater. Sci.,* **39**(3), 655 (2016).
20. S. Bose, T. Kuila, M. E. Uddin, N. H Kim, A. K. T., Lau, J. H. Lee, *Polymer*, **51**(25), 5921 (2010).
21. M. Ates, S. Caliskan, M. Gazi, *Fuller. Nanotub. Carbon Nanostructures,* **26**(10), 631 (2018).
22. P. Joshi, S. Mehtab, M.G.H Zaidi, *Bull. Chem. Soc. Jpn,* **95** (6), 855 (2022)
23. H. Lv, Y. Guo, Z. Yang, Y. Cheng, L.P. Wang, B. Zhang, Y. Zhao, Z. J. Xu, G. Ji, *J. Mater. Chem. C,* **5**(3), 491 (2017).
24. G. Liu, Y. Shi, L. Wang, Y. Song, S. Gao, D. Liu, L. Fan, *Carbon Lett,* **30**(4), 389 (2019).

Non-isothermal decomposition kinetics of copper benzene tricarboxylate metal organic framework

I. Joshi[1], V. Rani[2], P. Joshi[3], K. Khati[1], S. Mehtab[1], M.G.H. Zaidi[1*], P.K. Roy[4]

[1]*Department of Chemistry, G.B.Pant University of Agriculture and Technology, Pantnagar, Uttarakhand-263145, India*
[2]*Department of Physics, Sri Ram Singh Dhoni Government Degree College Jianti, Uttarakhand-263626, India*
[3]*Department of Chemistry, School of Allied Sciences, Dev Bhoomi Uttarakhand University, Naugaon-248007, India*
[4]*Centre for Fire, Explosive and Environment Safety, Defence Research Development Organisation, Timarpur, Delhi-110054, India*

The thermal decomposition of copper benzene tricarboxylate metal organic framework (HKUST-1) was studied by dynamic thermogravimetry. The decomposition proceeds *via* a single step and corresponding data was examined using various mathematical models. The Coats-Redfern (C-R) and Horowitz-Metzger (H-M) methods were used to compute the kinetic and thermodynamic parameters, including frequency factor (A), activation energy (Ea), change in enthalpy (ΔH), entropy (ΔS), and Gibbs free energy (ΔG). The mechanism of the degradation follows the non-evoking equation for three-quarters order mechanism ($F_{3/4}$), for which $[g(\alpha)=1 - (1 - \alpha)^{1/4}]$ and the rate-controlling method are the consequences of the chemical process. According to the C-R approach, Ea (KJ/mol), ΔH (KJ/mol), ΔS (KJ/mol-K) and ΔG (KJ/mol) for $F_{3/4}$ mechanism were 67.27, 61.92, -0.16 and 166.17, which are in close agreement with values determined by the H-M method, 67.30, 62.20, -0.26, 219.00, respectively. A (min^{-1}) provides considerably different values from both methods.

Keywords: Copper benzene tricarboxylate, Metal-organic frameworks, Non-isothermal kinetics, Thermal and kinetic parameters.

INTRODUCTION

The term **"**metal-organic frameworks" (MOFs) refers to unique functional materials made up of periodic spatial or planar arrangements of metal ions that are covalently bound to organic ligands. In the framework, the metal cluster serves as "lateral" and organic ligands act as "joint". MOFs have gained popularity in recent years as one of the most developed and used porous materials. Therefore, several scientists have synthesized a variety of porous materials with specialized properties and requirements based on their intended use such as highly efficient adsorbents [1], thin film devices [2], catalysts [3], and gas-storage materials [4]. MOFs are employed in a wide range of applications, including compound separation [5], sensors [6], supercapacitors [7] and particularly for selective adsorption and degradation [8]. This is due to their sizeable surface area, high and tunable porosity and accessibility of active sites [3]. The adjustable methods of synthesis, designs, and morphologies of numerous kinds of MOFs are fascinating research topics in electrochemical analysis such as oxidation of tiny molecules like nitrite [9], ethanol [10] and glucose, as well as reduction of hydrogen peroxide [11]**.** The stability of the MOFs should be one of the most important criteria for real-world applications.

For instance, stability of MOF offers ample potential for fluorescence sensing [12], photocatalysis [13]**,** drug delivery [14] and enzyme immobilization [15]. Therefore, MOFs stability must be ensured when they are utilised for specific applications in order to keep the desired functionalities and features. The three foremost kinds of stabilities are chemical, thermal and mechanical stability. However, it is crucial to consider that chemical and thermal stability are closely associated with each other. Heating often has the ability to change the chemical structure of MOFs by starting or accelerating the chemical reaction. This causes the associated framework to collapse by rupturing the metal-ligand coordination linkage, or occasionally it can also have an impact on the organic ligand itself [16]. Chemical and thermal stabilities are vital for catalytic operations [17], while mechanical stability is important for structuring MOF, such as creating pellets or other compressed shapes [18]. Chemical stability is also crucial for applications like molecule separation and drug delivery [19].

Thermally stable materials like polymers [20] and their composites [21] are highly prized and necessary for industrial applications. A MOF is said to be thermally stable if it can be heated to a relatively high temperature without experiencing

permanent changes to its chemical and physical composition [16]. When MOFs are subjected to heat treatment, they can degrade in a variety of ways including amorphization [22], graphitization [23], melting [24], and metal-oxo-cluster dehydration [25]. Therefore, thermogravimetric (TG), differential thermal analysis (DTA) and derivative thermogravimetric (DTG) techniques are employed to gauge the thermal stability of MOFs [26]. Thermal analysis can be used to identify characteristics such as composition, transition temperature, purity, stability, thermal expansion, loss of modulus, and energy dissipation [27].

Copper (Cu)-based MOFs, i.e., copper benzene tricarboxylate MOF are one type of MOFs that is still being extensively explored due to exceptional physical and chemical properties. HKUST-1 (Hong Kong University of Science and Technology-1) is unquestionably one of the most researched and quoted MOFs also known as MOF-199. HKUST-1 is composed of Cu_2 paddle-wheel clusters connected with benzene-1,3,5-tricarboxylic acid to form a three-dimensional porous network having the chemical formula $[Cu_3(BTC)_2(H_2O)_3]_n$. [28].

The current study aims to estimate the kinetic and thermodynamic parameters of solid-state decomposition of HKUST-1 using TG data. All metrics for HKUST-1 were analysed using the Coats and Redfern (C-R) and Horowitz and Metzger (H-M) techniques, including activation energy (Ea), frequency factor (A), change in enthalpy (ΔH), change in entropy (ΔS), and change in Gibbs free energy (ΔG).

EXPERIMENTAL

Materials and measurement

HKUST-1 was procured from the Centre of Fire, Explosives and Environment Safety Lab, Defense research Development Organization Delhi. The thermogravimetric measurement was carried out in air at a flow rate of 200 ml/min in the temperature range of 35°C-1000°C using EXSTAR TG/DTA 6300. For the experiment 10.34 mg sample weight was used at a heating rate of 10° C/min.

Table 1. Algebraic expressions for g(α) and its corresponding mechanism.

Symbol	g(α)	Rate determining process
Acceleratory rate equations		
$P_{1/2}$	$\alpha^{1/2}$	Nucleation
$P_{1/3}$	$\alpha^{1/3}$	Nucleation
$P_{1/4}$	$\alpha^{1/4}$	Nucleation
$P_{3/2}$	$\alpha^{3/2}$	Nucleation
Non evoking equations		
$F_{1/3}$	$1 - (1-\alpha)^{2/3}$	Chemical reaction
$F_{3/4}$	$1 - (1-\alpha)^{1/4}$	Chemical reaction
$F_{3/2}$	$1/(1-\alpha)^{1/2} - 1$	Chemical reaction
F_2	$1/(1-\alpha) - 1$	Chemical reaction
F_3	$1/(1-\alpha)^2 - 1$	Chemical reaction
Deceleratory rate equations		
Fo, P_1, R_1	α	Contracting disk
$F_{1/2}$, R_2	$1-(1-\alpha)^{1/2}$	Contracting cylinder
$F_{2/3}$, R_3	$1-(1-\alpha)^{1/3}$	Contracting spherical
D_1	α^2	One-dimensional diffusion
D_2	$\alpha + (1-\alpha)\ln(1-\alpha)$	Two-dimensional diffusion
D_3	$[1 - (1-\alpha)^{1/3}]^2$	Three-dimensional diffusion (spherically)
D_4	$(1 - 2\alpha/3) - (1-\alpha)^{2/3}$	Three-dimensional diffusion (cylindrically)
Sigmoidal rate equation		
A_1, F_1	$-\ln(1-\alpha)$	Nucleation and growth, n=1
$A_{3/2}$	$[-\ln(1-\alpha)]^{2/3}$	Nucleation and growth, n=1.5
A_2	$[-\ln(1-\alpha)]^{1/2}$	Nucleation and growth, n=2
A_3	$[-\ln(1-\alpha)]^{1/3}$	Nucleation and growth, n=3
A_4	$[-\ln(1-\alpha)]^{1/4}$	Nucleation and growth, n=4

Integral methods

The integral function g(α) dictated by the conversion process and the mathematical model for the most common solid-state reaction processes are shown in Table 1 [29, 30].

For the current study, two integral approaches were employed. One calculation strategy was based on the C-R method, and the other was based on the H-M method [31-33].

RESULTS AND DISCUSSION

Thermogravimetric analysis

Fig. 1. depicts the thermal degradation curve of HKUST-1 under air corresponding to dynamic TG-DTA-DTG experiment performed at a heating rate of 10°C/min. Before the decomposition, the temperature-dependent weight loss curve shows almost 25% losses from 30 to 137°C due to exclusion of residual solvents and guest molecules that are contaminated with HKUST-1. The subsequent weight loss of 4.2% at 137 to 280°C indicates loss of water molecules coordinated to Cu. It is evident that at high temperatures, coordinate bonds break rather than solvent is freed from the pores of MOFs [34]. The decomposition of HKUST-1 appeared in the temperature range from 286 to 380°C, leaving 26% weight residue (Fig. 1a). This was associated with an intense DTA signal at 0.599 mV with peak temperature of 373°C. DTA reveals exothermic decomposition of HKUST-1with - 4.20 J/ mg of heat of fusion. Decomposition of HKUST-1 terminated at 548°C, leaving 27.7% char residue. Further, fusion of HKUST-1 was observed at DTG peak temperature of 304°C with 7.2 mg/min (Fig. 1b).

Calculation of thermodynamic parameters from TGA

To calculate activation energy for the single-step decomposition of HKUST-1, first C- R equation [30] was used:

$$lng(\alpha) = \ln\left(\frac{ART2}{\beta Ea}\right) - \frac{Ea}{RT}$$

A plot of $lng(\alpha)$ *vs* 1000/T can be used to calculate the activation energy for each of the degradation processes described in Table 1. Table 2, shows activation energy and correlations for different mechanisms. Analysis of this table confirms that solid state thermo degradation mechanism may follow non evoking equation of three-quarter order ($F_{3/4}$) or decelerator rate equation following power law, *i.e.* ($F_{2/3}$) and Jander equation i.e. (D_3) (Fig. 1c). The Ea for the $F_{3/4}$ mechanism is 67.27KJ/mol, with a correlation value of 0.99613. The $F_{2/3}$ shows 62.72 and D_3 was found to be 125.44 KJ/mol, having almost the same correlation value.

All the thermodynamic parameters for these three mechanisms are described in Table 3. In order to confirm the exact degradation mechanism, we have also calculated activation energy and other thermodynamic parameters using the H-M equation [30].
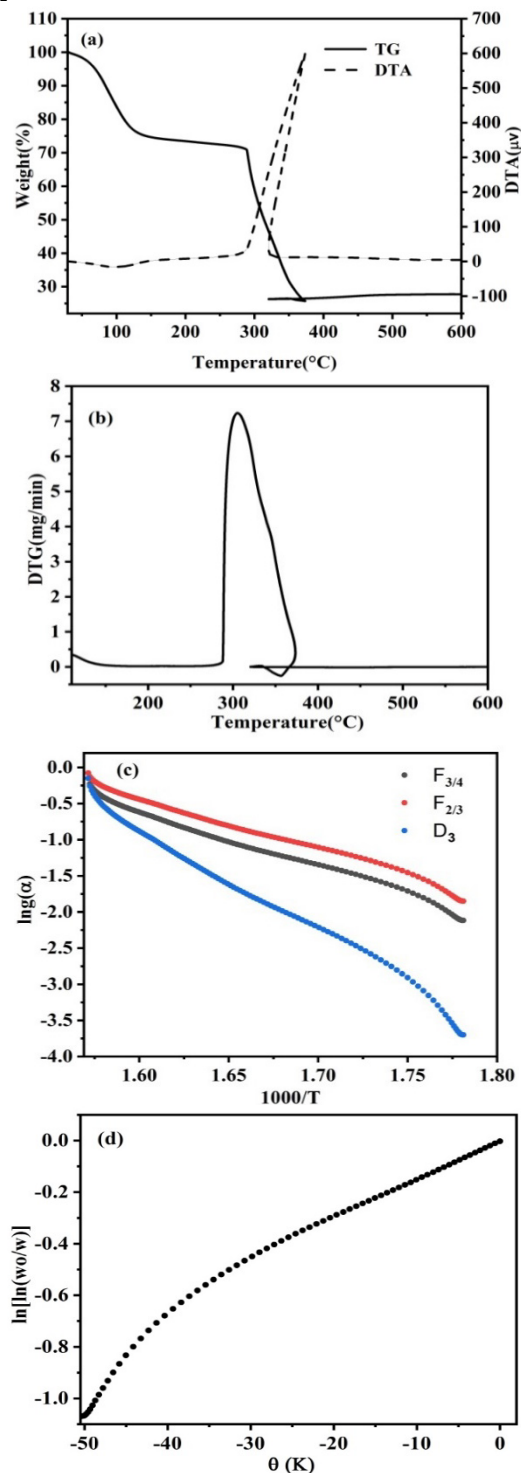

Figure 1. Graph obtained by (a) TG and DTA (b) DTG (c) Coats-Redfern and (d) Horowitz-Metzger method for HKUST-1.

$$\ln\left[\ln\left(\frac{w--o}{w}\right)\right] = \frac{Ea\theta}{RT2s}$$

The slope of $\ln\left[\ln\left(\frac{wo}{w}\right)\right]$ *vs* θ is used to determine the activation energy. From the H-M method (Fig. 1d), the value of Ea for single-step decomposition is 67.30 KJ/mol. The best agreement was found with C-R method corresponding to a chemical reaction, i.e., (F3/4) documented in Table 3.

Table 2. Activation energy obtained using C-R method for several solid-state processes.

Mechanism	Ea (KJ/mol)	R
$P_{1/2}$	18.33	0.97585
$P_{1/3}$	12.22	0.97585
$P_{1/4}$	9.17	0.97585
$P_{3/2}$	55.00	0.97585
$F_{1/3}$	47.66	0.98939
$F_{3/4}$	67.27	0.99613
$F_{3/2}$	124.63	0.96240
F_2	176.71	0.93251
F_3	298.01	0.90229
F_o, P_1, R_1	36.67	0.97585
$F_{1/2}, R_2$	54.60	0.99392
$F_{2/3}, R_3$	62.72	0.99612
D_1	73.33	0.97585
D_2	92.73	0.98729
D_3	125.44	0.99612
D_4	102.98	0.99192
A_1, F_1	83.09	0.99105
$A_{3/2}$	55.39	0.99105
A_2	41.54	0.99105
A_3	27.70	0.99105
A_4	20.77	0.99105

The Ea of decomposition was determined to be 67.29 KJ/mol. This high value reflects the thermal stability of the complex HKUST-1. Thermodynamic parameters ΔG, ΔH are positive whereas ΔS is negative, indicating a non-spontaneous response. The negative value of ΔS implies that the decomposition process occurs at a slower pace than the regular ones. As a result, it is obvious that the thermal decomposition process is unfavorable, signifying that complex HKUST-1 is thermally stable. Further, to validate our findings, the Ea of Cu complexes with various ligands were compared to the existing results. Cu complexes with 5-(2-carboxyphenylazo)-2-thiohydantoin [35], humic acid [36], pyrazole derivatives [37] and pyridine-dicarboxylate [38] revealed their Ea (KJ/mol) from 74.00 to 136.00, 38.82, 18.70 to 30.20 and 21.40 to 77.50, respectively. In our case, the Ea value of HKUST-1 is found to be 67.29, which is within the range of previously known Cu complexes.

CONCLUSION

The non-isothermal kinetics of HKUST-1 was investigated using simultaneous TG-DTG-DTA. The thermogram of HKUST-1 is of C-type, equivalent to single-step decomposition. The thermodynamic and kinetic parameters were examined using C-R and H-M methods. According to C-R method, thermal degradation of HKUST-1 follows either chemical process or deceleratory path. Further, H-M method, confirms that HKUST-1 follows a chemical process (F3/4) in the conversion range considered. The values of A are significantly different using both approaches, whereas the results for the remaining parameters Ea, ΔH, ΔS, and ΔG for F3/4 are comparable. As a result, it can be deduced that TG data may be utilised to provide matrices for the decomposition process. The comparison of the findings obtained with different calculating processes revealed that they are highly dependent on the mechanism function of the process selected. Therefore, it is critical to establish the most likely mechanism function for this objective. Some inferences about the mechanisms and features of the processes may be drawn based on accurately determined values of A, Ea, ΔH, ΔS, and ΔG. Hence, different practical concerns requiring solid phase involvement may be addressed.

Table 3. Thermodynamic and kinetic parameters of HKUST-1.

Parameters	C-R Method			H-M Method
	$F_{3/4}$	$F_{2/3}$	D_3	
A (min^{-1})	4.54×10^4	2.10×10^4	4.86×10^9	5.58×10^1
E_a (KJ/mol)	67.27	62.72	125.44	67.30
ΔH (KJ/mol)	61.92	57.37	120.08	62.20
ΔS (KJ/mol-K)	-0.16	-0.17	-0.07	-0.26
ΔG (KJ/mol)	166.17	165.73	162.43	219.00

REFERENCES

1. C.J. Wijaya, S. Ismadji, H.W. Aparamarta, S. Gunawan, *Molecules*, **26**(21), 6430 (2021).
2. H.C. Zhou, J.R. Long, O.M. Yaghi, *Chemical reviews*, **112**(2), 673 (2012).
3. T. Shen, T. Liu, H. Mo, Z. Yuan, F. Cui, Y. Jin, X. Chen, *RSC Advances*, **10**(39), 22881 (2020).
4. C.Y. Gao, H.R. Tian, J. Ai, L.J. Li, S. Dang, Y.Q. Lan, Z.M. Sun, *Chemical Communications*, **52** (74), 11147 (2016).
5. H. Jiang, K. Yang, X. Zhao, W. Zhang, Y. Liu, J. Jiang, Y. Cui, *Journal of the American Chemical Society*, **143**(1), 390 (2020).
6. H.Y. Li, S.N. Zhao, S.Q. Zang, J. Li, *Chemical Society Reviews*, **49**(17), 6364 (2020).
7. M.A. Tahir, N. Arshad, M. Akram, *Journal of Energy Storage*, **47**, 103530 (2022).
8. M. Wen, G. Li, H. Liu, J. Chen, T. An, H. Yamashita, *Environmental Science: Nano*, **6**(4), 1006 (2019).
9. B. Yuan, J. Zhang, R. Zhang, H. Shi, N. Wang, J. Li, F. Ma, D. Zhang, *Sensors and Actuators B: Chemical*, **222**, 632 (2016).
10. L. Yang, S. Kinoshita, T. Yamada, S. Kanda, H. Kitagawa, M. Tokunaga, T. Ishimoto, T. Ogura, R. Nagumo, A. Miyamoto, M. Koyama, *Angewandte Chemie International Edition*, **49**(31), 5348 (2010).
11. D. Zhang, J. Zhang, R. Zhang, H. Shi, Y. Guo, X. Guo, S Li, B. Yuan, *Talanta*, **144**, 1176 (2015).
12. X.J. Liu, Y.H. Zhang, Z. Chang, A.L. Li, D. Tian, Z.Q. Yao, Y.Y. Jia, X.H. Bu, *Inorganic Chemistry*, **55**(15), 7326 (2016).
13. L. Chi, Q. Xu, X. Liang, J. Wang, X. Su, *Small*, **12**(10), 1351(2016).
14. Z. Dong, Y. Sun, J. Chu, X. Zhang, H. Deng, *Journal of the American Chemical Society*, **139**(40), 14209 (2017).
15. X. Wang, P.C. Lan, S. Ma, *ACS Central Science*, **6**(9), 1497 (2020).
16. G. Mouchaham, S. Wang, C. Serre, *Metal-Organic Frameworks: Applications in Separations and Catalysis*, 1 (2018).
17. E. T. Vogt, B. M. Weckhuysen, *Chemical Society Reviews*, **44**(20), 7342 (2015).
18. K.W. Chapman, G.J. Halder, P.J. Chupas, *Journal of the American Chemical Society*, **131**(48), 17546 (2009).
19. P. Horcajada, T. Chalati, C. Serre, B. Gillet, C. Sebrie, T. Baati, J.F. Eubank, D. Heurtaux, P.Clayette, C. Kreuz, J.S. Chang, *Nature Materials*, **9**(2), 172 (2010).
20. J.S. Shukla, M.G.H. Zaidi, S.K. Dixit, *Asian Journal of Chemistry,* **6**(4), 739 (1994).
21. P. Varshney, S.K. Gururani, R. Singh, M.G.H. Zaidi, *Material Science Research India*, **4**(2), 353 (2007).
22. T. D. Bennett, T. K. Todorova, E. F. Baxter, D. G. Reid, C. Gervais, B. Bueken, B. van de Voorde, D. De Vos, D. A Keen, C. Mellot-Draznieks, *Physical Chemistry Chemical Physics*, **18**(3), 2192 (2016).
23. R. R. Salunkhe, Y. V. Kaneti, J. Kim, J. H. Kim, Y. Yamauchi, *Accounts of Chemical Research*, **49**(12), 2796 (2016).
24. D. Umeyama, S. Horike, M. Inukai, T. Itakura, S. Kitagawa, *Journal of the American Chemical Society*, **137**(2), 864 (2015).
25. L. Valenzano, B. Civalleri, S. Chavan, S. Bordiga, M. H. Nilsen, S. Jakobsen, K. P. Lillerud, C. Lamberti, *Chemistry of Materials*, **23**(7), 1700 (2011).
26. R. G. Chaudhary, P. Ali, N. V. Gandhare, J. A. Tanna, H. D. Juneja, *Arabian Journal of Chemistry*, **12**(7), 1070 (2019).
27. V. Rani, R. C. Srivastava, H. M Agarwal, M.G.H. Zaidi, *Materials Today: Proceedings*, **4**(9), 9471 (2017).
28. K. C. Chong, S. O. Lai, S. K. Mah, H. San Thiam, W. C. Chong, S. H. Shuit, S. S. Lee, W. E. Chong, in: *IOP Conference Series: Earth and Environmental Science,* **1135**(1), 012030 (2023).
29. L. Vlaev, N. Nedelchev, K. Gyurova, M. Zagorcheva, *Journal of Analytical and Applied Pyrolysis*, **81**(2), 253 (2008).
30. L. Núñez, F. Fraga, M.R. Nunez, M. Villanueva, *Polymer*, **41**(12), 4635 (2000).
31. S. Mehtab, M.G.H. Zaidi, N. Rana, K. Khati, S. Sharma, *Bulletin of Materials Science*, **45**(3), 162 (2022).
32. P. Joshi, G. Bisht, S. Mehtab, M.G.H. Zaidi, *Materials Today: Proceedings*, **62**, 6814 (2022).
33. S. Mehtab, M.G.H. Zaidi, N. Rana, K. Khati, S. Sharma, *Bull. Mat. Sci.* 45, 162(2022).
34. W.W. Lestari, M. Adreane, C. Purnawan, H. Fansuri, N. Widiastuti, S.B. R Ahardjo, in: *IOP Conference Series: Materials Science and Engineering,* **107**(1), 012030 (2016).
35. S. S. Kandil, G. B. El-Hefnawy, E. A. Bakr, A.Z. Abou El-Ezz, *Transition Metal Chemistry*, **28**, 168 (2003).
36. A. G. Prado, J. D. Torres, P. C. Martins, J. Pertusatti, L. B. Bolzon, E. A. Faria, *Journal of Hazardous Materials*, **136**(3), 585 (2006).
37. I.M. El-Deen, A.F. Shoair, M.A. El-Bindary, *Journal of molecular liquids*, **249**, 533 (2018).
38. O.Z. Yeşilel, İ. İlker, M.S. Refat, H. Ishida, *Polyhedron*, **29**(11), 2345 (2010).

Study of thermal properties of poly (α-methyl styrene) and polyurethane and their fullerene-based interpenetrating polymer network

M. M. Jafri[1]*, M. Kamal[2], R. K. Dwivedi[3]

[1]Department of Chemistry, School of Basic Sciences, Chhatrapati Shahuji Maharaj University, Kanpur, India
[2]Department of Chemistry, Christ Church Degree College, Kanpur, India
[3]Department of Physics, Christ Church Degree College, Kanpur, India

Thermal properties of pure poly (α-methyl styrene) (PAMS) and polyurethane (PU) and their fullerene based interpenetrating polymer network (IPN) was investigated by differential scanning calorimetry (DSC) and thermo-gravimetric analysis (TGA). Glass transition temperature (T_g) of pure PAMS and PU was recorded at 173°C and 120°C respectively and their thermal decomposition was found at 350°C and 348°C respectively and while glass transition temperature of their fullerene based IPN was recorded at 160°C and thermal decomposition was found at 392°C. A gradual increase in (T_g) value by the incorporation of vinyl polymer reveals the role fullerene as a nanomaterial in strengthening interpenetration as well as enhancement in thermal properties of reacting monomeric species. An enhanced thermal stability pattern of IPN than PAMS and PU was recorded, which indicates the incorporation of urethane and α-methyl styrene units into the polymeric network of fullerene surface. The conductivity pattern explains semiconductor character of the fabricated IPN. Scanning electron microscopic (SEM)exhibits dual phase morphology of IPN. Besides of these testing, IPN was also analyzed for permittivity and permeability which reveals enhanced dielectric as well as good electromagnetic properties. This interpenetration surely brings a great change in the various physiochemical and electrical properties and new class of IPN will be established. Such polymeric systems may be applicable in the field of semiconductor to a broader range. These IPN of moderate conductivity might be useful in the electronics science research area.

Keywords: Fullerene, polyurethane, interpenetrating polymer network, scanning electron microscopic technique.

INTRODUCTION

The concept of interpenetration was first introduced by Sperling *et al*. [1]. As we know, IPN is a mixture in a mesh form in which polymerization of one monomer occurs in the presence of other [2]. IPN is the combination of properties of the cross-linked to polymers. It is important know about sequential upgradation of IPN, which is of great concern, Buist and coworkers fabricated PU polymeric network, Gangopadhyay [3] prepared polypyrrole based IPN. IPN based biomaterial was observed by Banerjee *et al*. [4], Isiklan and coworkers [5] discussed application of IPN. Rokhade *et al*. [6] emphasized on drug release mechanism. Synthesis of dielectric elastomer was put forwarded by Patel *et al.* [7], Kulkarni *et al.* fabricated IPN hydrogel [8], Vlad *et al.* prepared immiscible IPN [9], Lu and Zang and coworkers [10] put forward their study on polymeric material based on castor oil and PU, Al *et al.* [11] synthesized chitosan-based semi-IPN, An *et al.* [12] gave a thermodynamic model of physical gels. A review was put forward by Patel and his coworkers [13], Singh *et al.* [14, 15] reported polyglycidyl methacrylate and acrylamide based IPN synthesis.

Athawale and Kolekar [16-18] synthesized glycerol and its IPN with poly (butyl methacrylate). Wang *et al*. [19] discussed the damping behavior of PU/poly (methyl methacrylate) (PMMA) simultaneous interpenetrating networks (SINs).

IPN-based hydrogels were fabricated from ethylene glycol dimethacrylate by Seon and co-workers [22] using free radical polymerization technique. Yufeng [20] and team members reported fullerene shape change. Karabanova [21] and co-workers studied miscibility study of (HEMA). Seon [22] and co-workers synthesized and characterized a semi-IPN. Vishal [23] and his co-workers recognized the importance of pH-sensitive delivery system of gelatin-polymethacrylic acid IPN. Russel and his group member [24] viewed tuning conversion.

Polymer-derived IPN involving fullerene has been known over decades for electronic applications. However, their thermal and electrical properties are not well explored. Monika [25] *et al*. synthesized fullerene films of ferrocenyl. They produced redox active films in a solution of Pd (II) derivatives of C_{60}. The film indicated the fullerene bonding to Pd atom, forming an IPN. In 2012 Bo [26] and co-workers reported high internal quantum. In 2015 Ting *et al.*

---

* To whom all correspondence should be sent:
E-mail: jafrimerajic05@gmail.com

[27] synthesized a polymer of fullerene and glycidyl azide. Thereafter in 2016 Jelena highlighted applications of IPN for vibration damping. Progress in fullerene-based OPV was reported by Ranjith [28] and co-workers. They had synthesized fullerene based semi-IPN using acrylonitrile and aniline, benzoyl peroxide and divinylbenzene. IPN was characterized by DSC, TGA, conductivity, FESEM, transmission loss (TL) and permittivity/ permeability techniques. As a result of backbreaking work of this group, a stronger, tougher and conducting semi IPN is produced [29, 30]. Another important nanomaterials towards the polymer research has been discovered. This is the fullerene molecule exhibiting hollow sphere. This is good to see that fullerenes are stable but are not totally unreactive. Thus, the combination of fullerene with the vinyl reactive monomers brings about a new hope for better interpenetration of these units. This interpenetration surely brings a great change in the various physiochemical and electrical properties and new class of IPN will be stablished.

EXPERIMENTAL

Urethane, α-methyl styrene, fullerene (C60), divinyl benzene (DVB) and benzoyl peroxide (BPO) were procured (purity >99.5%) from various resources available in India. The polymer samples were prepared from raw materials through polymerization over 2.5 hours at 70°C. Fabricated polymer was dried and taken out for the testing. IPNs were fabricated at different concentration of F-PAMS, PU, DVB and BPO in solvent (toluene) for some required time (3 hours) at 60°C under an inert atmosphere.

Characterization of IPN

The synthesized IPN characterized using thermal analysis techniques. IPN was examined for swelling data in dimethyl formamide, using Flory-Rehner equation. Sample of mass 3-5 mg was analyzed by DSC on a V2.2 Dupont calorimeter, in N_2 region (heating rate 10°C/min). TGA was carried out on TGA V% V5 1A 2100, under nitrogen atmosphere at a heating rate of 10°C/min. IPN was tested for permittivity ($\varepsilon^*=\varepsilon'-j\varepsilon''$) and permeability ($\mu^*=\mu_r'-\mu_r''$) values in X band (8.2-12.4 GHz) frequency region. IPN was characterized by SEM with a resolution of 100 nm.

RESULTS AND DISCUSSION

FTIR spectroscopy

FTIR for fullerene peaks are 1430, 527 (for C-C vibration) and 1600 cm^{-1} (–C=C-). For PAMS, it reveals peaks at 3000 (stretching), 1490 (-C-C- and

50

C-H stretching vibrations), 699 (benzene ring C=C bending) and 1444 cm^{-1} for bending vibrations and for PU linkage it assigns a signal at 3300 (NH units), 1710 (C=O stretching), 2913 (CH symmetric stretching), 2249 (−NCO) group) 1489 and 1441 cm^{-1} (CH$_2$ and CH bending). While the FTIR spectrum for IPN reveals the presence of fullerene at 549 for caged vibrations), 1600 cm^{-1} (for C=C mode). PAMS shows the peaks at 3055 (stretching), 1495 (-C-C- vibrations), 2981 (C-H) and 698 cm^{-1} (benzene ring C=C out of plane bending). PU peaks are at 3200 (NH units), 1742 (C=O stretching of urethane linkage), 2798 (CH stretching of CH$_2$) and 2000 cm^{-1} (−NCO) group. Change in the band positions of fullerene, PAMS and PU clearly explains that good interpenetration has taken place of IPN [31, 32] (Fig.1).
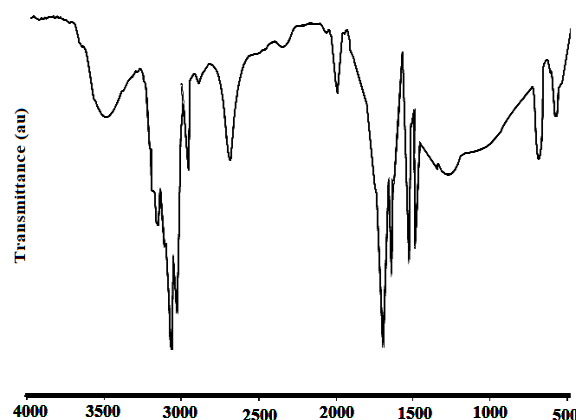

Fig. 1. FTIR spectrum of IPN

Thermal properties

Fig. 2a shows the TGA value at 392°C. Decomposition was found to be possessing higher value than PAMS and PU, which indicates incorporation of urethane into IPN. The enhancements in the thermal properties of the fabricated IPN is a result of proper interpenetration of the polymeric steps. This interpenetration strongly inhibits the chain mobility and improves the swelling behavior of the IPN and improves the T_g value and TGA value as well. DSC graph shows values (Fig. 2b) at 160°C, higher than T_g of PU (120°C) and lower than T_g of PAMS (173°C). The synthesized IPN reveals an increase in T_g value by 10-20°C, which may be the result of restricted chain mobility. PU are entangled to crosslink PAMS (interpenetration). PAMS provides stiffness and PU provides flexibility. Thus, it is clear that the IPN is a combination of both the strength and flexibility. It is important to note that IPN is also associated with the application of fullerene. Fullerene may be the answer for the toughness and conductivity of IPN. Fullerene works more or less towards the filler of

these fabricated IPNs and provides an overall stable and tough structure along with flexibility. It is also helpful in the interpenetration of the IPN.

Morphology

Structure of IPN of PAMS and PU is observed by SEM depicting dual phase morphology (Fig. 4). IPN is diversified and clear. The surface of fullerene, PAMS and PU is not smooth and possesses rough heterogeneous structure. It is expected that film morphology contains dual phase. One phase is the presence of fullerene- based PAMS and another phase is most probably the polymeric film of PU over this fullerene-based PAMS polymer in the form of interpenetration. Thus, a clear dual phase morphology and interpenetration is a signature of diversification and obviously enhanced physical, as well as thermal properties. Moreover, IPN species get a proper formation of the diversified product in better intermingled form. Thus, it is sure that the IPN structure is heterogeneous and different phases are clearly observed. This rough surface reveals the better interpenetration of the reacting species and cross-linker. Moreover, it may be deduced that dual phase morphology provides a chance for the bonding and interpenetration. Fullerene provides the proper conductivity to the IPN. Fullerene is also helpful in the interpenetration of the IPN.
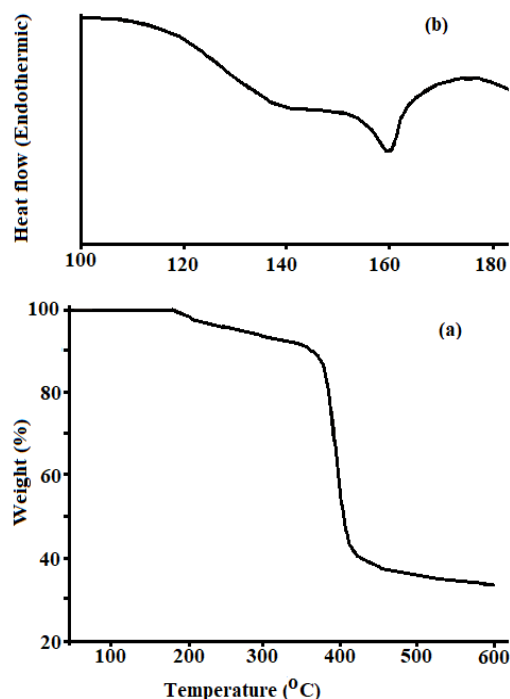
Fig. 2. TG (a) and DSC (b) curves of IPN

Electrical conductivity

Conductivity of IPN is 1.38×10^{-6} $\Omega^{-1}m^{-1}$ at frequency 20-50 Hz, revealing semiconductor nature. These value of conductivity falls in the range of conductor range and insulator range. Which is an indication of broad-spectrum application of such polymeric network. Such polymeric systems may be applicable in the field of semiconductor to a broader range. The IPN of moderate conductivity might be useful in the electronics science research area.
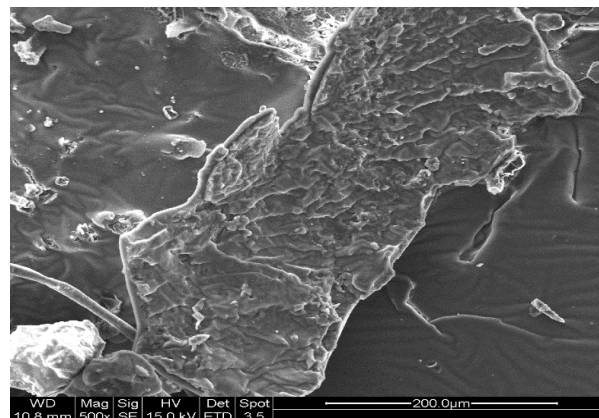
Fig. 3. SEM of IPN

Permittivity and permeability of IPN

Permittivity and permeability of any material is the property that throws light on the electromagnetic properties, dielectric properties along with the conductive behavior. The values of ε_r', ε_r'' and $\tan\theta$ for IPN are 2.47, 0.15 and 0.08, respectively. Values range from 0.92 to 1.20, 0.01 to 0.103 and from 0.01 to 0.08 for μ_r', μ_r'' and $\tan_r''$ respectively. Higher values of permittivity reveal good dielectric properties and enhanced permeability depicts enhanced electromagnetic properties. Such polymeric network may be used in various environments and domain such as defense field, medical, different laboratories, etc. These may be very useful as a semiconductor and they are applicable for dielectric purposes It is to be concluded that these IPNs are very useful in dielectric materials. Thus, a combination of overall properties of the IPN is established.

Effect of components

Incorporation of fullerene, PU and PAMS shows increased swelling behavior. This enhanced swelling is applicable in various domains. They may be used for water retaining purposes too. As PAMS contains benzene ring in the planar form, so this may provide a strong backbone structure which obviously enhances the T_g values and thermal decomposition temperature. Thus, PAMS is responsible for providing an ordered and tough form to the IPN. Higher concentration of PAMS usually enhances relative polymer crystallinity and toughness while

PU is responsible for providing flexibility to the IPN. Increase in concentration of PU is a function of flexibility and greater degree of crosslinking between PU and fullerene-based PAMS phase. Increase in the concentration of DVB is directly responsible for the crosslinking and hence low chain mobility, which causes an increase in T_g. It is true that DVB is very helpful in the interpenetration of IPN. Thus, a change in the concentration of DVB efficiently affects IPN formation.

PU is commercially a very important organic polymer used in various applications such as rigid PU foam, coatings, adhesives, building and construction, composite wood, medical and flooring, etc. Besides these applications PU is mainly popular for its flexibility. Second monomer used in the research is α-methyl styrene. PAMS which is a polymer of α-methyl styrene provides the mechanical strength to the IPN. This may result into enhanced mechanical, as well as physiochemical properties of the IPN. Thus, this molecule is very helpful in the formation of the IPN.

As discussed above, these important properties of the polymers such as flexibility of PU and the stiffness and compactness of PAMS may be combined to a new and unique combination. Such an IPN is being synthesized which reflects these combined properties in the increase of Tg and TGA values. Such polymeric structures are very useful in the environment which hold alternating thermal behavior. Thus, such polymeric network may be applicable in vast domains such as defense, medicine, electronics, etc. Fullerene also played a great role in the improvement of strength of IPN. Thus, the enhancement of the thermal properties may be the result of proper interpenetration of these distinct species: fullerene, PU and PAMS combination. Basically, fullerene not only enhances the interpenetration but it also helps the IPN for inbuilt conductive and electromagnetic properties. It may also be deduced that preparation of such IPN systems may the

CONCLUSIONS

The synthesized polymeric network exhibits better thermal properties than PAMS and PU. The DSC analysis depicts higher value of T_g for the IPN as compared to PU, the thermal decomposition pattern of IPN was found to be possessing higher value than ranges PAMS and PU, which shows insertion of urethane units into the polymeric network. Thus, such polymeric network may be applicable in vast domains such as defense, medical, electronics, etc. Fullerene also played a great role in the improvement of strength of IPN. IPN surface

contains fullerene, PAMS and PU, which is not smooth. This reveals the presence of rough and heterogeneous domains under the immediate layer and dual phase morphology. Thus, it may be predicted that due to this heterogeneity which is a result of proper interpenetration has a direct impact on the chain mobility of the polymeric chains inside the polymeric network. This effect of the interpenetration causes the increase and enhancement of the thermal properties. Conductivity testing reveals the semiconducting character of IPN. Thus, at last this to say that we have fabricated IPN which possesses the desired and all required properties for various purposes. The research has provided a combination of the flexibility, toughness, electrical conductivity along with the electromagnetic properties.

REFERENCES

1. H. Sperling, R. Hu, L. Utracki, Springer, Dordecht, the Netherlands, 2003, p. 417.
2. X. Zhao, *MechPhys Solids,* **60**, 319 (2012).
3. R. Gangopadhyay, A. De, *Mater Chem.,* **12**, 3591 (2002).
4. S. Banerjee, S. Ray, S. Maiti, *Int. J. Appd Pharmac.,* **2**, 28 (2010).
5. N. Isiklan, J. *Appl. Polym. Sci.,* **99**, 1310 (2006).
6. A. Rokhade, S. Patil, *Carbohydrate Polym.*, **67**, 605 (2007).
7. B. Patel, L. Patel, H. Shah, K. Modasiya, *Pharma,* **1**, 19 (2011).
8. R. Kulkarni, V. Sreedhar, S. Mutalik, C. Setty, B. Sa, *Biol. Macromol.*, **47**, 520 (2010).
9. S. Vlad, A.Vlad, S. Opera, *Eur. Polym.J.,* **38**, 829 (2002).
10. L. Zang, J. Zhou, J. Hunang, P. Gong, Q. Zhou, L. Zheng, Y. Du, *Ind. Eng. Chem.* **38**, 4284 (1999).
11. A. Al-Kahtani, H. Bhojya, S. Sherigara, *Carbohydrates,* **344,** 699 (2009).
12. Y. An, F. Solis, H. Jang, *Mech. Phys. Solids.* **58**, 2083 (2010).
13. H. Patel, H. Patel, Z. Shah Modasiya, *Pharma,* **1,** 19 (2011).
14. A. Singh, M. Kamal *Int. J. of Plastic Tech.*. **17,** 194 (2013).
15. T. Hsieh, P. Hsieh, C. Simon, *Polymer,* **40,** 3153 (1999).
16. K. Das, S. Lenka, *Appl. Polym. Sci.* **75**, 1487 (2000).
17. R. Greco, M. Iavarone, A. Fiedlerova, E. Borsig, *J. Macromol. Sci.,* **A37**, 433 (2000).
18. V. Athawale, S. Kolekar, *J. Appl. Polym. Sci.*, **75**, 825 (2000).

19. S. Wang, S. Zawadzki, L. Akcelrud, *Mater. Res.*, **4**, 27 (2001).
20. L.Yufeng, Yu. I. Boris, *Phys. Rev.*, 68, 2334031 (2003).
21. L. Karabanova, G. Boiteux, O. Gain, G. Seytre, L. Sergeeva, E. Lutsyk, *Polym. Int.,* **53**, 2051 (2004).
22. J. Seon, R. Su, M. Geoffrey, Y. In, I. Sun, *J. Appl. Polym. Sci.*, **96**, 867 (2005).
23. N. Vishal, C. Satish, H. Shivakumar, *Ind. J. Pharm. Sci.,* 64 (2007).
24. B. Russel, M. Cardona, B. Francis, M. Swain, G. Guldi, E. Sankaranarayanan, C. Brain, *Adv. Funct. Mater.*, **19**, 1 (2009).
25. M. W. Zolopa, K. Winkler, R. Cabalero, F, Langa, *Electrochim. Acta*, **56**, 5566 (2011).

26. B. Liu, R. QiPng, L. Zhao, L. Lay, R. Friend, P. Ho, *Nat. Commun.*, 1 (2012).
27. T. Huang, J. Bo, F. Peng, C. Di, R. Zheng, Y. He, S. Jin, *Polymers*, **7**, 896 (2015).
28. K. Ranjith, D. Arun, N. Vinila, C. Praveen, *Res. Dev. Mater. Sci.*, **1**, 1 (2017).
29. E. Katz, D. Faiman, S. Tuladhar, *J. Appl. Phys.*, **90**, 5343 (2001).
30. H. Kroto, J. Heath, O. Brien, R. Curl, R. Senalley, *Nature*, **318**, 162 (1985).
31. V. Agarwal, V. Vishnoi, M.G.H. Zaidi, S. Alam, A. K. Rai, *Fullerenes, Nanotubes, Carbon Nanostr.*, **15(5)**, 267 (2010).

Effect of substrate on the properties of calcite thin films prepared by dip coating method

J. Kumari[1], P. Kumar[1*], R. Singhal[2], A. K. Mukhopadhyay[3], M. G. H. Zaidi[4]

[1]Department of Physics, Manipal University Jaipur, Jaipur-303007, Rajasthan, India
[2]Department of Physics, Malaviya National Institute of Technology, Jaipur-302017, India
[2]Department of Physics, Sharda School of Basic Sciences and Research, Sharda University, Greater Noida 201310, Uttar Pradesh, India
[4]Department of Chemistry, College of Basic Science and Humanities, G.B Pant University of Agriculture and Technology, Uttarakhand, 263145, India

We report on the development of calcite thin film on two different glass substrates. The first film was deposited on pre-cleaned glass substrate and another film was deposited on the glass substrate treated with dilute hydrofluoric acid (HF), using dip-coating. The films were synthesized by dipping glass substrate and etched glass substrate alternatively into calcium metal salt solution Ca $(NO_3)_2.4H_2O$ and NaOH base solution. Several techniques were used to characterize the thin films that include X-ray diffraction, Fourier transform infrared spectroscopy (FTIR), field emission scanning electron microscopy (FESEM) and ultraviolet-visible spectroscopy (UV-Vis). From FESEM images of substrates it was observed that the etched sample has higher roughness than the plain glass substrate. Accordingly, the effect of roughness was monitored on the morphology of deposited calcite thin films. The rough surface of substrate lead to a bigger crystallite size of calcite thin films as calculated by XRD peaks and also observed in FESEM image. Subsequently, from optical studies, the bandgap of the thin films was found to decrease with increase in crystallite size. The present study on the calcite thin films might pave the way to understand the thin films and further use them in several applications in sensors, biomedical, environmental, and for fundamental research.

Keywords: Calcite, thin films, dip method, substrate effect, XRD

INTRODUCTION

Calcium carbonate ($CaCO_3$) is one of the substances that are found in plenty amount on the earth. Minerals that contain this element are found in rocks and are important components of pearls and shells of marine organisms. In general, calcium carbonate forms three distinct crystal forms, aragonite, vaterite, and calcite. Each crystal form has a characteristic morphology, such as rhombohedral, spherical, or needle-like [1]. Several industries use this mineral. It is a primary component in agricultural lime [2], utilized as a filler material in paper and collar industries, and extensively used as a building substance in the production industry [3, 4]. There are several important factors to consider, one of which is particle morphology, and recent studies have been directed toward crystal shape [5]. Many approaches have been developed to synthesize the calcite, including biomimetic synthesis [6], carbonization [7], and precipitation [8], reverse micro emulsion [9], microwave irradiation [10]. Ultrasonic intensity can also be used on it or surface morphology of calcium carbonate. A report by Tolba *et al*. and Mantilaka *et al*. has shown that it is common to find calcite $CaCO_3$ in cubic and flaky forms [13, 14]. As far as we know, there has been little research on calcite $CaCO_3$ thin films. Hence, gap of knowledge about calcite in literature becomes the scope of the present research.

In this study, we synthesized the thin films of calcium carbonate using chemical dip-coating method. The prepared thin films were characterized using several characterization techniques. The effect of substrate on the deposition of calcite thin films was studied.

EXPERIMENTAL

### Preparation of substrate

The calcite thin films were deposited on fresh glass substrate and etched glass substrate. Etched glass substrate was prepared by keeping the fresh glass substrate in a solution of HF (48%) and D.I. water in the ratio of (10:30) for 10 min. Before deposition, the substrates were thoroughly cleaned with deionised water and dried at room temperature. [15, 16].

Formation of $CaCO_3$ thin films

For the preparation of $CaCO_3$ thin films, the precursors of analytical grade reagents were used without any additional purification. The precursors 0.2M calcium nitrate tetrahydrate $Ca(NO_3)_2.4H_2O$ and 0.2 M sodium hydroxide (NaOH) were weighed

---

* To whom all correspondence should be sent:
E-mail: pushpendra.kumar@jaipur.manipal.edu

accurately and dispersed in D.I. water while the solution was constantly stirred. Two glass substrates were used to deposit thin films. The first one was fresh glass substrate and the second one was etched glass substrate. The fresh glass substrate was fixed in the sample holder and the dipping rate of the substrate in the individual solution was kept at 400 mm/min for 20 dips, alternatively in sodium hydroxide (NaOH) and calcium nitrate tetrahydrate Ca $(NO_3)_2.4H_2O$ solution and sample name was assigned as G1. The etched glass substrate was also fixed in a sample holder, dipped for 20 times alternatively in NaOH and $Ca(NO_3)_2.4H_2O$ aqueous solutions and the resulted calcite deposited thin film was named as sample G2. During this process calcium hydroxide thin film is formed, however it immediately reacted with CO_2 gas present in the environment and converted to calcium carbonate thin films. The following reactions take place during the calcite thin film formation.

Ca $(NO_3)_2.4H_2O$ + 2NaOH → Ca $(OH)_2$ + 2 $NaNO_3$ + 4 H_2O (1)

Ca $(OH)_2$ + CO_2 → $CaCO_3$ + H_2O (2)
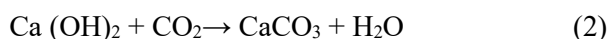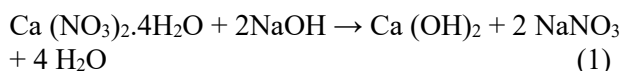
Characterization of CaCO₃ thin films

Rigaku Minifilm-II X-ray diffractometer with Cu Kα radiation of wavelength 1.54054 Å was used to analyse the structural properties, crystallite size and phase of the synthesized thin films. Optical studies were done by a Shimadzu UV-NIR 2600 spectrophotometer. Using a JEOL (JSM-7610FPlus) FESEM, we examined the thin films microstructure sof surface morphologies. FTIR was utilized to analyse the functional groups present in calcite thin films using a Bruker Alpha instrument (resolution of 0.8 cm^{-1} in the wavenumber range 4000-500 cm^{-1}).

RESULTS AND DISCUSSION

Structural study

In Figure 1, the XRD spectra of all the prepared samples are shown. According to the XRD spectra, different peaks can be classified into the following planes: (012), (104), and (108) at 2θ values of 22.35º, 29º and 48.45º, respectively. The main peak (108), which was observed at 2θ ~ 29º, is of the rhombohedral calcite phase of $CaCO_3$ (space group R-3C and no.: 167, PDF Card No. 00-005), and precisely matches the diffraction peak reported in literature [17, 18]. As indicated in Figure 1, XRD was used to determine the pure phase of the calcite thin film in both samples and to confirm that the synthesized thin films are nanocrystalline in nature. Average crystallite size (t_{ds}) of the samples was evaluated according to Scherrer equation [19]:

$$t_{ds} = \frac{k\lambda}{\beta \cos\theta} \quad (3)$$

Here, k is a correction factor that is often considered to be 0.9, and λ, β, θ represent the x-ray wavelength, full width at half maximum, and diffraction angle in turn. The calculated crystallite size of the thin film samples G1 and G2 was found to be 7.12 nm and 7.52 nm, respectively.
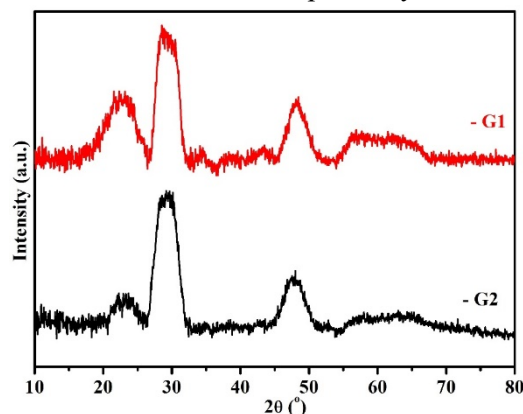

Fig. 1. XRD spectra of calcite thin films (G1) on plain glass and (G2) on etched glass substrate.

Morphological studies:

Fig. 2 (a) presents an FESEM image of the calcite thin film of sample G1 and Fig. 2(d) presents a FESEM image of the calcite thin films of sample G2 which is deposited on etched glass substrate. An illustration of the nanocrystalline structures with cubic shapes can be seen in Figure 2(a). As can be seen from Figures 2(a) and 2(d), both samples have uniform morphology. However, there is a small difference in the surface roughness. The sample G2 shows a higher surface roughness than the sample G1. Analogous results were also reported in the literature by Abdallah *et al.* in a ZnO thin film system on a different substrate [20]. Fig. 2(b) exhibits a higher magnification of Fig. 2(a) for a better representation of a cubic structure. In Fig. 2 (c), the EDAX pattern of sample G1 is shown and the substantial occurrence of C along with Ca and O is seen. Calcite thin film formation was further confirmed by the peak of carbon in EDAX pattern in the current paper and well supported by XRD data discussed in prior section. Similarly, in Fig. 2 (d) we exhibit the FESEM image demonstrating the spherical microstructure of sample G2. Fig. 2(e) displays the higher magnification of Fig. 2(d) for a better representation. As can be seen from the FESEM image, Fig. 2(d) shows higher roughness than Fig. 2(a). This difference in roughness can be attributed to the surface morphology of the substrate. Similarly, in Fig. 2(f) we exhibit the respective EDAX pattern of sample G2. It is further confirmed by the presence of carbon along with Ca and O in the
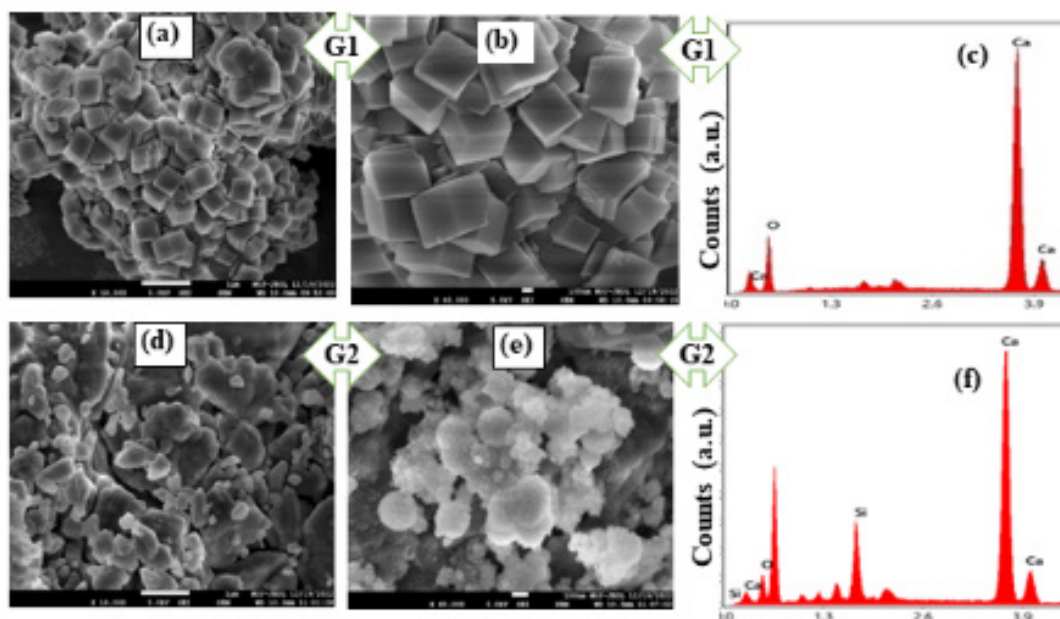
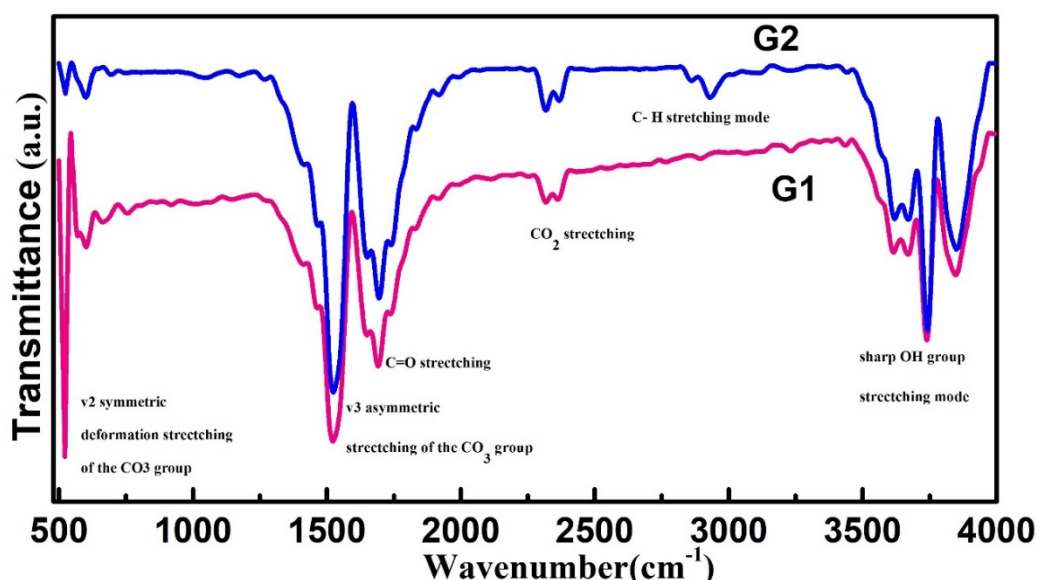**Fig. 2.** FESEM and EDAX patterns of G1 and G2.

Fig. 3. FTIR spectra of calcite thin films of G1 and G2.

EDAX pattern that calcite phase formation took place in the prepared thin film, which is also in agreement with the XRD results. Hence, EDAX and XRD results in both samples correlated well with each other and revealed a calcite phase with controllable microstructure of calcite thin films. Spherical-like microstructure appears rougher in sample G2 as can be seen in Fig. 2(d).

FTIR studies

Figure 3. illustrates the FTIR spectra of G1 and G2 samples. Both the spectra show an absorption band at 550 cm^{-1} corresponding to the CO_3 group stretching mode. The CO_3 absorption v3 symmetric stretching on the thin film sample causes the broad peak at 1500 cm^{-1}. The peak in the CO stretching mode appears at 1750 cm^{-1}. During atmospheric adsorption of CO_2, a small peak at 2400 cm^{-1} is observed. In the surface OH group stretching mode, there is a sharp absorption band at 3750 cm^{-1}. Every functional group available in both thin film samples G1 and G2. However, here is a minor difference in the peak's intensity of both samples. This can be due to samples deposited on different substrates.

The similar functional group for calcite is reported in literature [21]. The CO_3 absorption v2 symmetric stretching peak is decreasing with the change in substrate surface that can be seen in Figure 3. The FTIR spectra of each sample showed the functional group of $Ca(OH)_2$ and $CaCO_3$, as indicated.

Optical studies

Figure 4 shows the UV-Vis absorption spectra for synthesised $CaCO_3$ thin films on both the substrates in the wavelength range of (190-800 nm). A small increase in optical absorbance was observed in sample G2 with respect to G1, as illustrated in Figure 4. The latter shows the average absorption range dependency on surface roughness of the deposited thin film. In Figure 5 we show the related Tauc's plot of both samples. A red shift in the absorbance band edge was observed in sample G2, as seen in Fig. 4. This red shift in the band edge of absorbance was due to an increase in the crystallite size in sample G2. The following equation may be used to calculate the optical band gap of both samples:

$$(\alpha h\upsilon) = A\,(h\upsilon - E_g)^n \qquad (4)$$

Here n is a constant associated to the type of transition (n=1/2 for a direct band gap), α is the optical absorption coefficient, 'A' represents a constant and E_g is the energy gap. In order to calculate band gap energy, the straight section of the curve between "hυ" and $(\alpha h\upsilon)^2$ was extrapolated. As shown in Figure 5, the band gap energies of the $CaCO_3$ thin films are 3.74 eV and 3.72 eV for the sample G1 and G2, respectively. The similar observation of band gap as a function of crystallite size was also published in literature by other workers [22-24]. According to the XRD examination, the crystallite size in sample G2 was found to be greater than that in sample G1. Hence, bandgap values are changed accordingly. These changes in band gap are also supported by FESEM results, where the surface roughness gets bigger as the crystallite size increases

due to rough surface and accordingly the bandgap decreases.
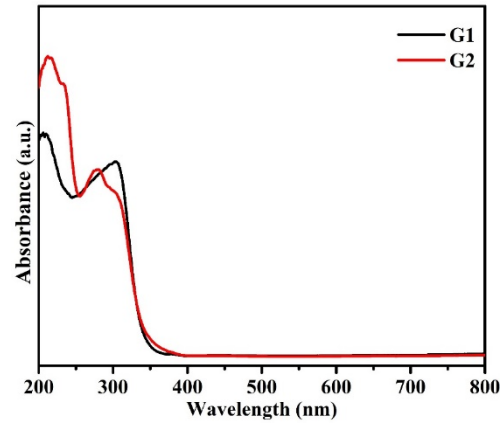
Fig. 4. Absorption spectra of calcite thin films of G1 and G2.

CONCLUSIONS

The calcite thin films were synthesized successfully using simple dip coating. Two different substrates were used in the present study. One is fresh glass substrate and the second is etched glass substrate. In etched glass substrate, the calcite thin film was found to be rougher than the plain glass substrate. From the FESEM images, it was seen that by changing the substrate surface different types of surface morphology of deposited thin films can be obtained. Small differences in the functional group intensity were observed that were attributed to the substrate surface effect. Further, it was seen from XRD results that the crystallite size in the film deposited on etched surface was larger than the thin film deposited on fresh glass substrate. Accordingly, the band gap of calcite thin film was found to decrease from 3.74 eV to 3.72 eV with increase in crystallite size. Moreover, the results suggest that calcite thin films can be tailored for future biomedical applications in both band gap and microstructure.
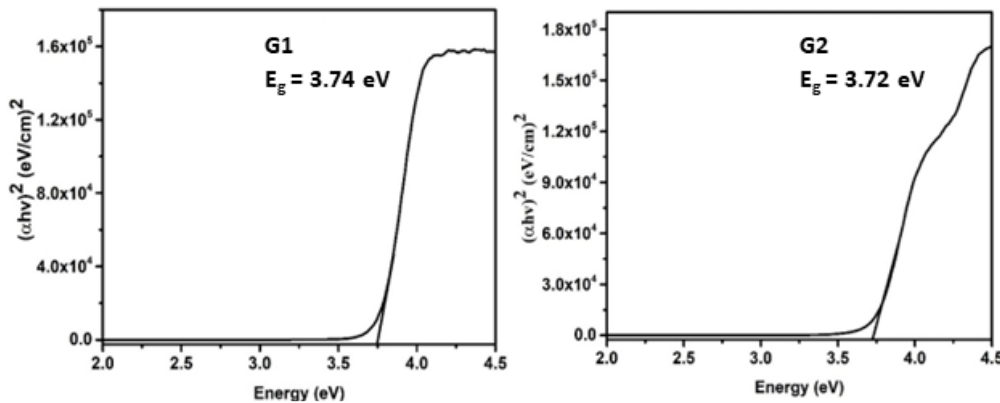

Fig. 5. Tauc's plot of $(\alpha h v)^2$ *vs.* (hv) energy for $CaCO_3$ thin films of G1 and G2.

REFERENCES

1. L. Minkowicz, A. Dagan, V. Uvarov, O. Benny, *Materials (Basel)*, **14,** 3525 (2021).
2. K.Y. Chan., D.P. Heenan, *Aust. J. Soil Res*., **36,** 73 (1998).
3. H. C. Sang, K. P. Jin, K. L. Seung, M. J. Sung, H. K. Im, W. A. Ji, K. Hwan, *Mater. Sci. Forum*, **10,** 881 (2007).
4. T. Matschei, B. Lothenbach, F. P. Glasser, *Cem. Concr. Res*., **37**, 551 (2007).
5. J. S. Christopher, F. L. Sophie, C. M. Fiona, et al., *Adv. Funct. Mater*.**, 20,** 2108, (2010).
6. Q Shen, L. C. Wang, X. P, Li, et al., *Cryst. Growth &Design*.**, 8**, 3879 (2008).
7. R. Y. U. Miyoung , J. H. Ahn, K. S. You, et al., *J. Ceram. Soc. Japan*, **117**, 106 (2009).
8. Yunlan Su, HR Yang, WX Shi, et al., *Colloids and Surfaces A: Physicochem. Eng. Aspects,* **355**, 158, (2010).
9. Y. T. Clifford, C. K. Chen, *Chemical Engineering Science*, **63,** 3632 (2008).
10. A. Rizzuti, C. Leonelli, *Powder Technology*, **186,** 255 (2008).
11. K Yoshiyuki, Y Kohei, N. Nobuyuki, *Ultrasonics Sonochemistry*, **17,** 617 (2010).
12. S. X. Li, Lyu, F Geng, et al.*, J. Cryst. Growth*., **312**, 1766, (2010).
13. E. Tolba, W.E.G. Muller, B.M.A. ElHady, M. Neufurth, F. Wurm, S. Wang, H. C Schröder, *Mater. Chem. B Mater. Biol. Med*., **4,** 376 (2016).
14. M.M.M.G.P.G. Mantilaka, H.M.T.G.A. Pitawala, R.M.G. Rajapakse, D.G.G.P. Karunaratne, K.G.U. Wijayantha, *Cryst. Growth*, **392,** 52, (2014).
15. Hai Yan Xu, Si Le Xu, Xu Dong Li, Hao Wang, Hui Yan, *Science*, **252,** 4091 (2006).
16. Dong Bo Fan, Hao Wang, Yong Cai Zhang, Jie Cheng, Bo Wang, Hui, *Materials Chemistry and Physics*, **80,** 44 (2003).
17. J. Kumari, Harish, Akash, A. Pandey, P. Kumar, M. K Singh, A. Singh, M. S. Shishodia, R. P. Joshi, A. K. Mukhopadhyay, *Material Science Chemistry Select*.,**7,** 24, (2022).
18. J. Kumari, Harish, Akash, A. Pandey, P. Kumar, M. K. Singh, R. P. Joshi, A. K. Mukhopadhyay, *Material Today Proceeding*, **60,** 6 (2022).
19. Akash, Harish, J. Kumari, A. K. Mukhopadhyay, P. Kumar, *Chemistry Select.*, **7**, e202200417 (2022).
20. B. Abdallah, A. Kader, J. Feras, *J. Nanostuct.*, **10,** 185 (2020).
21. A. Barhoum, H. Rahier, R. E. Abou-Zaied, Mohamed R. Thierry Dufour, G. Hill, A. Dufresne, *ACS Appl. Mater. Interfaces,* **26**, 2734, (2014).
22. Harish, P. Kumar, J. Kumari, P. Phalswal, P. K. Khanna, A. Salim, R. Singhal, A. K. Mukhopadhyay, R. P. Joshi, *J. Nano-Electron. Phys*., **13**, 01029, (2021).
23. P. Kumar, *ISRN Nanotechnology*, 2011 (2011) Article ID 163168, 6 pages.
24. P. Kumar, P. Lemmens, *RSC Advance*, **5**, 91134 (2015).

Synthesis and characterization of metal doped molecular sieve 5Å-based catalyst

L. Kumar[1], A. G. Chakinala[2], M. G. H. Zaidi[3], P. Kumar[1*]

[1]Department of Physics, Manipal University Jaipur, Jaipur-303007, Rajasthan, India
[2]Department of Biotechnology and Chemical Engineering, Manipal University Jaipur, Jaipur-303007, Rajasthan, India
[3]Department of Chemistry, College of Basic Science and Humanities, G.B Pant University of Agriculture and Technology, Uttarakhand, 263145, India

Conversion of waste to best in the form of valuable product using different catalysts is the need of present time for an emerging technological application. However, achieving the appropriate yield of best with negligible waste generation at low energy consumption is still a grand challenge. In the process of converting waste to best the catalyst plays an important role for green chemistry. In this report, we have synthesized metal, i.e., zinc- and iron-doped molecular sieve 5Å catalyst using chemical synthesis process. The synthesized catalyst was identified by diverse analytical techniques. Optical spectra revealed the reduction in band gap of metal-doped molecular sieve by 5Å, which was attributed to localized state formation within the band gap of base material molecular sieve 5Å. Such materials can find technological applications in green chemistry to convert waste into valuable chemicals.

Keywords: Molecular sieve 5Å, Metal doping, Chemical synthesis, FESEM.

INTRODUCTION

Nanotechnology's progress has sparked a surge of fascination in transition metal catalysts due to their versatile applications. These catalysts, composed of transition metals, find extensive use in various fields such as wastewater treatment, rechargeable batteries, and catalytic hydrogenation [1]. The use of transition metals, such as iron and zinc, offers several benefits, including being cost-effective and readily available in nature [2]. In recent years, the discharge of pollutants into water environments has emerged as a critical concern, endangering both human health and aquatic ecosystems. To combat this issue, extensive research has been conducted to develop metal nanoparticles as efficient catalysts for the elimination of these harmful contaminants [3].The incorporation of metallic and acidic sites within a unified nanocomposite material has been the subject of extensive research in catalytic applications for many years. The exceptional thermal stability, acidity, and distinctive nanoscale porous structure of molecular sieve 5Å (MS-5Å) have positioned it as a promising candidate for introducing acidic functionality. Various catalytic reactions have demonstrated the exceptional efficiency of composite materials combining metals and molecular sieve 5Å in catalysis [4].

The porous structure of molecular sieve 5Å has rendered it a promising candidate for hosting the synthesis of nanoparticles. These materials can be obtained through natural processes or laboratory techniques and typically comprise alumina (Al_2O_3), silica (SiO_2), alkali or alkaline-earth metals, as well as water molecules trapped inside the pores [5]. The molecular sieve 5Å exhibits a regular microsphere structure in one-, two-, and three-dimensions, resulting in an extensive network of cages and channels with precise shapes and sizes [6]. In this context, Xu *et al.* conducted a comprehensive assessment on the summary of metal nanoparticle catalysts [7]. Additionally, David *et al.* provided insights into the perspectives and applications of molecular sieve 5Å containing metal nanoparticles in catalysis [8]. Wu *et al.* investigated the confinement of noble nanometals within a molecular sieve 5Å matrix, highlighting the notable advantages in size and site adjustment, as well as nano-architecture model.

Recently, the scientific community has extensively investigated the influence of transition metal catalysts on catalytic capabilities. However, there is a notable absence of studies exploring the synthesis of Zn and Fe-doped MS-5Å composite nanomaterials. This knowledge gap in the literature motivated the scope of the present work. Building upon our interest in synthesizing new nanostructured compounds with applications in metal-organic framework synthesis and wastewater treatment [9, 10], we present a simple chemical synthesis process for making zinc and iron-doped MS-5Å materials. The synthesized samples were analyzed using XRD, FTIR spectroscopy, FESEM, and UV-Vis techniques. The synthesis of nanosized catalysts within the molecular sieve 5Å framework represents an innovative approach towards achieving efficient

---

* To whom all correspondence should be sent:
  E mail: pushpendra.kumar@jaipur.manipal.edu

catalytic reactions. These MS-5Å-based nanocomposites hold potential for various multifunctional applications, which will be the focus of our future endeavors.

EXPERIMENTAL

Material

For this research work, reagents: urea (CH_4N_2O), iron (III) nitrate nonahydrate ($Fe(NO_3)_3.9H_2O$) and zinc nitrate hexahydrate ($Zn(NO_3)_2.6H_2O$) were used without any purification. Molecular sieve-5Å was purchased from Gujrat Multi Gas Base Chemicals Pvt. Ltd. Ethanol was used for the synthesis.

Sample preparation

A straightforward chemical synthesis method was employed to fabricate composite nanostructures (CNs) of iron and zinc-doped molecular sieve 5Å (MS-5Å). At first, finely crushed MS-5Å (3 g) was added to ethanol (15 mL), followed by the addition of urea (1.5 g) dissolved in ethanol (15 mL). The resulting pinkish product was stirred for 1 hour. Subsequently, iron (III) nitrate nonahydrate ($Fe(NO_3)_3.9H_2O$) and zinc nitrate hexahydrate ($Zn(NO_3)_2.6H_2O$) solutions (1.6 g each) were slowly dropwise mixed into the solution while continuously stirring at 60°C for 2 hours. The resulting mixture was then sonicated for 1 hour, filtered, and dried overnight at room temperature. Finally, the dried samples (Zn/MS-5Å and Fe/MS-5Å) were calcined at 500°C for 5 hours and placed in a desiccator. In total, there were three samples - molecular sieve-5 Å named as sample S1, Zn-doped MS-5Å named as sample S2 and Fe-doped MS-5Å named as sample S3.

Characterization

The synthesized catalyst underwent comprehensive characterization using various methods to analyze its structural, morphological, functional, and optical properties. The UV-Vis spectra were recorded in absorbance mode on a Shimadzu UV-NIR 2600, Japan instrument in the range of 190-800 nm at ambient temperature. Prior to measurement, the synthesized samples were dissolved in deionized (DI) water and subjected to sonication for approximately 1 hour. The obtained absorbance data were utilized to evaluate the energy gap (E_g) of both samples by constructing Tauc plots that correlate energy with the square of the absorption coefficient ($\alpha h v)^2$. The structural analysis of the prepared materials showed various functional groups, using a Fourier transform infrared (FTIR) spectrometer model Bruker Alpha from the USA. The spectra were documented in the scale of 500-4000 cm^{-1}.

The structural characterization was made using a programmed multipurpose X-ray diffractometer (model: SMARTLAB) manufactured by Rigaku. The instrument employed a wavelength of Cu Kα radiation of 0.15406 nm. The detector was operated at a voltage of 40 kV with a filament current of 30 mA. The XRD patterns were recorded for all samples in the span of $10° \leq 2\theta \leq 80°$, with a scanning rate of 0.02 θ /s at room temperature. This analysis aimed to investigate the size, phase and crystal structure of the prepared materials. The morphology, shape, and size of the synthesized samples were analyzed using a field effect scanning electron microscope (FESEM) model JEOL-7610F, Japan. Additionally, the elemental constituents of the samples were analyzed by energy dispersive X-ray spectroscopy (EDX), which was integrated with the same FESEM instrument.

RESULTS AND DISCUSSION

Structural study

The XRD patterns of the prepared material are illustrated in Fig. 1. The XRD patterns exhibit multiple peaks, indicating the crystalline nature of the compounds. The diffraction peaks, observed at specific 2θ values, correspond to various crystallographic planes. Specifically, the peaks located at approximately 6.30°, 10.20°, 11.94°, 15.69°, 18.67°, 20.32°, 23.57°, 26.93°, 30.60°, 31.25°, 32.29°, and 33.90° can be indexed to the (200), (220), (311), (331), (511), (440), (533), (642), (660), (751), (840), and (664) planes, respectively, which are associated with the molecular sieve 5 Å present in our samples. The observed diffraction peaks closely correspond to the characteristic peaks of the alumina and silica tetrahedral framework. Notably, the dominant peak (200) is observed at an approximate 2θ value of 6.30° [11]. To determine the crystallite size (t_{DS}) of the sample for the respective crystal plane orientations, the Debye-Scherrer formula was employed [12]:

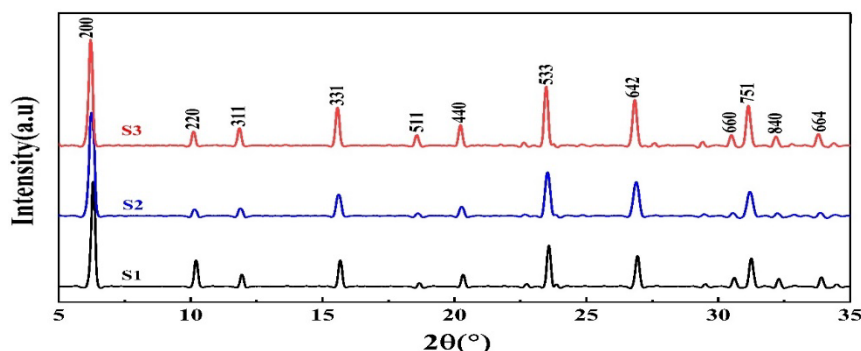$$t_{DS} = \frac{k\lambda}{\beta_{hkl}cos\theta_{hkl}} \tag{1}$$

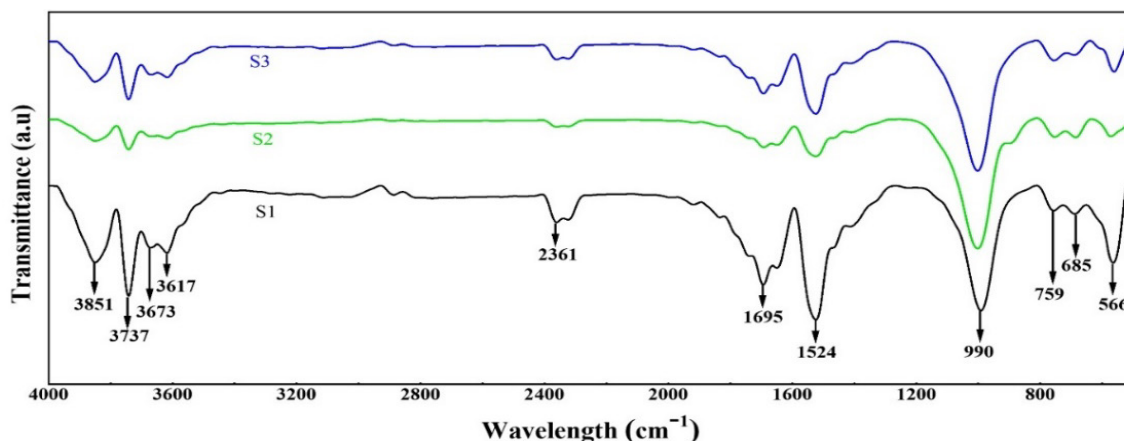**Fig. 1.** XRD spectra of MS-5Å (S1), Zn/MS5Å (S2) and Fe/MS5Å (S3)

Fig. 2. FTIR spectra of samples S1, S2, and S3.

The determined values of crystallite size for samples S1, S2, and S3 are 53.38 nm, 54.02 nm, and 56.23 nm, respectively. It is noted that the crystallite size of samples S2 and S3 is larger compared to sample S1. This increase in crystallite size can be attributed to the heating treatment that samples S2 and S3 underwent during the synthesis process. The supplied heat energy during calcination facilitates the diffusion and rearrangement of atoms or molecules within the sample, leading to the agglomeration and growth of existing crystallites. This phenomenon, known as crystallite growth or crystallite coarsening, causes the average crystallite size to increase after calcination.

FTIR study

The different groups contained in the materials were examinedby FTIR. Figure 2 illustrates the FTIR spectra of MS-5Å, Zn/MS-5Å, and Fe/MS-5Å composite nanomaterials (CNs) in the measurable range of 500 to 4000 cm^{-1}. The wave number corresponding to 566 cm^{-1} was attributed to the bending vibrations of the T-O (T = Al, Si groups) in the sieve [13, 14]. These peaks also represent the bending vibration of the internal tetrahedron TO_4 of the MS-5Å structure, indicating the existence of Al^{3+} and Si^{4+} in the sieve. The peak at 685 cm^{-1} is associated with Si-O-Si, while the peak at 759 cm^{-1} corresponds to the symmetrical stretching (T-O-T, T = Si, Al) [15]. The band near 990 cm^{-1} is related to the symmetric vibrations of Si-O (bridging) and Si-O- (non-bridging) bonds [16]. The bands detected at 1524 and 1695 cm^{-1} are related to the OH bending vibration of water molecules [17]. The band at 2361 cm^{-1} may be attributed to the interaction between Zn/MS-5Å, Fe/MS-5Å, and TO_4 in the sieve during the doping process [18, 19].The samples exhibit distinctive bands corresponding to AlO-H groups (at 3737 and 3673 cm^{-1}), Si-OH-Al acidic hydroxyls (at 3617 cm^{-1}) [20, 21], and external SiO-H groups (at 3851 cm^{-1}) (Figure 2), consistent with previous studies [22]. The introduction of metal ions into the molecular sieve directs to a significant decrease in the intensity of these bands (Figure 2), indicating that the zinc and iron species interact with several hydroxyl groups of the pristine support.
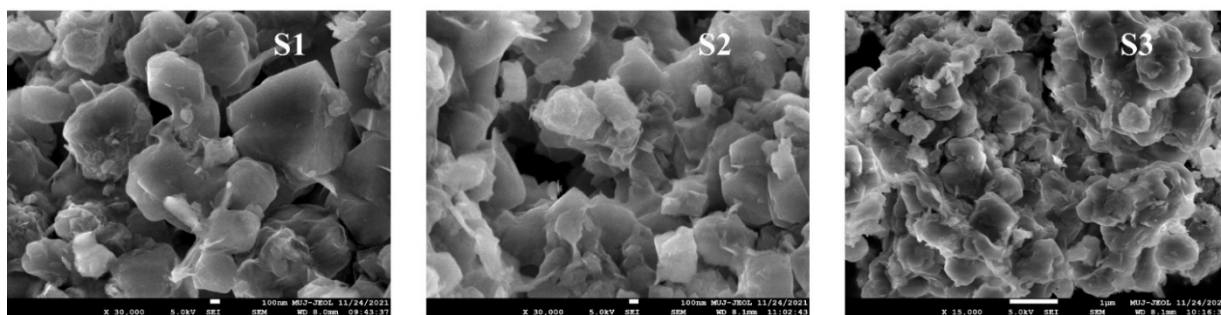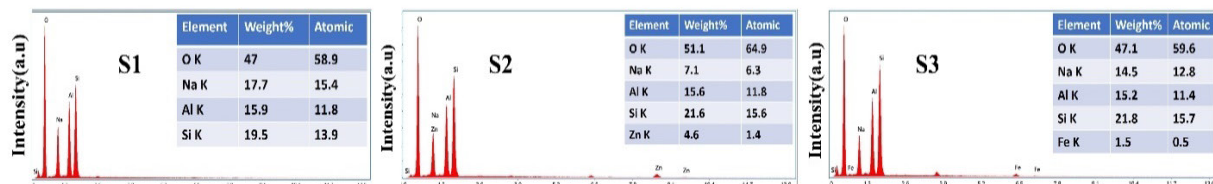
Fig. 3. FESEM images of the samples S1, S2 and S3

Fig. 4. XEDS spectra of the samples S1, S2 and S3.
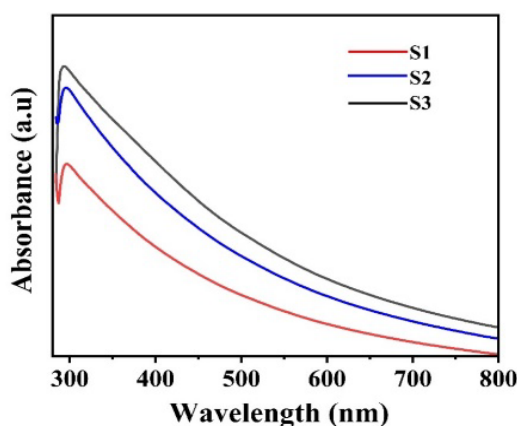

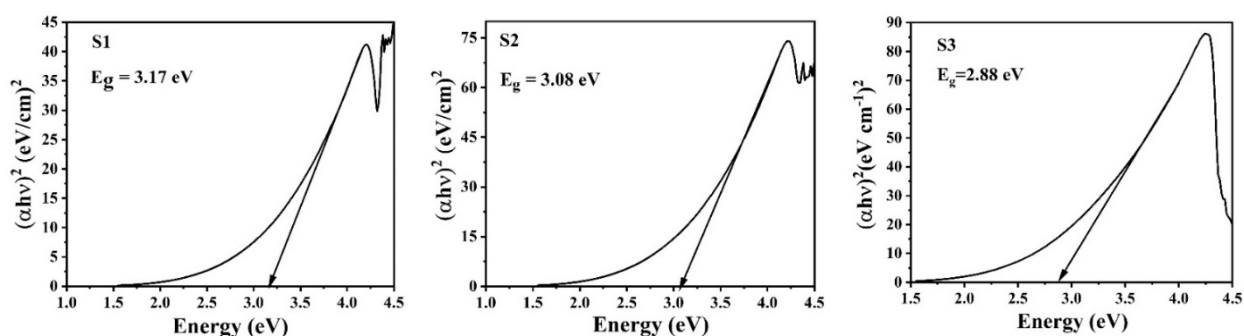**Fig. 5.** Absorbance spectra of the samples S1, S2 and S3

Fig. 6. Tauc plots of the samples S1, S2 and S3

Microstructural studies

FESEM analysis

The morphology of the samples was studied using high-resolution FESEM. The images exhibit that the mean diameter of the samples ranged from 100 nm to 1 μm and were aggregated in shape with a high density, as seen in Fig. 3. The findings suggest that the blending methodology used resulted in well-

formed Zn/MS-5Å and Fe/MS-5Å, as supported by previous studies [23, 24]. The results showed that the samples consisted of oxygen, iron, silicon, zinc, and aluminum, as seen in Fig. 4. The data from the selected area analysis by XEDS, which included a comparative elemental analysis, confirmed that the Zn/MS-5Å and Fe/MS-5Å are composed of the elements and no impurities were detected. The obtained Zn and Fe content agreed with the

theoretical zinc and iron content in the Zn/MS-5Å and Fe/MS-5Å, as seen in Fig. 4 [25].

Optical behavior

The optical study of the samples was performed in the wavelength scale of 190-800 nm, as depicted in Figure 5. The Tauc plots, based on the relation involving the absorption coefficient and the energy of the incident light, are shown in Figure 6. These plots were utilized to estimate the band gap energy [26-29].

$$(\alpha h\nu) = \beta (h\nu - E_g)^r \text{ for } h\nu > E_g \qquad (2)$$
and
$$(\alpha h\nu) = 0 \text{ for } h\nu < E_g \qquad (3)$$

where, absorption coefficient (α) was evaluated using absorbance (A) by the formula $\alpha = (2.303 * A / x)$, where x represents the width of the sample. A constant β was introduced, and the optical energy gap (E_g) was determined using a linear fit of the experimental data. The parameter r can take values of 1/2 and 2 for direct and indirect admitted transitions, respectively, which depends on the nature of electron transitions accountable for the optical absorption. Based on the linear fits, the band gap values for samples S1, S2, and S3 were evaluated to be around 3.177 eV, 3.08 eV, and 2.88 eV. It is observed that the band gap decreases with metal doping. This drop in band gap can be related to the increase in crystallite size, as evidenced by the XRD analysis.

CONCLUSION

In this study the synthesis of metal-supported MS-5Å nanoparticles was performed using a chemical method. The effect of heating during sample synthesis was evaluated in terms of its impact on crystallite size and optical properties. The results revealed that the increased agglomeration in the synthesized nanomaterials, due to heating, was the primary reason for the observed changes. The band gap of the sample showed a significant shift, from 3.17 eV in sample S1 to 3.08 eV in S2 and 2.88eV in S3, because of the alterations in structural parameters and crystallite size caused by the agglomeration. These findings demonstrate the feasibility of modulating the properties of molecular sieves 5Å through variations in synthesis parameters and doping with different transition metals. This study contributes to the advancement of knowledge in the field by providing insights into the behavior of the synthesis process of different molecular sieves and its potential applications in industries such as biomedical, wastewater treatment, and thermochemical heat storage.

REFERENCES

1. G. Allaedini, S. M. Tasirin, P. Aminayi, *Chemical papers,* **70**, 231 (2016).
2. X Du, H Su, X Zhang, *Journal of Catalysis,* **383**, 103 (2020).
3. A. Karbul, M. K. Mohammadi, R. J. Yengejeh, F. Farrokhian, *Material Research,* **24**, e20200292 (2021).
4. E Nyankson, J. Adjasoo, J. K. Efavi, A Yaya, G. Manu, A. Kingsford, R. Y. Abrokwah, *Scientific African,* **7**, e00257 (2020).
5. M. Yoldi, E.G.Fuentes-Ordoñez, S.A.Korili, A.Gil, *Powder Technology,* **366**,175 (2020).
6. H. Jahangirian, R. Moghaddam, N. Jahangirian, B. Nikpey, S. Jahangirian, N. Bassous, B. Saleh, K. Kalantari, T. J. Webster, *Int. J Nanomedicine,* **15**, 1005 (2020).
7. D. Xu, H. Lv, B. Liu, *Frontiers in Chemistry,* **6**, (2018).
8. D. Farrusseng, A. Tuel, *New Journal of Chemistry,* **40**,3933 (2016).
9. M. K. Mohammadi, A. Gutiérrez, P. Hayati, K. Mohammadi, R. Rezaei, *Polyhedron,* **160**, 20 (2019).
10. A. Derakhshan-Nejad, H. A. Rangkooy, M. Cheraghi, R. J. Yengejeh, *J Environ. Health Sci, Eng.*,**18**, 201 (2020).
11. R. M. Barrer, P. J. Denny, *J. Chem. Soc.*,**0**, 971 (1961).
12. Harish, P. Kumar, J. Kumari, P. Phalaswal, P. K. Khanna, A. Salim, R. Singhal, A. K. Mukhopadhyay, R. P. Joshi, *Journal of Nano- and Electronic Physics,* **13**, 01029 (2018).
13. B. Kwakye-Awuah, E.Von-Kiti, I. Nkrumah, R. ErdooIkyreve, I. Radecka, C. Williams, *Desalin.. Water Treat.,* **57**, 21654 (2016).
14. A. Zainal Abidin, Abu Bakar NHH, Ng. EP, W. Tan, *J. Taibah Univ. Sci*., **11**,1070 (2017).
15. H. L. Wang, J. Y. Cui, W. F. Jiang, *Mater. Chem. Phys*., **130,** 993 (2011).
16. B. Kwakye-Awuah, D. D. Wemegah, I. Nkrumah, C. Williams, I. Radecka, *Int J, Sci Res.,* **2**, 26 (2013).
17. M. S. Boroglu, M. A. Gurkaynak, *Polym Bull*., **66,**463 (2011).
18. X.Guo, A. Navrotsky, *Microporous Mesoporous Mater*., **268,** 197 (2018).
19. A. Asiedu, S. Kumar, *Ind. Eng. Chem. Res*., **58,** 15787 (2019).
20. E. Bourgeat-Lami, F. Fajula, D. Anglerat, T. Des Courieres, *Microporous Mater*.,**1**, 237 (1993).
21. A. Janin, M. Maache, J. C. Lavalley, J. F. Joly, F. Raatz, N. Szydlowski, *Zeolites.*, **11**, 391 (1991).
22. A. Jentys, N. H. Pham, H. J Vinek, *Chem. Soc. Faraday Trans.*,**92**, 3287 (1996)
23. X. Zhang, Q. Shen, C. He, C. Ma, J. Cheng, Z. Liu Z. Hao, *Catal. Sci. Technol*., **2**, 1249 (2012).
24. E. F. Iliopoulou, S. Stefanidis, K. Kalogiannis, A. C. Psarras, A. Delimitis, K. S. Triantafyllidis, A. A. Lappas, *Green Chem*., **16**, 662 (2014).
25. Y. Ding, Y. Wang, L. Zhang, H. Zhang, C. M. Li Y. Lei, *Nanoscale*, **3**, 1149 (2011).

26. P. Kumar, P. Lemmens*, RSC Adv.*, **5**, 91134 (2015).

27. Harish, P. Kumar, V. Kumar, R. K. Mishra, J. S. Gwag, M. K. Singh, R. Singhal, A. K. Mukhopadhyay, *Ceramic International*, **48**, 35771 (2022).

28. Harish, P. Kumar, S. Kumari, M. Debnath, A. Salim, R. Singhal, R. P. Joshi, and A. K. Mukhopadhyay, *Journal of Material Science*, **57**, 8241 (2022).

29. Akash, Harish, J. Kumari, A. K. Mukhopadhyay, P. Kumar, *Chemistry Select.*, **7,** e202200417 (2022).

Electrical behavior of graphite epoxy composite electrodes in humid environment

M. Pandey[1], D. Palariya[1], S. Mehtab[1]*, M.G.H. Zaidi[1]*, P. Kumar[2]

[1]*Department of Chemistry, College of Basic Sciences & Humanities, G.B. Pant University of Agriculture & Technology, Pantnagar, Uttarakhand-263145, India*
[2]*Department of Physics, Manipal University Jaipur, Jaipur-303007, Rajasthan, India*

The present study demonstrates the development of graphite (GR)-enriched epoxy composites for possible application as electrode materials for supercapacitors operating in humid environment. The study was conducted through development of a series of adhesive compositions involving epoxy resin supplemented with various proportions of GR (50 to 85 %w/w) and 4,4'-diaminodiphenyl sulfone (1%, w/w), followed by curing over stainless-steel current collectors at 110 °C. This has afforded a series of working electrodes (WEs) with improved electrical conductivity. The effect of temperature and voltage on the electrical behavior of WEs at varying composition was investigated in humid environment (40%, RH). The study demonstrates that WEs involving 50 wt% of GR exhibit a 10% increase in σDC at 1 V under 40% RH, 40°C. Arrhenius plots revealed that the activation energies (Ea, J/mole) of WEs were dependent on GR concentration (50 to 75% w/w) and were found in the range of 2.10 to 4.76. In comparison to the humidity at room temperature (36% RH), the humidity exposure (40% RH) of WEs derived at 50 wt% GR has shown an increase in σDC by 7.69%.

Keywords: Humidity, Epoxy, Graphite, Electrical conductivity, Working electrodes

INTRODUCTION

The current century has witnessed a growing need of inexpensive electronic materials for microelectronics [1], energy conservation and storage [2-4]. Working electrodes (WEs) constitute a crucial component in portable electronic devices, including batteries and supercapacitors pertaining to power generation and charge storage. The exploration of renewable and energy-efficient WEs for batteries and supercapacitors relies on the utilization of electrically conducting and electroactive materials possessing commendable temperature, voltage regulated conducting behavior [1], sustainability in humid environment [5] and ease of fabrication [6]. The adequate performance of WEs necessitates their high heat resistance and stability in humid conditions. In this regard, electrically conducting WEs with stability up to 200°C were developed from polyindole in presence of tungsten carbide [7]. Another study demonstrated an enhancement in the semiconducting behaviour of polypyrrole by incorporating haemoglobin [4]. A study reported that supercritical CO_2 assisted the green method for the synthesis of composite with improved DC conductivity and thermal stability [3]. In a recent study, thermally stable WEs (1000°C) were derived from carboxylate functional multi walled carbon nano tubes (MWCNTs) in presence of hexagonal boron nitride and polyvinyl butyral.

The study reveals an increase in σDC ranging from 0.96 to 1.14 under humidity exposure (40%) up to 3 h. However, further humidity exposure up to 9 h has marginally declined the σDC from 1.11 to 1.10 under identical conditions [8].

Graphite is widely known as an electrically conducting filler for polymer materials, especially epoxy resin to afford the polymer composites for electronic and electrochemical applications Over decades, considerable progress has been noticed in development of polymer nanocomposites through reinforcing various allotropic variants of graphite with epoxy resins. The key allotropic variants used in the development of electrically conducting polymer nanocomposites involving epoxies are expanded graphite, graphite [10, 11], graphite nanoparticles [12, 13] and carbon black [14]. A study involving expanded graphite (8 wt %) reveals an 11-fold increase in σDC of epoxy [9]. However, graphite as a filler poorly contributes to σDC of epoxy composite, as reported [10, 11].

Reinforcing graphite by 5 to 25 % contributes to the σDC ($\times 10^{-6}$) S/cm ranging from 2.5 to 3.39 [10]. In another study the increase in graphite loading up to 55 wt% imparts the σDC of epoxy composite in the order of 10^{-4} S/cm [11]. Reinforcing graphite nano particles (0.3 to 30 wt %) into epoxy imparts σDC of polymer composite by the order of 10^{-3} S/cm [12].

---

* To whom all correspondence should be sent:
E-mail: smiitr@gmail.com, mghzaidi@gmail.com

Although a wide range of allotropic variants of graphite has been investigated to develop the electrically conducting epoxy composites and their nano composite analogues, no efforts are yet reported on the investigation of their electrical behaviour in humid environment.

Epoxy is widely used as an insulating material, and its response to elevated humidity levels has been extensively studied [15-22]. Epoxy/epoxy compounds in humid environment can undergo dimensional changes [13-15], reduction in mechanical properties [16, 17], increased susceptibility to environmental stress cracking [19, 20] and altered thermal properties [23, 24]. Epoxy resins have shown different mechanisms of water absorption *via* hydrogen bonding under different RH exposure based on their structure and activation energies [25, 26]. In a study it was found that addition of MWCNTs (1 wt%) to epoxy resulted in moisture uptake similar to cured epoxy, however, reduction in diffusivity was observed [16]. The dependence of σDC of GR/epoxy composites on RH has not been extensively studied. The present study investigates the humidity and temperature dependence of electrical conductivity of epoxy GR composites at varying voltage.

EXPERIMENTAL

Materials and methods

Working electrodes (WEs) were fabricated using commercially available GR powder (purity 98%, surface area 250 μm) sourced from Loba Chemie Fine Chemicals Pvt. Ltd, India. Epoxy (CY-230, density 1.08 g/cc) and hardener (4,4'-diaminodiphenyl sulfone, HT-972) were obtained from Huntsman India Pvt Limited. Other chemicals and solvents (>99 %) were locally arranged and used without further purification.

Fabrication of working electrodes

A series of WEs was fabricated through curing of an adhesive composition involving epoxy resin supplemented with various proportions of GR in acetone medium over stainless steel current collectors (CC). The CC employed for development of WEs were of 1 cm^2 area and a thickness of 1.48 ± 0.01 mm. A representative procedure involving the adhesive composition of epoxy resin (CY-230) with GR (50 to 85 w/w%) was thoroughly mixed at 800 rpm, followed by thermal activation at 90ºC±1ºC for 1 h and curing over CC with 4,4'-diaminodiphenyl sulfone (1%, w/w) at 50ºC ± 1ºC. Prior to curing, the surface of CC was polished with emery paper and subsequently cleaned with acetone. WEs were post-cured at 110ºC. WEs with GR (% w/w) 0, 50, 65, 75

and 85 were fabricated and abbreviated as WE-0, WE-I, WE-II, WE-III and WE-IV, respectively. WEs with coating thickness of 0.23 ± 0.01 mm were isolated and stored at 50 ± 1°C/400 mm Hg [27]. The morphology of the electrode surface was examined through gold sputtering on its surface followed by scanning electron microscopy (SEM) imaging on JEOL JSM-6610 LV at 15 kV.

DC conductivity measurement

DC conductivity (σDC) measurements were conducted at 25 ± 1°C using a four-probe setup equipped with Keithley nanovoltmeter 2182A and a 6221 DC current source. The activation energy (Ea, J/mol) of the WEs was calculated within the temperature (K) range of 313.15 to 373.15 according to the Arrhenius equation $\sigma DC = \sigma_oDC \exp(-Ea/K_BT)$, where σDC is electrical conductivity (μS/cm) of WEs, Ea is activation energy (eV) which indicates the energy needed for an electron to skip and move to adjacent vacancy, σ_oDC is pre-exponential factor which corresponds to maximum electrical conductivity (that it would have at infinite temperature), T is absolute temperature, and K_B is Boltzmann's constant [28-30]. Oven-dried electrodes were aged in humid environment. Relative increase in σDC of WEs under humidity exposure at 36% and 40% were investigated at selected voltages over the interval of 1 h till 8 h at 40±1 ºC.

RESULTS AND DISCUSSION

Microstructure

Dispersion of GR into epoxy matrix of WEs was revealed through SEM (Figure 2). Dispersion of GR into epoxy has been associated with occasional phase separation in the epoxy matrix. The bright and dark phases associated demonstrate the epoxy- and GR-rich phases of WEs. Early studies revealed saturation of the epoxy matrix with 55 wt% of GR cured with aliphatic amine hardener without significant phase separation [11]. In the present investigation, WEs derived through dispersion of 50 to 85 wt% of GR revealed phase separation at 1KX, 10 μm, due to the insoluble nature of the solid phase hardener (HT-972) into epoxy resin (Figure 2b). The concerned phase separation was well distinct at 3KX, 5μm indicating the dispersion of graphene layers derived from GR into epoxy matrix.

In a study on GR/epoxy it was reported that at the elevated temperature employed during the curing process of epoxy, the viscosity of epoxy resin diminished, thereby enhancing the mobilization of the filler phase within the polymer phase. This increased the affinity of the filler to engage with the

matrix and establish conductive filler networks [31]. On further increase in GR concentration in epoxy (85%), the WE-IV resulted in dense clusters of graphene layers into the epoxy matrix (Figure 2d). WE-IV at 1KX, 10 μm revealed a saturation of the graphene layers within the epoxy matrix, displaying a significant presence of clusters formed by epoxy-bonded GR (Figure 2b). Another study revealed that reinforcement of GR (80 wt.%) results in decreased processability due to high viscosity. In the current investigation, the loading of 85 wt% of GR was found to adequately bind with epoxy matrix while preserving a phase-separated morphology over WEs (Figure 2d) [32].

Electrical behavior

Figure 2 reveals the trend of σDC of WEs (36% RH) with concentration of GR (wt%) at selected voltages at $25 \pm 1^{\circ}C$. In general, σDC of WEs increased with GR concentration (wt%) and voltage. The increase in σDC of WEs with GR concentration

attributes to long-range conductive interconnections between the filler and the epoxy matrix. This observation is supported by the early reports of σDC on the close agreement with σDC epoxy nanocomposites involving MWCNT and GR [11, 33]. However, the relative difference in σDC for individual WEs was marginal at 1V and 10V. These observations revealed the electrically insulating behaviour of WEs up to 10V. This observation was in close agreement with epoxy nanocomposites prepared out of expanded graphite [9]. Present observations indicated that WE-IV with 85 wt% reinforcement of GR imparts enhanced σDC (859.80 μS/cm) at 100V over the epoxy composite (100 μS/cm) involving expanded graphite (8 wt%) at 1000 V. Moreover, an increase in voltage from 1 V to 100 V has raised the σDC of WE-IV 11 times over WE-0 [34]. Dispersion of carbonaceous fillers plays constructive role towards enhancing the electrical behavior of epoxy composites [35].
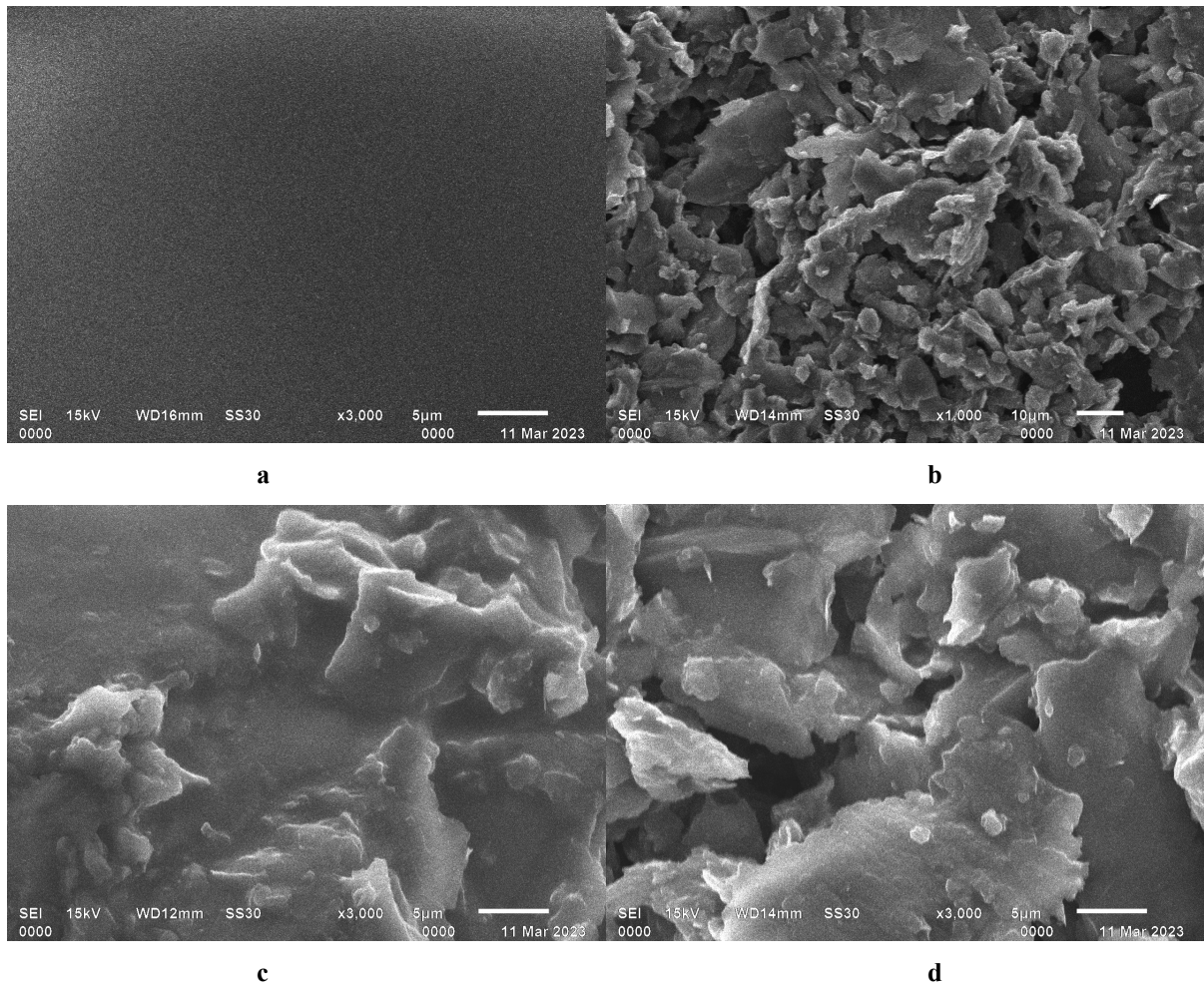

Fig. 1. SEM of WE-0 (a) and WE-IV (b) at 1KX, 10 μm, WE-I(c) and WE-IV(d) at 3KX, 5μm

In the present investigation the exceptionally enhanced σDC (859.80 µS/cm) of WE-IV at 100 V was supported by SEM which indicates the prominent dispersion of graphene layers (bright phase) into epoxy matrix (dark phase) (Figure 1c).

Figure 3. demonstrates the linear I-V characteristics of WEs at 25 ± 1°C. The ohmic behavior of WEs appeared in the range of 0.10 to 2.08 µA with corresponding voltage ranging from 20 to 55 V [36]. Table 1 shows the increase in σDC of WEs with varying voltage (1V–100V) and temperature ranging from 293 to 393 K. Figure 4 illustrates a decline in σDC of WE-IV with temperature (K) ranging from 333 to 393 at 100 V. This consistent trend attributes to the enhancement in the collaborative motion of the macromolecular segments of epoxy, triggered with temperature elevation. This movement leads to a greater dissipation of energy, thereby contributing to the observed decrease in σDC [37]. Using the theoretical Arrhenius model, the calculated activation energies from plots of log (σDC) against 1000/T at 100 V revealed Ea (J/mol) for WEs in the sequence of WE-0 (4.19), WE-I (2.10), WE-II (3.97), WE-III (4.76) (Figure 5).
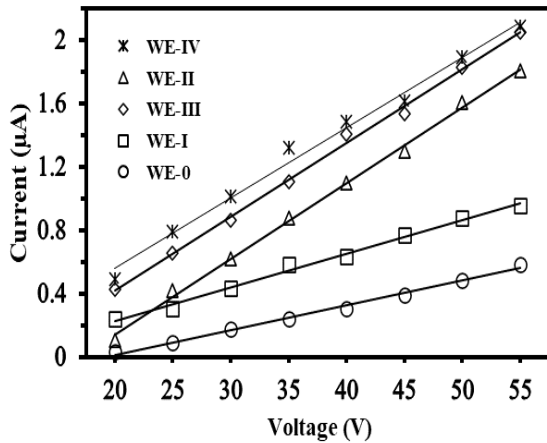
Fig. 4. Arrhenius plots of the DC conductivity for WEs
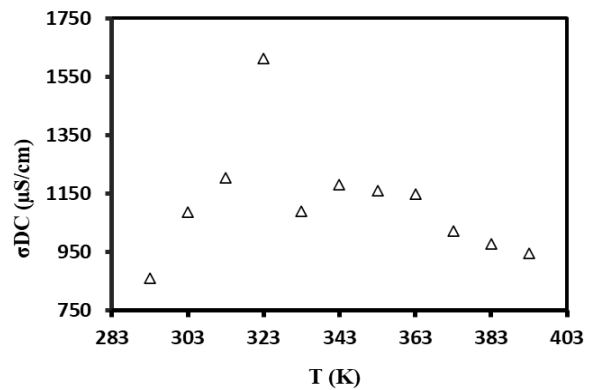
Fig. 5. Effect of temperature on σDC of WE-IV at 100 V

Effect of humidity

WEs were developed at selected wt% of GR and investigated for the electrical behavior after 8 h of exposure at 40% RH%. In general, the σDC (µS/cm) of WEs was dependent on their composition. Figure 6 demonstrates the effect of wt% of GR and voltage (V) on σDC of WEs. The σDC of WE-I was increased by 10.30% at 1 V and by 7.55% at 100 V. WE-II has shown an increase in σDC by 5.23 % at 1 V. However, at 100 V, WE-II has shown an increase of σDC by 1.44 % .The rest of the WEs has shown a significant decrease in their σDC (µS/cm) ranging from 859.39 to 822.2. Duration of humidity on WEs based on GR oxide/epoxy revealed an increase in their σDC from 10^{-6} to 10^{-2} S/cm when RH was increased from 30% to 100% [5]. Epoxy resins cured with amines are associated with inherrent hygroscopic nature due to the formation of hydroxyl group in their macromolecular segment [8, 15]. A study on carbon/epoxy composites has reported that the presence of carbonaceous fillers reduced the moisture-absorbing capacity of the composite by 3% [38]. For such reasons, WE-I, WE-II developed at higher proportion of epoxy absorbed the moisture to a great extent over those prepared at low proportion of epoxy (WE-III, WE-IV).

Fig. 2. Effect of voltage on σDC (µS/cm) of WEs

Fig. 3. Ohmic behavior of WEs

A detailed insight into the effect of humidity on σDC of Wes and their electrical behavior was obtained at competitive RH% selected at 36 and 40 (Figure 7). The increase in RH from 36 to 40, has raised the σDC of WE-I from 650 to 700 at 100 V. The calculations revealed that the increase in RH by 4% imparts 7.69% increase in σDC of WE-I at 100 V. However, subsequent Wes were found resistant towards humidity and have not contributed to further increase in their σDC under the differential exposure of RH by 4% at 100 V. The present investigation is in agreement with the literary report that reveals insulating properties of graphene oxide thin films at low RH. Presence of epoxy contributes to the ion conducting mechanism within the polymer matrix that causes an increase in σDC of WEs [39]. However, with increase in % GR, the relative proportion of epoxy decreased, that delivers the WEs, wherein the σDC is insignificantly increased, thus leaving WEs with intact electrical behavior.
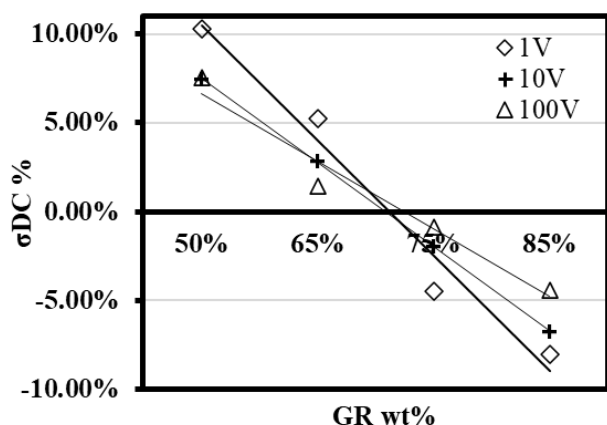
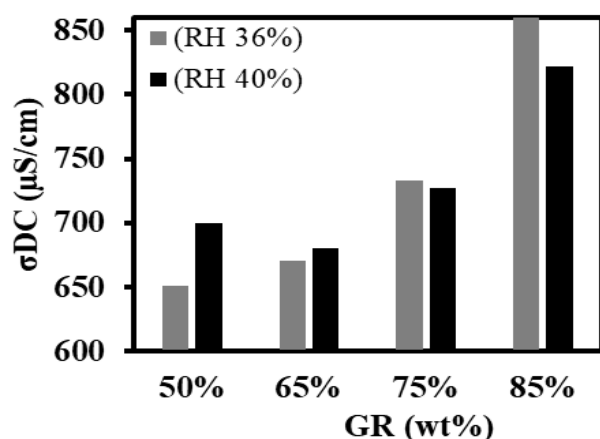**Fig. 6**. Effect of composition and voltage on σDC of WEs at RH (40%)

Fig. 7. Effect of composition and RH % on σDC of WEs.

Table 1. Effect of temperature on the conductivity of WEs at 100V

T(K)	WE-0	WE-I	WE-II	WE-III	WE-1V
393	486.35	650.95	670.24	743.54	946.71
383	543.97	667.41	707.84	791.04	977.17
373	594.69	694.72	717.84	826.94	1023.29
363	639.38	716.35	765.46	901.34	1024.20
353	654.49	733.11	797.00	963.84	1082.01
343	691.67	768.37	842.29	992.35	1092.13
333	729.38	783.39	899.00	1043.77	1389.70
323	732.77	784.14	902.77	1084.25	1612.37
313	754.89	800.25	958.71	1119.85	1319.50
303	751.18	796.64	963.08	1160.35	1096.13
293	771.11	792.29	998.98	1197.09	859.88

CONCLUSIONS

Working electrodes (WEs) based on epoxy supplemented with graphite (GR) (wt% 50 to 85) were developed *via* curing process on a stainless-steel current collector. The developed WEs revealed saturation at 85 wt% GR which showed clear phase separation and dense clusters of graphene layers within the epoxy matrix. With GR wt% the σDC (μS/cm) of WEs was found to increase by 859.80 for WE-IV at 100V, 36% RH and 25 ± 1°C. The study demonstrated an 11-fold increase in σDC of WE-IV over WE-0 at variable voltage ranging from 1 V to 100 V. The present investigation suggests that dispersion of carbonaceous fillers plays a constructive role towards enhancing the electrical behaviour of epoxy composites. The study also demonstrated that with the rise in temperature from 293 to 393 K and varying voltage (1 V–100 V) the WEs exhibited an increase in σDC with temperature. A detailed investigation on the effect of humidity on σDC of WEs revealed that σDC is greatly influenced by changes in relative humidity. WEs under differential exposure of RH by 4% at 100V showed an increase of 7.69 % in σDC of WE-I, however, other electrodes were insignificantly affected. The WE-I at 40% RH showed an increase in σDC by 10.30 % at 1 V and 7.55 % at 100 V. The present study demonstrates that the presence of relatively higher wt% of epoxy in WE-I, II, has significantly contributed to increased σDC owing to its hygroscopic nature and hydroxyl groups.

REFERENCES

1. S. Mahtab, P. Joshi, B. Arya, M.G.H. Zaidi, T. I. Siddiqui, N. K. Ahirwar, *Mat. Sci. Res.,* India, **17**, 08 (2020).

2. L. Spinelli, F. Roncaglia, R. Biagi, A. di Bona, M. Romagnoli, A. Mucci, (*In E3S Web of Conf.*, Vol. 334). EDP Sciences (2022).

3. S. Sharma, S. Mehtab, M. G. H. Zaidi, *Mater. Chem. Phys.*, **296**, 127278 (2023).

4. S. Mehtab, M. G. H. Zaidi, N. Rana, K. Khati, S. Sharma, *Bull. Mater. Sci.*, **45** (3), 162 (2022).

5. V. A. Smirnov, N. N. Denisov, A. E. Ukshe, Y. M. Shul'ga, *High Energy Chem.*, **47**, 242 (2013).

6. S. S. Yao, D. Jiang, Q. Z. Zhang, X. X. Wang, (*In IOP Conf. Ser.*, *MSEB,* Vol. 740). IOP Publishing (2020).

7. S. Mehtab, M.G. H. Zaidi, R. Kunwar, K. Singhal, T. I. Siddiqui, *Int. J. Polym. Anal.*, **26** (3), 204 (2021).

8. S. Sharma, S. Mehtab, M. G. H. Zaidi, *Mater. Today: Proc.*, 62, 6494 (2022).

9. N. Jović, D. Dudić, A. Montone, M. V. Antisari, M. Mitrić, V. Djoković, *Scr. Mater.*, **58** (10), 846 (2008).

10. A. Kaushik, P. Singh, Jyoti, *J. Reinf. Plast.*, **29** (7), 1038 (2010).

11. J. M. L.Reis, S. A. Martins, H. S. da Costa Mattos, *J. Braz. Soc. Mech.*, **42**, 1 (2020).

12. S. K. Joshi, A. Kumar, M. G. H. Zaidi, *Def. Sci. J.,* **70** (3) (2020).

13. A. Caradonna, C. Badini, E. Padovano, M. Pietroluongo, *Materials*, **12** (9), 1522.

14. P. Kuzhir, A. Paddubskaya, A. Plyushch, N. Volynets, S. Maksimenko, J. Macutkevic, I. Kranauskaite, J. Banys, E. Ivanov, R. Kotsilkova, A. Celzard, V. Fierro, J. Zicans, T. Ivanova, R. Merijs Meri, I. Bochkov, A. Cataldo, F. Micciulla, S. Bellucci, Ph. Lambin, *J. Appl. Phys.,* **114** (16) (2019).

15. N. Sharp, C. Li, A. Strachan, D. Adams, R. B. Pipes, *J Polym Sci B Polym Phys.,* **55** (15), 1150 (2017).

16. Y. Zheng, G. B. McKenna, *Macromolecules*, **36**(7), 2387 (2003).

17. O. Starkova, S. T. Buschhorn, E. Mannov, K. Schulte, A. Aniskevich, *Eur. Polym. J.,* **49** (8), 2138 (2013).

18. E. Pérez-Pacheco, J. I. Cauich-Cupul, A. Valadez-González, P. J. Herrera-Franco, *J. Mater. Sci.*, 48, 1873 (2013).

19. M. M. Khotbehsara, A. Manalo, T. Aravinthan, W. Ferdous, K. T. Nguyen, G. Hota, *Constr. Build. Mater*., *249*, 118846 (2020).

20. C. Zou, J. C. Fothergill, S. Zhang, X. Zhou, (*In 10th IEEE International Conf. Solid Dielectrics*) (2010).

21. H. Dhieb, J. G. Buijnsters, K. Elleuch, J. P. Celis, *Compos. B. Eng.,* 88, 252. (2016).

22. B. C Ray, *J. Colloid Interface Sci.,* **298** (1), 111 (2006).

23. W. Peng, X. Huang, J. Yu, P. Jiang, W. Liu, *Compos. Part A Appl. Sci. Manuf*., **41** (9), 1201 (2010).

24. M. Lettieri, M. Frigione, *Constr. Build. Mater.*, **30**, 753 (2012).

25. P. Fischer, J. J. De Luccia, *Am. Soc. Test. Mater.,* **50** (1976).

26. G. C. Papanicolaou, T. V. Kosmidou, A. S. Vatalis, C. G. Delides, *J. Appl. Polym. Sci.*, **99** (4), 1328 (2006).

27. M. Pandey, S. Mehtab, M. G. H. Zaidi, *Mater. Today: Proc.,* **65**, 3278 (2022).

28. P. Joshi, S. Mehtab, M. G. H. Zaidi, T. Tyagi, A. Bisht, *J. Anal. Sci. Technol.,* **10**, 33 (2020).

29. J. Vila, P. Ginés, J. M. Pico, C. Franjo, E. Jiménez, L. M. Varela, O. Cabeza, *Fluid Ph. Equilibria*, **242** (2), 141 (2006).

30. S. Mehtab, M. G. H. Zaidi, N. Rana, K. Khati, S. Sharma, *Bull. Mater. Sci.,***45** (3), 162 (2022).

31. H. Suherman, J. Sahari, A. B. Sulong, R. N. Royan, (*Key Eng. Mater.*, **447**, 643), Trans. Tech. Publications Ltd (2010).

32. H. Suherman, A. B. Sulong, J. Sahari*, Ceram. Int.*, 39 (2013)

33. H. Suherman, A. B. Sulong, J. Sahari, *Int. J. Mech. Mater. Eng.*, **5** (1), 74 (2010).

34. N. Jović, D. Dudić, A. Montone, M. V. Antisari, M. Mitrić, V. Djoković, *Scr. Mater.,* **58** (10), 846 (2008).

35. G. E. Guloglu, M. C. Altan, *J. Compos. Sci.*, **4** (1), 21 (2020).

36. D. O'Hare, J. V. Macpherson, A. Willows, *Electrochem. Commun.,* **4** (3), 245 (2002).

37. Y. Yao, X. Chen, J. Zhu, B. Zeng, Z. Wu, X. Li, *Nanoscale Res. Lett.*, **7** (1), 1 (2012).

38. L. Du, S. C. Jana, *J. Power Sources*, **172** (2), 734. (2007)

39. H. Suherman, R. Dweiri, A. B. Sulong, M. Y. Zakaria, Y. Mahyoedin, *Polymers*, **14** (3), 502 (2022).

Thermal degradation and kinetic analysis of fly ash-enriched epoxy composites

M. Pandey[1]*, P. Joshi[2], S. Mehtab[1], M. Aziz[1], M. Pandey[1], P. Kumar[3], M.G.H. Zaidi[1]*

[1]*Department of Chemistry, College of Basic Sciences and Humanities, G.B. Pant University of Agriculture and Technology, Pantnagar, U.S Nagar-263145, Uttarakhand, India*
[2]*Department of Chemistry, School of Allied Sciences, Dev Bhoomi Uttarakhand University, Naugaon, 248007, India*
[3]*Department of Physics, Manipal University Jaipur, Jaipur-303007, Rajasthan, India*

Present investigation demonstrates the enrichment of fly ash (FA, 27.23 nm) into cured epoxy resin (CE) and the study of the non-isothermal kinetic mechanism and thermodynamic data of solid-state decomposition under oxidative media. Thermal study and degradation behavior of FA-enriched polymer composite (FEPc) were determined by simultaneous thermogravimetric (TG) - differential thermogravimetric (DTG) - differential thermal analysis (DTA). The kinetic parameters of FEPc were measured through Coats–Redfern (CR) and Horowitz–Metzger (HM) models under best-fit analysis and further evidenced by linear regression analysis. FEPc revealed two step decomposition with improved TG onset by 25 ºC over CE due to the inherent thermal stability of FA. Results demonstrated that thermal behavior, kinetic and thermodynamic parameters of FEPc were improved with the enrichment of FA into CE. HM and CR models at reaction orders (n) ranging from 0 to 3 revealed the steadiness in order of solid-state degradation for CE (n = 2), FA and FEPc (n = 1) with negative value of entropy difference. CR method calculated higher values of activation energy (E_a) over HM method. These applied methods delivered higher differences in the values of E_a, change in enthalpy and Gibbs free energy of solid-state degradations, but marginal changes in pre-exponential factor and change in entropy of FEPc over CE and FA. Kinetic and thermodynamic parameters disclosed modification in thermal stability of FEPc over CE due to the intrinsic thermal stability of FA.

Keywords: Fly ash, Cured epoxy, Polymer composite, Non-isothermal kinetics, Thermogravimetric analysis, Solid state degradation

INTRODUCTION

Over past years, the kinetic analysis of non-isothermal decomposition procedures has been attracting the interest of many investigators along with modern history of thermal degradation. The kinetic analysis is necessary for correlating the kinetic and thermodynamic parameters to degradation mechanism [1, 2]. Thermal degradation mechanism allows the postulation of kinetic equations, and kinetics is the preliminary point to understand the mechanisms for decomposition [3]. Over other methods thermogravimetric analysis (TGA) is the most appropriate technique to study the kinetics [2, 4].

Epoxy resin (ER) is a thermosetting polymer which is characterized by at least one or more oxirane functional groups in the polymeric material and is regarded as reactive intermediate. ERs are primarily synthesized y the reaction of epichlorohydrin with active hydrogen of alcohols, phenols, acids, amines and through oxidation of olefins with peroxide [5, 6]. Di-glycidyl ether bisphenol-A (DGEBA) is a widely used bifunctional epoxy resin, synthesized by the reaction of epichlorohydrin with bisphenol A [7].

Furthermore, ERs can also react with active hydrogen of polyamines, polyphenols, polymercaptans and polyacids through polyaddition mechanism. Curing reaction of ER may be initiated in presence of UV light or appropriate catalysts at room or elevated temperatures through attack of a curing agent on the C-O-C ring. The curing reaction of ER is exothermic and mostly proceeds through step-growth polymerization [5, 7, 8]. High toughness, corrosion resistivity, moisture resistivity, mechanical and fatigue strength allows CE to be utilized in the field of protective coating, casting, automotive primer, glass sizing, electronic encapsulants, adhesives and aerospace composites [6, 9].

Various investigations have concluded to boost the thermal performance of ER through modification with electrical and thermally stable reinforcing agents [10]. Epoxy-based polymer composites (PCs) are of wide interest from an industrial and scientific viewpoint due to their exceptional characteristics over conventional composites [11]. Incessant demand of highly efficient materials encourages innovations in fabrication of PCs. Generally, PCs are incorporated with light-weight materials as fillers which attribute high mechanical and thermal

---

* To whom all correspondence should be sent:
E-mail:minakshipandey2912@gmail.com,
mghzaidi@gmail.com

performance. These lightweight PCs are widely used in transportation, structural, automotive, aerospace, electronics, turbines and leisure industry [12-14]. The reinforcement of additives in ER have been under substantial attention over decades. Studies have shown that the thermal performance of epoxy composites has been improved by the reinforcement of various metallic [15], carbon-based materials [16, 17], hybrid [18], ceramic [19] and fly ash (FA) [2, 20] fillers.

Over the past decades FA has attracted interest due to its high abundance. It is made up of metallic oxides such as SiO_2, Fe_2O_3, CaO and Al_2O_3. The presence of metallic oxides rises the thermo-mechanical performance of polymer composites [20]. FA is an industrial byproduct that results from the combustion of coal from thermal power plants, pulp, paper, brick making industries and incineration of municipal solid waste [21]**.** Composition of FA produced from different resources depends upon the type of coal, conditions of burning, combustion rate and cooling control. Global survey reveals production of about 780 MT / year of FA across the world out of which, 226.13 is nationally produced [22]. Globally, FA has been utilized in concrete and cement industries [23], synthesis of zeolites for wastewater treatment [24], geopolymer production [25]**,** soil stabilization [26], and fabrication of polymer composites (PCs) [27, 28]. High bulk density, porosity, particle size and surface area allow FA usage as a suitable filler in the development of high-performance PCs [27]. Over the past years, FA has been used as reinforcement in epoxy-based polymers due to its enhanced electrical, mechanical thermal and electrochemical performance [28].

FA-enriched polymer composite (FEPc) has received emerging attention as naturally abundant, inexpensive and viable substitute for synthetic PCs applicable in thermal insulation of electrical and electronic devices [29]. Thermal insulation properties of PCs in construction industries play an important role for minimization the operational energy consumption. Thermal response of FEPc in the fire environment mainly depends on the thermal decomposition of FA. For this reason, Tiwari *et al.,* [2] developed different kinetic models for thermal degradation and curing kinetics tests on FA-reinforced PCs (2.5 to 7.5 wt%) to obtain the reaction kinetic parameters of the material and to explore decomposition mechanism. Thermal analysis of FA derived PCs reveals the kinetic and thermodynamic parameters, including pre-exponential factor, reaction order, change in entropy, enthalpy, Gibbs free energy and activation energy. Kinetic analysis reveals the higher value of

activation energy for Coats-Redfern (20.36 to 30.84) over Broido´s (17.79 to 26.43) and Horowitz – Metzger (19.20 to 29.43) for first-order kinetics.

In the present investigation, FEPc was prepared and characterized through simultaneous TG-DTA-DTG. Kinetic and thermodynamic parameters such as activation energy (E_a), frequency factor (A), enthalpy change (ΔH), entropy change (ΔS) and Gibbs free energy change (ΔG) associated with the materials were estimated from TGA through CR and HM methods.

Materials

FA was collected from a thermal power plant, Kashipur, Uttarakhand, ground into 0.70 mm mesh size and dried at 40±1 ºC. Commercially available DGEBA (ER, LY-556), with density 1.09 $g/cm^3$and epoxy equivalent197 g/Eq was used for development of FEPc. TETA (CY-230) and hexane (99.98%) were procured from Huntsman India Pvt Limited. Other chemicals and solvents (purity >99.55) were locally arranged and used without further purification.

Preparation of FEPc

Stainless steel panels with 1 cm^2 area and 1.50±0.1 mm thickness were polished with emery paper followed by ultrasonic cleaning with acetone for 20 min. FEPc was developed through valorization of FA under enriched concentrations (60 phr) into epoxy resin. The process of development of FEPc involved dispersion of FA into ER in ethanol (2.0 mL) @ 500 rpm over 5 h to afford a suspension, followed by sequential thermal activation at 90±1°C over 1 h. The suspension was cooled to 40±1°C and cured with TETA hardener. This was followed by deposition of FEPc suspension on 316-SS current collectors. FEPc was kept at 25±1ºC over 24 h thereafter post cured at 400 mm Hg/70°C.

CHARACTERIZATION

Crystallite size (d) of FA was calculated through Debye Scherer equation D=$K\lambda/\beta cos\theta$, where K=order of diffraction (K=1), λ=wavelength of X-ray, β=full width half maximum of peak, Θ=scattering angle [29]. Simultaneous TG-DTA-DTG was performed on EXSTAR TG/ DTA 6300 in air @ 10 °C/min from ambient to 600°C with reference to alumina.

Kinetic models such as Horowitz–Metzger (HM) and Coats–Redfern (CR) were employed for calculation of the kinetic parameters including; order of reaction (n), E_a, A, ΔS, ΔH and ΔG. These methods depend on the conditions of experiments

and mathematical analysis of data fraction of thermal decomposition (α), was evaluated from TG data

$$\alpha = \frac{w_o - w_t}{w_o - w_f}$$

according to the relation: where, w_o = initial weight, w_t = weight at particular temperature and w_f = final weight of sample [30].

Coats–Redfern model

CR equation revealed the kinetic parameters in every stage of thermal degradation. CR method employs the plot of log g(α) against 1000/T which reveals the value of E_a through the slope $\left(-\frac{E_a}{R}\right)$ and pre-exponential factor (A) through the intercept $ln\left(\frac{ART^2}{\beta E_a}\right)$.

$$log_{10}\left[\frac{g(\alpha)}{T^2}\right] = log_{10}\left[\frac{AR}{\beta E}\left(1 - \frac{2RT}{E_a}\right)\right] - \frac{E_a}{2.303RT}$$

For n = 0, $g(\alpha) = \alpha$; n = 1, $g(\alpha) = -ln(1-\alpha)$; n =2 $g(\alpha) = \frac{1}{1-\alpha}$; n=3 $g(\alpha) = \frac{1}{(1-\alpha)^2}$ and for n^{th} order $g(\alpha) = [(1-\alpha)^{1-n} - 1]/(n-1)$

where β = heating rate, R = gas constant (8.314 J/mol K) and T = degradation temperature.

The values of ΔH (kJ/mol), ΔS (kJ/mol.K) and ΔG (kJ/mol) were calculated according to the respective relation; $E_a - RT$, $Rln\left(\frac{Ah}{kT}\right)$ and $\Delta H - T\Delta S$.

where k = Boltzmann constant ($1.38×10^{-23}$ J/K), h = Plank constant ($6.626 × 10^{-34}$ J.s) and R is universal gas constant (kJ/K. mol) [31].

Horowitz-Metzger model

HM equation illustrates the kinetic parameters of FA-reinforced PCs through the plot of $log_{10}\left[log_{10}\frac{w_o}{w_t}\right]$ over θ, which reveals the value of activation energy through the slope $\left(-\frac{E_a}{2.303RT_s^2}\right)$ and pre-exponential factor (A) through the intercept

$$log_{10}\left[\frac{w_o - w_t}{w_o - w_f}\right] = \frac{E_a\theta}{2.303RT_s^2}$$

where, R is gas constant, w_o = initial weight of sample, w_t = weight of sample at a particular temperature and w_f = final weight of sample, T_s is reference temperature and is appraised as the temperature at which w_f/w_o = 0.37 for n = 1 of the degradation process, θ is the difference between the peak temperature and the temperature at a particular weight loss (θ = T – Ts) [30]. The values of ΔH, ΔS and ΔG were calculated according to the above- mentioned relation.

RESULTS AND DISCUSSION

Thermogravimetric analysis

Thermal stabilities of FA CE and a respective FEPc were examined through simultaneous TG-DTA-DTG from ambient conditions to 600°C. TG reveals the weight loss (%wt) with respect to temperature @ 10°C/min in air. DTG demonstrates the maximum rate of degradation (µg/°C) at the respective peak decomposition temperature. However, DTA reveals the fusion temperature at the respective peak temperatures (°C).

TG of FA revealed single step rapid decomposition up to 600°C leaving a weight residue (Wr) of 96.7 % and was associated with 0.8% moisture content. This was supported by DTG @ 5.8 (µg/°C) at 212°C. Not any single peak was observed in DTA analysis which attributes to amorphous nature of FA.

TG of CE revealed three-step decomposition - first step decomposition with TGo at 185°C leaving 87.5% Wr due to degradation of residual monomers of CE and untreated reagents. Such decomposition of CE was supported with a DTG signal @ 27.5 µg/°C at 219 °C. Prior to this temperature, CE was decomposed leaving 98.3 % Wr at 163°C due to loss of moisture content (0.40 %) and untreated reagents. Second step decomposition of CE revealed TGo at 300 °C leaving 74.2% Wr. Within the range of temperature 300–363 °C, the maximum weight loss (38%) was due to breakage of ether bond and C-C bond of benzene ring. Major decomposition of CE was supported with DTG signal @ 88.0 µg/°C at 350 °C. CE has revealed a DTA signal of 49.2 µV at 360 °C with heat of fusion -136.3 J/g. Third step decomposition of CE showed TGo at 363 °C leaving 36.2% Wr. This decomposition was further supported with a DTG signal @ 37.5 µg/°C at 418°C. TGe of CE appeared at 458 °C leaving 7.5 % char residue.

Thermal degradation of FEPc showed two-step decomposition. FEPc revealed first step decomposition with TGo at 210°C leaving 94.7 % Wr. Such decomposition progressed with @ 6.9 µg/°C at 183°C. Prior to this temperature, weight loss of 5.3% attributed to expulsion of moisture content (1.8%) and untreated residual monomer of CE. Second step decomposition of FEPc was initiated with TGo at 301 °C leaving 91.9 %Wr. Such decomposition was further supported with DTG

signal @ 54.0 μg/°C at 370°C. TGe of FEPc appeared at 500 °C leaving 55.1 % char residue.

Table. 1. Thermal parameters of FA, CE and respective FEPc.

	[TG$_o$ (TG$_e$)]^A	DTG^B
CE	162 (98.3) 500 (7.5)	27.5 (219), 88.0 (350), 418 (37.5)
FA	200 (98.8) 600 (97.7)	5.9 (220) 3.5 (500)
FEPc	200 (94.7) 500 (55.1)	54.0 (370)

^{A}: TG$_o$= %Wr at TG onset (°C), TG$_e$= %Wr at TG endset (°C). ^{B}: Rate of degradation, μg/ °C (Peak temperature, °C).
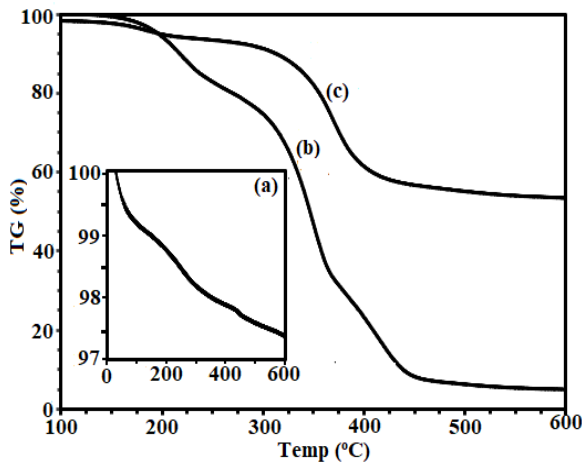
Fig. 1. TG of FA(a), CE(b) and FEPc(c)
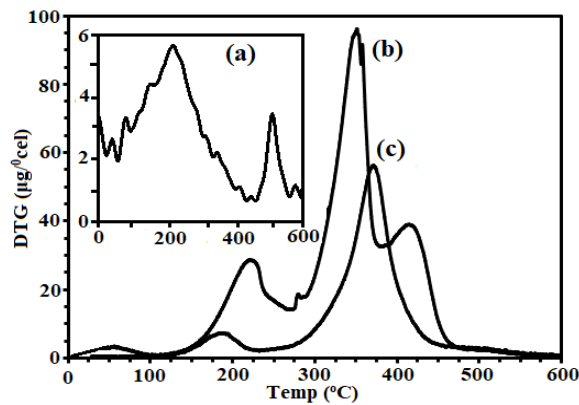
Fig. 2. DTG of FA(a), CE(b) and FEPc (c)

Kinetic analysis

Kinetic analysis of FA, CE and FEPc through non-isothermal decomposition methods revealed Ea, A, ΔS, ΔH and ΔG. Respective thermodynamic and kinetic parameters were deduced from TGA analysis using HM and CR for n = 0, 1, 2, 3 and are also summarized in Table 2. Regression coefficients (R^2) (n = 0 to 3) of order.

74

evaluated from CR and HM plots attributed their satisfactory linear relation (Table 2).

In general, the respective A and Ea of FA, CE and FEPc evaluated from CR method have higher value over HM method in the entire range .
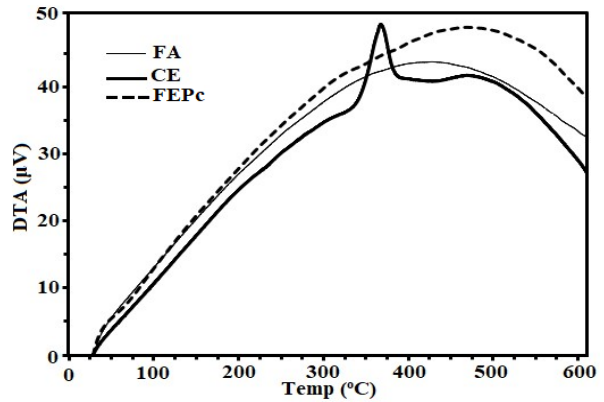

Fig. 3. DTA of FA(a), CE(b) and FEPc(c)

Generally, CR method reveals higher E$_a$ over HM method [2]. CR and HM methods have disclosed larger variation in the values of E$_a$, ΔG and ΔH but only a slight difference in the values of ΔS. In general, FA, CE and FEPc, their respective Ea and A evaluated from CR method were higher over HM method. However, an insignificant difference was observed in the values of ΔS evaluated from HM and CR methods.

FA revealed that E$_a$ ranges between 45.16 and 26.87 (50.30 to 35.39). For CE and related FEPc, CR (HM) methods disclosed E$_a$ ranging from 11.43 to 14.56 (15.23 to 24.25) and 33.01 to 53.31 (42.74 to 40.23), respectively. Exceptionally higher values of E$_a$ for FA and related FEPc, revealed enhanced thermal stability. For FA, CR the HM method revealed A ranging from 0.34 to 5.66 (0.23 to 4.32). For CE and respective FEPc, CR the HM method revealed A ranging from 1.23 to 1.31 (1.25 to 1.32) and 2.94 to 2.71 (2.68 to 2.89), respectively.

For FA, CR the HM method revealed (-ΔS) ranging from 0.12 to 0.22 (0.15 to 0.24). CE and related FEPc attributed (-ΔS) ranging from 0.25 to 0.28 (0.24 to 0.29) and 0.25 to 0.12 (0.32–0.15) respectively. For FA, CR the HM method attributed (ΔH) ranging from 39.98 to 21.69 (45.13 to 30.11). For CE and related FEPc, CR the HM method attributed (-ΔH) ranging from 6.00 to 9.21 (10.05 to 19.07) and 27.82 to 48.13 (37.56 to 35.06) respectively. For FA, CR the HM method attributed (ΔG) ranging from 114.74 to 158.75 (138.58 to 179.63). For CE and related FEPc, CR the HM method attributed (ΔG) ranging from 166.75 to 182.80 (159.57 to 199.74) and 183.57 to 122.89 (217.60 to 131.51), respectively.

Table. 2. Kinetic and thermodynamic parameters of FA, CE and respective FEPc evaluated from CR and HM models.

	T (K)	n	Method	E_a^a	A^b	$-\Delta S^c$	ΔH^a	ΔG^a	R^2
FA	623	0	HM	45.16	0.34	0.12	39.98	114.74	0.9951
			CR	50.30	0.23	0.15	45.13	138.58	0.9952
		1	HM	25.36	0.25	0.25	20.18	175.93	0.9982
			CR	30.24	0.24	0.23	25.06	168.35	0.9987
		2	HM	50.90	1.79	0.32	45.72	245.08	0.9972
			CR	52.32	0.26	0.35	47.14	265.19	0.9965
		3	HM	26.87	5.66	0.22	21.69	158.75	0.9921
			CR	35.29	4.32	0.24	30.11	179.63	0.9952
CE	623	0	HM	11.35	1.23	0.25	6.00	166.75	0.9953
			CR	15.23	1.25	0.24	10.05	159.57	0.9952
		1	HM	17.53	0.98	0.27	12.18	185.79	0.9923
			CR	23.89	1.00	0.29	18.71	199.38	0.9914
		2	HM	19.28	0.85	0.19	13.93	136.10	0.9989
			CR	20.36	1.25	0.21	15.18	146.01	0.9982
		3	HM	14.56	1.31	0.28	9.21	182.80	0.9912
			CR	24.25	1.32	0.29	19.07	199.74	0.9920
FEPc	643	0	HM	33.01	2.94	0.25	27.82	183.57	0.9893
			CR	42.74	2.68	0.28	37.56	217.60	0.9912
		1	HM	43.74	5.54	0.23	38.56	181.85	0.9993
			CR	52.36	5.23	0.25	47.18	207.93	0.9985
		2	HM	36.09	7.75	0.31	30.91	224.04	0.9975
			CR	36.95	5.63	0.32	31.77	237.53	0.9982
		3	HM	53.31	2.71	0.12	48.13	122.89	0.9912
			CR	40.23	2.89	0.15	35.06	131.51	0.9923

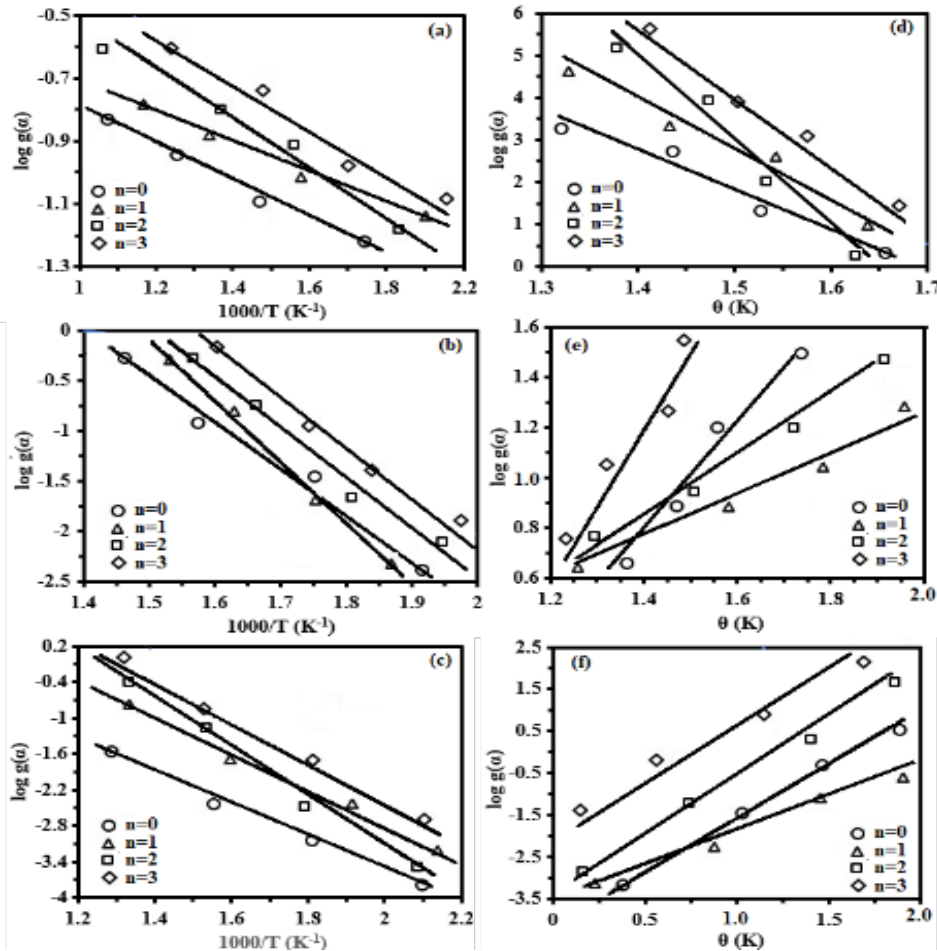[a]: $KJmol^{-1}$; [b]: min^{-1}; [c]: $KJmol^{-1} K^{-1}$

Fig. 4. CR thermogram of FA (a), CE (b), FEPc (c) and HM thermogram of FA (d), CE (e) and FEPc (f).

CONCLUSION

Fly ash-enriched polymer composite (FEPc) was prepared through curing reaction of fly ash (FA, 60 wt%) with an epoxy based reactive binder. For this investigation, FA (0.80% moisture content) was procured from nearby thermal plant. Non-isothermal kinetic, thermal and thermodynamic data of FEPc were compared with FA and CE. Thermogravimetric analysis @10°C heating rate was employed to evaluate the kinetic and thermodynamic parameters of the materials through Coats–Redfern (CR) and Horowitz–Metzger (HM) models at n = 0, 1, 2 & 3. The activation energy, pre-exponential factor and order of reaction of FEPc were improved due to the enrichment of FA into cured epoxy (CE). CR model attributed greater value of activation energy (E$_a$) and frequency factor (A) over HM model for all materials. Non-isothermal kinetic parameters were obtained through plotting calculated values of log g(α) against decomposition temperature. E$_a$ and A values of the materials attributed that CE follows second order kinetics while FA and FEPc follow first order kinetics. The obtained results concluded that FA is the most impressive reinforcing agent for improving the thermal stability of the CE, which leads to shifting of weight loss stages to higher decomposition temperatures along with an increment in the char residue @ 600°C. Higher thermal stability of FEPc makes them suitable to use in anticorrosive coatings, electrical and microelectronic devices.

REFERENCES

1. J. B. Dahiya, K. Kumar, M. Muller-Hagedorn, H. Bockhorn, *Polym. Int.*, **57**, 722 (2008).
2. S. Tiwari, C. L. Gehlot, K. Srivastava, D. Srivastava, *J. Ind. Chem. Soc.*, **98** (5) 100077 (2021).
3. G. Léonard, D. Toye, G. Heyen, *Int. J. Greenh. Gas Control.*, 30(6), 171 (2014).
4. R. Ebrahimi-Kahrizsangi, M. H. Abbasi, *Trans. Nonferrous Met. Soc. China*, **18** (1), 217 (2008).
5. C. Chen, B. Li, M. Kanari, D. Lu, *Adhes. Adhes. Joints Ind. Applications*, 37 (2019).
6. Z. Yan, J. Tian, K. Wang, K. D. Nigam, G. Luo, *Chemical Engineering Science*, **229**, 116071 (2021).
7. W. Zhou, D. Lv, H. Ding, P. Xu, C. Zhang, Y. Ren, ... P. Ma, *React. Funct. Polym.*, **180**, 105383 (2022).
8. C. Liu, M. Sun, B. Zhang, X. Zhang, G. Xue, X. Zhang, *Eur Polym. J.*, **121**, 109304 (2019).
9. A. C. Marques, A. Mocanu, N. Z. Tomić, S. Balos, E. Stammen, A. Lundevall, ... S. Teixeira de Freitas, *Materials*, **13** (24), 5590 (2020).
10. Z. R. Jia, Z. G. Gao, D. Lan, Y. H. Cheng, G. L. Wu, H. J. Wu, *Chin. J. Phys. B.*, **27** (11), 117806 (2018).
11. M. Hemath, S. Mavinkere Rangappa, V. Kushvaha, H. N. Dhakal, S. Siengchin, *Polym. Compos.*, **41** (10), 3940 (2020).
12. G. Roviello, L. Ricciotti, O. Tarallo, C. Ferone, F. Colangelo, V. Roviello, R. Cioffi, *Materials*, **9** (6), 461 (2016).
13. A. Pattanaik, M. Mukherjee, S. B. Mishra, *Compos. B: Eng.*, **176**, 107301 (2019).
14. R. Manimaran, I. Jayakumar, R. Mohammad Giyahudeen, L. Narayanan, *Energ. Source. Part A: Recovery, Utilization. Env. Effects*, **40** (8), 887 (2018).
15. A. I. Misiura, Y. P. Mamunya, M. P. Kulish, *J. Macromol. Sci. Part B.*, **59** (2), 1216 (2020).
16. I. Bustero, I. Gaztelumendi, I. Obieta, M. A. Mendizabal, A. Zurutuza, A. Ortega, B. Alonso, *Adv. Compos. Hybrid Mater.*, **3**, 31 (2020).
17. E. C. Senis, I. O. Golosnoy, J. M. Dulieu-Barton, O. T. Thomsen, *J. Mater. Sci.*, **54** (12), 8955 (2019).
18. M. W. Akhtar, J. S. Kim, M. A. Memon, M. M. Baloch, *Compos. Sci. Technol.*, **195**, 108183 (2020).
19. Y. Ouyang, L. Bai, H. Tian, X. Li, F. Yuan, *Compos. Part A: Appl. Sci. Manuf.*, **152**, 106685 (2022).
20. S. Tiwari, K. Srivastava, C. L. Gehlot, D. Srivastava, *Int. J. Waste Resour.*, **10**, 1 (2020).
21. S. S. Alterary, N. H. Marei, J. King Saud Univ. Sci., **33** (6), 101536 2021.
22. S. K. John, Y. Nadir, K. Girija, *Constr. Build Mater.*, **280**, 122443 (2021).
23. S. Pangdaeng, T. Phoongernkham, V. Sata, P. Chindaprasirt, *Mater. Des.*, **53**, 269 (2014).
24. C. L. Hwang, C. H. Chiang, T. P. Huynh, D. H. Vo, B. J. Jhang, S. H. Ngo, *Constr. Build Mater.*, **135**, 459 (2017).
25. Z. Zhang, H. Wang, Y. Zhu, A. Reid, J. L. Provis, F. Bullen, *Appl. Clay Sci.,* **88**, 194 (2014).
26. Z. Luo, B. Luo, Y. Zhao, X. Li, Y. Su, H. Huang, Q. Wang, *Polymer,* **14** (2), 307 (2022).
27. J. Sim, Y. Kang, B. J. Kim, Y. H. Park, Y. C. Lee, *Polymer.*, **12** (1), 79 (2020).
28. M. Gnanavel, T. Maridurai, K. M. Kumar, *Mater. Res. Express.*, **6** (9), 095507 (2019).
29. M. Pandey, S. Mehtab, M. G. H. Zaidi, *Mater. Today: Proc.*, **65**, 3278 (2022).
30. P. Joshi, G. Bisht, S. Mehtab, M. G. H. Zaidi, *Mater. Today: Proc.*, **62**, 6814 (2022).
31. H. Li, N. Wang, X. Han, H. Yuan, J. Xie, *Polymer*, **13** (4), 569 (2021).

Review on the green synthesis of reduced graphene oxide

N. S. Karki[1], T. Bisht[2], A. Kalkhundiya[3], H. Mudila[4], K. Khati[5], M. Bisht[1]*

[1] Department of Chemistry, L.S.M. Govt. P.G. College, Pithoragarh, Uttarakhand, India
[2]Department of Chemistry, Indira Priyadarshini Gov. Girls College, Haldwani, Uttarakhand, India
[3]Department of Zoology, S.S.J. University, Campus Almora, Uttarakhand, India
[4]Departments of Chemistry, Faculty of Technology and Sciences, Lovely Professional University, Punjab, India
[5] Department of Chemistry, R.H. Govt. P.G. College, Kashipur, Uttarakhand, India

Carbon-based material, *i.e.,* reduced graphene oxide (RGO), is a chemical substance obtained from graphite powder, which is of great interest since the last two decades. It is used in a large number of fields, like heterogeneous catalysis, bio-sensing, energy storage, drug delivery, etc. Graphite powder is oxidized and exfoliated to generate graphene oxide (GO) by using the traditional modified Hummer's method, which after reduction generates the RGO. Synthesis of RGO from GO can be done by using chemical reduction methods, as well as by using green methods. Due to their environmentally friendly and less hazardous nature, green methods are preferred over chemical reduction methods t, prepare the RGO from GO. The RGO and GO synthesized were characterized using XRD, UV-visible, TGA, FESEM and FTIR techniques.

Keywords- Graphene oxide, Reduced graphene oxide, Graphite oxide, Green synthesis.

INTRODUCTION

Graphene has a hexagonal network structure of sp^2 hybrid carbon atoms arranged with each other to construct a one-atom-thick sheet [1]. In this one-atom-thick sheet of graphene all the carbon-carbon bond lengths are 1.42 Å, intermediate with respect to C-C and C=C bond lengths. Graphene was discovered in 2004 by researchers at Manchester University. For this great discovery, they won the Nobel prize in physics in 2010 [2]. Over the recent years graphene has been focused as a good research material due to its large surface area and high conductivity-based technological applications [3]. Due to its excellent outcomes from various experiments, it is used in a large number of fields like bio-sensing [4], drug delivery [5], catalysis [6], and energy storage [7].

This makes it suitable for a wide range of applications, like Li-ion batteries [8], thin film transistors [9], and solar cells [10, 11]. Till now, a large number of methods have been developed for the large-scale production of graphene and these methods include chemical vapor deposition [8], [12, 13], mechanical exfoliation [14, 15], aerosol pyrolysis [16], solvothermal methods [17] and chemical reduction methods [18, 19]. By the reason of cost-effective nature and good yield of RGO obtained from GO, the chemical reduction method is considered as the best method [20].

To prepare RGO from GO reducing agents like hydrazine, dimethyl hydrazine, hydroquinone, or sodium borohydride can be used. Still, due to these reducing agents' poisonous, non-environmentally friendly nature, they can exert some harmful effects during bio-related applications [21, 22]. Synthesis of RGO can also be done by using green methods. Among the green methods, phytoextracts like green tea [23], carrot roots [24], bacteria (*Escherichia coli*) [25], orange (*C.Sinensis peel*), cloves (*S. Aromaticum*), cherry (*P.Serrulate*) [26], salvia spinosa [27], *Hibiscus Sabdarrifa L* [28], rose water [29], etc. can be used to synthesize reduced RGO. Synthesis of RGO can also be done by using the environmentally friendly method, in which RGO is prepared by UV irradiation of exfoliated GO nanosheets [30]. Aqueous phytoextracts like mango (*Mangifera indica L*) leaves extract and potato (*Solanum tuberosum L*) extract are good reducing agents to produce RGO from GO [31]. These phytoextracts are easily available, environmentally friendly, non-hazardous reducing agents to prepare RGO [25]. Mango and potato phytoextracts containing phenolic compounds like caffeic acid, chlorogenic acid, gallic acid, protocatechuric acid, salicylic acid, vanillic acid [32-36], etc., which have hydroxyl groups, use the reduction of oxygen functionality present in GO as a mild reducing agent [37, 38].

* To whom all correspondence should be sent:
E-mail: manishatanuja@gmail.com

Green methods are environmentally friendly and less hazardous in comparison to the chemical methods to prepare RGO from GO. However, still, there are some limitations of green methods like high time consumption [39], and poor stability [40-42] which are not favorable for obtaining a good yield of RGO.

EXPERIMENTAL

Synthesis of graphene oxide (GO) by modified Hummer's method

GO can be synthesized from graphite powder by using modified Hummer's method [43, 44]. Modified Hummer's method does not involve NaNO$_3$ but gives the yield of GO approx. equal to the usual Hummer method. The modified Hummer's method is eco-friendly because it eliminates the evolution of toxic gases like NO$_2$, N$_2$O$_4$ [45], etc. In this method, 2 g of graphite powder is mixed with 50 ml of concentrated sulfuric acid while stirring constantly. The mixture is then cooled in an ice bath, which makes a suspension. Below 100°C, 6 g of KMnO$_4$, which is an oxidizing agent, is slowly added to this suspension (caution: blast can occur if KMnO$_4$ is added quickly). Now the suspension is stirred at 25°C for 25 minutes followed by sonication in an ultrasonic bath for 8 minutes.
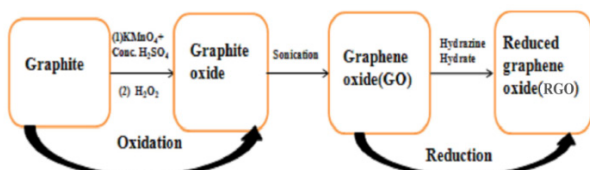
Fig. 1. General path for the synthesis of GO and RGO

After ultrasonication 250 ml of distilled water is introduced to the mixture with 10-fold repetition of the stirring and sonication process. Now 30 ml of H$_2$O$_2$ is introduced into the exfoliated graphite oxide obtained after ultrasonication of the dispersed solution for 1 hour. Ultrasonication of this content at 10000 rpm GO is prepared, which is washed by 2M HCl and distilled water until pH 7. The graphene oxide obtained in this way is dried at room temperature for 24 hours [46]. The general pathway for synthesizing GO and RGO from graphite powder is represented in Fig. 1 [46].

Preparation of reduced graphene oxide (RGO) through graphene oxide (GO)

Green synthesis to prepare RGO from GO is an environmentally friendly method, such as using various plant materials or bio-molecules as reducing agent. These are eco-friendly and non-hazardous methods to prepare RGO from GO. For the green synthesis of RGO firstly a reducing agent containing phytoextract is prepared. Now, this phytoextract is mixed with GO prepared by a customized Hummer's method, by which the reducing agent present in the phytoextract causes the reduction of GO into RGO.

Green synthesis of reduced graphene oxide (RGO) from graphene oxide (GO) by using mango leave extract

For this purpose, fresh mango leaves (*Mangifera indica L.*) are washed and dried and then ground to obtain the powder form. This powder is placed in a conical flask and 100 ml of Millipore water is added, followed by stirring for 1 hour at 50°C by a magnetic stirrer until a homogenous mixture is obtained. This mixture is centrifuged and filtered by using Whatman 42 filter paper. Mango leaves extract prepared is added to the GO dispersion obtained from the ultrasonicated mixture of GO prepared by modified Hummer's method and deionized water (maintaining a 1:1 volume ratio of GO and phytoextract) and stirring is done for 12 hours at 60°C by using a magnetic stirrer. This reaction mixture is refluxed in an oil bath at 70-80°C for 8 hours, as a result of which the brownish color of GO is converted into dark black color. After centrifuging and washing with deionized water and acetone, this black solution gives RGO, which is dried in a vacuum desiccator for 48 hours [31].

Green synthesis of reduced graphene oxide (RGO) from graphene oxide (GO) by using potato extract

For this purpose, at first thinly sliced potatoes are washed with hot distilled water, then sliced potato is taken in 100 ml of Millipore water and ground to convert it into potato paste. Now the mixture is centrifuged, and the supernatant liquid is collected as potato extract. Potato extract prepared is added to the GO dispersion obtained from the ultrasonicated mixture of GO prepared by the modified Hummer's method and deionized water (maintaining a 1:1 volume ratio of GO and phytoextract) and stirring is done for 12 hours at 60°C by using a magnetic stirrer. This reaction mixture is refluxed in an oil bath at 70-80°C for 8 hours, as a result of which the brownish color of GO is converted into dark black color. At last, this dark-colored solution is centrifuged, washed with deionized water, and then cleaned with acetone to produce RGO, which is then dried for 48 hours in a vacuum desiccator [31].

Green synthesis of reduced graphene oxide (RGO) from graphene oxide (GO) by using S. Spinosa leaf extract

To prepare *S. Spinosa* leaf extract, *S. Spinosa* leaves are washed with distilled water and dried for five days in the shade. Now the dried leaves of *S. Spinosa* are ground with double distilled water in the grinder. Finally, this ground mixture is extracted using a Soxhlet extracting apparatus, as a result of which *S. Spinosa* leaf extract is obtained and stored at 4°C. The *S. Spinosa* leaf extract is mixed with GO suspension (which is made by mixing graphene oxide made by a modified version of Hummer's method and distilled water in a mixer) This mixture is stirred for 12 hours in an oil bath at 95°C. This changes the color of the solution and shows that RGO has formed. Now on centrifuging (at 10000 rpm for 10 minutes) and washing the top layer containing an aqueous solution of GO by de-ionized water, solid reduced RGO is obtained, which is dried and stored [27, 47].

Green synthesis of reduced graphene oxide (RGO) from graphene oxide (GO) by using Hibiscus Sabdarriffa L. extract

To obtain the *Hibiscus Sabdarriffa L.* extract, the powder form of the flower of *Hibiscus Sabdarriffa L.* plant is mixed with deionized water, heated and stirred on a magnetically stirred hot plate for 30 minutes. Now the mixture is filtered, and the filtrate is cooled at 25°C. to obtain *Hibiscus Sabdarriffa L.* extract which is mixed with a suspension of GO obtained from an ultrasonicated mixture of GO and deionized water. This mixture is stirred for 150 minutes using a mechanical stirrer under sonication by which the brown color of GO is changed into black which conforms to the formation of RGO [28].

Green synthesis of reduced graphene oxide (RGO) from graphene oxide (GO) by using green tea extract

In this method, about 1.5 g of GO powder is added to 150 ml of green tea extract and stirred for 72 hours. Now the sample mixture is diluted using deionized water and centrifuged twice at 5000 rpm for 15 minutes. Finally, solid RGO is obtained on filtration, which is dried in an oven at 80°C for 24 hours [45].

Green synthesis of reduced graphene oxide (RGO) from graphene oxide (GO) by using lemon juice

For this synthesis, lemon juice is extracted by squeezing a yellow lemon and centrifugation at 13000 rpm for 10 minutes. Now after filtration, the filtrate is obtained as lemon juice which is stored at 4°C for further use. The lemon juice is mixed with GO with sonication and the pH of the mixture is maintained at 12.3 with the help of 4 ml of aqueous NaOH solution. Now on stirring the mixture in an oil bath at 80°C for 2 hours, a black-colored mass is collected. This black-colored mass on centrifugation and washing by deionized water gives pure RGO after drying at 50°C for 24 hours, which is stored at 25°C [48].

Green synthesis of reduced graphene oxide (RGO) from graphene oxide (GO) using Plectranthus amboinicus leaf extract

First, *Plectranthus amboinicus* leaves are washed through running tap water, then with deionized water. The *Plectranthus amboinicus* leaves are dried at 50°C using a hot air oven and converted into powder form using mortar and pestle. Now the *Plectranthus amboinicus* leaf powder is mixed with deionized water and the mixture is refluxed for 2 hours. Finally, on filtration using Whatman No 1 filter paper, the leaf extract of *Plectranthus amboinicus* is obtained. The GO prepared previously is mixed with *Plectranthus amboinicus* leaf extract in 2:1 ratio and ultrasonicated for 1 hour. This mixture is placed in a stainless-steel autoclave for 12 hours at 100°C. The color change from brown to black indicates the reduction process to produce RGO from GO. This solution is washed by sonication at 9000 rpm, initially using deionized water and then ethyl alcohol. This sample is dried at 60°C in a vacuum oven to obtain RGO [49].

Green method for reduction of GO into RGO by hydrothermal treatment

For the purpose of preparing RGO from GO, at first GO with de-ionized water is sonicated with the help of ultrasonic bath cleaner about 30 minutes by which a homogenous yellow-brown dispersion is obtained. This yellowish-brown mixture is heated in an autoclave for 4 hours at 150°C, and then RGO is obtained by filtering and washing it with deionized water and then drying it in a vacuum oven at 60°C for one night [50].

Other than the above green synthesis to prepare RGO from GO, some other plant extracts like leaf extract, fruit extract, flower extract, peel extract, bark/stem extract, seed extract, root extract, and pollen grain extract are also used as reducing agents to make RGO from GO using green methods. Table 1 [51] lists all of these plant extracts as green reducing agents (1.1 to 1.8).

Table 1. Leaf extracts for the reduction of GO into RGO

S.No	Botanical Name	Reduction Method	S.No	Botanical Name	Reduction Method
1	*Colocasia esculenta*	Stir, reflux	21	*Ocimum sanctum*	Reflux
2	*Mesua ferrea L.*	Stir, reflux	22	*Anacardium occidentale Linn*	Stir
3	*Spinacia oleracea*	Stir	23	*Eucalyptus*	Reflux
4	*Ginkgo biloba*	Stir	24	*Ocimum sanctum L.*	Stir
5	*Eichhornia crassipes*	Reflux	25	*Stigma phyllonovatum*	Stir
6	*Pulicaria glutinosa Prunus serrulate Magnolia Kobus Platanus orientalis*	Reflux	26	*Euphorbia cheiradenia Boiss*	Reflux
7	*Diopyros kaki Pinus desiflora Acer palmatum Ginkgo biloba*	Reflux	27	*Mentha arvensis*	Reflux
8	*Azadirachta indica*	Stir, reflux	28	*Tribulus terrestris Mentha piperita*	Autoclave
9	*Euphorbia wallichii*	Reflux	29	*Urtica dioica L.*	Stir
10	*Spinacia oleracea Ficus religiosa*	Reflux	30	*Euphorbia milli*	Stir
11	*Artemisia vulgaris*	Reflux	31	*Thymbra spicata*	Reflux
12	*Paederia foetide L.*	Stir	32	*Euphorbia heterophylla (L.)*	Reflux
13	*Platanus orientalis*	Reflux	33	*Memecylonedule*	Water bath
14	*Oleae uropaea*	Water bath	34	*Elaeis guineensis*	Reflux
15	*Melissa officinalis L.*	Stir	35	*Zataria multiflora*	Reflux
16	*Annonas quamosa*	Reflux	36	*Azadirachta indica*	Stir
17	*Eucalyptus*	Water bath	37	*Telfairia occidentalis*	Stir
18	*Camellia sinensis*	Reflux	38	*Murray akoenigii*	Autoclave
19	*Aloe vera*	Reflux	39	*Acalypha indica*	Autoclave
20	*Aloe vera (L.) Burm.f.*	Reflux	40	*Erythrina senegalensis*	Reflux

Table 2. Fruit extracts for the reduction of GO into RGO

S.No	Botanical Name	Reduction Method	S.No	Botanical Name	Reduction Method
1	*Cocos nucifera L.*	Oil bath	6	*Zante currants*	Water bath
2	*Punica granatum*	Stir	7	*Phyllanthus emblica*	Reflux
3	*Ficu scarica*	Stir	8	*Phyllanthus emblica*	Autoclave
4	*Vitis vinifera*	Reflux	9	*Fragaria ananassa*	Reflux
5	*Terminalia bellirica*	Water bath	10	*Helicteres isora*	Sonication

Table 3. Flower extracts for the reduction of GO into RGO

S. No	Botanical Name	Reduction Method
1	*Tagetes erecta*	Stir
2	*Rosa damascena*	Autoclave
3	*Syzygium aromaticum*	Reflux
4	*Chrysanthemum morifolium*	Water bath

Table 4. Peel extracts for the reduction of GO into RGO

S. No	Botanical Name	Reduction Method
1	*Citrus sinensis*	Stir
2	*Sugar cane bagasse*	Stir
3	*Citrus hystrix*	Stir

Table 5. Bark / stem extracts for the reduction of GO into RGO

S. No	Botanical Name	Reduction Method
1	*Cinnamomum verum*	Reflux
2	*Saccharum officinarum*	Autoclave
3	*Cinnamomum zeylanicum*	Reflux
4	*Alstonia scholaris*	Stir

Table 6. Seed extracts for the reduction of GO into RGO

S. No	Botanical Name	Reduction Method
1	*Phaseolus aureus L.*	Stir
2	*Glycine max (L.) Merr.*	Stir
3	*Vitis vinifera*	Stir
4	*Terminalia chebula*	Reflux

Table 7. Root extracts for the reduction of GO into RGO

S. No	Botanical Name	Reduction Method
1	*Daucus carota subsp. sativus*	Stir
2	*Salvadora persica L. (miswak)*	Stir
3	*Allium cepa (onion)*	Stir
4	*Daucus carota*	Stir
5	*Zingiber officinale Roscoe*	Reflux

Table 8. Pollen grain extract for the reduction of GO into RGO

S. No	Botanical Name	Reduction Method
1	*Peltophorum pterocarpum*	Stir heat-treated in Ar gas

Characterization of graphene oxide (GO) and reduced graphene oxide (RGO)

With the help of XRD, UV-VIS, FTIR, TGA, and FESEM analysis the formation of GO and RGO was confirmed in the following way.

X-ray diffraction analysis

When the XRD patterns of GO and RGO are taken with an x-pert powder diffractometer using a copper rotating anode and an incident beam with a wavelength of 154 nm, the d-spacing (according to Bragg's equation $n\lambda = 2d\sin\theta$) of the most intense peak from the (001) plane is 1.45 nm for GO and 379 nm for RGO (Fig. 2) [46]. This occurs by reason of hydroxyl, epoxy, and carbonyl groups present in GO [44] and in RGO d-spacing is decreased due to the smaller number of oxygen containing functionalities

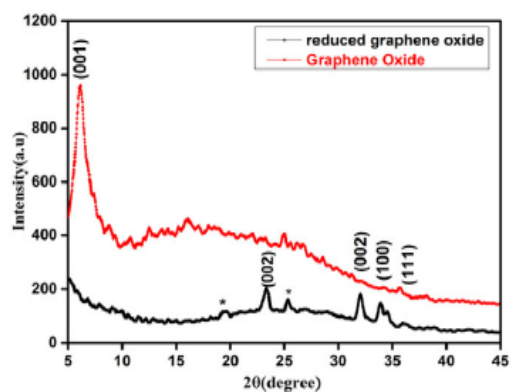[52]. This observation will indicate the reconstitution of the sp^2 framework on reduction [46].

Fig. 2. X-ray diffraction pattern of GO and RGO

UV-visible spectroscopy analysis

When GO is obtained after the reduction of graphite, then oxygen atoms are attached to the graphene layer. Because of this, polarity is increased. This results in water's increasing solubility, which can be observed by a color change from yellow to brown. The brown-colored solution (GO solution) exhibits absorption maxima of different intensity according to the concentration of GO formed [53]. The absorption maximum for GO is 225 nm in the oxidized material. When UV-visible absorption spectra were analyzed, GO and RGO exhibited absorption peaks at 226 nm and 257 nm, respectively (Fig. 3) [53]. This shift in UV-visible absorption maxima conforms to the formation of RGO, as well as the recovery of the π-conjugated structure of graphene after the reduction process of GO into RGO. This result also matches with the other reported literature [54].
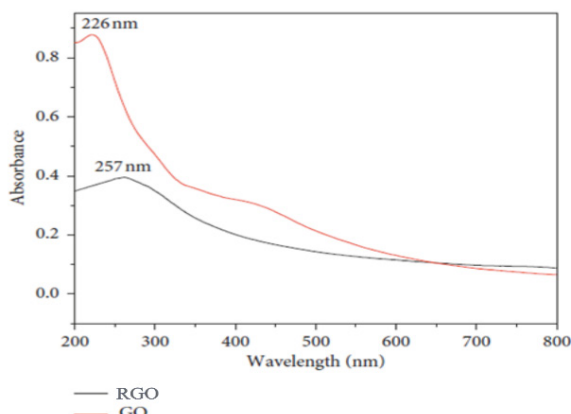
Fig. 3. UV-visible spectra of GO and RGO.

Fourier transform infrared spectroscopy analysis

Fig. 4 [55] represents the FTIR spectra of graphite oxide (GrO) and GO. Both GrO and GO exhibit the FTIR spectral peaks at 1050 cm^{-1} (stretching peak of C-O bond), 1310 cm^{-1} (peak of C-OH bond), 1630 cm^{-1} (stretching peak of C=C), 1740 cm^{-1} (stretching peak of C=O) and 3320 cm^{-1} (stretching peak of –OH group). All these peaks indicate the presence of alkene, hydroxyl, and carbonyl functional groups in the GrO and GO, which conform to the synthesis of GO [54]. Both GrO and GO exhibiting the same FTIR spectra means that both these have the same skeleton. There is only one difference that GO is the exfoliated sheet of GrO.
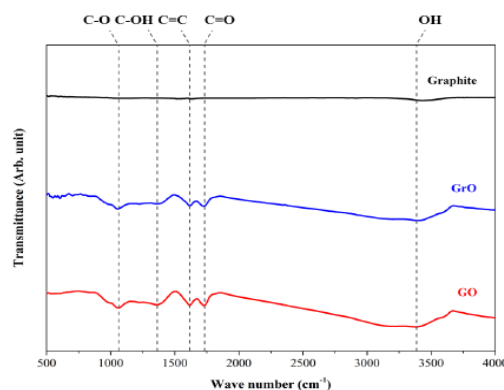
Fig. 4. FTIR spectra of graphite, GrO, and GO

RGO is prepared from GO by a reduction process. Fig. 5 [55] represents the FTIR spectra of RGO, as well as the effect of the functional groups on the annealing process of GO in the oven.
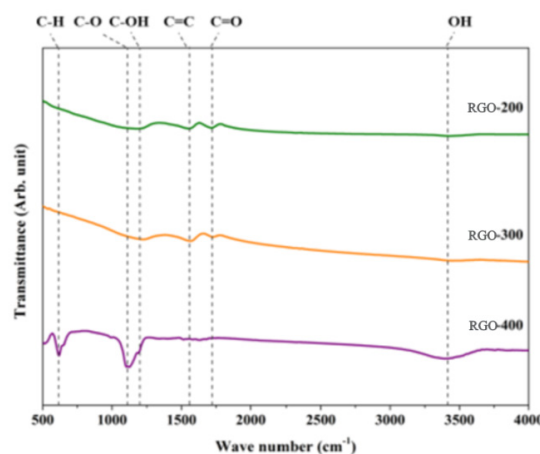

Fig. 5. FTIR spectra of RGO under annealing conditions of GO

The absorbance of oxygen-related functional groups is higher in Fig. 4 compared to Fig. 5. This indicates the formation of RGO by the reduction process of GO [45, 55].

Thermogravimetric analysis

For the measurement of thermal stability of GO and RGO, TGA measurement was used in the temperature range between 0ºC and 800ºC in nitrogen atmosphere, as shown in Fig. 6 [48]. This TGA of GO and RGO shows that weight loss in RGO is less than in GO under different temperature conditions (Fig. 6). This will indicate the smaller number of oxygen containing functionalities in RGO with respect to GO. This type of result in weight loss for GO and RGO agrees with the reported work of Gan *et al.* [56].
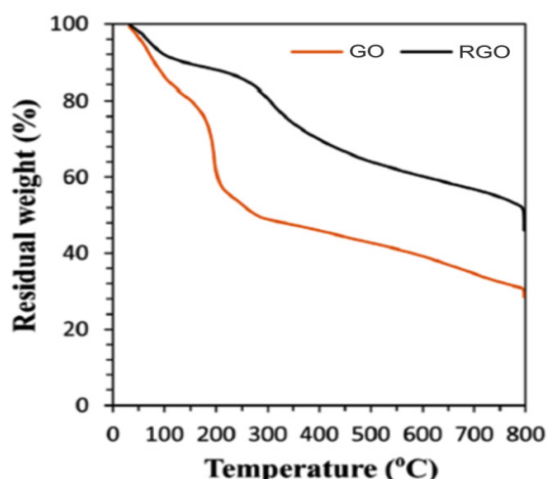
Fig. 6. TGA spectra of GO and RGO

Field emission scanning electron microscope analysis

This analysis is used to study the surface morphology of GO and RGO. This is observed in Fig. 7 [46]. It indicates the highly wrinkled structure of RGO in comparison to GO, which concludes that the surface of GO gets crimped on converting into RGO because of eliminating oxygen-containing functional groups from the surface.
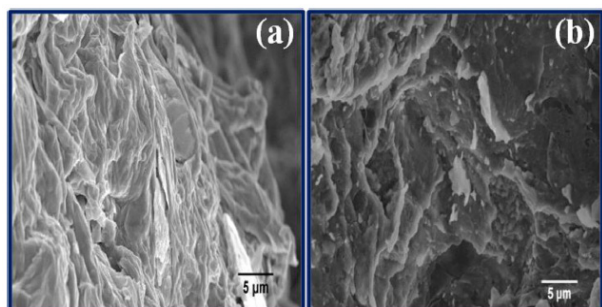

Fig. 7. FESEM image of GO (a) and RGO (b)

CONCLUSIONS

GO obtained from graphite powder by modified Hummer's method can be reduced by using chemical processes, as well as green methods to prepare the RGO, but from the different reported results, green methods using different plant extracts are preferred over the chemical methods due to the environmentally friendly nature of green methods. Green methods are preferred, particularly during the biologically related application of RGO, because poisonous or hazardous chemicals involved or generated by using chemical methods cause harmful effects. Since the yield of RGO prepared using chemical reduction methods is higher than the yield obtained using green methods, in this respect, green methods are not considered suitable for preparing RGO.

REFERENCES

1. A. K. Geim, K. S. Novoselov, *Nature*, **6**, 183 (2007).
2. M. S. Dresselhau, P. T. Araujo, *ACS Nano*, **4,** 6297 (2010).
3. R. Udayabhaskar, R. V. Mangalaraja, T. Pandiyarajan, B. Karthikeyan, H. D. Mansilla, D.Contreras, *Carbon*., **124**, 256 (2017).
4. C. H. Lu, H. H. Yang, C. L. Zhu, X. Chen, G. N. Chen, *Angew. Chemie Int. Ed*., **48**, 4785 (2009).
5. X. Sun, Z. Liu, K. Welsher, J. T. Robinson, A. Goodwin, S. Zaric, H. Dai, *Nano Res*., **1**, 203 (2008).
6. Y. Song, K. Qu, C. Zhao, J. Ren, X. Qu, *Adv. Mater*., **22**, 2206 (2010).
7. H. Cheng, X. Sha, L. Chen, A. C. Cooper, M.L. Foo, G. C. Lau, W. H. Bailey 3rd, G. P.Pez, J. *Am. Chem. Soc*., **131**, 17732 (2009).
8. K. S. Kim ,Y.Zhao, H. Jang, S. Y. Lee, J. M. Kim, K. S. Kim, J.H. Ahn, P. Kim, J.Y.Choi B.H. Hong, *Nature*., **457**, 706 (2009).
9. J. H. Jung, D. S. Cheon, F. Liu, K. B. Lee, T. S. Seo, *Angew. Chemie Int. Ed*., **49**, 5708 (2010).
10. F. Schedin, A. K. Geim, S. V. Morozov, E. W. Hill,P. Blake,M. I. Katsnelson, K. S. Novoselov, *Nat. Mater*., **6**, 652 (2007).
11. G. Eda, G. Fanchini, M. Chhowalla, *Nat. Nanotechnol*., **3**, 270 (2008).
12. X. Li, W. Cai, J. An, S. Kim, J. Nah, D. Yang, R. Piner, A. Velamakanni, I. W. Jung, E. Tutuc, S. K. Banerjee, L. Colombo, R. S. Ruoff, *Science*, **324**, 1312 (2009).
13. A. Reina, X. Jia, J. Ho, D. Nezich, H. Son,V. Bulovic, M. S. Dresselhaus, J. Kong, *Nano Lett*., **9**, 30 (2009).
14. K. S. Novoselov, A. K. Geim, S. V. Morozov, D. Jiang, Y. Zhang, S. V. Dubonos, I. V. Grigorieva, A. A. Firsov, *Science*, **306**, 666 (2004).
15. X. Lu, M. Yu, H. Huang, R. S. Ruoff, *Nanotechnol*., **10**, 269 (1999).
16. J. C. Delgado, J. M. R.-Herrera, X. Jia, D. A. Cullen, M. S. Dresselhaus, M. Terrones, *NanoLett*., **8**, 2773 (2008).
17. M. Choucair, P. Thordarson, J. A. Stride, *Nat. Nanotechnol*., **4**, 30(2009).
18. S. Stankovich, D. A.Dikin, R. D. Piner, K. A. Kohlhaas, A. Kleinhammes, Y. Jia, Y. Wu, S. T. Nguyen, R.S. Ruoff, *Carbon*., **45**, 1558 (2007).
19. D. R. Dreyer, S. Park, C. W. Bielawski, R. S. Ruoff, *Chem. Soc. Rev*., **39**, 228 (2010).
20. P. Joshi, S. Mehtab, M.G.H. Zaidi, *Bull. Chem. Soc. Japan,* **95** (6), 855 (2022).
21. J. I. Paredes, S. Villar-Rodil, M. J. Fernández-Merino, L. Guardia, A. Martínez-Alonso, J. M. D. Tascón, *J. Mater. Chem.*, **21**, 298 (2011).
22. D. Y. Lee, Z. Khatun, J.-H. Lee, Y. Lee, I. In, *Biomacromolecules*, **12**, 336 (2011).
23. Y. Wang, Z. Shi, J. Yin, *ACS Appl. Mater. Interfaces*., **3**, 1127 (2011).
24. T. Kuila, S. Bose, P. Khanra, A. K. Mishra, N. H. Kim, J. H. Lee, *Carbon*., **50**, 914 (2012).
25. S. Gurunathan, J. W. Han, V. Eppakayala, J.H. Kim, *Colloids Surf. B: Biointerfaces*, **102**, 772 (2013).

26. S. Thakur, N. Karak, *Carbon.*, **94**, 224 (2015).
27. J. Yang, X. Xia, K. He, M' Zhang, S. Qin, M. Luo, L. Wu, *J. Mol. Struct.*, **1245**, 131064 (2021).
28. H. A. Alshamsi, S. K. Ali, S. H. Alwan Altaa, *J. Phys. Conf. Ser.*, **1664**, 012058 (2020).
29. B. Haghighi ,M. A. Tabrizi, *RSC Adv.*, **3**, 13365 (2013).
30. Y. H. Ding, P. Zhang, Q. Zhuo, H. M. Ren, Z. M. Yang, Y. Jiang, *Nanotechnol.*, **22**, 215601 (2011).
31. S. Sadhukhan, T.K.Ghosh, D. Rana , I. Roy, A. Bhat tacharyya, G. Sarkar, M. Chakraborty, D.Chattopad hyay, *Mater. Res. Bull.*, **79**, 41 (2016).
32. C. R. Brown, *Am. J. Potato Res.*, **82**, 163 (2005).
33. J. A. Severi, Z. P. Lima, H. Kushima, A. R. M. S. Brito, L. C. Dos Santos,W. Vilegas, C. A. Hiruma-Lima, *Molecules.*, **14**, 1098 (2009).
34. T. H. Ibrahim, Y. Chehade, M. A. Zour, *Int. J. Electrochem.Sci.*, 6542 (2011).
35. S.Andreas, *Global Science Books*, 23(2009).
36. K. Singhal, S. Mehtab, M. Pandey, M. G. H. Zaidi, *Current Res. Green Sustain. Chem.* 5, 100266 (2022).
37. R. Rikhari, B. Saklani, A. Bisht, S. Mehtab, M. G. H. Zaidi, *Sensor Lett.* **17**, 511 (2019).
38. S. M. R. Ribeiro, L. C. A. Barbosa, J. H. Queiroz, M. Knödler, A. Schieber, *Food Chem.*, **110**, 620 (2008).
39. J. Zhang, H. Yang, G. Shen, P. Cheng, J. Zhang, S. Guo, *Chem. Commun.*, **46**, 1112 (2010)
40. C. Shan, H. Yang, D. Han, Q. Zhang, A. Ivaska, L. Niu, *Langmuir.*, **25**, 12030 (2009).
41. M. J. F.Merino, L. Guardia, J. I. Paredes, S. V. Rodil, P. S. Fernández, A. M. Alonso, J. M. D. Tascón,*J. Phys. Chem. C.*, **114**, 6426 (2010).
42. O. Akhavan, E. Ghaderi, S. Aghayee, Y. Fereydooni, A. Talebi, *J. Mater. Chem.*, **22**, 13773 (2012).
43. S. Abdolhosseinzadeh, H. Asgharzadeh, H. Seop Kim, *Sci. Rep.*, **5**, 10160 (2015).
44. Z. Fan, K. Wang, T. Wei, J. Yan, L. Song, B. Shao, *Carbon*, **48**, 1686 (2010).
45. M. J. Y. Tai ,W. W. Liu, C.-S. Khe, N. H. Md Said, Y. P. Teoh. C. H. Voon, H. C. Lee, *AIP Conf. Proc.*,020032 (2018).
46. N. Sharma, V. Sharma, Y. Jain, M. Kumari, R. Gupta, S. K. Sharma, K. Sachdev, *Macromol. Symp.*, **376**, 1700006 (2017).
47. A. Abubakar, M. Haque, *J. Pharm. Bioallied Sci.*, **12**, 1 (2020).
48. M. Mahiuddin, B. Ochiai, *Technol.*, **9**, 96 (2021).
49. R. M. Dominic, P. Punniyakotti, B. Balan, S. Angaiah, *Bull. Mater. Sci.*, **45**, 2 (2022).
50. M. Zhi, Q. Liu, H. Chen, S. Feng, Y. He, *J. Phys. Conf. Ser.*, **1213**, 052047 (2019).
51. D. Perumal, E. L. Albert, C. A. C. Abdullah, *J. Composites Science*, **6**, 58 (2022).
52. V. Loryuenyong, K. Totepvimarn, P. Eimburanapravat, W. Boonchompoo, A. Buasri, *Advances in Materials Science and Engineering,* **2013**, 1 (2013).
53. A. T. Habte, D. W. Ayele, *Advances in Materials Science and Engineering*, **2019**, 1(2019).
54. H. Saleem, M. Haneef, H. Y. Abbasi, *Mater. Chem. Phys.*, **204**, 1 (2018).
55. R. Hidayat, S. Wahyuningsih, A. Ramelan, *IOP Conf. Ser. Mater. Sci. Eng.*, **858**, 12009 (2020).
56. L. Gan, B. Li, Y. Chen, B. Yu, Z. Chen, *Chemosphere*, **219**, 148 (2019).

Impact of biopolymer *Commiphora wightii* (guggul) oleo gum resin fumes on indoor environment

N. Singh[1*], V. Gupta[2]

[1]*Tropical Forest Research Institute, Jabalpur P.O.R.F.R.C. Jabalpur (M.P.) 482001, India*
[2]*Faculty of Science, Motherhood University, Roorkee, India*

The present study focuses on the physico-chemical composition of *C. wightii* oleo-gum resin, a biopolymer comprising steroids, diterpenoids, aliphatic esters, carbohydrates, and various inorganic ions. The ash, water-soluble, and alcohol-soluble extractive content of the resin were found to be 4.47±0.78%, 25.76±0.15%, and 10.65±0.25%, respectively. Additionally, the oleo-gum resin contained 0.85±0.21% essential oil. Biologically active chemicals, guggulsterone-E and guggulsterone-Z were estimated 0.05±0.01%, and 0.53±0.07%, respectively. Moreover, this study assessed the inhibitory effect of oleo-gum resin fumes on the indoor microbial environment and the concentration of inorganic pollutants. Exposure to guggul resin fumes for 30 minutes resulted in a significant reduction of 82%-90% in colony-forming units (CFU) of environmental microbes, including bacteria and fungi. Furthermore, the impact of guggul fumes on inorganic pollutants, specifically SO_2 and NO_2 concentrations, was investigated in the study area. Before treatment, SO_2 and NO_2 levels were observed to be 4.6 ppm and 0.021 ppm, respectively. Following fumigation, there was a reduction in SO_2 levels ranging from 8.47% to 26.73%, while NO_2 levels increased by 9.52% to 14.85%. This comprehensive study sheds light on the potential of *C. wightii* oleo-gum resin to influence indoor microbial contamination and inorganic pollutant levels, showcasing its significance in environmental and health-related applications.

Keywords: *Commiphora wightii*, guggulsterones, microbial contamination, bacterial colonies, colony forming units, SO_2, NO_2

INTRODUCTION

Medicinal values of guggul, *Commiphora wightii* oleo gum resin, are reported in Atharva Veda [1]. It is found effective in treatment of several diseases [2-4]. Besides, it is also used in incense, lacquers, varnishes, ointments as a fixative and in perfumes. It has very high demand in national and international herbal industries. National Medicinal Plant Board, Ministry of Ayush, New Delhi has considered it as one of the priority species for research and development [5].

The significance of this gum-resin is due to the presence of a steroid "guggulsterone", in two active isomers, guggulsterone E and Z which are responsible for the hypolipidemic activity [6, 7]. Guggulsterone and guggulipid have been demonstrated to reduce risk of cardiac function in clinical studies [8] and also inhibit platelet aggregation and provide protection from myocardial ischemia in rats [9, 10] due to antioxidant property. The plant extracts of guggul were used as major components in the preparation of 100% natural disinfectants[11]. The potential antioxidant and antimicrobial activities of guggul against different organisms, *viz.*, *Klebsiella pneumoniae*, *Bacillus subtilis*, *Staphylococcus aureus*, *Proteus vulgaris*, *Escherichia coli*, and *Staphylococcus epidermidis*

were also documented [12]. Guggulsterone Z and gugulipid (GL) possess anti-cancer activity [13]. The fresh guggul plant extract was found more effective compared to its distillate. The antibacterial efficacy of guggul gum was assessed against gram-positive and gram-negative bacterial strains [14, 15]. The efficacy of guggul resin fumes was compared with some weeds; maximum reduction was observed in oleo-gum resin fumes. Fumes of weed species were also found effective for reducing bacteria population in the laboratory rooms. The bhils tribes inhale the fumes of gum resin of guggul to cure fever and bronchial diseases [16]. The inhalation of medicinal smoke is a simple way of administering a drug. Since ancient times, fumes of frankincense and myrthwere used for religious purposes, had hygienic functions, also to remove bad smell, and reduce pollutants of air. The bactericidal, germicidal, antiviral, and fungicidal properties of benzoin resin and oil due to the presence of biocidal constituents- benzoic acid, benzaldehyde, and benzyl benzoate were assessed [17, 18]. Similarly, fumes of odoriferous medicinal herbs and wood were used to purify the environment [19]. Keeping these facts in mind, the present study deals with the effect of fumes on air quality and the anti-microbial activities of oleo-gum-resin *C. wightii*.

---

* To whom all correspondence should be sent:
E-mail: singhn@icfre.org

MATERIALS AND METHODS

Collection of sample and determination of quality of guggul

Samples of guggul were collected from the forest of Bhuj (Gujarat). Quality of resin, i.e., moisture%, water soluble, ethanol soluble extractive value, total ash and acid insoluble ash value were determined by following methods as per WHO guidelines [20].

Estimation of bioactive chemicals- guggulsterone E & Z

The quantity of biologically important chemicals guggulsterone-E and guggulsterone-Z was estimated with the help of chromatographic technique - high performance thin layer chromatography (HPTLC) [21]. Standard solution of both chemicals was prepared in separate 10 ml volumetric flasks by dissolving 1000 µg in 3 ml of ethyl acetate and final volume was made up with methanol. 50 mg resin was dissolved in 2 ml of ethyl acetate and the volume was made up with methanol in a 10 ml volumetric flask. A standard graph was plotted with different concentrations of the standard (200, 400, 600 and 800 ng/spot).

Development of HPTLC plate and quantity estimation of guggulsterone - E&Z

Standard and 20 µg/spot samples were applied in three replicates using Linomet 5 (CAMAG) on 20 cm × 10 cm, 200 µm silica gel 60 F254 coated aluminum plates. A toluene:acetone (6:1) solution was used as mobile phase to develop plate in a CAMAG derivatization chamber. 100 µm/step data resolution was used to scan developed plates in a wavelength range of 200 to 400 nm. WinCATs Planner Chromatography manager software (CAMAG) Switzerland Excel (Microsoft Office 10) USA was used to quantify guggulsterone E & Z through the calibration curve of standards (Figs. 9a to 9f, 10a to 10c) and their peak area. Following formula was used to calculate guggulsterone E & Z percentage:

$$E - GS \text{ and } Z - GS \ (\%)$$
$$= \frac{\text{Estimated amount (µg)} \times 100}{\text{Dry amount spotted on the track (µg)}}$$

Testing of microbial activity

Fumigation was carried out by burning 10 g of guggul [22] in the room (8 m × 10 m × 3.5 m). Settle plate method as passive sampling was used to determine the total microorganisms (bacterial and fungal) in the air. The efficacy of fumes was assessed by microbial count, CFU before and after exposure of plates of nutrient agar (NA) and potato dextrose agar (PDA) for 30 min, placed at different distances (1, 1.5, 2, 2.5, 3, 3.5 and 4 feet). After exposure the plates were incubated at 37°C.

Effect of fumes on NO_2 and SO_2 levels

NO_2 in air was collected by scrubbing a known volume of air through an alkaline solution of arsenite. The nitrite ions thus formed reacted with sulfanilamide and N-(1-naphthyl) ethylenediamine (NEDA) in phosphoric acid to form the colored azo dye, which was measured on a spectrophotometer at 540 nm. SO_2 from the air stream was absorbed in a sodium tetra-chloromercurate solution, it forms a stable dichlorosulfomercurate complex, which then behaves effectively as fixed SO_3^{2-} in solution. The amount of SO_2 was then estimated by the color produced when prosaline-hydrochloride and formaldehyde were added to the solution, measured on a spectrophotometer at 560 nm.

RESULTS AND DISCUSSION

Guggul, oleo-gum resin physico-chemical properties were assessed. The physical nature of the resin is viscous, moist and granulous. It burns in fire, melts in the sun light, and forms milky emulsion in hot water. The ash, water-soluble and alcohol-soluble parts were 4.47±0.78, 25.76±0.15 and 10.65±0.25%, respectively. The quantity of essential oil in the oleo-gum resin was estimated as 0.85±0.21%. The bioactive constituents, i.e., guggulsterone-E, guggulsterone-Z (Fig. 1) and total guggulsterone were quantified as 1.45±0.30, 0.05±0.010, and 0.53±0.07%, respectively. The results of this study are in accordance with earlier studies on the quality of guggul reported [23, 24]. However, some variation was observed in quantity which might be due to collection of material from different geographical regions.

Efficacy of fumes on air micro flora

The efficacy of oleo-gum-resin on bacterial and fungal population in air is depicted in Table 1 and Fig. 2. Colony forming units (CFU) were reduced significantly after burning of resin. The CFU of environmental microbes/bacteria decreased by 82-90% compared to the control. The percent reduction of fungal colonies varied from 88.55 to 91.72% over control. The results of the study show that the bacterial and fungal population decreased after fumigation with guggul resin in the area, the number of CFU before fumigation varied 1 to 13.
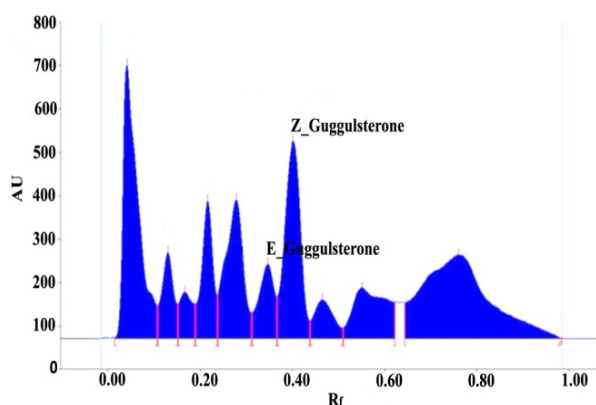
Fig. 1. HPTLC fingerprint profile of oleo-gum resin of *C. wightii* showing guggulsterone-E&Z

The result of this study is in the agreement with the findings of a study, determined potential efficacy of guggul against six gram-positive and four gram-negative bacteria [14]. Several studies have been undertaken to develop ecofriendly fungicides to reduce their harmful effect of synthetic carcinogenic [25]. Benzoin oil showed biological activities due to the presence of benzoic acid, benzaldehyde, and benzyl benzoate, and its smoke worked as a disinfectant [17, 18]. The present study was supported by the study on the effectiveness of guggul to inhibit gram-negative and gram-positive bacteria [16]. Further, the results of our study are in the line of a previous work which studied the effect of different weed fumes on the microbial population and compared with guggul and observed potential reduction of microbial population by oleo-gum resin fumes in comparison to other plants [15]. The result of the study is consistent with the findings of recent studies, reported the ability of the smoke to purify the air. The ability of traditional ayurvedic

fumigation practices in environmental disinfection is also reported in several studies [26]. The white benzoin resin fumes inhibit bacterial strains of *Staphylococcus aureus*, *Pseudomonas aeruginosa*, and *Candida albicans* [27]. The fumes lead to purification of air by oxidizing the carbonic compounds and along with that they have antimicrobial properties which benefit the people around. They have disguising effect on various pollutants in the atmosphere including the oxides of sulfur. The present investigation reports the potential of fumes of oleo-gum resin on microflora in the environment. The results clearly disclosed the effect of oleo gum resin on different microbes in air.

Efficacy of C. wightii oleo-gum-resin fumes on SO_2 and NO_2 levels in air

In the study area, for investigation of effect of guggul fumes on inorganic pollutants, i.e., SO_2 and NO_2, concentrations had been undertaken. The concentrations of SO_2 and NO_2 before treatment were 4.6 ppm and 0.021 ppm while after fumigation, SO_2 decreased from 1.23 to 0.39 ppm, corresponding to 8.47 to 26.73% decrease in SO_2 level and NO_2 increased from 0.025 to 0.051 ppm (Fig. 3). Our results are in conformity with the study conducted on the effect of fumes onSO_2 and NO_2 levels in ambient air [26]. In the present study, it was assessed that guggul fumes reduce microbial load and SO_2 levels, while a slight increase in NO_2 levels was observed in the air. However, it was below the threshold limit as per the guidelines of National ambient air quality standards (NAAQS) of 0.053 ppm.

Table 1. Effect of fumes of oleo gum resin on reduction of microbes

Treatment number	Distance (ft)	% of bacterial colonies after fumigation (mean)	% of fungal colonies after fumigation (mean)
1	1.0	9.526±1.065	15.86±0.078
2	1.5	11.78±1.725	14.56±0.181
3	2.0	12.51±1.595	18.77±0.295
4	2.5	13.68±2.44	12.10±0.108
5	3.0	14.98±2.77	11.80±0.378
6	3.5	12.78±3.635	17.06±0.178
7	4.0	14.81±0.94	10.41±0.505

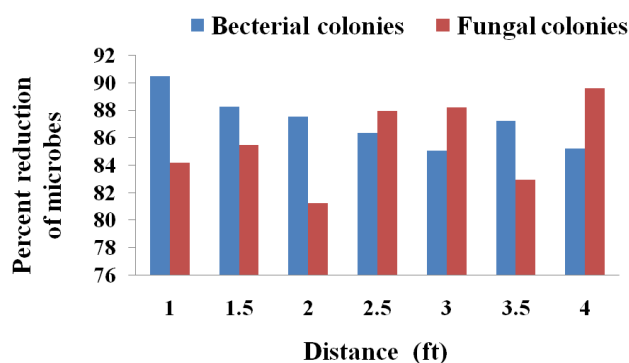Values are mean ± standard deviation (three replicates)

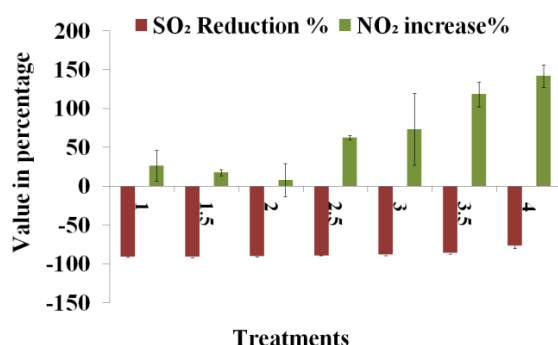**Fig. 2.** Effect of fumes of guggul on reduction of microbes (bacteria and fungi)

Fig. 3. Effect of fumes on reduction/increase of SO_2 and NO_2 levels

CONCLUSIONS

In the present study, the potential of *C. wightii*, oleo gum resin fumes was observed in environment purification. The phytochemical analysis of guggul revealed the presence of 4.47±0.78% ash, 25.76±0.15% water-soluble ash, 0.65±0.25% alcohol-soluble part and 0.85±0.21% essential oil. The quantity of bio active ingredients in guggulsterones was observed to be 1.45±0.30%. Moreover, this study assessed the inhibitory effect of oleo-gum resin fumes on the indoor microbial environment and concentration of inorganic pollutants. Exposure to guggul resin fumes for 30 minutes resulted in a significant reduction (82%-90%) in colony-forming units (CFU) of environmental microbes. Furthermore, the concentrations of the inorganic pollutants SO_2 and NO_2, were also found changed due to burning of guggul. A reduction in SO_2 levels ranging from 8.47% to 26.73% was observed, while NO_2 levels increased by 9.52% to 14.85%. On the basis of our study it was revealed that fumigation with *Commiphora wightii* oleo-gum resin is effective to improve air quality through minimizing/ reducing microbes and effects on toxic gaseous pollutants have potential. The use of fumes of this medicinal oleo-gum resin can reduce bacterial and fungal growth, as well as toxic gaseous pollutants of atmosphere. Findings of the study may pave the way to develop integrated approach to use bioproducts of *Commiphora wightii* (guggul), an important natural resource, to manage air quality.

REFERENCES

1. S. Kumar, V. Shankar. *J. Arid Environ.,* **5,** 1 (1982).
2. S. Dev, *Environ. Health Perspec.,* **107,**783(1999).
3. G.V. Satyavati, *Indian J. Med. Res.*, **87,** 327 (1988).
4. X. Wang, J. Greilberger, G. Ledinski, G. Kager, B. Paigen, G. Jurgens, *Atherosclerosis*, **172,**9 (2004).
5. C. P. Kala, B. S. Sajwan, *Curr. Sci.*, **93 (6),** 797(2007).
6. R. B. Singh, M. A. Niaz, S. Ghosh, *Cardiovasc. Drugs Ther.,* **8,** 659 (1994).
7. N. L. Urizar, D. D. Moore. *Annu. Rev. Nutr.*, **23,** 303(2003).
8. C. Ulbricht, E. Basch, P. Szapary, P. Hammerness, S. Axentsev, H. Boon, D., Kroll, L. Garraway, M. Vora, J. Woods, *Complement Ther. Med.,* **13,** 279 (2005)
9. L. Mester, M. Mester, S. Nityanand, *Planta Medica*, **37**(4), 367 (1979).
10. R. Chander, F. Rizvi, A. K. Khanna, R. Pratap, *Ind. J. Clin. Biochem.,***18,** 71(2003).
11. S.A. Mandavgane, V.V. Pattalwar, A.R. Kalambe, *Nat. Pro. Rad.*, **4**(4) (2005).
12. J. Jerald, T. Peck, F. Steinicke,M. Whitton, in: APGV'08: Proceedings of the 5th Symposium on applied perception in graphics and visualization, 155 (2008).
13. W. Jiang, B. David, C. David, Z. Feng, M.A. Luciano, *Nat. Biotechnol.*, **31,** 233 (2013).
14. B. K. Ishnava, Y.N. Mahida, J.S.S. Mohan, *J. Pharmacogn. Phytother.*, **2,**91 (2010).
15. N. Singh, S. Kumar, Chitra, *Ind. J. Weed Sci.*, **49**(4), 417 (2017).,

16. P. Vani, D. Sreekanth, P. Manjula, B. Keerthi, S. Kistamma, B. Mohan, A. N. Reddy, C.H. Mohan *J. Pharmacogn. Phytochem.*, **5**(5) (2016)

17. M.A. Hanif, A.Y. Al-Maskri, Z.M.H. Al-Mahruqi, J.N. Al-Sabahi, A. Al-Azkawi, M.Y. Al-Maskari. *Nat. Prod. Commun.,***5** (5),751 (2011).

18. A. Sharif, H. Nawaz, *Int. J. Chem. Biochem.*, **10,** 106(2016).

19. M. L. Grbić, N. Unković, I. Dimkić, P. Janaćković, M. Gavrilović, O. Stanojević, M. Stupar, L Vujisić, A. Jelikić, S. Stanković, J. Vukojević, *J. Ethnopharmacol.*, **219**,1 (2018).

20. Anon., *Off. J. Europ. Comm.,* **L 330**, 32 (1998).

21. A. Kulhari, A. Sheorayan, N. Saxena, M. Chander, M. Mangal, A. Chaudhury, A. K. Dhawan, K. K. Rajwant, *Genet. Res. CropEvol*., **60,** 1173 (2013).

22. N. Prabhu, J. Rengaramanujam, P. A. Joice, *Indian J. Tradit.Knowl*., **8(2),** 278 (2009).

23. A. Jain, V. B. Gupta, *Indian J. Tradit. Knowl*., **5,** 478 (2006).

24. P. Goyal, A. Chauhan, P. Kaushik*, J. Med. Med. Sci.,***1**(3),071 (2010).

25. Al-Sabri, M.A. Moslem, S. Hadi, M.A. Yassin, *J. Pure Appl. Microbiol.,***8 (**5), 3951 (2014).

26. B. S. Bhatwalkar, P. Shukla, R. K. Srivastava, R. Mondal, R. Anupam, *J. Ayurveda Integr. Med.*, **10**(3), 203 (2019).

27. W. Alruways, E. E. Intisar, Mansi A. Mariam, *Int. J. Med. Res. Health Sci.* (*IJMRHS*), **9**(11),5629 (2020).

Goos-Hänchen shift in monolayer graphene with electrostatic barriers

N. Agrawal[1*], S. Rathore[2], S. Kumar[3]

[1]Department of Physics, University of Allahabad, Prayagraj, Uttar Pradesh, India
[2]Materials Physics Research Laboratory, Department of Physics, Government PG College Budaun-243601, Uttar Pradesh, India
[3]Department of Computer Science, Hansraj College, University of Delhi, New Delhi, 110007, India

We analysed the electron transport and Goos-Hänchen (GH) lateral shifts in graphene. We discuss recent studies on the GH shift in monolayer graphene. We describe the theoretical framework for calculating the GH shift and its electronic analogue in monolayer graphene. Further we discuss the enhancement in the GH shift corresponding to the resonant positions arising due to quasi-bound states formation in the presence of well-formed in the double barrier structure.

INTRODUCTION

The Goos-Hänchen (GH) shift is a phenomenon in which the lateral displacement of a beam of light occurs as it is reflected off a surface. This effect was first observed in the context of optics and has since been found to occur in a variety of physical systems [1-3]. In recent years, the GH shift has been studied in the context of graphene, a two-dimensional material consisting of a single layer of carbon atoms arranged in a hexagonal lattice. Graphene exhibits a number of unique electronic and optical properties [4-9], and the GH shift in graphene has been found to have some particularly interesting and useful characteristics. The GH shift in graphene arises due to the strong interaction between light and electrons in the material. As a beam of light enters graphene, it excites the electrons and creates a surface plasmon polariton (SPP), which is a collective oscillation of the electron density. This SPP interacts with the incident light and causes it to experience a lateral shift as it reflects off the surface. Understanding and controlling the GH shift in graphene has important implications for the development of new technologies, such as ultra-compact photonic circuits and sensors. Additionally, the GH shift provides a unique tool for studying the electronic and optical properties of graphene and other two-dimensional materials.

The Goos-Hänchen (GH) shift in monolayer graphene can be understood within the framework of the surface plasmon polariton (SPP) theory. When light enters graphene, it can excite an SPP, which is a collective oscillation of the electron density on the surface of the material. This SPP can then interact with the incident light and cause a lateral shift in its reflection angle. The GH shift can be calculated using the Fresnel coefficients, which describe the reflection and transmission of light at an interface between two materials with different refractive indices. In the case of graphene, the Fresnel coefficients depend on the angle of incidence and the polarization of the incident light, as well as the doping level and Fermi energy of the material. This shift in graphene can be enhanced by controlling the doping level and Fermi energy of the material. For example, doping graphene with impurities can increase the density of states and enhance the interaction between the incident light and the SPP, leading to a larger GH shift.

In addition to its practical applications, the GH shift in graphene can also provide insights into the fundamental properties of two-dimensional materials. For example, the GH shift can be used to probe the electronic properties of graphene and to study the coupling between light and matter in low-dimensional systems. Overall, the GH shift in monolayer graphene is a fascinating phenomenon with a wide range of potential applications in photonics and nanotechnology. In addition to the Goos-Hänchen (GH) shift, monolayer graphene exhibits another type of lateral shift known as the Imbert-Fedorov (IF) shift [10]. The IF shift is similar to the GH shift in that it arises from the interaction between light and surface plasmon polaritons (SPPs) in the material, but it differs in the way that it is calculated and its physical origin.

The IF shift arises when light reflects off a surface with a non-uniform refractive index profile. In the case of graphene, this non-uniformity can arise due to the presence of a strain gradient or a spatially

---

varying doping profile. The IF shift can be described as the lateral displacement of the reflected beam relative to the incident beam, and it depends on the angle of incidence and the polarization of the incident light, as well as the refractive index profile of the material. The IF shift in graphene has been experimentally observed in a number of studies. For example, it has been shown that the presence of a strain gradient in graphene can lead to a significant IF shift, which can be controlled by applying a mechanical strain to the material. Similarly, the IF shift can be enhanced by doping graphene with impurities or by patterning the material into a non-uniform structure. Like the GH shift, the IF shift in graphene has potential applications in the development of new photonic devices and sensors. The ability to control the lateral displacement of light in graphene could be useful for designing ultra-compact and highly sensitive photonic circuits, as well as for studying the fundamental properties of low-dimensional materials.

Theoretical framework

The Fresnel coefficients can be used to calculate the Goos-Hänchen (GH) shift at the interface between two media, such as strained graphene and air. The Fresnel coefficients describe the reflection and transmission of electromagnetic waves at the interface and depend on the refractive indices of the two media. In the case of strained graphene, the refractive index of graphene is affected by the mechanical strain, which changes the electronic properties of the material. The refractive index of strained graphene can be calculated using the following formula $n = 1 - \delta + i\alpha$, where δ is the real part of the refractive index, which is affected by the mechanical strain, and α is the imaginary part, which accounts for the absorption of light by the material.

The Fresnel coefficients for the reflection and transmission of electromagnetic waves at the interface between strained graphene and air can be expressed as $r = (n_1 - n_2)/(n_1 + n_2)$ and $t = 2n_1/(n_1 + n_2)$, where n_1 is the refractive index of strained graphene and n_2 is the refractive index of air. With this, the GH shift can be calculated using $\Delta x = -2\text{Im}(t/r)\ \partial\theta(q/k)$, where Im is the imaginary part, $\partial\theta(q/k)$ is the derivative of the surface plasmon wave vector with respect to the incident angle, and q and k are the wave vectors of the surface plasmon and incident light, respectively.

Electronic analogue of Goos-Hänchen-like shift in graphene

Many optics like behavior of ballistic electrons in graphene have been demonstrated due to the quantum-mechanical wave nature of electrons [4]. In graphene, electrons near the Fermi level, namely the transport electrons no more obey quadratic dispersion law, a typical characteristic of their nonrelativistic nature, but rather obey a linear dispersion relation, an archetype of the ultra-relativistic massless particles. The transport of such massless Dirac fermions in the presence of an electrostatic potential barrier is analogous to negative refraction through meta materials [9]. It was shown that a precise focusing can be achieved by fine-tuning the densities of carriers on either side of the barrier. This can be used to turn the electrostatic barrier (or n-p-n junction) into a Veselago lens for electrons.

Further, the unique electronic and transport properties of graphene including anomalous quantum hall effect and Klein tunnelling has opened very new exciting prospects in terms of analogy between optics and electron propagation in ballistic regime. Many optics-like phenomena such as collimation, Fabry Perot interference and Bragg reflection have been predicted with graphene-based structures. Further, quantum Goos-Hänchen effect has been investigated at the single graphene interface and in graphene based electric and magnetic barriers which are analogous to the phenomenon of the lateral shift of the light beam total internally reflected from dielectric surface [10-22]. However, in general the magnitude of quantum Goos-Hänchen shift is of the order of Fermi wavelength which impedes its direct measurement and broad applications. Later on, Chen *et al.* investigated the lateral shifts for Dirac fermions in transmission through monolayer graphene barrier, based on a tunable transmission gap [21, 22]. This shift has same physical origin that is due to the beam reshaping since each plane wave component undergoes different phase shift, however it has nothing to do with the evanescent waves which play an all important role in the lateral shift of total internally reflected wave function. For this reason, this shift can be termed as Goos-Hänchen-like (GHL) shift. It can be considered as an electronic analogue of the lateral shifts of light beam transmitted through a meta-material slab. Very recently a giant Goos-Hänchen shift has been reported for electron beam tunnelling through graphene double barrier structures [18, 19]. It is found that inside the transmission gap for the single barrier, the shift displays sharp peaks with magnitude up to the order of electron beam width which may be utilized to design valley and spin beam filters. A detailed investigation of the physics behind such giant Goos-Hänchen shift is required.

Theory: tunable transmission gap and GHL shift for single electrostatic barrier in monolayer graphene

We consider the massless Dirac fermions with the Fermi energy E and incidence angle ϕ with respect to the x axis incident upon a barrier of height V_0 and width d. Since the charge carriers in graphene are formally described by Dirac like Hamiltonians, the wave functions in region I (x<0), region II (0<x<d) and in region III (x>d) are obtained as:

$$\psi_I = \begin{pmatrix} 1 \\ se^{i\phi} \end{pmatrix} e^{i(k_x x + k_y y)} + r \begin{pmatrix} 1 \\ -se^{-i\phi} \end{pmatrix} e^{i(-k_x x + k_y y)}$$

$$\psi_{II} = a \begin{pmatrix} 1 \\ s'e^{i\theta} \end{pmatrix} e^{i(q_x x + q_y y)} + b \begin{pmatrix} 1 \\ -s'e^{-i\theta} \end{pmatrix} e^{i(-q_x x + q_y y)}$$

$$\psi_{III} = t \begin{pmatrix} 1 \\ se^{i\phi} \end{pmatrix} e^{i(k_x x + k_y y)}$$

Eq. (1)

Here k_x and k_y are the parallel and perpendicular wave vector components outside the barrier while q_x and q_y are the corresponding components inside the barrier. Using Eq. (1) the transmission coefficient is determined as:

$$T = \frac{4k_x^2 q_x^2}{k_x^2 q_x^2 + \left(k_y^2 + k_F k_F'\right)^2} e^{-2iq_x d}$$

Here k_F and k_F' are the Fermi wave vectors outside and inside the barrier region, respectively. In the next section we present the result and analysis of transmission and GHL shift using above expression.

RESULTS AND DISCUSSION

Tunable transmission gap & Goos-Hänchen shift for single and double electrostatic barrier

We calculated the tunable transmission gap occurring in the presence of single electrostatic barrier in graphene, and the associated Goos-

Hänchen-like (GHL) shift. This is shown in Figs. 1 (a) and (b). Further, we obtained the shift in the presence of a double electrostatic barrier and showed that inside the tunable transmission gap for the constituent single barrier, the shift displays giant, sharp peaks at the position of the bound states formed due to the well between the two barriers.

When the electrons are incident at an angle greater than the critical angle:

$$\phi > \phi_c = \sin^{-1}\left|\frac{V_0 - E}{E}\right|$$

the wave vector inside the barrier corresponds to an evanescent wave and the transmission probability is damped exponentially. Due to this reason, there occurs an angle-dependent gap as we plot transmission as a function of incident energy. The amount of this angle-dependent gap can be evaluated analytically as $\Delta E = 2V_0 \sec\phi \tan\phi$. Further, using the transmission coefficient expression and applying the stationary phase approximation the GHL shifts of the transmitted beam through a barrier in graphene can be obtained using $\sigma_t = \delta\phi_t / \delta k_y$ corresponding to the wave vector at central incidence angle. The analytical expression for GHL shift is thus obtained as:

$$\sigma_t = d \tan\phi_0 \cdot T \cdot \left[\left(2 + \frac{k_0^2}{k_x^2} + \frac{k_0^2}{q_x^2}\right)\frac{\sin 2q_x d}{2q_x d} - \frac{k_0^2}{q_x^2}\right]$$

where $k_0^2 = k_{y0}^2 - ss' k_F k_F'$, the central wave vector being k_0.

Depending on the sign of the product $ss' = \pm 1$ the GHL shifts can be negative or positive and can be enhanced by the transmission resonances. Importantly, we clearly show that the giant GHL shifts correspond to the resonant positions arising due to quasi-bound states formation in the presence of well-formed double barrier structure.
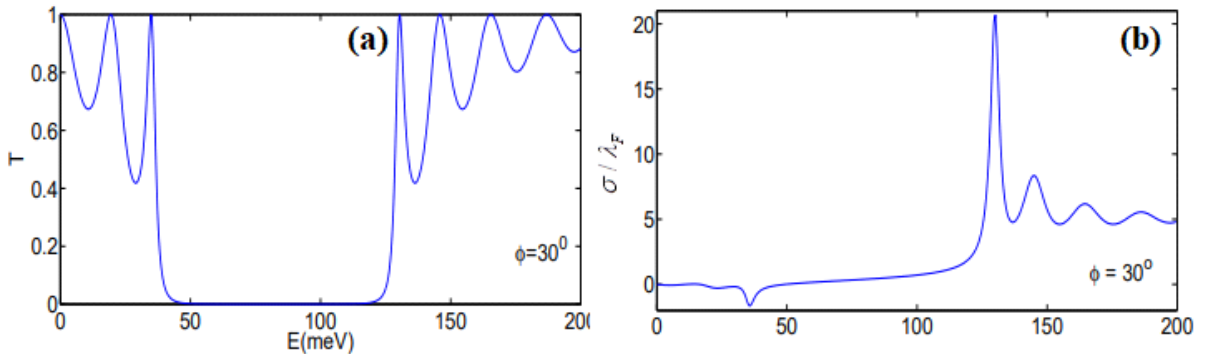

Fig. 1. Tunable transmission gap & Goos-Hänchen shift for single electrostatic barrier in monolayer graphene
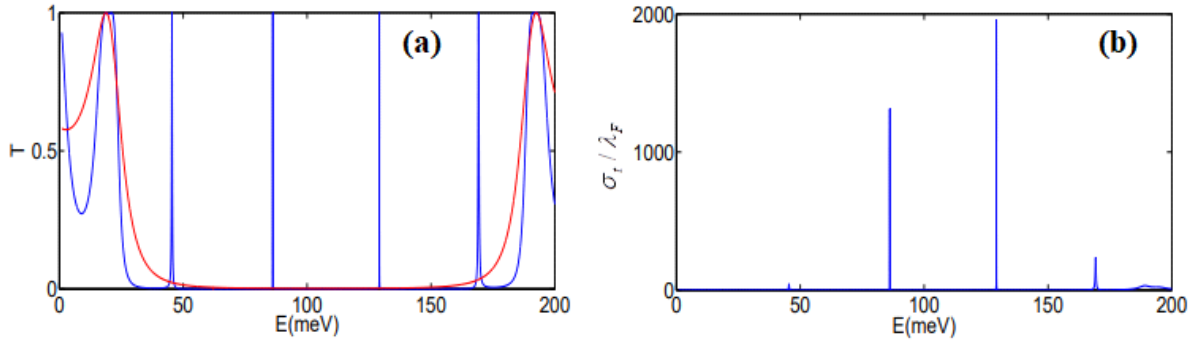
Fig. 2. Tunable transmission gap & Goos-Hänchen shift for double electrostatic barrier in monolayer graphene.

CONCLUSION

In this paper we discussed the GHL shift in monolayer graphene. Depending on the Klein tunnelling regime or classical motion regime, the GHL shifts can be negative or positive and can be enhanced by the transmission resonances. Here we point out that applying magnetic barriers with commensurate electrostatic potential will provide better tunability to the system. The vector potential of a magnetic field couples differently at the two valleys of graphene and hence can be used to obtain valley polarisation.

REFERENCES

1. C. Imbert, *Phys. Rev.,* **D 5**, 787 (1972).
2. C. F. Li, *Phys. Rev.,* **A 76**, 013811 (2007).
3. O. Hosten, P. Kwiat, *Science,* **319**, 787 (2008).
4. S. Sharma, S. Mehtab, M. G. H. Zaidi, *Materials Chemistry and Physics*, **296**, 127278 (2023).
5. A. H. Castro Neto, F. Guinea, N. M. R. Peres, K. S. Novoselov, A. K. Geim, *Rev. Mod. Phys.,* **81**, 109 (2009).
6. C. W. Beenakker, *Rev. Mod. Phys.,* **80**, 1337 (2008).
7. S. Mehtab, M. G. H. Zaidi, N. Rana, K. Khati, S. Sharma, *Bull. Mat. Sci.*, **45** (3), 162 (2022).
8. Y. Zhang, Y. W. Tan, H. L. Stormer, P. Kim, *Nature (London),* **438**, 201 (2005).
9. M. I. Katsnelson, K. S. Novoselov, A. K. Geim, *Nat. Phys.*, **2**, 620 (2006).
10. M. Shah, M. Sajid, M. Shah, *J. Opt. Soc. Am.,* **B 38**, 2736 (2021).
11. L. Zhao, S. F. Yelin, *Phys. Rev.,* **B 81**, 115441 (2010).
12. C. W. J. Beenakker, R. A. Sepkhanov, A. R. Akhmerov, J. Tworzydlo, *Phys. Rev. Lett.*, **102**, 146804 (2009).
13. F. Goos, H. Hänchen, *Ann. Phys.*, **436**, 333 (1947); **440**, 251 (1949).
14. K. V. Artmann, *Ann. Phys.* **437**, 87 (1948).
15. M. Sharma, S. Ghosh, *J. Phys.: Condens. Matter,* **23**, 055501 (2011).
16. N. Agrawal, S. Ghosh, M. Sharma, IJMPB, **27** (10) 1341003 (2013).
17. W. Bao, F. Miao, Z. Chen, H. Zhang, W. Jang, C. Dames, C. N. Lau, *Nat. Nanotechnol.*, **4** (9), 562 (2009).
18. F. Guinea, M. I. Katsnelson, A. K. Geim, *Nature Phys.*, **6**, 30 (2009).
19. V. M. Pereira, A. H. Castro Neto, *Phys. Rev. Lett.*, **103**, 046801 (2009).
20. Yu. Song, *App. Phys. Lett.,* **100**, 253116 (2012).
21. K. I. Sasaki, R. Saito, *Prog. Theor. Phys. Suppl.*, **176**, 253 (2008).
22. X. Chen, Y. Ban, C. F. Li, *J. Appl. Phys.,* **105**, 093710 (2009).
23. X. Chen, C.F. Li, Y. Ban, *Phys. Rev.,* **B 77**, 073307 (2008).

Synthesis of PANI-GO and PANI-rGO nanocomposites and their electrochemical performance

Nisha[1], G. Singh[1], A. Kumar[1], P. Prasher[2], H. Mudila[1]*

[1]Department of Chemistry, Lovely Professional University, Phagwara, Punjab-144411, India
[2]Department of Chemistry, UPES, Dehradun, 248007, India

In this work, a series of binary nanocomposites (PGs and PGRs) were synthesized by adding a varying percentage of GO and rGO to the matrix of polyaniline (PANI). PANI was synthesized by the chemical oxidative method, while GO was synthesized through the modified Hummers method and was further reduced to rGO. All the individual material and composite materials were analyzed through FTIR, XRD, TGA-DSC, and SEM analysis. The electrochemical performance was studied *via* cyclic voltammetry for the PANI, GO, PGs, and PGRs in the potential range of -0.5 to 0.5 V at varying scans (1 to 500 mV/s). The specific capacitance of PANI, GO, and rGO was found to be 169.57, 248.69, and 279.34 F/g while the maximum specific capacitance for the binary composites for PG-5 and PGR-5 was found to be 367 and 1231 F/g respectively.

Keywords: Polyaniline, Reduced graphene oxide, Electrochemical sensor, Clean energy, Cyclic voltammetry.

INTRODUCTION

Conductive polymers (CPs) are of great interest because of their incomparable properties like high surface area, multi-redox reaction, thermal resistance, and chemical stability. Out of various CPs, polyaniline (PANI) possesses a wide range of electrical properties and is a great choice because of its ease of synthesis [1, 2]. Apart from the CPs, nowadays carbon-containing materials like graphite oxide (GO) and reduced graphite oxide (rGO) provide a capable preliminary material for the fabrication of composites with CPs due to defects and potential functionalization [1, 2]. GO is a single sheet having oxygen-containing functional groups like -OH, C-O-C, and –COOH groups [3] whereas rGO has extraordinary physical and chemical properties, a 2D form of graphite, sp^2 hybridization, great mechanical properties, electron transport, high surface area, and great conductivity. rGO has a honeycomb-like structure in which one strong bond C-C is present in the plane and another π-bond is present out of the plane having a delocalized network, this structure is important for the availability of electrons for conduction [2, 3]. Numerous improvements have been made to CPs and carbon-containing compounds to form their composites for the reason that they provide low cost, save time, and give a better result of conductivity by acting as electroactive material [4-6].

In this experimental work, systematic studies have been carried out on the fabrication and electrochemical activity of the PANI-GO (PGs) and PANI-rGO (PGR) composites. The present work involves the formation of a binary composite with different ratios of PANI with GO and rGO (w/w %) by a simple route of *ex-situ* polymerization. The fabricated composites were characterized using FTIR, XRD, TGA, DSC, and SEM. These composites were found to have great electroactive properties when studied for their specific capacitance determined by cyclic voltammetry (CV).

MATERIALS AND METHOD

Materials

Chemicals like aniline (p=1.021 g/ml, LOBA Chemie), SDS (sodium dodecyl sulfate, Qualikems Fine chem.) ferric chloride (Alpha Chemika), graphite (LOBA Chemie Pvt Ltd), sulfuric acid (Avantor Performance Materials India Ltd), potassium permanganate (Hi-Media Laboratories Pvt. Ltd.), sodium nitrate (Avarice Industries), hydrogen peroxide, hydrochloric acid, hydrazine hydrate and ethanol were procured from LOBA Chemie Pvt Ltd and the chemicals were not further purified because all chemicals were of analytical quality.

Preparation of PANI, GO, and rGO

Preparation of PANI from aniline was carried out by the process mentioned by Bangade *et al. 2020,* in the presence of an anionic surfactant and an oxidant $FeCl_3$ [7]. GO was formed by the modified Hummers method as explained by Mudila *et al. 2014* [8]. In a beaker deionized water (250 ml) was taken to which

---

2g of GO was added and was subjected to stirring over a magnetic stirrer (1100 rpm). Then 2 ml of hydrazine hydrate was dropwise added to the above solution. The mixture was heated at 80 °C for 72 hours with continuous stirring. Fine black particles were observed after the reaction completion which were separated by centrifugation (~5000 rpm).

Fabrication of binary composites PANI-GO (PGs) and PANI-/rGO (PGRs)

Table 1. Composition, ratio, and code for PANI-GO composites

PANI	0.1 g	0.1 g	0.1 g	0.1 g	0.1 g	0.1 g
GO	0.025 g	0.05g	0.075g	0.1 g	0.2g	0.3 g
Ratio	4:1	2:1	4:3	1:1	1:2	1:3
Code	PG-1	PG-2	PG-3	PG-4	PG-5	PG-6

Table 2. Composition, ratio, and code for PANI-rGO composites

PANI	0.1 g	0.1 g	0.1 g	0.1 g	0.1 g	0.1 g
rGO	0.025 g	0.05 g	0.075 g	0.1 g	0.2 g	0.3 g
Ratio	4:1	2:1	4:3	1:1	1:2	1:3
Code	PGR-1	PGR-2	PGR-3	PGR-4	PGR-5	PGR-6

Electrode preparation

The working electrode was prepared of stainless steel(304-SS) which was de-greased by acetone. The material to be coated over the SS electrode was containing 0.05 g of electroactive material added with graphite (0.005 g) in a binder polystyrene (5 g/dL in xylene). The material was dried and weighted (~ 0.01 g) and was further used as a working electrode in 1M KOH solution [8]. The electrochemical measurement of PANI, GO, rGO, PANI-GO, and PANI-rGO was done by cyclic voltammetry (CV) in a -0.5 to 0.5V potential window range at a scan rate of 1 to 500 mV. The specific capacitance (C_s) of the active materials calculated from the cyclic voltammograms curves is given by the equation.

$$C_s = A/2mk.\Delta V$$

where, A= area under the CV curve, m= mass loaded of the electro-active material, k=applied scan rate (1 to 500 mV/s), ΔV=applied potential window -(0.5 to 0.5 V).

RESULTS AND DISCUSSION

Electrochemical measurement

Electrochemical performance of PANI, GO, and rGO. Fig. 1. shows the electrochemical behavior of PANI, GO, and rGO. Specific capacitance values increase progressively from PANI to GO and rGO due to their structural property which possesses the availability of free electrons for electric conduction, this may be attributed to the increased surface area and porous structure of all the materials. CV curves show a regular increase in the range of cathodic and anodic current with enhanced scan rate but this trend was not continuous and led to a decrease in specific capacitance indicating the stability of the materials. Table 3 depicts the C_s values of PANI, GO, and rGO at various scan rates with the highest capacitance value of 169.5, 248.69, and 279.34 F/g, respectively at 1 mV/s and the values decreases regularly as the scan rate increases from 1 to 500 mV/s [6, 8].

Table 3. Specific capacitance of PANI, GO, and rGO at different scans

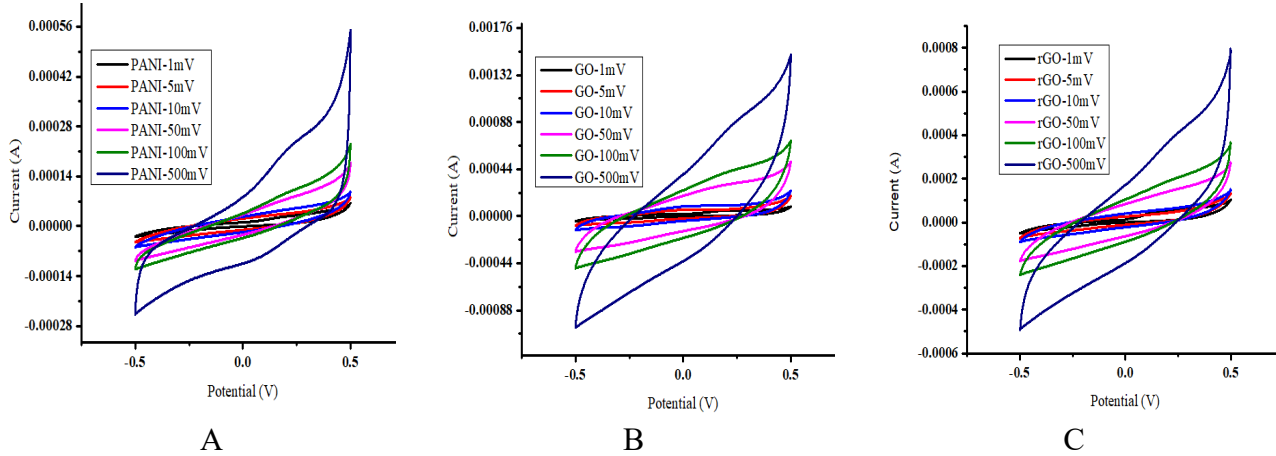| Scan Rate	Specific capacitance (C_s) F/g		
	PANI	GO	rGO
1mV/s	169.5	248.69	279.34
5mV/s	50.77	100.46	72.50
10mV/s	32.60	73.89	46.60
50mV/s	10.79	38.32	19.60
100mV/s	6.40	27.18	13.07
500mV/s	2.58	11.04	5.05

Figure 1. Cyclic voltammogram of (A) PANI (B) GO (C) rGO at different scan rate

Table 4. Specific capacitance of PGs at different scans rates

Scan rate	Specific capacitance (C_s) F/g					
	PG-1	PG-2	PG-3	PG-4	PG-5	PG-6
1mV/s	85.32	95.6	161.0	210.0	367.0	181.0
5mV/s	15.13	69.3	46.96	46.08	132.54	66.03
10mV/s	11.8	48.1	23.48	24.57	96.52	40.5
50mV/s	4.29	22.9	10.8	11.26	47.39	23.87
100mV/s	3.04	16.2	6.3	8.4	34.08	16.89
500mV/s	1.7	6.9	4.8	4.8	15.7	5.8
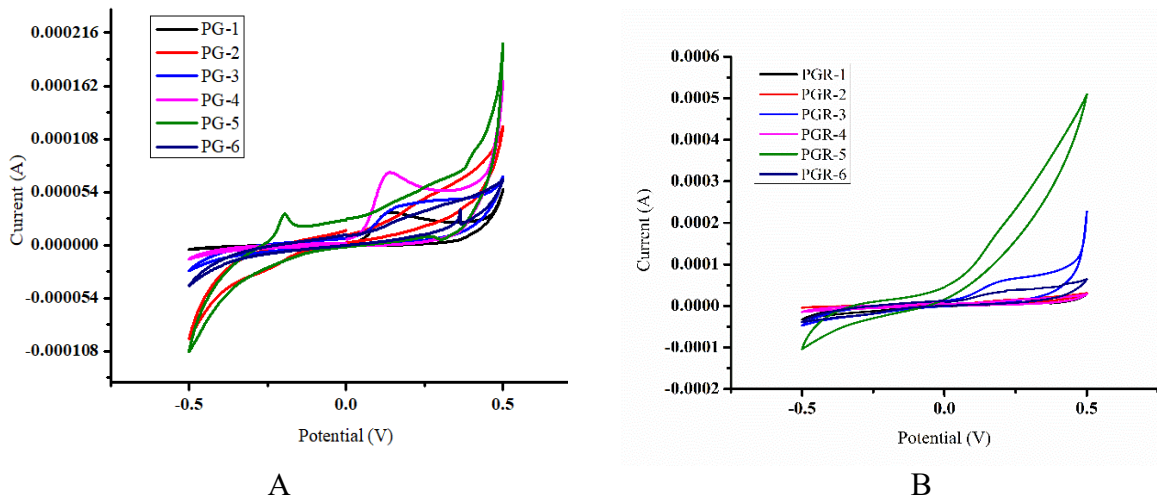
Figure 2. Comparative cyclic voltammogram of (A) PGs all ratios at 1mV/s (B) PGRs all ratios at 1mV/s

Table 5. Specific capacitance of PGRs at different scans rates

Scan rate	Specific capacitance (C_s) F/g					
	PGR-1	PGR-2	PGR-3	PGR-4	PGR-5	PGR-6
1mV/s	102.0	226.2	305.2	323.4	1231.9	310
5mV/s	24.5	155.7	76.6	56.7	305.8	105.2
10mV/s	14.8	122.1	49.3	43.7	73.2	69.3
50mV/s	12.7	53.9	23.1	22.3	61.2	34
100mV/s	9.3	37.1	39.9	16	38.4	25.8
500mV/s	4.4	14.4	8.5	6.8	14.1	13.5

Electrochemical performance of binary composites PGs and PGRs

The specific capacitance of PANI increases with the addition of specific weight percentages of GO and rGO because they get homogeneously grafted on the PANI matrix and surface area gets enhanced, but this increase was not regular (Tables 4, 5). The maximum value of C_s was achieved for PG-5 (367 F/g) and PGR-5 (1231.9 F/g), afterward, there is a decrease in C_s due to more addition of GO and rGO layers on PANI inhibiting the conduction and reducing the active surface area. Well-aligned PGs and PGRs show excellent performance as electrode materials. Maximum C_s values of PGR-5as compared to PG-5 were shown for the reason that it facilitates electrolyte diffusion in the honeycomb-like carbon structure (more available in PGR) and π-bond that is present out of the plane having a delocalized network, this structure is important for the availability of electrons for conduction [2]. Fig. 2 shows the voltammogram of PGs and PGRs in all ratios at 1mV/s.

Fig. 3 depicts that the binary composite in the ratio PG-5 (1:2) and PGR-5 (1:2) was found to have the highest C_s.
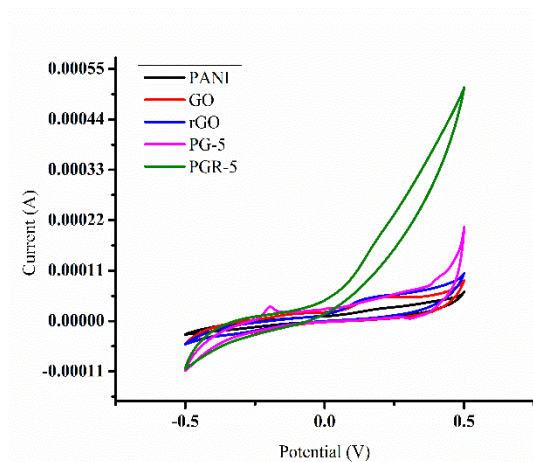
Figure 3. Cyclic voltammograms of PANI, GO, rGO, PG-5 and PGR-5

The slope, as well as the area of the CV curve of PGR-5 and PG-5 is higher than PANI, GO, and rGO

signifying the reduced resistance, fast ion diffusion rate, and good capacitance behavior in composite material. As a result, the CV dimensions of the composite 1:2 shows the utmost current and reveal a large surface area of CV curves indicating the enhanced specific capacitance attributed to synergic consequence among GO and PANI matrix as well as rGO and PANI matrix [18].

Fourier transform infrared (FTIR)

The powdered samples (PANI, GO, rGO, PG, and PGR) were characterized by using FTIR (Perkin Elmer Spectrum IR Version 10.6.1). PANI showed characteristic peaks at 3412, 2978, 1549, 1450, 1293, 1230, 1036, and 783 cm^{-1} corresponding to N-H str., C-H str., C=C bond, benzenoid ring, C-N bond, N-H bend., C-H bend., and quinoid ring respectively [10, 11]. The peaks at 3164, 1712, 1618, and 1039 cm^{-1} were the characteristic peaks of O-H stretching, C=O stretching, C=C bond, and C-O stretching of graphene oxide (GO) [12, 13]. rGO showed peaks at 1544, 3389, and 1709 cm^{-1} for skeletal vibrations, -OH stretching and C=O stretching [14] as shown in Figure 4. The peaks at 1711, 1560, 1107, and 799 cm^{-1} correspond to the C=O stretching, N-H bending, C-H stretching of the benzenoid ring, and C-H out-of-plane bending vibrations in binary composite PG [15, 16]. Another binary composite PGR showed peaks at 1708, 1453, 1292, and 1096 cm^{-1} owing to the presence of the C=O group, C=C str. of benzenoid rings, and C-N bend. of the benzenoid ring, and C-H stretching of the quinoid ring [17, 18] as shown in Figure 4.

X-ray diffraction (XRD)

The XRD of all samples was studied by using an X-ray diffractometer (Bruker D8 advance) using Cu-Kα radiation. The broad peak at about 2θ = 25° is the characteristic peak of PANI [26]. The characteristic peak of the graphite 2θ = 26.4° (Fig 5A) was transformed to 2θ = 10.61° (Figure 5B) when converted to GO, which was attributed to the presence of oxygenated groups and water molecules inserted in the interlayer of graphite. For rGO samples weak broad peak at approximately 2θ = 24.5° is observed (Fig 5B) [13].
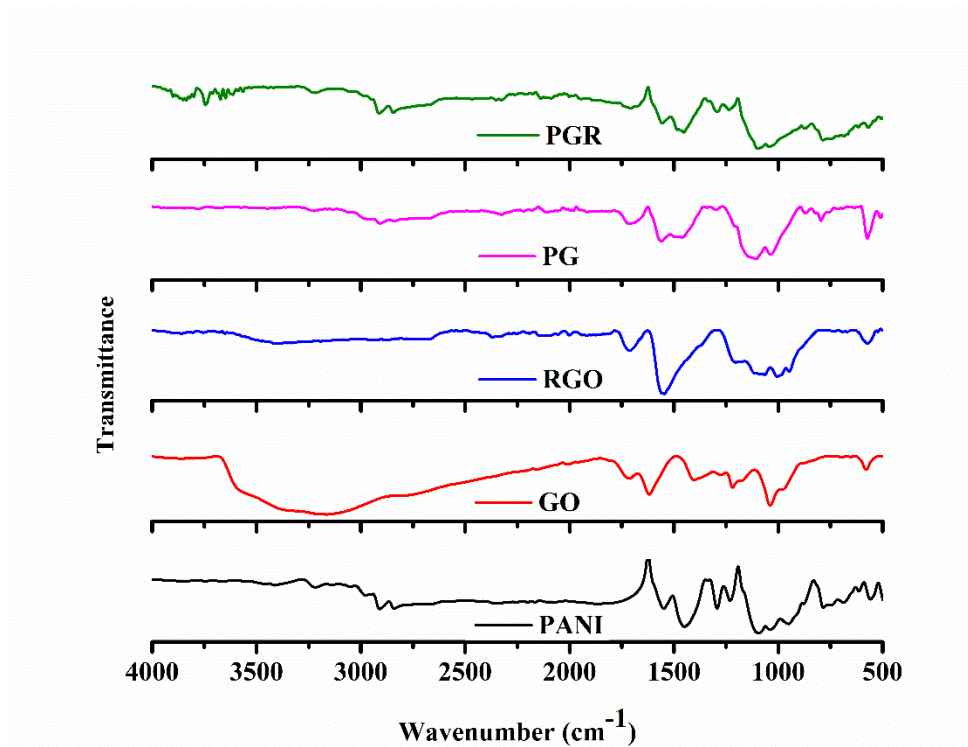
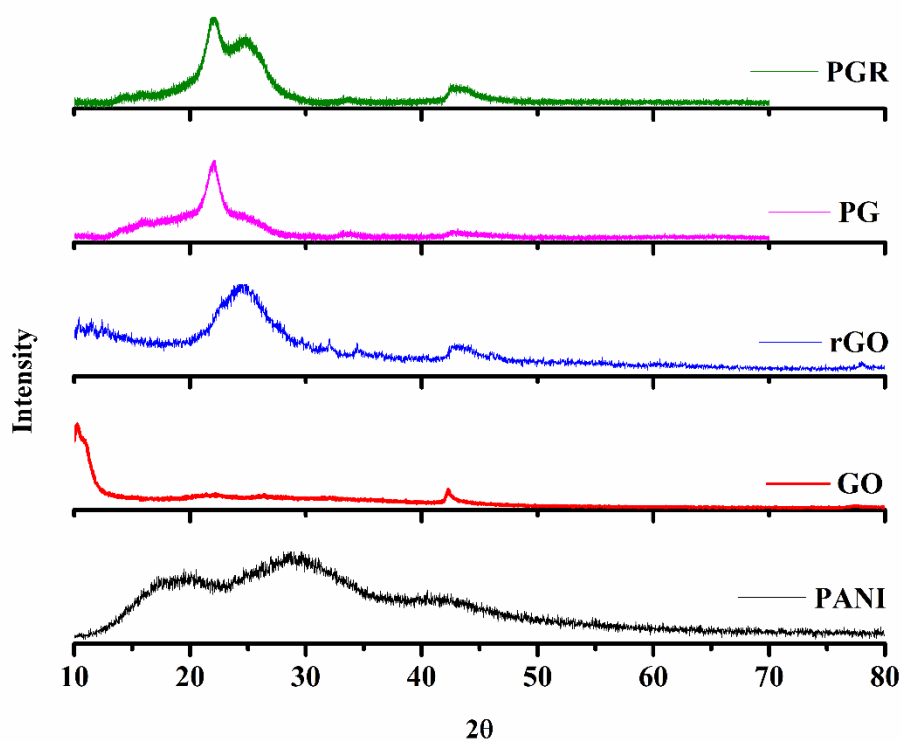**Figure 4.** FTIR spectra of all the individual materials and composites

Figure 5. XRD of all individual materials and composites
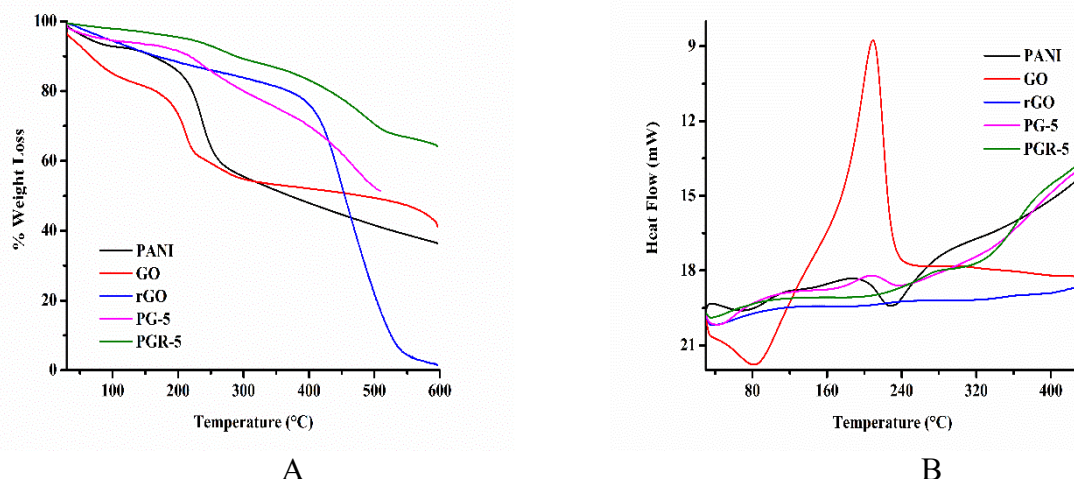
Figure 6. (A)TGA and (B) DSC of individual and composite materials

Thermogravimetric analysis (TGA)

TGA was executed to predict the thermal stability of a material, the data was recorded on the instrument (TGA)-50H of Perkin Elmer. A material of the weight (x mg) was heated under an inert(N_2) atmosphere with a flow of 10 °C/min (room temperature to 600°C) to record the TG data. For PANI a three-step weight loss was observed, and two minima were depicted which are due to weight loss. The first weight loss is due to the loss of adsorbed water at 100˚C and the second weight loss of 27 % is due to the decomposition of PANI between100˚C to 300˚C. The third weight loss of 12% started above 300 ˚C due to the degradation of the polymeric backbone of PANI [19].

For GO the TGA plot shows that the weight loss (%w) occurred in three steps, initially a mass loss (20%) occurred below the temperature of 117 ˚C because of the removal of the water absorbed. In the 2nd step, mass loss (30%) occurs up to the temperature of 200˚C due to the thermal decomposition of functional groups containing oxygen (-OH, -COOH, etc.) to yield CO, and CO_2 [20]. It was observed that there was smaller weight loss taking place in rGO as compared to GO, which is by reason of the presence of less percentage of groups like -OH, -COOH, etc. in rGO [21]. It has been observed that the percentage mass loss of PG is nearly positioned at the weight loss range of individual components Go and PANI, however, the weight loss curve of PG was somewhat closer to GO indicating the stability of PG. Thus, it can be inferred that PANI has been successfully grafted on the surface of GO [22]. The composite PGR below 150°C showed a minute weight loss suggesting low moisture absorbed by the sample. Maximum weight loss occurred at a temperature range of 200 to 300°C

and weight loss at approx. 550°C was due to the probable decomposition of rGO [23]. The comparative TGA of individual materials and their binary composite has been shown in Fig. 6 A.

Differential scanning calorimetry (DSC)

DSC is a very successful technique to determine the heat flow in the sample by using a DSC analyzer 50H of Perkin Elmer. A material of the known weight was heated under an inert (N_2) atmosphere at a 10 °C/min flow rate (from room temperature to 500 °C) to record the DSC data. DSC of PANI showed endothermic peaks at a lower temperature due to loss of water molecules and another endothermic peak was observed due to the decomposition of amine units as depicted by TGA results also. The endothermic peak below 100 ˚C was related to the evaporation of water molecules and the 2nd endothermic peak was observed at 230 ˚C due to the decomposition of the dopant, while the exothermic peak at 431˚Caccounted for the breakdown of PANI backbone [24]. In GO the endothermic peak below 100°C indicates evaporation of water molecules and also signifies that the de-oxygenation reaction starts below this temperature. A peak at 212˚C (endothermic) corresponds to the breakdown of oxygenated functional groups (-OH and -COOH etc.) with the evolution of CO and CO_2 [20]. In the case of rGO due to absorbed moisture an endothermic peak (below 100 °C) due was encountered, also an exothermic peak near 200 °C was observed due to the loss of oxygenated functional groups. However, these peaks were less intense as compared to the peaks observed in GO due to a smaller number of -OH and -COOH gr. The reduction of GO into rGO results in a decline in the number of functional groups, hence peak intensity

decreases [25]. In the presence of GO, and PANI there is a cross-linking reaction that results in thermodynamically destitute at lower temperatures. The binary composite showed an endothermic peak below 100 °C owing to the loss of moisture, an exothermic peak (209°C) due to the release of certain gases, and an exothermic peak at 433 °C due to the breakdown of the backbone of the polymer, which signifies the successful formation of the binary composite. Another binary composite PANI-rGO (PGR-5) shows an endothermic peak at 107 °C and two exothermic peaks, one at 278°C and the second at 435 °C. The peak intensity was found to be lower in binary composite because of enhancement in thermal stability [26, 27] as shown in Fig. 6B.

Scanning electron microscopy (SEM)

SEM image shows the average size of nanoparticles of PANI was about 60 nm [28]. These micrographs confirm the approximately spherical shape of the nanoparticles. In GO numerous folded and wrinkled sheet-like structures can be easily seen, and the GO presented a randomly arranged structure. SEM images of rGO showed that the wrinkled and folded sheets present in GO were reduced and were changed to exfoliated sheet-like appearance which might lead to a better exfoliated surface area thus leading to better electron navigation [29]. PANI was homogeneously surrounded by GO fibers in binary composite PG [27]. PGR composites show that the PANI nanoparticles lie on the RGO's surface [17].
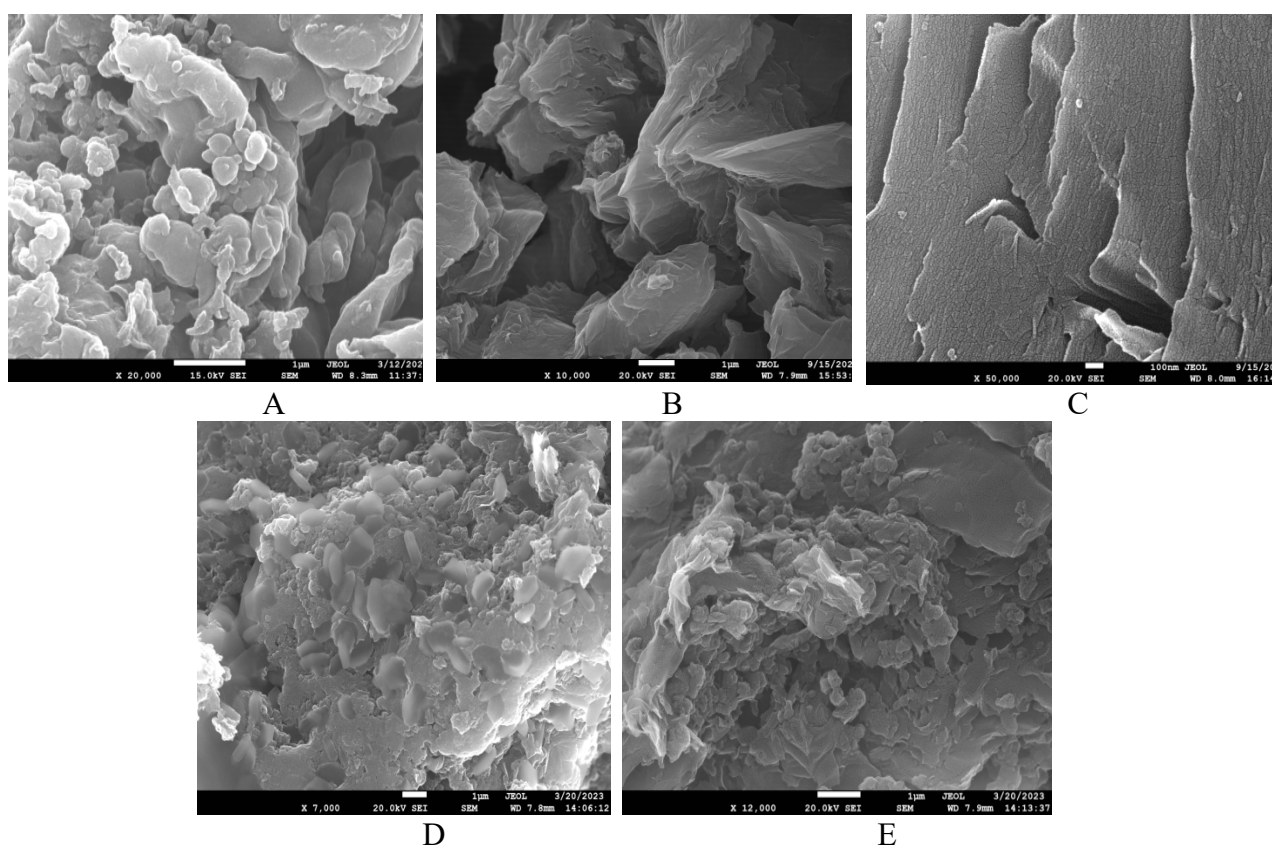
Figure 7. SEM micrographs of (A) PANI (B) GO (C) rGO (D) PG-5 and (E) PGR-5

CONCLUSION

A series of binary nanocomposites of PANI with GO (PG) and rGO (PGR) were successfully prepared *via* the *ex-situ* method in various ratios. These binary composites were compared for their electrochemical behavior by studying their associated specific capacitance measured by cyclic voltammetry. The results show a maximum specific capacitance of 169.5, 248.5, and 279.34 F/g for PANI, GO, and rGO at 1 mV/s. In the binary composition, the PG-5 has a ratio of 1:2 and was found to have the greatest C_s of 367 F/g, while 1231.9 F/g was the maximum capacitance of PGR-5 nanocomposite with a 1:2 ratio. Further, the fabricated nanocomposites (PG and PGR) and individual materials (PANI, GO, and rGO) were analyzed by FTIR, XRD, SEM, TGA, and DSC for their chemical, structural and thermal characteristics.

Conflicts of interest: *No conflicts of interest are declared by the authors.*

REFERENCES

1. T. N. A. B. T. A. Mutalib, S. J. Tan, K.L. Foo, Y. M. Liew, C. Y. Heah, M.M.A.B. Abdullah. *Pol. Bull.,* **78**, 4835 (2020), doi:10.1007/s00289-020-03334-w

2. D. George, G. James, J.K. Manjally, J. Thomas, M.S. Kuriakose, K.S. Aryamol, S.C. George. Application. *Mater. Today: Proc*, **24**, 1734 (2020), doi:10.1016/j.matpr.2020.03.597

3. G. Xu, N. Wang, J. Wei, L. Lv, J. Zhang, Z. Chen, Q. Xu. *Ind. Eng. Chem. Res.,* **51**, 14390 (2012), doi:10.1021/ie301734f

4. M. Ates M. Yildirim. *Pol. Bull.*, **77**, 2285 (2019), doi:10.1007/s00289-019-02850-8

5. F. Soysal, Z. Çıplak, B. Getiren, C. Gökalp N. Yıldız. *Mat. Res. Bull.*, **124**, 110763 (2020), doi:10.1016/j.materresbull.2019.110763

6. Shruthi, K.M. Vighnesha, Sandhya, D.N. Sangeetha M. Selvakumar, *Surf. Eng. Appl. Electrochem.,* **54**, 359 (2018), doi:10.3103/s106837551804018x

7. S.S. Bangade, V.M. Raut, S.E. Bhandarkar D.P. Gulwade. *Mater. Today: Proc.,* **29** (2020), doi:10.1016/j.matpr.2020.04.790

8. H. Mudila, V. Joshi, S. Rana, M.G.H. Zaidi S. Alam . *Carbon Lett.*, **15**, 171 (2014), doi: 10.5714/CL.2014.15.3.171

9. H.Mudila, M.G.H. Zaidi, S. Rana, V.Joshi, S. Alam. *Int. J. Chem. Anal. Sci.*, **4**, 139 (2013), doi:10.1016/j.ijcas.2013.09.001

10. B. Butoi, A. Groza, P. Dinca, A. Balan V. Barna, V. *Polymers*., **9**, 732 (2017), doi: 10.3390/polym9120732.

11. B.S. Singer, S. Palaniappan, S. Pabba. *J. Electrochem. Soc.,* **159** (2020), doi: 10.1149/2.036201jes

12. S. Drewniak, R. Muzyka, A. Stolarezky, T. Pustelny, T.M.K. Moranska M. Setkiewicz. *Sensors*., **16**, 103 (2016), doi: 10.3390/s16010103

13. X. Jiao, Y. Qiu, L. Zhang and X. Zhang. *RSC Adv.,* **7**, 52337 (2017), doi:10.1039/c7ra10809e

14. F.T. Thema, M.J. Moloto, E.D. Dikio, N.N. Nyangive, L. Kotsedi, M. Mazza M. Khenfouch. *J. Chem.,* **2013**, 150536 (2013), doi: 10.1155/2013/150536

15. M. Manoj, K.M.A. kumar, B. Jinisha S. Jayalekshmi. *J Mater Sci Mater Electron*, **28**, 14323 (2017), doi:10.1007/s10854-017-7292-9

16. M. Mahadik, H. Patil, G. Bodkhe, N. Ingle, P. Sayyad, T. A. Gahaouri, S. M. Shirsat, M. Shirsat. *Front. Mater.*, **7** (2020), doi: 10.3389/fmats.2020.00081

17. Y. Zhang, J. Liu, Y. Zhang, J. Liu Y. Duan. *RSC Adv.*, 7, 54031 (2017), doi:10.1039/c7ra08794b

18. S. Palsaniya, H. B. Nemade, A. K. Dasmahapatra. *J Phys. Chem. Solids*, **154**, 110081 (2021), doi:10.1016/j.jpcs.2021.110081

19. A. Kumar, A. Kumar, H. Mudila, K. Awasthi V. Kumar. *J. Phys.*, **1531** (2020), doi:10.1088/1742-6596/1531/1/012108

20. S.N. Alam, N. Sharma, L. Kumar, L. *Graphene.*, **6** (2017), doi: 10.4236/graphene.2017.61001

21. N. Sharma, V. Sharma, Y. Jain, M. Kumari, R. Gupta, S, K. Sharma K. Sachdev *Macromol. Symp.*, **376**, 1700006 (2017), doi:10.1002/masy.201700006

22. Q. Fan, Y. Yang, Y. Hao, X. Zhao Y. Feng. *J. Mol. Liq.*, **212**, 557, (2015), doi:10.1016/j.molliq.2015.10.008

23. Y. Wang, X. Wu, W. Zhang S. Huang. *Syn. Metals*, **210**, 165 (2015), doi:10.1016/j.synthmet.2015.09.022

24. M. Matoetoe, F. Okumu, C. Maphale O. Fatoki. *Asian J. Chem.*, **27**, 1411 (2015), doi:10.14233/ajchem.2015.18061

25. J. Singh A.S. Dhaliwal (2022). *J. Phys Chem Solids.*, **160**, 110358 (2022), doi:10.1016/j.jpcs.2021.110358

26. A. L. Ahmad, U. R. Farooqui, N. A. Hamid, *RSC Adv.*, **8**, 25725 (2018), doi:10.1039/c8ra03918f

27. L.R. Vargas, A.K.D.S. Poli, R. de C.L. Dutra, C. B. De Souza, M.R. Baldan E.S. Gonçalves. *J. Aerosp. Technol. Manag.*, **9**, 29 (2017), doi:10.5028/jatm.v9i1.697

28. A. Abdelrahmeen M.F. Elkady. *Alex. Engg J.,* **57**, 3291 (2018), 10.1016/j.aej.2018.01.012

29. B. Thirumalraj, C. Rajkumar, S.M. Chen S. Palanisamy. *Sci. Rep.,* **7** 41213 (2017), doi:10.1038/srep4121

Microwave-assisted synthesis of curcumin-encapsulated silica-chitosan composite for drug release study

P. Kumar[1]*, N. Khan[1], D. Kumar[1, 2], M. Ali[1], R. Tandon[3]

[1]*Department of Applied Chemistry, M. J. P. Rohilkhand University, Bareilly-243006 (U.P.), India*
[2]*Constituent Government College, Richa, Baheri, MJPRU Bareilly, (U.P.), India*
[3]*Department of Chemistry, Bareilly College, Bareilly-243001, (U.P.), India*

The synthesis of curcumin-encapsulated silica-chitosan composite in a domestic microwave oven has been reported. The composite was synthesized through sol-gel route. Chitosan, a bio-compatible polymer, was used as capping agent while TEOS was used as silica precursor. The optimized composite samples were characterized by scanning electron microscopy (SEM), Fourier transform infrared spectroscopy (FTIR), thermo-gravimetric analysis (TGA) and X-ray diffraction (XRD) analysis. The feasibility of the drug release was monitored by setting up *in vitro* drug release experiments. The latter were performed in phosphate buffer saline (PBS) at pH 7.4 and room temperature (30ºC). Sustained curcumin release was found which took place up to 76% in regular manner in 90 h. The curcumin release kinetics was calculated using Higuchi, Korsmeyer – Peppas, zero order and first order models of drug release kinetics by fitting the values of curcumin release data in their respective equations. The Higuchi model of drug release was found best suited for the curcumin release from the composite among all the models studied for drug release.

Keywords: Curcumin, Silica, Chitosan, Composite, TEOS, Sol-gel

INTRODUCTION

Derivations of medicines from plants has been an important part of health care since ancient time and is playing a crucial role in present too [1, 2]. Curcumin is a prominent naturally occurring multitherapeutic agent [3]. Curcumin is obtained by the extraction of the rhizome of *Curcuma longa* which is commonly known as turmeric, a herbaceous plant of zingiberaceae family [4]. The rhizome is crushed to a fine powder of turmeric. Turmeric is yellow colored common kitchen spice which has been used for a long time for medicinal purpose as well. Turmeric contains only ~2% curcumin which is extracted in the form of curcuminoid along with bis-desmethoxycurcumin (BDMC) and desmethoxycurcumin (DMC). Curcumin is supposed to be a most vital fraction of turmeric and responsible for most of the biological functions associated with it. Curcumin is well of terpene and contains them predominantly in mono and sesqui form [5]. Curcumin is natural polyphenol which is hydrophobic in nature, hence shows poor solubility in water but charming one in other organic solvents like ethanol, methanol, acetone and dimethyl sulfoxide [6]. The phenol and diketone moieties of curcumin make it rich of antioxidant character. Curcumin shows charming anti-inflammatory, wound healing, antimicrobial and antiproliferative properties and hence is widely studied for the healing of different types

cancers [7]. In spite of different valuable features associated with curcumin, its area of clinical applications is limited due to its hydrophobicity which restricts its easy bioavailability moreover, quick degradability and rapid metabolism also limit up its applications [7-9].

Bioavailability of naturally obtained drugs is needed to be enhanced to promote their oral consumption. Since last few decades, designing of drug delivery systems to carry such types of hydrophobic or lipophilic drugs like curcumin are drawing huge attention as it successfully carries the drugs to targeted area and enhances their bioavailability by providing sustained release [10]. Among various types of drug delivery systems, those based on mesoporous silica (MS) are being introduced as potential drug carriers due to their promising aptitude for drug delivery [11]. As the MS-based materials are rich in pore volume and surface area, therefore, they provide more significant hand for carrying a higher quantity of drug. Earlier research has affirmed that MS is able to increase the solubility of insoluble drugs like hydrophobic medicines used to treat the cancer, moreover they neglect the consumption of hazardous organic solvents and are more stable in thermal and chemical respect [12]. MS-based drug delivery systems show highly hydrophilic behavior, novel nonreactive attitude towards chemicals and excellent

---

* To whom all correspondence should be sent:
E-mail: pramendra2002@gmail.com

biocompatibility which makes them a suitable material for both *in vitro* and *in vivo* drug delivery systems [12]. There are a number of interactions formed between mesoporous surface of silica and drug moiety like electrostatic interaction, ionic bonding, hydrogen bonding, etc. which facilitate the hold of silica over drug moiety [13]. On discussing the mesoporous silica with respect to drug delivery system, a big deal of virtues is associated with it. We may utilize these in developing a significant curcumin delivery system using which various drawbacks associated with curcumin delivery like its bioavailability may be improved. A number of researchers worked to develop curcumin release systems using mesoporous silica as drug carrier [14, 15].

Kuang *et al.* built up a curcumin delivery system based on mesoporous silica for the treatment of cancer by photodynamic therapy (DPT) in which curcumin was being used as photosensitizer. The silica worked perfectly in mediating the curcumin in the DPT by carrying it up and made intracellular release [13]. Kotcherlakota *et al.* designed an amine functionalized series (S2, S4 and S6) based on mesoporous silica for curcumin release. MSU-2, KIT-6 and MCM-41, highly porous silica materials, were being used as model. Among all curcumin containing samples, the S4 was found to be more significant against cancer cells feasibility [16]. Mullassery *et al.* synthesized the composite of mesoporous silica using acrylamide β-cyclodextrin grafted 3-aminopropyltriethoxysilane bentonite (AMCD-g-APSB) for *in vitro* drug release study [17]. Nasab *et al.* prepared mesoporous silica-based drug carrier system to enhance the biocompatibility and bioavailability of curcumin. The curcumin was being capped by chitosan and the system worked perfectly as a shield to carry the drug successfully [18].

Due to success and positive results associated with drug carrier systems, a hydrophobic drug like curcumin might be encapsulated into hydrophilic polymer hydrogel or polymeric micelles for controlled release of the drug at targeted area [19]. The role of polymer is very crucial for the synthesis of MB-based system. Chitosan was found significant for the purpose due to its biocompatibility and bio-degradability [20].

Chitosan is a cationic polysaccharide which can be obtained by deacetylated chitin. Chitosan is a well-known polysaccharide which is also one of the trusty applicants among biopolymers due to its wide area of applications like good antibacterial and antifungal properties and high metal binding capacity [21]. Moreover, it has power over a range of biological properties, like antimicrobial, antioxidant, anti-inflammatory, anti-cholesterol, cytocompatible and analgesic [22] which make it crucial for various applications, most relevant in pharmaceutical and medical fields like drug delivery and wound dressing [23]. Chitin is obtained from various kinds of living organisms, mostly from the cell wall of yeast and fungi. Chitosan has biodegradability, biocompatibility, non-toxic and mucoadhesive nature which enlarge its applications area aspects [24]. Chitosan is an only polymer with cationic character keeping it distinguishable from others. As chitosan is a polyaminoglycoside, the cationic character of chitosan is associated with its amino groups. This feature permits the modulation of its physicochemical properties through covalent links to other residues and responsible for its tendency to conjugate with different medicinal agentsm hence it plays a crucial role in drug delivery systems. In the present work, focusing on stable presentation of curcumin *via* delivery platform, we synthesized the curcumin-encapsulated silica-chitosan composite hydrogel to facilitate and regulate the curcumin delivery. Chitosan worked as pH responser polymer shell on silica surface [25, 26].
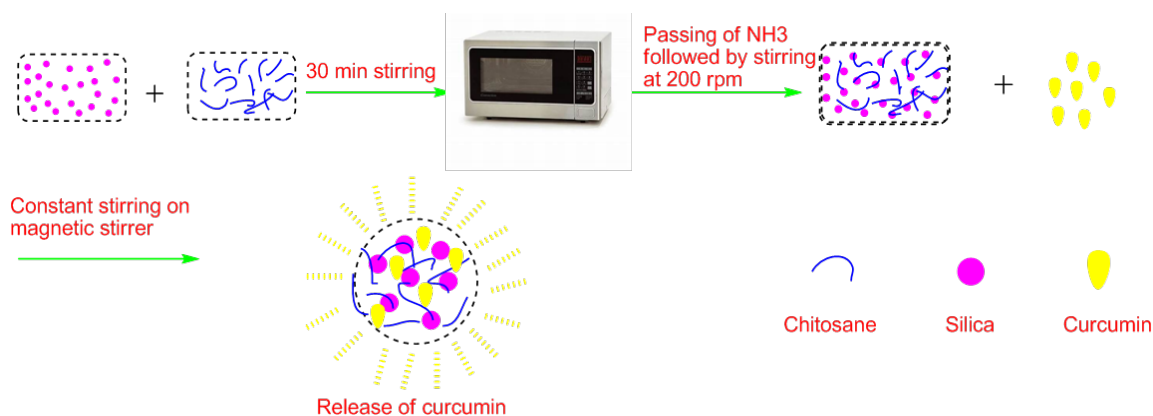
Scheme 1. Schematic representation of the synthesis of curcumin-encapsulated silica-chitosan composite.

EXPERIMENTAL

Materials and reagents

Tetraethoxysilane (TEOS 98%) was being used as silica precursor and was purchased from Merck, Mumbai, India. Chitosan, a natural polymer, was supplied from Otto chem. private Ltd. India; ethanol, curcumin and PBS buffer were provided from Merck. All chemicals were being used as supplied without further purification. LG Microwave (MH 2548QPS model), was used as energy source to conduct the respective chemical reactions. The solution's pH was evaluated with the help of digital pH meter from Globe instruments. All the quantitative analyses for the determination of curcumin released were carried out on Systronics double beam UV-VIS spectrophotometer.

Synthesis of silica-chitosan composite and encapsulation of curcumin

The synthesis of silica/chitosan composite with chitosan was based on the sol-gel method as reported previously [24]. Firstly, a 1% w/v solution of chitosan was prepared by dissolving 500 mg of chitosan in 50 ml of citric acid followed by 10 h continuous stirring to prepare a homogenous solution. Separately in a flask, 1 ml of TEOS was dissolved in 1 mL of ethanol and that solution was added dropwise to the already prepared solution of chitosan with constant stirring. After 30 min of stirring, the mixture solution was heated in a microwave for 30 sec at 20 microwave power (180 W). The solution was kept to cool down to room temperature for the introduction of ammonia current for small extent and then the flask was kept again on magnetic stirrer at 200 rpm. After around 10 h of stirring, the solution started thickening. Meanwhile, the solution of curcumin was also prepared in ethanol and was added slowly. After around 1 h a transparent gel was formed that was dried and washed up by ethanol.

Characterization of silica-chitosan composite

The curcumin-embedded silica-chitosan composite as synthesized, was characterized with the help of appropriate analytical techniques: Fourier transform infrared (FTIR) spectroscopy was employed to recognize the different functional groups in the composite sample, working in the range from 500 cm^{-1} to 4000 cm^{-1}, on a Thermo-Scientific (Nicole 6700); X-ray diffraction (XRD) technique was used to record the pore structure from 5° to 40° 2θ angle, carried out on Bruker D 8 advance instrument (Shimadzu, Japan). The thermal treatment of the samples was carried out in a differential scanning calorimeter (Mettler Toledo DSC1) by heating up to 800°C at 10 K min^{-1} heating rate to analyze its behavior towards thermal treatment; the morphology and the structure of the synthesized composite was established by scanning electron microscopy (SEM) carried out on a Leo 435 VP model.

In vitro release study of curcumin from silica-chitosan composite

Drug release study was performed based on previously reported work with slight modifications [27]. The amount of curcumin-loaded composite sample containing 10 mg of curcumin was weighed and dispersed into 100 mL solution of phosphate buffer saline (PBS) of pH 7.4 containing 25% ethanol. The release medium as prepared was placed on a thermostatic shaker (100 rpm) at room temperature. At regular and definite time intervals, 3 mL release medium was withdrawn and replaced with same amount of fresh PBS buffer solution. The withdrawn solution was centrifuged for 5 min at 5000 rpm, then the measurement of the amount of curcumin released was done by UV–VIS spectrophotometer at $\lambda_{max} = 425$. First the instrument was calibrated by curcumin then the amount of released curcumin was analyzed with the help of a calibration curve [28-31]. The amount of curcumin released was quantified by using eq. 1 given below:

$$\text{Release \%} = \frac{\text{Amount of curcumin released}}{\text{Total amount of curcumin present}} \times 100 \quad .. (1)$$

Kinetics of release

Release kinetics of drug from the composite and its mechanism was analyzed using different types of models such as Higuchi, zero order and first order models by fitting the drug release data in the equations given below [32, 33].

Higuchi model

In the Higuchi model, the graph is plotted between drug release and $t^{1/2}$. This model shows the graph representing the constant release of drug in a rational period of time which generally corresponds to inactive matrix and straight line is formed in the graph [34]. Higuchi model is represented by the equation (2):

$$M_t/M_\infty = K_H t^{1/2} \qquad (2)$$

where M_t/M_∞ represents the fractional of released drug in t time while K_H is Higuchi constant.

Korsmeyer-Peppas model of drug release

It is also called a power law model which describes the release of drug from the polymeric system. This model is able to explain the release mechanism of drug in a simultaneous manner like water diffusion in the matrix, dissolution of matrix and swelling of matrix. The model is represented by equation (3):

$$M_t/M_\infty = kt^n \tag{3}$$

where M_t/M_∞ symbolizes the fractional of released drug in t time, K is Korsmeyer constant and n is release exponent.

Zero-order reaction

This type of kinetic study attributes to the constant release of the given drug; hence the drug release is only a function of time and is independent of drug concentration. Zero-order kinetic model is important in explaining the mechanism of different types of drugs like the drugs administrated to maintain the blood pressure and pain control drugs. The equation for calculating zero-order release kinetics is represented as equation (4):

$$M_t/M_\infty = k_0 t \tag{4}$$

where M_t/M_∞ symbolizes the fractional of released drug in t time while K_0 is zero-order constant.

First-order reaction

This model was developed to present the release of water-soluble drug. This model states that the release of drug at time 't' is only dependent of drug concentration. The first-order release kinetics model is represented by equation (5):

$$M_t/M_\infty = 1 - \exp(-k_1 t) \tag{5}$$

where M_t/M_∞ symbolizes the fractional of drug released at time t, K_1 is first-order constant.

RESULTS AND DISCUSSION

Synthesis of curcumin-encapsulated silica-chitosan composite

Scheme 1 represents the systematic plan of silica-chitosan composite synthesis and curcumin encapsulation, in diagrammatic form. Mixture of TEOS and ethanol was added slowly and drop wise manner to the pre dissolved chitosan solution with constant stirring forming a homogenous solution. Then the solution was microwaved for 30 seconds followed by passing of ammonia current with constant stirring at 200 rpm. When the hydrogel started to be formed, curcumin solution was introduced to it.

Characterization of the samples

SEM

Figure 1 represents the SEM image of the curcumin loaded silica-chitosan composite. The external view of composite shows slightly porous and roughly arranged solid surface. The particles in the composite appear to be present in agglomerated form which is suggested due to the viscous nature of chitosan to entrap curcumin and silica in to the composite [34].
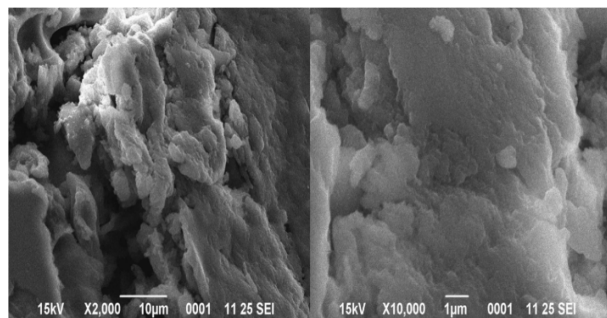
Figure 1. SEM image of the surface of curcumin-encapsulated silica-chitosan composite.

Thermal analysis

The result of thermal treatment of curcumin loaded silica-chitosan composite was studied by its TGA curve, shown in Figure 2. The TGA curve of silica-chitosan composite shows two weight loss steps. First one starts from 50 °C which leads to very slow and gradual decrease in weight till 300 °C while the second one starts at 350 °C. The TGA curve of the composite clarifies that there is negligible loss in weight till 200°C which demonstrates the thermally stable behavior of the composite. This also confirms that the curcumin present in the composite did not lose its properties during the experiments [35].
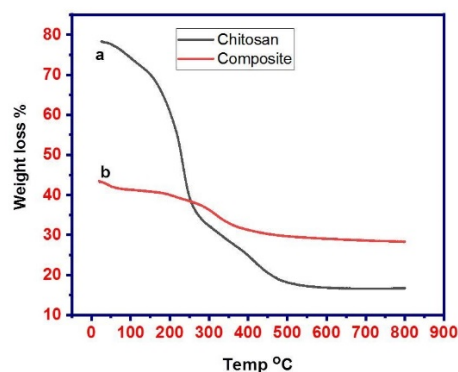

Figure 2. Thermogravimetric analysis of chitosan (a) and composite (b).

X-ray diffraction

The XRD outline of synthesized composite and chitosan is represented in Figure 3. As the XRD analysis pattern of curcumin is certain and already reported in literature, the behavior of curcumin was found to prove a highly crystalline nature [36]. The XRD diffractograms of chitosan, silica and synthesized composite are represented in Figure 3 revealing the semi-crystalline nature of chitosan and composite while the crystalline one of silica [37]. However, after the encapsulation of crystalline curcumin into chitosan-silica composite, no finely resolved crystalline peak was found in the XRD pattern of the composite suggesting that curcumin is well dispersed into the semi-crystalline chitosan matrix of composite [36].
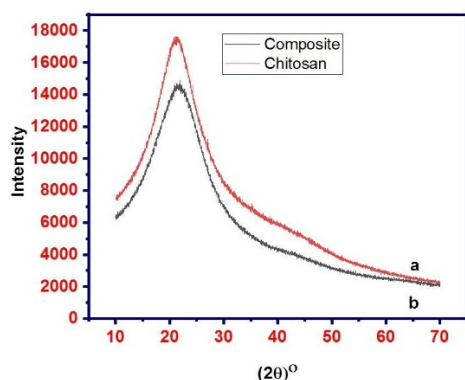
Figure 3. X-ray diffraction analysis graphs of chitosan (a) and composite (b).

FTIR spectra

The FTIR spectra of curcumin-loaded silica-chitosan composite are represented in Figure 4. The spectrum of curcumin shows the characteristic bands of −OH stretching at 3250 cm^{-1}, C=C and C=O mixed vibrations at 1630 cm^{-1}, C−O and C−C mixed vibrations at 1510 cm^{-1}, olefin C−H bending vibration at 1430 cm^{-1}, C−O−C stretching vibration at 1030 cm^{-1} and C−C−H aromatic bending vibration at 850 cm^{-1} [38]. In the spectrum of chitosan, the band at 3400 cm^{-1} is due to N-H stretching of amine group while the one at 1690 cm^{-1} is due to C=O stretching of carbonyl group of amide. The band at 1050 cm^{-1} represents the C-O stretching of secondary hydroxyl group [27]. In the spectrum of composite, there is slight shifting of some bands with the appearance of few new ones like the band at 1160 cm^{-1} representing the Si-O-Si stretching of silica in the composite. The height of the band at 3400 cm^{-1} slightly decreases due to the lower probability of hydrogen bonding due to a lesser number of hydroxyl groups present on the composite as compared with chitosan. The band at 1690 cm^{-1} in

chitosan is shifted to a higher frequency value at 1750 cm^{-1} in the composite and the appearance of few new ones like a band present at 1160 cm^{-1} represents the Si-O-Si stretching of silica in the composite. The height of the band at 3400 cm^{-1} slightly decreases due to the lower probability of hydrogen bonding due to a lesser number of hydroxyl groups present on the composite as compared with chitosan. The band at 1690 cm^{-1} in chitosan is shifted to higher frequency value at 1750 cm^{-1} in the composite [27].
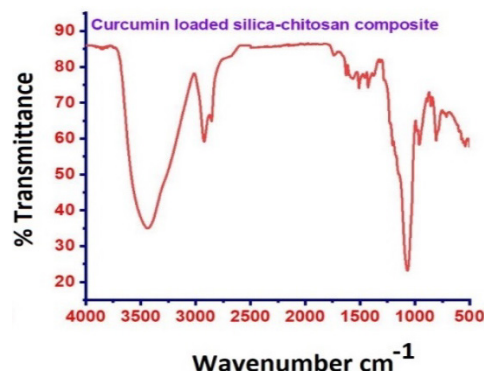

Figure 4. FTIR spectrum of curcumin-loaded silica.

In vitro curcumin release experiments

The *in vitro* experiments for curcumin release from the silica-chitosan composite were carried out at pH 7.4. Figure 5 shows that the curcumin release from the encapsulated silica-chitosan composite took place in a controlled way. In the first 10 hours just 30% of curcumin was released from the composite, which increased in a steady manner up to 52% after 24 hours. This regulation and maintenance of release was supported by the crucial role of amine groups of chitosan [39]. A sustained and gradual release was being observed up to 90 hours when 76% of drug was released. After that the rate of curcumin release was so slow that it was not noticeable.
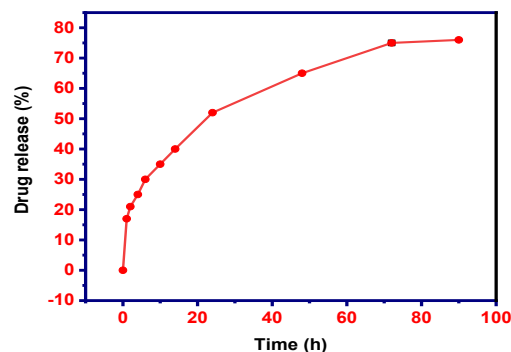

Figure 5. *In vitro* release of curcumin (%) with time from curcumin-encapsulated silica-chitosan composite in PBS (pH 7.4) at 30 ºC.
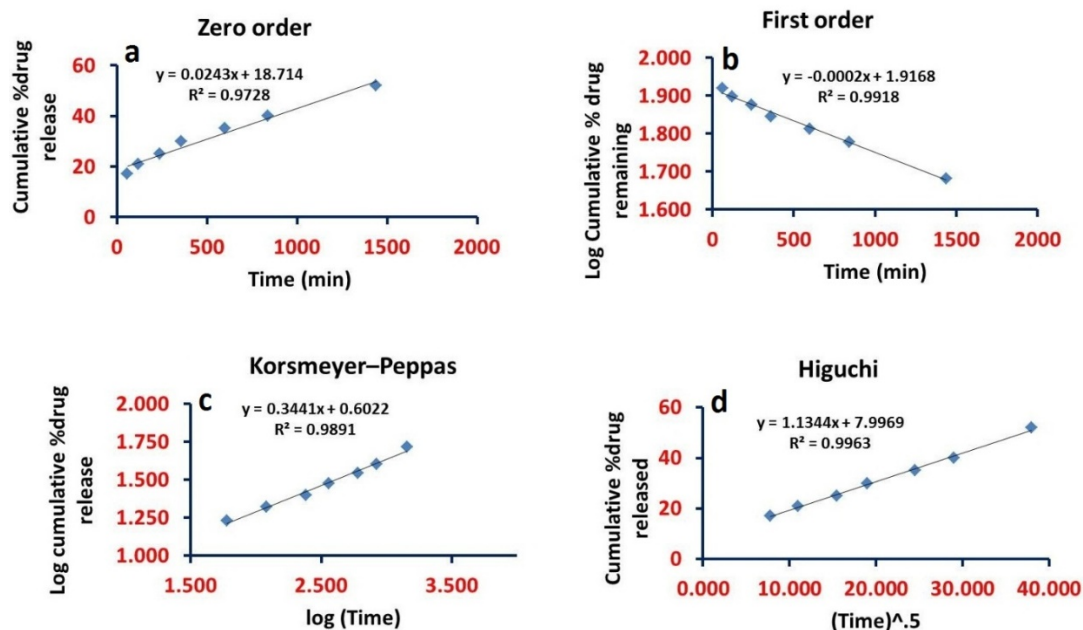
Figure 6. Kinetic study of curcumin release by zero order, first order, Korsmeyer-Peppas and Higuchi models of drug release.

Table 1. Kinetic models study and their various parameters.

S.N.	Kinetic Models	Plot	Parameters
1.	Kinetic equation for zero order	$M_t/M_\infty = k_o t$	$K_0 = 0.024$, $R^2 = 0.972$
2.	Kinetic equation for first order	$M_t/M_\infty = 1 - e^{(-k_1 t)}$	$K_1 = 0$, $R^2 = 0.991$
3.	Kinetic equation of Korsmeyer-Peppas	$M_t/M_\infty = kt^n$	$K = 2.688 \times 10^{-2}$, $R^2 = 0.989$
4.	Kinetic equation for Higuchi model	$M_t/M_\infty = kt^{1/2}$	$K_H = 0.996$, $R^2 = 0.996$

Kinetic study of drug release

Figure 6 plots represent the kinetics of drug release through different models. In order to find out the kinetics of curcumin release from the curcumin-encapsulated silica-chitosan composite, we evaluated the regression coefficient for different kinetic models by fitting the *in vitro* drug release data of curcumin in the following four mathematical models, i.e., zero order, first order, Korsmeyer-Peppas and Higuchi models of drug release. The values of R^2 signify that the Higuchi model for drug release best fits curcumin release kinetic data. The kinetic drug release parameters (correlation coefficient (R^2) and rate constant) were calculated from Figure 6 and are shown in Table 1.

CONCLUSION

The successful synthesis of curcumin-encapsulated silica-chitosan composite by using sol-gel method and microwave radiation as energy source was reported. The structure, morphology and presence of different functional groups in the synthesized composite was ascertained by SEM and FTIR analytical techniques while the thermal behavior and crystal orientation were enlightened by TGA and XRD techniques. Curcumin is a versatile polyphenol which is applicable in a number of medical applications like antioxidant, antimicrobial, and anti-cancer agent. The bioavailability of curcumin was approached to enhance by its encapsulation into silica-chitosan composite. Silica-based drug delivery systems, being good carriers, provided an easy room to carry the sufficient amount of curcumin with additional qualities of chitosan in regulating the sustained release of drug. *In-vitro* drug release study experiments were performed in PBS (pH 7.4) at room temperature (30°C). Drug release took place in continuous manner and maximum up to 76% curcumin was released in 90 h. The kinetics of the release was also evaluated by using Higuchi, Korsmeyer-Peppas, zero order and

first order models of drug release kinetics by fitting the curcumin release data in their respective equations. The value of regression coefficient suggested that Higuchi model (R^2 value = 0.996) is best fitted for the release of curcumin from curcumin-encapsulated silica-chitosan composite.

Conflict of Interest: *All authors have no conflict of interest.*

REFERENCES

1. P.V. Licciardi, J.R., *Int. Immunopharmacol.*, **11**, 390 (2011).

2. A. Prasansuklab, J.M. Brimson, T. Tencomnao, *J. Tradit. Complement. Med.*, **10**, 301 (2020).

3. A. Askarizadeh, G.E. Barreto, N.C. Henney, M. Majeed, A. Sahebkar, *Int. J. Pharm.*, **585,** 119476 (2020).

4. D. Kang, B. Li, L. Luo, W. Jiang, Q. Lu, M. Rong, R. Lai, *Biochimie*, **123,** 73 (2016).

5. I.O. Alisi, A. Uzairu, S.E. Abechi, S.O. Idris, *J. Adv. Res*, **12,** 47 (2018).

6. M. Sökmen, M.A. Khan, *Inflammopharmacol.,* **24** , 81 (2016).

7. R. Prabhuraj, K. Bomb, R. Srivastava, R. Bandyopadhyaya, *J. Drug Deliv. Sci. Technol.,* **57,** 101722 (2020).

8. W. Su, T. Wei, M. Lu, Z. Meng, X. Chen, J. Jing, J. Li, W. Yao, H. Zhu, T. Fu, *Eur. J. Pharm. Sci.,* **134,** 246 (2019).

9. A. Abusnina, T. Keravis, I. Yougbaré, C. Bronner, C. Lugnier, *Mol. Nutr. Food Res.,* **55**, 1677 (2011).

10. Y. Abo-zeid, G. Mantovani, W.L. Irving, M.C. Garnett, *J. Drug Deliv. Sci. Technol.,* **46,** 354 (2018).

11. S. Malekmohammadi, H. Hadadzadeh, Z. Amirghofran, *J. Mol. Liq.*, **265,** 797 (2018).

12. J. Lin, Q. Cai, Y. Tang, Y. Xu, Q. Wang, T. Li, H. Xu, S. Wang, K. Fan, Z. Liu, *Int. J. Pharm.,* **536**, 272 (2018).

13. *RSC Adv.,* **10**, 24624 (2020).

14. V. S. Bollu, A. K. Barui, S. K. Mondal, S. Prashar, M. Fajardo, D. Briones, A. Rodriguez-Dieguez, C. R. Patra, S. Gómez-Ruiz, *Mater. Sci. Eng. C,* **63**, 393 (2016).

15. H. Fu, L. Wu, L. Duan, S. Lü, *Acta Pharm. Sin.,* **52,** 468 (2017).

16. R. Kotcherlakota, A.K. Barui, S. Prashar, M. Fajardo, D. Briones, A. Rodríguez-Diéguez, C.R. Patra, S. Gómez-Ruiz, *Biomater. Sci.,* **4,** 448 (2016).

17. D.M. Manohar, B.F. Noeline, R. Surya, *Asian. J. Pharm. Clin. Res.,* **11,** 372 (2018).

18. N. Ahmadi Nasab, H. Hassani Kumleh, M. Beygzadeh, S. Teimourian, M. Kazemzad, *Nanomed. Biotechnol.,* **46,** 75 (2018).

19. M. Abedanzadeh, M. Salmanpour, F. Farjadian, S. Mohammadi, A.M. Tamaddon, *J. Drug Deliv. Sci. Technol.,* **58,** 101793 **(**2020).

20. S. Bajpai, N. Chand, S. Ahuja, *Int. J. Biol. Macromol.*, **79,** 440 (2015).

21. M. Monier, *Int. J. Biol. Macromol.* **50**, 773 (2012).

22. M. Kong, X.G. Chen, K. Xing, H.J. Park, *Int. J. Biol. Macromol.* **144**, 51 (2010).

23. J. Bonilla, L. Atarés, M. Vargas, A., *Food Hydrocoll.,* **26,** 9 (2012).

24. H. Moussout, H. Ahlafi, M. Aazza, M. Bourakhouadar, *Polym. Degrad. Stab.,* **130,** 1 (2016).

25. A. Bernkop-Schnürch, S. Dünnhaupt, *Eur. J. Pharm. Biopharm.,* **81,** 463 (2012).

26. J. H. Hamman, *Marine Drug,* **8**, 1305 (2010).

27. R. K. Das, N. Kasoju, U. Bora, *Nanomed.: Nanotechnol. Biol. Med.,* **6,** 153 (2010).

28. D. Kumar, A. Gautam, P. P. Kundu, *J. App. Polym. Sci.,* **139,** 51552 (2022).

29. D. Kumar, A. Gautam, P.P. Kundu, *Int. J. Pharma.,* **635**, 122735 (2023).

30. D. Kumar, A. Gautam, S. Rohatgi, P. P. Kundu, *Int. J. Biol. Macromol.* **218**, 82 (2022).

31. D. Kumar, A. Gautam, D. K. Tripathi, K. M. Poluri, P. P. Kundu, *J. Drug Deliv. Sci. Technol.,* **77**, 103875 (2022).

32. D. Kumar, S. Kumar, S. Kumar, S. Rohatgi, P. P. Kundu, *Int. J. Biol. Macromol.* **183**, 962 (2021).

33. D. Kumar, V. Raj, A. Verma, P. Kumar, J. Pandey, *Int. J. Biol. Macromol.* **131**, 184 (2019).

34. Q. Wang, S. Zhang, Z. Deng, Y. Zhang, Z. Jiao, *Microporous and Mesoporous Mater,* **357**, 112612 (2023).

35. S. A. Gaware, K. A. Rokade, S. Kale, *J. Drug Deliv. Sci. Technol.,* **49,** 345 (2019).

36. M. Gallo, F. Giudice, M. Banchero, S. Ronchetti, L. Manna, B. Onida, *J. Sci. Technol*, **96**, 236 (2020).

37. N. G. Madian, N. Mohamed, *J. Mater. Res. Technol.,* **9**, 12970 (2020).

38. K. Liu, R.-L. Huang, X.-Q. Zha, Q.-M. Li, L.-H. Pan, J.-P. Luo, *Carbohydr. polym.,* **232** , 115810 (2020).

39. S. Malekmohammadi, H. Hadadzadeh, Z. J. Jo, M. L. Amirghofran, *J. Mol. Liq.*, **265,** 797 (2018).

Thermodynamics and non-isothermal kinetics of solid-state decomposition of poly-2-dimethyl amino ethyl methacrylate NFGs derived from supercritical CO_2

P. Joshi[1*], M. Pandey[3*], M. Aziz[2], I. Joshi[2], D. Palariya[2], M. Pandey[2], S. Mehtab[2], M.G.H. Zaidi[2]

[1]*Department of Chemistry, School of Allied Sciences, Dev Bhoomi Uttarakhand University, Naugaon 248007, India*
[2]*Department of Chemistry, College of Basic Sciences and Humanities, G.B. Pant University of Agriculture and Technology, Pantnagar, U.S Nagar 263145, Uttarakhand, India*
[3]*Department of Chemistry, School of Science, IFTM University, Moradabad-244102, Uttar Pradesh, India*

Nanoferrogels (NFGs) are potentially valuable materials for various agricultural and biomedical applications, where thermal resistance is crucial for effectiveness and safety. In this study, the thermodynamic and non-isothermal kinetic properties of the solid-state decomposition of supercritically synthesized poly-2-dimethyl amino ethyl methacrylate (PDMAEMA) and its NFG were investigated. NFGs were prepared by incorporating ferrite nanoparticles (FNPs) of size ~ 10.5 nm through a chemical method. Kinetic and thermodynamic characteristics of NFGs were demonstrated through thermal analysis. By comparing NFGs non-isothermal kinetic, thermal and thermodynamic data with that of FNP and PDMAEMA, this study aimed to gain insight into the unique properties of NFG. PDMAEMA have shown three-step decomposition, leaving a char residue of 25.7%. NFG has shown four-step decomposition, leaving 9.1% weight residue which suggests that NFG has better thermal stability and resistance to decomposition than PDMAEMA. Coats-Redfern (CR) and Horowitz-Metzger (HM) methods were used to evaluate the thermodynamics and kinetics of degradation and the thermodynamic stability of materials. HM method yielded higher values of activation energy (E_a) and pre-exponential factor (A) compared to the CR method. A slight variation was observed in ΔS and ΔH values obtained from the HM and CR methods during the evaluation process.

Keywords: Nanoferrogel, non-isothermal kinetics, supercritical, acrylate

INTRODUCTION

Ferrogels are a type of hydrogels that contain magnetic particles, such as iron oxide nanoparticles, dispersed throughout hydrophilic monomers, e.g., acrylic acid or acrylamide [1, 2]. Ferrite nanoparticles (FNPs) are incorporated into the hydrogel network either by embedding them within the polymer chains or by coating them onto the surface of the polymer chains [3, 4]. Ferrogels have the potential to revolutionize agriculture by improving soil remediation, nutrient delivery, plant growth, and crop monitoring [5, 6].

In agriculture, ferrogels can be used to remediate contaminated soils by absorbing and immobilizing heavy metals, pesticides, and other pollutants [7-9]. These smart materials can be loaded with nutrients and fertilizers and used to deliver them directly to plant roots [10]. The magnetic particles in the ferrogel can be manipulated with an external magnetic field to guide the gel to the desired location, resulting in more efficient nutrient uptake and reduced fertilizer waste [11-13].

Ferrogels are synthesized using sol-gel synthesis, co-precipitation, electrospinning and supercritical synthesis [14-18]. Supercritical methods are used to tune the porosity and morphology of the ferrogel, which can affect its magnetic and mechanical properties [19, 20-22]. Thermal stability of ferrogels is essential in agriculture because it allows for the controlled release of fertilizers and pesticides over an extended period of time, which can increase their efficacy and reduce the negative impact on the environment [23, 24]. The thermal stability of ferrogels ensures that the encapsulated compounds remain intact and do not degrade or evaporate due to high temperatures or UV exposure, which can reduce their efficacy [25]. When the soil temperature reaches a certain threshold, the ferrogels can undergo a phase transition and release the encapsulated compounds into the soil. By controlling the release of these compounds, ferrogels can reduce the amount of runoff and leaching that occurs, which can lead to water pollution and soil degradation [26, 27].

Common methods for examining the thermal characteristics of materials include differential thermogravimetry (DTG), thermogravimetry (TG), and differential thermal analysis (DTA) [28–31]. Coats-Redfern (commonly known as CR) and Horowitz - Metzger (commonly known as HM) techniques have been used to analyze thermal data

---

in order to calculate the activation energy (E_a) and pre-exponential factor (*A*) for the thermal degradation of a material [32, 33]. The slope of the straight line and its intercept may be used to determine changes in entropy (ΔS), enthalpy (ΔH), and free energy (ΔG) from the presented data. Generally speaking, the HM and CR approaches are helpful for examining the thermal behavior of materials, including ferrogels, and can offer relevant data on their thermal stability and breakdown kinetics [13, 34].

EXPERIMENTAL

Materials

The compounds AIBN, MBA and simazine (99%) were procured from MS HiMedia Chemicals in India whereas 2-dimethyl amino ethyl methacrylate (DMAEMA) was purchased from Poly Science in the United States. The remaining substances — chemicals, solvents, and CO_2 (with 99.5% purity) —were purchased locally and were used without additional purification.

Preparation of NFG in SCC

A reactor under high-pressure with a 100 mL stainless steel vessel and temperature control was utilized to synthesize NFG. DMAEMA, AIBN, MBA and FNP with concentrations of 6.30×10^{-3} mol/dL, 1.50×10^{-3} mol/dL, 9.80×10^{-4} mol/dL and 0.03 g, w/w 3% respectively, were all added to the reactor. After this the reaction mixture was cooled down to 10°C over the course of ten minutes, CO_2 was added to raise the pressure to 1200 psi at 90 ± 1°C. After allowing the reaction mixture to heat for 6 hours, the reactor vessel's temperature was brought down to 25 ± 1°C, and the contents were depressurized at a rate of 1 mL/min to produce NFG. In SCC, PDMAEMA was produced by polymerizing DMAEMA in the absence of FNP under the same reaction conditions.

CHARACTERIZATION

Utilizing alumina as a reference, the thermo-oxidative stability of the samples was examined utilizing simultaneous TG-DTG-DTA over EXSTAR TG/DTA 6300 at a heating rate of 10 °C/min in air (200 ml/min). TG data were interpreted for evaluation of moisture content, char yield, % weight residue of samples along with kinetic and thermodynamic factors.

Interpretation of TG

TG data of PDMAEMA, NFG were evaluated for their weight loss (%) with reference to temperature, decomposition stages involved and kinetic parameters through a series of calculation-based methods such as CR and HM methods.

Plotting the double logarithm of the reciprocal of the weight fraction of the reactant component against temperature is what is entailed in the HM method. The following equation (Eq. (1)) serves as a description of the HM approximation expression:

$$\log\left(\log\left(\frac{w_0}{w}\right)\right) = \frac{E_a \theta}{2.303 R T_s^2} \tag{1}$$

with w_0: the initial weight; *w*: the weight at temperature T; $w/w_0 = 0.368$ for 1st order reaction and T_s: the experimental reference temperature such that $T-T_s = \theta$.

For the CR method, the equation is as follows:

$$\log_{10}\left[-\frac{\log_{10}(1-\alpha)}{T^2}\right] = \left[\log_{10}\left(\frac{AR}{aE_a}\right)\left\{1-\frac{2RT}{E_a}\right\}\right] - \frac{E_a}{2.303RT} \tag{2}$$

where: T is the temperature in Kelvin, α is the fraction of the original sample left at temperature T and R is the universal gas constant with a value of 8.314 $JK^{-1}mol^{-1}$ in SI units. CR method implies a plot of $\log_{10}[-\log_{10}(1-\alpha)/T^2]$ *vs* T^{-1} for determining the energy of activation which is calculated by the straight line's slope obtained from $-(E_a/2.303R)$.

RESULTS AND DISCUSSION
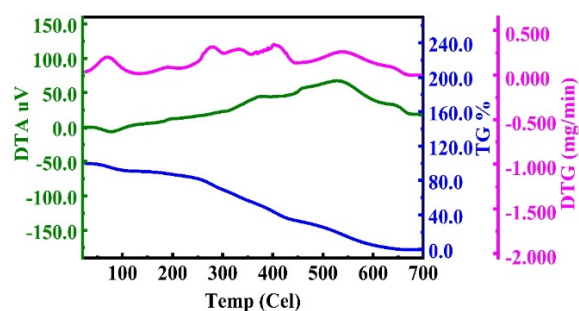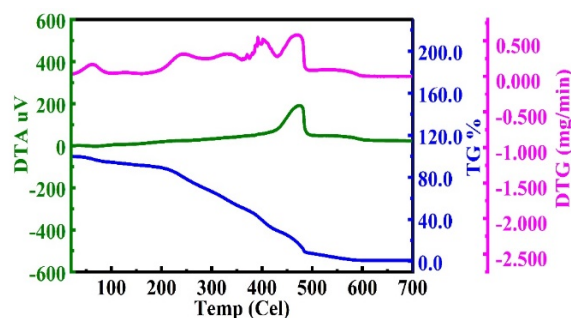
Thermal stability

The TG-DTA-DTG analysis results of PDMAEMA and NFG are summarized in Table 1. PDMAEMA showed 1st decomposition step with TGo at 200°C, leaving a Wr of 87.0%. The DTG showed a 2nd decomposition step at 300°C with a Wr of 69.4%. A 3rd decomposition step occurred at 400°C, leaving a Wr of 44.1%. The TG endset of PDMAEMA showed up at 500°C, leaving a char residue of 25.7%. NFG showed 1st decomposition step with TGo at 200°C, leaving a Wr of 89.0%. A 2nd decomposition step occurred at 300°C with a Wr of 66.4%. A 3rd decomposition step occurred at 400°C, leaving a Wr of 39.3%, and a 4th decomposition step occurred at 485°C, leaving a Wr of 9.1%.

Table 1. Thermal data of PDMAEMA and respective NFG

Polymers	TG[A]		DTA[B]		-ΔH[C]	DTG[D]	
	TGo	TGe					
PDMAEMA	87.00 [200]	25.70 [500]	-6.40 [76]	67.10 [532]	0.17	20.10 [71]	26.10 [539]
NFG	89.00 [200]	9.10 [485]	190.50 [476]		-2.79	16.90 [63]	58.30 [471]

[A]: TGo= %Wr at TG onset (ºC), TGe= %Wr at TG endset (ºC)
[B]: DTA signal (Peak temperature, ºC)
[C]: Heat of fusion (J/g)
[D]: R= Rate of degradation, kJ/g. (Peak temperature, ºC)

Table 2. Kinetic and thermodynamic parameters of PDMAEMA and NFG evaluated from HM and CR methods

	T(K)	n	Method	E_a[A]	A[B]	-ΔS[C]	-ΔH[D]	ΔG[E]	R²
PDMAEMA			CR	8.3	0.04	0.34	2.68	2.18	0.99396
	651	0	HM	25	0.07	0.40	19.3	2.02	0.99490
			CR	13	0.02	0.34	7.38	2.13	0.99516
		1	HM	32	0.03	0.37	26.3	2.14	0.99511
			CR	28	0.47	0.33	22.3	1.92	0.99712
		2	HM	38	1.20	0.36	32.3	2.02	0.99676
			CR	28	0.47	0.71	22.3	4.39	0.99894
		3	HM	42	6.18	0.28	36.3	1.45	0.99728
NFG	612	0	CR	8.7	0.04	0.34	2.51	2.05	0.99024
			HM	18	0.24	0.32	11.8	1.84	0.99705
		1	CR	20	0.01	0.34	13.8	1.94	0.99486
			HM	45	7.70	0.30	38.8	1.44	0.99861
		2	CR	42	0.10	0.33	35.8	1.66	0.99180
			HM	75	10.2	0.28	68.8	1.02	0.99736
		3	CR	67	32	0.33	58.8	1.43	0.99169
			HM	77	38	0.27	70.8	0.94	0.99731

Fig. 1a. Graph simultaneously showing TG-DTA-DTG of PDMAEMA

Fig. 1b. Graph simultaneously showing TG-DTA-DTG of NFG

Kinetic analysis

Utilizing alumina as a reference, the thermo-oxidative stability of the prepared samples was examined by simultaneous TG-DTG-DTA over EXSTAR TG/DTA 6300. The examination was done at a heating rate of 10ºC/min in air. TG data was interpreted for evaluation of moisture content, char yield, % weight residue of samples along with kinetic and thermodynamic parameters. CR method was applied to calculate the thermodynamic and non- isothermal kinetic parameters from the TG data. CR method implies a plot between $\log_{10}$ [- $\log_{10}(1-\alpha)/T^2$] and T^{-1} in order to determine activation energy calculated by the straight line's slope obtained from (E_a/ 2.303R)

The kinetic and thermodynamic parameters that were deduced from the TG data using the CR and HM methods for n = 0 to 3 are summarized in Table 2. Table 2 also shows the regression coefficients (R^2) evaluated from the plots. The values of R^2 being approximately equal reveal their linearity. FNPs, PDMAEMA and respective NFG, reveal higher values for E_a and A evaluated from HM method over CR method. For PDMAEMA (Fig. 2a), and respective NFG HM (CR) methods reveal E_a ranging

111

from 25 to 42 (8.3-28) and from 23 to 76 (9.8 to 55), respectively (Figs. 2a-2d). The very high values of activation energy (E_a) in Table 2 reveal enhanced thermal stability of hydrogels and related NFG. The values of the frequency factor for CR (HM) were ranging 0.03-6.18 (0.02-0.47) and 0.24-38 (0.04-32), respectively (Figs. 2a-2d). The methods reveal (-ΔS) ranging 0.40-0.28 (0.71-0.33) and 0.34-0.33 (0.33-0.32), respectively (Figs. 2a-2d). The ΔG of PDMAEMA evaluated by HM (CR) methods was found ranging 1.45 to 2.14 (1.92-4.39), respectively (Fig. 2). Under similar conditions for NFG, HM (CR) method revealed ΔG ranging 0.94 - 1.84 (1.43 to 2.05) [35].
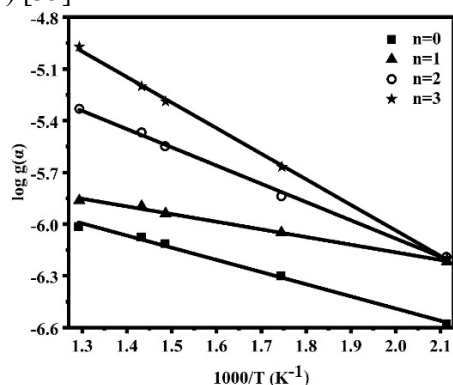
Fig. 2a. CR plots of PDMAEMA
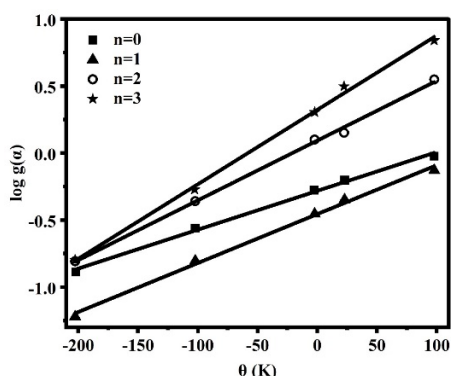
Fig. 2b. HM plots of PDMAEMA
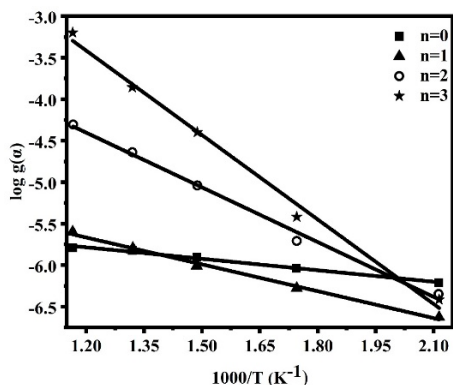
Fig. 2c. CR plots of NFG
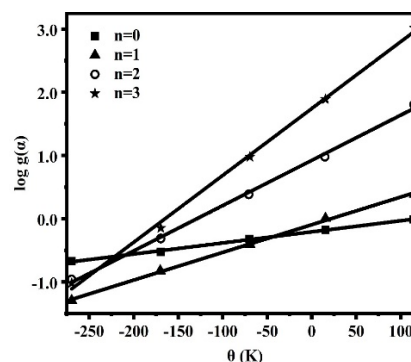
Fig. 2d. HM plots of NFG

CONCLUSIONS

Supercritical carbon dioxide was used to synthesize poly-2-dimethyl amino ethyl methacrylate (PDMAEMA) and related nanoferrogels (NFG). Coats-Redfern, commonly known as the CR method and Horowitz-Metzger, commonly known as the HM method, were employed to investigate their kinetics and the thermodynamics of solid-state decomposition at various levels (n = 0, 1, 2, and 3). Both methods are widely used for the analysis of chemical reactions and are applicable to a wide range of systems. The non-isothermal kinetics were examined by plotting the log(a) functions, which were calculated from TG data, against the decomposition time from thermograms. The values of E_a (activation energy) and A (frequency factor) revealed that the ferrite nanoparticles follow first-order kinetics, while PDMAEMA and NFG follow third-order kinetics. The HM method reveals higher values for E_a and A, but DS and DH showed identical results. The overall results obtained from CR and HM methods can be used to compare the reaction kinetics and thermodynamics of different systems, and to optimize reaction conditions for desired outcomes.

REFERENCES

1. C. Boztepe, M. Daskin, A. Erdogan, *React. Funct. Polym.*, **173**, 105219 (2022).
2. A. P. Safronov, B. J. Stadler, J. Um, M. R. Zamani Kouhpanji, J. Alonso Masa, A. G. Galyas, G. V. Kurlyandskaya, *Materials*, **12**, 2582 (2019).
3. S. Awasthi, *JOM*, **73**, 2440(2021).
4. R. Messing, N. Frickel, L. Belkoura, R. Strey, H. Rahn, S. Odenbach, A. M. Schmidt, *Macromolecules*, **44**, 2990 (2011).

5. B. Narjary, P. Aggarwal, S. Kumar, M. D. Meena, ICAR (2013).
6. M. R. Guilherme, F. A. Aouada, A. R. Fajardo, A. F. Martins, A. T. Paulino, M. F. Davi, A. F. Rubira, E. C. Muniz, *Eur. Polym. J.*, **72**, 365 (2015).
7. J. Y. Lim, S. S. Goh, S. S. Liow, K. Xue, X. J. Loh, *J. Mater. Chem. A*, **7**, 18759 (2019).
8. L. M. Sanchez, D. G. Actis, J. S. Gonzalez, P. M. Zélis, V. A. Alvarez, *J. Nanopart. Res.*, **21**, 1 (2019).
9. O. V. Kharissova, H. R. Dias, B. I. Kharisov, *RSC Adv.*, **5**, 6695 (2015).
10. D. Fouad, Y. Bachra, G. Ayoub, A. Ouaket, A. Bennamara, N. Knouzi, M. Berrada, in: Chitin and chitosan-physicochemical properties and industrial applications, IntechOpen, 2020.
11. S. Agila, J. Poornima, in: 15th International Conference on Nanotechnology (IEEE-NANOIEEE), 2015, p 1058.
12. R. D. Silva, L. T. de Carvalho, R. M. de Moraes, S. D. F. Medeiros, T. M. Lacerda, *Macromol. Chem. Phys.*, **223**, 2100501 (2022).
13. P. Joshi, G. Bisht, S. Mehtab, M. G. H. Zaidi, *Mater. Today Chem.*, **62**, 6814 (2022).
14. E. I. Wisotzki, D. Eberbeck, H. Kratz, S. G. Mayr, *Soft Matter*, **12**, 3908 (2016).
15. R. Hernández, V. Zamora-Mora, M. Sibaja-Ballestero, J. Vega-Baudrit, D. López, C. Mijangos, *J. Colloid Interface Sci.*, **339**, 53(2009).
16. N. A. Elkasabgy, A. A. Mahmoud, *AAPS PharmSciTech*, **20**, 256 (2019).
17. P. Joshi, S. Mehtab, M. G. H. Zaidi, *Bull. Chem. Soc. Jpn.*, **95**, 855 (2022).
18. S. Daneshyan, G. Sodeifian, *J. Supercrit. Fluids*, **188**, 105679 (2022).
19. F. Hadizadeh, E. Khodaverdi, F. Oroojalian, P. Rahmanian-Devin, S. H. M. Hashemi, N. Omidkhah, K. Asare-Addo, A. Nokhodchi, H. Kamali, *Int. J. Pharm.*, **631**, 122507 (2023).
20. J. Shi, X. Kang, L. Mao, Y. Jiang, S. Zhao, Y. Liu, B. Zhai, H. Jin, L. Guo, *Chem. Eng. J.*, 141608 (2023).
21. L. Jia, L. Xu, Y. Liu, J. Hao, X. Wang, *CCS Chem.*, **5**, 510 (2023).
22. Á. Miguel, N. García, V. Gregorio, A. López-Cudero, P. Tiemblo, *Polymers*, **12**, 1336 (2020).
23. L. M. Sanchez, D. G. Actis, J. S. Gonzalez, P. M. Zélis, V. A. Alvarez, *J. Nanopart. Res.*, **21**, 1 (2019).
24. H. M.Nizam El-Din, A. W. M. El-Naggar, *Des. Monomers Polym.*, **17**, 322(2014).
25. D. Das, P. Prakash, P. K. Rout, S. Bhaladhare, *Starch-Stärke*, **73**, 1900284 (2021).
26. J. W.Tay, D. H. Choe, A. Mulchandani, M. K. Rust, *J. Econ. Entomol.*, **113**, 2061 (2020).
27. B. Tomadoni, C. Casalongué, V. A. Alvarez, *Poly. Agri-Food Appl.*, 99 (2019).
28. E. T. Tenório-Neto, T. Jamshaid, M. Eissa, M. H. Kunita, N. Zine, G. Agusti, H. Fessi, A. E. El-Salhi, A. Elaissari, *Polym. Adv. Technol.*, **26**, 1199 (2015).
29. M. R. Rahman, S. Hamdan, J. L. C. Hui, in: MATEC web of conferences, vol. 87, EDP Sciences. 2017, p. 03013.
30. M. S. H. Akash, K. Rehman, M. S. H. Akash, K. Rehman, *Ess. Pharma. Anal.*, 207 (2020).
31. R. R. F. Ramos, D. D. Siqueira, R. M. R. Wellen, I. F. Leite, G. M. Glenn, E. S. Medeiros, *J. Polym. Environ.*, **27**, 1677 (2019).
32. H. Gul, A. U. H. A. Shah, S. Gul, J. Arjomandi, S. Bilal, *Iran. J. Chem. Chem. Eng.*, **37**, 193 (2018).
33. A. S. Kipcak, F. T. Senberber, E. Moroydor Derun, N. Tugrul, S. Piskin, *Res. Chem. Intermed.*, **41**, 9129 (2015).
34. V. Rani, R. C. Srivastava, H. M. Agarwal, M. G. H. Zaidi, *Mat. Today: Proceed.*, **4** (9), 9471 (2017).
35. S. Mehtab, M. G. H. Zaidi, N. Rana, K. Khati, S. Sharma, *Bull. Mat. Sci.*, **45**, 162 (2022).

Effect of ferrite on electrical and optical properties of fly ash enriched nanohybrids

P. Singh*, D. Palariya, M. Pandey, S. Mehtab*, M. G. H. Zaidi**

Department of Chemistry, College of Basic Sciences and Humanities,G.B. Pant University of Agriculture and Technology, Pantnagar, U.S Nagar-263145, Uttarakhand, India

For a variety of applications in the production of sustainable composite materials, fly ash (FA)-enriched ferrite nanohybrids (NHs) have emerged as an effective and trending technology in the field of nanohybrids. For the purposes of the current research, NHs were fabricated, characterized and examined for electrical conductivity (σDC) in a wide range of physical conditions. Development and stability of NHs was confirmed by UV spectroscopy. Surface morphology of NHs was ascertained through scanning electron microscopy. The effect of temperature on σDC of NHs was evaluated over the range of 25^0C to 115 ($\pm2^o$C). I-V characteristics of all the specimens were recorded in the voltage range of 5 to 45 V at RT.

Keywords: FA, BF, DC conductivity, SEM, NHs.

INTRODUCTION

FA is a byproduct of coal combustion in thermal power plants, and black ferrite (BF) is a type of ceramic material composed of iron oxide (Fe_2O_3) and other metal oxides [5]. The chemical composition of the FA particles consists of Al_2O_3 (24.80%), SiO_2 (50.50%), Fe_2O_3 (12.68%), MgO (1.61%), CaO (1.02%), SO_3 (1.02%) and other elements (10.21%), as reported by different sources [4]. Combining FA with BF creates a composite material that can have several useful properties depending on the intended application. Because of its dominant-negative surface charge, FA is a promising adsorbent. Numerous uses for wastewater treatment have been documented [12]. The combination of FA and BF can be utilized to develop magnetic composites with potential applications in various fields, such as electronics, energy storage, and environmental remediation [10].

BF is known for its magnetic properties, making it suitable for applications in magnetic data storage, magnetic sensors, and electromagnetic devices. The most thermodynamically stable iron oxide phase in the family is hematite (Fe_2O_3), and it has a number of benefits, including natural availability, biocompatibility, and low cost [11].

By incorporating FA into the BF matrix, it is possible to create magnetic composites with tailored properties. The combination of FA and BF can result in materials with enhanced electromagnetic interference shielding properties.

Such composites can be used to protect electronic devices and sensitive equipment from unwanted electromagnetic radiation [13].

Composite materials of FA and BF might exhibit catalytic properties, enabling them to accelerate certain chemical reactions [14]. This could find applications in environmental cleanup and industrial processes. Depending on the composite's mechanical properties, it may have applications in structural engineering and construction [8]. The FA could provide a lightweight filler or reinforcement within the BF matrix. It's important to note that the properties of the composite heavily depend on the specific composition, manufacturing process, and ratio of FA to BF. Extensive research and experimentation would be required to optimize the material for specific applications [16].

According to a global survey, around 780 MT of FA are generated annually worldwide, of which 226.13 are produced domestically. The type of coal, burning circumstances, combustion rate, and cooling control all affect the composition of FA produced from various resources [17]. FA can be used as a filler for high-performance PCs because of its high bulk density, porosity, particle size, and surface area. Due to their improved electrical, mechanical, thermal, and electrochemical properties, FAs have been incorporated as reinforcement in BF-based polymers over the years [1].

The addition of BF to FA can significantly affect its electrical conductivity. FA is typically a non-

---

* To whom all correspondence should be sent:
E-mail: smiitr@gmail.com, mghzaidi@gmail.com

conductive material, as it mainly consists of silicon dioxide (SiO_2) and other non-metallic components [7]. On the other hand, BF is a ceramic material composed of iron oxide (Fe_2O_3) and other metal oxides and is known to be a semi-conductor or insulator depending on its composition and doping. When BF is added to FA, it can introduce certain changes to the electrical properties of the composite material. Depending on the concentration and type of BF used, the addition of BF to FA can increase the electrical conductivity of the NHs [2]. BF particles may act as conductive pathways within the non-conductive FA matrix, allowing for the movement of electrons. In this case, the electrical conductivity of the composite material would lie between that of a conductor and an insulator. The conductivity can be modulated by adjusting the BF content [3]. In some cases, the addition of BF may not significantly alter the electrical conductivity of FA, especially if the BF content is relatively low, or if the specific type of BF used is more insulating in nature. The conductivity of NHs may also be temperature-dependent, as both BF and FA can show variations in their electrical properties with temperature changes. The specific electrical behavior of the NHs will depend on factors like the percentage of BF in the mixture, the type of BF used (e.g., magnetite, hematite, etc.), the distribution and size of the BF particles within the FA matrix, and any additional processing or treatment applied during composite fabrication. These variations in electrical conductivity can have practical applications [4]. For example, if a certain level of electrical conductivity is desired in a composite material for specific electronic or electromagnetic applications, the proper selection and incorporation of BF can help achieve that objective.

It's worth noting that experimental research and testing would be necessary to determine the exact electrical conductivity characteristics of a specific FA composite with BF, as there can be a wide range of possible outcomes based on the mentioned factors. Incorporating BF into FA can lead to magnetic composites suitable for applications in data storage, magnetic sensors, or electromagnetic devices. Additionally, the combination may also offer benefits in terms of waste management, environmental remediation, and structural engineering [6].

EXPERIMENTAL

Materials

FA was collected from pulp and paper industry situated nearby area of the University. FA was finely ground into 0.80 mm mesh size, stored at 50 ± 1^oC

and used for preparation of NHs. All the chemicals and solvents (purity >99.55) were locally arranged and used without further purification. Commercially available ferrite was procured from Research-Lab Fine Chem Industries, Mumbai, India. The moisture content of FA was deduced according to a procedure reported earlier [9]. The disk-shaped specimens (diameter 1 cm) of FA, ferrites and NHs for electrical conductivity measurements were fabricated in 2.20 ± 0.01 mm thickness through mixing a series of compositions of ferrite with FA under hydraulic press at 100 kg/cm^2 for 5 minutes.

Characterization

Scanning electron microscopy (SEM) measurements were performed on a JSM 6610 (LV) at 0.2 KX (1 mm) and 15 kV. UV-vis absorbance experiments were carried out at room temperature with UV-vis Specord-200 using quartz cuvettes. The energy band gap of specimens was estimated from Tauc plot. Electrical conductivity measurements were performed on a Keithley nanovoltmeter (2182A) equipped with current source (6221) and a temperature-controlled four-probe arrangement. The activation energy (Ea) was deduced through Arrhenius equation: $\sigma = \sigma_o exp(-Ea/kT)$, where σ is electrical conductivity of the specimen at temperature (T, K), σ_o is pre-exponential factor, and k is Boltzmann constant.

RESULTS AND DISCUSSION

Electrical behavior of FA, BF and NHs

Electrical conductivity of FA, BF and NHs containing pellets was examined at different experimental conditions to estimate the working performance and durability of developed NHs.

Electrical conductivity at variable voltages

In order to ascertain the relative electrical behavior of FA, BF and NHS their σDC (mS/cm) were examined in the voltages ranging 1 to 100 V at 25 ± 1^oC (Fig. 1). Results indicate that at 1 V and 10 V for all pellets, σDC values were comparatively low. Maximum σDC were obtained at 100 V with maximum value of 1.03 for BF-derived pellets. The conductivity response of BF was found to be higher over FA and NHs at all voltages.

Effect of temperature

In order to determine the relative electrical behavior of FA, BF and NHs, their σDC (mS/cm) were examined at variable temperatures ranging from 25 to 115^oC (Fig. 2). Plot of FA, BF and NHs-derived pellets shows a linear increase in σDC with temperature. Ea was also calculated for BF, FA and

NHs and it was found to be 7.08 Jmol^{-1}, 0.61 Jmol^{-1} and 2.24 Jmol^{-1} for BF, FA and NHs, respectively.
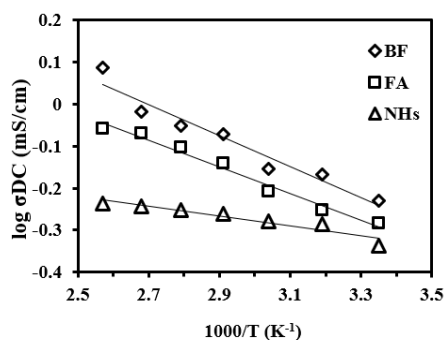

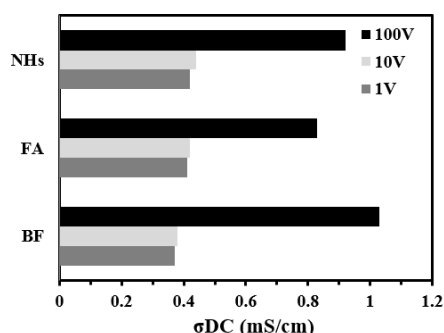**Fig. 1.** Effect of voltage variation on σDC

Fig. 2. Effect of temperature on σDC

I-V characteristics of FA, BF and NHs

I-V characteristics of pellets were recorded in the voltage range of 5 to 45 V at RT. Electrical characteristics examinations reflect those conductivities of BF-derived pellets was higher over FA and NHs-based pellets. Fig. 3 demonstrates the I-V plot of FA, BF and NHs derived showing a linear increase in current with voltage at room temperature that implies Ohmic conductive behavior of pellets.
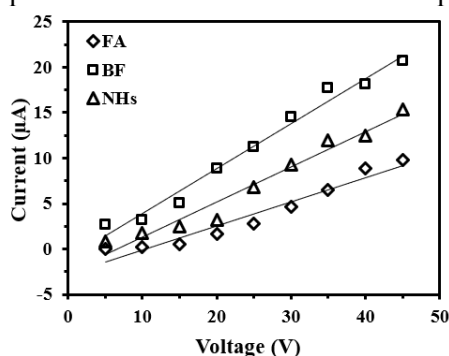
Fig. 3. I-V characteristics of FA, BF and NHs

Moisture content analysis of FA

Percent moisture content of FA was analyzed by loss on drying method and average moisture content was found to be 0.0175% [18].

Surface morphology of FA, BF and NHs

In order to have comparable results FA and NHs were imaged at a common scale of 1 mm and 25 kx. FA is primarily composed of compact or hollow spheres with a consistent smooth texture, as shown in the figure. The presence of solid deposits or small crystals, such as soluble alkaline sulfates, iron mineral dendrites, mullite crystals, etc., could frequently be seen on the surface of spheres. Small spherical particles with some agglomerated particles in the FA pores can be seen. Additionally, some quartz flakes, unburned coal residue, or even vitreous unformed pieces could be noticeable. It was determined that the ferrosphere in the figure is of the dendritic type. High levels of iron oxide are seen in the ferrosphere, and this type of particle structure rarely occurs in FA. The images show that the development of NHs is significantly influenced by the ferrosphere [20]. In the case of NHs, no such agglomerated particles are observed, a smooth surface indicating that ferrite is completely distributed into the pores of FA, leading to formation of more stable NHs.

(a)   **(b)**
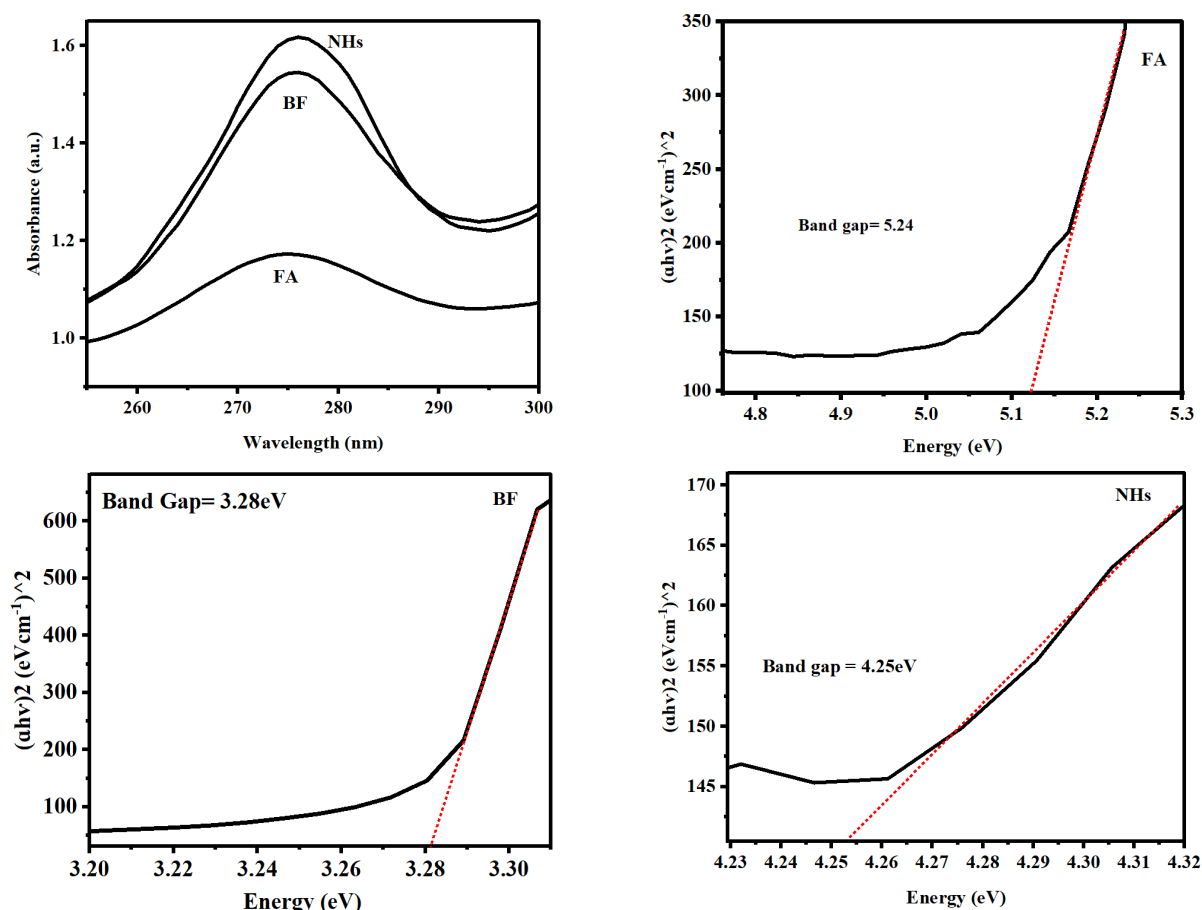

(c)
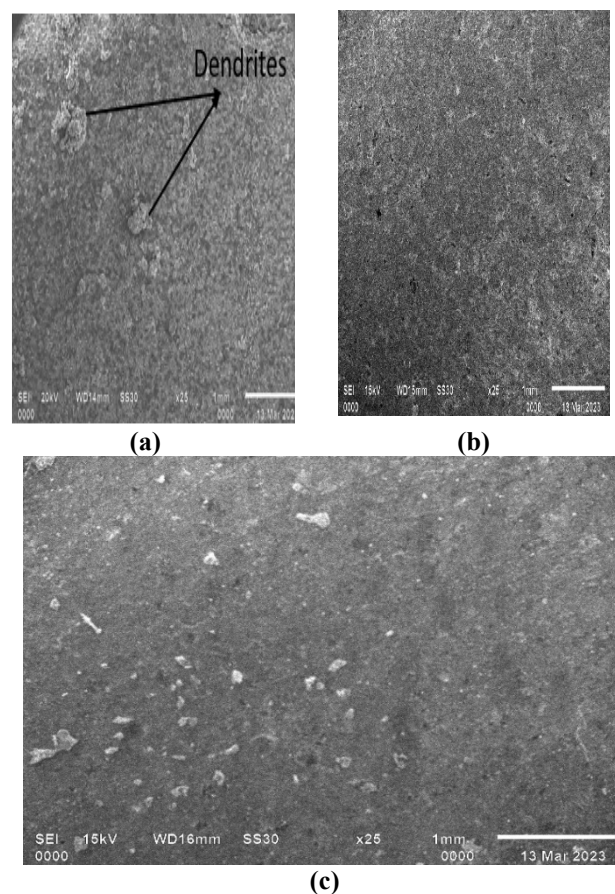
Fig. 4. SEM images of a) FA b) NHs (c) BF

Fig. 5. UV-Vis spectra of a) FA, BF and NHs; b) band gap energy graph of FA; c) band gap energy graph of BF; d) band gap energy graph of NHs.

Optical spectroscopy

The absorption spectra of FA, BF and NHs are shown in Fig. 5. In our present study FA exhibited a maximum absorption spectral peak at 274 nm and most of the peaks were observed in the region of 270 nm-280 nm but were absent in the region of 600-900 nm. In the case of BF the maximum absorption peak is observed at 275 nm which is in close resemblance with the maximum absorption peak of NHs at 276 nm. Band gap energy was also calculated with the help of Tauc plot for FA, BF and NHs (Table 1) [19].

Table 1. Band gap energy for FA, BF and NHs

Samples	Band gap energy (eV)	λ_{max} (nm)
FA	5.24	274
BF	3.28	275
NHs	4.25	276

CONCLUSION

Pellets of FA, BF and NHs were fabricated using a hydraulic press. Surface morphology of FA and NHs was investigated by FESEM analysis revealing that BF-based pellets showed maximum σDC (mS/cm) of 1.03±0.20 at 100 V and ambient temperature. I-V plot of FA, BF and NHs-derived pellets shows a linear increase in current with voltage at room temperature that implies Ohmic conductive behavior of the pellets, The moisture content was also evaluated for FA and it was found to be 0.0175%. The band gap energy obtained from UV reflectance spectra analysis was 5.24, 3.28, and 4.25 eV for FA, BF and NHs, respectively. Synergic compatibility of FA with BF plays an important role in electron channeling that results in optimization of conductivity over time in harsh environments that make NHs an interesting choice of electrically conducting material to use in microelectronics, microwave absorption and batteries.

REFERENCES

1. R. Raja, K. Satheesh, V. Manisekar Manikandan, *Mater. Desig.*, **55**, 499 (2014).
2. K. G. Barbara, A. G. Kim, *Fuel*, **85**, 2537 (2006).
3. S. Angelo, R. Overhof, T. Green, J. Pels. *Waste Manag.*, **32**, 144 (2012).
4. S. R. Chauhan, S. Thakur. *Mater. Desig.*, **51**, 398

(2013).

5. T. Zhandos, S. Azat, A. Baibatyrova, *Int. J. Coal Prep. Util.,* **42**, 1968 (2022).
6. W. Franus, M. Wdowin, M. Franus, *Environ. Monitor. Assess.*, **186**, 5729 (2014).
7. S. Golbad, P. Khoshnoud, N. A. Zahra, *Int. J. Environ. Sci. Technol.,* **14**, 135 (2017).
8. J. Brassell, T. Philip, V. Ojumu, L. F. Petrik, Zeolites-useful minerals, 2016, p. 203.
9. P. Khoshnoud. PhD diss., The University of Wisconsin-Milwaukee, 2017.
10. P. Khoshnoud, S. Gunashekar, M. Murtatha, N. Jamel, A. Zahra, *J. Minerals Mater. Character. Eng.,* **2**, 554 (2014).
11. S. Liu, J. Zhu, X. Guo, J. Ge, H. Wu. *Col. Surf. A: Physicochem. Eng. Asp.*, **484**, 434 (2015).
12. O. Jan, I. Stubna, V. Trnovcova, T. Hulan, L. Vozar. *Adv. Mater. Res.,* **1126**, 123 (2015).
13. M. Revanasiddappa, D. S. Swamy, K. Vinay, Y. T. Ravikiran, S. C. Raghavendra, in: *AIP Conf. Proc.*, **1953**, 090070-090081(2018).
14. G. Noreen, K. Zubair, M. F. Shakir, M. Zahid, Y. Nawab, Z. A. Rehan, *J. Superconduct. Novel Magn.,* **33**, 3519 (2020).
15. S. Varshney, A. Ohlan, V. K. Jain, V. P. Dutta, S. K. Dhawan, *Indust. Eng. Chem. Res.,* **53**, 14282 (2014).
16. S. B. Kondawar, A. D. Dahegaonkar, V. A. Tabhane, D. V. Nandanwar, *Adv. Mater. Lett.,* **5**, 360 (2014).
17. S. Kashi Gupta, R. K. Baum, T. N. Kao, S. N. Bhattacharya, *Mater. Des.,* **95**, 119 (2016).
18. H. Mudila, S. Rana, M. G. H. Zaidi, S. Alam, *Nanostructures*, **23**, 20 (2015).
19. J. C. Jeyageetha, V. Sankaragomathi, M. Bharathi, R. Muthumari, P. S. Priya, *Int. J. Recent Sci. Res.,* 14466 (2016).
20. E. Gerasimova. *Procedia Eng.*, **150**, 1553 (2016).

Strontium-doped lanthanum nickelate (LaNiO₃) nano-materials for alkaline water splitting

P. Mishra[1], P. Sharma[1], V. Singh[2], N. K. Singh[1*]

[1]Department of Chemistry, Faculty of Science, University of Lucknow, Lucknow-226007, India
[2]Department of Chemistry, Maharana Pratap Govt. P.G. College, Hardoi, U.P. India, Pin code- 241001, India

Innovative perovskite-type oxides, specifically $La_{1-x}Sr_xNiO_3$ (where $0 \leq x \leq 0.8$), were skillfully synthesized using a low-temperature citric acid sol-gel approach. These novel materials were then subjected to comprehensive scrutiny to explore their remarkable electrocatalytic potential in the context of alkaline water splitting. Characterizations were performed by using oxide material as anode at which oxygen evolution reaction (OER) takes place. Through X-ray diffraction (XRD) examination, it was unveiled that the material was predominantly composed of an almost pure phase. Delving into the cyclic voltammogram (CV) data, a mesmerizing duo of redox peaks emerged, one anodic and its counterpart cathodic, observed just before starting of OER within the potential range of 0-0.7V in 1 M KOH solution at room temperature. The research brought to light a remarkable boost in electrocatalytic activity upon Sr substitution for La in LaNiO₃. Additionally, an intriguing discovery unfolded, showing a unity order for the OER concerning shifts in OH^- concentration, accompanied by Tafel slopes spanning the fascinating range of 85 to 101 mV decade⁻¹. The lower values of electrochemical activation energy ($\Delta E^o_{el}{}^\#$) and highly negative values of entropy of activation ($\Delta S^{o\#}$) favor a high rate of electrochemical formation of oxygen, which arises through adsorption phenomenon.

Keywords: XRD, Perovskite; Sol-gel; Water splitting; Tafel plot; Electrocatalytic activity

INTRODUCTION

Transition metals (Mn, Fe, Co, Ni) mixed oxides with perovskite type structure are important electrode materials for various applications such as efficient oxygen anode in water electrolysis [1-5] and as a cathode in solid oxide fuel cells and metal air batteries [6-8]. The major problems associated with electrocatalytic activity of the electrode for OER were the higher potential value and deterioration of electrode materials. It was further observed that electrocatalytic efficiency towards OER decreases with cell operation due to formation of a very thin resistant layer of NiO over the nickel electrode [9, 10]. In order to reduce internal resistance several suitable membranes, *viz*., reinforced asbestos, sintered nickel, PTFF bonded zirconia, nickel net backed porous cermets membrane, etc., have been developed. Nickel is unstable and not suitable for the anodic polarization conditions. So, work is continued to reduce the oxygen overpotential with low-cost electrode material. For the purpose, investigations were carried out to obtain economical electrode materials by powder coating [11], raney nickel coating [12], electrodeposition [13, 14], plasma spraying [15] methods to improve the porosity and hence the surface area of the nickel electrodes. Several other materials have also been investigated for oxygen evolution reaction other than nickel. Transition

metals oxides with spinel (e.g. Co_3O_4 and $NiFe_2O_4$) and perovskite (e.g. $La_{1-x}Sr_xCoO_3$, $La_{1-x}Sr_xNiO_3$, $La_{1-x}Sr_xMnO_3$, etc.) structure, their cost-effectiveness, widespread accessibility, and remarkable resistance to corrosion in alkaline media, are setting them apart as a distinguished choice in the scientific community [16]. In the dawn of research, conventional ceramic and thermal decomposition methods reigned supreme for the synthesis of these materials at elevated temperatures [17-19]. Conventional methods in earlier studies yielded oxides with larger particle sizes and lower specific surface areas, while recent low-temperature synthetic approaches utilizing solid organic precursors have shown promising results in producing oxides with significantly enhanced specific surface areas [20-23]. Through the implementation of advanced low-temperature synthesis techniques and the utilization of organic precursors, scientists effectively created Sr-substituted perovskite materials. These pioneering substances demonstrated a remarkable improvement in electrocatalytic performance, surpassing those generated through conventional high-temperature ceramic and thermal decomposition methodologies. In a recent seminal research endeavor, Lal *et al*. [24] embarked on a comprehensive exploration of the electrochemical behavior governing the oxygen evolution reaction (OER) in $La_{1-x}Sr_xCoO_3$ materials,

---

where x ranged from 0 to 0.4. Notably, these intriguing specimens were meticulously synthesized using the sophisticated stearic acid sol-gel method. Furthermore, the team diligently investigated the physicochemical attributes of these compounds, employing state-of-the-art techniques. The investigation uncovered a striking resemblance between the roughness aspect of the oxide surface and the evident electrocatalytic behavior in both the Sr-substituted lanthanum cobaltites and the Sr-substituted lanthanum manganite. The latter was produced using the sol-gel technique, employing malic acid and polyacrylic acid.

The interfacial and electrocatalytic properties of these materials are widely recognized to be significantly influenced by various preparation variables. These include the concentration of the starting substances, pH of the solution, temperature, method of preparation, characteristics of precursors, and ionic substitution. Given the mentioned considerations, we meticulously examined the electrocatalytic behavior of copper-substituted lanthanum cobaltites, which was synthesized *via* sol-gel technique in acidic medium [25]. Encouragingly, our findings unveiled favorable outcomes in terms of its performance towards the oxygen evolution reaction (OER).

MATERIALS AND METHODS
Chemical and reagents

All the chemicals used were either AR-grade or purified grade, so, no further purification has been done. Perovskite-type oxides of La, Sr and Ni having composition $La_{1-x}Sr_xNiO_3$ ($0 \leq X \leq 0.8$), were synthesized by adopting the low-temperature citric acid sol-gel method reported by Vassiliou *et al.* [26]. In this method, metal nitrates, citric acid and ethylene glycol were mixed together in double distilled water in appropriate proportions. Gel formation was catalyzed by the addition of few drops of HNO_3. The excess nitric acid was boiled off and the gel so obtained was heated on a hot plate till the gel burnt out completely into solid mass with evolution of brown fumes. The solid was then crushed into fine powder and further annealed at 650 °C for 6 hours in a muffle furnace (ASCO) to get the desired material.

Equipments and measurements

The presence of a single perovskite phase in the prepared oxides was confidently ascertained by capturing X-ray diffraction patterns with the XPERT-PRO diffractometer (Model PW3050/60) employing a Cu-Kα (λ = 1.54048 Å) radiation source. To determine the crystallite size, Scherrer's

formula was diligently utilized. Furthermore, the texture of the oxide in its powder form underwent thorough examination through scanning electron microscopy (JEOL JSM 6490LV). For the precise execution of cyclic voltammogram (CV) and Tafel experiments, we employed the advanced capabilities of an electrochemical workstation, the Gamry Reference 600 ZRA. This workstation is equipped with a potentiostat/galvanostat and specialized corrosion & physical electrochemistry software, facilitating accurate control and comprehensive measurements throughout the entire electrochemical testing procedure. Throughout the experiment, we harnessed the power of three exceptional electrodes: a platinum foil (serving as the auxiliary electrode, boasting an area of ~2 cm²), Hg/HgO/1M KOH (taking on the role of the reference electrode, showcasing an electrode potential of E° = 0.098 V *vs* NHE at 25°C), and an oxide film on Ni-support (our working electrode, expertly prepared following well-established literature procedures [27, 28]). To ensure seamless connections and minimize the iR drop, we seamlessly integrated a Luggin capillary, infused with gel prepared by mixing agar-agar and potassium chloride in a definite stoichiometry, into the electrochemical cell. This ingenious setup ensured a precision-driven measurement experience and empowered full control throughout the captivating electrochemical journey.

RESULTS AND DISCUSSION
X-ray diffraction (XRD)

Intriguing X-ray diffraction patterns (XRD) of $LaNiO_3$ and $La_{0.2}Sr_{0.8}NiO_3$ were explored from 20° to 100° (Figure 1). Astonishingly close matches to JCPDS ASTM file 25-1060 and COD ID 1000308 confirmed their exceptional crystallinity. In our extensive investigation, we have made captivating discoveries concerning the diffraction patterns of $LaNiO_3$ and $La_{0.2}Sr_{0.8}NiO_3$. Notably, the CA-SG method showcased its remarkable efficiency, producing materials with near-pure perovskite phases, highlighting its exceptional capabilities. To delve deeper into their characteristics, we employed Scherer's formula [$S = \frac{0.9\,\lambda}{B\,Cos\theta}$] [29] to calculate the crystallite size, yielding fascinating results. $LaNiO_3$ exhibited an impressive crystallite size of approximately 25 nm, while $La_{0.2}Sr_{0.8}NiO_3$ displayed a slightly smaller size, measuring around 18 nm. The obtained X-ray diffraction patterns for $LaNiO_3$were subjected to Rietveld refinement using Full Prof suite to calculate accurate unit cell dimensions. From the refined data the crystals were found to be of hexagonal structure with space group R -3 c and cell parameters a = b = 5.46, c = 13.19; α=β=90°,γ=120°.
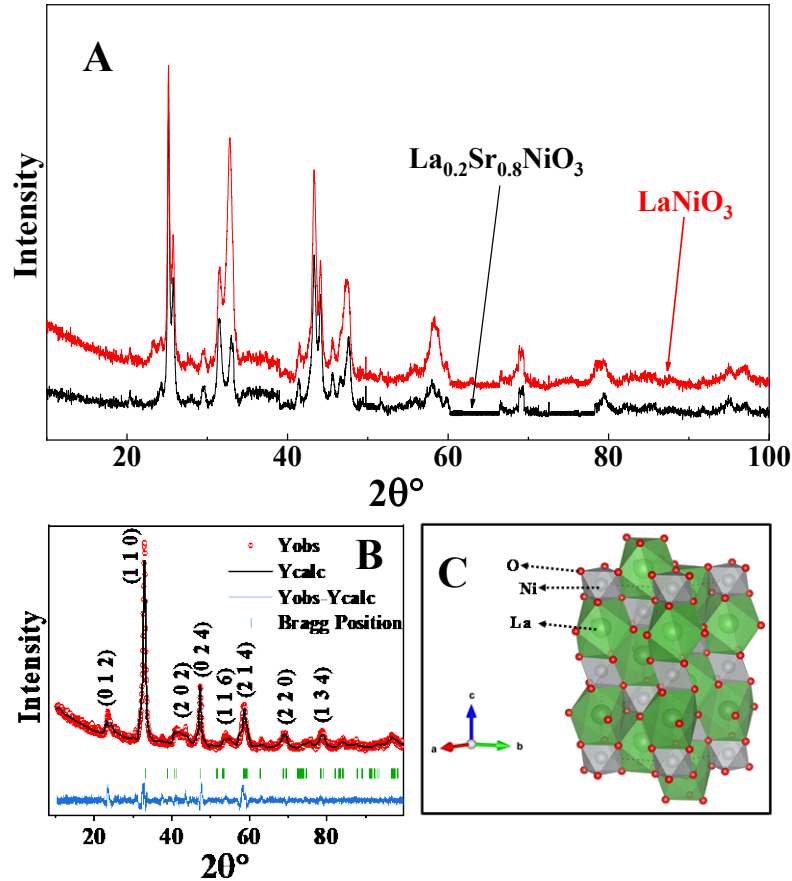
Figure 1 (A). XRD powder patterns of LaNiO₃; **(B)** Refined XRD profile of LaNiO₃; **(C)** Crystal structure of LaNiO₃
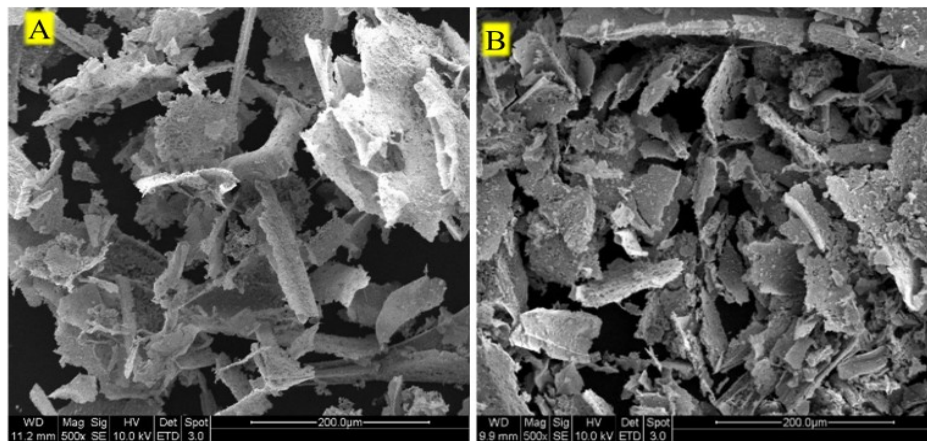
Figure 2. SE micrographs of **(A)** LaNO₃; **(B)** La$_{0.2}$Sr$_{0.8}$NiO₃ oxide powder sintered at 650°C for 6 h.

Table 1. Values of the cyclic voltammetric parameters of Ni/La$_{1-x}$Sr$_x$NiO₃ ($0 \leq x \leq 0.8$) in 1 M KOH at 25°C (scan rate = 20 mVsec^{-1})

Electrode Materials	E$_{Pa}$ (mV)	E$_{Pc}$ (mV)	ΔE$_P$ (mV)	E°= (E$_{Pa}$+E$_{Pc}$)/2 /mV	j$_{pa}$ (mA cm^{-2})	j$_{pc}$ (mA cm^{-2})	$\dfrac{j_{pa}}{j_{pc}}$	Q (mC cm^{-2})
LaNiO₃	475	382	93	428	0.66	0.33	2.0	5.8
La$_{0.8}$Sr$_{0.2}$NiO₃	481	382	99	431	0.65	0.40	1.6	8.7
La$_{0.5}$Sr$_{0.5}$NiO₃	478	381	95	430	0.94	0.57	1.6	11.3
La$_{0.2}$Sr$_{0.8}$NiO₃	482	398	84	440	1.16	0.96	1.2	23.6

The quality factors of the refined profile are in an acceptable range with χ^2 value = 2.4926 for LaNiO₃.

Scanning electron micrography (SEM)

Figure 2 shows the SE micrographs of the materials annealed at 650°C for 5 h at magnification ×500. Materials represented a flake-like structure with slightly small size for La₀.₂Sr₀.₈NiO₃, which shows better performance in the splitting of alkaline water.

Cyclic voltammetry (CV)

Behold Figure 3(A), presenting a mesmerizing cyclic voltammogram of the exquisite electrocatalyst film electrodes gracing the surface of Ni. With grace and precision, this enchanting data was measured at a scan rate of 20 mV/sec, exploring the captivating potential region of 0.0 - 0.7 V. Bathed in the brilliance of a 1 M KOH solution at a serene 25°C. Observe each voltammogram, adorned with a delightful set of redox peaks, just before the fascinating event of water splitting takes place. The corresponding redox peak potentials were found to vary with 478 ± 4 and 390 ± 8, respectively. Singh *et al.* [27] has also observed similar redox peaks with LaNiO₃ oxide electrode. According to their research, the captivating redox peaks arise from the process of gaining or losing electrons in the Ni. The formal redox potential was calculated by averaging the positive and negative potential which are almost similar with each oxide electrode. Other voltammetric parameters such as anodic & cathodic peak potential difference (ΔE_P), anodic (j_{p_a}) & cathodic (j_{p_c}) maximum current and total charge (q) obtained from the integrated CV curve are tabulated in Table 1. The enchanting value of j_{p_a}/j_{p_c}, surpasses unity, hinting at the captivating irreversibility of the redox couple. Behold, the values of the esteemed cyclic voltammetric parameters proudly grace Table 1, revealing their mystical secrets. It is noteworthy that the significant increase in charge with Sr-substitution for La in the oxide matrix leads to the improvement in catalytic activity for OER. Maximum charge value (~4 times) was observed with 0.8 mol Sr-substitution. Delving into the allure of the experiment, we ventured to study the impact of scan rate on the CV parameters. With fervor and precision, we meticulously recorded CV curves across a range of 20-120 mV sec⁻¹ in the enchanting realm of 1M KOH at STP (25°C). The voltammogram for La₀.₂Sr₀.₈NiO₃ is given in Figure 3(B). With each step of our study, a bewitching transformation unfolded: the anodic peak potentials (23-37 mV) shifted towards higher potentials, while the cathodic peak potentials (7-22 mV) drifted towards lower potentials. This mesmerizing phenomenon emerged as we increased the scan rate, promising to reveal enthralling insights into the system's dynamics. The shifting in potential indicates the irreversible [27, 28] process of electron transfer. The integrated voltammetric charge (q) was obtained by combining the positive and negative segments of the curve, up to just preceding the onset of the OER. With exception to La₀.₂Sr₀.₈NiO₃, the value of charge was found to decrease with increase of scan rate. The voltammetric charge (q) against (scan rate)⁻¹/² shows direct relation (Figure 3(C)) which indicates diffusion of species-controlled formation of redox couple at oxide/electrode interface [28, 30].

Electrocatalytic activity

The alluring world of electrocatalytic activity unfolded before our eyes as we meticulously recorded iR-compensated anodic Tafel experiments (E *vs* log j) (Figure 3(D)). This captivating endeavor took place at a leisurely scan rate of 0.2 mV/sec, immersed in 1M KOH solution at a serene 25°C. The catalyst represents similar nature in the curves regardless of the substitution of Sr for La in the LaNiO₃ lattice. For Tafel slope, we focused on initial linear section of the curve and observed that the Tafel slope value decreased with Sr-substitution except La₀.₈Sr₀.₂NiO₃ oxide. Among the oxide electrode tested, the oxide with 0.8 Sr-substitution was found to be the most active electrode towards water splitting. Gathering insights from the data relating to current density at 800 mV, a mesmerizing revelation takes shape, unveiling the distinctive order of electrocatalytic activity among the diverse oxide electrodes La₀.₂Sr₀.₈NiO₃ (j= 25.2mAcm⁻²) > La₀.₅Sr₀.₅NiO₃ (j= 4.4mAcm⁻²)> La₀.₈Sr₀.₂NiO₃ (j=3.4 mAcm⁻²) > LaNiO₃ (j= 1.9 mAcm⁻²). It is noteworthy that the Tafel slopes (85-101 mV decade⁻¹) observed with the oxide catalysts were almost similar to those reported in literature particularly for La₀.₈Sr₀.₂MnO₃ (108 mV decade⁻¹), La₀.₆Sr₀.₄MnO₃ (108 mVdecade⁻¹), La₀.₆Sr₀.₄MnO₃ (103 mVdecade⁻¹) and La₀.₇Sr₀.₃MnO₃ (92 mVdecade⁻¹) obtained by malic acid [20], citric acid [21], polyacrylic acid [22], citric acid-ethylene diamine [23] and La₀.₆Cu₀.₄CoO₃ [25] sol-gel routes, respectively. Although these oxides have similar Tafel slope values yet have better electrocatalytic activity towards OER as compared to oxides reported in the present work. But, La₀.₇Sr₀.₃MnO₃ synthesized by auto combustion technique [31] (j = 2 mA cm⁻² at 750 mV in 1M LiOH) has lower electrocatalytic property. Unveiling the order required a captivating pursuit, leading us to record the anodic polarization curve

(Figure 3(E) for $La_{0.2}Sr_{0.8}NiO_3$) across various KOH concentrations. Throughout the experiment, we ensured the uniformity of electrical intensity for each electrolytic solution. To achieve this objective, we fixed the ionic strength of 1.5 for each electrolyte by introducing KNO_3. The enchanting curve provided us with a wealth of current density data (log j in A cm^{-2}) at a specific potential. This mesmerizing data was then plotted against log [OH$^-$], creating the captivating Figure 3(F). The inclination of the line divulged an almost unity slope value for the order of reaction in every instance (Table 2). The enthralling Tafel slopes and order of the OER listed in Table 2, suggest the compelling proposition: the OER occurring at the electrocatalysts goes on with the similar mechanism.
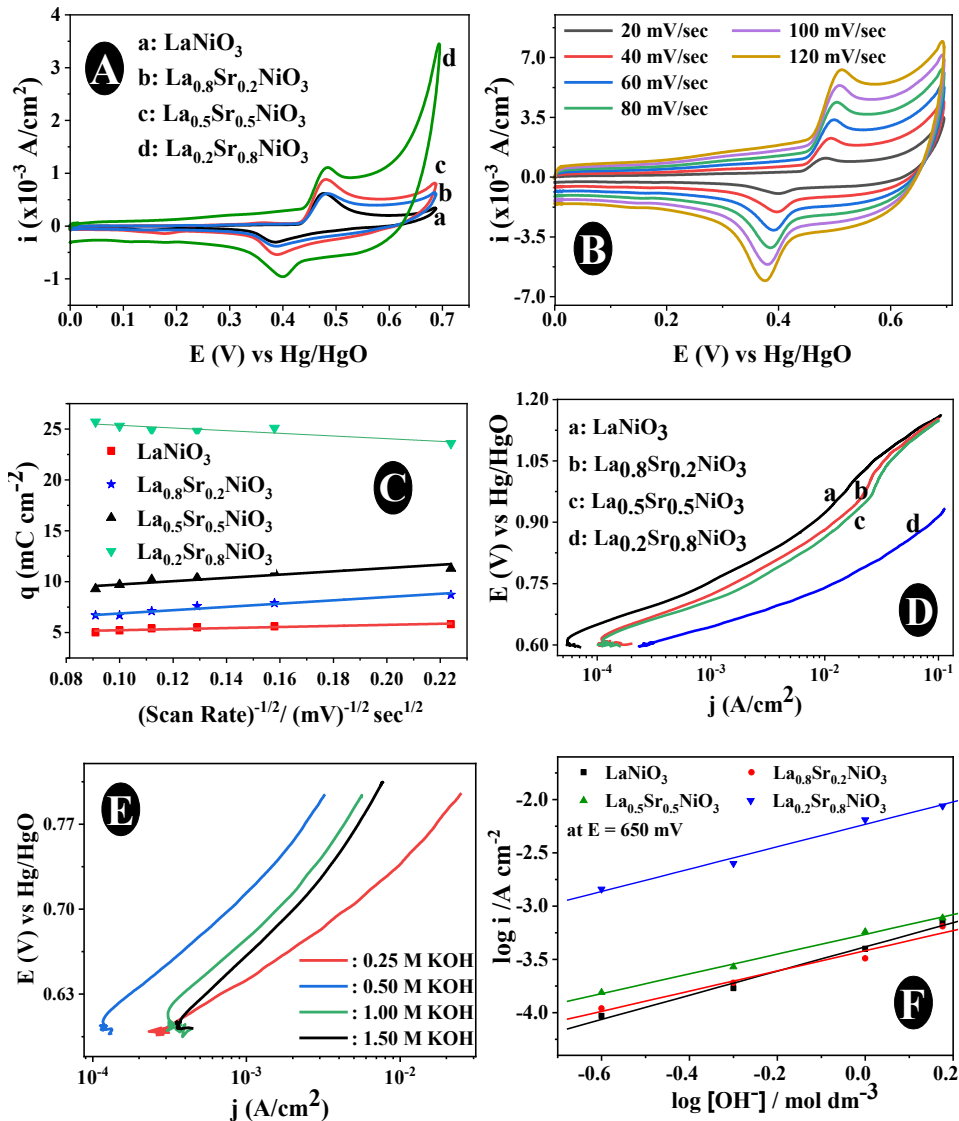
Figure 3. (A) Cyclic voltammograms of Ni/$La_{1-x}Sr_xNiO_3$ ($0 \leq x \leq 0.8$) film electrode at 20 mV sec^{-1} scan rates in 1M KOH (25°C); **(B)** CV of Ni/$La_{0.2}Sr_{0.8}NiO_3$ film electrode at different scan rates in 1M KOH (25 ˚C); **(C)** Plot of voltametric charge (q) *vs* (scan rate)$^{-1/2}$ for the oxide film electrode on Ni; **(D)** Anodic polarization curve for Ni/$La_{1-x}Sr_xNiO_3$ ($0 \leq x \leq 0.8$) in 1M KOH (25°C); SR: 0.2 mVsec^{-1}; **(E)** Tafel curves of Ni/$La_{0.2}Sr_{0.8}NiO_3$ in different KOH concentrations ($\mu = 1.5$) at 25°C; **(F)** Plot of log j *vs* log [OH$^-$] for the oxide electrode at 25°C

Table 2. Electrode kinetic parameters for oxygen evolution reaction on Ni/La$_{1-x}$Sr$_x$NiO$_3$ ($0 \leq x \leq 0.8$) in 1 M KOH at 25 ˚C

Electrode	Tafel slope / mVd^{-1}	Order (p)	E/ mV at j (mA cm^{-2})		j (mA cm^{-2}) at E / mV		
			10	100	700	750	800
LaNiO$_3$	95	1.2	926	1162	0.3	0.9	1.9
La$_{0.8}$Sr$_{0.2}$NiO$_3$	101	0.9	885	1159	0.6	1.5	3.4
La$_{0.5}$Sr$_{0.5}$NiO$_3$	89	0.9	867	1150	0.8	2.0	4.4
La$_{0.2}$Sr$_{0.8}$NiO$_3$	85	1.0	740	916	4.0	11.5	25.2
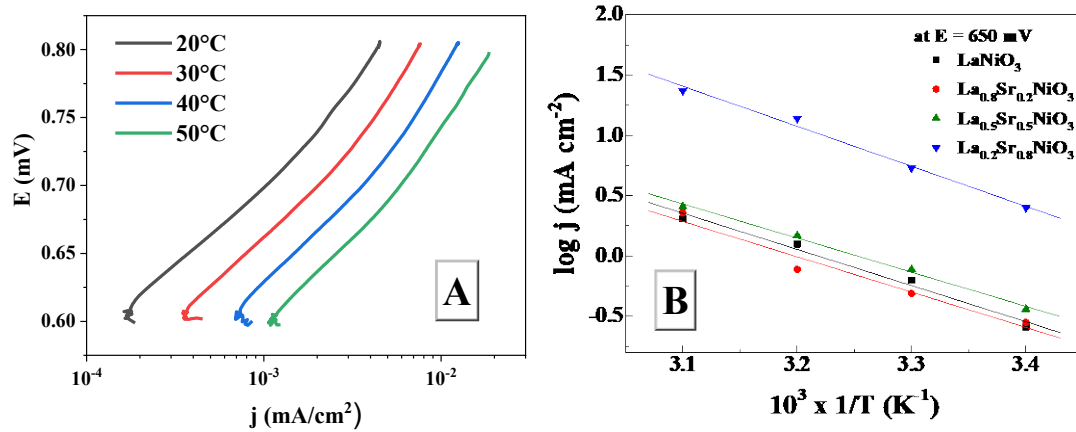
Figure 4. (A) Anodic polarization curve for the oxide film electrodes, La$_{0.2}$Sr$_{0.8}$NiO$_3$, at different temperatures; **(B)** Arrhenius plot for the oxide electrode at a constant applied potential (650 mV) in 1 M KOH

Table 3. Thermodynamic parameters for O$_2$ evolution on Ni/La$_{1-x}$Sr$_x$NiO$_3$ ($0 \leq x \leq 0.8$) in 1 M KOH

Electrode	$\Delta H_{el}^{\circ \neq}$ (KJ mol^{-1}) at E = 650 mV	$-\Delta S^{\circ \neq}$ (J deg^{-1} mol^{-1})	α	$\Delta H^{\circ \neq}$ (KJ mol^{-1})
LaNiO$_3$	36.9	227.4	0.6	57.7
La$_{0.8}$Sr$_{0.2}$NiO$_3$	36.9	227.4	0.6	57.7
La$_{0.5}$Sr$_{0.5}$NiO$_3$	34.5	233.5	0.5	51.5
La$_{0.2}$Sr$_{0.8}$NiO$_3$	39.6	199.5	0.6	61.0

Thermodynamic study

Embarking on a captivating journey into thermodynamic parameters, we recorded anodic polarization in 1M KOH at varying temperatures. Witness the enchanting Figure 4(A), featuring a set of mesmerizing polarization curves at 20, 30, 40, and 50°C for La$_{0.2}$Sr$_{0.8}$NiO$_3$ at unwaveringly maintained steadfast temperature for the reference electrode. From the captivating Arrhenius plot, log j vs 1/T (Figure 4(B)), at a specific potential of 650 mV, we derived the standard apparent enthalpy of activation ($\Delta H_{el}^{\neq}$). This mesmerizing parameter was skillfully evaluated inclination of the plots. The value of log j (in mA cm^{-2}) was diligently deduced from the curve, meticulously measured at varying temperatures. Furthermore, by using relations (1) and (2) [32, 33] more thermodynamic parameter was investigated:

$$\Delta H_{el}^{\circ \#} = \Delta H^{\circ \#} - \alpha F \qquad (1)$$

$$\Delta S^{\circ \#} = 2.3R \left[\log j + \Delta H_{el}^{\circ \#} / 2.3RT - \log(nF\omega C_{OH^-}) \right] \qquad (2)$$

The terms mentioned in relation (1) and (2) have their general meanings. The transfer coefficient (α) was determined by using the relation 2.303RT/bF. In this captivating pursuit, the gas constant (R), Faraday constant (F), Tafel slope ('b') in mV decade^{-1} and overpotential (η) [34], absolute temperature (T) played pivotal roles. Within the realm of equation (2), an enthralling frequency factor ω (= k$_B$T/h) emerges, with k$_B$ and h signifying the universal constants. Embarking on meticulous calculations, we derived the values of these captivating thermodynamic parameters, tabulated in the illustrious Table 3. From the table, it is observed that each oxide electrode has almost similar value of activation energy. The emergence of a profoundly negative value for $\Delta S^{\circ \#}$ holds captivating implications, pointing to the intriguing involvement

124

of captivating interactions during the oxygen evolution reaction.

CONCLUSION

The captivating findings from this research work unveil the profound influence of Sr substitution in the base oxide (LaNiO$_3$) on both its physicochemical and electrocatalytic properties. The oxide, La$_{0.2}$Sr$_{0.8}$NiO$_3$, boasts an astonishing 12-fold increase in catalytic power compared to LaNiO$_3$ in the realm of alkaline water splitting. Additionally, the XRD data showcases nearly pure phases of the oxide materials, adding to their enchanting allure.

REFERENCES

1. Y. Matsumoto, E. Sato, *Electrochim. Acta*, **24,** 421 (1979).
2. Y. Matsumoto, S. Yamada, T. Nishida, E. Sato, *J. Electrochem. Soc.,* **127,** 2360 (1980).
3. S. Yamada, Y. Matsumoto, E. Sato, *J. Electrochem. Soc. Jpn.,***49,** 269 (1981).
4. B. JO'M, T. Otagawa, Young, *J. Electroanal. Chem. Interfacial Electrochem.,* **150** 633 (1983).
5. S. Tiwari, P. Chartier and R. N. Singh, *J. Electrochem. Soc.,***142,** 148 (1995).
6. D. Meadowcroft, *Nature,* **226,** 847 (1970).
7. Y. Shimizu, H. Matsuda, N. Miura, N. Yamazoe, *Chem. Lett.,* **21,** 1033 (1992).
8. J. Suntivich, H. A. Gasteiger, N. Yabuuchi, H. Nakanishi, J. B. Goodenough, Y. Shao-Horn, *Nat. Chem.,***3,** 546 (2011).
9. J. Chang, Y. Xiao, M. Xiao, J. Ge, C. Liu, W. Xing, *ACS Catal.,***5,** 6874 (2015).
10. S. Jin, *Acs Energy Letters,* **2,** 1937 (2017).
11. D. E. Hall, *J. Electrochem. Soc.*, C41 (1985).
12. L. Chen, A. Lasia, *J. Electrochem. Soc.*, **138,** 3321 (1991).
13. J. De Carvalho, G. Tremiliosi Filho, L. A. Avaca, E. Gonzalez, *International Journal of Hydrogen Energy,***14,** 161 (1989).
14. Y. Ogata, H. Hori, M. Yasuda, F. Hine, *J Electrochem. Soc,*, **135,** 76 (1988).
15. D. E. Hall, *J Appl Electrochem*, 107 (1984).
16. K. Zeng, X. Zheng, C. Li, J. Yan, J. H. Tian, C. Jin, P. Strasser, R. Yang, *Adv. Funct. Mater.,***30,** 2000503 (2020).
17. J. O. M. Bockris, T. Otagawa, *J. Electrochem. Soc.,***131,** 290 (1984).
18. J. Balej, *Int. J. Hydrogen Energy,***10,** 89 (1985).
19. A. Kobussen, F. Van Buren, T. Van den Belt, H. Van Wees, *J. Electroanal. Chem.,***115,** 131 (1980).
20. N. K. Singh, S. Tiwari, R. N. Singh, *Int. J. Hydrogen Energy,* **23,** 775 (1998).
21. T. Sharma, N. K. Singh, S.K. Tiwari, R. N. Singh, *Ind. J. Eng. Mat. Sci.*, **5,** 38 (1998)
22. N. K. Singh, B. Lal, R. N. Singh, *Int. J. Hydrogen Energy,***27,** 885 (2002).
23. B. Lal, N. K. Singh, R. N. Singh, *Indian J. Chem.,***40A***,* 1269 (2001).
24. B. Lal, M. Raghunandan, M. Gupta, R. N. Singh, *Int. J. Hydrogen Energy,* **30,** 723 (2005).
25. N. K. Singh, M. Yadav, C. Fernandez, *Int. J. Electrochem. Sci.,***12,** 7128 (2017).
26. J. K. Vassiliou, M. Hornbostel, R. Ziebarth, F. J. Disalvo, *J. Solid State Chem.,***81,** 208 (1989).
27. R. N. Singh, S. Tiwari, S. Singh, A. Jain, N. K. Singh, *Int. J. Hydrogen Energy,* **22,** 557 (1997).
28. R. N. Singh, S. K. Tiwari, S. P. Singh, N. K. Singh, G. Poillerat, P. Chartier, *J. Chem. Soc. Faraday Trans.,***92,** 2593 (1996).
29. N. Fradette, B. Marsan, *J. Electrochem. Soc.,***145,** 2320 (1998).
30. N. K. Singh, P. Sharma, M. K. Yadav, R. Parihar, *Int. J. Electrochem. Sci.,***15,** 7001 (2020).
31. B. Shin, S. Choi, Y. Tak, *Int. J. Electrochem. Sci,* 5900 (2016).
32. N. K. Singh, P. Sharma, I. Kumar, A. S. Chaddha, *Int. J. Electrochem. Sci*, **14,** 11379 (2019).
33. E. Gileadi, Electrode Kinetics, VCH Publishers Inc, New York, USA, 1993, p. 151.
34. R. N. Singh, J. Pandey, N. K. Singh, B. Lal, P. Chartier, J.-F. Koenig, *Electrochim. Acta*, **45,** 1911 (2000).

Modification in thermal and electrical characteristics of royal palm frond (*roystonea regia*) through blending with high-density polyethylene

R. Patwal[1], V. Arya[1], M. Aziz[1], S. Pandey[1], T.I. Siddiqui[2], S. Mehtab[1*], M.G.H. Zaidi[1*]

[1]*Department of Chemistry, College of Basic Sciences and Humanities, G. B. Pant University of Agriculture and Technology, Pantnagar, U. S. Nagar (213145), India*
[2]*Department of Chemistry, Sir Syed Faculty of science, Mohammad Ali Jauhar University, Rampur 244901, India*

The objective of this research is to characterize royal palm fronds (RPFs) and fabricate biocomposites (BCs) by reinforcing the RPF powder with high-density polyethylene (HDPE). RPF was grinded into powder, and various analyses were conducted to determine their moisture content, lignin content, and water and alcohol-benzene solubility. HDPE was dissolved in xylene solvent and RPF powder was mixed with molted HDPE to fabricate polymer BCs. The fabricated polymer BCs underwent examination for their electrical conductivity and thermal stability using direct current (σDC) conductivity and thermogravimetric-differential thermal analysis-differential thermogravimetry (TG-DTA-DTG). The results showed that the electrical conductivity and thermal stability of the BCs were significantly lower compared to the original royal palm frond fibers.

Keywords: Biocomposites, Royal palm, Lignocellulosic biomass, HDPE.

INTRODUCTION

Agricultural waste has received growing attention over decades for sustainable development of society and industries. Worldwide production of biomass per year is estimated to be approximately 140 gigatons (Gt) [1]. Palm waste is a major portion of agriculture waste which accounts for millions of metric tons annually [2]. It consists of solid waste (empty fruit bunches, palm kernel shells, fibers, trunk residues) and liquid waste (palm oil mill effluent) [3]. It requires proper management to reduce environmental impact. Management practices include waste-to-energy conversion, composting, biomass utilization, sustainable production practices and wastewater treatment [4, 5]. Efficient management of palm waste reduces pollution, offers economic opportunities, and promotes sustainability in the palm oil industry [6].

Royal palm is a kind of ornamental palm tree, mostly planted at the roadsides [7]. Royal palm tree sheds fronds periodically as a waste material. These fronds can be utilized in various ways such as building material for roofs, buckets, furniture, utensils, and polymer composites [8-10]. Palm fronds, a common waste material produced by palm tree residues, often present challenges in terms of disposal due to the environmental pollution caused by burning them. However, there are several alternative methods available for managing palm fronds in a more sustainable manner. Composting is a popular option, where palm fronds are decomposed under controlled conditions to create nutrient-rich soil. This process not only eliminates waste but also produces organic fertilizer or soil amendments, benefiting plant growth and soil health [11, 12]. Another method is mulching, where shredded or chipped palm fronds are spread around plants to retain moisture, suppress weeds, and improve overall soil quality [13]. As the fronds gradually break down, they release valuable nutrients into the soil.

Modification of wood through reinforcing polymer materials has received growing attention since decades [14]. Lignocellulosic biomass represents a promising solution for sustainable development, capable of meeting the growing global demand. The fronds of the Royal palm (*Roystonea regia*) can be classified as lignocellulosic waste, which presents an opportunity for resource utilization. Royal palm fiber-based products have emerged as cost-effective and potent materials for the production of composites [15]. By harnessing the lignocellulosic properties of the waste from the Royal palm, it becomes feasible to convert this material into valuable resources, thereby contributing to sustainability and resource optimization. Royal palm-derived composites find applications in diverse fields such as construction materials, sound barriers, agriculture, eco-friendly materials, bioplastics, and biocomposites [16].

---

* To whom all correspondence should be sent:
E-mail: mgh_zaidi@yahoo.com, smiitr@gmail.com

Palm waste has advantages over other agrowaste derived from stubble, straw, bagasse, and low-grade wood. It is abundantly available, grows quickly, producing fronds multiple times a year, making it a more preferable renewable and sustainable resource for composite development [17]. Also, palm fronds possess strength and flexibility, enhancing composite performance. They are lightweight, reducing overall product weight for practical applications. Palm frond waste is often cost-effective due to its availability and lower cost compared to other materials [18].

Biomass conversion technologies offer an innovative approach to managing palm fronds. Processes such as anaerobic digestion and gasification can convert the fronds into biogas, biofuels, or other forms of energy [19, 20]. This not only reduces waste but also generates renewable energy, contributing to a more sustainable energy mix. Additionally, palm fronds can be used as providing insulation and moisture absorption for livestock or animal shelters [21]. Palm fronds also have creative applications. They can be woven into baskets, mats, or used as material for crafting decorative items [22]. This approach promotes recycling and repurposing, reducing waste and adding aesthetic value to the fronds. While landfill disposal can be a last resort when no other options are available, it should be avoided due to its negative environmental impact.

EXPERIMENTAL

Material and method

In this research study, a novel approach was adopted to fabricate a polymer bio-composite by combining high-density polyethylene (HDPE) and RPF powder. Initially, both HDPE and RPF were ground into powder. Next, HDPE was dissolved in xylene solvent at a temperature of 90 ºC while continuously stirring in isolated conditions. In the following step, RPF was added to the thick HDPE slurry with continuous stirring at a speed of 1000 rpm. The bio-composites (BCs) were prepared using HDPE and RPF in 10:90 wt %, respectively. A masterbatch was prepared by blending melted HDPE powder and RPF powder, which underwent compression pressure of 2000 psi and heating to a temperature of 200 ºC at a rate of 1.25 ºC per minute for a duration of 2 hours. During this process, the pressure gradually stabilized at around 1800 psi, indicating the completion of the compression. Efforts have been made to develop the BCs with uniform thickness and stable mechanical strength. The binding capability of HDPE with RPF powder

was found appropriate in fabrication of bio-composite.

RESULTS AND DISCUSSION

Moisture content

The RPF was transformed into powder (Fig. 2). This RPF powder was utilized to determine its moisture content. 5gm of RPF powder was dried in an oven at 50°C. The weight of the RPF powder was measured at regular intervals, typically every hour, until a constant weight was achieved, indicating complete drying of RPF powder. % Moisture content = $(5 - 4.53 / 5) \times 100 = 9.41$ %.
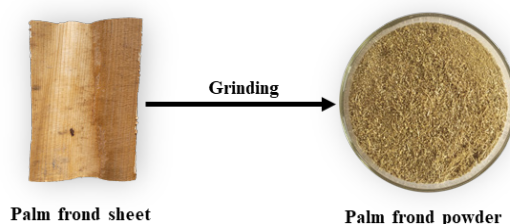

Fig. 1. Conversion of RPF sheets into powder

Water solubility analysis

ASTM D1106-56 was followed to determine the solubility of the RPF powder in distilled water as a solvent. Adding 2 g of the RPF powder to a beaker with 300 ml of distilled water at 23 ± 2°C and stirring it thoroughly for 48 h the insoluble residue was filtered out with the help of filter paper and oven dried at 50°C for 4 h. The weight of insoluble residue found was 1.6 g.

% Water solubility = (Wt. of powder sample - Wt. of residue / Wt. of powder sample) × 100
% Water solubility = $(2 - 1.6 / 2) \times 100 = 20$ %

Alcohol-benzene solubility

ASTM D1107-56 was followed for the alcohol and benzene solubility test of the RPF powder. 5 g of the previously dried RPF powder was packed in muslin cloth and placed in the Soxhlet and examined. This whole process of Soxhlet extraction method took 6 h, after that the residue was dried and weighed several times until its weight got constant, indicating that the residue is free from solvent. Total weight of the residue was found to be 4.48 g.

% Alcohol-benzene solubility = (Wt. of powder sample - Wt. of residue / Wt. of powder sample) × 100
% Alcohol-benzene solubility = $(5 - 4.48 / 5) \times 100 = 10.4$ %.

Lignin content

ASTM D1106-96 is a standard test method for acid-insoluble lignin in wood and lignocellulosic materials like RPF powder. A representative palm frond sample was finely ground and transferred to a

500 mL Erlenmeyer flask. To the flask, 72 mL of 72 % sulfuric acid and 8 mL of 37 % hydrochloric acid were added and mixed thoroughly. The flask was heated on a 100°C water bath for 1 hour. After acid extraction, the flask was cooled, and the acid-insoluble residue was filtered using pre-weighed filter paper and vacuum filtration. The residue was washed with hot water until neutral, dried in a 50°C oven until a constant weight was achieved, and then weighed and recorded.

% Lignin = (Wt. of powder sample - Wt. of residue / Wt. of powder) × 100

% Lignin = (1 – 0.45/1) × 100 = 55 %.

Electrical conductivity

I-V characteristics for BCs derived from RPF and HDPE powder were determined with increasing voltage from 5 to 30 V [23]. RPF has rendered gradual rise in current ranging from 0.0439 to 0.17 A whereas BCs showed a rise in current from 0.028 to 0.138 A. The fabricated biocomposite exhibits lower electrical conductance compared to the RPF (Fig. 2).
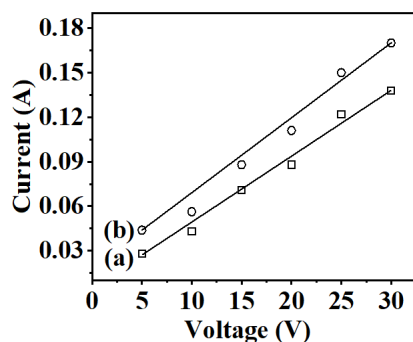
Fig. 2. I-V characteristics of (a) BCs, (b) RPF.

Thermal stability

Thermal stability of the materials and BCs was ascertained through DTG-TG-DTA [24-26]. The relative thermal stability of HDPE (Fig. 3a), RPF powder (Fig. 3b), and BCs (Fig. 3c) was investigated through their respective TG-DTA-DTG. TG demonstrates the weight loss rendered by the material with reference to temperature at a constant heating rate. Decomposition of material in TG is expressed as TG onset. Prior to TG onset, weight loss associated with material was attributed to moisture content. TG endset is the temperature at which the thermal decomposition of material is concluded. Beyond TG endset the residual weight associated with the sample is termed as char yield. Multiple steps in TG demonstrate the various stages of the decomposition process which is revealed through DTA. DTG demonstrates a rate of degradation of materials. Wide DTA peaks demonstrate the amorphous behavior of HDPE, RPF

128

powder and BCs. Fig. 3a showing simultaneous TG-DTA-DTG of HDPE reveals TG onset at 400°C leaving 98.0 % weight residue. Prior to TG onset, 0.1 % weight loss by HDPE at 99.9°C corresponds to moisture content associated with HDPE. DTG reveals the single step degradation of HDPE with weight loss at a rate of 3.527 mg/min at 473°C. Major peaks correspond to degradation temperature (weight residue %) at 100 (99.9) and 400 (98.0), and have shown endset at 95°C leaving 1.1 % weight residue.
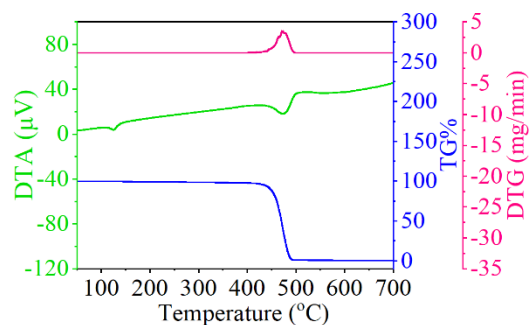

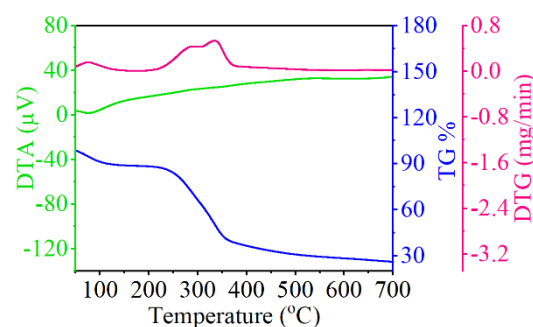**Fig. 3 (a).** TG-DTA-DTG of HDPE.

Fig. 3 (b). TG-DTA-DTG of RPF.

Fig. 3b represents simultaneous TG- DTA- DTG of RPFP which reveals TG onset at 223.0°C leaving 87.49 % weight residue. Prior to TG onset 8.7 % weight loss attributes to residual moisture associated with RPF powder at 99.9°C without appearance of any rate of dehydration. RPF powder has shown major peaks corresponding to degradation temperature (weight residue %) at 289 (75.4) and 338.5 (53.3) with the degradation rate of 0.440 and 0.532 mg/min, respectively. The endset corresponds to 363.2°C leaving 40.1 % weight residue. It is also showing a minor peak at 75°C with the rate of 0.159 mg/min.

Fig. 3c represents simultaneous TG- DTA- DTG of BCs, revealing TG onset at 241.0°C leaving 88.1 % weight residue. Prior to TG onset 6.4 % weight loss by BCs at 99.9°C attributed to residual moisture with BCs. DTG reveals the expulsion of moisture from BCs at the rate of 0.102 mg/min at 99.9°C. BCs shows major peaks corresponding to degradation temperature (weight residue %) at 278 (75.4) and

329.5 (53.3) with the degradation rate of 0.372 and 0.596 mg/min, respectively. The endset corresponds to 347.2°C leaving 49.5 % weight residue.
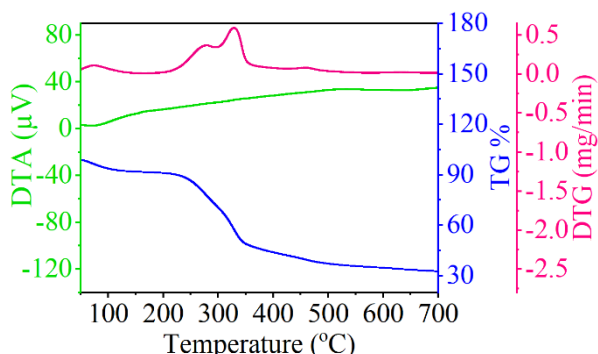

Fig. 3(c). TG-DTA-DTG of RPF.

The research findings indicate that the moisture content of RPF powder was determined to be 9.41 %. Furthermore, the percent water solubility of RPF powder was found to be 20 % and the percent alcohol-benzene solubility was found to be 10.4 %, indicating the solubility of RPF powder in different solvents. The lignin content of the RPF powder was found to be 55 %, suggesting a significant presence of lignin in the sample.

The resulting polymers BCs were subjected to examinations for electrical conductivity, and thermal stability using direct current (σDC) conductivity, and thermogravimetric-differential thermal analysis-differential thermogravimetry (TG-DTA-DTG), respectively. The findings revealed a decrease in electrical conductivity and an increase in thermal stability in the BCs compared to the original royal palm frond fibers.

CONCLUSION

In conclusion, the research findings provide valuable insights into the characteristics of RPF powder and its resulting polymer BCs. The moisture content of the RPF powder was determined to be 9.41 %, indicating a relatively low moisture content. The solubility tests showed that the RPF powder had a water solubility of 20 % and alcohol-benzene solubility of 10.4 %, suggesting its solubility in different solvents. The presence of lignin in the RPF powder was significant, with a content of 55 %.

Moreover, the examination of the resulting polymer BCs revealed interesting observations. The electrical conductivity of the BCs was found to decrease compared to the original royal palm frond fibers. This indicates that the transformation process from RPF powder to BCs resulted in a decrease in electrical conductivity. On the other hand, the thermal stability of the BCs increased, suggesting improved resistance to high temperatures. These findings suggest that the transformation process

alters the properties of the fibers, making them more suitable for applications requiring enhanced thermal stability.

Overall, this research provides important information about the composition and characteristics of RPF powder and its resulting polymer BCs. It contributes to our understanding of the potential applications of RPF powder and the effects of the transformation process on its properties. Further studies can build upon these findings to explore the practical implications and potential uses of RPF powder and BCs in various fields.

REFERENCES

1. N. Tripathi, C. D. Hills, R. S. Singh, C. J. Atkinson, *NPJ Clim. Atmos. Sci.*, **2**, 35 (2019).
2. M. K. Sridhar, O. O. AdeOluwa, *Biotechnology for Agro-Industrial Residues Utilisation: Utilisation of Agro-Residues*, 341 (2009).
3. P. F. Rupani, R. P. Singh, M. H. Ibrahim, N. Esa, *World Appl. Sci. J.*, **11** (1), 70 (2010).
4. S. D. Oseghale, A. F. Mohamed, A. O. Chikere, *OIDA Int. J. Sustain. Dev.*, **10** (12), 41 (2017).
5. M. K. Awasthi, S. Sarsaiya, A. Patel, A. Juneja, R. P. Singh, B. Yan, M. J. Taherzadeh, *Renew. Sustain. Energy Rev.*, **127**, 109876 (2020).
6. Y. D. Tan, J. S. Lim, *Renew. Sustain. Energy Rev.*, **111**, 507 (2019).
7. U. Adzkia, N. Nugroho, I. Z. Siregar, L. Karlinasari, *Biodiversitas*, **21** (3), (2020).
8. C. Belgacem, F. Serra-Parareda, Q. Tarrés, P. Mutjé, M. Delgado-Aguilar, S. Boufi, *Polymers*, **13** (14), 2335 (2021).
9. R. Kumar, A. Thakur, R. Thakur, P. K. Dogra, *Recent Advanced Future Persp.*, 129 (2022).
10. M. A. Binhussain, M. M. El-Tonsy, *Constr. Build. Mater.*, **47**, 1431 (2013).
11. U. Ali, N. Sajid, A. Khalid, L. Riaz, M. M. Rabbani, J. H. Syed, R. N. Malik, *Env. Pro. Sustain. Ener.*, **34** (4), 1050 (2015).
12. P. F. Rupani, R. P. Singh, M. H. Ibrahim, N. Esa, *World Appl. Sci. J.*, **11** (1), 70-81 (2010)
13. A. Alfarisi, T. Mandang, A. Sutejo, *Earth Environ. Sci.*, **1038** (1), 12064 (2022).
14. S. Mahtab, S. Masroor, N. Siddiqui, M. G. H. Zaidi, *Mater. Today: Proceed.*, **26**, 1831 (2020).
15. J. Agarwal, S. Sahoo, S. Mohanty, S. K. Nayak, *J. Thermoplast. Compos. Mater.* **33** (7), 978 (2020).

16. O. Faruk, J. Tjong, M. Sain (eds.), Lightweight and Sustainable Materials for Automotive Applications, Boca Raton, CRC Press, 2017.

17. S. K. Agarwal, Air Pollution, APH Publishing, New Delhi, 2005.

18. A. Karimah, M. R. Ridho, S. S. Munawar, D. S. Adi, R. Damayanti, B. Subiyanto, A. Fudholi, *J. Mater. Res. Technol.*, **13**, 2442 (2021).

19. H. A. Umar, S. A. Sulaiman, M. M. Said, A. Gungor, M. Shahbaz, M. Inayat, R. K. Ahmad, *Biomass and Bioenergy*, **151**, 106179 (2021).

20. S. S. Harsono, P. Grundmann, S. Soebronto, *J. Clean. Prod.*, **64**, 619 (2014).

21. J. Ly, L. Ayala, *Cuban J. Agric. Sci.*, **52** (4), (2018).

22. I. U. Hag, S. Ijaz (eds.), Etiology and Integrated Management of Economically Important Fungal Diseases of Ornamental Palms, Springer, 2020.

23. S. Mehtab, M.G.H. Zaidi, A. Singh, M. Pandey, A. Mahra, S. Sharma, M. Aziz, D. Palariya, B. Singhal, *Environ. Sci. Pollut. Res.*, **30**, (2023).

24. M. Kumar, P. L. Sah, M. G. H. Zaidi, A. Srivastav, *Advanced Mater. Research*, **214**, 392 (2011).

25. B. Kumar, M. G. H. Zaidi, S. Rathore, A. K. Rai, I. S. Thakur, P. L. Sah, *Instrum. Sci. Technol.*, **34** (1), 67 (2006).

26. T. K. Joshi, M. G. H. Zaidi, P. L. Sah, S. Alam, *Polymer International*, **54** (1), 198 (2005).

Synthesis and characterization of xanthan gum and carboxymethylcellulose sodium salt based ionic crosslinked hydrogels for agricultural application

R. Yadav, Ayush, Manu, A. Rani*

Department of Applied Chemistry, Delhi Technological University, Delhi-110042, India

Ever-growing world population is creating immense pressure on the agriculture sector leading to the overexploitation of resources, soil degradation, and water scarcity which in turn significantly reduces crop yield. To break this destructive loop, a current investigation is initiated aiming at the development of new materials, carboxymethylcellulose sodium salt (NaCMC)-based ionic (Fe^{3+}) cross-linked hydrogels ($XG-Fe_{1-5}$, $NaCMC_{1-5}$, and $XG-Fe-NaCMC_{1-5}$). The hydrogels were characterized using Fourier-transform infrared spectroscopy, thermogravimetric analysis, scanning electron microscopy, and X-ray diffraction analysis. The study confirms that the hydrogel, XG-Fe-NaCMC with maximum thermal stability and swelling index, has potential application in agriculture improving the water holding and retention capacity of the soil. Moreover, a significant positive effect on the growth of wheat grass *(Triticum aestivum)* was recorded in a pot experiment. It showed that the plants grew faster in the soil treated with urea-loaded XG-Fe-NaCMC than the plants raised in soil treated directly with urea. The current investigation, for the first time, approached the development of hydrogels by crosslinking dual anionic natural polysaccharides *via* trivalent ions for agricultural applications.

Keywords: Hydrogel; NaCMC; Xanthan gum; Agriculture

INTRODUCTION

The efficient use of water resources for crop production is a major step toward sustainable agriculture. In this context, the Government of India has sponsored a scheme "per drop more crop." It promotes water management mainly through micro irrigation (Drip and Sprinkler irrigation systems) and the adoption of micro-level water storage systems in agricultural fields [1]. The application of 3-D polymeric matrices (hydrogels, HGs), with the ability to absorb and hold a large amount of water, to agricultural fields is a chemical approach to support the scheme. These hydrogels act as on-the-spot tiny water reservoirs, releasing up to 95% of adsorbed water into the soil during drought water stress [2-4]. Also, they amend the properties of the soil in favor of plant growth [2]. Most synthetic and semi-synthetic hydrogels employed in agriculture today contain acrylic acid derivatives and polyacrylamide in their basic skeletal framework [6, 7]. Their persistence in the soil is a serious environmental problem. Moreover, the residual acryl amide in polyacrylamide is a potential soil and food contaminant [3]. It necessitates the utilization of benign materials to design safer hydrogels for agricultural applications [8-11].

The use of cellulose (a natural polysaccharide) for the synthesis of hydrogels has been rising in popularity day-by-day as it is ubiquitous in nature,

less expensive, and environmentally safe. Agro-wastes [12, 14], office waste papers [15, 16], and waste products of cotton industries (cotton linters, and knitted rag) [4,5] are rich sources of cellulose. The presence of many reactive hydroxyl groups on polymeric chains facilitates their structural modifications thereby introducing a new set of physicochemical properties [6]. Carboxymethyl cellulose (CMC), is one such derivative of cellulose synthesized by reacting sodium mono chloroacetate and cellulose in an alkaline medium [20, 21]. Its sodium salt (NaCMC) is non-toxic, biocompatible, bioadhesive, biodegradable, and water-soluble. More COO^- functional groups increase the water storage ability of polymers due to an increase in oxygen content in the framework. The introduction of carboxylate functional groups also allows the polymeric chains to link together *via* multivalent ionic crosslinkers to develop 3-D network of hydrogels [22-26]. It is evident that trivalent iron (Fe^{3+}) is a safe and non-toxic crosslinking agent.

Xanthan gum (XG) is a water-soluble, anionic, exocellular microbial polysaccharide (PS). It is produced by the microbe *Xanthomonas campestris*. It consists of β(1→4) linked glucan backbone with alternating charged trisaccharide side chain containing a glucuronic acid residue between two mannose units [7]. XG plays diverse roles in food, medical, cosmetic industries and oil fields [8].

---

* To whom all correspondence should be sent:
E-mail: archanarani@dce.ac.in

Presently, it is attracting enormous attention of scientists by exhibiting ~~positive~~ synergistic action with different polysaccharides such as partially hydrolyzed polyacrylamide (HPAM) [9], galactomannans (guar gum and locust bean gum) [30, 31], gum Arabic [10], Konjac gum [11]. It is now well established that the synergistic combination brings about additional functional properties to the mixture, compared to polysaccharide alone. Studies also confirm that positive results are obtained with XG/PS in 1:1 ratio (w/w) [11,12].

To our knowledge, combined effect of XG/NaCMC has been rarely investigated. The current investigation, therefore set out to develop a series of hydrogels (XG-Fe-NaCMC 1-5) by crosslinking XG, NaCMC (1:1) through Fe^{3+} ions for agricultural applications. Swelling test demonstrated the optimum concentration for crosslinker. Thus, optimal hydrogel XG-Fe-NaCMC was characterized by Fourier Transform infrared (FTIR) spectroscopy, scanning electron microscopy, energy dispersive X-ray analysis (SEM/EDX), and thermogravimetric analysis (TGA). We also report herein the impact of hydrogel on the growth of wheat grass (*Triticum aestivum*) in terms of average number of germinated seeds, average shoot height (cm), average root length (cm), total fresh weight (g) and total dry weight (g) of wheat grass raised for 15 days in normal environmental conditions.

MATERIALS AND METHODS

Chemicals

Commercial XG powder was purchased from the local market, anhydrous iron (III) chloride was procured from Merck Lifesciences Pvt Ltd, NaCMC and urea were purchased from CDH Pvt. Ltd., Milli Q grade water was used to prepare aqueous solutions.

Synthesis of hydrogels (HGs)

Three sets of HGs were prepared using varied amounts of Fe^{3+} as crosslinker; i) xanthan gum hydrogel (XG-Fe 1-5), ii) carboxy methylated cellulose hydrogels (NaCMC-Fe 1-5), and iii) xanthan gum, carboxy methylated cellulose (1:1) hydrogels (XG-Fe-NaCMC 1-5) (Table 1). Briefly, the desired amount of xanthan gum and /or sodium carboxy methylated cellulose was stirred in 40 mL of distilled water with the help of magnetic stirrer until a uniform thick solution is obtained. 40 ml of $FeCl_3$ solution with requisite amount of $FeCl_3$ was added to this aqueous-viscous solution and kept for 2 days at room temperature. The resultant hydrogels were washed thoroughly in distilled water to avoid unreacted materials and then dried in an oven at 70°C until constant weight.

Swelling study

The swelling of HGs was investigated by gravimetric analysis. Dried samples of hydrogels were accurately weighed and immersed in 250 mL of distilled water. At predetermined time intervals, swollen gels were taken out and blotted with filter paper to remove extra water. Weight of the gel was recorded and it was placed in water again. This process was repeated until a constant weight was reached. The % swelling index (SI) of hydrogels was calculated using equation 1 [13,14]

$$SI\ (\%) = \frac{(Ws - Wd)}{Wd} \times 100 \qquad \text{Eq. 1}$$

where W_s and W_d are the weights of swollen and dry hydrogels, respectively.

Table 1. Swelling indices of hydrogels of different formulations

Formulation	Xanthan Gum(g)	NaCMC (g)	Distilled Water(ml)	Crosslinker-$FeCl_3$(g/40 ml)	Swelling Index (%)
XG-Fe₁	0.4	0	40	0.04	ns
XG-Fe₂	0.4	0	40	0.08	702.1
XG-Fe₃	0.4	0	40	0.12	521.5
XG-Fe₄	0.4	0	40	0.16	479.7
XG-Fe₅	0.4	0	40	0.20	413.5
NaCMC-Fe₁	0	0.4	40	0.04	ns
NaCMC-Fe₂	0	0.4	40	0.08	364.8
NaCMC-Fe₃	0	0.4	40	0.12	343.2
NaCMC-Fe₄	0	0.4	40	0.16	241.4
NaCMC-Fe₅	0	0.4	40	0.20	231.3
XG-Fe-CMC₁	0.2	0.2	40	0.04	ns
XG-Fe-NaCMC₂	0.2	0.2	40	0.08	526.4*
XG-Fe-NaCMC₃	0.2	0.2	40	0.12	412.2
XG-Fe-NaCMC₄	0.2	0.2	40	0.16	360.3
XG-Fe-NaCMC₅	0.2	0.2	40	0.20	310.2

* XG-Fe-NaCMC formulation with maximum % SI represents optimum concentration of crosslinker and therefore selected for detailed analysis. ns- not synthesized

Characterization

The XRD analysis of XG-Fe-NaCMC, XG-Fe, and NaCMC-Fe hydrogels was carried out by Perkin Elmer spectrum version 10.5.3 model in solid-state form. FTIR spectroscopy was performed using Perkin Elmer spectrum two. Thermo-gravimetric analysis (TGA) of XG-Fe-NaCMC hydrogel was carried out using a PerkinElmer, TGA 4000 in N_2 atmosphere in the temperature range from 25°C to 800°C with 10°C/min of uniform heating rate. The surface morphology of XG-Fe-NaCMC hydrogel was analyzed by SEM on EVO 18 research, Zeiss, instrument**.**

Maximum water holding capacity of soil (MWHC)

Air-dried soil, collected from DTU garden, was filtered through a 3 mm sieve. 0.1 g of hydrogel was mixed in 50 gm of this soil. The mixture was then placed in a PVC tube (diameter - 2.5 cm, length - 10 cm) with small holes at the bottom covered with filter paper inside the lower surface. Weight of this set up is recorded as W1. The soil samples were then gradually soaked with distilled water from the top of the tube until the water began to leak out of the bottom of the tube. Once there was no longer leakage of water at the bottom, the tube was weighed again and recorded as W2. For control, soil was taken without hydrogel. % MWHC of the soil was calculated using equation 2 [15,16].

$$\text{MWHC (\%)} = \frac{(W2 - W1)}{50} \times 100 \qquad \text{Eq. 2}$$

Plant growth study

The effects of the hydrogel-treated soil on the growth of *T. aestivum* were investigated in terms of i) average number of seeds germinated; ii) total fresh and dry weight and iii) average shoot height and root length. In this process, 300 g of soil, collected from DTU garden, was taken in different pots. 0.1 g of urea-loaded hydrogels (XG-Fe, NaCMC-Fe and XG-Fe-NaCMC) was placed at a depth of 5 cm in soil in all the ~~different~~ pots. For control, soil without hydrogels was directly treated with urea solution. Fifteen wheat seeds were sowed in each pot and exposed to natural environmental conditions with occasional irrigation. Number of seeds germinated in each set was recorded. The appearance of radicle alone was considered as a sign of seed germination. After a period of 15 days, the whole plant was removed from the soil, cleaned, weighed and length of the shoots and roots was carefully measured. In order to determine the dry biomass, the plant material was dried for 24 hours at 70°C [17].

RESULTS AND DISCUSSION

Synthesis

Formation of water-insoluble mass from water soluble precursors, XG and/or NaCMC, in the presence of Fe^{3+} ions with the ability to hold large amount of water clearly indicates the creation of a hydrogel. Both XG and NaCMC contain anionic carboxyl functional groups. Thus, ionic crosslinking arises *via* Fe^{3+} ions to develop 3D polymer network (Fig. 1). The extent of crosslinking is significantly influenced by the concentration of Fe^{3+}, which is also demonstrated by the % swelling index. 0.04 g/40 ml of $FeCl_3$ fails to develop efficient interaction between the chains in the identical synthetic conditions, hence, hydrogel is not obtained. With gradual increase in $FeCl_3$ concentration from 0.08 to 0.2 g/40 ml aq. solution, a regular decrease in % swelling index was observed indicating reciprocal correlation between crosslinking and water storage capacity of the hydrogels. Based on these findings the optimal XG-Fe-NaCMC hydrogel (XG:NaCMC in 1:1 ratio and 0.08 g/40 ml of aqueous $FeCl_3$ solution) was selected for detailed analysis.
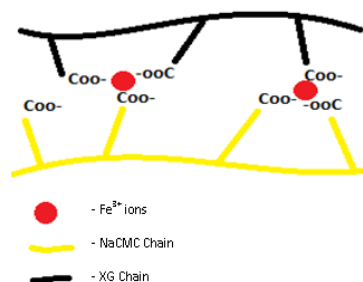

Fig. 1. Binding of carboxylate groups of XG and NaCMC with Fe^{3+} ions.

Characterization of synthesized hydrogels

X-ray diffraction

X-ray diffraction pattern (Fig. 2) confirms that the crystallinity of XG and NaCMC is adversely affected by the crosslinking. Thus, XG-Fe and NaCMC-Fe have more disordered structure than that of their precursors. It may be assumed that polymeric chains undergo the order → disorder transition to form ionic bonds with trivalent Fe ions [18]. This transition is more prominent in XG-Fe-NaCMC hydrogel. It has a completely amorphous structure. Carboxylate functional groups are attached to two different polymeric chains in a different way. Probably, for crosslinking either the electrostatic force of attraction between Fe^{3+} and COO^- and/or the repulsive interaction between XG and NaCMC, both being anionic polysaccharides, causes

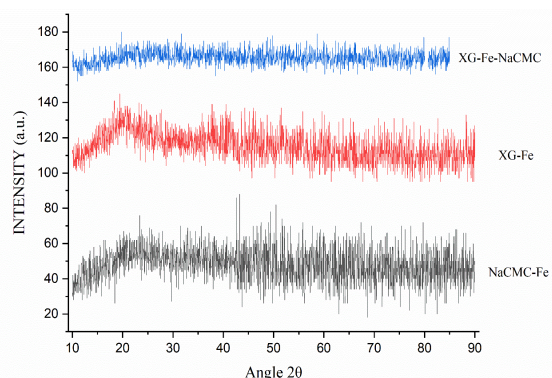rearrangement of basic polysaccharide network leading to loss of crystallinity.

Fig. 2. XRD spectra of hydrogels.

Fourier Transform infrared spectroscopy

Fig. 3 represents the FTIR spectra of XG-Fe-NaCMC, XG-Fe and NaCMC-Fe. The absorption band in the range of 3200-3300 cm^{-1} confirms the presence of OH groups in the hydrogels. Two broad bands between 1609 and 1390 cm^{-1} arise from the asymmetrical and symmetrical stretching mode of –COO^- groups. The absorption bands at 2920 and 2850 cm^{-1} of XG-Fe hydrogel correspond to the asymmetric and symmetric methylene C-H stretching of XG, respectively [19]. Absorption band in the range of 1050-1030 cm^{-1} shows the presence of symmetrical stretching of -COO^- group of glucuronic acid and at 1037 cm^{-1} is due to the C-O-C stretching of the ether group.
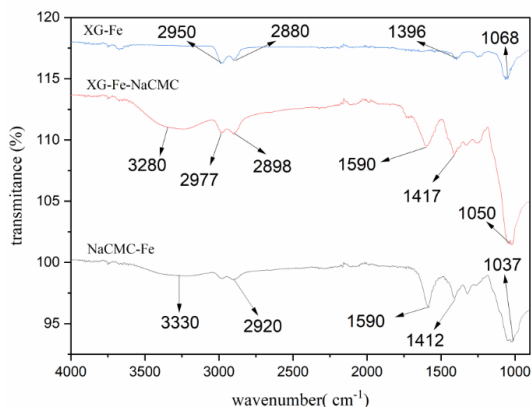
Fig. 3. FTIR spectra of hydrogels

Thermogravimetric analysis

Thermogravimetric assessment of hydrogels is presented in Fig. 4. The first phase in the range of 50-200°C is observed in all samples, probably due to desorption of moisture bound to the saccharide structure through water hydrogen [20]. The significant weight loss observed between 250-800 °C is attributed to breakdown of main polymeric chain [20]. In NaCMC-Fe, the primary degradation began at ~240°C, with weight loss from the inorganic portion followed by pyrolysis occurred after 335°C. XG-Fe followed a multi-step degradation pattern. TGA also confirms that hydrogel (XG-Fe-NaCMC) is thermally more stable than the hydrogels prepared using single natural polymeric chains (XG-Fe or NaCMC-Fe).
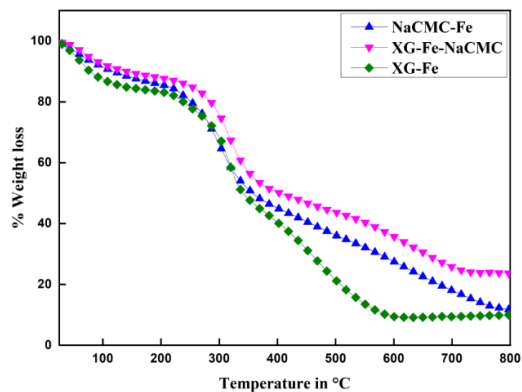
Fig. 4. TGA thermograms of XG-Fe, NaCMC-Fe and XG-Fe-NaCMC

Scanning electron microscopy

The surface morphologies of XG, NaCMC, and their hydrogels and EDX were studied (Fig. 5). The XG is found to have a smoother surface than its hydrogel XG-Fe which has a relatively rougher and coarser surface. NaCMC too has a smooth surface but NaCMC-Fe has smooth surface with abrupt ruptures and cracks exposing rough and irregular morphology [21]. The porosity of XG-Fe-NaCMC is surprisingly very high. It supports our assumption that repulsive interaction between two different anionic polysaccharide chains and their order → disorder transition during crosslinking favors the development of highly porous 3D network of hydrogel.

Swelling study

The amount of crosslinker was varied from 0.04 to 0.20 g/40 ml aq. solution of $FeCl_3$ for the synthesis of different sets of hydrogels. In general, it was observed in each case that the % swelling index decreases with increase in Fe^{3+} concentration. Maximum % SI was attained in about 25 hours (Fig. 6 a, b). The extensive analysis of % SI of different formulations (Table 1) revealed a significant fact: the % SI of single polysaccharide hydrogel, NaCMC-Fe$_2$, is 364.5 with 0.08 g/40 ml of aq. FeCl$_3$ solution, whereas, with the same amount of crosslinker % SI is enhanced to 526.4 when dual polysaccharide frame work is developed using XG:NaCMC in 1:1 ratio (formulation XG-Fe-NaCMC$_2$). Similar trend was exhibited by other formulations also confirming the positive interaction between XG and NaCMC.
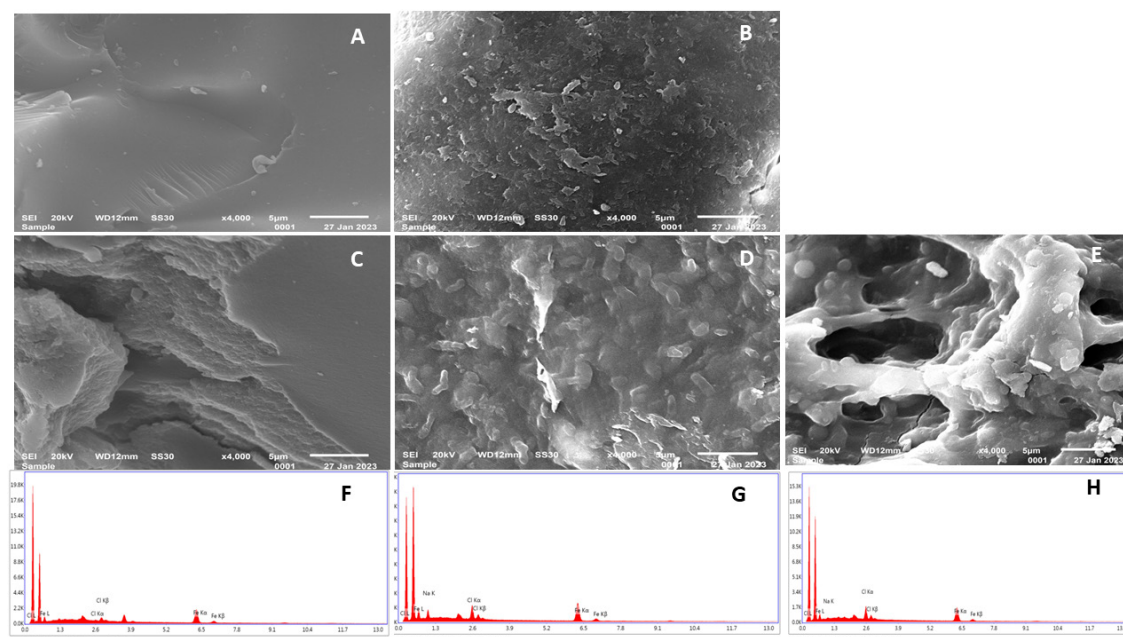
Fig. 5. SEM images and EDX graphs of hydrogels, (A) XG, (B) XG-Fe hydrogel, (C) NaCMC, (D) NaCMC-Fe hydrogel, (E) XG-Fe-NaCMC hydrogel (F) EDX of XG-Fe, (G) EDX of NaCMC-Fe, and (H) EDX of XG-Fe-NaCMC.
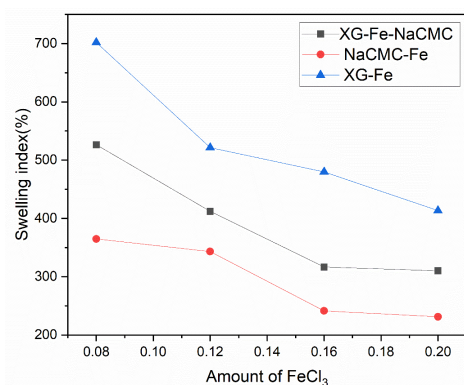

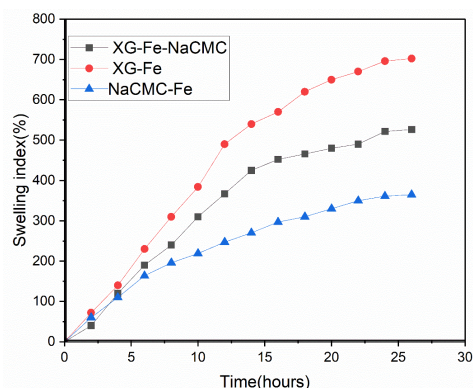**Fig. 6 (a).** % Swelling index with different amounts of FeCl$_3$.

Fig. 6 (b). % Swelling index with time

Maximum water holding capacity (MWHC)

MWHC of soil was determined in control (without applying hydrogels) and in soil treated with hydrogels: XG-Fe, NaCMC-Fe and XG-Fe-NaCMC. In control, MWHC of soil was 20 ml per 50 g of soil, which increased by 10% (22 ml per 50 g of soil) by application of NaCMC-Fe hydrogel. Application of XG-Fe-NaCMC and XG-Fe demonstrated an increase in MWHC by 30% (26 ml per 50 g of soil) and 40% (28 ml per 50 g of soil), respectively [15].

Plant growth

The influence of hydrogel (0.1 g per 300 g of soil) on growth of wheat grass is shown in Table 2 and Fig. 7. Water is a vital input in agriculture. It not only triggers the seed germination, but is also responsible for the utilization of nutrients in fullest by plants [22]. It is also well known that seeds grow better when urea is available for a longer period. Current investigation confirms that hydrogel XG-Fe-NaCMC is a potential component of agricultural field for better growth of the plant by maintaining urea and water level in soil.
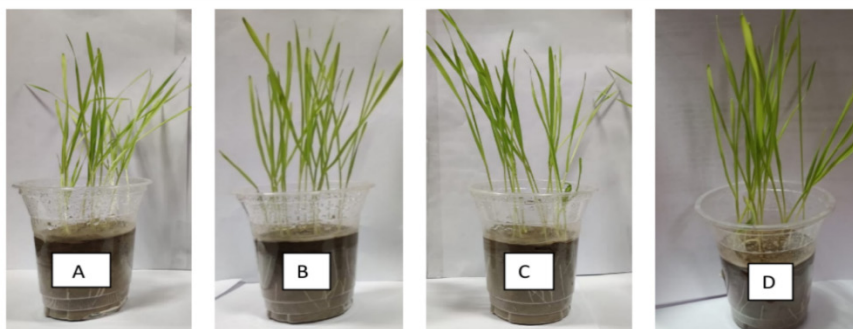
Fig. 7. Plant growth, (A)- Control (soil without hydrogel), (B)- soil with NaCMC-Fe, (C)- soil with XG-Fe, and (D)- soil with XG-Fe-NaCMC.

Table 2. Wheat grass growth assessment by pot experiment

Sample	Total fresh weight (g); % increase	Total dry weight (g); % increase	Average number of germinated seeds; %	Average shoot height (cm); % increase	Average root height (cm); % increase
XG-Fe	2.2696; 52.07%	0.2403; 56.24%	14; 93.33%	18.92; 18.69%	6.48; 15.50%
NaCMC-Fe	1.7680; 18.46%	0.1814; 17.95%	14; 93.33%	17.11; 7.34%	5.88; 4.81%
XG-Fe-NaCMC	2.6164; 75%	0.2745; 78.48%	15; 100%	19.14; 20.07%	6.71; 19.60%
Ctrl	1.4924	0.1538	13; 86.67%	15.94	5.61

CONCLUSION

In current time the efficient use of available water in agriculture sector is a worldwide serious challenge. To fulfil the food demand of ever-growing population and make agriculture sustainable and future-ready multidirectional efforts are urgently needed, including development of new technologies and effective management of agriculture practices. With this view the current study explored the use of gainful interaction between two different polysaccharides (xanthan gum and carboxymethylated cellulose) crosslinked through Fe^{3+} ions for agricultural applications. An optimal formulation (XG:NaCMC in 1:1 ratio and 0.08 g/40 ml of aqueous $FeCl_3$ solution) exhibited promising benefits on seed germination (100 % seed germination), plant growth (up to 75% increase in total fresh weight and 78.84% increase in total dry weight) and MWHC of soil. Besides, carboxymethylated cellulose can be obtained from waste plant materials, thus, offers a benign way for agro-waste management.

REFERENCES

1. GOI, Operational Guidelines of Per Drop More Crop Component of Pradhan Mantri Krishi Sinchayee Yojana, 2021.
2. M. S. Johnson, C. J. Veltkamp, *J. Sci. Food Agric.*, **369**, 789 (1985).
3. S. Keivanfar, R. Fotouhi Ghazvini, M. Ghasemnezhad, A. Mousavi, M. R. Khaledian, *Agric. Conspec. Sci*, **84**, 383 (2019).
4. S. K. Patra, R. Poddar, M. Brestic, P. U. Acharjee, P. Bhattacharya, S. Sengupta, P. Pal, N. Bam, B. Biswas, V. Barek, P. Ondrisik, M. Skalicky, A. Hossain, *Int. J. Polym. Sci.,* **2022**, 1 (2022).
5. S. Malik, K. Chaudhary, A. Malik, H. Punia, M. Sewhag, N. Berkesia, M. Nagora, S. Kalia, K. Malik, D. Kumar, P. Kumar, E. Kamboj, V. Ahlawat, A. Kumar, K. Boora, *Polymers (Basel)*, **15**, 161 (2022).
6. S. Kim, G. Iyer, A. Nadarajah, J.M. Frantz, A.L. Spongberg, *Int. J. Polym. Anal. Charact.,* **15**, 307 (2010).
7. H. Rodrigues Sousa, I. S. Lima, L. M. L. Neris, A. S. Silva, A. M. S. Santos Nascimento, F. P. Araújo, R. F. Ratke, D. A. Silva, J. A. Osajima, L. R. Bezerra, E. C. Silva-Filho, *Molecules,* **26**, 2680 (2021).
8. S. Mishra, N. Thombare, M. Ali, S. Swami, Applications of Biopolymeric Gels in Agricultural Sector. In: V. Thakur, M. Thakur, S. Voicu (eds.) Polymer Gels. Gels Horizons: From Science to Smart Materials, Springer Nature, Singapore, 185 (2018).

9. M. A. Qureshi, N. Nishat, S. Jadoun, M. Z. Ansari, *Carbohydr. Polym. Technol. Appl.,* **1**, 100014 (2020).

10. B. Song, H. Liang, R. Sun, P. Peng, Y. Jiang, D. She, *Int. J. Biol. Macromol.,* **144**, 219 (2020).

11. E. P. Miri Klein, *J. Sci. Food Agric.,* **100**, 2337 (2020).

12. J. Li, M. Jiang, H. Wu, Y. Li, *J. Agric. Food Chem.,* **57**, 2868 (2009).

13. E. V. R. Campos, J. L. de Oliveira, L. F. Fraceto, B. Singh, *Agron. Sustain. Dev., 3***5**, 47 (2015).

14. P. Tasaso, *Int. J. Chem. Eng. Appl.,* **6**, 101 (2015).

15. W. L. Shuailong Li, Gang Zhou, Zongqi Liu, Naiguo Wangd, Zunyi Wei, *J. Clean. Prod..* **258**, 120620 (2020).

16. G. Joshi, S. Naithani, V.K. Varshney, S.S. Bisht, V. Rana, P.K. Gupta, *Waste Manag,* **38**, 33 (2015).

17. A. B. M. Fakrul Alam, M. I. H. Mondal, *J. Appl. Polym. Sci.,* **128**, 1206 (2013).

18. I. A. Jahan, F. Sultana, M. N. Islam, M. A. Hossain, J. Abedin, *Bangladesh J. Sci. Ind. Res.,* **42**, 29 (1970).

19. A. Di Martino, Y. A. Khan, S. Durpekova, V. Sedlarik, O. Elich, J. Cechmankova, *J. Clean. Prod.,* **285**, 124848 (2021).

20. M. S. Rahman, M. S. Hasan, A. S. Nitai, S. Nam, A. K. Karmakar, M. S. Ahsan, M. J. A. Shiddiky, M. B. Ahmed, *Polymers (Basel),* **13**, 1345 (2021).

21. R. Saberi Riseh, M. Gholizadeh Vazvani, M. Hassanisaadi, Y. A. Skorik, *Polymers (Basel),* **15**, 440 (2023).

22. M. Szekalska, A. Puciłowska, E. Szymańska, P. Ciosek, K. Winnicka, *Int. J. Polym. Sci.,* **2016**, 1 (2016).

23. P. Joshi, S. Mehtab, MGH Zaidi, *Bull. Chem. Soc, Japan* **95** (6), 855 (2022).

24. M. Kurdtabar, H. Nezam, G. Rezanejade Bardajee, M. Dezfulian, H. Salimi, *Polym. Sci. - Ser. B,* **60**, 231 (2018).

25. P. Joshi, G. Bisht, S. Mehtab, M. G. H. Zaidi, *Mat. Today: Proceed.,* **62**, 6814 (2022).

26. G. O. Akalin, M. Pulat. *J. Nanomater.,* **2018**, 1 (2018).

27. N. H. Ahmad, S. Mustafa, Y. B. Che Man, *Int. J. Food Prop.,* **18**, 332 (2015).

28. S. Chaturvedi, S. Kulshrestha, K. Bhardwaj, R. Jangir, A Review on Properties and Applications of Xanthan Gum, In: A. Vaishnav, D.K. Choudhary, (eds.) Microb. Polym., Springer, 87, Singapore, Singapore, 87, (2021).

29. S. Cai, X. He, K. Liu, A. M. Rodrigues, R. Zhang, *RSC Adv.,* **7**, 41630 (2017).

30. F. Poret, A. Cordinier, N. Hucher, M. Grisel, G. Savary, *Carbohydr. Polym.,* **255**, 117500 (2021).

31. S. P. Giuliano Copetti, M. Grassi, R. Lapasin, *Glycoconj. J.,* **14**, 951 (1997).

32. Y. Shi, J. Li, L. Gu, Y. Su, W. Chen, M. Zhang, C. Chang, Y. Yang, *Int. J. Food Sci. Technol.,* **58**, 1037 (2023).

33. X. Yu, Y. Wang, W. Zhao, S. Li, J. Pan, S. Prakash, X. Dong, *Food Hydrocoll.,* **137**, 108333 (2023).

34. I. C. M. Dea, E. R. Morris, D. A. Rees, E. J. Welsh, H. A. Barnes, J. Price, *Carbohydr. Res.,* **57**, 249 (1977).

35. A. Rashidzadeh, A. Olad, A. Reyhanitabar, *Polym. Bull,* **72**, 2667 (2015).

36. S. G. Warkar Khushbu, A. Kumar, *Polymer (Guildf)*, **182**, 121823 (2019).

37. F. F. Montesano, A. Parente, P. Santamaria, A. Sannino, F. Serio, *Agric. Sci. Procedia,* **4**, 451 (2015).

38. P. A. Williams, P. Annable, G. O. Phillips, K. Nishinari, Mixed Polysaccharide Gels Formed between Xanthan Gum and Glucomannan, in: 2nd edn.; Caballero, B., (eds.). Food Hydrocoll., Springer US, Boston, MA, 2992 (1994).

39. M. Kang, O. Oderinde, S. Liu, Q. Huang, W. Ma, F. Yao, G. Fu, *Carbohydr. Polym.,* **203**, 139 (2019).

40. D. Hua, S. Gao, M. Zhang, W. Ma, C. Huang, *Carbohydr. Polym.,* **247**, 116743 (2020).

41. B. Kumar, R. Priyadarshi Sauraj, F. Deeba, A. Kulshreshtha, K. K. Gaikwad, J. Kim, A. Kumar, Y. S. Negi, *Gels,* **6**, 1 (2020).

42. M. R. Blatt, F. Chaumont, G. Farquhar, *Plant Physiol.,* **164**, 1555 (2014).

Recent advances in thin film hydrogen sensors, materials and methods

R. S. Pandhre[1], N. Suthar[1], A. Hakeem K K[1], D. Dashora[1], M. G. H. Zaidi[2], P. Kumar[1*], A. K. Mukhopadhyay[3]

[1]Department of Physics, Manipal University Jaipur, Jaipur-303007, Rajasthan, India
[2]Department of Chemistry, College of Basic Science and Humanities, G.B Pant University of Agriculture and Technology, Uttarakhand, 263145, India
[3]Department of Physics, Sharda School of Basic Sciences and Research, Sharda University, Greater Noida 201310, Uttar Pradesh, India

Hydrogen has become the center of attraction from the research point of view because of its renewable and pollution-free characteristics and its use in many fields. Hydrogen is now being used in various industrial areas in order to generate green energy and power for numerous purposes. It is used as fuel in aircraft and spacecraft because of its renewability and lightness. It is used in storage tanks, refueling stations, automotive vehicles, metal smelting, glassmaking, semiconductor processing, petroleum extraction, etc. Green hydrogen can be used to generate electricity at night. Due to the wide range of use of hydrogen, it is vital to make the technology safer for the people. Hence, in this paper we shall discuss the need for hydrogen sensors and how useful are they in industries as hydrogen usage is growing rapidly. The detailed overview about the bulk and thin film sensors like "Thin film bulk acoustic resonator sensors" and carbon nanotubes-based sensors, etc. and main materials used such as palladium as catalyst in hydrogen sensing was briefed. Further, the discussion about materials and methods of fabrication and future scopes in this technology was an important component of this paper. Finally, we will conclude this review with recent advancements and types of hydrogen sensors such as mechanical, electrical, optical sensors, etc.

Keywords: hydrogen sensors, thin films, palladium, electrical sensors

INTRODUCTION

Hydrogen is the lightest element and attracted a significant attention of researchers around the world from fundamental, as well as technological point of view. Earth has around 70% of water which is one of the biggest sources of hydrogen. The huge use of hydrogen in several applications has made it one of the hot topics of current research. The use of hydrogen specially for renewable green energy in automotive vehicles is the best green fuel for the future [1]. Hydrogen, because of its lightness and renewability nature, is one of the best fuels for spacecraft. Because of the broad range of use of hydrogen in several fields, it is vital to make the technology safer for everyone [1-5]. More than 156 countries revealed their new 'Hydrogen Policies' in Glasgow in 2021, and formulated strategies to alter their energy usage and infrastructure to become 'Carbon-Zero' by 2030 [1]. The realization of hydrogen policies depends on the production, storage, transportation, and extensive applications of hydrogen [6-10]. As we know, hydrogen is a very inflammable gas and has a very high flame propagation velocity. Since hydrogen molecule has a very small size, it can leak through many materials and can be the cause of explosive disasters. In the past there have been many disasters happened, as the

FUKUSHIMA NUCLEAR DISASTER (loss of reactor cooling resulted in a nuclear meltdown and 3 hydrogen explosions which led to the release of radioactive contamination), the Kennedy space center disaster (large H_2 tank got ruptured causing the shuttle Challenger to explode and killing all 7 astronauts onboard) and many more. Therefore, the detection of hydrogen leakage and its concentration monitoring is very necessary to give the public confidence in using this technology.

Hydrogen monitoring is highly required for nuclear reactor safety, mines, industries, hospitals, households, storage tanks, pipelines, hydrogen production plants, refueling stations, spacecraft, etc. and for that reason, hydrogen sensors have been introduced. Hydrogen sensors that are preferred to be small for mass production, must work at room temperature to make it sustainable with respect to energy, and response and recovery time must be as low as possible, should be affordable by cost, reliability must be high for longevity. As we have seen above how dangerous hydrogen is if not used appropriately. There are several types of sensors that were reported in literature, e. g., palladium capped rare earth thin film hydrogen sensors, TFBAR, CNTs [11-16]. These sensors work great in room temperature ranges which is an essential desirable component for any device. The widespread

applications and the increase in commercial interest for these sensors led to an exponential increase in related publications since the year 1970, as shown in Figure 1 (a). Some types of sensors are shown in Figure 1 (b). However, despite the significant importance of the present field, not much attention was given in hydrogen sensing field by the scientific community. This lack of knowledge base documentation makes the scope of the present paper. In this review paper, we shall discuss various aspects of types of sensors, methods of fabrication, bulk and thin film sensors, materials used, and future scope.
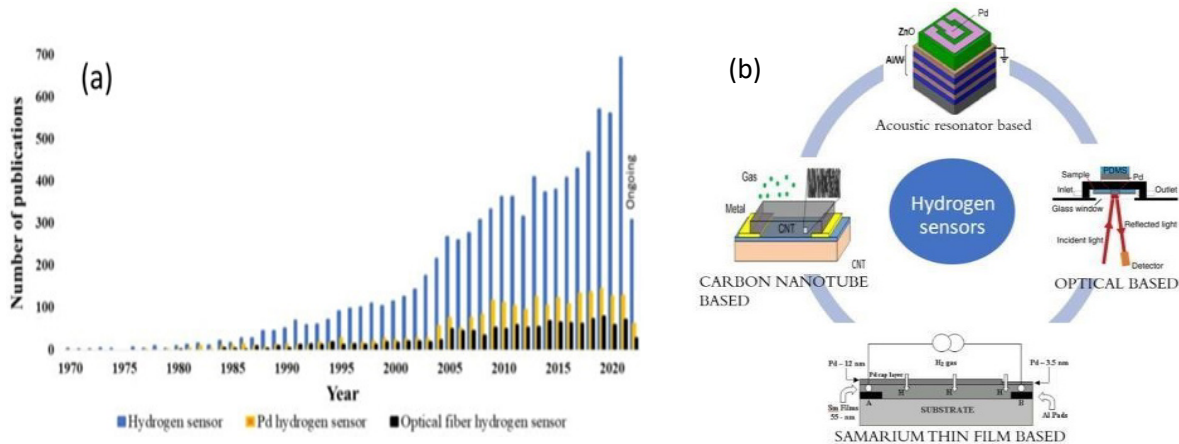
Figure 1. (a) Trends in increase in the publication on hydrogen sensors since 1970 as per SCOPUS (June 2022) [1]; **(b)** Different kinds of hydrogen sensors.
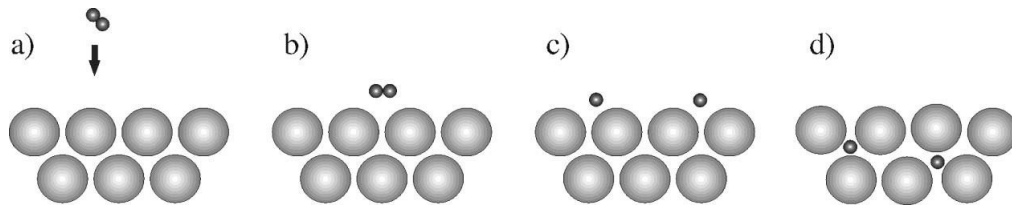
F igure 2. Reaction steps between hydrogen molecule and Pd [2].

Several types of hydrogen sensors

There are many types of hydrogen sensors that are used these days, e. g., thermal-based hydrogen sensors, work function-based hydrogen sensors, mechanical-based hydrogen sensors, electrical-based hydrogen sensors, optical-based hydrogen sensors. We shall mainly discuss electrical and optical based hydrogen gas sensors in this paper.

Electrical-based hydrogen sensors

These sensors work on the basis of electrical resistivity shift of the sensor material when exposed to hydrogen gas concentrations, the main material here is palladium that acts as a catalyst to dissociate hydrogen molecule into atomic hydrogen that further diffuses into underneath materials and results in the change of resistance. The advantage of these sensors is that based of substrate these can be modified for different working temperature ranges.

Optical based-hydrogen sensors

These sensors work on the basis of catalytic and absorption properties of palladium during hydrogen-ation that results in changes of reflectance, transmittance, absorbance and refractive index. The major advantage of these sensors is that they have good response time compared to other sensors and are very safe as they don't generate any sparks during the detection process. Further discussion shall be conducted in the following sections.

Pd NPs-based electrical H$_2$ sensors with different substrates

When Pd is placed in hydrogen-rich environment, the hydrogen gas gets absorbed by it exothermally. At the equilibrium state it is reversible in nature. Hydrogen reacts with Pd atoms through Van der Waals interactions. The absorbed gas molecule of hydrogen breaks down into hydrogen atoms and gets diffused in metal. The reaction can be written as:

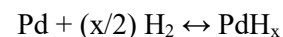$$Pd + (x/2) H_2 \leftrightarrow PdH_x$$

Figure 2 illustrates the process of hydrogen diffusion in Pd step by step. The structural change of Pd caused by its interaction with hydrogen results in alterations of its electrical, mechanical, and optical

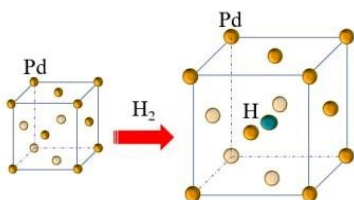properties due to increase in lattice volume of Pd, as illustrated in Figure 3.

Figure 3. Hydrogen absorption results in expansion of the Pd lattice [2].

Building a hydrogen sensor frequently involves fabrication of either optical or electrical devices. The most universally found Pd NPs-based sensors for H_2 sensing are electrical. The system's modification in resistivity or work function upon exposure to H_2 takes place in these kinds of sensors [2]. The electrical and optical hydrogen sensors are normally based on Pd NPs. In one of the reports by Joshi *et al*. Pd nanoparticles and Pd thin films were exposed to hydrogen to study sensing properties. The experimental setup used for sensing is shown in Fig. 4 (a) where the green part in the measurement chamber is the sensing element. In general, an experiment involves cyclical switching from a carrier gas to an H_2 enriched atmosphere within a gas chamber containing a sensing sample, while measuring the resulting changes in the system's resistance or conductance. Here gas rates are controlled by mass flow controllers (MFC) [4].

The response time of the film was taken to the 90% of the maximum resistance attained by a film when exposed to the hydrogen environment. In this study by Joshi *et al*., the comparative hydrogen sensing of the film deposited on Si substrate by two methods, i.e, electrochemically and via sputtering has been reported. It was observed in this study that the electrochemically deposited films have shown better hydrogen response than the film deposited by

sputtering. The response time observation can be seen in Fig. 4(b). Further it was also concluded that the grain size plays a significant role in hydrogen sensing response time. In Fig. 4(b), we can see that overall gas sensing response increases in smaller grain size that was attributed to the activation of surface states in nano size particles. It is also known that the smaller particle size has more active sites which leads to improved chemical sensitization phenomena. Electrical hydrogen sensors based on Pd NPs can be categorized as per the design of the setup used. In these types of systems, Pd NPs can be deposited on different types of substrates like silicon; oxide materials like ZnO, WO_3, etc.; sometimes they functionalize carbon materials like CNTs. Different types of substrates used are described here [2].

Pd NPs on silicon carbide (Ta₂O₅/SiC)

Silicon is a most abundant material on earth and extensively used as a substrate for semiconductor devices. Si has a very small band gap that restricts the maximum working temperature of Si to below 250 °C. Alternatively, silicon carbide (SiC) has a wide band gap, stability and chemical inertness that made SiC a better substrate candidate for high-temperature operations. Kim *et al*. reported the fabrication of Pd/Ta_2O_5/SiC-based hydrogen gas sensors. Here the thin layer tantalum oxide (Ta_2O_5) on SiC was used to improve the sensitivity due to its stability at higher temperature with high permeability for hydrogen gas. The schematic diagram of the sensing device is displayed in Fig. 5 (a) and the hydrogen sensing arrangement in Fig. 5(b). The I-V characteristics and capacitance response properties of the device were investigated on exposure to hydrogen concentration in the temperature range from room temperature to 500°C. In this study they have reported a good performance of device for hydrogen gas sensing at high temperatures [9].
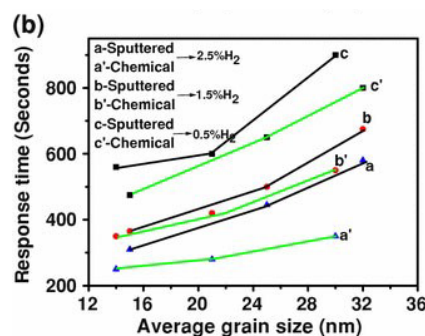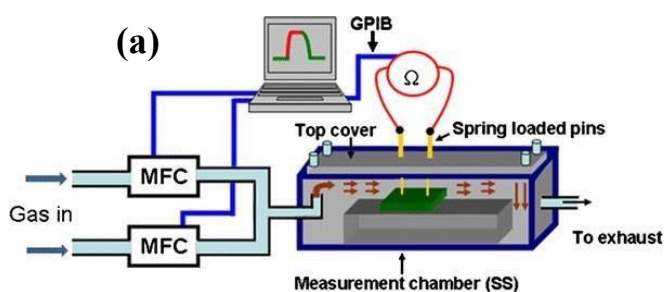

Figure 4 (a) Typical H_2 electrical sensing experiment setup; **(b)** Response time of Pd nanoparticles thin films prepared by electrochemical and sputtering technique of thickness 150 nm as function of grain size [4] open access source.
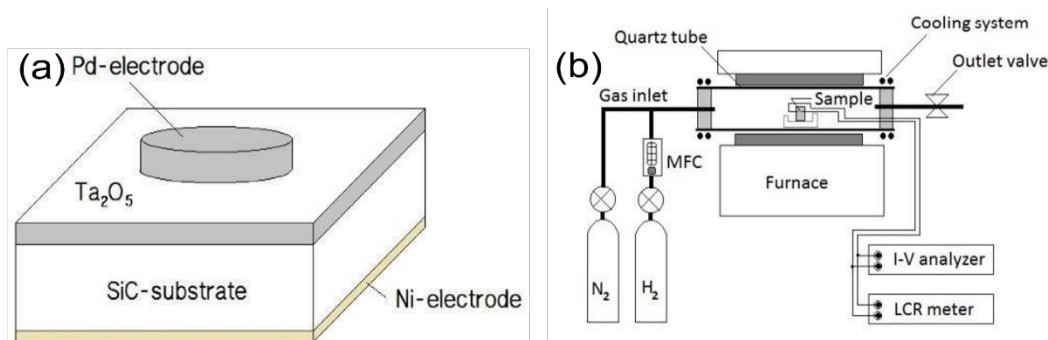
Figure 5 (a) Pd on SiC substrate with thin layer of Ta_2O_5; (b) complete setup for hydrogen sensing [9] open access source.

In Fig. 6, it can be seen that a drastic change in capacitance of the device was observed when exposed to the hydrogen concentration at the working temperature of 500 °C.
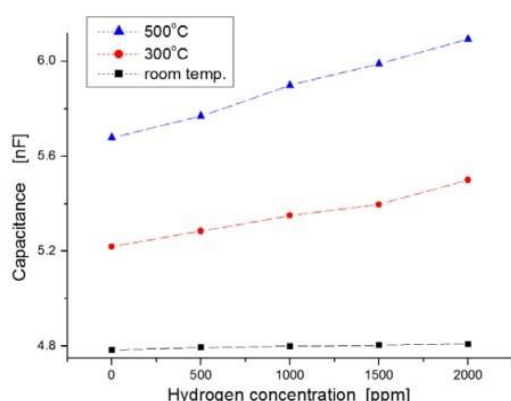

Figure 6. Change in capacitance as a function of hydrogen concentrations at different temperatures [9].

However, change in capacitance was almost consistent at room temperature when the device was subjected to hydrogen environment. Further it was also seen quantitatively that the capacitance was enhanced from 5.6 nF to 6.1 nF after the hydrogen concentration varied from zero to 2000 ppm at 500 °C. From the observation it was concluded in this paper that Ta_2O_5 dielectric thin layer provides great possibilities for hydrogen sensing application at high temperatures [9].

Pd NPs on carbon nanotubes

In one of the reports published by Sayago *et al.* [8], Pd has been integrated to CNTs to amend their hydrogen sensitivity. They prepared three different types of sensing materials: (1) SWNTs (single-walled nanotubes); (2) SWNTs functionalized with palladium; (3) SWNTs doped with palladium. These sensing materials were deposited on alumina substrate. Sensing concentrations of hydrogen varied from 0.5 to 4% and the carrier gas used was nitrogen with 99.99% purity with a constant flow of 200 ml/min. The response and recovery time was found

to be 30 and 60 min respectively. The effect of temperature on the sensor with SWNTs was studied on Heraeus MSP 769 instrument in the temperature range of 100-250°C. After the complete study they found the results that only the sensors functionalized with Pd detect H_2 at room temperature and as the Pd content is increased, the sensor starts to give better response. Unfortunately, these sensors do not attain saturation throughout exposure time, but they provide good response time of 2 min. The sensor with SWNTs on alumina substrate (Heraeus MSP 769) only detects H_2 for temperatures higher than 200 °C and same condition was also observed with Pd-doped SWNTs. Because of random distribution of CNTs arrays, gas can be adsorbed at multiple active points (like tube ends, edges and valleys outside, inner and between) and that's the reason of longer exposure time. As a conclusion we can say that all these sensors show very low response, and their resistance doesn't vary much with H_2 concentration and hence the practical utility of such sensors needs more research to improve.

Pd-based optical H_2 sensors

A number of optical hydrogen sensors have been developed based on the permittivity fluctuation and catalytic characteristics of Pd during hydrogenation. Pd has a weaker optical sensitivity than other sensing materials like Mg and Y because hydrogenation only causes a minor change in its dielectric constant. For other hydrogen sensing materials, hydrogen absorption is quite typical as they have need of catalysts to dissociate hydrogen molecules into atoms which can enhance the expense of sensor. To prevent the hydrogen poisoning on Pd from other gases a kind of protection layer (e.g., PMMA, PTFE) can be applied on the sensing materials. Optical sensors are safer than other sensors because of the absence of any ignition source. Different measurement techniques, including reflectance, interferometry, surface plasmon resonance, and evanescent light, can be used for optical detection. Its adaptability for various sensing applications is further increased by fibre Bragg gratings and field interaction. In this section

141

we will discuss various kinds of optical response-based sensors.

Pd-PMMA bilayer on a soft PDMS substrate (PPBE)

She *et al.* in his work on hydrogen sensor tried to make a sensor based on light scattering, a low price and high contrast hydrogen sensor that can produce enormously high reflectance variation due to the conversion of specular to diffusion reflection during surface wrinkling [10]. They studied the reflectance change of PPBE (Pd-PMMA bilayer on an elastomer like polydimethylsiloxane (PDMS)), with Pd and polymethyl methacrylate (PPMA) as protecting layer. They used PPBE because it is of low cost and simple to manufacture. In order to fabricate PPBE a thin Pd film was first deposited on it. The Pd film was then covered with a PMMA/PAA bilayer on a quartz substrate. Lastly, after polyacrylic acid (PAA) was mixed in water, the PMMA film coating on the Pd film was left behind. Here they chose PMMA because of its high selective filtration of H_2. The schematic diagram of same is shown in Fig. 7 for better understanding. In this work, they measured the reflectance spectra of the sensor in order to show the effect of PMMA on its performance. The thickness of Pd film and PMMA is 25 and 22 nm, respectively. The variation in reflectance spectra in the visible band and response time for Pd on PMMA at 0% and 4% exposure of H_2 gas mixed with N_2 and air are shown in Fig. 8. They further investigated the effect of thickness of Pd film on response time and it was found that the latter increases with increase in thickness. It was also seen that thinner the PMMA, more reflectance changes are in lesser time. When

thickness of PPMA was taken of 16 nm the hydrogenation time decreased from 15 to 5 seconds, heading to quick response rate of the sensor. In practical application here the response time and reflectance change decreased with increase in temperature. The reflectance change was found more than 22.7% in the whole visible band with reflectance contrast over 370% in wrinkle surface. The response time can be 1 second if the alarm point is set at a 4% change in reflection at wavelength 600 nm. Hence the PPBE is extremely appropriate for real hydrogen sensing.

Sensor based on tunable laser diode spectroscopy (TDLAS)

Avetisov *et al.* used tunable laser diode spectroscopy [TDLAS] as it can detect hydrogen gas without collecting gas samples (which is safer compared to other types of sensors) and has low maintenance cost and operational costs [14]. Cavity ring down spectroscopy (CRDS), intro cavity output spectroscopy (ICOS), etc. were not preferred because of contamination of reflective mirrors that were a major concern in industrial uses. The sensor consists of two units i.e., transmitter unit that contains diode laser, microprocessor board, input output electronics and receiver unit which contains photodetector, amplifier, mixer, etc. The sensor diagram is given in Fig. 9 for reference.

The absorption spectrum of hydrogen in the infrared region is very weak, the first band is located between 1100-1500 nm, this is also due to the low mass of the H_2 molecule. From HITRAN simulation they concluded that 3 transition bands were suitable for H_2 sensing, i.e., 2407 nm, 2223 nm, 2122 nm.
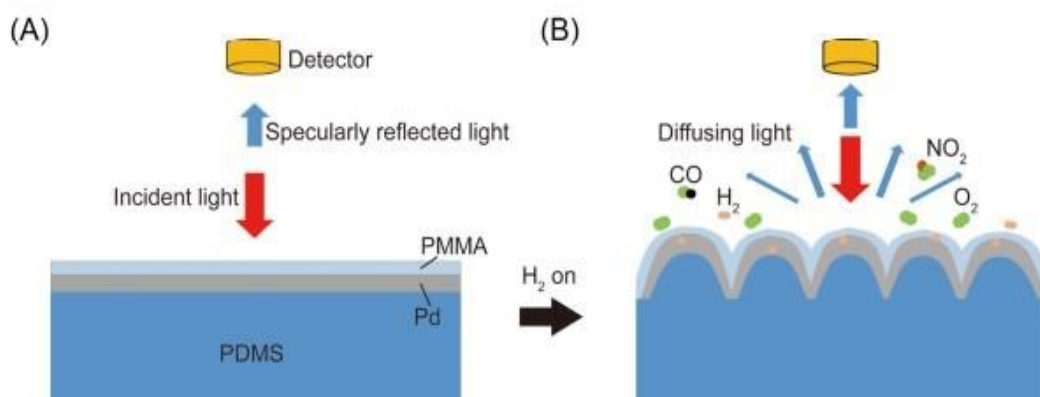

Figure 7. Schematic exhibiting the sensing mechanism of the PPBEs. (A) The specularly reflected light by the flat Pd/PMMA bilayer before hydrogenation and (B) diffused reflectance by the wrinkling surface generated by volume expansion of Pd thin film after hydrogenation [10]- open access source.
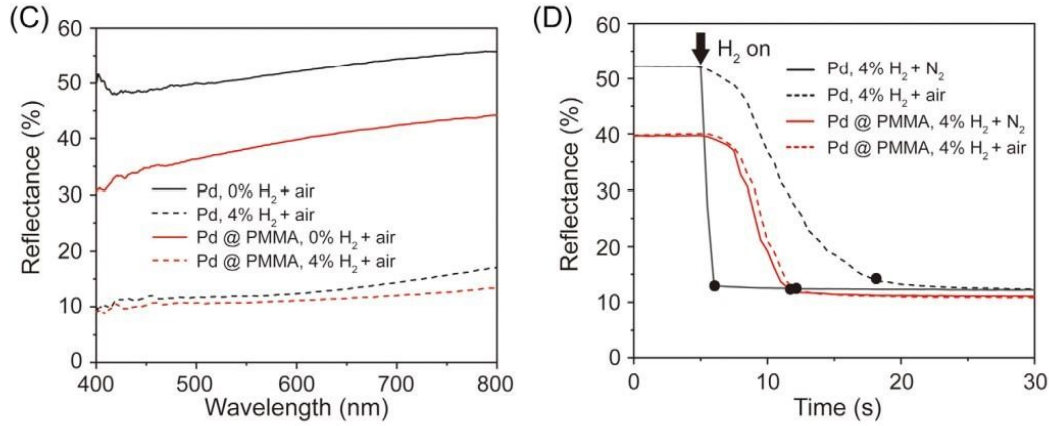
Figure 8. (C) Reflectance spectra as function of wavelength of the PPBE and a Pd film on PDMS when exposed to 0% and 4% H_2 mixed with dry air, respectively. (D) Reflectance change as function of time at a fixed wavelength of 600-nm of a PPBE (red line) and a Pd film on PDMS (black line) on exposure to 4% H_2 mixed with N_2 (solid line) and dry air (dash line), respectively [10] open access source.
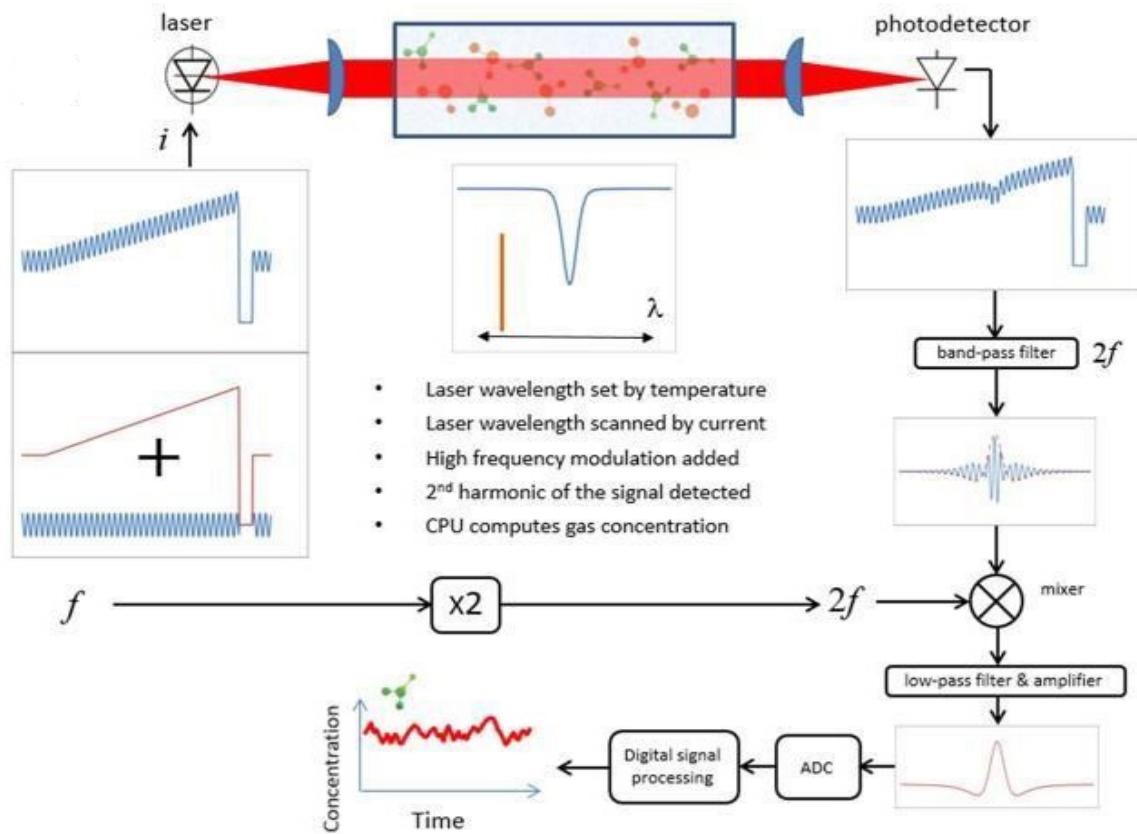

Figure 9. Typical arrangement for a spectroscopy-based H_2 gas sensor [14] open access source.

The best suitable line is the one that doesn't coincide with spectral lines of other gases such as CO_2, H_2O, CO, etc., as shown in Figure 10.

During the experimental session major issues faced with TDLAS sensors were optical fringe noise and coupling of stray light in the active laser area. These were solved by AR coating the surfaces and tilting them. For estimating the sensor performance, the transmitter and receiver unit were kept 1 m away and the cell was maintained at ambient temperature,

also the sensor was calibrated with known values of H_2 and N_2, the H_2 concentration was reduced from 10-0.1 percent and the concentration set *vs*. measured result was plotted and shown in Fig. 11. Measurement precision of 0.02%v H_2 was found within 1s of integration time. As we increase the pathlength, the absorption also increases that results in the increase of sensor precision. Which indeed makes it more suitable for industry uses.
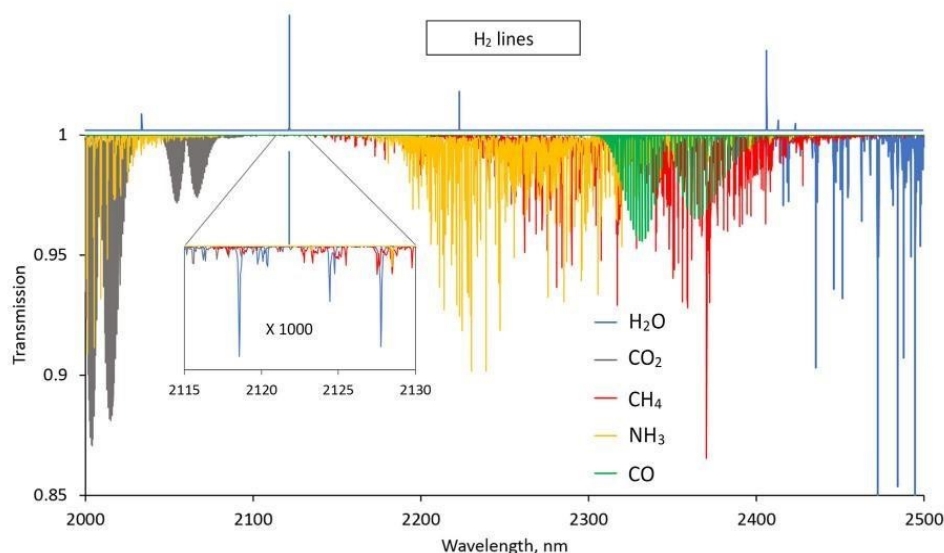
143

Figure 10. HITRAN simulation for the absorption spectrum of various gases and H_2 which might be present in typical usage environments of the sensor [14] open access source.
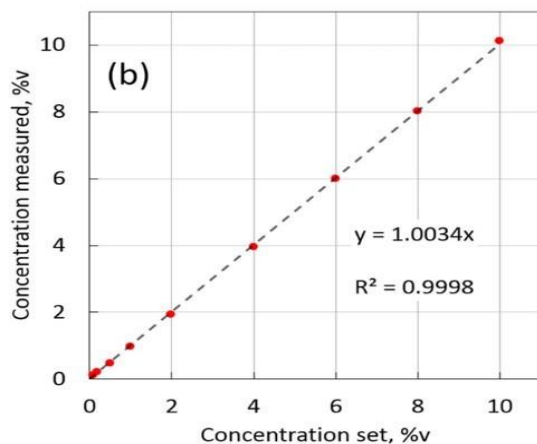

Figure 11. Graph of concentration of H_2 in chamber with detection precision [14].

Future scopes and applications

With its multiple uses in fertilizer factories, nuclear power plants, refineries, and other emerging technologies like eco-friendly fuels, hydrogen has a bright future. A hydrogen sensing system is necessary because the hydrogen has distinctive characteristics including strong flammability, low viscosity, low density, high escape rate, and the ability to burn with an unnoticeable flame. The sensitivity, reaction time, accuracy, detection range, durability, and dependability of gas sensors are the main determinants of their use. The current study focuses on the application of these sensors for a variety of businesses, including those that produce fertilizers, refineries, hydrogenating agents, and fuel cell-powered cars [1]. To monitor hydrogen concentrations and optimize process settings for optimal efficiency, hydrogen sensors can be used in

hydrogen generation processes such steam methane reforming, electrolysis, and biomass gasification. In addition to the above hydrogen sensors can also be employed for safety monitoring, leak detection, and risk avoidance. In order to monitor hydrogen concentrations at various points throughout the operation of the fuel cell, including the hydrogen input, fuel cell stack, and exhaust gases, hydrogen sensors can be employed in hydrogen fuel cell systems. By guaranteeing enough hydrogen supply and averting any dangers, hydrogen sensors can aid in maximizing the efficiency of fuel cells. In chemical companies, early detection of hydrogen leaks using hydrogen sensors can assist to avoid accidents, reduce losses, and guarantee safety. The car industry and the US DOE have examined the need for H_2 safety sensors. The recommended range for sensors per vehicle is 2 to 6. The cost of sensors per vehicle will be reduced and operational costs will be better managed if one kind of sensor can function in all these diverse operating situations [2]. It may also be utilized inside automobiles to look for potential hydrogen leaks in the fueling system, hydrogen storage system, or other hydrogen infrastructure components. To ensure safety and avoid risks like explosions or fires, early identification of hydrogen leakage is essential. In order to ensure the safe storage of hydrogen in high-pressure tanks or other types of hydrogen storage systems used in cars, hydrogen sensors are essential. In the event of leaks or other safety issues, they can set off alarms or shut off the system. Vehicles using hydrogen internal combustion engines may monitor hydrogen concentrations during combustion using hydrogen

sensors. They offer feedback for effective engine running and aid in ensuring safe hydrogen combustion. These car's hydrogen sensors generally gauge the amount of hydrogen present in the intake or exhaust gases. Hydrogen sensing might undergo a revolution if other technologies, such as the Internet of Things, artificial intelligence, and wireless communication, were integrated with hydrogen sensors. Algorithms powered by artificial intelligence can increase sensor selectivity, dependability, and calibration, resulting in better sensor performance and fewer false alarms. In the current paper, the electrical and optical hydrogen sensors based on different systems with their advantages and disadvantages were elaborated in detail. This information at one place will definitely help scientific society for future expansion in the field of hydrogen sensing.

REFERENCES

1. A. K. Pathak, S. Verma, N. Sakda, C. Viphavakit, R. Chitaree, B. M. A. Rahman, *Photonics*, **10**, 122 (2023).
2. C. C. Ndaya, N. Javahiraly, A. Brioude, *Sensors*, **19**, 4478 (2019**)**.
3. P. Kumar, L.K. Malhotra, *Mater. Chem. Phys.,* **88**, 106 (2004).
4. R. K. Joshi, S. Krishnan, M. Yoshimura, A. Kumar, *Nanoscale Res. Lett.*, **4,** 1191 (2009).
5. A. M. Díez-Pascual, *Macromol.*, **1**, 64 (2021).
6. P. Kumar. L. K. Malhotra, *Thin Solid Films*, **491,** 270 (2005).
7. P. Kumar, L. K. Malhotra, *Jpn. J. Appl. Phys*, **43**, 909 (2004).
8. I. Sayago, E. Terrado, E. Lafuente, M. C. Horrillo, W. K. Maser, A. M. Benito, R. Navarro, E. P. Urriolabeitia, M. T. Martinez, J. Gutierrez, *Synth. Meth.,* **148**, 15 (2005).
9. K. Seongjeen, C. Jehoon, J. Minsoo, J. Sungjae, K. Sangchoel, *Sensors*, **13**, 13575 (2013).
10. S. Xiaoyi, Y. Qiankun, Y. Guowei, S. Yang, J. Chongjun, *Nano Select.,* **3**, 655 (2022).
11. P. Kumar, L. K. Malhotra, *Electrochim. Acta,* **49,** 3355 (2004).
12. P. Kumar, L. K. Malhotra, *Appl. Surf. Sci.*, **236**, 461 (2004).
13. N. Bavili, T. Balkan, B Morova, M. Eryürek, Y. Uysallı, S. Kaya, A. Kiraz, *Sens. Actuators B: Chem.,* **310**, 127806 (2020).
14. V. Avetisov, O. Bjoroey, J. Wang, P. Geiser, K. G. Paulsen, *Sensors,* **19**, 5313 (2019).
15. P. Kumar, L. K. Malhotra, *Jpn. J. Appl. Phys.*, **45**, 9094 (2006).
16. P. Kumar, R. Philip, G. K. Mor L. K. Malhotra, *Jpn. J. Appl. Phys.,* **41,** 6023 (2002).

Conducting polymer nanocomposites for energy storage applications: recent progress and future challenges

S. Rawal[1*], P. Kumar[2], P. K. Singh[1], A. K. Mukhopadhyay[1*]

[1]*Department of Physics, Sharda School of Basic Sciences and Research, Sharda University, Greater Noida 201310, Uttar Pradesh, India*
[2]*Department of Physics, Manipal University Jaipur, Jaipur 303007, Rajasthan, India*

These days, the requirement of developing new energy storage devices to store large amount of energy in high-rate applications is increasing. Thus, the cconducting polymers (CPs) hold a good future in energy storage field. This is related to their flexibility, light weight, high conductivity ($>10^3$ S cm^{-1}), cost effectiveness, controlled resistance over a wide range and excellent electrochemical properties. In particular, these materials can be used as an active material in rechargeable batteries and supercapacitors. CPs-based pseudocapacitors are capable to deliver large amount of energy that can last millions of cycles. Therefore, the current review summarizes how the choice of monomers and physical characteristics of dopants affect the electrical behavior of polymers and their widespread applications. The possible challenges to be overcome for their futuristic developments are also identified.

Keywords: Conducting polymer, Pseudocapacitance, Polyaniline, Polypyrole, Polythiopene, Supercapacitance.

INTRODUCTION

In today's scenario utilization of renewable and clean source of energy is very much needed. To use energy, it needs to be produced and stored. Since last few decades the field of energy generation and storage in an eco-friendly manner has evolved as a matter of huge significance. Hence, it is an area of intense research focus. It is also a fact that world population is growing at an alarming rate and so is the energy demand. Thus, it comes as no surprise that there is a continuously increasing gap between the demand and supply of energy. This is why efficient storage of energy is even more needed today than yesterday. In energy storage technologies initially, energy is stored in different forms such as chemical, mechanical, thermal, electromagnetic, electrochemical and electrical energy. This is done by different storage mechanisms i.e., direct storage and indirect storage (Fig. 1).

This stored energy is further used in electric form later on. There exist many forms of energy storage devices: (1) chemical energy storage (e.g. biofuels, hydrogen storage system), (2) mechanical energy storage (e.g. flywheel or hydropower), (3) thermal energy storage (e.g., steam accumulator), (4) electromagnetic energy storage (e.g. superconducting magnetic energy storage or SMES), (5) electrochemical energy storage (e.g. rechargeable batteries and supercapacitors), (6) electrical energy storage (e.g., a capacitor).

Supercapacitors or electrochemical capacitors are electrochemical devices based on the same principle as conventional capacitors (i.e. two electrodes separated by an electrolyte medium). But in the case of supercapacitors the distance between the electrodes is of atomic dimension which leads to significantly higher energy density in comparison to conventional capacitors [1]. Henceforth, electrochemical capacitors are supposed to serve as option capacitors and lithium ion-based devices [2, 3].

Due to their superior features [4-10], the applications of supercapacitors are increasing in portable, automotive systems and energy storage devices in comparison to the applications of the lithium ion batteries. Electric double layer capacitors (EDLCs) consist of carbon material-based electrodes [11, 12]. However, in pseudocapacitors the electrodes are made up of oxides of transition metals [13] or electroactive polymers [14, 15].

Power capability of electric double layer capacitors is generally high due to fast ionic adsorption and desorption of the electrolyte, however, their specific capacitance (Cs) is not up to the mark. On the other hand, pseudocapacitors can give rise to higher Cs values but cycling performance is not so good [16, 17]. In comparison to the relatively expensive transition metal oxides, the CPs are considered as the low-cost potential candidate electrode material for the pseudocapacitors.

* To whom all correspondence should be sent:
E-mail: sangeeta.4@sharda.ac.in,
anoop.mukhopadhyay@sharda.ac.in

If the electrode material is prepared from the combination carbon material/ CPs or metal oxide/ CPs then both the electric double layer formation and faradaic reactions add to the capacitance value and comparatively high Cs value is obtained (Fig. 2). The data displayed in Fig. 2 presents a comparative account of average specific values for electric double layer capacitors, pseudocapacitors and hybrid materials. The performance of the electrodes is influenced by the individual active constituents, as well as the interfacial characteristics and morphology of materials [1]. Charge storage mechanism of both EDLCs and pseudocapacitors is different due to the different charge-storing property of the electrode materials. In EDLCs charge is stored by the accumulation of the charge (due to double layers) on the electrode/electrolyte interface, whereas in pseudocapacitors (Fig. 3) [12] electric charges are confined in as electric double layers sandwiched between the carbon electrode and

.

ionically conducting electrolyte. These layers are separated by atomic distances (~10 Å). Different models such as Helmholtz model, Gouy and Chapman diffuse model, and Stern model have been proposed for the explanation of double layer formation in EDLCs. The behavior of electrolyte ions, microstructure of electrode material, and the compatibility of the electrolyte ions by electrode material affects the performance of EDLCs. On the other hand, in pseudocapacitors whether the electrode material is transition metal oxides [13] or CPs [16] charge is stored by the reversible and fast redox faradaic reactions occurring in the electrode material (Fig. 4) [12]. Calation and intercalation of the electrolyte ions plays an important role in determining the pseudocapacitance performance. In comparison to other pseudocapacitive materials, the CPs possess high redox contributions, good flexibility and intrinsic conductivity
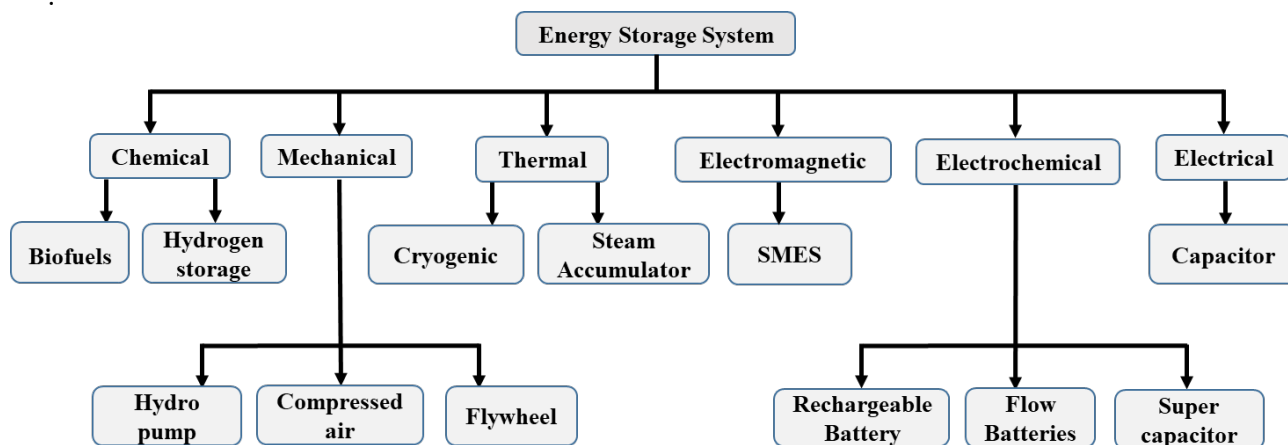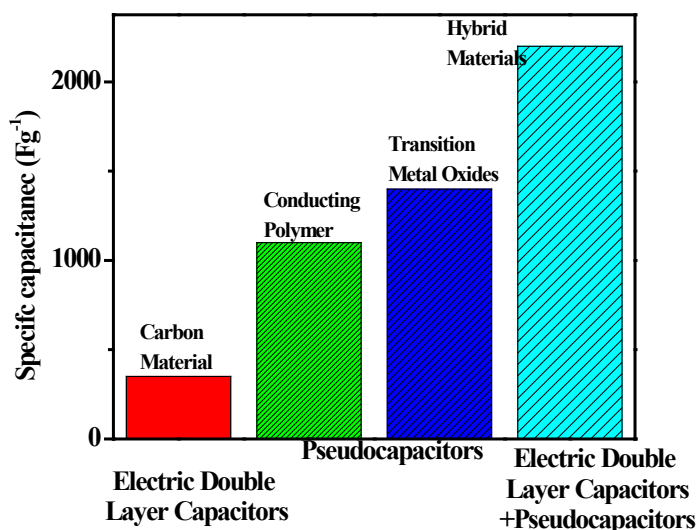

Fig. 1. Energy storage classifications

Fig. 2. Comparison of Cs values for different kinds of supercapacitor electrode materials
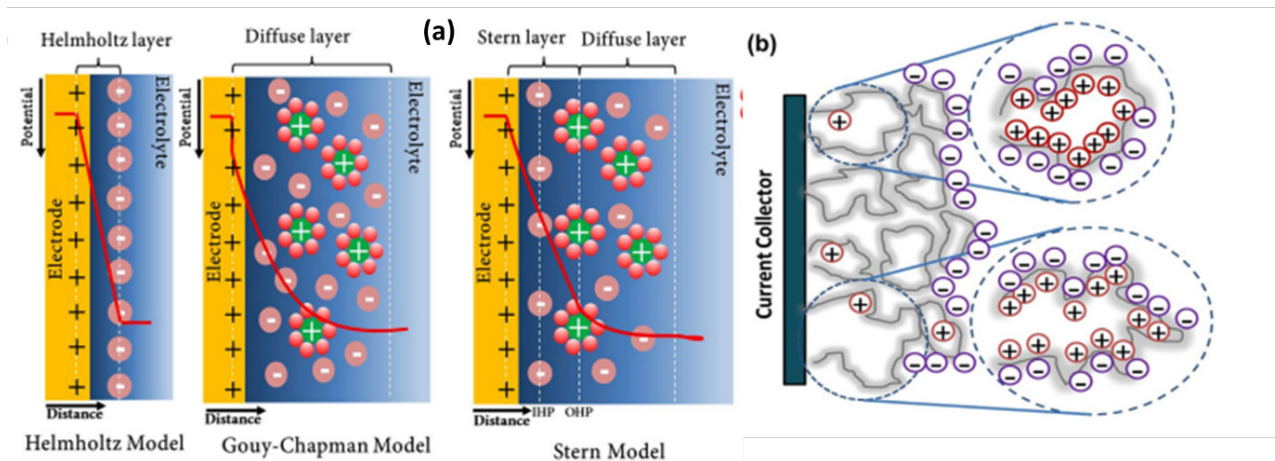
Fig. 3. (a) Different models (Helmholtz model, Gouy–Chapman model and Gouy-Chapman–Stern model) for the charge storage mechanism, and (b) Schematic illustration of charge storage mechanism of EDLC [12].
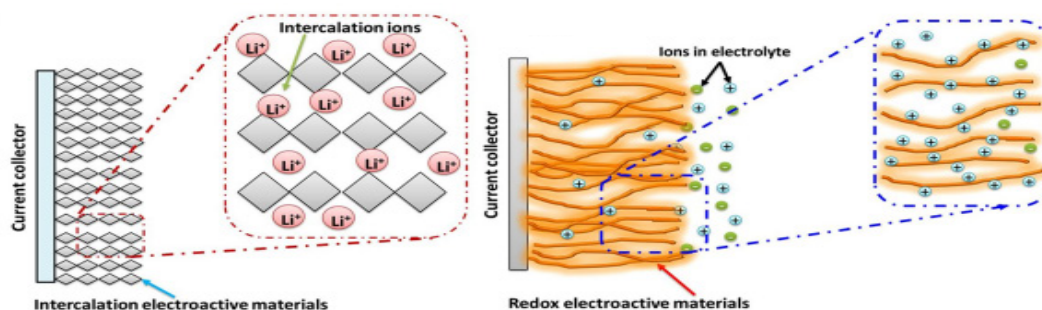

Fig. 4. (a) Pictorial illustration of the calation and intercalation of electrolyte ions in pseudocapacitors. (b) Redox mechanism of charge storage mechanisms in pseudocapacitors. [12]

The current review is mainly focused on the CPs-based pseudocapacitors. Different type of CP-based supercapacitors, their designing concepts and fabrication methods are discussed. It outlines the recent developments, finally point towards the future challenges for the route of flexible CP-based electrode materials and relevant device fabrications.

Properties of Conducting Polymers and Composites

Polyphenylene vinylene or PPV (10^{-3}–100 S cm^{-1}), polyacetylene or PA (3–1000 S cm^{-1}) polypyrole (PPy, 0.3–100 S cm^{-1}), polythiopene (PTh, 2–150 S cm^{-1}), polyaniline (PANI, 0.01–5 S cm^{-1}), and polyphenylene are few examples of conducting polymers (CPs) [21, 22]. Since discovery, the CPs have been praised by industry and academia for their applications in sensors [23, 24], and electrochromic devices [25].

CPs are obtained by vapor phase synthesis, electrochemical polymerization, solvothermal, hydrothermal, electrospinning, inclusion, template assisted, and plasma polymerization methods [26-29]. Though CPs offer good electrical conductivity and it can be tuned by the synthesis methods, their mechanical properties are not good. The CPs consist of sp^2 hybridized carbon atoms and one electron of these carbon atoms is present in a p_z orbital and is orthogonal to the other 3 sigma bonds. All the p_z orbitals of a molecule combine together and form a wide delocalized set. The electrons from these delocalized orbitals give rise to high mobility if the material is doped by oxidation. So, undoped or neutral conjugate polymers are found to have typically low electrical conductivity (10^{-10} to 10^{-8} S/cm) and it is found that even a small amount of doping can cause an increase of several orders of magnitude in electrical conductivity. The conductivity of the doped CPs depends on both the type and amount of the dopant. Doping in the CPs is a reversible process (Fig. 5). The CPs consist of long chains of Π conjugate polymers. The Π conjugate polymers are polymers consisting of alternating single and double or triple bonds. There can be also covalent bonds. Their charge transport phenomena are independent of their charge transport characteristics and intrinsic conductivity.

The application of CPs in energy storage devices such as grid scale storage, electrical vehicles, and portable electronic devices is attracting technological and scientific interest and it will

148

increase in future. Energy stored per unit weight or volume, power density, Cs, rate capability, cycle life, environment safety and cost are the few parameters which affect the overall performance of the CPs-based electrochemical energy storage devices or pseudocapacitors. Lithium-ion batteries are the main energy storage device. Although they have high energy density, cycle life and charge discharge rate are comparatively low. In comparison, the supercapacitors (both electric double layer and pseudocapacitors) possess high power density but at the cost of low energy density.

To enhance the performance of these novel electrical energy storage devices, the exploration of novel resources and methods to optimize the properties is therefore an area of major, emerging global research focus. For instance, the usage of nanomaterial for pseudocapacitors offers shortened pathways for mass or charge transport and new reaction pathways which are not possible to become available for the bulk material. Also, nanomaterial-based electrodes may lead to other potential advantages, e.g., (a) better accommodation of strain value induced by the electrochemical reactions, (b) high surface area, (c) flexibility, and (d) excellent mechanical properties [30].
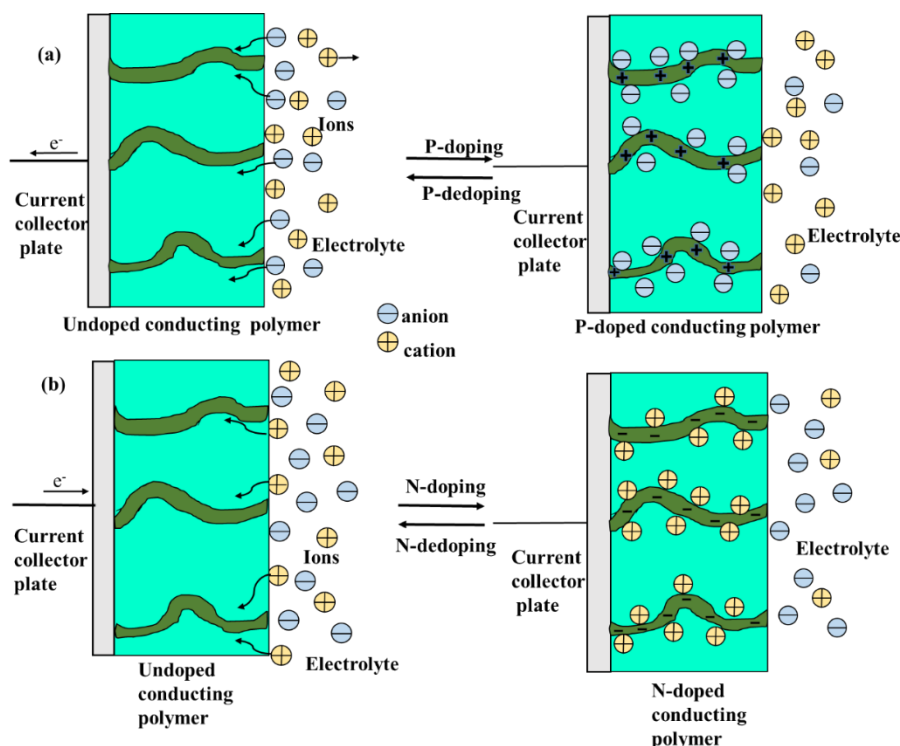

Fig. 5. Schematic representation of charging and discharging over CPs-derived electrodes associated with (a) p-doping and (b) n-doping.

Conductive polymers and composites for energy storage applications

Although a very high value of Cs value can be obtained from the CP based pseudocapacitors but some CP such as PPy and PANI lack in cycling stability [31]. During the charging and discharging process the CPs suffers from swelling and shrinkage problem which leads to cyclic instability. The CPs exhibit the greatest electrochemical performance in acidic electrolytes. PANI is the most studied CPs for the electrochemical performance. Research reported by others [32-34] confirm that it shows poor mechanical instability, volumetric shrinking and swelling during doping-dedoping process. This process leads to crack formation. Crack formation leads to breaking. The breaking ultimately leads to fast capacitance decay [32-34]. The eelectrochemical performance of polypyrrole and polyindole (PIn) have been also studied in various applications including sensors, organic light emitting diodes and energy storing devices [35-38]. Owing to their excellent mechanical strength, optical properties, and chemical activity, these CPs find applications in other fields such as chemical sensors [39], biosensors [40], and also electromagnetic shielding [41].

Combination of CPs and carbon material

Superior electrochemical properties can be obtained if composite materials are made from CPs and carbon material. Carbon material not only provides substrate backbone but also gives highly conductive pathways. Therefore, the carbon materials of all dimensions i.e., 1D, 2D, and 3D such

as activated carbon, graphene nanoribbons (GNRs), carbon nanofibers (CNFs), and carbon nano tubes (CNTs) have been combined with CPs to be used as an electrode material [42]. These composites provide electrochemical performance much superior than that of the CPs. This performance enhancement happens due to a synergistic effect between the electrostatic ions from the electric double layers and faradaic reactions of the of the CPs [43, 44].

The Cs (F g^{-1}) are calculated by the following equation (1).

$$C_s = \frac{i\Delta t}{m\,\Delta V} \tag{1}$$

where i (Amp) is the discharge current, m (g) is the mass of one working electrode, Δt (sec) is the discharge time in seconds and the ΔV (V) represents the voltage change (exclusive of the IR drop for the duration of the discharge process) in volt.

The Cs can also be calculated from the area of the CV cycle by the following equation (2),

$$Cs = \int IdV/(s\,m\,\Delta V) \tag{2}$$

The term $\int Idv$ is the integral area of the CV cycle, s is the scan rate, m is the mass of materials, and ΔV is the potential range.

The energy density E (Wh g^{-1}) of the electrode materials can be calculated using the equation (3):

$$E = \frac{C_s \times \Delta V^2}{2 \times 3.6} \tag{3}$$

where C_s (F g^{-1}) represents the specific capacitance and ΔV (V) is the potential window.

The power density P (W kg^{-1}) of the electrode material can also be evaluated from the energy density by the equation (4):

$$P = \frac{3600 \times E}{\Delta t} \tag{4}$$

Here E represents the energy density and Δt corresponds to the discharge time.

The Coulombic efficiency (η) can be calculated from the results of galvanostatic charge-discharge experiment and can be expressed as:

$$\eta = \frac{t_D}{t_C} \times 100 \tag{5}$$

The hydrothermal carbon coating on the PANI nanowire improves the cycling stability (95% retention) after 10000 cycles by the three-electrode system [45]. Deposition of carbonmaterial on CPs including enhances the cycling stability. Liu and Co workers deposited cloth shell on PANI and PPy pseudocapacitive material (i.e, PANI@C and PPy@C) and reported a cycling retention value of 95% and and 85 %, respectively, after 10000 cycles as shown in Fig. 6. Fig. 6 represents the variation of the areal capacitance of PANI, PANI@C, PPy, and PPy@C at varying current densities. In comparison to bare CPs (PANI and PPy) core shell structures display higher areal capacitance values but it decreases rapidly at higher current densities.

At higher current densities the presence of carbon shell on the polymer surface decreases the movement of electrolyte ions towards the polymer surface which leads to the increase of *iR* drop. But the presence of the carbon shell increases the cycling performance of the bare polynomial, where PANI@C shows 95% cycling retention value which is very high in comparison to 20% capacitance retention for PANI. PPy@C also shows enhancement in cycling retention value (85%) in comparison to bare PPy (25%) (Fig. 7).
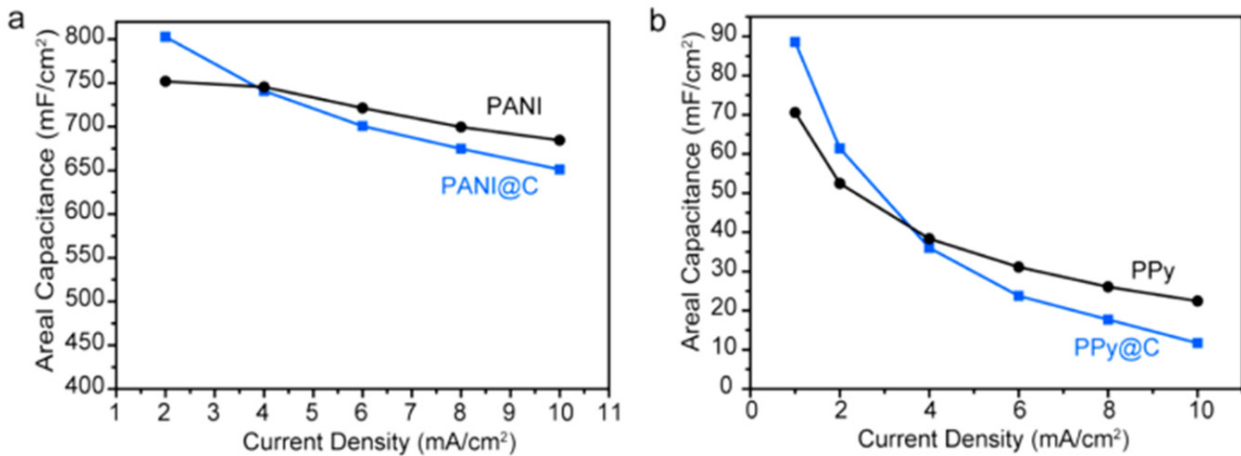

Fig. 6. Areal capacitance of (a) PANI, PANI@C and (b) PPy, PPy @C electrodes collected at different current densities [46].
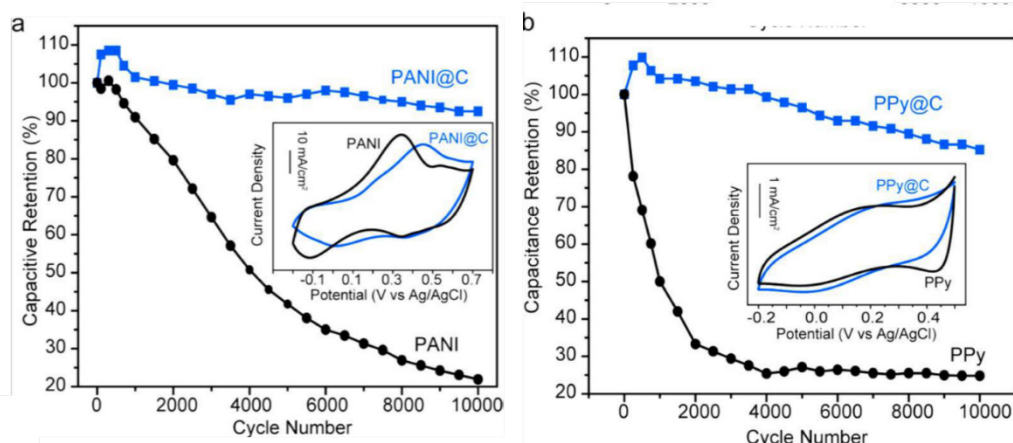
Fig. 7. Cycling performance of (a) PANI and PANI@C and (b) PPy and Ppy@C electrodes [46].
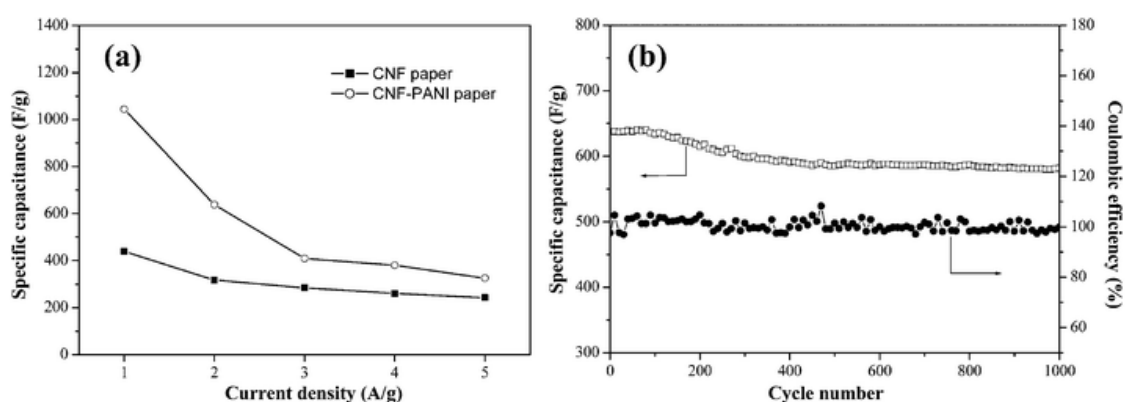

Fig. 8. (a) Variation of Cs of CNF and CNF/PANI with current density. (b) Variation of Cs and Coulomb efficiency of CNF/PANi at a current density of 2 A g^{-1} [51].

The graphene/PANI nanofiber composite films prepared by the vacuum filtration method give better Cs of 210 F g^{-1}[47]. Hybrid films of SWNT and PANI also enhances the energy density value without deteriorating the power capabilities [48-50]. Carbon nanofiber (CNF)/PANI composite produces synergistic effect as both electric double layer and pseudocapacitance contributes to the charge storage mechanism and hence, an increased capacitance value (638 F g^{-1}) (Fig. 8) [51]. For a composite material of carbon (any form) and CPs, thickness of both kinds of material (base or core material and shell material) plays a vital role in defining the electrochemical properties. It is indeed observed that the electrochemical performance of the GNR/PANI composite material is better than that of the base material (GNRs) but if the thickness of the PANI exceeds a certain limit then the Cs start decreasing because more loading of PANI in the composite material leads to reduction in the conductivity. The optimized GNR/PANI composite exhibits high Cs, e.g., 264 Fg^{-1} [52].

It needs to be noted here that the 2D carbon materials such as graphite nanoflakes (GFs),

graphene oxide (GO), and reduced graphene oxide (rGO) also have high surface area and can act as good substrate for making composite material with CPs. GO has a good compatibility with the CPs due to the presence of oxygenated groups such as hydroxyl, carboxyl, and epoxide functional groups on its basal planes and edges [53]. The comparative morphological and electrochemical studies on 1D PANI, GO and PANI/Go nanocomposite reveal that the ratio of aniline to GO plays the main role in determining the morphology of the final composite material. In terms of electrochemical performance, the PANI/GO nanocomposite gives better results, e.g., (555 F g^{-1}) [54].

Further, the 3D carbon materials such as carbon cloth, carbon fibers, activated carbon, and carbon aerogels provide good distribution of macro, meso and micropore sizes. Such activated carbons (AC) also provide charge transport pathways. Thus, *in situ* polymerized PANI/AC composite exhibits Cs value (943 Fg^{-1}) (Fig. 9) higher than that (371 Fg^{-1}) of the pure PANI material at low scan rate [55].

Although loading of PANI on AC decreases the specific surface area but Cs value enhances because

now capacitance is given by both processes, i.e., electric double layer formation due to AC and redox reactions due to the PANI. Cs decreases with increase in scan rate because high scan rate restricts low diffusion of electrolyte ions.

Similarly, the PEDOT (i.e., polyethylenedioxy thiophene)-coated carbon provides 181 Fg^{-1} of Cs for the solid-state device [56]. In a similar manner, the 3D porous polypyrole film synthesized by template-assisted method exhibits a high capacitance of 313 Fg^{-1} and 81.3% retention after 10,000 cycles by three electrode system. Here $CaCO_3$ is used as template as it creates more pores. That increases the surface area and hence, aids the diffusion-controlled process. In

addition, it enhances the total amount of redox reactions [57].

It follows that this composite design philosophy works mainly on the concept of a perfect match of the pore size of the 3D carbon material with the electrolyte ion size. When that happens, it gives rise to charge accumulation by the electric double layer formation. That is why, the CP (i.e., CPs)-3D carbon composites provide improved electrochemical properties [58, 59]. Further, the RuO_2 shell-PANI nanofiber core composites are reported [60] to have the highest Cs of 710 Fg^{-1} at 5 mVs^{-1} along with 94% retention from 5 to 100 mVs^{-1} coupled with 88% cycling stability improvement (*ca.* 65% for PANI nanofiber), (Fig. 10).
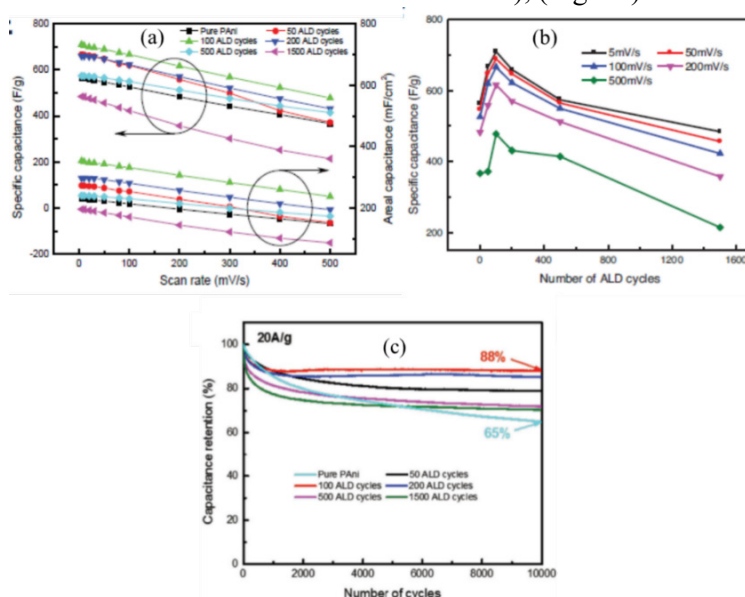

Fig. 9. Variation of Cs values of PANI and PANI/AC composite at varying (a) scan rates and (b) current density. (c) Energy density and power density of PANI and composite materials.
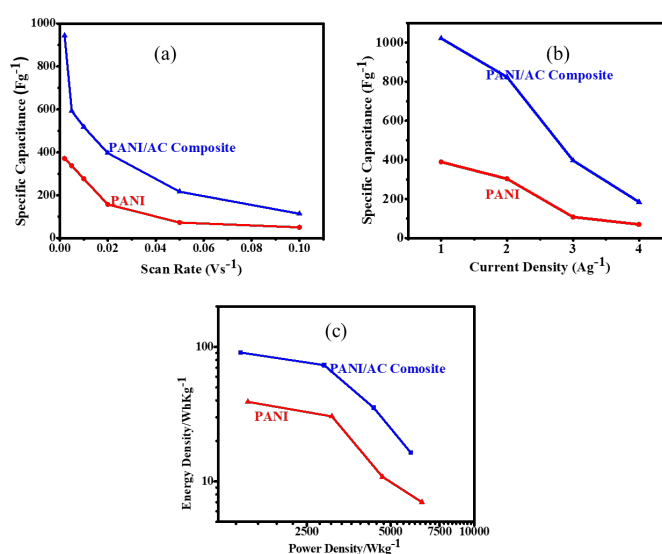

Fig. 10. Electrochemical performance of PANI/RuO_2 core shell (a) Variation of Cs and areal capacitance with scan rate, (b) variation of Cs with atomic layer deposition ALD: atomic layer deposition), (c) cyclic stability of pure PANI and core shell structure [60].

Table 1. Cs, energy and power density, and cyclic performance of CPs and its composites.

Electrode Material	Electrolyte	Cs ($F g^{-1}$)	Power density ($kW kg^{-1}$)	Energy Density ($Wh kg^{-1}$)	Cyclic Stability	Ref.
PANI-benzoquinone	H_2SO_4 (1M)	524	-	-	>5000	14
Poly(isothianaphthene)	Propylene carbonate+ 1 M Bu_4NBF_4	40				22
PPy	H_2SO_4 (0.5 M)	586	-	-	-	31
PANI/CNT	H_2SO_4-polyvinyl alcohol	350			1000	32
PPy /Polyethylene geotextile	$LiCl_4$ (1M)	545				38
PANI/MWNT	$LiPF_6$ (1M) + ethylene carbonate and dimethyl carbonate	238 (F/cm^3)	220	100 kW	-	43
SWNT/Polyaniline	H_2SO_4 (0.5 M)	706				44
PANI/Carbon cloth	H_2SO_4 (1M)	724			10,000	46
PPy/Carbon cloth	H_2SO_4 (1M)	99			10,000	46
Graphene/PANI nanofiber	-	210			800	47
SWNT/PANI	-	236	62.5	131		48
PANI/SWNT		541				50
PANI/CNF	H_2SO_4 (1M)	638			1000	51
PANI/GNRs	H_2SO_4 (1M)	340	3.2	7.56	4200	52
PANI/GO	H_2SO_4 (1M)	555			1000	54
PANI/AC	Na_2SO_4 (1M)	937	5.9	16.3	2000	55
PEDOT/CF	PVA-H_2SO_4	112	-	5.1	12000	56
PPy	-	313	-	-	10000	57
PANI/RuO_2		710	42.2	10	10000	60
PPy/CA	KOH ($mol L^{-1}$)	433			500	61
PANI/Cdots	676					66
PPy/Cdots	529					66

Though pure PPy has low Cs in comparison to PANI but composites of PPy/carbon material gives enhanced performance. For instance, the PPy/carbon aerogel composites synthesized by the chemical oxidation polymerization method gives many times increment in the Cs value (433 Fg^{-1}) in comparison to that of the pure PPy. Doping PPy with organic molecules (such as *p*-toluenesulfinate) exhibits a 96% retention after 500 cycles [62]. In addition, the ccombination of CPs with inorganic material gives a synergistic effect to provide better plastic property and electrical conductivity [63-65]. The Cs values are reported to be 529 Fg^{-1} for PANI doped with carbon dots and 676F g^{-1} for PPy doped carbon dots [66]. This work uses the *in situ* chemical oxidative polymerization method. Polythiopene has low conductivity and usually shows lower Cs values in comparison to those of PANI and PPy but it can work for a wider potential window [67, 68]. Due to its high environmental stability [69, 70] the PEDOT CP is also gaining popularity as a supercapacitor electrode material. Table 1 shows the

electrochemical performance (Cs, energy and power density, and cyclic performance) of few CPs and their composites.

Future challenges

The future developmental challenges of pseudocapacitors are deeply linked with the development of CPs and CP-(1D/2D/3D) Carbon composites. The future of CPs lies in exploring new chemistry and new molecular design along with the exploration of both existing and new fields for commercialization. Despite great progress, the n-doped CPs are yet to be able to meet the ambient stability and conductivity level of p doped polymers. Another important factor that will govern this emerging field is the development of efficient synthesis methodologies for development of new CPs. Despite the immense progress in recent research, the relationship between chain structure morphology, and conductivity is yet to be comprehensively understood. However, the immense importance of this aspect stems very much from the fact that the properties of the CPs are hugely affected by the chain length distribution of the monomers and hence, even a small amount of bond connectivity defects and undesirable crosslinking may drastically change the charge transport properties. The most obvious need of the hour is that the cycling stability of the CP based pseudocapacitors must be significantly enhanced. The rate and cycling performance of CP based electrodes can be improved by making composites of CP with other materials (e.g., carbon-based materials, nanomaterials, hydroxides, sulfides or oxides).

The major challenge is to develop these new hybrid materials in a pre-designed fashion so that they can deliver the required output for future generation of supercapacitors. Both AI and ML can play a big role here in defining the design of such exotic materials.

Thus, there can't be any doubt that there is a plenty of room for these hybrid material in supercapacitors. PANI is the most explored CPs foe energy storage application [32, 43,4 6-55, 60]. Other CPs such as poly(isothianaphthene) [22], PPy [31, 38, 46, 57, 61, 66], PEDOT [56], and PIn also have the potential for energy-storage applications. The current topic of research for carbon materials is zero dimensional (nanosized) carbon materials. Although C-dots are less conductive in comparison to conductive polymers but the synergistic effect of electric double layer and redox oxidation phenomenon may lead to better electrochemical phenomenon of the hybrid materials synthesized form the C-dots and CPs [66]. For instance, as mentioned above; if a nanocomposite of CPs and carbon material is synthesized then both electric double layer formation and pseudocapacitance can enhance the performance of the energy storage device. As and when this dream is realized, the CPs composite electrodes may play a vital role in smart, economical, and flexible energy storage applications in the future generations of pseudocapacitors.

Summary and Conclusions

This review focuses on the current state of the knowledge on existing and new materials for development of better pseudocapacitors as efficient energy storage devices. It specifically describes the developments that has taken place to enhance the specific capacitance (Cs) of CPs and their composites with (e.g., 0D, 1D, 2D, and 3D carbon), C-dots, and suitable metal oxides, e.g. RuO_2, etc. Further, it identifies the future challenges that need to be addressed for further development of CPs (PANI, PPy, PEDOT, PIn, etc.) and their composites with (0D, 1D, 2D, 3D carbon), C-dots, and suitable metal oxides, e.g. RuO_2, etc. Finally, it also suggests the need for more efficient scalable synthesis technologies for large-scale production of pseudocapacitor materials, especially the CPs so that more efficient energy storage devices can be developed in days to come.

REFERENCES

1. B. Conway, Electrochemical Supercapacitors: Scientific Fundamentals and Technological Applications, Kluwer Academic/Plenum Publishers, New York, 1999.
2. E. Frackowiak, *Phys. Chem. Chem. Phys.,* **9,** 1774 (2007).
3. F. Beguin, E. Frackowiak, M. Lu, Supercapacitors: Materials, Systems and Applications, Wiley-VCH, 2012.
4. R. Kotz, M. Carlen, *Electrochim. Acta,* **45,** 2483 (2000).
5. A. Burke, *J. Power Sources*, **91**, 37 (2000).
6. K. H. An, W. S. Kim, Y. S. Park, J.-M. Moon, D. J. Bae, S. C. Lim, Y. S. Lee, Y. H. Lee, *Adv. Funct. Mat.*, **11**, 387 (2001).
7. S. Arepalli, H. R. Fireman, P. G. Moloney, C. B. Huffman, P. Nikolaev, L. Yowell, C. D. Higgins, S. P. Turano, K. Kim, P. A. Kohl, W. J. Ready, *JOM*, **57**, 26 (2005).
8. Y. Zhang, H. Feng, X. Wu, L. Wang, A. Zhang, T. Xia, H. Dong, X. Li, L. Zhang, *Int. J. Hydrogen Energy*, **34**, 4889 (2009).

9. H. Chen, T. N. Cong, W. Yang, C. Tan, Y. Li, Y. Ding, *Prog. Nat. Sci.*, **19**, 291 (2009).

10. J. Y. Lee, K. Liang, K. H. An, Y. H. Lee, *Synth. Met.*, **150**, 153 (2005).

11. S. Rawal, B. Joshi, Y. Kumar, *J. Energy Storage*, **20**, 418 (2018).

12. S. Balasubramaniam, A. Mohanty, S. K. Balasingam, S. J. Kim, A. Ramadoss, *Nano-Micro Lett.*, **12**, 1, (2020).

13. P. Simon, Y. Gogotsi, *Nat. Mater.*, **7**, 845 (2008),

14. D. Vonlanthen, P. Lazarev, K. A. See, F. Wudl, A. J. Heeger, *Adv. Mater.*, **26**, 5095 (2014).

15. A, M. Bryan, L. M. Santino, Y. Lu, S. Acharya, J. M. D'Arcy, *Chem. Mater.*, **28**, 5989 (2016).

16. L. L. Zhang, X. S. Zhao, *Chem. Soc. Rev.*, **38**, 2520 (2009).

17. I. Shown, A. Ganguly, L. C. Chen, K. H. Chen, *Eng. Sci. and Eng.*, **3**, 2 (2015).

18. G. Wang, L. Zhang, J. Zhang, *Chem. Soc. Rev.* **41**, 797 (2012).

19. Y. Kumar, S. Rawal, B. Joshi, S. A. Hashmi, *J. Solid State Electrochem.*, **23**, 1118 (2019).

20. V. Augustyn, P. Simon, B. Dunn, *Energy Environ. Sci.* **7**, 1597 (2014).

21. G. A. Snook, P. Kao, A. S. Best, *J. Power Sources*, **196**, 1 (2011).

22. S. Sivakkumar, R. Saraswathi, *J. Power Sources*, **137**, 322 (2004).

23. C. S. Park, C. Lee, O. S. Kwon, *Polymers*, **8**, 249 (2016).

24. F. S. Omar, N. Duraisamy, K. Ramesh, S. Ramesh, *Biosens. Bioelectron.*, **79**, 763 (2016).

25. V. K. Thakur, G. Ding, J. Ma, P. S. Lee, X. Lu, *Adv. Mater.*, **24**, 4071 (2012).

26. R. Brooke, P. Cottis, P. Talem, M. Fabretto, P. Murphy, D. Ewans, **86**, *Front. Chem.*, 127 (2017).

27. C. S. Park, D. H. Kim, B. J. Shinm, D. Y. Kim, H. K. Lee, H. S. Tae, *Materials*, **9**, 812 (2016).

28. Q. Tang, J. Wu, X. Sun, Q. Li, J. Lin, *Langmuir*, **25**, 5253 (2009).

29. A. Deronzier, J. C. M., C.C. R. *Photo Chemical*, **147**, 339 (1996).

30. Y. Shi, L. Peng, Y. Ding, Y. Zhao, Y. Guihua, *Chem. Soc. Rev.*, **44**, 6684 (2015).

31. D. P. Dubal, S. H. Lee, J. G. Kim, W. B. Kim, C. D. Lokhande, *J. Mater. Chem.*, **22**, 3044 (2012).

32. C. Meng, C. H. Liu, L. Z. Chen, C. H. Hu, S. S. Fan, *Nano Lett.*, **10**, 4025 (2010).

33. T. Kombayashi, H. Honeyama, *J. Electroanal. Chem.* **177**, 281 (1984).

34. C. Choi, D.S. Ashby, D. M. Butts, R. H. DeBlock, Q. Wei, J. Lau, B. Dunn, *Nature Review Materials*, **5**, 5 (2019).

35. R. B. Choudhary, S. Ansari, B. Purty, *J. Energy Storage*, **29**, 101302 (2020).

36. Y. Huang, H. Li, Z. Wang, M. Zhu, Z. Pei, Q. Xue, Y. Huang, C. Zhi, *Nano Energy*, **22**, 422 (201),.

37. M. Gross, D. C. Muller, H. G. Nothofer, U. Scherf, D. Neher, C. Brauchle, K. Meerholtz, *Nature*, **405**, 661 (2000).

38. A. Yavuz, N. Ozdemir, H. Zengin, *Int. J. Hydrog. Energy*, **451**, 8876 (2020).

39. M. H. Naveen, N. G. Gurudatt, Y. B. Shim, *Appl. Mater. Today*, **9**, 419 (2017).

40. M. Gerard, A. Chaubey, B. D. Malhotra, *Biosensors, Bioelectron.* **17**, 345 2002).

41. S. K. Dhawan, N. Singh, D. Rodrigues, *Sci. Technol. Adv. Mater.* **4**, 105 (2003).

42. G. Yu, X. Xie, L. Pan, Z. Bao, Y. Cui, *Nano Energy,* **2**, 213 (2013)

43. M. N. Hyder, S. W. Lee, F. Ç. Cebeci, D. J. Schmidt, Y. Shao-Horn, P. T. Hammond, *ACS Nano,* **5**, 8552 (2011).

44. J. Liu, J. Sun, L. Gao, *J. Phys. Chem. C,* **114**, 19614 (2010).

45. J. Ge, G. Cheng, L. Chen, *Nanoscale,* **3**, 3084 (2011).

46. T. Y. Liu, L. Finn, M. H. Yu, H. Y. Wang, T. Zhai, X. H. Lu, Y. X. Tong, Y. Li, *Nano Lett.,* **14**, 2522 (2014).

47. Q. Wu, Y. X. Xu, Z. Y. Yao, A. R. Liu, G. Q. Shi, ACS *Nano,* **4**, 1963 (2010).

48. Z. Q. Niu, P. S. Luan, Q. Shao, H. B. Dong, J. Z. Li, J. Chen, D. Zhao, L. Cai, W. Y. Zhou, X. D. Chen, S. S. Xie, *Energy Environ. Sci.*, **5**, 8726 (2012).

49. K. L. Klein, A. V. Melechko, T. E. McKnight, S. T. Retterer, P. D. Rack, J. D. Fowlkes, D. C. Joy, M. L. Simpson, *J. Appl. Phys.*, **103**, 061301 (2008).

50. I. V. Panasenko, M. O. Bulavskiy, A. A. Iurchenkova, Y. Aguilar-Martinez, F. S. Fedorov, E. O. Fedorovskaya, B. Mikladal, T. Kallio, A. G. Nasibulin, *J. Power Sources,* **541**, 231691 (2022).

51. X. Yan, Z. Tai, J. Chen, Q. Xue, *Nanoscale,* **3**, 212 (2011).

52. L. Li, A. R. O. Raji, H. Fei, Y. Yang. E. L. Samuel, J. M. Tour, *ACS Appl. Mater. Interfaces,* **5**, 6622 (2013).

53. B. Genario, W. Lu, A.M. Dimiev, Y. Zhu, A. R. O. Raji, B. Novosel, L. B. Alemany, J. M. Tour, *ACS Nano,* **6**, 4231 (2012).

54. J. J. Xu, K. Wang, S. Z. Zu, B. H. Han, Z. X. Wei, *ACS Nano,* **4**, 5019 (2010).

55. S. Rawal, U.K. Mandal, A. Kumar, Y. Kumar, B. Joshi, *Nano Express,* **2**, 010013 (2012).

56. B. Anothumakkool, A. Torris, S. N. Bhange, M. V. Badier, S. Kurungot, *Nanoscale,* **6**, 5944 (2014).

57. T. Wang, Y. Wang Di, Zhang, X. Hu, L. Zhang, C. Zhao, Y. S. He, W. Zhang, N. Yang, Z. F. Ma, *ACS Appl. Mater. Interfaces*, **13**, 17726 (2021).

58. F. Fu, H. Wang, D. Yang, X. Qiu, Z. Li, Y. Qin, *J. Colloid Interface Sci.,* **617**, 694 (2022).

59. M. Seredych, D. Hulicova-Jurcakova, G. Q. Lu, T. J. Bandosz, *Carbon,* **46**, 1475 (2008).

60. C. Xia, W. Chen, X. Wang, M. N. Hedhili, N. Wei, H. N. Alshareef, *Adv. Energy. Mater.*, **5**, 1401805 (2015).

61. H. An, Y. Wang, X. Wang, L. Zheng, X. Wang, L. Yi, X. Zhang, *J. Power Sources,* **195**, 6964 (2010).

62. A. Kumar, R. K. Singh, H. K. Singh, P. Srivastava, R. Singh, *J. Power Sources,* **246**, 800 (2014).

63. L. Shao, J.-W. Jeon, J. L. Lutkenhaus, *Chem. Mater.*, **24**, 181 (2011).

64. G. Liu, S. Xun, N. Vukmirovic, X. Song, P. Olalde-Velasco, H. Zheng, V. S. Battaglia, L. Wang, W. Yang, *Adv. Mater.,* **23**, 4679 (2011).

65. Y. E. Miao, W. Fan, D. Chen, T. Liu, *ACS Appl. Mater. Interfaces*, **5**, 4423 (2013).

66. B. Devadas, T. Imae, *ACS Sustainable Chem. Eng.,* **6**, 127 (2018).

67. L. Yuan, B. Yao, B. Hu, K. Huo, W. Chen, J. Zhou, *Energy Environ. Sci.*, **6**, 470 (2013).

68. A. Laforgue, P. Simon, C. Sarrazin, J. F. Fauvarque, *J. Power Sources*, **80**, 142 (1999).

69. K. Lota, V. Khomenko, E. Frackowiak, *J. Phys. Chem. Solids*, **65**, 295 (2004).

70. Z. Su, C. Yang, C. Xu, H. Wu, Z. Zhang, T. Liu, C. Zheng, Q. Yang, B. Li, F. Kang, *J. Mater. Chem. A*, **1**, 12432 (2013).

Ultrasonic studies on molecular interaction of a fragrant moiety with aprotic polar solvent in their binary mixtures

S. Gupta[1,2,4]*, A. Mohan[1,4], R. Agarwal[1,4], N. U. Siddiqui[2,4], V. Jain[1,4], M. Kumar[3,4]

[1]*Department of Chemistry, Bareilly College, Bareilly-243005, Uttar Pradesh, India*
[2]*Department of Chemistry, G. F. College, Shahjahanpur-242001, Uttar Pradesh, India*
[3]*Department of Physics, K. C. M. T, Bareilly-243122, Uttar Pradesh, India*
[4]*M. J. P. Rohilkhand University, Bareilly-243006, Uttar Pradesh, India*

Ultrasonic study is an enabling technique for understanding the nature of molecular interactions in binary mixtures. Ultrasonic velocity (u), density (ρ), and viscosity (η) for binary mixtures of dihydromyrcenol (DHMOH: a commercial fragrant entity) with acetone, bearing different molar concentrations were measured at the temperatures 298.15K, 303.15K, and 308.15K. The acoustic derived parameters such as adiabatic compressibility (κ), acoustic impedance (Z), intermolecular free length (L_f), and molar volume (V_m) were also determined. The effect of molar concentration and temperature variations on various parameters was taken into consideration. The measured values of ultrasonic velocity, density and viscosity were found to increase with the increase in concentration of the solute and decrease with increase in temperature. The chosen acoustic parameters revealed a strong relationship with both concentration and temperature of binary mixtures.

Keywords: Ultrasonic velocity, Viscosity, Density, Acetone, Intermolecular interactions.

INTRODUCTION

The experimental determination of density, viscosity and ultrasonic velocity provides a better tool to understand the nature of molecular interactions in a binary mixture. The properties of the binary mixture depend upon its composition and find many applications in different chemical, industrial and biological processes [1, 2]. Therefore, the study of intermolecular interactions in the binary liquid mixtures is of considerable importance. Hence, to study the thermodynamic properties and nature of molecular interactions in the binary mixtures of dihydromyrcenol (DHMOH, 2,6-dimethyl-7-octen-2-ol) with acetone, the ultrasonic velocity, density and viscosity were measured in different compositions at 298.15, 303.15, and 308.15 K. Dihydromyrcenol is widely used as a fragrance ingredient in many useful products [3]. The molecular structure of dihydromyrcenol is shown in Figure 1. The molecules of acetone have a carbonyl functional (C=O) group. It is the simplest and smallest ketone having polar aprotic nature. Acetone is a colourless liquid solvent miscible with water. Thus, the growing demand of acetone and dihydromyrcenol in various products emphasizes the need to study the thermodynamic properties of liquids and their binary mixtures at different temperatures. Hence, in the present work, the density, viscosity, and ultrasonic velocity were measured at three temperatures,

298.15, 303.15, and 308.15 K. By using the experimental values, parameters such as adiabatic compressibility (κ), acoustic impedance (Z), molecular free length (L_f), and molar volume (V_m) were calculated by using the standard relation [1, 2, 4-7] and discussed in the next section. These parameters were helpful in understanding the nature of molecular interaction between solute and solvent. The variations in the derived parameters with temperature and molar concentration were further discussed in terms of molecular interaction between the components of the binary mixtures. Thus, the present study gives a better understanding of the intermolecular interactions in the binary system.
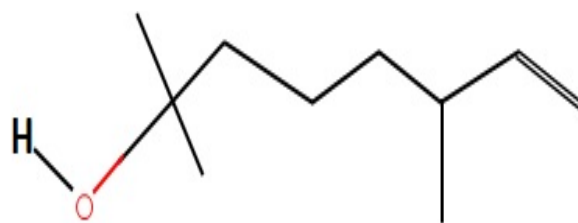

Figure 1. Structure of dihydromyrcenol (2,6-dimethyl-7-octen-2-ol) in 2D.

EXPERIMENTAL

The chemical liquid used as a solvent was purchased from S. D. Fine Chemicals, India and dihydromyrcenol (DHMOH) from Hina Chemicals,

---

* To whom all correspondence should be sent:
E-mail: shalu123gupta21@gmail.com

Gujarat (India). Binary mixtures were prepared by weighing the liquids in specially designed ground glass stoppered weighing bottles. After that, a stock solution was prepared which was diluted to different desired molar concentrations. An electronic balance of sensitivity OF 0.0001 g was used for weighing appropriate mass of the solute. The densities and viscosities of the liquids were measured at three temperatures with a specific gravity bottle and Cannon Fenske viscometer. The time taken for the flow of liquids in Cannon Fenske viscometer was measured by an electronic digital stop watch with an accuracy of ±0.01 sec. An electrically operated constant temperature-circulating water bath (Mittal Enterprises, New Delhi) was used to keep the temperature constant during the experimental observations. The ultrasonic velocities were determined by using a single frequency ultrasonic interferometer of frequency 2 MHz (Model: F-05 Mittal Enterprises, New Delhi). Before starting the experimental measurements with the ultrasonic interferometer, its measuring cell of capacity 10 mL was properly cleaned and dried to eliminate any factor which may create experimental error in the measured values. For accurate calibration of instruments some pure solvents such as 1-propanol, 2-propanol, 1-butanol, 2-butanol and acetone were used to determine the density (ρ), viscosity (η) and ultrasonic velocity (u) at 303.15 K, related to the

standard data described in the available literature and depicted in Table 1.

RESULTS

The experimental values of density, viscosity and ultrasonic velocity of the binary mixtures of DHMOH and acetone as a function of molar concentration at three temperatures are listed in Table 2. Experimental values of these fundamental parameters were further used to compute parameters, such as adiabatic compressibility (κ), acoustic impedance (Z), molecular free length (L_f) and molar volume (V_m). The expressions used for the calculation of the derived parameters, which are available in literature [1, 4-7] are as follows:

Adiabatic compressibility $\quad \kappa = \frac{1}{\rho u^2} \quad$ (1)

Acoustic impedance $\quad\quad Z = \rho u \quad$ (2)

Molecular free length $\quad\quad L_f = \frac{K_T}{u \rho^{1/2}} \quad$ (3)

where K_T is Jacobson constant that depends on temperature and is given by:

$K = (93.875 + 0.345) \times 10^{-8}$.

Molar volume of the liquid mixture is:

$$V_m = \frac{\bar{M}}{\rho} \quad\quad (4)$$

where $\bar{M}$ is mean molecular weight of the mixture.

Table 1. Comparison of density (ρ), viscosity (η) and ultrasonic velocity (u) with available literature data.

Liquids	Density (ρ) kg/m^3		Viscosity (η)mPa.s		u (ms^{-1})	
	Expt.	Lit.	Expt.	Lit.	Expt.	Lit.
1-propanol	795.42	798.00 [12] 795.71 [14]	1.590	1.610 [12]	1191.2	1189.2 [12] 1189.8 [14]
2-propanol	777.75	776.80 [10,11] 776.50[14]	1.812	1.800 [10,11]	1127.6	1126.3 [14]
1-butanol	802.80	802.60 [8] 804.40 [9] 804.00 [12]	2.104	2.222 [8] 2.151 [9] 2.054 [12]	1228.8	1228.1 [8] 1229.1 [9] 1228.4 [12]
2-butanol	796.42	798.12[15] 798.80 [16]	2.352	2.553 [16]	1193.6	1194.0 [15]
Acetone	780.23	779.00 [13] 780.33 [15]	0.313	0.292 [13] 0.295 [15]	1142.2	1141.2 [13]

Table 2. Measured values of density (ρ), viscosity (η) and ultrasonic velocity (u) of binary mixtures in terms of molar concentration at different temperatures.

Conc. (Moles/lt)	Density, ($\rho \times 10^3$kg/m^3), at different temperatures (K)		
(M)	298.15K	303.15K	308.15K
0.00	0.7851	0.7802	0.7761
0.01	0.7857	0.7808	0.7770
0.02	0.7864	0.7814	0.7775
0.03	0.7870	0.7821	0.7781

0.04	0.7877	0.7827	0.7786
0.05	0.7885	0.7835	0.7794
0.06	0.7891	0.7842	0.7801
0.07	0.7899	0.7850	0.7806
0.08	0.7906	0.7857	0.7812
0.09	0.7914	0.7866	0.7819
0.10	0.7922	0.7874	0.7825

Viscosity, η (mPa.s), at different temperatures (K)			
0.00	0.3157	0.3132	0.2990
0.01	0.3191	0.3164	0.3024
0.02	0.3225	0.3198	0.3058
0.03	0.3260	0.3235	0.3095
0.04	0.3301	0.3274	0.3134
0.05	0.3332	0.3305	0.3165
0.06	0.3363	0.3336	0.3196
0.07	0.3391	0.3364	0.3224
0.08	0.3419	0.3392	0.3252
0.09	0.3451	0.3424	0.3284
0.10	0.3479	0.3452	0.3312

Ultrasonic velocity, u (ms^{-1}), at different temperatures (K)			
0.00	1153.21	1142.20	1122.00
0.01	1156.30	1145.31	1128.06
0.02	1161.31	1150.11	1135.70
0.03	1166.40	1155.20	1139.12
0.04	1172.81	1160.28	1143.88
0.05	1176.50	1165.12	1149.08
0.06	1182.73	1171.66	1155.28
0.07	1186.40	1176.68	1160.12
0.08	1193.74	1180.44	1164.02
0.09	1199.30	1186.04	1169.56
0.10	1203.11	1193.27	1174.92

Table 3. Calculated values of adiabatic compressibility (κ_s), acoustic impedance (Z), molecular free length (L_f) and molar volume (V_m) at different concentrations and temperatures.

Conc. (Moles/lt) (M)	Adiabatic compressibility K$\times 10^{-10}$ (m^2/N)		
	298.15K	303.15K	308.15K
0.00	9.578	9.825	10.235
0.01	9.519	9.764	10.113
0.02	9.429	9.675	9.972
0.03	9.340	9.581	9.904
0.04	9.230	9.490	9.816
0.05	9.163	9.401	9.717
0.06	9.059	9.289	9.605

0.07	8.994	9.201	9.518
0.08	8.876	9.134	9.448
0.09	8.785	9.037	9.349
0.10	8.720	8.919	9.258

Acoustic impedance $Z \times 10^5$ (Kg m^{-2} s^{-1})

0.00	9.054	8.911	8.708
0.01	9.085	8.943	8.765
0.02	9.133	8.987	8.830
0.03	9.180	9.035	8.863
0.04	9.238	9.082	8.906
0.05	9.277	9.129	8.956
0.06	9.333	9.188	9.012
0.07	9.371	9.237	9.056
0.08	9.438	9.275	9.093
0.09	9.491	9.329	9.145
0.10	9.531	9.396	9.194

Intermolecular free length $L_f \times 10^{-11}$ m

0.00	6.3653	6.5056	6.7002
0.01	6.3459	6.4854	6.6603
0.02	6.3157	6.4559	6.6134
0.03	6.2857	6.4246	6.5910
0.04	6.2486	6.3940	6.5615
0.05	6.2259	6.3642	6.5284
0.06	6.1907	6.3258	6.4905
0.07	6.1684	6.2956	6.4613
0.08	6.1278	6.2728	6.4372
0.09	6.0963	6.2396	6.4038
0.10	6.0739	6.1986	6.3722

Molar volume, $V_m \times 10^{-4}$ (m^3/mol)

0.00	0.7398	0.7444	0.7484
0.01	0.7517	0.7564	0.7601
0.02	0.7635	0.7684	0.7723
0.03	0.7754	0.7803	0.7843
0.04	0.7872	0.7922	0.7964
0.05	0.7989	0.8040	0.8082
0.06	0.8107	0.8158	0.8200
0.07	0.8223	0.8274	0.8321
0.08	0.8340	0.8392	0.8440
0.09	0.8456	0.8507	0.8558
0.10	0.8571	0.8623	0.8677

ANALYSIS OF THE RESULTS

The experimental values of density, viscosity and ultrasonic velocity at temperatures 298.15K, 303.15K, and 308.15 Kare listed in Table 2. The values of adiabatic compressibility (κ), acoustic impedance (Z), molecular free length (L_f), and molar volume (V_m) at three different temperatures are given in Table 3. The experimental values of ultrasonic velocity, density, and viscosity are plotted as a function of molar concentration as shown in Figs. 1, 2 (a) & 2(b). From these figures, it can be observed that the experimental values of fundamental parameters increased with the increase in molecular concentration of DHMOH. However, the experimental values of said parameters decreased with the increase in temperature. This shows that the intermolecular forces decrease due to increase in thermal energy causing agitation in molecules of the system [2, 9]. From Table 2, it can be easily inferred that the measured values linearly increase with the increase in solute concentration. There may be an intermolecular interaction in the binary system which contributes to this behaviour [2, 6]. Further, the values of derived parameters, i.e., κ, Z, L_f and V_m, given in Table 3, are plotted in terms of molar concentration (M) as shown in Figs. 3(a,b,c &d).The results show that the adiabatic compressibility and intermolecular free length values show inverse relationship with ultrasonic velocity which is on expected lines as it is clear from the derived equations. These said parameters decreased with molecular concentration. The decreasing behaviour of 'κ' and L_f indicates that there is strong interaction between the molecules which causes the molecules to become closer together, thus resulting in a less compressible nature [6]. This may be due to the formation of a strong envelope around the solute molecules by the solvent leading to a decrease in compressibility. This fact is also supported by the increase in acoustic impedance. Eyring and Kincaid model [17] proposed that ultrasonic velocity increases with the decrease in intermolecular free length and *vice versa* when mixing two components. Similar trends were observed in the present study for intermolecular free length and ultrasonic velocity.

Acoustic impedance is the resistance of propagation of ultrasonic waves through the medium. Table 3 and Fig. 3(b), clearly reflect that the values of acoustic impedance decrease with the increase in temperature and increase with the increase in molar concentration. The changes observed in acoustic impedance with temperature and molar concentration further confirm the intermolecular interaction between the molecules [18, 19]. Besides these, the molar volume (V_m) is also found to increase with the increase in concentration of DHMOH.
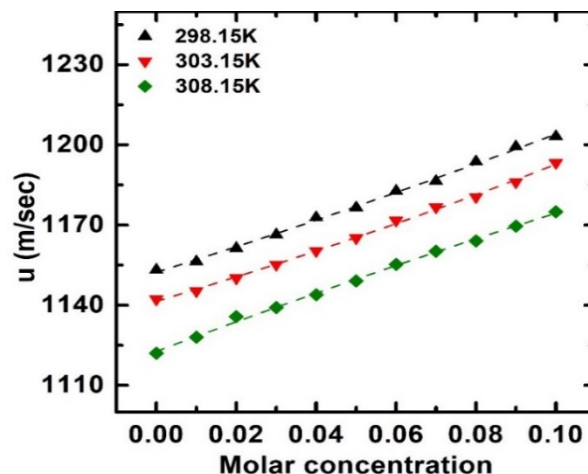
Figure 1. Variation in measured ultrasonic velocity as a function of concentration at different temperatures.

CONCLUSION

The measured values of fundamental parameters were found to increase with concentration of solute in binary mixtures whereas these values decreased with the increase in temperature, thus indicating presence of intermolecular interactions in the experimental binary mixtures. It was also observed that the ultrasonic velocity increased with the concentration of DHMOH whereas the intermolecular free length decreased. On the contrary, ultrasonic velocity showed a reduction in values with the increase in temperature which may be due to the rise in thermal energy of binary system. The decrease in adiabatic compressibility suggests a formation of solvation layer around the solute molecules which indicates a marked molecular interaction in binary mixtures.
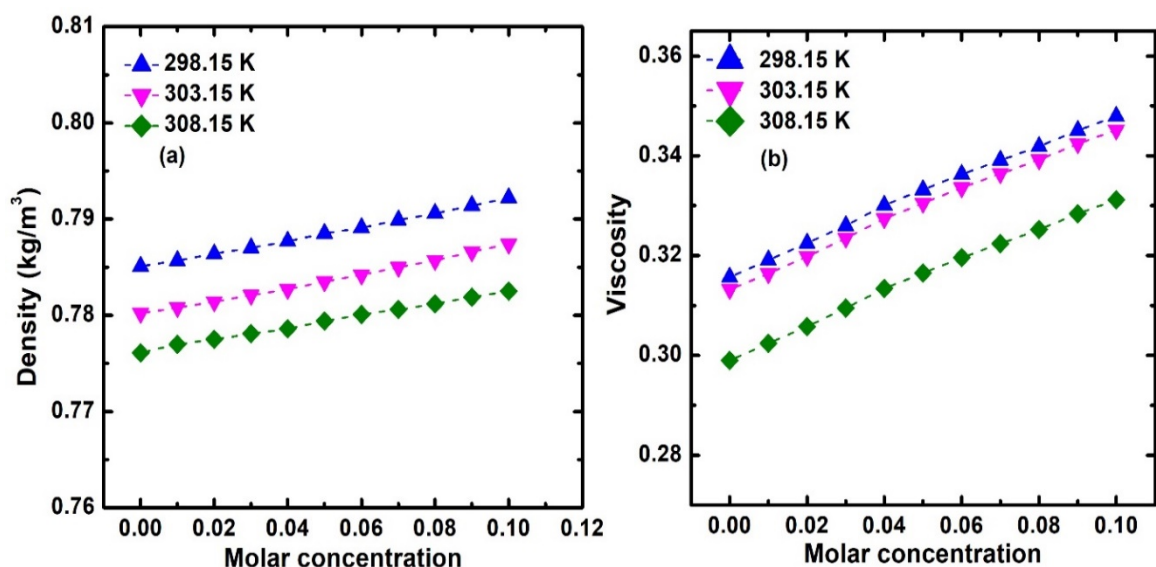
Figure 2. Measured values of density (ρ), viscosity (η) at different molar concentrations and temperatures.
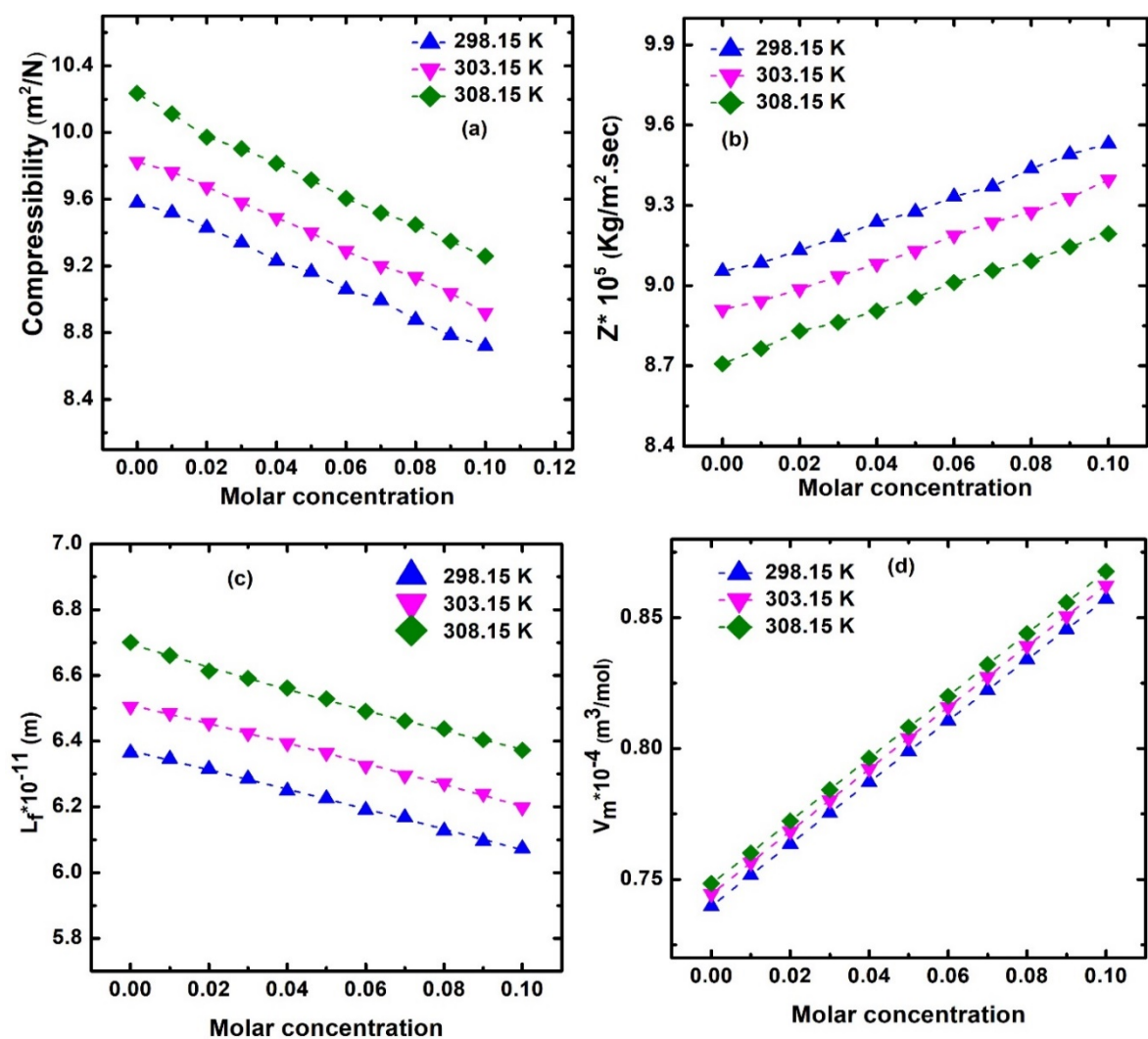

Figure 3. Variation in derived parameters; adiabatic compressibility (κ), acoustic impedance (Z), molecular free length (L_f), and molar volume (V_m)sat different molar concentrations at three different temperatures.

REFERENCES

1. A. Ali, Abida, S. Hyder, *Phys. Chem. Liq*., **42**, 4 411 (2004).
2. M. Srilatha, D. Chinnarao, B. V. Rao, C. V. Padmarao, N. Murali, B. A. Kumar, B. K. Babu, *Spectrochimica Acta A Mol. Biom. Spectroscopy,* **202**, 174 (2018).
3. V. T. Politano, E. M. Lewis, A. M. Hoberman, M. S. Christian, R. M. Diener, *Api, Int. J. Toxicol*., **28**, (2009), 80.
4. A. N. Kannappan, V. Rajendran, *J. Pure Appl. Ultrason,* **13,** 27 (1991).
5. A. Pal, R. K. Bhardwaj, *Z. Phys. Chem.,* **216**, 1033 (2002).
6. R. Kumar, R. Mahesh, B. Shanmugapriyan, V. Kannappan, *Ind. J. Pure Appl. Phys.*, **50**, 633, (2012).
7. B. Kumar Sarkar, A. Choudhury, B. Sinha, *J. Solution Chem.***, 41**, 53 (2012).
8. M. Srilatha, B. V. Rao, B. V. Saradhi, *Current Sci.,* **113**, 1553 (2017).
9. S. Elangovan, S. Mullainathan, *Elixir Ultrasonic*, **58A**, 15048 (2013).
10. F. M. Pang, C. Seng, T. Teng, H. M. Ibrahim, *J. Mol. Liq.,* **136**, 71 (2007).
11. S. Heydarian, M. Almasi, Z. Saadati, *J. Chem. Thermodynamics,* **135**, 345 (2019.
12. S. Sreehari Sastry, S. Babu, T. Vishwam, K. Parvateesam, H. SieTiong, *Physica B*, **420**, 40 (2013).
13. K. Rajagopal, S. Chenthilnath, *J. Chem. Therms.,* **42,** 675 (2010).
14. A. Ali, A. Nain, D. Chand, R. Ahmad, *Phys. Chem. Liq.,* **43**, 205 (2005).
15. J. A. Riddick, W. B. Bunger, T. Sakano, Organic Solvents: Physical Properties and Methods of Purification, fourth Edn., Wiley Interscience, New York, 1986.
16. A. Ali, A. K. Nain, B. Lal, D. Chand; *Int. J. Thermos.,* **25**, 6 (2004).
17. J. F. Kincaid, H. Eyring, *J. Chem Phys.,* **6**, 620 (1938).
18. M. Das, M. N. Roy, *Phy. Chem. Liq*., **44**, 663 (2006).
19. J. D. Pandey, Ranjan Dey J. Chhabra, *Phys. Chem. Comm.,* **6**, 55 (2003).

Microwave synthesis of starch-G-polymethylmethacrylate-G-polyvinyl alcohol for sustained urea release

Shashi Verma*, Raj Kishore Tiwari

Department of Chemistry, University of Lucknow, Lucknow, (U.P.) India

To address agro-environmental pollution concerns, a fully biodegradable formulation was developed by grafting potato starch with polymethylacrylate and polyvinyl alcohol (St-g-PMA-g-PVA). This eco-friendly formulation was synthesized using microwave irradiation. The successful grafting of polyvinyl alcohol onto the potato starch-poly(methylacrylate) backbone was verified using FTIR, confirming the desired chemical structure. TGA analysis provided evidence of the formulation's thermal stability under varying conditions. SEM images provided visual confirmation of the successful grafting process. The formulation's properties, including urea entrapment efficiency, equilibrium water absorption, and urea release kinetics from the copolymer, were investigated. The incorporation of hydrophilic PMA-PVA content significantly enhanced the swelling capacity of the starch matrix. Moreover, the control over the release rate of urea from the loaded copolymer could be achieved by adjusting the graft efficiency. This innovative approach demonstrates potential in mitigating environmental impact while offering controlled nutrient management in agriculture.

Keywords: Microwave synthesis, Characterization, Controlled release, Graft copolymers, Urea

INTRODUCTION

The realm of controlled drug delivery has emerged as a multidisciplinary field focused on enhancing drug administration. The purpose of drug delivery systems is to optimize drug release methods. Polymers have been instrumental in advancing drug delivery by enabling the controlled dispensation of therapeutic agents, ensuring consistent dosages over prolonged periods, cyclic administrations, and customizable release of both hydrophilic and hydrophobic medications [1]. The category of responsive polymers applicable to drug delivery encompasses hydrogels, micelles, polyplexes, and polymer-drug conjugates, which will be elaborated upon below.

Hydrogels represent hydrophilic networks formed by (co)polymers with the capacity to absorb substantial amounts of water or biological fluids [2]. Over time, biodegradable carbohydrate graft copolymers have been explored to address specific needs within the realm of polymer-based drug delivery. Carbohydrate-PVA based hydrogels, beads, and scaffolds have found extensive utility in sectors such as agriculture, biomedicine, environment, and food packaging [3-5]. Amidst the diverse polymer options for drug delivery, natural polymers stand out due to their remarkable biocompatibility, minimal toxicity, and efficient enzymatic degradation [6, 7]. Counteracting the limitations of raw starch in terms of mechanical strength and rapid release, chemical modifications have been conventionally undertaken to enhance its properties. Synthetic polymers offer favorable attributes, and the combination of natural and synthetic polymers yields both mechanical stability and biocompatibility, leveraging the synergies between the two materials for controlled drug delivery [8-14]. To achieve this, alterations have been applied through grafting, blending, or crosslinking [15-19]. Grafting of vinyl monomers onto natural polymers is a widely accepted strategy [20-24], having practical and academic significance in controlling drug molecule release. It presents a convenient avenue for modifications catering to the agrochemical field's needs, including sustained fertilizer release to reduce pollution and health hazards.

Recent strides have been made with hydrophilic starch graft copolymers exhibiting high swellability, prominent in crafting controlled release mechanisms for highly water-soluble agrochemicals and nutrients in agricultural applications [25-27]. These graft copolymers have outperformed individual conventional polymers in controlled release devices, thus expanding their scope and applications [28, 29]. Urea, among various fertilizers, stands out for its high nitrogen content and cost-effectiveness. However, its significant solubility results in economic losses and environmental pollution [30-33], issues that controlled release techniques effectively address. Utilizing controlled release formulations for agrochemical delivery offers economic advantages [34-36].

* To whom all correspondence should be sent:
E-mail: sverma.lkouni@gmail.com

Earlier studies have investigated controlled release of diverse herbicides like simazine, 2,4,5-trichlorophenoxy acetic acid, and triazine, employing polymeric matrices [37-39]. Starch-based hydrogels have been employed for carbendazim delivery [40]. St-g-polylactide and St-g-polyacrylic acid have facilitated urea release [8, 41]. Grafting synthetic monomers onto the starch backbone emerges as a potent strategy to enhance starch properties. In the present study, we explore grafting polyvinyl alcohol onto St-g-PMA matrix, aiming to enhance the mechanical strength of natural graft copolymers [42]. These composites are formulated into graft copolymers, subsequently loaded with agrochemicals.

EXPERIMENTAL

Materials

The graft copolymer synthesis was conducted utilizing a household microwave oven, specifically the LG Intellocook TM-MS-1947 C model, operating at a frequency of 2450 MHz and capable of delivering up to 800W of power. The polyvinyl alcohol (PVA) used, with a molecular weight of 125,000, was sourced from Sd Fine Chemical limited in Mumbai, India, and was employed without additional purification. The procurement of potassium persulfate ($K_2S_2O_8$) was from Merck, India. The entirety of the study relied on distilled water. The St-g-PMA copolymers, integral to this synthesis, were prepared as detailed in the subsequent sections.

Synthesis of starch-g-PMA

In a 250 ml flask, the starch solution (0.1 g dissolved in 30 ml of hot distilled water) served as the base. To this solution, thiourea (TU) (0.01M) and $K_2S_2O_8$ (0.02M) were introduced. Following thorough stirring, methylmethacrylate (MA) (0.11 M) was incorporated into the reaction mixture. Subsequently, the flask was placed within a microwave oven and exposed to irradiation. The irradiation process occurred under microwave power (MW) of 320 W for a duration of three minutes. After the reaction reached completion, the initial product was obtained, which was then precipitated using a methanol:water mixture (3:1 ratio), where the homopolymer dissolves. The resultant graft copolymer solid was subsequently cleansed with a methanol:water mixture to eliminate any unreacted monomers and reagents. Finally, the graft copolymer solid was dried in a vacuum oven at 40°C until a consistent weight was achieved.

Synthesis of St-g-PMA-g-PVA

The PVA solution (5% w/v) was formulated by dissolving the requisite PVA amount in hot distilled water (100 ml). The dispersion of starch graft PMA in water was achieved through heating at 100°C under continuous stirring, ensuring a uniform blend. Into this mixture, 0.02 M $K_2S_2O_8$ was introduced while maintaining constant stirring. Following this, the flask underwent exposure to microwave irradiation for three minutes at 640 W. Upon completion of the reaction, the mixture underwent cooling, and the resultant product was precipitated using a methanol:water mixture (3:1 ratio). The preliminary product was filtered, washed twice with water, and dried at room temperature until reaching a consistent weight.

Urea encapsulation

The encapsulation process for urea involved immersing a precisely weighed quantity of the prepared matrix (on a dry basis) into a saturated urea solution at room temperature, allowing it to achieve swelling equilibrium. Once equilibrium was reached, the swollen graft copolymers were removed, and excess liquid on their surface was absorbed using filter paper. The subsequent step involved gradual evaporation of the water at 40°C. Before initiating the release experiments, the samples underwent two rounds of thorough washing with water to eliminate surface-exposed urea from the graft copolymers.

CHARACTERIZATION

FTIR spectrum

Fourier-transform infrared (FTIR) spectra measurements were conducted using a Perkin-Elmer FTIR spectrophotometer from the USA, utilizing KBr pellet technique. The FTIR spectrum analysis of pure PVA (depicted in Figure 1c) exhibited a broad peak approximately at 3426.1 cm^{-1}, indicating the presence of intramolecularly hydrogen-bonded hydroxyl groups within singular bridge compounds. Notably, peaks observed at 3022.1 and 1217.1 cm^{-1} were attributed to C-H stretching, denoting the presence of a hydrocarbon chromophore in the PVA structure. Regarding the St-g-PMA spectrum (illustrated in Figure 1a), distinctive peaks emerged at 3450.6 and 1047.8 cm^{-1}, likely attributed to –OH stretching and skeletal (C-O-C) vibrational stretching arising from the starch component. Furthermore, a discernible band at 1746.1 cm^{-1} was observed, indicative of the presence of a carboxylic group (>C=O) in the structure.

The FTIR spectrum of the St-g-PMA-g-PVA matrix (depicted in Figure 1c) demonstrated a distinct peak at 3434.3 cm^{-1}, suggestive of intermolecular hydrogen-bonded hydroxyl groups that contribute to polymeric association. Alongside these observations, the graft copolymer matrix also exhibited peaks at 3025.1 and 1217.8 cm^{-1}, which are indicative of the presence of a hydrocarbon chromophore. Notably, the characteristic peak associated with the carboxylic group at 1746.1 cm^{-1} was absent, indicating the absence of >C=O groups in this structure [42]. This absence strongly suggests that all the carboxylic groups of St-g-PMA have been engaged in the grafting process, signifying the successful grafting of PVA onto the St-g-PMA backbone.
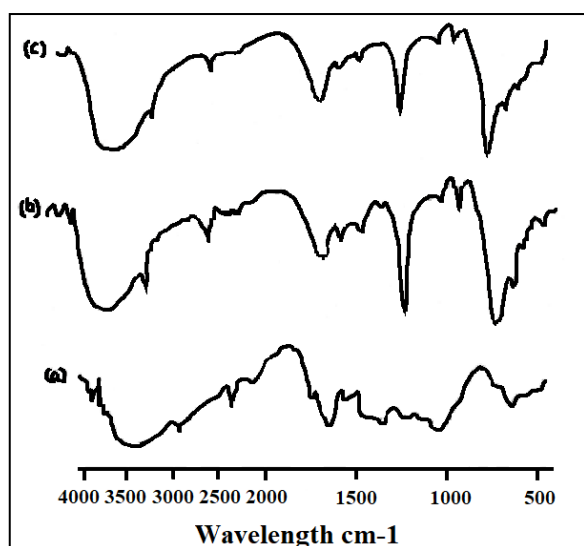
Fig. 1. FTIR spectra (a) St-g-PMA (b) St-g-PMA-g-PVA (c) PVA

Thermogravimetric analysis

The thermal stability and degradation patterns of the St-g-PMA and St-g-PMA-g-PVA matrices were assessed using an EXSTAR TG/DTA 6300 instrument under atmospheric conditions. Melting studies were conducted over a temperature range of 25°C to 800°C, employing a heating rate of 20°C/minute in an oxygen environment. The TGA results are graphically presented in Figure 2. The thermogram of St-g-PMA (Figure 2b) exhibits a three-stage weight loss profile. Initially, up to 100°C, a weight loss of 3.7% occurred, likely attributed to moisture loss. Subsequent weight losses were observed at 9.4%, 41.8%, and 86.2%. These losses occurred at temperatures of 200°C, 300°C, and 500°C. Previous reports have indicated that pure PVA undergoes decomposition in two stages and remains thermally stable up to around 265°C, with a weight loss of approximately 15% [42, 43].

Decomposition products of pure PVA have also been documented [44]. Turning to the TG curve of the St-g-PMA-g-PVA matrix (Figure 2a), the graft copolymer demonstrated a gradual weight loss until 290°C, primarily due to 1.3% residual surface water loss. Beyond this point, a rapid weight decrease was evident. The matrix exhibited decomposition temperatures at 200°C, 300°C, 400°C, 500°C, and 600°C, resulting in weight losses of roughly 7.3%, 33.3%, 48.2%, 69.6%, and 89.0%, respectively. A comparative thermal analysis underscores the enhanced thermal resistance of the prepared graft copolymer, St-g-PMA-g-PVA, up to 600°C.

Swelling equilibrium

A precisely weighed composite matrix sample was immersed in distilled water at room temperature until equilibrium was reached. Subsequently, the swelled samples were extracted from the water and gently dried using filter paper to remove excess water. The equilibrium water absorbancy (Qev) of the matrix was calculated by weighing the swollen samples and employing the following equation [45]:

$$Qev\ (g/g) = \frac{M2 - M1}{M1}$$

where M_2 is the weight of the swelled sample and M_1 is the weight of the dried sample. Qev is expressed in gram/g.
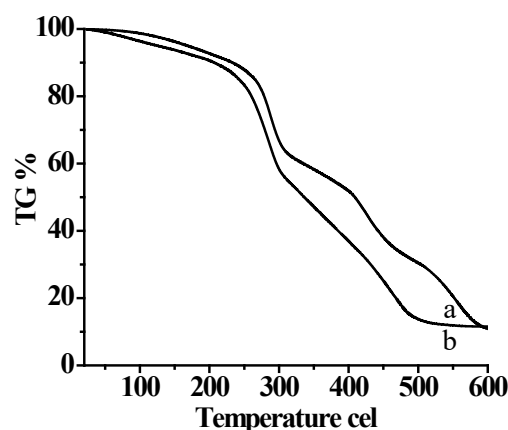

Fig. 1. Comparative TGA graph of St-g-PMA (b) St-g-PMA-g-PVA (a).

Encapsulation efficiency

The encapsulation efficiency of the matrix is indicated by the total weight percentage of the substance enclosed within it. To accurately quantify the amount of encapsulated urea, the samples were weighed and subjected to washing with 20 ml of water to eliminate excess surface-bound urea. The urea content in the water was subsequently determined spectrophotometrically at 420 nm [46].

The encapsulation efficiency was computed using the following formula:

$$EE\ (\%)\ =\ \frac{[1-W2\ ]\ X100\%}{[WoxC]}$$

where W_0 is weight of loaded urea sample, W_2 is the urea exposed on surface of the grafted matrix and C is the urea content of the matrix calculated from the feed composition.

Urea release study

The investigation into the *in vitro* release of urea from the St-g-PMA-g-PVA matrix involved placing 200 mg of dried and loaded samples in 500 ml of distilled water at 25°C. At set intervals, a 2 ml portion of the solution was extracted, and an equivalent volume of water was introduced to maintain a constant volume. The measurement of the released urea amount was conducted using a UV-spectrophotometer at 420 nm [46].

Surface morphology

The surface morphology assessment of both the St-g-PMA matrix and the prepared St-g-PMA-g-PVA matrix was carried out using an LEO 430 SEM model. Before examination, the specimen surfaces were coated with a layer of gold through sputter coating. In the SEM micrographs of the grafted starch matrix, a relatively coarse surface was observed, indicating that the amorphous starch had undergone partial miscibility with poly(methylacrylate) (as depicted in Figure 3). Figure 4 showcases the polyvinyl alcohol dispersion within the St-g-PMA matrix, revealing a relatively smooth surface with voids. This is in contrast to the agglomerated surface of St-g-PMA. Furthermore, Figure 5 displays the SEM images of the graft copolymer matrix loaded with urea. Evidently, the grafting of polyvinyl alcohol occurred uniformly onto the grafted starch backbone. The SEM analysis of the St-g-PMA-g-PVA matrix unveiled that the grafting of PVA and PMA resulted in physical and chemical crosslinking, as discernible pores are evident in the micrographs. It's hypothesized that these pores correspond to regions of water permeation and interaction sites for external stimuli with the hydrophilic groups of the graft copolymers.

RESULTS AND DISCUSSION

In the St-g-PMA matrix, the unbound carboxylic groups ($>C=O$) of PMA engage with OH groups of PVA through microwave irradiation, resulting in the formation of the graft copolymer. During this grafting process, only a minimal quantity of homopolymer is produced. The grafted product and PVA can be conveniently separated through cold water treatment, as PVA exhibits solubility in this condition. This solubility tends to increase with the augmentation of poly(methylacrylate) content. The graft copolymerization involving synthetic hydrophobic monomers like poly(methylacrylate) distinctly reduces the swellability of the St-g-PMA matrix. Conversely, water absorbancy shows an increase with elevated PVA content. This is attributed to the abundance of free hydroxyl groups, leading to a greater presence of hydrophilic groups and subsequently enhancing water absorbancy. A comparative assessment of the swelling equilibrium for both St-g-PMA and St-g-PMA-g-PVA copolymers is presented in Table 1. The optimal swelling equilibrium is achieved when the contents of St-g-PMA and PVA are in equal proportions. Similarly, maximum urea loading is attained under these balanced conditions. The resulting graft copolymer matrix exhibits an equilibrium swelling of 364% after eight hours, and this value remains relatively constant for up to 250 hours. This equilibrium swelling is anticipated to diminish after this duration.
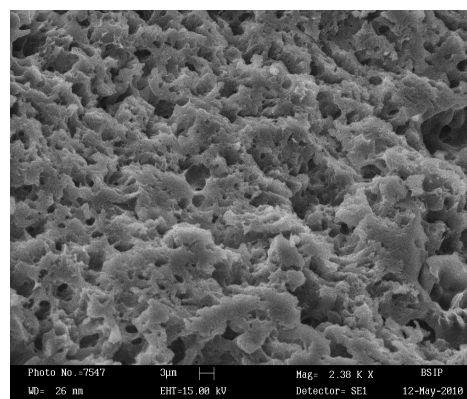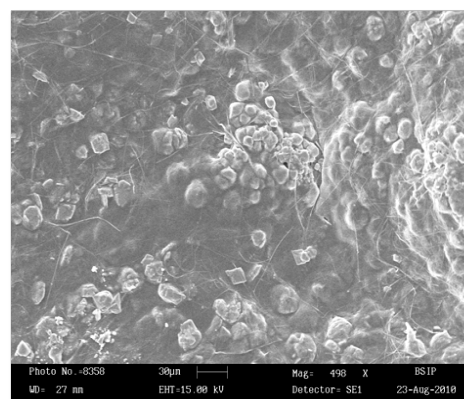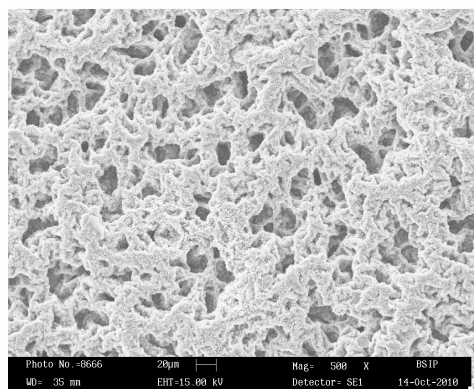

Fig. 3. SEM of St-g-PMA copolymer

Fig. 4. SEM of St-g-PMA-PVA copolymer

Table 1. Swelling equilibrium of St-g-PMA and St-g-PMA-g-PVA copolymer

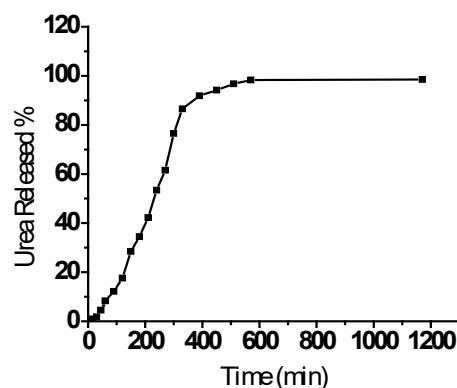| GSC	WH %	UH %	SW Qeq
St-g-PMA: PVA (25:75)	6.1	43.70	286
St-g-PMA: PVA (50:50)	4.2	69.98	364
St-g- PMA:PVA (75:25)	2.5	32.1	186
St-g-PMA (100)	1.5	14	150

GSC* starch graft copolymers, WH* water holding %, UH* urea holding%, SWQeq* swelling equilibrium

Fig. 5. Urea loaded St-g-PMA-g-PVA copolymer

Fig. 6. Urea released percentage with time

The graft copolymer matrix exhibits enhanced urea encapsulation, primarily attributed to the presence of voids within the graft copolymer structure. In Figure 5, SEM micrographs of urea-loaded graft copolymers clearly illustrate the presence of these voids. The loading capacity for urea displays an upward trend with increasing PVA content, reaching its maximum capacity at 50% PVA content, corresponding to a grafting efficiency of 50% for PVA. The impact of graft modification and grafting ratio on the urea release rate from the grafted matrix is outlined in Table 1. Generally, the release rate of urea from the grafted matrix is diminished compared to the St-g-PMA matrix. The diffusion nature of urea into the graft copolymer matrix was predicted using the following equation.

$$F = M_T/M_0 = Kt^n$$

The fractional release of urea at time "t" denoted by M_T/M_∞, where "k" stands for the constant linked to the network structure, and the exponent "n" signifies the diffusion exponent indicative of the release mechanism. In instances of regular Fickian diffusion, the value of "n" equals 0.5. For Case II diffusion, "n" equals 1.0, and for non-Fickian diffusion, "n" ranges between 0.5 and 1.0. The release mechanism for urea from the grafted matrix is assumed to exhibit a non-Fickian diffusion behavior.

The maximum urea release from the St-g-PMA-g-PVA matrix reached approximately 98.38% within 26 hours (as demonstrated in Figure 6). During the initial stage, the release rate exhibited rapid progress, nearly reaching its maximum value within 6-7 hours. The pattern observed in the plot indicates a linear release rate behavior during the initial six-hour period, followed by a slower release rate that ultimately leads to almost complete release within ten hours. The graft copolymer matrix effectively releases the encapsulated urea in a controlled and prolonged manner, which is a critical requirement for the controlled use of agrochemicals to mitigate environmental and health concerns.

CONCLUSIONS

A St-g-PMA-g-PVA matrix was successfully synthesized through microwave irradiation, yielding a high product yield. The hydrophobic nature of poly(methylacrylate) contributed to a reduction in the swelling capacity of the grafted matrix, resulting in enhanced water resistance. The incorporation of PMA was effective in bolstering the mechanical properties of the compatible composite, along with fostering biodegradation. The grafting of PVA onto the St-g-PMA backbone led to improved swelling efficiency and enhanced thermal behaviors. Comparatively, the urea release rate from the St-g-PMA-g-PVA matrix exhibited a decrease compared to ungrafted starch. The release mechanism was

characterized as non-Fickian diffusion. The prepared graft copolymer matrix exhibits potential for application as a controlled-release carrier in environments involving heavy water.

REFERENCES

1. B. Begines, T. Ortiz, M. Pérez-Aranda, G. Martínez, M. Merinero, F. Argüelles-Arias, A. Alcudia, *Nanomaterials (Basel,* **10**, 1403, (2020)

2. V. Tyagi, A. Thakur, R. L. Kroen*, Materials Today: Proceedings* **(**2023)**.**

3. R. H. Gabriela, A. R. Marilena, M. M. Patricia, L. S. Mirna, *Internat. J. Pharmaceutics,* **600**, 120478, (2021).

4. J. Pushpamalar, A. K. Veeramachineni, C. Owh, X. J. Loh, *Chem. Plus. Chem.,* **81**, 504, (2016).

5. C. Wang, T. Yokota, T. Someya. *Chemical Reviews,* **121**, 4, 2109 (2021).

6. R. P. Singh, S. Pal, S. Krinamurti , P. Adnard, S. K. Akber , R. P. Singh, S. Pal , S. Krishnamoorthy, P. Adhikary, S.K. Ali. *Pure Applied Chem.,* **81**, 525, (2009).

7. P. Vitor, F. Lemos, H. R. Marcelino, L. G. Cardoso, C. O. de Souza, J. I. Druzian, *Internat. J. Biolog. Macromolecules*, **184**, 218, (2021).

8. Y. Niu, H. Li., *Ind. Eng. Chem. Res.,* **51**, 38, 12173, (2012).

9. J. Nath, A. Ahmed, P. Saikia, A. Chowdhury, S. K Dolui*, Applied Clay Science,* **190**, 105569, (2020).

10. L. Dai, C. L. Si, *Mat. Letters,* **207,** 213 (2017)

11. L. Pang, Z. Gao, H. Feng, S. Wang, Q. Wang, *J. Controlled Rel.,* **316**, 105, (2019).

12. J. Meimoun, V. Wiatz, R. Saint-Loup, J. Parcq, A. Favrelle, F. Bonnet, P. Zinck, *Starch-Stärke,***70** (1-2), 1600351, (2018).

13. D. F. Apopei, M. V. Dinu, E. S. Dragan, *Digest J. Nanomaterials,* **7** (2), 707 (2012).

14. N. F. A. Ghapar, H. Baharin, K. J. A. Karim, *AIP Conference Proceedings,* **1985**, 050001 (2018).

15. S. Mehtab, M. G. H. Zaidi, N. Rana, K. Khati, S. Sharma, *Bull. Mat. Sci.* **45**, 162 (2022).

16. M. C. Li, X. Ge, U. R. Cho, *Macromolecular Research,* **21**, 519, (2013).

17. H. Chen, L. Yu, Z. Wang, ul Abdin, Y. Chen, J. Wang. *Q RSC Adv.,***5**, 67459, (2015).

18. A. Gandhi, S. Verma, S. S Imam, M. Vyas*, Plant Archives,* **19(2)**, 972 (2019).

19. P. Duan, S. Jiang, F. Chen, Z. Li, L. Ma, Y. Song, X. Yu, Y. Chen, H. Liu, L. Yu. *Industrial Crops Products,* **192,** 116075, (2023).

20. P. Joshi, S. Mehtab, M. G. H. Zaidi, *Bull. Chem. Soc. Jpn.*, **95**, 855 (2022).

21. P. Joshi, G. Bisht, S. Mehtab, M. G. H. Zaidi, *Mater. Today Chem.,* **62**, 6814 (2022).

22. S. Moolsin, N. K Robishaw, *J. Curr. Sci. Technol.,* **5(1),** 99 (2015).

23. T. T Hong, H. Okabe, Y. Hidaka, K. Hara, *Environment. Pollution,* **242(B),** 1458, (2018).

24. U. Yasmeen, F. Haq, M. Kiran, A. Farid, A. N. Vallah, T. Aziz, *Molecules,* **27 (18**), 5844, (2022)

25. T. Bal, S. Swain, *J. Pharmaceutical Sci.,* **28**, 33, (2020).

26. R. Liang, H. Yuan, G. Xi, Q. Zhou, *Carbohydrate Polym.*, **77,** 181 (2009).

27. H. Wei, H. Wang, H. Chu, J. Li. *Int. J. Biol. Macromolecules,* **133**, 1210 (2019).

28. A. Chang, *Iranian Polym. J.*, **24**, 161 (2015).

29. Q. Wei. *Iranian Polym., J.,* **23**, 637 (2014).

30. S. Chen, M. Yang, C. Ba, S. Yu, Y. Jiang, H. Zou, Y. Zhang. *Sci. Total Environ.,* **615,** 431 (2018).

31. A. M. Dave, M. H. Mehta, T. M. Aminabhavi, A. R. Kulkarni, K. S. Soppimath, *Polym. Plastics Technology Eng.,* **38**, 675 (1999).

32. Y. Naz, S. A. Sulaiman. *J. Controll. Rel.*, **225**, 109 (2016).

33. L. Xie, M. Liu, B. Ni, X. Zhang, Y. Wang. *Chemical Eng. J.,* **167** (1), 342 (2011).

34. E. V. R. Campos, J. L. De Oliveira, L. F. Franceto, *Advanced Sci. Eng. Medicine*, **6**, 373, 1538, (2014).

35. A. Singh, D. Dhiman, A. K. Kar, D. Singh, M. P. Purohit, *J. Hazardous Mat.,* **384**, 121525 (2020).

36. E. V. Piletska, N. W. Turner, A. P. F. Turner, S. A. Piletsky, *J. Cont. Rel.,* **108,** 132 (2005).

37. G. R. Mahdavinia, S. B. Mousavi, F Karimi, G. B. Marandi, *e-Polymers,***144**, 1618 (2009).

38. L. D. Moreno, L. S. Moreno, A. Pena, *Environment.,* **378**, 119 (2007).

39. B. Singh, D. K. Sharma, S. Negi, A. Dhiman, *Internat. J. Plastics Technol.,* **19**, 263 (2015).

40. C. Bai, S. Zhang, L. Huang, H. Wang, W. Wang, *Carbohyd. Polym.,* **125**, 376 (2015).

41. F. Chen, C. Miao, Q. Duan, S. Jiang, H. Liu, L. Ma, *Ind. Crops Products*, **191(A),** 115971, (2023).

42. M. Patil, S. N. Mathad, A. Y. Patil, M. N. Arshad, H. S. Alorfi, M. Puttegowda, A. M. Asiri, A. Khan, N. Azum, *Polymers*, **14,** 350 (2022).

43. B. S. Kaith, S. Kaliya. *Polymer J.,* **39**, 1319 (2007).

44. R. Watanabe, H. Hagihara, H. Sato, *Polymer J.*, **50,** 1067 (2018).

45. V. Vijan, S. Kaity, S. Biswas, J. Issac, A. Ghosh, *Carbohyd. Polymer,* **90**, 496, (2012).

46. F. L. David, J. E. Sherwood, P. S. Francis, *Aust. J. Soil Res.,* **42(7),** 709 (2004).

Sustainable development of essential oils coated antimicrobial cellulosic fabric

S. Massey[1]*, S. Mehtab[2]

[1]Department of Clothing and Textiles, College of Community Sciences,
[2]Department of Chemistry, College of Basic Sciences and Humanities, Govind Ballabh Pant University of Agriculture and Technology, Pantnagar-263145, Uttarakhand, India

Novel finishing of fabrics through sustainable route has always raised demand for eco-friendly textiles and apparels intended for hygiene and medical applications. This research reports the antimicrobial activity of four essential oils (eucalyptus, clove, mint and neem oil) at 10 to 60 µl against bacteria *S. aureus* and fungi *A. niger*. Neem oil showed minimum zone of inhibition (0.7mm) against bacteria followed by clove oil (1mm) and mint oil (3.16mm) at 60 µl. Eucalyptus oil showed maximum zone of inhibition (7 mm) against *S. aureus*. The antifungal activity of neem oil was found to be negligible, whereas clove and mint oil had 3 to 3.16mm of zone of inhibition. Again, eucalyptus oil showed maximum antifungal activity (4.15mm) at 60 µl. The reduction in bacterial colonies was 75% in case of eucalyptus oil, 56% by clove oil and 37% by mint oil. Neem oil efficacy was lowest against fungi. Reduction in fungal growth was found to be highest by eucalyptus oil (85%) at 60 µl. Spray technique was done to finish fabric with selected oil and fabric properties were tested. The structural properties of finished fabric were not affected by finish although fabric thickness increased due to deposition of oil layer. The finish decreased drape coefficient of finished fabric and showed marginal effect on water vapour transmission and air permeability thus increasing comfort properties. There was marginal reduction in tensile strength of essential oil treated fabric however abrasion loss % showed better resistance against abrasion. Our findings highlight the development of sustainable cellulosic fabric using plant-based potential antimicrobial agents for finishing.

Keywords: Antimicrobial activity, Essential oils, Tensile strength, Water vapor transmission, Air permeability

INTRODUCTION

Since prehistoric times, medicinal plants have been used worldwide as natural remedy to cure various health problems including asthma, skin allergies, respiratory, urinary and cardiovascular diseases [1, 2]. According to the Botanical Survey of India, more than 8,000 indigenous medicinal plants are found in India. Medicinal plants are considered important and promising sources for traditional healing therapies, medications and have therapeutic benefits [3]. They contain several important phytochemicals such as flavonoids, alkaloids, tannins and terpenoids. These phytochemicals contain various disease-curing properties like antimicrobial, non-inflammatory, antioxidant and antiviral effects. Earlier, the crude extracts from leaves, roots, stem, flowers and fruits of medicinal plants were utilized [4]. However, recent advances in natural medicinal remedies derived essential oils as they are concentrated natural extracts with highly volatile secondary plant metabolites [5, 6]. These active bio components present in essential oils can be further utilized for diverse applications for development of functional clothing, anti-odor apparels and nano finished textiles [7, 8].

The recent global pandemic has hard hit the lifestyle. Consumers nowadays have elevated awareness to control the spread of infection through clothes or textile materials and demand hygienic or safe textiles [9]. The area of contact with skin during wear, body secretions, fabric composition and age of consumer are the determinant parameters for growth of microbes on clothes [10-12]. It is posed that susceptibility for microbial degradation of natural fibres is due to the generic composition of fabric (cellulose/ proteins/ polysaccharides), elevated body temperature, high humidity (70%–90%) and sweat secretion [13, 14]. Previous studies reported that bacteria like *Staphylococcus aureus, Escherichia coli* leads to body odor, skin irritation and hospital-acquired infections whereas fungi like *Aspergillus niger, Pencillium* cause loss in tensile strength and weight of cotton fabrics [9, 15]. Therefore, there is emerging demand for antimicrobial finished apparels that have significant impact against bacteria and viruses, environment friendly and safe [16].

A lot of chemicals mainly mineral and silver based are used to develop antimicrobial finished fabrics. These textiles are making their way into the

---

* To whom all correspondence should be sent:
E-mail: shefali.massey@gmail.com

global market and may affect health and environment [17]. The commonly used antimicrobial agents in textiles are triclosan, and quaternary ammonium compounds which are found to be poisonous and cause skin inflammation [9]. The plant-based antimicrobials can be the possible alternative in combating microbial growth as they are environment friendly, safe and nontoxic. Review from previous studies reported that bioactive compounds (gallic acid, cypellocarpin A, eucaglobulin, cuniloside, azadirachtinin, mentha) present in species of eucalyptus (*Eucalyptus globulus*), mint (*Mentha arvensis*), clove (*S. aromaticum*) and neem (*Azadirachta indica*) have benefits as antimicrobial, antioxidant and anti-inflammatory [18-21]. Earlier studies reported that aloe gel extract was used for treating cotton fabric for antimicrobial activity [22], chamomile, sage and green tea [23], and pine bark (*Pinus brutia*) [24], against bacteria (G+ and G-), yeasts and fungi.

The current research project tests the efficacy of antibacterial and antifungal properties of essential oils on organic cotton fabric. In addition, the antimicrobial finished fabric was evaluated on various performance parameters including structural, strength and comfort properties, adds to the literature. Therefore, this research reports the efficacy of essential oils which produce an eco-friendly antimicrobial finished organic fabric and the fabric performance finished fabric with essential oil.

MATERIALS AND METHODS

Materials

In the present study, an extensive investigation of literature was done on researches related to antimicrobial efficacy of plant-based herbs and their comparative constituents. Based on the review, eucalyptus *(Eucalyptus globulus),* neem *(Azadirachta indica)*mint *(Mentha arvensis)* and clove *(Syzygium aromaticum)* oils were procured from Central Institute of Medicinal and Aromatic Plants, Pantnagar, Uttarakhand. Plain-woven organic cotton fabric of GSM 146.34 g/m² was procured from Paramount Syntex Pvt. Ltd., Ludhiana (Punjab).

Test inocula

The strains of *Staphylococcus aureus* (Gram positive bacteria) and *Aspergillus niger* (Fungi) were taken as the representative of bacteria and fungi. These pathogenic strains are highly infectious that invade the textile materials. *Staphylococcus aureus* and *Aspergillus niger* multiply at a faster rate in the skin regions which have increased pH and prolonged wetness [25]. The antimicrobial tests were conducted against the bacteria and fungi to evaluate the effectiveness of essential oils against microbes. The strains were collected from Department of Microbiology, College of Veterinary and Animal Sciences, GBPUAT, Pantnagar.

Antimicrobial analysis

The percentage reduction rates (% R) in growth of bacteria and fungi on the fabric was evaluated by Colony Formation Units (CFU) of selected microorganisms, i.e., *S. aureus* and *A. niger* using AATCC test method 100:2004. Both the untreated and treated organic cotton fabric was tested for antimicrobial activity against the pathogenic strains of bacteria and fungi. The test inoculum was prepared which consist of nutrient broth culture having 2.7×10^5/ml colony forming units (CFU) of bacteria/fungi. Test inoculum of 1.0 ml was laden on fabric samples of 4.8 cm ± 0.1 cm diameter. The strains were cultivated in nutrient agar and test samples were put in contact for 24 h. The reduction in number of colonies was calculated by counting viable colonies of bacteria/fungi on the agar plate using following formula:

R = 100% X (B-A)/B

where A - number of bacteria recovered from the inoculated specimen after 24 h; B - number of bacteria recovered instantly after inoculation, 0 h.

For qualitative tests, agar diffusion test of textile fabrics (SN 195920-1992) was conducted where nutrient agar was prepared and test specimens (28.6mm) and control samples which were cut circularly were placed in nutrient agar for 24 h. The plates were incubated for 18 to 24 hours at 37ºC. The formula used for calculating the zone of inhibition:

W = T-D/2

where T - total diameter of the test specimen and clear zone measured in mm; W - width of the clear zone of inhibition; D - diameter of the test specimen.

To determine the washing fastness of the finish, test on finished fabric samples was done in "Laundrometer" to determine the efficacy of antimicrobial finish after ten washes with the procedure ISO 2, IS 15370:2005. The recipe for laundry test was:

Laundry soap solution - 5 g/l;
Sodium carbonate (Na₂CO₃) - 2 g/l;
M:L ratio - 1:50;
Temperature - 35–37 °C ;
Time - 30 min.

Evaluation of properties of finished fabrics

Structural properties

The physical properties were tested as per their fabric construction which includes fabric count, fabric thickness, cover factor and fabric weight per unit area.

a) Fabric count - It was determined with calibrated square magnifying glass called "Pick glass" and expressed in ends × picks/inch^2.

b) Fabric thickness - The samples for fabric thickness were tested as per ISI (IS: 7702-1975) method by using Shirley's thickness tester.

c) Fabric weight - The fabric weight of both samples (treated and untreated) was determined as per IS: 1964-1970 and calculated by the formula:

Fabric weight (g/m^2) = W/A

where W is the fabric weight measured in grams and A is the area of the fabric in meter^2.

d) Cover factor - Cover factor is determined by calculating threads/inch (both warp and weft) in the fabric as well as by counts of the thread. It is defined as the portion of the fabric area covered by both warp and weft yarns. It was calculated by the formula:

K = n/√N

where K= cover factor; n= threads/inch; N = cotton count.

Comfort/end use properties

The comfort properties were tested for the treated fabric finished with essential oil and comparison was done with the untreated fabric sample. The comfort properties include water vapor transmission rate, air permeability, bending length, drapability and thermal insulation.

a) Water vapor transmission. Water vapor transmission of the fabric samples was checked by the water dish method (ASTM: E 96-00). The distilled water was maintained in a test dish at a level of 3/4± ¼ from the specimen in a controlled test chamber. Periodically weighing, determine the rate of water vapor which was calculated and expressed as G/m^2/d.

WVT = (G/t)/A

where, WVT is water vapor transmission rate, G is weight change, t is time during which G occurred and A is the test area (cup mouth area).

b) Air permeability. Air permeability of the specimen was done on Eureka air permeability tester and the sample was cut in a circular shape according to the area (10 cm^2). The pressure was set at 5KPa into the pressure vessel. The amount of air passed through sample was read on a manometer in cubic centimetre/ minute for treated and untreated fabric samples.

c) Drapability. Drape meter was used to check the drapability of the treated fabrics and expressed as "Drape coefficient". The paper was cut according to the template and the drape coefficient was calculated with the help of following formula:

$$F = \frac{Ws - Wd}{W_D - Wd}$$

where F= drape coefficient; WD = area of specimen which is equivalent to the area of weight of the paper; Wd - area of supporting disc, which is equivalent to the area of weight of the paper; Ws = area equal to the projected area of specimen. Here, 'F' value determines the drapability, i.e., small 'F' value indicates better drapability while large value of 'F' indicates the poor drapability.

Qualitative assessment of antimicrobial activity of essential oils

Antimicrobial activity of selected essential oils of eucalyptus, clove, mint and neem was examined at 10–60 µl against *S. aureus* and *A. niger*. The essential oil of clove, mint and neem at 10-30 µl was not sensitive against strains of *S. aureus* and *A. niger* (Fig. 2).

d) Thermal insulation. The thermal insulation (clo value) of finished fabrics was assessed using Sasmira thermal conductivity apparatus. The fabric sample was cut according to the template and was placed on a hot plate. The round plate was finally used to cover the sample and the temperature was allowed to fall to 50ºC. The hot plate was allowed to cool down from 51ºC to 50ºC and time was measured with the help of a standard stop watch. Average time was divided by two and then divided with 250 to determine the clo value.

Strength properties

The strength of the fabric is an important parameter. The strength of the treated samples was calculated for tensile strength and abrasion resistance.

a) *Tensile strength.* The tensile strength of the fabric was measured with the instrument named "Electronic tensile tester". It was based on the principle of constant rate of extension and ASTM test method D-1682-94 (1994) and Ravelled strip test method of ISI (IS: 1969-1968) was used to determine the breaking strength of samples (25 cm × 5 cm) in both warp and weft direction.

b) Abrasion resistance. The fabric resistance against abrasion was measured on a "Martindale abrasion tester". The abrasion loss % of the test samples was calculated using the formula:

Abrasion loss % = $\dfrac{\text{wt. of sample before abrasion} - \text{wt. of sample after abrasion}}{\text{wt. of sample before abrasion}} \times 100\%$
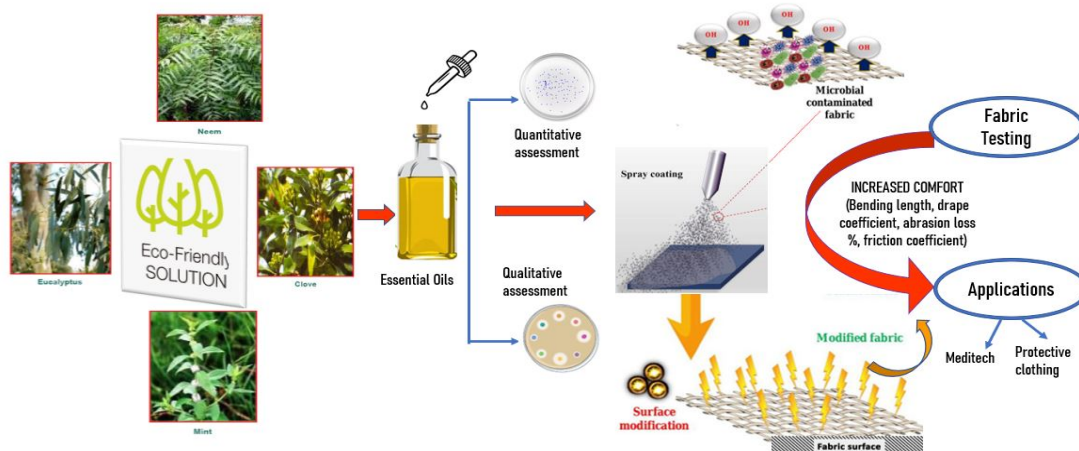

Fig. 1. Schematic development of essential oils coated antimicrobial cellulosic fabric

RESULTS

Fig. 1 demonstrates that the leaves of herbal plants, namely eucalyptus, clove, mint and neem were used to extract the essential oils. All essential oils were assessed for antimicrobial activity through qualitative and quantitative assessment. The essential oil which exhibited best antimicrobial activity was selected for finishing the fabric and spray method was used to apply the antimicrobial finish. The oil got adsorbed on the fabric surface and fabric was tested for comfort properties. Results indicated the increase in comfort of the fabric properties which leads to its application in medical textiles and protective clothing.

A significant zone of inhibition was formed against *S. aureus* at 60 µl by essential oils of neem (2.0 mm), clove (2.5 mm), mint (2.7 mm) and eucalyptus (10 mm) (Fig. 2). In case of *A. niger,* eucalyptus oil inhibited fungi at a minimum amount of 20 µl while clove and mint oil was not very sensitive till 30 µl. However, there was no effect of neem oil against *A. niger* even at higher concentration (60 µl). The essential oil of mint and clove oil displayed only moderate antifungal activity with zone of inhibition 2.5 mm and 4.16 mm, respectively, at 60 µl (Figs. 2 and 3). Eucalyptus oil formed highest antifungal zone of inhibition (6.5 mm) at tested amount.

Based on the results, essential oils at 60 µl amount showed maximum antimicrobial efficacy, thus, highest amount of oils (60 µl) was used for quantitative test. In general, eucalyptus oil was more effective among essential oils and showed maximum antibacterial and antifungal activity.

Fig. 2. Qualitative assessment of antimicrobial activity against a) *S. aureus,* b) *A. niger*.

(i)

(ii)
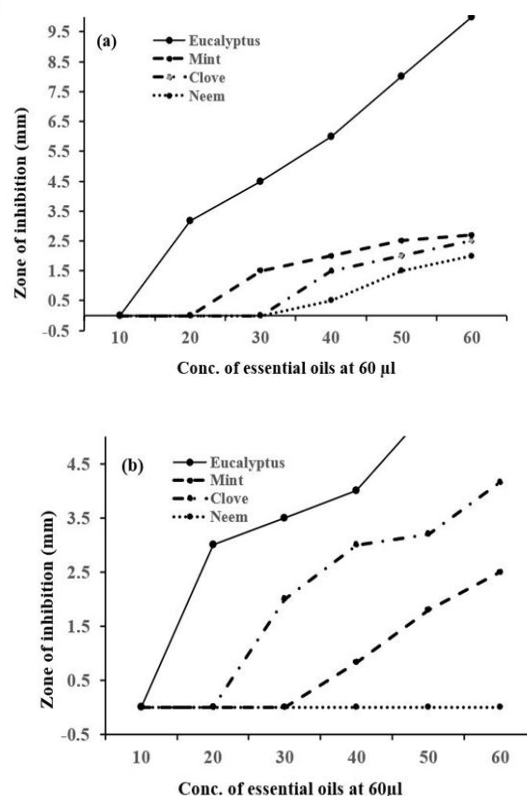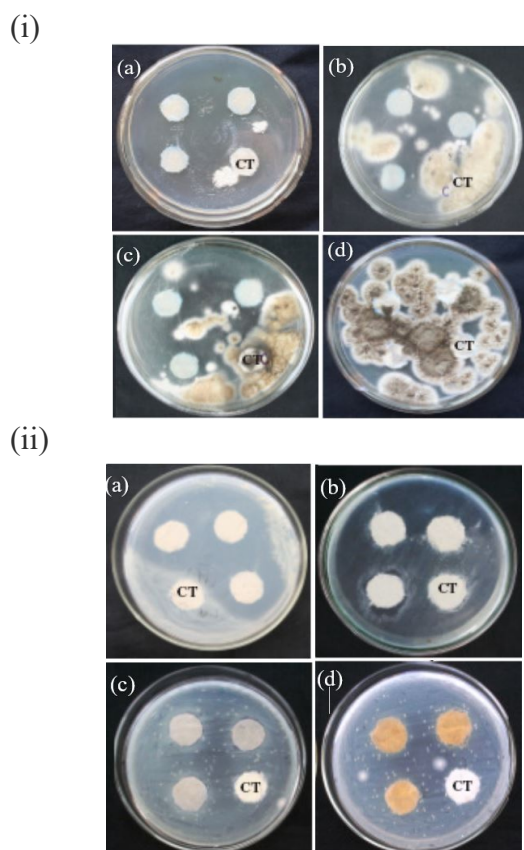
Fig. 3. Inhibition zone formed against i) *A.niger,* ii) *S. aureus* at 60 µl by (a) eucalyptus oil (b) mint oil, (c) clove

Quantitative assessment of antimicrobial activity of essential oils

The quantitative antimicrobial test (ASTM:E 2149-01) revealed that active oils were eucalyptus, clove and mint which managed to achieve reduction in bacterial and fungal colonies. In case of fabric finished with clove oil, the percent reduction of bacteria was much higher (56%) than for mint (37%) and neem oil (14%). The oil of eucalyptus showed excellent resistance against bacteria *S. aureus* (75%) (Fig. 4). Notably, eucalyptus oil was highly effective against fungi *Aspergillus niger* with 84% fungal growth reduction. Thepercent reduction of fungal colonies with clove oil was marginally higher (27%) than mint oil (23%). There was no percent reduction in the growth of fungal colonies in case of neem oil.

For the fabric finished with eucalyptus oil and clove oil, the decrease in the percent reduction of microorganism after five washes was in the range of 0.5-0.79%. This represents the good efficacy in resisting the microbial growth, i.e., against both bacteria and fungi.
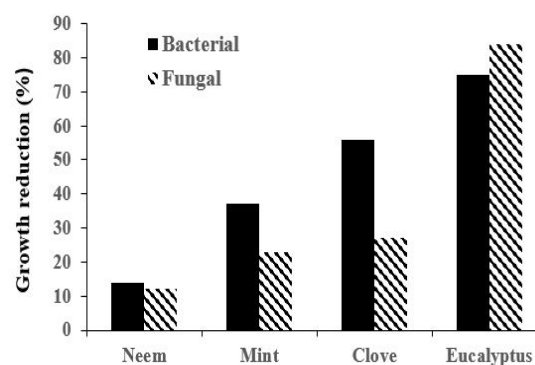
Fig. 4. Quantitative assessment of antimicrobial activity of essential oils

A marginal decrease in the percent reduction of *Staphylococcus aureus*, (Gram+ve bacteria) and *Aspergillus niger* (fungi) is noted in mint oil after laundering. In case of neem oil, the essential oil on the fabric was washed off. This results in decrease in antimicrobial reduction and less effectiveness of the finish. Overall, it can be inferred that after 5 washes of less than 1% reduction in microbial growth indicates a temporary finish.

Structural properties

Results from Table 1 indicate no difference between the fabric count of untreated and treated organic cotton samples. The fabric cover factor is good as densely woven plain weave fabric contributed to good covering power and application of essential oil did not indicate any change for the finished cotton fabric. Statistically, oil caused non-significant difference between thicknesses of fabric samples.

It is noticeable that there was increase in the weight (GSM) of finished cotton fabric (255.70 g/m²) compared to unfinished fabric (146.34 g/m²). The added weight or increased GSM of the fabric resulted due to the adsorption of essential oil in the interstices of fabric structure.

Table 1. Structural properties of essential oil treated fabric with untreated samples

Fabric samples	Fabric Count (ends × picks/inch²)	Fabric Thickness (mm)	GSM (g/m²)	Cover Factor	
				Warp	Weft
Untreated	64 × 64	0.41	146.34	14.44	14.26
Treated	64 × 64	0.42	255.7	14.44	14.35

Comfort properties

a) Water vapor transmission (WVT). A marginal decrease in WVT was found in the finished fabric (1575.39 Gm/m$^{2/}$d) compared to unfinished fabric (1595.90 Gm/m$^{2/}$d). Water vapor reduction of the fabric samples revealed that essential oils were adsorbed by the cotton fabric as the interspaces within yarn/fabric structure were filled with oils thus, reducing water vapour transmission through fabric.

b) Air permeability. The air permeability of untreated and treated organic cotton fabric samples was 10.75 ccf/min and 10.53 ccf/min, respectively. It is apparent from the results that there was slight decrease in the air permeability of finished sample. The reason may be that due to deposition of eucalyptus oil layer, the interstices or open spaces of woven sample were blocked or filled by oil and air permeability was decreased. Above results were supported by the study of Sarkar *et al.* (2002) that the air permeability of control fabric is higher (15.32cc/s/cm^2) whereas 1% clove oil-treated fabric shows lower air permeability (12.57 cc/s/cm^2) [26].

c) Drapability. While comparing the drape coefficient of unfinished and finished fabric samples with eucalyptus oil finish, it was found that drape coefficient of finished fabric (0.25%) was less (approx. half) than the unfinished sample (0.53%). Therefore, the drapability of treated fabric sample was more as lower the drape coefficient, higher will be drapability. The reason may be that after oil finish treatment, the smoothness and softness of fabric was increased. The woven and loop pile samples became lesser stiff as compared to untreated woven and loop thus in turn influencing improved drapability.

Statistically it was found that the effect of oil caused significant difference at 1% level between the drapability of unfinished and finished fabric samples

d) Thermal insulation. It was found that the thermal insulation of treated fabric (0.45 clo) was marginally higher more than the untreated fabric sample (0.39 clo).

According to Tortora (1982) [27], thermal insulation is related to heat conductivity of fabric, fabric thickness and entrapment of still air by the fabric. In the present study, the application of herbal oil finish may have sealed the interstices between the warp and weft of woven fabric, thus enhanced and trapped the level of still air. Therefore, thermal insulation of the treated sample was found more as compared to untreated fabric sample.

Strength properties

a) Tensile strength. The results indicate that tensile strength of finished fabric in warp direction was slightly reduced (9.43 kgf/cm) than that of unfinished fabric (9.67 kgf/cm) whereas a moderate drop in tensile strength of finished fabric (4.95 kgf/cm) when compared to unfinished cotton fabric (6.51 kgf/cm) was observed in the weft direction. The factors that lead to adsorption of oil in fabric structure are fibrelength, crimp and cross-sectional shape. In the present study, staple length, bean shaped cross section and crimp of cotton fibresled to the absorption of essential oil finish on treated fabric. The pH of the eucalyptus oil was slightly acidic (5.1-5.6) and as cotton fibres are sensitive to acids, the adsorption of oil in the cotton structureanticipated reduction in tensile strength.

b) Abrasion loss percentage. While comparing the abrasion loss percent of samples, results indicated that abrasion loss percent of unfinished sample (2%) was marginally higher than the finished fabric (1.62%).

The reason may be that after application of oil finish on treated sample, the fabrics became soft leading to less short fibre ends on the surface than the unfinished fabric sample, hence, abrasion loss of treated sample was also reduced.

CONCLUSION

In today's competitive world, one of the top priorities for many textile manufacturers is finishing of cotton textiles with antimicrobial properties for hygiene applications. Results indicated that eucalyptus oil showed maximum antimicrobial activity against both bacteria and fungi when compared with clove, mint and neem oil. The efficacy of neem oil against bacteria and fungi was lowest and no percent reduction in microbial colonies was seen. The antimicrobial efficacy was not much reduced (less than 1%) after five washes, showing a temporary finish. The tensile strength of the finished organic cotton fabric was slightly dropped compared to that of unfinished fabrics. However, it can be inferred that statistically essential oils caused non-significant difference on count and cover factor of finished fabric. However, water vapor transmission and air permeability are little bit reduced indicating oil deposition in fabric interstices. Compared to other finishing, this essential oil finish on cotton fabric introduced suppleness and reduced the drape coefficient and abrasion loss %.

The research findings establish the possibilities in averting the transmission of microbial infections through clothes or textile materials in most safe and eco-friendly way. Furthermore, utilization of plant-based antimicrobials for finishing textiles are totally safe, both for human usage and environment when compared with synthetic chemicals or compounds. The easy availability of the plant-based herbs and method to apply or replenish finish is an add on advantage for the commercial use of the finish.

REFERENCES

1. X. R. Tian, G. T. Feng, Z. Q. Ma, N. X. Zhang, X. Zhang, *Phytochem.*, **10**, 168 (2014).
2. V. Wyk, B. Erick, M. Wink, Medicinal plants of the World, CABI, 2018.
3. N. Vaou, E. Stavropoulou, C. Voidarou, C. Tsigalou, E. Bezirtzoglou, *Microorganisms,* **9**, 2041 (2021).
4. U. A. Khan, H. Rahman, Z. Niaz, M. Qasim, J. Khan, Tayyaba, B. Rehman, *Eur. J. Microbiol. Immunol.*, **3**, 372 (2013).
5. R. Mahmoudi, A. Kaboudari, B. Pakbin, Applications of Medicinal Herbs and Essential oils in Food Safety, A. Hany (ed.), 2019.
6. A. Man, L. Santacroce, R. Jacob, A. Mare, L. Man, *Pathogens,* **8**, 108 (2019).
7. K.Chhouk, H.K.Wahyudiono, M.Goto, *J. Environ. Chem. Eng*, **6**, 2944 (2018).
8. W.H. Talib, A.M. Mahasneh, *Molecules,***15**,1811 (2010).
9. D. P. Venkatraman, U. Sayed, S. Parte, S. Korgaonkar, *Text. Res. J*, **92**, 5015 (2022).
10. S. E. Abney, M. K. Ijaz, J. Mckinney, C. P. Gerb, *Appl. Environ. Microbiol,*, **87**, 14 (2021)
11. C. Callewaert, E. D. Maeseneire, F. M. Kerckhof, A. Verliefde, T. V. Wiele, N. Boon, *Appl. Environ. Microbiol*, **80**, 6611(2014).
12. S. Massey, S. Jahan, *Text. Mag.,* **51**, 45 (2010).
13. M. Kozowski, J. Walentowska, Handbook of Natural Fibres, Second Edition, Volume 1: Types, Properties and Factors Affecting Breeding and Cultivation, Woodhead Publishing Series in Textiles, 2020, p. 693.
14. S. Massey, A. Goel, *Man-Made Text. India*, **51**, 172 (2008).
15. H. R. Taghiyari, R. Majidinajafabadi, R. Vahidzadeh, *Ann. Acad. Bras. Cienc.,* **90**, 2797 (2018).
16. S. Massey, R. Kholiya, A. Hussain, *Asian J. Agric. Ext. Economics Sociol.,***40**, 250 (2022).
17. R. Kholiya, S. Massey, A. Hussain, *Int. J. Mod. Trends Sci. Technol.*, **8**, 41 (2022).
18. M. A. Alzohairy, Therapeutics Role of *Azadirachta indica* (Neem) and Their Active Constituents in Diseases Prevention and Treatment. Hindawi Publishing Corporation, 2016.
19. N.Z. Immaroh, D.E. Kuliahsari, S.D. Nugraheni, International Conference on Green Agro-industry and Bioeconomy. IOP Publishing. IOP Conf. Series: Earth and Environmental Science, 2021, p.733.
20. L. Nuñez, M. D. Aquino, *Braz. J. Microbiol.*, **43**, 1255 (2012).
21. A.S. Yeshwantrao, *Int. J. Creat. Res. Thoughts,* **9**, 108 (2021).
22. D. Jothi, *Afr. J. Microbiol. Res.*, **3**, 228 (2009).
23. A. M. El-Shafei, S. S. Shaarawy, *Egypt. J. Chem,* **6**, 317 (2018).
24. S. P. Karakava, S. P. Meitner, Y. O. Ceilktas, *Cytotechnology*, **73**, 423 (2021).
25. S. Kotowa, *Int. Biodeterior. Biodegradation,*, **53**, 165 (2004).
26. R. K. Sarkar, P. De, P. D. Chauhan, *Indian J. Fibre Text. Res*, **28**, 322 (2002).
27. P. G. Tortora. Understanding Textiles, Macmillan Publishing Company, UK, 1982.

Electrical characterization of polyindole/haemoglobin composites

S. Rawat[1], S. Mehtab[2]*, M.G.H. Zaidi[2]*, Jitendra[1], T.I. Siddiqui[3], J. Maheshwari[2]

[1]Department of Chemistry, Hemvati Nandan Bahuguna Garhwal University, SrinagarGarhwal (246174), Uttarakhand, India
[2]Department of Chemistry, College of Basic Science and Humanities, Govind Ballabh Pant University of Agriculture and Technology, Pantnagar, U. S. Nagar (263145) Uttarakhand (U.K.), India
[3]Department of Chemistry, Sir Syed Faculty of science, Mohammad Ali Jauhar University, Rampur 244901, India

The present research investigates the electrochemical characteristics of Polyindole (PIN) and Hemoglobin (Hb) composites, namely PIN/Hb, as conductive polymers comprising benzene and pyrrole rings as structural units. Working Electrodes (WEs) coated with PIN/Hb were fabricated, varying Hb concentrations and denoted as C-I, C-II, and C-III, respectively. Al WEs exhibited a linear I-V relationship. Electrical conductivities of the WEs were measured at room temperature (RT) by varying voltages at 1 V, 10 V, and 100 V. The results showed that the direct current conductivity (σDC) of the composites was higher than that of pure PIN, with C-III exhibiting the highest conductivity of 0.1×10^{-2} S cm^{-1} at 100 V. Furthermore, the conductivities of the developed WEs were analyzed at variable temperatures ranging from 25°C to 125°C. It was observed that for all WEs, the conductivity initially increased with temperature, reaching a peak value at 75°C, after which it gradually decreased. C-III coated WE achieved the highest conductivity value of 0.16×10^{-2} S cm^{-1} at 100 V. Initially, the conductivity of the baked WEs increased with baking time and temperature up to 3 hours at 50°C, followed by a gradual decrease in conductivity until 6 hours, after which it stabilized. For C-III coated WEs, the maximum conductivity of 0.51×10^{-2} S cm^{-1} was achieved at 50°C after 3 hours of baking, showing similar trends at 100°C baking temperature.

Keywords: Working electrodes, Polyindole, Haemoglobin, DC Conductivity

INTRODUCTION

Massive amount of fossil fuels was used to power the economy at the start of industrial revolution, which contributed to the overall development of society and therefore the energy crisis and environmental pollution are two major concerns in today's world, not only because the main source of energy i.e., fossil fuels are running out, but also because fossil fuels contaminate the environment by releasing CO_2 and other toxic gases. As a result, there is a high expectation that renewable energy would eventually replace traditional fuels as the dominant source of energy in our daily life. However, some renewable energies, such as solar and wind energy, are inherently unstable and intermittent, leading to necessitating the use of energy storage in systems with long-term energy output. Various batteries with high energy density such as Pb/PbO$_2$ and lithium ion batteries, are commonly used in electric energy storage systems. Most batteries, on the other hand, have a slow power delivery or uptake that can't keep up with faster and higher-power energy demands [1]. Researchers have been challenged to develop green and sustainable energy storage technologies due to rise in energy consumption, fossil fuel depletion, and global warming. Because of its highpower density, extended cycle life, fast charge-discharge process and environmental friendliness, the supercapacitor is thought to be one of the most promising candidates among other energy storage devices [2]. Since the discovery of highly conducting polyacetylene (PAc) in 1977, CPs have been the dominant materials in Polymer Science. Hideki Shirakawa, Alan J. Heeger, and Alan G. MacDiarmid were the first to discover oxidation of acetylene by iodine, which produced PAc with increase in conductivity [3]. Conductivity of iodine-doped PAc can match that of silver, which is one of the easily accessible electrical conductors. They were awarded with the Nobel Prize in Chemistry in 2000 for their groundbreaking discovery, which opened up new avenues for the study of electric organic polymers.

Conducting polymers (CPs) are polymers having conjugated chain structures. They have unique bonding patterns along the polymer backbones, consisting of alternating double and single bonds, which gives them semiconducting characteristics [4]. A number of factors influence polymer conductivity, including conjugation length, total chain length, and charge transfer to adjacent molecules [5]. These neutral conjugated polymers can be transformed into semi-conductive or

* To whom all correspondence should be sent:
E-mail: smiitr@gmail.com, mghzaidi@gmail.com

conductive states *via* chemical or electrochemical redox processes. CPs are routinely doped with other functional materials to generate composites in order to extend the functionalities or increase the performances of these polymers [6]. CP composites with high stabilities and conductivities can be used as a key component in transistors [7, 8], light emitting diodes [9, 10], electrochromic devices [11, 12], electrochemical capacitors [13, 14], actuators [15, 16], sensors [17, 18], and photovoltaic cells [19, 20].

PIN is a well-known conductive polymer comprising benzene and pyrrole rings as structural units. It is an electroactive polymer produced via electrochemical oxidation of indole or chemical oxidation with $FeCl_3$ or $CuCl_2$. Due to its simple polymerization, high redox activity, thermal stability, tuneable conductivity and environmental stability, PIN has been widely considered as an extrapolative material among many CPs [21]. Recently, PIN have been doped with NiO [22], ZnO [23], CuO [24], Co_3O_4 [25] and Fe_2O_3 [26]. Hb is a redox respiratory protein found in red blood cells. It is made up of four polypeptide chains, each with one iron haem group. Because of its commercial accessibility, high stability, affordability and high capability rate, Hb can be considered to as an ideal model for good electrochemical performance in supercapacitor applications [27]. Present investigation provides a pioneer attempt towards the development of working electrodes (WEs) of PIN/Hb composites and the effect of temperature on their conductivities.

MATERIALS AND METHODS

Materials

Pre-synthesized PIN and its composites with Hb were obtained from Department of Chemistry of College of Basic Sciences and Humanities, G.B.P.U.A.&T, Pantnagar, India [28]. PIN and its composites with 100 mg, 200 mg and 300 mg concentration of Hb were represented as C-I, C-II and C-III respectively. Polyvinyl butyral (PVB, Himedia, Delhi, India) and Tetrahydrofuran (THF, ≥99%, Merck, Mumbai, India) were purchased from respective firms. Graphite (Gr, 98.0%, 500 μm) was purchased from Loba-Chemi, Mumbai, India while N-methyl-2-pyrollidone (NMP, ≥99%) was purchased from Sigma Aldrich, Bangalore, India. Acetone (>98%) was procured from Sd. Fine, Chandigarh, India. Sulphonated polysulphone (SPS) used was pre-synthesized in lab [28]. Hb was purchased from (Otto Kemi, India). Distilled water was obtained from Merck Millipore water purification system. All other chemicals and solvents were of AR grade and were used without further purification. SS plates of 1 cm^2 area were fabricated by cutting and used as current collector for the development of WEs.

Optimization of coating materials and fabrication of WEs

For the development of stable working electrodes of uniform surface morphology several binders, fillers were optimized with composites in different solvents.

Table 1. Surface morphologies of the developed WEs

S. No	Composite	Binder	Filler	Solvent	Surface Morphology on SS
1.	PIN (35mg)	SPS (15mg)	Gr (10mg)	NMP (1.5mL)	Uniform and even surface
2.	C-I (35mg)	PVB (15mg)	Gr (15mg)	THF (1.5mL)	Flaky and unable to adhere
3.	C-I (35mg)	SPS (15mg)	Gr (10mg)	NMP (1.5mL)	Uniform and even surface
4.	C-II (35mg)	SPS (15mg)	Gr (10mg)	NMP (1.5mL)	Uniform and even surface
5.	C-III (35mg)	SPS (15mg)	Gr (10mg)	NMP (1.5mL)	Uniform and even surface
6.	C-III (35mg)	PVB (7.5mg)	Gr (5mg)	THF (1.5mL)	Uneven surface
7.	C-III (65mg)	SPS (70mg)	Gr (10mg)	NMP (1.5mL)	Coating material delaminates and unable to adhere
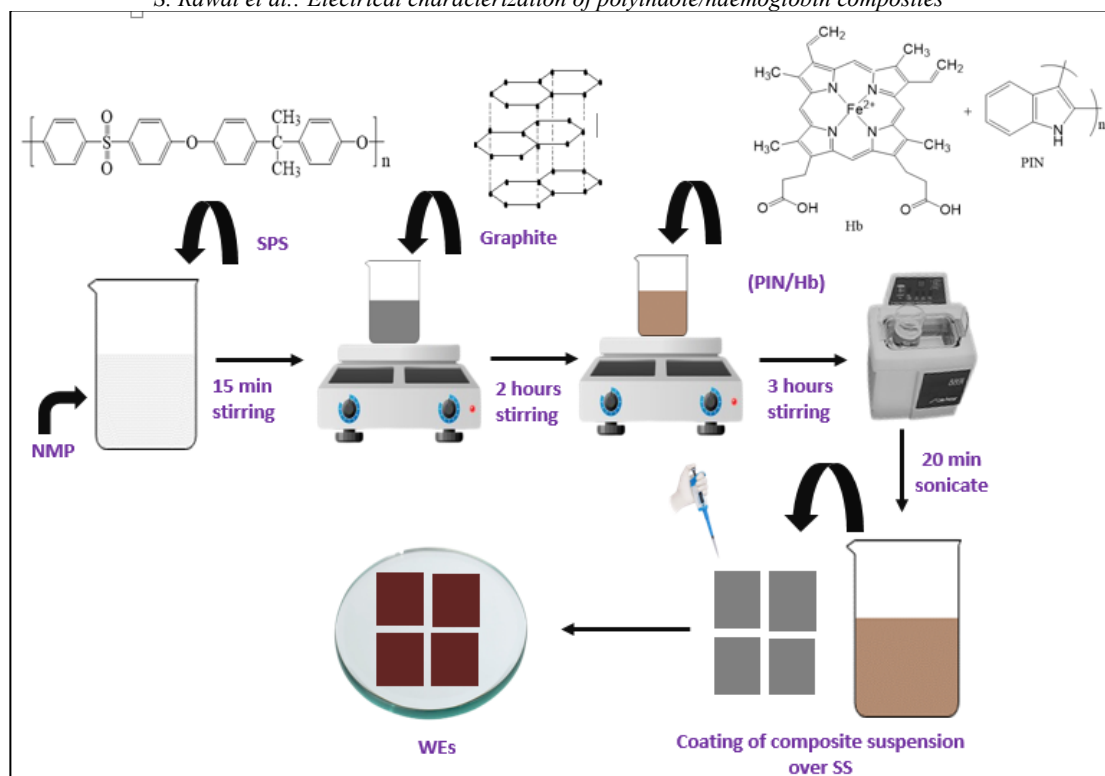
Fig. 1. Schematic representation for fabrication of WEs

Fabrication of WEs using PVB as binder and THF as solvent

SS (1 cm^2) was finished with emery paper and thenpre-treated with different solvents (distilled water and acetone, respectively) in order to get smooth and shiny surface. PVB was weighed and dissolved in 1.5 mL of THF and then stirred for 15 min at Room temperature (RT). To this mixture, Gr was added and continued to stir for 2 h until the Gr get dispersed to obtained homogenous suspension. 35 mg of electroactive material (PIN/Hb) was added to the above suspension and stirred for 3 h at RT. Obtained suspension was then ultrasonicated for 20 min in ultrasonicator, then 50 µL of prepared composite suspension was applied over SS using a micropipette and left to dry at RT for 24 h. Similar procedure was used for the development of WEs of C-III (Fig. 1).

Fabrication of WEs

Surface of SS was cleaned similarly as discussed as above. SPS was added to 1.5 mL NMP and stirred on magnetic stirrer for 15 min. To this 15 mg Gr was added and again stirred for 2 hr, till the Gr dispersed in the solution. PIN was added to the solution and stirred for another 3 hr and then ultrasonicated for 20 min. The developed suspension (50 µL) was applied over SS and left to dry at RT for 1 week. Similar procedure was used for the development of WEs for all composites C-I, C-II and C-III. WEs were fabricated at different concentrationsand their conductivity was measured by varying conditions.

Instrumentation and electrical characterization of WEs

DC conductivity (σDC, S cm^{-1}) data and I-V graphs were recorded over Keithley four-probe DC conductivity meter having current source (6221A) and voltage source (2182 V). The conductivities of PIN and its composites C-I, C-II and C-III were measured at variable temperature ranging from 25-125°C (298-398 K). For this purpose, a temperature regulated oven (±1°C) probe is enclosed in DC conductivity meter of Keithley four-probe nano-voltmeter. The effect of baking temperature on σDC of WEs was investigated with variation in time. Developed electrodes of PIN and its respective composites were baked at temperature ranging from 50-100°C in oven from 3-9 hr and their conductivity was measured on Keithley four-probe DC conductivity meter.

RESULTS AND DISCUSSION

Fabrication and optimization of WEs

The WEs of PIN and its Hb composites C-I, C-II and C-III were prepared using different combination and amounts of filler, binder and solvent. It was observed that the WEs that were obtained using PVB as binder and Gr as filler in THF solvent were unstable and showed delamination of coating material after sometime over SS. This may be due to

179

formation of non-homogeneous mixture of composites in THF and its poor binding over SS. WEs of PIN, C-I, C-II and C-III that were prepared using SPS as binder, Gr as filler and NMP as solvent were found to stable due to formation of homogeneous mixture, strong binding and even coating of suspension over SS [28]. Based on surface morphology and stability of coating over SS, SPS binder electrodes were used for further studies.

Electrical characterization of WEs

I-V data of fabricated WEs were recorded over Keithley four-probe DC conductivity meter having current source (6221 A) and voltage source (2182 V)in the voltage range of 5–25 V at RT. Electrical characteristics examinations reflect that

conductivity of developed composites (C-I, C-II, C-III) was higher over PIN and found to be maximum for C-III [29]. Fig. 2 reflects I-V graphs of PIN, C-I, C-II and C-III that show a linear variation of I-V at RT and implies ohmic conductive behavior of Hb in PIN [30].

The electrical conductivities of WEs were measured over temperature range of 25-125°C (298-398 K). It was found that all composites showed best conductivities at 100 V, therefore it was selected for further studies to check conductivities at variable temperatures (Fig. 3). At 100 V, σDC was measured at temperature of 25, 50, 75, 100 and 125°C in a temperature regulated oven (±1°C) probe enclosed in DC conductivity meter (Fig. 4).
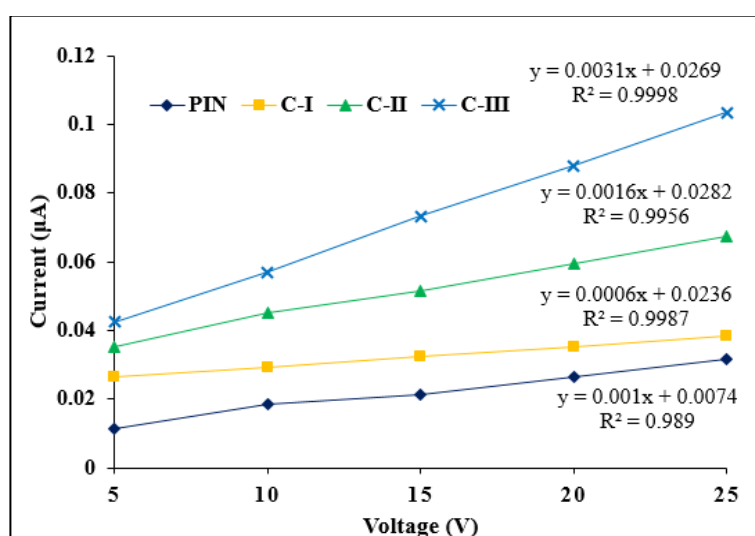
Fig. 2. I-V Characteristics of WEs at RT
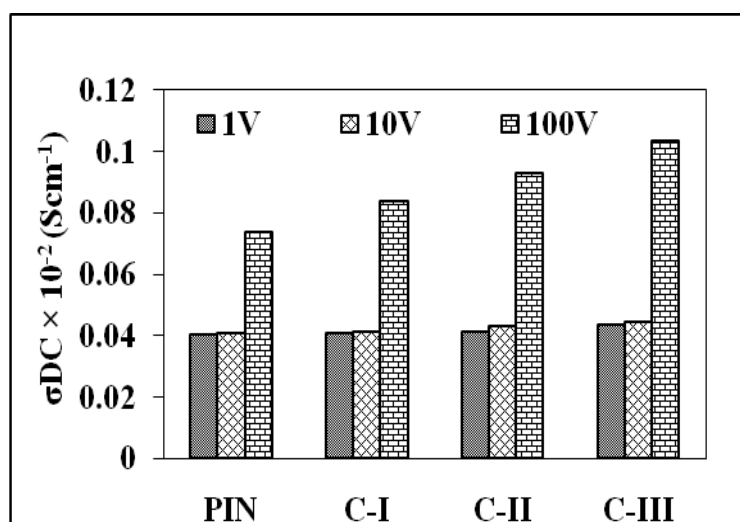
Fig. 3. Electrical conductivity of WEs at variable temperature

180

It was observed that the maximum conductivity was obtained at 75°C for all WEs. The conductivity of WEs were found to gradually increase till 75°C and then starts decreasing till 100°C, after this it become almost constant. The conductivity of composites was found to higher than that of PIN and maximum conductivity $(0.16 \times 10^{-2}$ S cm$^{-1})$ was obtained for C-III at 75°C. Increase in the value of σDC with temperature indicate the semiconducting behaviour of PIN/Hb composites. The increased up to 75°C may be due to increase in conductivity with temperature as a result of polymer chain hoping, inter-chain ion exchange, and segmental movement of polymerized units. Raising temperature to a certain points aids electron mobility and also helps in overcoming the energy potential barrier. Increasing temperature generates alternate conducting paths for charge conduction, revealing PIN to be a better CP at elevated temperatures. However, above this temperature, the conductivity is inversely affected due to dopant loss and other factors [25]. After 75°C the conductivity starts decreasing due to morphological changes of coating material over the surface of SS. As the coating cannot withstand high temperature and it starts delaminating and the surface becomes uneven.

Electrical conductivity of baked WEs with time

To check the durability of developed WEs at higher temperature over time their baking characteristics were examined in a temperature regulated Oven. WEs of PIN and its composites were baked at temperature range of 50-100°C in oven and their conductivities were measured over the time duration of 3-9 h (3, 6 and 9 h). The conductivity of baked WEs were measured over voltage range of 1-100V and it was observed that there was slight change in conductivity at 1 V and 10 V with maximum values at 100 V (Figs. 5 & 7).
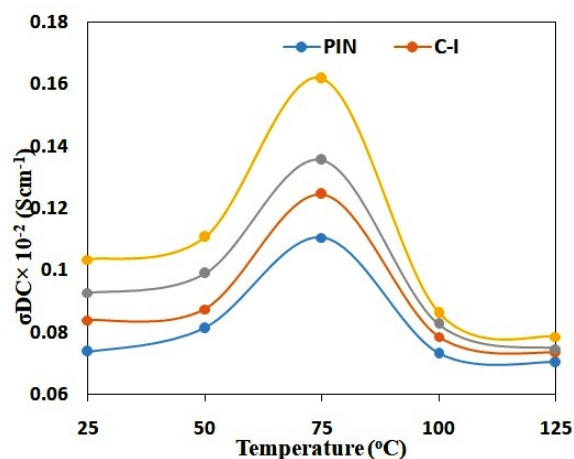
Fig. 4. Electrical conductivity of WEs at variable temperature over 100 V

At 50°C, it was observed that the baked electrodes showed a high increase in their conductivities till 3 h and then decreased up to 6 h and on further baking, conductivity remained constant (Fig. 6). This may be due to interchain hopping within the composites. When the temperature rises, the total charge migration is cut-off, causing a mechanical blockage in the flow of charge across the hole in PNCs [31]. Similar results were observed at 100°C but the conductivities of at this temperature was lower than that of 50°C (Fig. 8).

From the data it can be observed that composites have higher conductivity than PIN and maximum conductivity of 0.51×10^{-2} S cm^{-1} was observed for C-III at 50°C for 3 h. At 100°C the conductivity of C-III was found to be 0.25×10^{-2} S cm^{-1}. Highly doped composite C-III, exhibit higher conductivity over PIN, C-I, and C-II at baked conditions. Baking studies suggested that initially baking promote conductivity but after 3 h of baking the surface morphology of WEs changed and the coating layer starts to delaminate over SS.
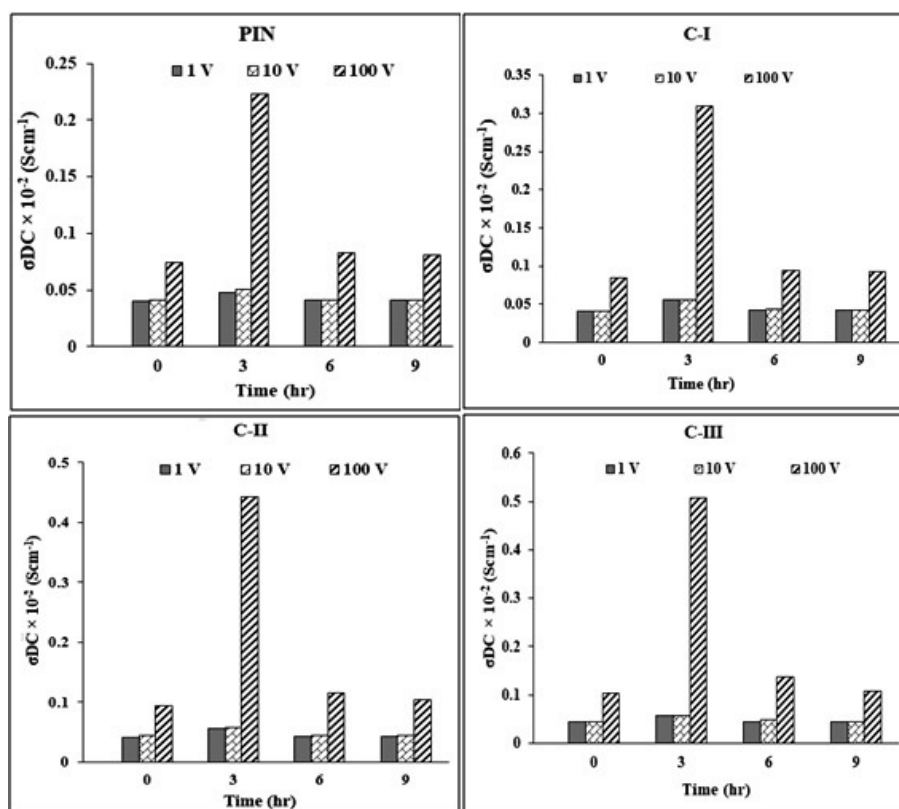
Fig. 5. Conductivity of different baked composites based WEs at 50°C at all voltages of 1, 10 and 100 V with time.
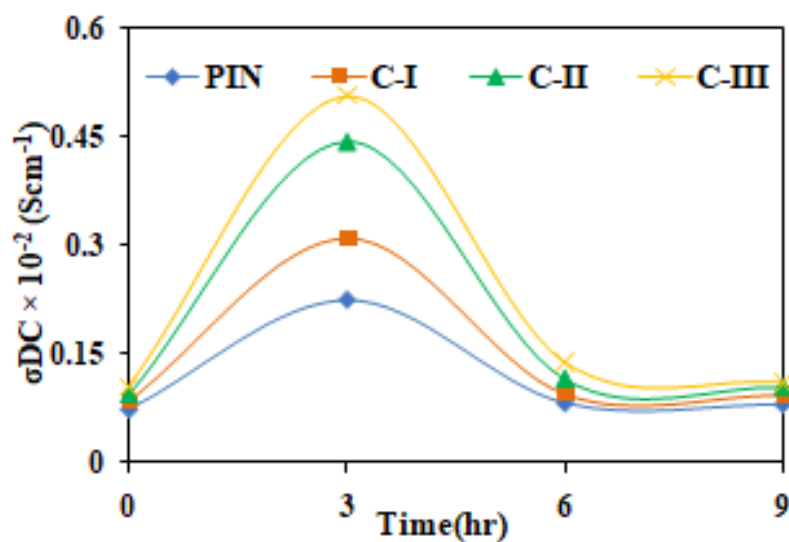
Fig. 6. Conductivity of baked WEs at 50°C over 100V with time
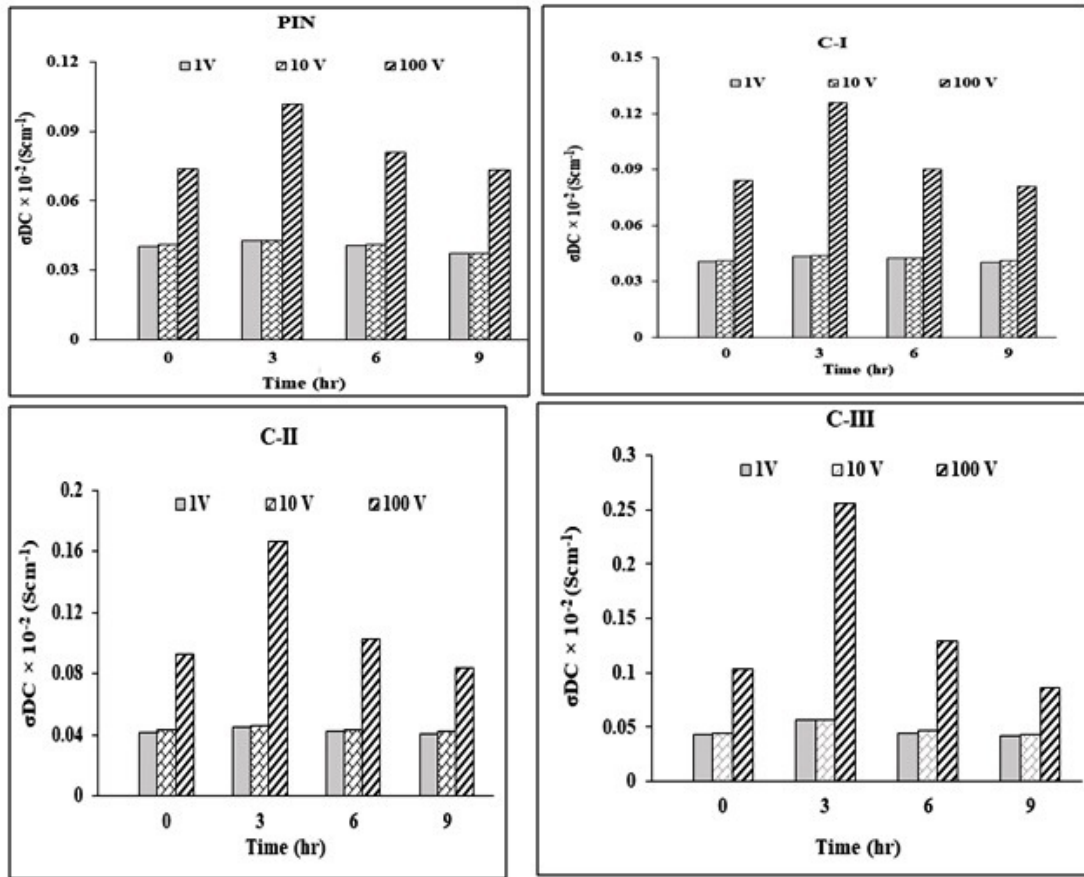
Fig. 7. Conductivity of different baked composites based WEs at 100°C at all voltages of 1, 10 and 100 V with time
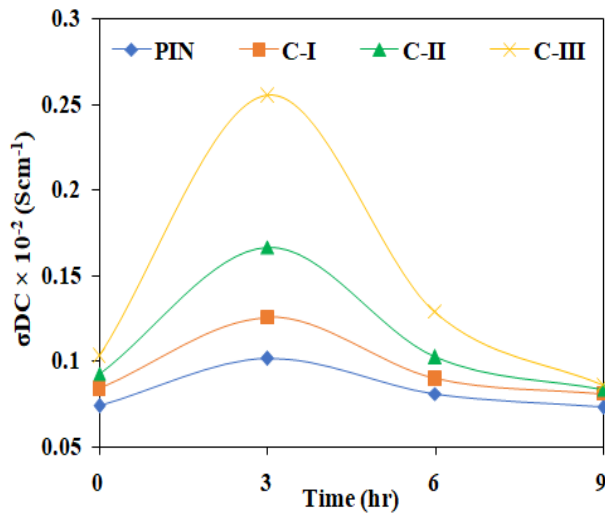

Fig. 8. Conductivity of baked WEs at 100°C over 100V with time

CONCLUSIONS

In this investigation, working electrodes (WEs) based on Polyindole (PIN) and its Hemoglobin (Hb) composites were successfully fabricated and their electrical conductivities were thoroughly examined under different thermal conditions. The fabrication process involved coating PIN and its composites (C-I, C-II, and C-III) with an optimized combination of filler Gr, binder PVB or SPS, and solvents THF or NMP. Through experimentation, it was found that filler Gr, binder SPS, and solvent NMP yielded a compatible and uniform coating over stainless steel (SS), resulting in stable and durable WEs. Electrical characterization of the WEs, including PIN, C-I, C-II, and C-III, demonstrated a linear I-V relationship, indicating Ohmic behavior in the developed WEs. Moreover, the electrical conductivities of the WEs were measured at room temperature (RT) under various voltages (1 V, 10 V, and 100 V). The results revealed that the composites exhibited higher direct current conductivity (σDC) than pure PIN, with C-III displaying the maximum conductivity of 0.1×10^{-2} S cm^{-1} at 100 V. The conductivity increased with the concentration of Hb and was most significant at 100 V, while remaining constant at 1 V and 10 V. Subsequently, the conductivities of the WEs were assessed at variable temperatures (25°C to 125°C) while maintaining a constant voltage of 100 V. It was observed that all WEs initially showed an increase in conductivity with rising temperature, peaking at 75°C, followed by gradual decreases. The highest conductivity value (0.16×10^{-2} S cm^{-1}) was achieved for C-III at 100 V. Furthermore, the WEs were subjected to baking at temperatures ranging from 50°C to 100°C for up to 9 hours, and their conductivities were evaluated at 3, 6, and 9 hours.

The maximum conductivity of 0.51×10^{-2} S cm^{-1} was attained for C-III coated WEs at 50°C after 3 hours of baking, with similar trends observed at 100°C baking temperature. However, at 100°C and a baking time of 3 hours, the conductivity (0.25×10^{-2} S cm^{-1}) of C-III WEs was lower than that at 50°C. This investigation presents a simplified and optimized approach for fabricating stable WEs with enhanced electrical conductivities across variable temperature ranges, baking conditions, and time durations.

REFERENCES

1. K. Wang, H. Wu, Y. Meng, Z. Wei, *Small*, **10**, 14 (2014).
2. R. P. Raj, P. Ragupathy, S. Mohan, *J. Mater. Chem. A*, **3**, 24338 (2015).
3. S. Hideki, E. J. Louis, A.G. MacDiarmid, C. K. Chiang, A. J. Heeger, *J. Chem. Soc., Chem. Commun.*, **16**, 578 (1997).
4. T. H. Le, Y. Kim, H. Yoon, *Polymers,* **9**, 150 (2017).
5. M. Naseri, L. Fotouhi, A. Ehsani, *Chem. Rec*, **18**, 599 (2018).
6. L. Xiang, Y. Wang, X. Yang, J. Chen, H. Fu, T. Cheng, *TrAC, Trends Anal. Chem,* **39**, 163 (2012).
7. C. T. Kuo, W. H.Chiou, *ACS Appl. Mater. Interfaces,* **88**, 23 (1997).
8. H.Tang, P. Kumar, S. Zhang, Z. Yi, G. D. Crescenzo, C. Santato, F. Soavi, F. Cicoira, *ACS Appl. Mater. Interfaces*, **7**, 969 (2015).
9. O. L. Gribkova, O. D. Omelchenko, A. R. Tameev, D. A. Lypenko, A. A. Nekrasov, O. Yu. Posudievskii, V. G. Koshechko, A. V. Vannikov, *High Energy Chem.*, **50**, 134 (2016).
10. B. Philip, J. Xie, J. K. Abraham, V. K. Varadan, *Smart Mater. Struct.*, **13**, N105 (2004).
11. L. Zhao, L. Zhao, Y. Xu, T. Qiu, L. Zhi, G. Shi, *Electrochim. Acta*, **55**, 491 (2009).
12. K. Y. Shen, C. W. Hu, L. C. Chang, K. C. Ho, *Sol. Energy Mater. Sol. Cells*, **98**, 294 (2012).
13. X. Jiang, S. Setodoi, S. Fukumoto, I. Imae, K. Komaguchi, J. Yano, H. Mizota, Y. Harima, *Carbon*, **67**, 662 (2014).
14. M.A. Memon, W. Bai, J. Sun, M. Imran, S. N. Phulpoto, S. Yan, Y. Huang, J. Geng, *ACS Appl. Mater. Interfaces*, **8**, 11711 (2016).
15. J. C. García-Gallegos, I. Martín-Gullón, J. A. Conesa, Y. I. Vega-Cantú, F. J. Rodríguez-Macías, *Nanotechnology*, **27**, 015501 (2016).
16. M. Tahhan, V. T. Truong, G. M. Spinks, G. G. Wallace, *Smart Mater. Struct.*, **12**, 626 (2003).
17. J. Janata, M. Josowicz, *Nat. Mater.*, **2**, 19 (2003).
18. H. Yoon, H. *Nanomaterials*, **3**, 524 (2013).
19. J. Lee, H. Kang, S. Kee, S. H. Lee, S. Y. Jeong, G. Kim, J. Kim, S. Hong, H. Back, K. Lee, *ACS Appl. Mater. Interfaces*, **8**, 6144 (2016).
20. E.M.J. Johansson, L. Yang, E. Gabrielsson, P.W. Lohse, G. Boschloo, L. Sun, A. Hagfeldt, *J. Phys. Chem., C*, **116**, 18070 (2012).
21. N. B. Taylan, B. Sari, H. I. Unal, *J. Polym. Sci. B Polym. Phys.*, **48**, 1290 (2010).
22. G. Rajasudha, A. P. Nancy, T. Paramasivam, N. Boukos, V. Narayanan, A. Stephen, *Int. J. Polym. Mater.*, **60**, 877 (2011).
23. G. Rajasudha, H. Shankar, P. Thangadurai, N. Boukos, V. Narayanan, A. Stephen, *Ionics*, **16**, 839 (2010).
24. G. Rajasudha, L. M. Jayan, D. D. Lakshmi, P. Thangadurai, N. Boukos, V. Narayanan, A. Stephen, *Polym. Bull.*, **68**, 181 (2012).
25. K. Khati, S. Mehtab, M.G.H. Zaidi, I. Joshi, S. Rathore, *Mat. Tod.: Proceed.*, **1**, 5 (2021).
26. S. Mehtab, M.G.H. Zaidi, N. Rana, K. Khati, S. Sharma, *Bull. Mat. Sci.*, **45**, 162 (2022).
27. M. Khairy, S. A. El-Safty, *Chem. Comm.*, **50**, 1356 (2014).
28. K. Khati, I. Joshi, A. Bisht, M. G. H. Zaidi, *Bull. Mater. Sci.*, **42**, 1(2019).
29. M. T. Ramesan. *Polym. Compos.*, **33**, 2169 (2012).
30. P. Joshi, S. Mehtab, M. G. H. Zaidi, T. Tyagi, A. Bisht, *J. Nanostructure Chem.*, **10**, 33 (2020).
31. S. Mehtab, M. G. H. Zaidi, R. Kunwar, K. Singhal, T. I. Siddiqui, *Int. J. Polym. Anal.*, **26**, 204 (2021).

Nanohybrid-modified working electrodes for electrochemical sensing of chlorpyrifos

S. Sharma[1], S. Mehtab[2]*, M.G.H. Zaidi[2], U. R. Mallik[1], R. Singh[1]

[1]Department of Chemistry, Surajmal Agarwal Pvt. Kanya Mahavidhyalaya, Kichha, Uttarakhand, India
[2]Department of Chemistry, College of Basic Science and Humanities, G.B Pant University of Agriculture and Technology, Uttarakhand (U.K.), India-263 145

Present work demonstrates that development of Nanohybrids (NHs) based working electrodes (WEs) for electrochemical (EC) sensing of chlorpyrifos (CPS). Synthesized c-MWCNT/h-BN NHs in presence of polyvinyl butyral binder in NMP medium was used to modify the surface of stainless-steel plate that worked as working electrode (WE) in EC studies. The EC behavior of CPS was studied by cyclic voltammetry (CV) and square wave voltammetry (SWV) in KCl (0.1 M) at 7.2 pH. SWV data reveals CPS can be quantified upto LOD of 2.62 ng/L and LOQ 7.96 ng/L over WE. The overall result reveals that developed electrode material for EC sensing provides highly sensitive, selective and reproducible estimation of CPS upto nano molar level.

Keywords: Nanohybrid, Electrochemical sensing, Cyclic voltammetry, Chlorpyrifos

INTRODUCTION

Organophosphates (OPs) are a large group of synthetic compounds, including esters, amides, or thiol derivatives of phosphoric, phosphonic, phosphorothioic, or phosphonothioic acids. They are commonly used as insecticides, herbicides, and fungicides, as well as in the production of plastics, gasoline additives, and flame retardants. OPs work by inhibiting the activity of acetylcholinesterase, an enzyme that regulates the transmission of nerve impulses in the body [1]. This leads to the accumulation of acetylcholine, a neurotransmitter in nerve synapses which can result in overstimulation of the nervous system and can be toxic to humans and other animals. Prolonged exposure to OPs can lead to a range of health problems, including nausea, headache, dizziness, confusion, and muscle weakness. In severe cases, OPs exposure can cause seizures, respiratory failure and even death [2]. For such reasons, there is a need of sustainable methodologies for routine, continuous, accurate, reproducible and on spot detection of OPs in real samples. In this context, different chromatographic [3], electrophoretic [4], and electrochemical (EC) [5] techniques were developed for identification of OPs.

CPS (*O,O*-diethyl-*O*-3,5,6-trichloro-2- pyridyl phosphorothioate) is a widely used OPs insecticide that has been used for several decades to control a variety of pests on crops. CPS has a low water solubility and high soil sorption coefficient; these characteristics make it possible so that CPS can remain in the natural environment for a long time [6]. CPS is absorbed in mammals by all routes wherein, inhalation leads to fastest appearance of symptoms, followed by oral and dermal routes. Prolonged exposure of CPS cause cancer, reproductive and neurological disorders, allergic reactions and neuro-developmental impairment in growing children [7]. In this context, the quantification of CPS through High performance liquid chromatography (HPLC) [8-10], Thin layer chromatography (TLC) [11], Surface-enhanced raman spectroscopy (SERS) [12], laser-induced breakdown spectroscopy (LIBS) [13, 14], UV spectra [15] and electrochemical (EC) [16, 17] methods have been well established. Recently, EC methods specially based on SWV overcome the problems associated with traditional analytical methods as these are cost effective, highly sensitive, selective and low sample volume, reusable, require less organic solvents and short analysis time. SWV has emerged as most sustainable approach for detection and quantification of OPs [18, 19].

NHs synthesized through dispersion of Nanomaterials over different substrate like MWCNT, graphene can be effectively used in the development of EC sensors. The NHs used for detection of CPS were GO/Fe_3O_4 [20], TiO_2/CA [21], TGO/UiO-66 [22], $MWCNT@SiO_2$-MIP [23] and PIN-WC [24]. The modification of WE surface by NHs is mainly responsible for the efficiency of EC sensors towards CPS detection. Modification of MWCNT with h-BN has been of interest in attempt to develop the NHs that find their future applications

---

in hydrogen energy storage [25], as electrode materials for high temperature supercapacitors and further may be utilized for quantification of CPS [26]. The present work proposed a novel and economical sensor for the trace level EC detection of CPS, using h-BN doped c-MWCNT NHs.

MATERIALS AND METHODS
Materials

Standards of CPS (99.5 %) were procured from Sigma, Aldrich, USA. Poly vinyl butyral (PVB) (Mw = 3.05 × 10^4 g/mol) was procured from Himedia, India and N-methyl-2-pyrrolidone (NMP) was used as solvent was purchased from Loba Cheme. All solutions were prepared in DW (Deionized water) (>18 MΩ-cm). NHs comprising c-MWCNT/h-BN was directly used as provided by Department of Chemistry, G.B. Pant University of Agriculture and Technology, Pantnagar [27]. Rest of the chemicals and solvents (Purity 99.5 %) were used without further purification.

Fabrication of electrodes

WEs were developed according to procedure reported earlier [28]. A series of WEs were fabricated through cast of an electroactive material supplemented with appropriate polymeric binder over current collectors (CC). Prior to deposition, stainless steel plate electrodes (SSPE) were finished through polishing with emery paper, then washed with DW and further ultrasonication in acetone over 10 min. SSPE with mirror like finish were dried and stored at 50 ± 1°C/400 mmHg. Electroactive compositions for deposition over SSPE were prepared through mixing of (35.0 mg) of NHs supplemented with PVB (7.50 mg) in NMP (1 mL) under stirring over 2 h followed by additional ultrasonic treatment over 20 min to afford a slurry. WEs with required thickness were prepared through cast of slurry (125 µL) over SSPE followed by gelation at room temperature for 1 h and then drying it at 50±1°C/400 mmHg. WEs developed by NHs with 5 wt% h-BN were abbreviated as WE-II.

EC characterization

EC studies of fabricated electrodes were performed in a triple electrode cell assembly over Potentiostat-Galvanostat, IVIUM Netherlands in KCl (0.1 M) at optimized pH. Electrode assembly was consist of WE-II, Pt foil (1 cm^2) as auxiliary electrodes and Ag/AgCl as reference electrodes. EC performance of WE-II was examined through CV at scan rate (mV/s) ranging 25 to 150 under compatible current and sweep potential. EC response of OPs over WE-II was optimized under judicious EC conditions. EC data obtained from SWV of standard solutions of CPS were simulated to achieve calibration plots for quantitative estimation of CPS.

RESULTS
EC behavior of WE-II

EC behavior of WE-II was investigated through CV studies in 0.1 M KCl [Fig. 1]. Comparative cyclic voltammograms were obtained for SSPE and WE-II at a common scan rate (SR) of 50 mV/s within potential window of -1.5 to +0.0 V. A pair of well-defined redox peaks was observed on the SSPE and WE-II with the Epa (V) at - 0.675 and -0.670, and Epc (V) values of -1.228 and -1.231 respectively. Magnitudes of redox peak current rapidly increased, on modification of SSPE with NHs (5 wt% h-BN) that indicates better EC behavior of WE-II [29]. CV studies was performed in different solvent medium *viz.*, KCl, PBS, H_2SO_4 and KOH and among all KCl showed best response and selected for onwards EC investigations [Fig. 2].

Effect of the scan rate on the EC detection of CPS was examined at different SR of 25, 50, 80, 100, 150 and 200 mV/s. Fig. 3 reflects that, Ipa increases from 0.767 to 1.912 mA and Ipc reduces from -1.202 to -2.231 mA with linear dependence on SR ranging from 25 to 150 mV/s. Data reveals that fabricated WE-II function as an electron conducting tunnel and releases more electrons with high SR, suggesting a typical surface-controlled electrode process. Further, the polarization of the electrode under high SR attributes to increased potential difference between anodic and cathodic peaks [30].
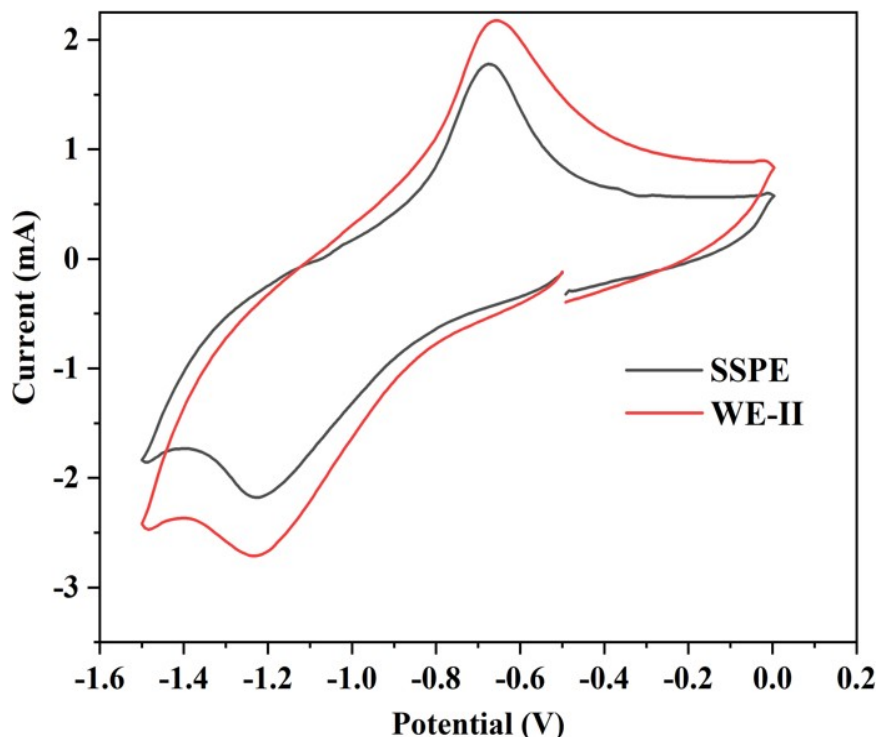
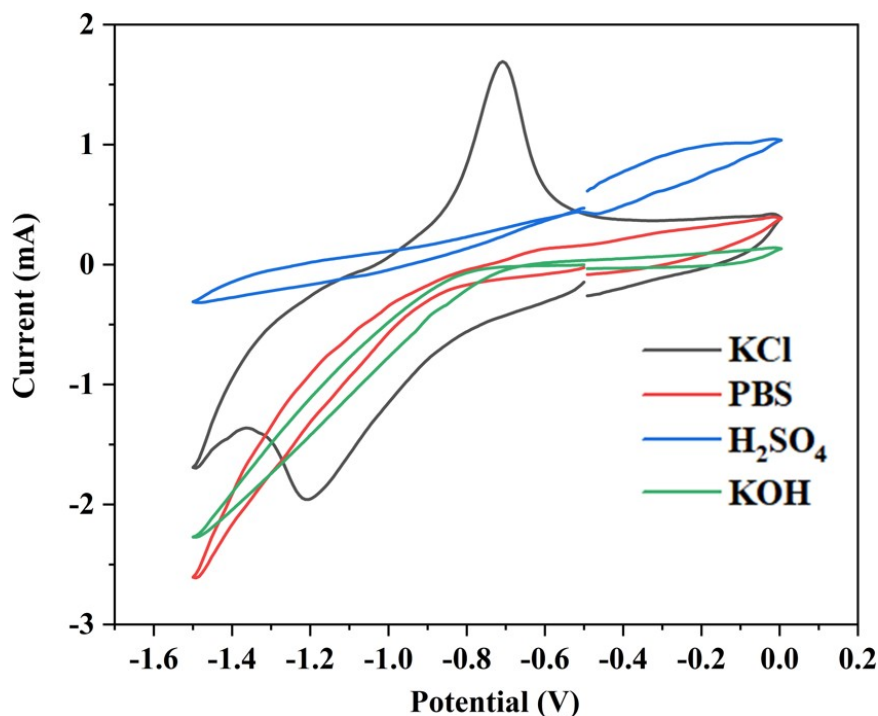**Fig. 1.** Comparative CV curves of SSPE and WE-II

Fig. 2. Electrochemical compatibility of electrolyte media with WE-II

Quantification of OPs through SWV

EC quantification of CPS, was examined through SWV at developed WE-II as sensing device [Fig. 4a]. SWV performed within optimal parameters of potential ranging -2.0 V to 2.0 V, E step of 8 mV @10 Hz pulse amplitude at 100 mV over WE-II.

Calibration curve for CPS was obtained by sequential addition of CPS (10^{-3} M methanolic solution) in KCl (0.1 M aqueous solution, pH 7.4). Calibration graph showed linear relation between Ip (2.79 to 3.61 mA) and successive addition of CPS (5 to 25 ng/L) added with regression coefficient of 0.98

[Fig. 4b]. The LOD and LOQ were estimated from calibration curves using relations, LOD = 3.3 (S.D. of intercept/slope) and LOQ = 10 (S.D. of intercept/slope) [31]. The proposed EC sensor demonstrates acceptable quantification of CPS with quite low LOD and LOQ values at WE-II as 2.62 ng/L and 7.93 ng/L, respectively.
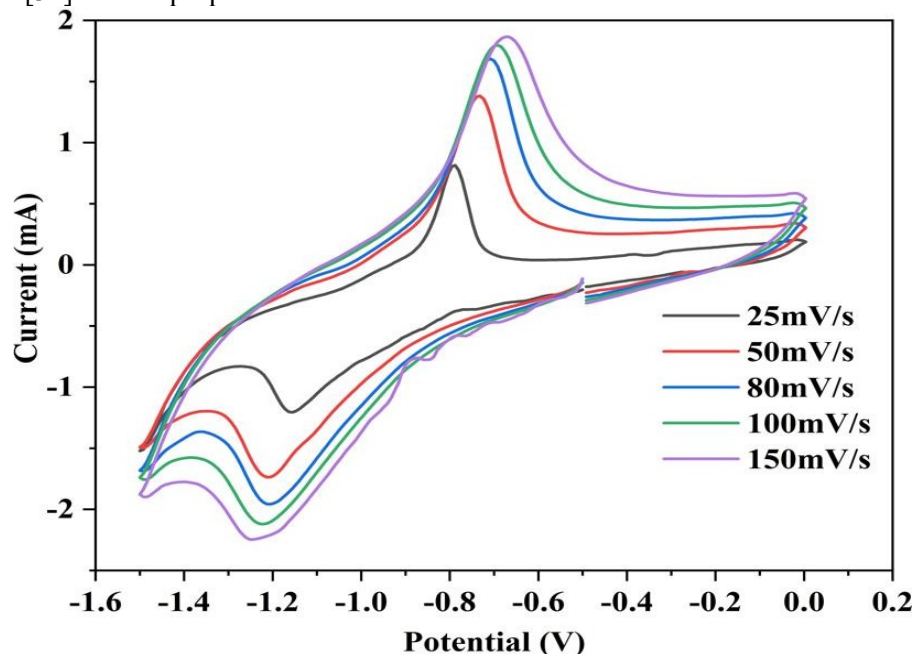
Fig. 3. Effect of SR (mV/s) ranging 25 to 150 on CV of WE-II
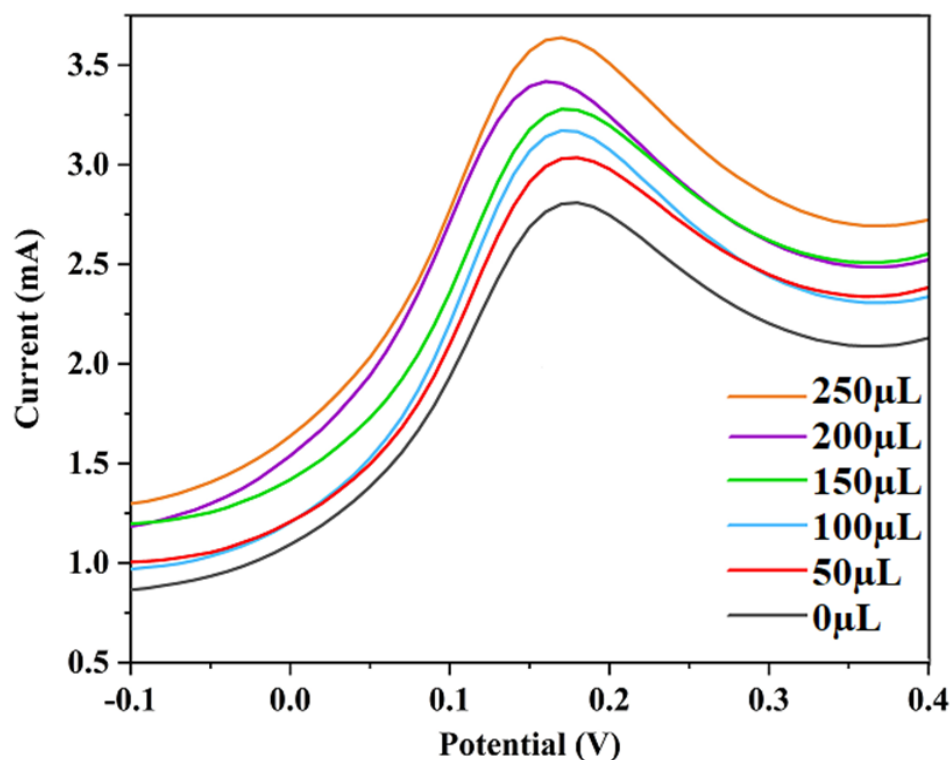
Fig. 4a. Effect of concentration of CPS on current response in SWV at WE-II
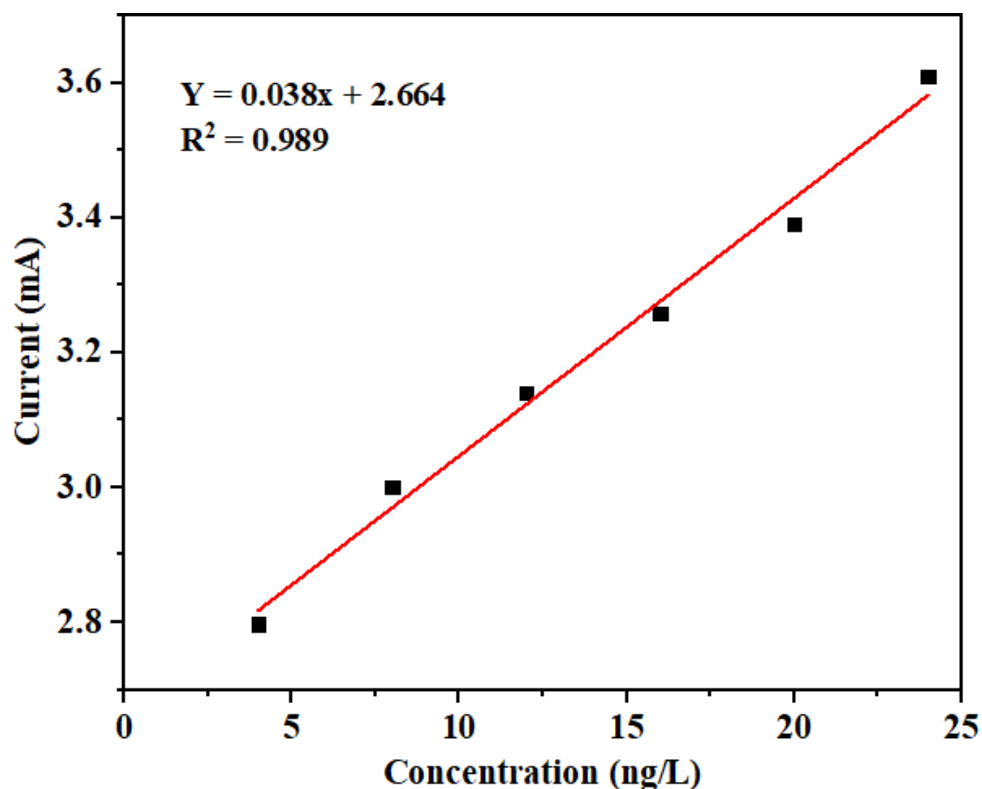
Fig. 4b. Calibration curve drawn from SWV for CPS at WE-II
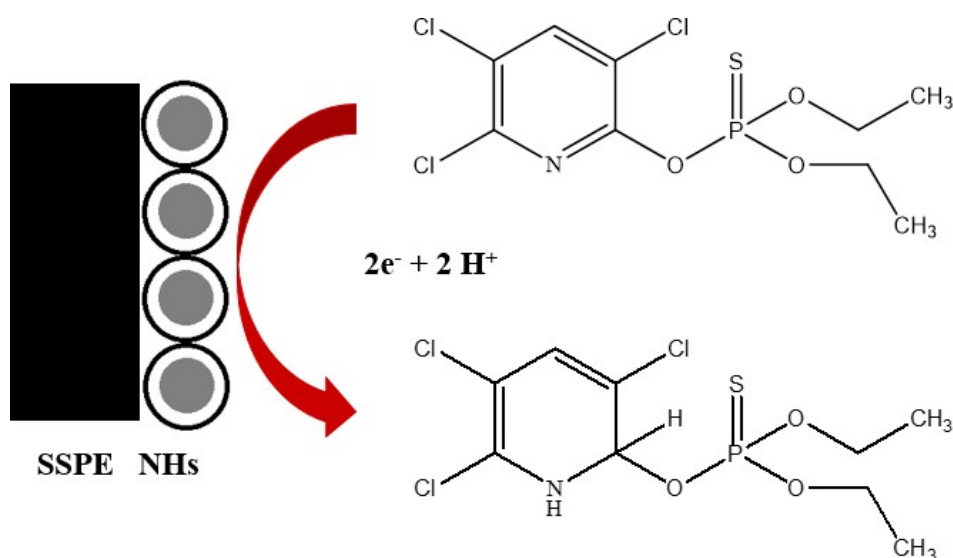
Fig. 5. Mechanism of electro reduction of CPS at WE-II

SWV showed two reductions peaks for CPS, out of them first strong reductionpeak was selected for quantification. In SWV, peak appears due to electro-reduction of CPS at pyridine ring (-C=N-) *via* $2e^-$ /$2H^+$ transfer step at pH 7.4 (Fig. 5). Reduction peaks of CPS at ~ -0.1 V and 0.6 V, appeared due to reduction of pyridine nitrogen and carbon ring respectively. Three chlorine atoms attached at pyridine ring facilitate delocalization of electrons at -C=N- bond and thus enhances the reduction of -C=N- bond of pyridine ring at low negative potentials. It revealed that the coated material act as an electron-conducting tunnel and facilitates the electron transfer kinetics that enhanced EC properties of WE-II. The enhancement in Ip may be attributed to their high surface area of NHs (5 wt% h-BN) and good electrical conductivity of WE-II that increases its sensitivity towards pesticides monitoring [32].

CONCLUSION

The present research has been focused on coating the NHs as potential electrode material for EC detection of CPS. WEs were derived from NHs in presence of PVB binder in NMP. WEs have rendered highly sensitive, selective and reproducible EC

response in KCl 0.1 M. The EC behavior of WE-II was investigated through CV studies under optimized parameters of SR of 50 mVs⁻¹, Estep 8 mV, within the potential window d-1.5 to +0.0 V. CV reveals enhanced redox behavior and EC stability of WEs in KCl at 7.2 pH. EC methods based on SWV reveal immense feasibility of electrodes towards quantification of CPS. SWV data reveals CPS can be quantified upto LOD of 2.62 ng/L and LOQ 7.96 ng/L over WE-II. The developed sensor exhibits high sensitivity, selectivity and shows an excellent recovery that can be employed in real sample analysis.

REFERENCES

1. J. Kaushal, M. Khatri, S.K. Arya, *Ecotoxicol. Environ. Saf.,* **207**, 1 (2021).
2. H. Mali, C. Shah, B.H. Raghunandan, A.S. Prajapati, D.H. Patel, U. Trivedi, R.B. Subramanian, *J. Environ. Sci.,* **127**, 234 (2022).
3. X. Guardino, J. Obiols, M.G. Rosell, A. Farran, C. Serra, *J. Chrom. A.*, **823**, 91 (1998).
4. M. Saunders, B.L. Magnanti, S.C. Carreira, A. Yang, U. Alamo Hernández, H. Riojas-Rodriguez, A. Bartonova, *Environ. Health,* **11**, S5 (2012).
5. M.L. Yola, N. Atar, *J. Electrochem. Soc.,* **164**, B223 (2017).
6. R.S. Bhende, U. Jhariya, S. Srivastava, S. Bombaywala, S. Das, N.A. Dafale, *Appl. Biochem. Biotechnol.,* **194**, 2301 (2022).
7. J.N. Seiber, L.A. Kleinschmidt, *J. Agric. Food Chem.,* **59**, 7536 (2011).
8. R.E. Mauldin, T.M. Primus, T.A. Buettgenbach, J.J. Johnston, G.M. Linz, *J. Liq. Chromatogr. Relat. Technol.,* **29**, 339 (2006).
9. Q. Ullah, N. Fatema, A. Mohammad, *JPC–J. Planar Chromat.,* **33**, 533 (2020).
10. V. Kumar, N. Upadhay, A.B. Wasit, S. Singh, P. Kaur, *Curr. World Environ.,* **8**, 313 (2013).
11. J. Sherma, R. Slobodien, *J. Liq. Chromatogr.,* **7**, 2735 (1984).
12. P. Ma, L. Wang, L. Xu, J. Li, X. Zhang, H. Chen, *Eur. Food Res. Technol.*, **246**, 239 (2020).
13. X. Du, D. Dong, X. Zhao, L. Jiao, P. Han, Y. Lang, *RSC. Adv.*, **5**, 79956 (2015).
14. X. Zhao, C. Zhao, X. Du, D. Dong, *Sci. Rep.,* **9**, 1 (2019).
15. Y. Makino, S. Oshita, Y. Murayama, M. Mori, Y. Kawagoe, K. Sakai, *Trans. ASABE,* **52**, 1955 (2009).
16. N.Y. Sreedhar, M.S. Kumar, K. Krishnaveni, *Sens. Act. B: Chem.*, **210**, 475 (2015).
17. R. Vera, S. Insa, C. Fontas, E. Antico, Talanta, **185**, 291 (2018).
18. D. Sharma, A. Nagpal, Y.B. Pakade, J.K. Katnoria, *Talanta*, **82**, 1077 (2010).
19. G.V. Guerreiro, A.J. Zaitouna, R.Y. Lai, *Anal. Chim. Acta.*, **810**, 79 (2014).
20. Y. Jiao, W. Hou, J. Fu, Y. Guo, X. Sun, X. Wang, J. Zhao, *Sens. Actuators B: Chem.,* **243**, 1164 (2017).
21. A. Kumaravel, M. Chandrasekaran, *J. Agric. Food Chem.,* **63**, 6150 (2015).
22. N. Karimian, H. Fakhri, S. Amidi, A. Hajian, F. Arduini, H. Bagheri, *New J. Chem.,* **43**, 2600 (2019).
23. W. Huang, X. Zhou, Y. Luan, Y. Cao, N. Wang, Y. Lu, T. Liu, W. Xu, *J. Sep. Sci.,* **43**, 954 (2020).
24. P. Joshi, S. Mehtab, M.G.H. Zaidi, T. Tyagi, A. Bisht, *J. Nanostructure Chem.*, **10**, 33 (2020).
25. M. Sankaran, B. Viswanathan, S.S. Murthy, *Int. J. Hydrog. Energy,* **33**, 393 (2008).
26. N. Jain, E. Gupta, N.J. Kanu, *Smart Sci.,* **10**, 1 (2022).
27. S. Sharma, S. Mehtab, M.G.H. Zaidi, *Materials Today: Proceedings* 62, 6494 (2022).
28. S. Sharma, S. Mehtab, M.G.H. Zaidi, *Mater. Chem. Phys.*, **296**, 127278 (2023).
29. M. Amatatongchai, W. Sroysee, P. Sodkrathok, N. Kesangam, S. Chairam, P. Jarujamrus, *Anal. Chim. Acta*, **1076**, 64 (2019).
30. B.G.S. Raj, R.N.R. Ramprasad, A.M. Asiri, J.J. Wu, S. Anandan, *Electrochim. Acta,* **156**, 127 (2015).
31. J.C. Miller, J.N. Miller, *Analyst,* **113**, 1351 (1988).
32. N. Karimian, H. Fakhri, S. Amidi, A. Hajian, F. Arduini, H. Bagheri, *New J. Chem.,* **43**, 2600 (2019).

Microwave synthesis and characterization of organophilic clay/polyacrylic-g-polycarbonate nanocomposites

S. Pandey [1], S. Mahtab [1], S. K. Gururani [2], M. G. H. Zaidi [1]*

[1] *Department of Chemistry, G. B. Pant University of Agriculture & Technology, Pantnagar-Uttraakhand-263 145, India*
[2] *Department of Chemistry, M.B. Post Graduate College, Kumaun University, Nainital-263 631, India*

Polymer nanocomposites (PNCs) were synthesized through graft copolymerization of polyacrylic acid onto polycarbonate followed by solution intercalation of organophiic montmorillonite (OMMT) into graft copolymer under microwave irradiation. PNCs were characterized through diverse spectral, thermal methods and scanning electron microscopy (SEM). Formation of PNCs was ascertained through UV-visible, FTIR spectra, X-ray diffraction and scanning electron microscopy. The matrix of the graft copolymer has been found to contain micropaticulate distributions of OMMT, leading to the formation of PNCs. Simultaneous thermogravimetric-differential thermal analysis-differential thermogravimetry reveals moderate thermal stability of PNCs.

Keywords: Polymer nanocomposites, Graft copolymerization, Montmorillonite, Characterization.

INTRODUCTION

Recently, there has been an increased interest in development of polymer nanocomposites (PNCs), involving phylosilicates for their potential applications in environmental cleanup [1], packaging, aerospace, and automotive industries [2-4]. Montmorillonite (MMT) belongs to the family of smectite clay holding 2:1 phylosilicates arrangement comprising two tetrahedral sheets along with one octahedral sheet of aluminosilicates. MMT has received enormous attention over decades as the inexpensive phylosilicates as filler for development of PNCs [5-6]. The high abundance, and rich intercalation chemistry allows MMT to serve as preferred choice for designing of two-dimensional PNCs [7]. Majority of thermoplastic and thermosetting polymers are hydrophobic and are not compatible with MMT. In order to afford the enhanced binding with polymers matrix, treatment of clays with surfactants offers a viable method to achieve their enhanced reinforcement into polymer matrix to develop the PNCs with improved barrier properties, structural rigidity, heat resistance, flame retardency, superhydrophobicity, promising mechanical, dynamic mechanical behavior and antimicrobial activities [8].

Chemical pretreatment of clays is well established methods to develop the organophilic clays as fillers for development of PNCs [5-7]. The viable pretreatment leads in presence of amino acids, organic quaternary ammonium salts, tetra organic phosphonium halides as modifiers for clay materials [5]. Functional amphiphilic graft polymers has been considered as compatibilizers to achieve the PNCs with key examples of polyethylene-graft-polymethacrylic acid [8], polystyrene (PS)-graft-cellulose [9], PS-graft-cellulose acetate [10], syndiotactic PS-g-polymethyl methacrylate [11], starch-g-PS [12].

Over the years, MW irradiation-based polymer manufacturing has gained popularity as a quick, efficient, and environmentally benign method of producing polymer products. Microwave treatment offers the dielectric way of heating where molecules bearing permanent dipole moment align to the applied electromagnetic field, resulting in rotation, friction, and collision of molecules that facilitates polymerization reactions [13, 14]. The present investigation deals with MW-assisted synthesis of (PAA)-g-polycarbonate (PC) and its solution intercalation with organophilic montmorillonite (OMMT) to afford the PNCs. In this process, OMMT was synthesized through cation exchange of commercially available MMT (K10) with cetyl pyridinium bromide (CPBr) in [14]. Synthesized PAA-g-PC and respective PNCs were characterized through diverse spectral, thermal methods and scanning electron microscopy [15-17].

---

* To whom all correspondence should be sent:
E-mail: smiitr@gmail.com, mgh_zaidi@yahoo.com

EXPERIMENTAL

Starting materials

Acrylic acid and PC (Tg. 150-160ºC, density 1.2 g/cc at 25 ºC) were procured from Sigma Aldrich Chemicals. Azobisisobutyronitrile (AIBN), Na-MMT (K-10) and cetyl pyridinium bromide (CPBr) were procured from Himedia, India. AIBN was re-crystallized from methanol and dried under reduced pressure at room temperature (mp 102-104ºC). Other chemicals and solvent (purity > 99%) were locally arranged and used without further purification. OMMT was prepared through dispersing Na-MMT (2.0 g) in de-ionized water (800 ml) followed by sonication over 1h. A solution of CPBr (20 mL, 0.36 M) in water was slowly added into the suspension of MMT under sonication (500 W) over 1 hr. OMMT was then isolated through filtration from the suspension and washed several times with distilled water until the testing of the mother liquor with AgNO$_3$ (0.1) M showed negative test for silver bromide. OMMT was dried overnight at 110°C and ground to pass a 400-mesh sieve. The % yield and % G 47.50 and 18.50 of PAA-g-PC was deduced according to the reported procedure and was found as 47.50 and 18.50, respectively[7].

MW-assisted synthesis of PNCs

AA (2.90 ×10^{-2}mole/dl) , PC (1.0 g) and AIBN (1.21×10^{-3} mol/dl) were dissolved in dichloromethane (5 ml) in a 100 mL-borosilicate glass vial and irradiated under MW at 100W over 5 min. The PC-g-PAA was isolated through successive washing of the crude product several times with methanol followed by filtration till achieving the uniform weight of the solid residue. The isolated PC-g-PAA (1.0 g) was subsequently subjected to solution intercalation in presence of OMMT (5 phr) in dichloromethane (25 ml) under MW irradiation at 100W over 5 min. The PNCs were isolated in 98 % yield through removal of dichloromethane followed by drying at 50 ºC/ 400 mmHg over 3 h. PAA was also synthesized under similar reactions conditions and used as reference for comparing the results.

Characterization

Uv-visible spectra were recorded in methanol on a Genesis 10 Thermospectronic spectrophotometer in tetrahydrofuran. FTIR spectra were recorded on Galaxy 300 Mattson FT-IR infrared spectrometer in KBr disks. XRD spectra were recorded at 25⁰C on a Rigaku-Geiger flex diffractometer using Cu-Kα radiation (λ= 0.154056). The crystallite size of OMMT and gallery spacing of OMMT was deduced through Debye Scherer method [16]. Thermograms were recorded on Perkin Elmer Pyris Diamond

thermal analyzer at sample size ranging in N$_2$@ 10 ºC/min with reference to alumina. SEM were recorded on JEOL-JSM-6610LV. TEM was recorded on JEOL 1011 (Tokyo, Japan) instrument with a primary beam voltage of 80 kV.

RESULTS AND DISCUSSION

Spectra

UV spectra reveal characteristic absorption maxima (nm) for PC (a), PC-g-PAA (b) and PNCs (c) at 266, 269 and 264 respectively (Fig. 1). The carboxylate functionalities extended by acrylic acid contribute red shift to the absorption of PC in the respective PC-g-PAA, whereas PNCs have shown a blue shift over graft copolymers due to binding of the OMMT with functionalities of the graft-co-polymers [17].
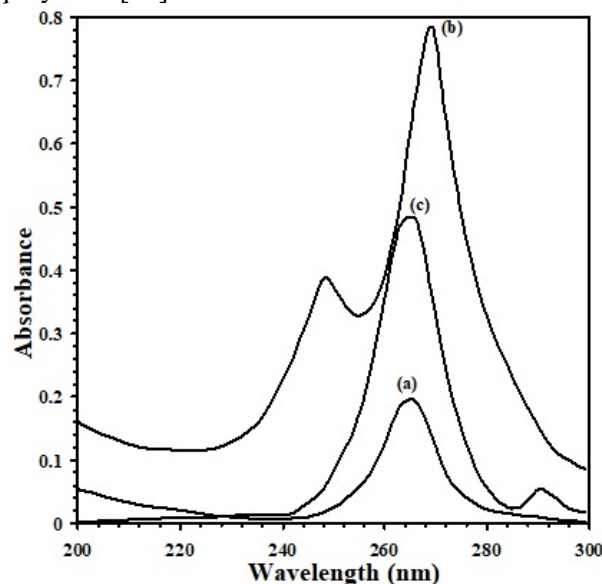

Fig. 1. UV spectra of PC (a), PC-g-PAA (b) and PNCs

Fig.2 demonstrates the FTIR spectra of OMMT (a), PC (b), PAA-g-PC (c) and PNCs (d).

FTIR spectrum of OMMT reveals the characteristic wave numbers (cm^{-1}) corresponding to 3396.93 (ν OH), 3004.35 (ν Ar. C-H), 2918.61 (ν CH$_2$, as.), 2852.09 (ν CH$_2$,sy.), 1630.43 (δ OH), 1481.72 (δ CH$_2$, scissoring), 1373.91 (δ CH$_3$,as.), 1317.39 (δ CH$_3$,sy.), 1317.39 (δ CH$_3$,sy.), 1169.57-1040.07 (ν Si-O), 782.61-717.39 (ρ CH$_2$), 673.91 (δ Si-O), 523.50 (ν Si-O/Si-O-Al), 465.31 (ν Si-O/Si-O-Fe) (Fig. 2a) [14]. PC shows wave numbers at 3784(ν COOH), 3439.7(ν O-H), 2360(ν C-H, as.CH$_2$), 1632.9 (δ, H$_2$0), 771.1(ρ C-H) (Fig. 2b) [17]. PAA-g-PC shows wave numbers at 3895.3 (ν C=O), 3022.3-2926.3(ν =C-H, CH$_2$), 2360.9(ν(C-H, as, CH$_2$), 1654.6(δ, H$_2$0), 1216.9 (ν C-O-C, as), 1027.6 (ν C-O), 929.2 (ν C…O), 764 (ρ C-H) (Fig. 2c). PNCs shows wave numbers at 3747.4-3600.5 (ν

C=O), 3021.7(ν =C-H, CH_2), 2925.4 (ν CH_3 as), 2854.2 (ν CH_2 sy), 1652.5(δ H_2O), 1216.4(ν C-O-C, as), 1017.4(ν C-O), 928.8(ν C…O) and 762.6(ρ C-H). This was associated with additional functionalities corresponding to 520.50 (ν Si-O/Si-O-Al), 450.31 (ν Si-O/Si-O-Fe), which reveals the formation of PNCs[14].
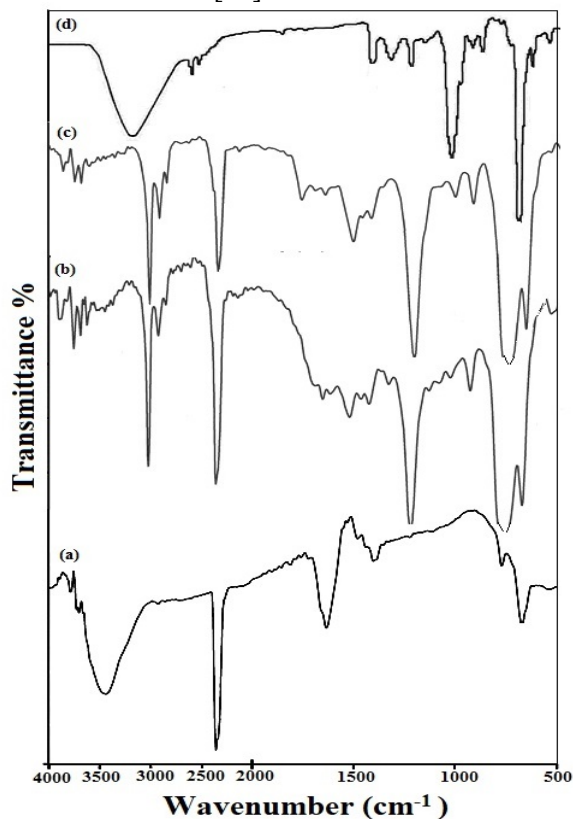

Fig. 2. FTIR spectra of OMMT (a), PC(b), PAA-g-PC (c) and PNCs (d)

Microstructure

XRD spectrum of OMMT reveals its amorphous characteristics with appearance of characteristic indexing of 2θ at 24.01° (001), 22.76° (005), 19.57° (02; 11), 27.47° (007) (Fig. 3a) [14,18]. XRD spectrum of PC demonstrates the characteristic crystalline zone at 2θ (d) corresponding to 14.54 (6.07). The indexing appeared at 3.46 (25.69) and 2.03 (31.44) attributes to semi-crystalline zones of PC (Fig. 3b). PC, PC-g-PAA (Fig. 3c) and PNCs (Fig. 3d) reveals common peaks ranging 2θ=21 to 24 ° corresponding to the van der Waals distance of neighboring polymer chains segments [20]. The indexing at 14.54 (6.07) and 15.15 (5.82) attributes to reduction in gallery spacing of PC due to graft copolymerization .The appearance of (001) indexing in the range of 2θ=21 to 28 attributes to binding of OMMT with PAA-g-PC.

TEM images reveal the formation of spherical micro particles of OMMT with particle size ranging 10 to 55 nm (Fig. 4a). The crystallite size of OMMT deduced from Debye Scherer methods (48 nm) is in closed agreement to particle size deduced from TEM (Fig. 4a).The samples for SEM imaging were made through cast of their films in dichloromethane. In order to have the comparable results, all the SEM images were recorded at 1000X, 10 μm. The cast films of PC reveal occasional appearance of air pockets due to evaporation of dichloromethane during their formation (Fig. 4b). PC-g-PAA reveals characteristic phase separation due to immiscibility of PAA into PC phase (Fig. 4c) [19]. PNCs has shown random distribution of assemblies of OMMT agglomerates into PC matrix (Fig. 4d).

Thermal stability

Fig. 5 demonstrates the simultaneous TG-DTA-DTG curves for PC (a), PAA (b), PAA-g-PC (c) and PNCs (d). The color codes for TG, DTA and DTG curves are black, green and violet. The pertinent thermal data are summarized in Table 1.

Table. 1. Thermal data deduced PC, PAA, PAA-g-PC and respective PNCs from thermograms

Sample	M^A	TG		DTG			DTA
		Onset	Endset	R_1^b	R_2^c	PT^d	$-\Delta H$ $(SV)^e$
PC	0.29	94.64 (431)	0.26 (600)	1.22 (448)	1.51 (479)	586	3168 (54.0)
PAA	2.20	89.50 (199)	0.10 (536)	0.63 (244)	0.59 (587)	499	2140 (63.6)
PC-g-PAA	1.50	90.90 (200)	0.00 (552)	0.55 (235)	0.21 (523)	511	1820 (40.4)
PNCs	4.5	86.87 (200)	9.61 (500)	0.62 (240)	0.82 (400)	407	4400 (35.2)

A: Moisture content (wt%); B : Rate of thermal decomposition at first step; C; Rate of thermal decomposition at second step; D: DTA peak temperature (°C); E:-ΔH $(SV)^e$ =Enthalpy of thermal decomposition in mJ/mg (DTA signal voltage in μV
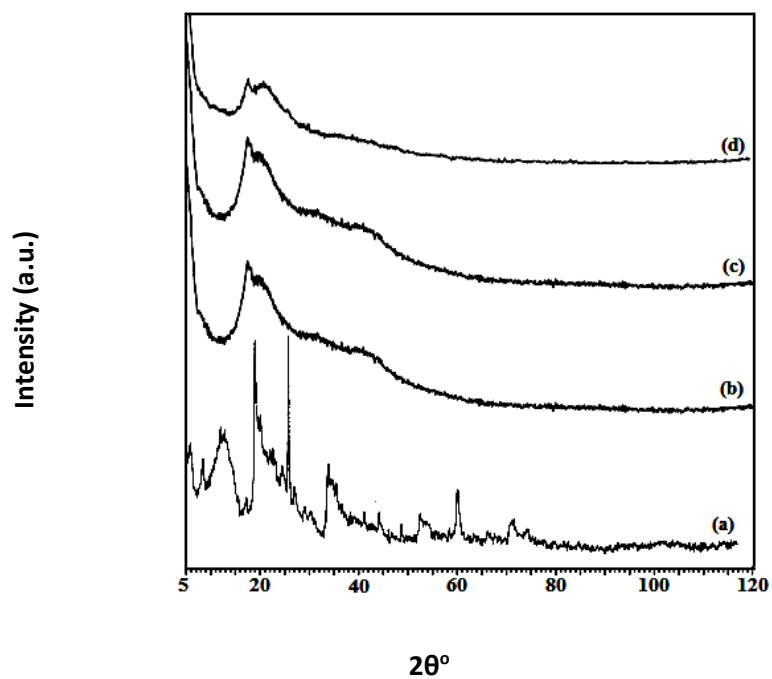
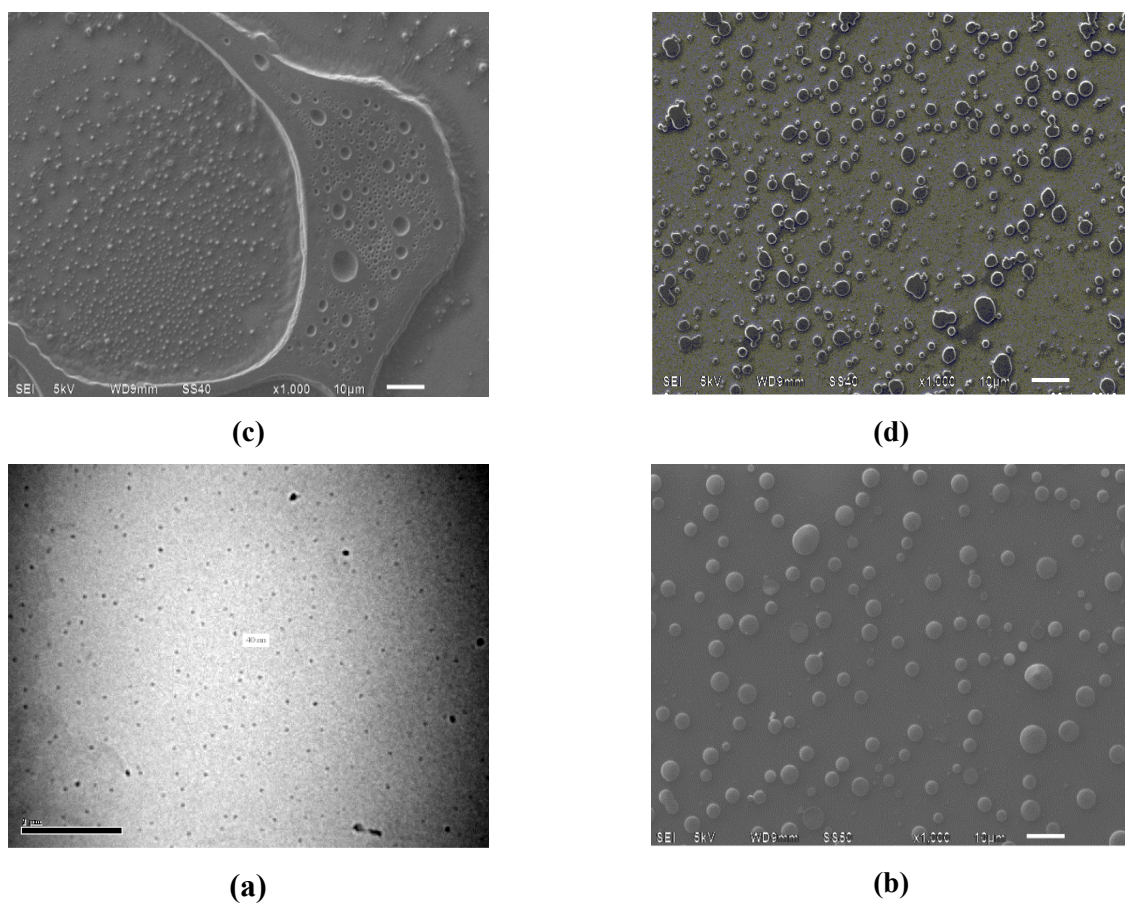**Fig. 3.** XRD spectra of OMMT (a), PC (b), PAA-g-PC(c) and PNCs (d)

(c)

(d)

(a)

(b)

Fig. 4. TEM of OMMT (a).SEM of PC (b), PAA-g-PC (c) and PNCs (d)
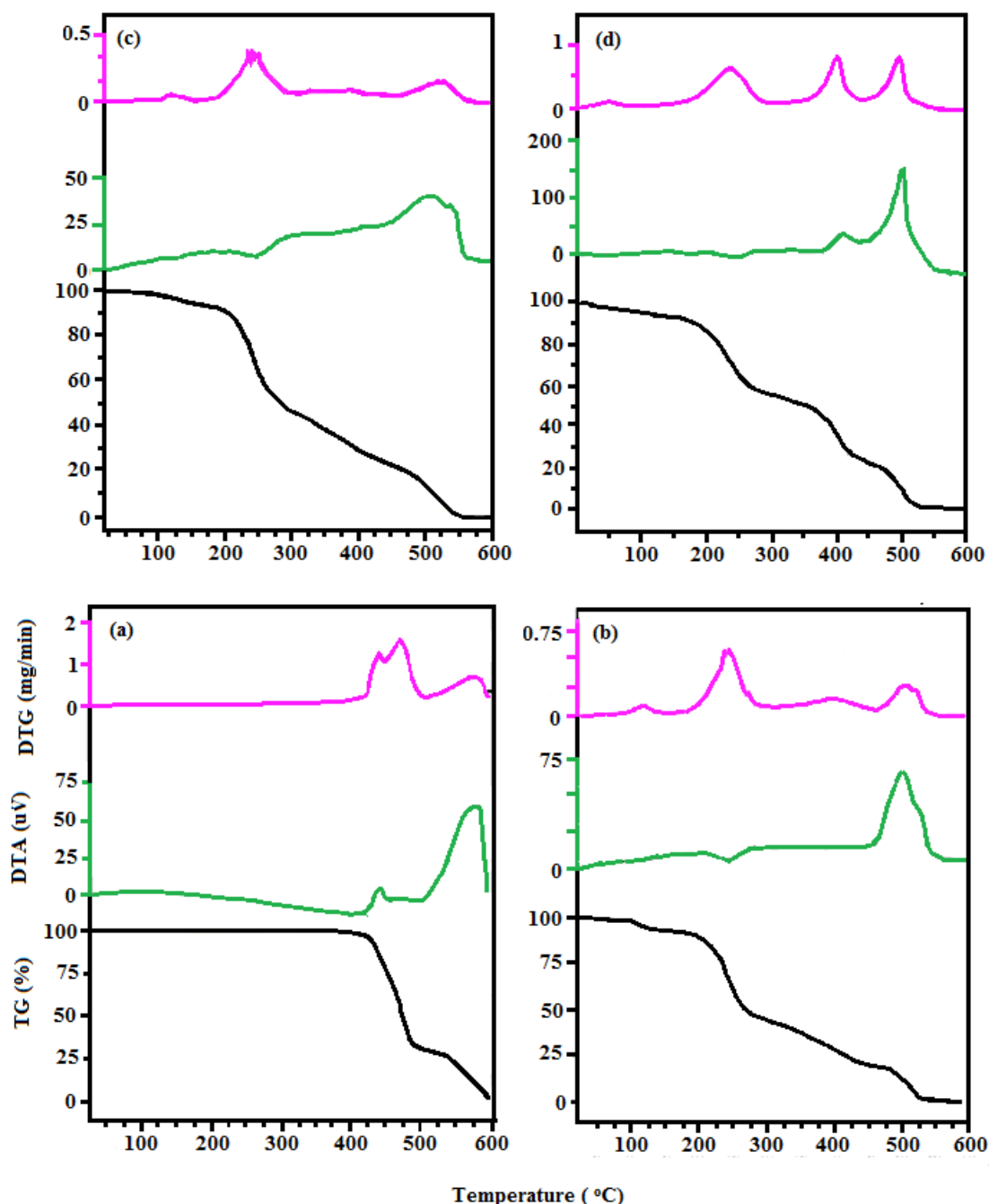
.

Fig. 5. Simultaneous TG-DTA-DTF of PC (a), PAA (b), PAA-g-PC (c) and PNCs (d).The color codes for TG, DTA and DTG are black, green and violet.

TG reveals two step decompositions by all the samples. Graft copolymerization of PAA onto PC and onward modification of PAA-g-PC with OMMT has liberated the PNCs with moderately improved thermal stability. PC shows TG onset at 431 °C leaving 94.64% Wr (weight residue). Prior TG onset, the 0.29 wt% loss at 100°C attributes to the moisture content associated with PC. DTG reveals two stage decomposition of PC at 448 °C and 479 °C with respective degradations (mg/min) @ 1.22 and 1.51. Thermal decomposition of PC has rendered the

exothermic DTA at 54 µV with evolution of -3168 mJ/mg of heat at 586 °C.

PAA was decomposed with TG onset at 199 °C leaving 89.50% Wr. Due to the inherent hygroscopic nature of PAA, has rendered enhanced moisture content (2.20 wt%). Decomposition of PAA was concluded at TG endset of 536 °C, leaving 0.10% Wr. DTG reveals the major decomposition of PAA at 244 °C and 587 °C @ (mg/min) 0.63 and 0.59, respectively.

Thermal decomposition of PAA has rendered the exothermic DTA at 63.6 μV with evolution of -2140 mJ/mg of heat at 499 °C. The high moisture content of PAA-g-PC (1.50 wt %) over PC (0.29 wt%) is due to the grafting of the hygroscopic macromolecular signets over PC. No significant change in TG onset and corresponding Wr % of PAA-g-PC and respective PNCs was observed over PAA. However, PAA-g-PC was completely volatilized at 552 °C due to inferior thermal stability [21]. DTG reveals usual two step decomposition of PAA which were initiated at 235 °C and 553 °C @ (mJ/mg) 0.55 and 0.21 respectively. PAA-g-PC (500 °C) has rendered a substantial reduction in TG onset over PC (600 °C). However, the controlled rare of degradation of PAA-g-PC revealed through DTA indicates their enhanced thermal stability of PC [17]. Thermal decomposition of PAA-g-PC has rendered the exothermic DTA at 40.41 μV with evolution of -1820 mJ/mg of heat at 523 °C.

The contribution of OMMT as a thermal stabilizer for PAA-g-PC was revealed at TG endset appeared at 500 °C leaving 9.61%Wr by PNCs. The high moisture content of PNCs (4.5 wt%) probably attributes to the insignificant loading of OMMT. However, high %Wr (9.61) at TG endset (500 °C) attributes to moderate thermal stability of PNCs over PAA-g-PC, PAA and PC respectively. However, the second step decomposition appeared of PNCs was progressed @0.82 mg/min, that was relatively higher over PC and PAA-g-PC. PNCs was exothermically decomposed with DTA at 35.20 μV leaving 4400mJ/mg of heat at 407 °C. Thermograms reveals that grafting of PAA onto PC and their onward modification with OMMT has rendered PNCs with enhanced moisture uptake (4.5 wt%) without any improving in TG onset temperatures over PAA. Thermal stability of PNCs was moderately compromised at TG endset. However, the highest liberation of heat (4400 mJ/mg) reveals the thermal stability of PNCs prior to their TG endset.

CONCLUSION

The present investigation demonstrates a clean, rapid and viable process of synthesis of polymer nanocomposites under microwave irradiation at 100W. The process involves microwave assisted synthesis of polyacrylic acrylic-graft-polybisphenol A-carbonate (PAA-g-PC) with graft yield and efficiency of 47.50% and 18.50, followed by their solution intercalation with organophilic montmorillonite (OMMT). For this purpose, OMMT was synthesized through cationic exchange of cetyl

pyridinium bromide with montmorillonite (K 10). The crystallite size of OMMT deduced from XRD (48 nm) was in closed agreement with transmission electron microscopy data (~55 nm). Diverse spectral and thermal methods revealed the formation of OMMT, PAA-g-PC and respective PNCs. Scanning electron microscopy revealed the random distribution of the microparticles of OMMT into the matrix of PAA-g-PC. PNC has shown moderate thermal stability over PC and respective PAA-g-PC.

REFERENCES

1. M. Hanmate, A. K. Pulikkal, *Chemosphere*, **307** (2), 135869 (2022).
2. M. Okamoto, Poly. Nanocompos. *Eng.*, **4** (1), 457 (2023).
3. S. Gul, A. Kausar, B. Muhammad, S. Jabeen, *Polym. Plast. Technol. Eng.,* **55** (3), 684–703 (2016).
4. F. Guo, S. Aryna, Y. Han, Y. Jiao, *Appl. Sci.*, **8** (9), 1696 (2018).
5. S. L. Bee, M. A. A. Abdullah, S. T. Bee, L. T. Sin, A. R. Rahmat, *Prog. Polym. Sci.* **85** (5), 57 (2018).
6. S. Pandey, M.G.H. Zaidi. S. K. Gururani , *Sci. J. Rev.*, **2** (11), 296 (2013).
7. R. Wang, H. Li, G. Ge, N. Dai, J. Rao, H. Ran, Y. Zhang, *Mol.*, **26** (9), 2521 (2021).
8. N. Sibold, C. Dufour, F. Gourbilleau, M. N. Metzner., C. Lagreve, L. L. Pluart, P. J. Madec, T. N. Pham, *Appl. Clay Sci.,* **38** (1-2), 130 (2007).
9. S. Murugesan, T. Scheibel, *Adv. Funct. Mater.*, **30** (17), 190801 (2020).
10. M. Abbasian, M. Bakshi, M. Jaymand, S. G. Karaj-Abad, *J. Elast. Plast.,* **51** (5), 473 (2019).
11. G. Moreira, E. Fedeli, F. Ziarelli, D. Capitani, L. Mannia, L. Charles, S. Viel, D. Gigmes, C. Lefy, *Polym. Chem.*, **6** (3), 5244 (2015).
12. M. Jaymand, *Polym. J.*, **43** (2), 901 (2011).
13. H. Namazi, A. Dadkhah, M. Mosadegh, *J. Polym. Environ.*, **20** (3), 794 (2012).
14. R. Hoogenboom, U. S. Schubert, *Macromol. Rapid Commun.*, **28** (6), 368 (2007).
15. H. Negi, T. Agarwal, M. G. H. Zaidi, A. Kapri, R. Goel, *Biotech. J.,* **6** (1):107 (2010).
16. T. Agarwal, K. A. Gupta, M. G. H. Zaidi, *J.Chem. Chem. Eng.*, **55** (3):62 (2012).
17. S. Mehtab, M. G. H. Zaidi, P. Joshi, D. Bawari, *IOP Sci. Notes*, **1**, 034201(2020).
18. S. K. Joshi, J. C. Kapil, A. K. Rai, M. G. H. Zaidi , *Phyica Status Solidi,* **199** (2): 321 (2003)
19. A. S. Pakdaman, J. Morshedian, Y. Jahani, J. Appl. Polym. Sci., 127 (2), 1211 (2013).
20. M. Spirkova, J. Pavlicevic, A. Strachota, R. Poreba, O. Bera, L Kapralkova, J. ldrian, M. Slouf, M. Lazic, J. Budinski , *Eur. Polym. J.*, **47** (3), 235 (2011).
21. D. Debier, A. M. Jonas, R. Legras, *J. Polym. Sci. B*, **36** (5), 2197 (1987).
22. V. Agarwal, M. G. H. Zaidi, S. Alam, A. K. Rai *Int. J. Polym. Anal. Charact.*, **14** (1), 52 (2009).
23.

Green development of methyl blue dyed electroactive cellulose fabric

S. Pathak[1], M.G.H. Zaidi[*1], S. Mehtab[1], M. Pandey[1], Shazia Mehtab[2], A. Bughani[1]

[1]*Department of Chemistry, C.B.S.H., G.B. Pant University of Agriculture and Technology, Pantnagar, India*
[2]*Fabric & Apparel Science Department, Institute of Home Economics, Delhi University, Delhi, India*

The traditional aqueous dyeing of textiles is a water-intensive process. The textile business frequently involves wet processing and finishing methods to improve the aesthetics and utility of textile fabrics, which have a highwater usage. According to estimates, to colour 1 kg of fabric 100 and 150 L of water is required. As a result, over 280,000 tonnes of carcinogenic textile dye effluents are disposed off into the water bodies every year, endangering both human health and aquatic life. Present study demonstrates the development of a series of green methodologies pertaining to dyeing of cellulose fabrics (CFs) with methyl blue (MYB, 200 μL). Green procedures of dyeing were conducted over CFs (1 inch^2) followed by either of hot air drying (10 min), MW irradiation (3 min) and SCC treatment (3 h), each at 70°C. The produced dyed fabrics (DFs) were investigated for their DC conductivity (σDC) through four probe arrangement. Cyclic voltammetry of MYB was performed at variable scan rates (25-100 mV/s) to check the cyclic stability. The leaching of dye from the DFs with time (over 120 min) was investigated through square wave voltammetry (SWV) in KCl (0.1 M). SWV reveals that the limits of detection and quantification (mg/L) of MYB up to 4.10×10^{-3} and 12.60×10^{-3}, respectively. The current study reveals that CFs undergoing SCC treatment show good dye uptake, better σDC and minimum leaching of the dye thereby making it the most efficient green methodology for dyeing in comparison to hot air and MW treatment.

Keywords: Cellulose fabric, Supercritical carbon dioxide, Cyclic voltammetry, Square-wave voltammetry, Microwave.

INTRODUCTION

Cellulose fabrics (CFs) are predominantly used in textile across the world and are tremendously employed in the apparel, décor, sanitation, and health industries[1].It is one of the most abundant natural biopolymers, which is composed of glucose chains that comprises many hydroxyls functional groups. CFs are characterized with excellent hygroscopicity, breathability, flexibility, biodegradability, heat retaining and sanitary property [2]. These characteristics make cellulose a desirable material for making conductive fabrics [3]. Conductive fabrics are now being used as wearable sensors [4], textile-integrated batteries [5], and fabric-based energy storage systems [6]. Reactive dyes are commonly used for dyeing and printing the CFs [7,8] due to strong intermolecular bonding with cellulose macromolecules[9]. Methyl blue (MYB) dye is frequently employed as a nuclear stain because it is a basic dye that can react with anionic groups like carboxylates, phosphates, and sulphates [10]. For biological staining, the dyes are used at high concentrations, which allows low affinity binding of dyes [11].

However, over a past decades, the traditional industries of textile manufacturing process have become one of the fundamental sources of environmental pollution due to discharging of large amounts of wastewater to the environment [12]. The wet processing of textile industries such as dyeing, printing and finishing techniques is a water-intensive process. It has been estimated that in a conventional dyeing, about 100-150 litres of water is used to dye 1 kg of fabric [13]. As a result, about 280,000 tons per years of textile dyes are dumped in wastewater industrial effluents and impose hazard to aquatic life and human health [14]. Dye effluents contain high chemical and biological oxygen demand which are very rich in organic and inorganic pollutants such as chlorinated compounds, heavy metals, nitrates, naphthol, sulphur, soaps, formaldehyde, chromium compounds, benzidine, sequestering agents and pigments [15, 16]. However, several toxic elements remain in the wastewater even after certain treatment processes and causes multi-contamination effects on plants, soil, air and water resources. Due to these environmental impacts, recently supercritical carbon dioxide (SCC) and microwave (MW) assisted dyeing procedures, which avoid the use of water, have been receiving growing attention [17, 18].

Over a past few years, green methodologies have been received growing consideration in the development of sustainable technologies at the cost of reduced disposal of hazardous substances to environment [19,20]. SCCis the most frequently utilised material over other supercritical fluids due to

---

* To whom all correspondence should be sent:
E-mail: mgh_zaidi@yahoo.com

its inexpensive, harmless, low surface tension, non-flammable nature and has critical conditions that are simple to access at Tc = 304.2 K and Pc = 7.37 MPa[21]. The low gas-like viscosity of SCC allows it to penetrate various solid substrates, and its liquid-like solvent power allows it to solubilize a wide range of organic molecules [22]. The high diffusion rates and low mass transfer resistance of SCC has reduced the dying time [23]. Hence, SCC has shown numerous advantages, such as short dyeing time highuptake rate, recycling of CO_2, no usage of water and any effluent discharged into environment over conventional aqueous dyeing process [24,25].

Another green methodology employed for dying is MW irradiation due to its mass transfer kinetics, which consumes less time, energy and solvent [26]. This technology provides an eco-friendly and pollution-free heating source for cotton dyeing due to its non-contact, uniform, efficient and quick heating properties [27-30]. This technique provides more colour depth in a shorter time over traditional dying methods [31]. The mass transfer effect provides good dye exhaustion, higher absorption abilityand energy consumption, resulting in a high treatment speed [32,33]. Inthis method, microwave energy penetrates easily to inside CFs and all particles of CFs can be heated simultaneously which leads to reduce the heat transfer problem [34].

In the present investigation, a kind of electrically conducting CFs has been fabricated through dying with methyl blue followed by conventional, SCC and MW assisted methods. Electrochemical behavior of DFs has been investigated in KCl (0.1 M) at 7.0 pH in view to explore their future applications in biomedical research of staining.

EXPERIMENTAL

Materials

MYB (purity ≥99.98%) and CFs were procured from Ms Molychem India PVT Limited and Abdos India PVT Limited, respectively. Other chemicals and solvents including carbon dioxide (≥99.0%) were locally organised and used without further purifications. MYB solution (0.04g) was dissolved in 100 mL of deionized water to create a 400 ppm-strength solution for dying CFs.

Dyeing of CFs under hot air

Specimen of CFs were dyed in a bath with an alcoholic solution of MYB (200μL) in two aliquots of 100 μL followed by hot air (70°C) drying over 10 min. DFs were stored at 400mmHg/25±1°C.

Dyeing of CFs under MW irradiation

Specimen of CFs were placed in a dying bath and was dyed with MYB solution (200μL) in aliquots of 100 μL followed by MW irradiation (22.4Hz, 70°C) over 3min. DFs was stored at 400mmHg/25±1°C.

Dyeing of CFs in SCC

A 100 mL high-pressure supercritical fluid reaction system equipped with needle valves, a chiller, and PID-controlled heating tape was used to dye CFs. A required mass of CO_2 and MYB (200 μL) moistened were introduced to the reactor vessel at a temperature of 25±1°C. For the vessel to achieve the requisite supercritical pressure (psi), between 1400 and 1800 over 3 h, the temperature was raised to 70±1°C. Depressurizing the reactor system at a rate of 10 psi per minute at 10±1°C allowed DFs to be separated from the vessel.

DFs of identical size were developed through hot air, MW irradiated, SCC treatment at 1400 and 1800 psi and were abbreviated as CF_1, CF_2, CF_3 and CF_4.

Characterizations

DC conductivity measurements were conducted over Keithley nanovoltmeter equipped with 6221 DC current source and 2182A nano voltmeter at selected voltages ranging 1 to 100 V at 25±1°C. Electrochemical behaviour of CFs and respective DFs was performed over IVIUM Potentiostat-Galvanostat equipped with triple electrode cell assembly comprising glassy carbon electrode as working electrode, Pt foil (1 cm^2) as auxiliary electrode and Ag/AgCl as reference electrode in KCl solution (0.1M). Calibration curve was plotted at selected concentrations of MYB over current response in SWV. Limit of detection (LOD) and limit of quantification (LOQ) of MYB were obtained from calibration curve using the relation: LOQ = 10×S/m, LOD = 3.33×S/m, where s represents standard deviation of the peak current for the blank and m indicates slope of the analytical curve in calibration curve [35].

RESULTS AND DISCUSSION

Electrical conductivity

I-V characteristics of undyed fabric (CF_0) and their respective DFs has revealed ohmic behaviourin current range 0.18 to1.01 μA up to 30V at 25±1 °C (Fig. 1). Fig. 2 demonstrates the effect of voltage ranging 1 to 100 V on σDC of CFs and respective DFs at 25±1 °C. CF_0 and respective DFs has shown comparable σDC (mS/cm) at 1V ranging 0.30 to 0.35. Further increase in voltage to 10 V, no remarkable changes were observed in value of σDC, which revealed the electrically insulating nature of

CF_0 and DFs up to 10V [36]. However, at 100 V, σDC of CF_0 and respective DFs increased due to their electrically conducting nature. CF_0 showed lower value of σDC (0.38) over hot air (0.45) and MW (0.56) assisted DFs. Furthermore, SCC assisted DFs showed relatively higher value of σDC at 1400 psi (0.68) and 1800 psi (0.64) over the rest of DFs.
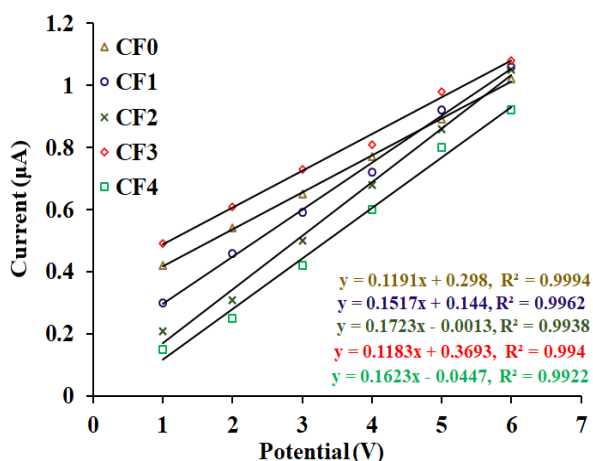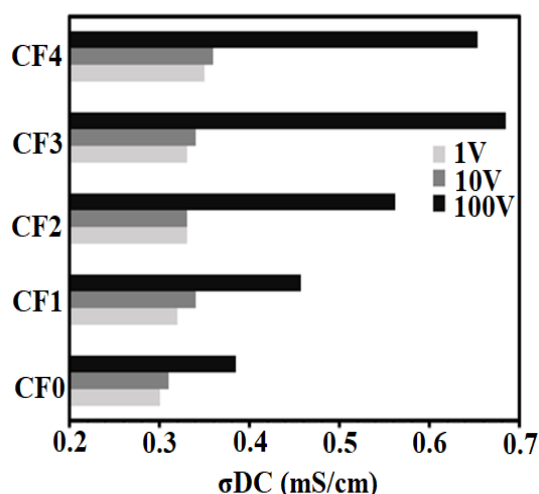

Fig. 1. I-V characteristics of DFs

Fig. 2. Effect of voltage on σDC of DFs

Electroanalysis

In order to investigate the I/V characteristics of MYB dye (400 ppm), CV measurements were conducted at pH 7.0, 25±1 °C under potential window -0.4 to 1.0 V with 25-100 mV/s scan rate (SR) in KCl (0.1 M) (Fig. 3). CV reveals free from redox characteristics of MYB in current range (-2 to 23 μA) and a potential window (-0.52 to 0.9V). MYB has shown relatively higher anodic peak current (I_{Pa}) over cathodic peak current (I_{Pc}) with SR.

With SR, MYB showed I_{Pc} (μA) ranging 143.50 to 182.50 at constant 0.29 V anodic peak potential (E_{pa}). However, MYB showed I_{Pc} (μA) 236.90 at 25 mV/s SR. Further rise in SR ranging 50 to 100 marginally raised I_{Pa} in the range of 303.00 to 316.00. Results showed the highest I_{Pa} value obtained for MYB dye at 100 SR.
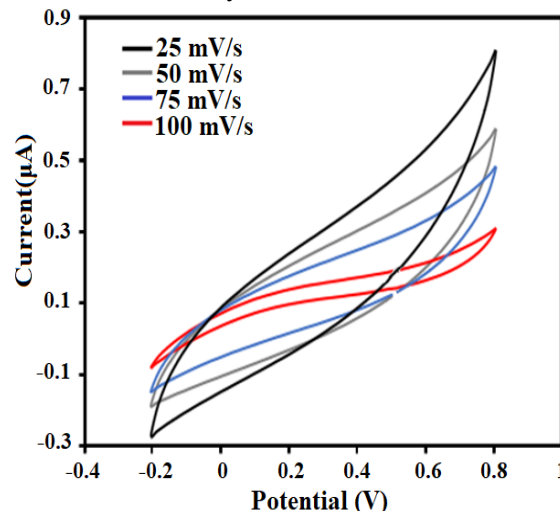
Fig. 3. CV of MYB in KCl (0.1M) at variable SR

Quantitative analysis of MYB released from DFs was performed by SWV. Trends of SWV for CF_1 (Fig. 5), CF_2 (Fig. 6) and CF_3 (Fig. 7) and CF_4 (Fig. 8) were investigated through SWV of DFs in KCl (0.1 M). Different green assisted dying procedures rendered a remarkable effect on the compatibility of MYB with dyed CFs. In general, DFs derived through hot air and MW assisted dying showed significant and identical quantitative release of MYB from DFs. However, DFs derived through SCC assisted methodology showed enhanced compatibility of MYB with DFs. Quantification of MYB during release from DFs was monitored through SWV in the potential range varying from -1.20 to 1.00 V, within specified optimal parameters at 50 Hz and pulse amplitude of 10 mV.

Prior to investigation of quantitative release of MYB from DFs, a calibration curve was drawn between the peak current of SWV against successive increase in concentration of MYB (ppm) ranging 0.006 to 0.14 in KCl (0.1M at pH 7.0, 25 ±1 °C). In the calibration curve peak current linearly increased ranging from 0.003 to 0.057 mA (regression coefficient of 0.99) with the concentration of MYB (Fig. 4). The calculated value of LOD and LQD for MYB was 4.1×10^{-3} mg/L and 12.6×10^{-3} mg/L, respectively.

$$y = 0.4051x + 0.0006$$
$$R^2 = 0.9979$$
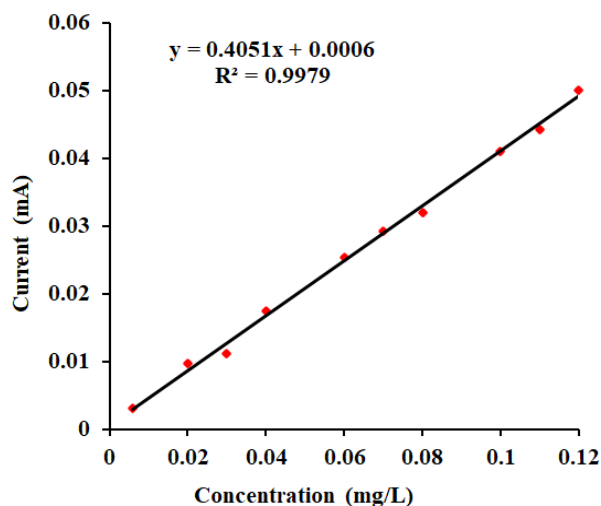
Fig. 4. SWV derived calibration curve of MYB
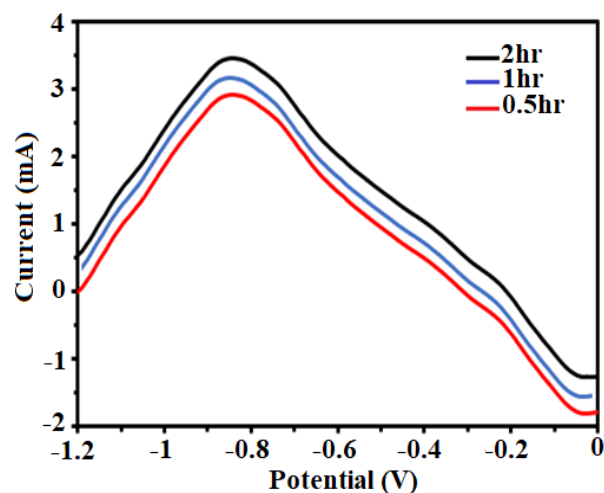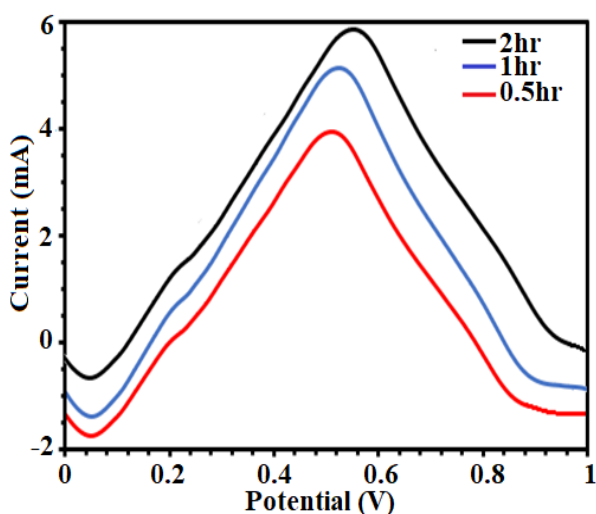

Fig. 7. Monitoring of MYB release from CF_3 in KCl (0.1M)
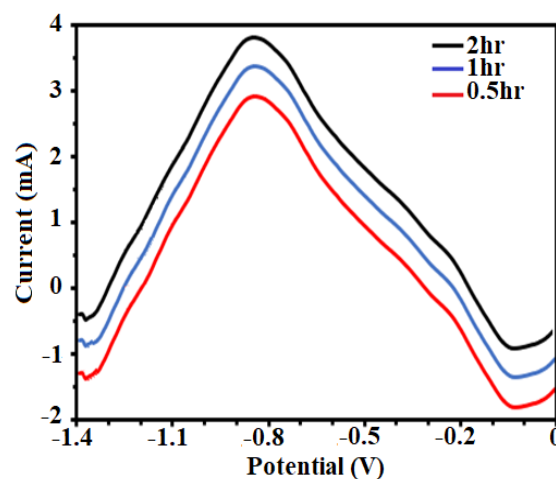

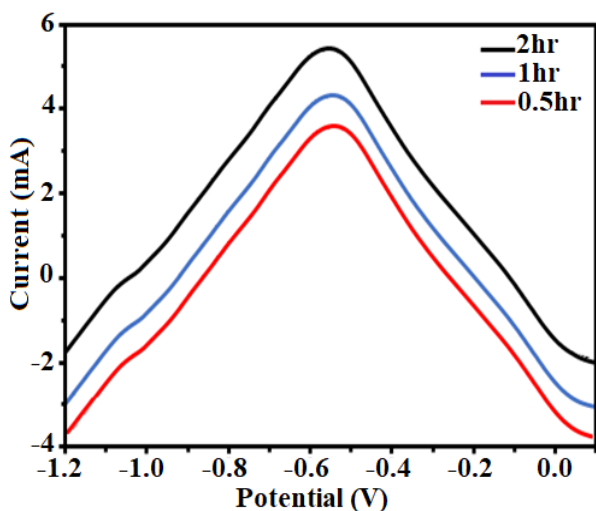**Fig. 5.** Monitoring of MYB release from CF_1 in KCl (0.1M)

Fig. 8. Monitoring of MYB release from CF_4 in KCl (0.1M)

CONCLUSION

Methyl blue (MYB)-dyed electroactive cellulose fabrics (CFs) has been developed through implication of a series of different green methodologies. In this context CFs (1.0 inch^2) was investigated for dying with methyl blue (400 ppm, 200μL) in hot air, microwave irradiation (MW) and supercritical carbon dioxide (SCC) treatments at 70°Cover selected periods. Study reveals enhanced potential of SCC towards dyeing of CFs in comparison to MW and hot air. I-V characteristics of undyed fabric (CF_0) and their respective dyed fabrics (DFs) has shown ohmic behaviour in voltage (V) ranging from 5 to 30 under four probe conditions at 25±1^{0}C. All DFs showed comparable σDC (mS/cm) at 1V ranging 0.30 to 0.35 at 25±1^{0}C. Increase in voltage to 10V showed no remarkable change in σDC of DFs at 25±1^{0}C. CF_3 (0.62 mS/cm) and CF_4 (0.59 mS/cm) showed higher value of σDC over CF_1

Fig. 6. Monitoring of MYB release from CF_2 in KCl (0.1M)

and CF_2 at 100V. Cyclic voltammetry (CV) revealed the redox behavior of MYB @ 25, 50, 75, and 100 mV/s. Release of MYB from DFs was performed by square wave voltammetry (SWV) in KCl (0.1 M) in the potential range -1.20 to 1.00 V. LOD (4.1×10^{-3} mg/L) and LOQ (12.6×10^{-3} mg/L) of MYB were obtained over GCE through SWV in KCl (0.1 M).

REFERENCES

1. S. Katayama, L. Zhao, S. Yonezawa, Y. Iwai,*J. Supercrit. Fluids*, **61**, 199 (2012).
2. S. El-Ghazali, M. Khatri, S. Kobayashi, I. S. Kim, *Med. Text. Nat. Resour.*, 3 (2022).
3. H. Kim, J.Y. Yi, B.G. Kim, J.E. Song, H.J. Jeong, H.R. Kim, *Plos One*, **15**, 0233952 (2020).
4. S. Majumder, T. Mondal, M. Deen, *Sens.,* **17**(12), 130 (2017).
5. Y. Lee, J. Kim, J. Noh, I. Lee, H. Kim, S. Choi, *Nano Lett.*, **13**, 5753 (2013).
6. Q. Huang, D. Wang, Z. Zheng, *Adv. Energy Mater.,***6**, 1600783 (2016).
7. K. Xie, A. Gao, M. Li, X. Wang, *Carbohydr. Polym.,* **101**, 666 (2014).
8. S. Kalia, A. Dufresne, B. M. Cherian, B. S. Kaith, L. Avérous, J. Njuguna, E. Nassiopoulos, *Int. J. Polym. Sci.*, **2011**, 1 (2011).
9. A. Khatri, M.H. Peerzada, M. Mohsin, M. White, *J.Clean. Prod.*, **87**, 50 (2015).
10. T. Veuthey, G. Herrera, V. I. Dodero, *Front. Biosci.,* **19,** 91 (2014).
11. P. Prentø, *Biotech. Histochem.,* **84**, 139 (2009).
12. A. Patti, G. Cicala, D. Acierno, *Polymers*, **13**, 134 (2020).
13. H. Zheng, J. Zhang, J. Yan, L. Zheng, *J.CO$_2$ Util.*, **16**, 272 (2016).
14. T. Hussain, A. Wahab, *J. Clean. Prod.,* **198**, 806 (2018).
15. B. Bharathiraja, I. A. E. Selvakumari, J. Iyyappan, S. Varjani, Curr. *Opin. Environ. Sci. Health*, **12**, 6(2019).
16. N. Methneni, J. A. Morales-González, A. Jaziri, H. B. Mansour, M. Fernandez-Serrano, *Environ. Res.*, **196**, 110956 (2021).
17. M. Banchero, *Color. Technol.*, **136**, 317(2020).
18. S. Adeel, M. Saeed, A. Abdullah, F. Rehman, M. Salman, M. Kamran, M. Iqbal, *J. Nat. Fibers*, **15**, 517 (2018).
19. E. P. Zovinka, A. E. Stock, *J. Chem. Educ.,* **87**, 350 (2010).
20. P. Söderholm, *Sustain. Earth.*, **3**, 1 (2020).
21. K. Y. Khaw, M. O. Parat, P. N. Shaw, J. R. Falconer, *Molecules*, **22**, 1186 (2017).
22. M. Banchero, *Color. Technol.,* **129**, 2 (2013).
23. T. A. Khattab, M. S. Abdelrahman, M. Rehan, *Environ. Sci. Pollut. Res.,* **27**, 3803 (2020).
24. M. L. Goñi, N. A. Gañán, R. E. Martini, *J.CO$_2$ Util.*, **54**, 101760 (2021).
25. H. A. Eren, İ. Yiğit , S. Eren, O. Avinc , Springer, Cham. ,**179**, (2020).
26. S. Kiran, S. Adeel, F. U. Rehman, T. Gulzar, M. Jannat, M. Zuber, *Glob. NestJ.*, **21**, 43(2019).
27. El-Khatib EM, Ali NF, El-Mohamedy RSR, *J.chem. pharm.,***8**, 614 (2016).
28. I. T. Karabegovic, S. S. Stojicevic, D. T. Velickovic, N. C. Nikolic, M. L. Lazic, *Int. J. Bio. Biomol. Agri. Food Biotech., Eng.,***6**, 997 (2012).
29. V. Sivakumar, K. Rani, M. Kumari, *Int. Wood Prod. J.,***8**, 6 (2017).
30. M. Hashem, A.M. Taleb, F.N. El-Shall, K. Haggag, *Carbohydr. Polym.,***103**, 385 (2014).
31. K. Haggag, M.M. El-Molla, Z.M. Mahmoued, *Indian J. Fibre Text. Res.,* **39**, 406 (2014).
32. M. J. Kale, N. V. Bhat, *Color. Technol.*, **127**, 365 (2011).
33. S. Adeel, M. Zuber, K. M. Zia, *Environ. Sci. Pollut. Res.*, **25**, 11100 (2018).
34. A. Hou, X. Wang, L. Wu, *Carbohydrate Polymers*, **74**, 934 (2008).
35. K. E. Klymus, C. M. Merkes, M. J. Allison, C. S. Goldberg, C. C. Helbing, M. Hunter, E., C. A. Richter, *Environ. DNA*, **2**, 271 (2020).
36. S. Mehtab, M.G.H. Zaidi, A. Singh, M. Pandey, A. Mahra, S. Sharma, M. Aziz, D. Palariya, B. Singhal. *Environ. Sci. Pollut. Res.*, **30**, 35 (2023).

Size analysis of CdS nanoparticles for the synthesis of polymer nanocomposites

A. Tyagi[1], S. Rathore[2], S. Jain[1]*

[1]*Physics Department, Daulat Ram College, University of Delhi, Delhi-110007, India*
[2]*Materials Physics Research Laboratory, Department of Physics, Government PG College, Badaun-243601 UP, India*

In this emerging era, polymer nanocomposites proved to be cornerstones for sustainable environment and energy applications like solar cells, optoelectronic devices, efficient drug delivery. Polymer combined with Inorganic semiconductor material provides the advantages of both constituting compounds providing high stability and enhanced electrical and optoelectrical properties. CdS has attracted the attention of many researchers, being a N-type semiconductor, it possesses wide energy band gap value 2.42eV and thus making it worthy material in optical switches, lasers, photoconductive devices and much more. In the present work, uniform thin films of CdS of varying thickness at different time interval (5min, 10 min and 15 min, respectively) have been synthesized and analyzed for the dependency of reaction time on the size of nanoparticle. These films were analyzed using different characterization tools such as X-Ray Diffraction (XRD), UV-Visible spectroscopy and atomic force microscopy (AFM) which tells about crystallographic structure, absorption spectra and morphological features of sample respectively. It was found that the size of nanoparticles deposited on substrates have been increased with increase in reaction time from 5 min to 15 min. The monodispersed particle has been deposited on the substrate obtained after 5 minutes of reaction time resulting in good quality thin film. Thus, it can be used to synthesize polymer nanocomposites for various electrical, optoelectrical and biological applications.

Keywords: Nanocomposites, Sustainable, Cadmium sulfide, Drug delivery

INTRODUCTION

In the recent times, polymer nanocomposites have been extensively used in various fields like for medical purposes, sustainable energy, and environmental applications due to their high-performance and unique physical and chemical properties [1, 2]. Nanocomposite are formed by the combination of different materials to have the best properties of the materials added in which at least one of them is of the nano regime [3, 4]. The inorganic(semiconductor) and organic (polymer) nanocomposites have fascinated many researchers or various applications such as solar cells, Light emitting diodes, transistors, and biological imaging [5]. The organic polymers engrossing the inorganic nanomaterial provides stability by passivating defects and dangling bonds, flexibility and the functional tunability. However, the inorganic semiconductor material enhances their optoelectronic properties with long lifetime [6, 7].

Amongst many inorganic semiconductors materials, cadmium sulfide (CdS) nanoparticles have been investigated by many researchers due to its good thermal stability and chemical resistance. Moreover, its physical and chemical nature changes significantly with size. It is the II–VI, direct band gap semiconducting nanomaterials having auspicious potential in the field of optics, electronic, optoelectronic, and medical applications[8]. Cadmium sulfide, a yellowish pigment, has many applications such as optical, electrical, optoelectrical. CdS (n-type semiconductor) has a wide energy band gap of 2.42 ev [9,,10].

The physical, chemical, biological, electronic, and optoelectronic properties of the nanocomposites can be varied by making changes in the shape, size and size distribution of nanomaterials incorporated [11-13]. The nanoparticle can be synthesized by different methods like chemical methods - chemical bath deposition, sol–gel method, electrodeposition and vacuum-sputtering [14, 15]. Based on literature survey, chemical methods are founds to be of low cost, very simple and quick. Also, they are very easy to change the parameters like temperature of reaction, pressure of reaction, reaction time, etc., which play an important role in the determination of the size and size distribution [11]. In the present work, the effect of size variation of CdS nanoparticles was analyzed. The CdS nanoparticles were synthesized by the chemical bath deposition (CBD) method. It is a method based on controlled precipitation of desired constituents from compound solution. The thin films synthesized with this method are uniform, pin-hole free, as ions are the basic building blocks. It is a fast, simple, and economical approach with desired particle-size, shape, composition, and aggregation of particles.

Three thin film samples were deposited with the variation in reaction time for 5 minutes, 10 minutes and 15 minutes, respectively. The samples deposited were characterized for structural, morphological, and optical characterisics.

MATERIAL AND METHOD

Material required and characterization

The chemicals used to synthesize CdS are purchased from Aldrich and used without further purification. CdS has been obtained from 3mM cadmium sulfate ($CdSO_4$) as a cationic precursor. Ammonia (NH_4OH) solution was used to maintain pH of the solution, 20mM thiourea (CH_4N_2S) was an anionic precursor. Distilled water, acetone, and 2-propanol were used.

The CdS samples synthesized using the CBD method were characterized using Philips X-ray diffractometer (XRD). The crystalline structure of CdS nanoparticles was determined by the spectra measured in the range of 20°-60° with copper Kα radiation at 1.5418Å wavelength. The optical characterization was done using the UV-Visible spectrometer (Shimadzu-UV1650PC) in the wavelength range of 425 to 750 nm. The morphological measurements were performed using an atomic force microscope (AFM). The images were obtained using a Multimode V NSV, Veeco instrument. The imaging was done in tapping mode at the resonant frequency of 300 kHz with a force constant 40 N/m.

Synthesis

The thin films of CdS nanoparticles were synthesized using a common bath deposition method (CBD) with some modifications [16]. In a beaker, some distilled water was taken and thiourea was mixed in it. In another beaker, distilleed water was taken and $CdSO_4$ was mixed in it. These two solutions were then sonicated for 10 min to ensure uniform mixing. Then, ammonium solution was added to the $CdSO_4$ solution and stirred for 10 sec. The thiourea solution was mixed to the $CdSO_4$ solution and the final solution was prepared. The solution was then heated on a hot plate with continuous stirring at a temperature of 65°-80° C. After that, the samples substrates were loaded in the beaker keeping mixture at low speed and waited for some time depicted in Fig. 1. The samples of CdS thin film were collected for an interval of 0 min, 5 min, 10 min and15 min.

The deposition process includes slow release of Cd^{2+} and S^{2-} ions through controlled setting of appropriate chemical equilibrium. The scheme of CdS thin films obtained after various time intervals of 0 min, 5 min, 5 min and 10 min is depicted in Fig. 2.
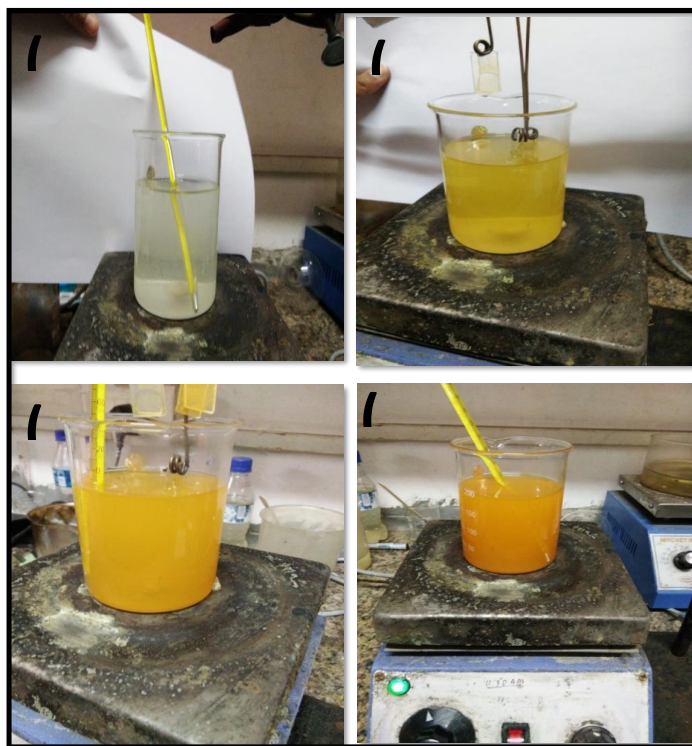

Fig. 1. Experimental steps for CdS thin film preparation: (a) 0 min; (b) 5min; (c) 10 min and (d)15min, respectively.
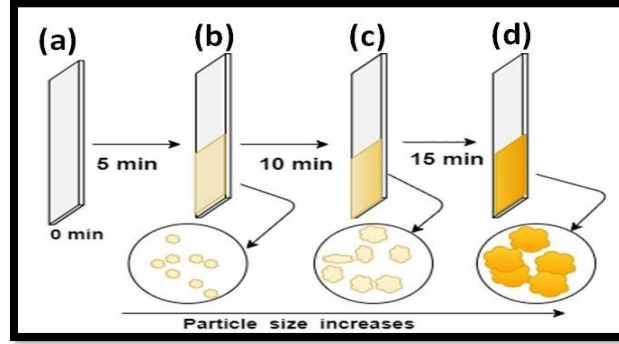
Fig. 2. CdS thin films obtained after specific intervals: (a) 0 min; (b) 5 min; (c) 10 min and (d) 15 min.

RESULTS AND DISCUSSION

Structural characterization

X-ray diffraction (XRD) analysis

Fig. 3 shows the XRD pattern of different CdS thin films synthesized *via* common bath deposition (CBD) technique. Fig. 4(A) shows the diffraction peak at 29.7 which is attributed to the (200) planes of CdS thin film. Similarly, Figs. 4(B) and 4(C) show the peaks at 26.7 and 29.7° which are assigned to (111) and (200) planes of CdS, respectively. It matches well with the standard JCPDS (10-0454) suggesting that the thin films are in cubic (zinc blend, ZB phase) form and in good agreement with the literature on CdS [17, 18]. The absence of other peaks corresponding to other phases confirms the pure phase synthesis of thin film.

It was observed that the peak intensity (Table 1) of CdS thin film decreases when reaction time increases from 5 minutes to 15 minutes. This decrease in intensity shows a decrease in crystallinity of the thin film. The FWHM values of the XRD peak provide the value of crystallite size of nanomaterials. The particle size decreases with increasing FWHM [19]. The crystallite size was calculated using Scherer's equation [20] and tabulated in Table 1.

$$D = k\left(\frac{\lambda}{\beta \cos\theta}\right) \qquad (1)$$

where, K = a constant of value equal to 0·89, λ = wavelength of X-ray (0·154 nm), β = full width at half maximum, θ = half diffraction angle.

The increase in crystallite size can be observed with the decreased value of FWHM. The estimated X-ray crystallite size of CdS varies from ~12 nm to ~31 nm as the time of reaction increases from 5 minutes to 15 minutes.

Lattice constant for the CdS nanoparticles forming the thin film can be calculated using equation (2) [21].

$$d^2 = a^2/(h^2+k^2+l^2) \qquad (2)$$

where a = lattice constant, (h, k, l) = Miller indices (MI). Lattice constant calculated was found to be 0.60 nm for our sample (CdS), which matches well with the earlier reported value for cubical CdS thin film [18].

Optical characterization

UV-Visible analysis

The optical studies of the CdS thin films were carried out using the absorption spectra in the visible range. Figs. 4 (A), (C) and (E) show the absorption spectra of the as fabricated CdS thin films. However, Figs. 4 (B), (D) and (F) show the corresponding Tauc's plots. The optical band gap (BG) energy of the nanomaterials which allows direct transition can be governed using the following equation (3) [22]:

$$\alpha h\nu = A(h\nu - E_g)^{1/2} \qquad (3)$$

where, E_g = band gap energy; α = absorption coefficient, ν = incident photon frequency and h = Planck's constant.
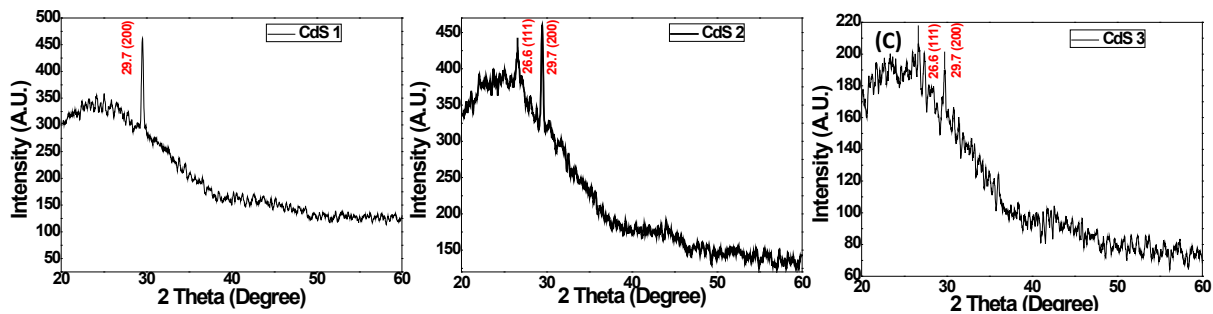
Fig. 3. XRD pattern for: (A) CdS 5 minutes (B) CdS; 10 minutes; (C) CdS 15 minutes, respectively

Table 1. Particle size as calculated from XRD analysis

Sample	2 theta (Degree)	(hkl)	Peak Intensity (A.U.)	FWHM (β)(Degree)	D (nm)
CdS 1 (5 minutes)	29.7	200	462	0.732	~12
CdS 2 (10 minutes)	29.7	200	459	0.285	~30
	26.6	111	442	0.351	~24
CdS 3 (15 minutes)	29.7	200	201	0.273	~31
	26.6	111	218	-	-

The optical band gap can be observed by extrapolating the linear region of the plot $(\alpha h\nu)^2$ *versus* photon energy (hν) and having intercept on the x-axis [23]. Decrease in band gap from 2.55 eV to 2.46 eV was observed in CdS thin films as the time of reaction increased from 5 minutes to 15 minutes (Figs. 4(B) and (F)). This blue-shift in the values of energy band gap w.r.t bulk CdS reflects the quantum confinement in the as synthesized CdS nanoparticles in thin film form. Furthermore, dual band gaps can be observed in CdS thin film synthesized with the reaction time of 10 minutes. These two bandgaps indicate the presence of different-sized nanoparticles which signifies polydispersity.

The effective mass approximation (EMA) proposed by Brus can be used to find the particles size as given by equation (4) [12] for different band gap CdS:

$$E_n = E_g^{bulk} + \frac{\hbar \pi^2}{2R^2}\left(\frac{1}{m_e^*} + \frac{1}{m_h^*}\right) - \frac{1 \cdot 8e^2}{4\pi\varepsilon_0\varepsilon R} \quad (4)$$

where,

R = radius of the nanoparticle,
m_e^* = effective mass of (e-)electron (0.19me),
m_h^* = effective mass of hole (0.80me),
m_e = mass of electron,
ε = dielectric constant of material (for CdS = 5.7) and
εo = permittivity of free space.

Applying EMA, the size (radius) of CdS nanoparticles was calculated as 14 nm, 31 nm and 43 nm, respectively with reaction time of 5 minutes, 10 minutes, and 15 minutes. Thus, the decrease in the band gap was observed with increasing particle size as the time of reaction varies from 5 minutes to 15 minutes which is in good agreement with the XRD analysis. Furthermore, the lower band gap of 2.0 eV observed in a CdS thin film synthesized after 10 minutes reaction time indicates bulk or very large sized nanoparticles and confirms the polydispersity as obtained above by XRD. Thus, the film obtained after reaction time of 10 minutes is not favorable for

polymer nanocomposites and thus, for many device applications like photovoltaics and photocatalysis.

Morphological characterization

Atomic force microscopy (AFM)

The high uniformity and smoothness of thin film are very important properties as they provide a good interface with less lattice mismatch and pin hole defects [24]. The uniformity and other morphological characteristics of the CdS thin films were investigated by atomic force microscopy (AFM) in the present study.

Fig. 5 shows the AFM images of CdS thin films in 2-dimension and 3-dimension, respectively. Figs. 5(A), (C) and (E) represent the 2-dimensional view of CdS thin films, which shows the shape and particle size distribution of CdS nanoparticles. It shows spherical-shaped CdS nanoparticles in all cases. However, there is an increase in particle size as the reaction time increases from 5 minutes to 15 minutes. Fig. 5(C) shows that a CdS thin film obtained after 10 minutes of reaction has polydispersity which is in good agreement with XRD and UV analysis.

The different particle size of CdS nanoparticles in different films results in morphological variation of the thin film. Figs. 5(B), (D) and (F) show the 3-dimensional view of thin films corresponding to different-sized CdS nanoparticles. The RMS roughness value of these films was found to be 21.0, 28.2 and 32.3, respectively. From these it can be observed that increasing particle size results into an increase in roughness of films. This leads to an increase in non-uniformity of the films and defects in the thin film. These defects may cause bad interface contacts with other films in the device which results into bad quality device. Thus, for good quality of film and thus, of nanocomposites, nanoparticles should be monodispersed with small size, which can be obtained with a shorter reaction time.
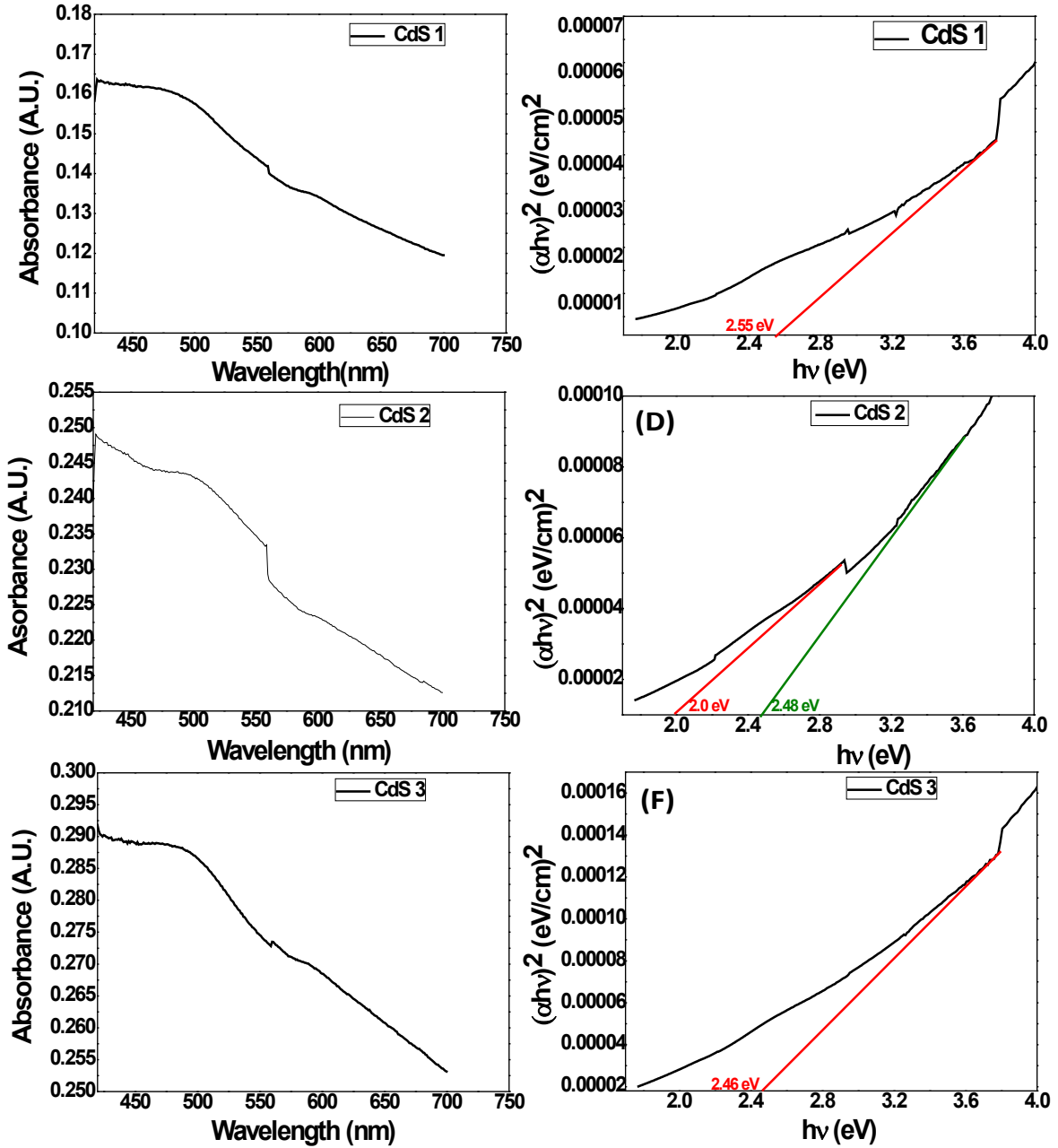
Fig. 4. Absorbance curve and corresponding Tauc's plot for (A & B) CdS 5 minutes, (C & D) CdS 10 minutes and (E & F) CdS 15 minutes, respectively
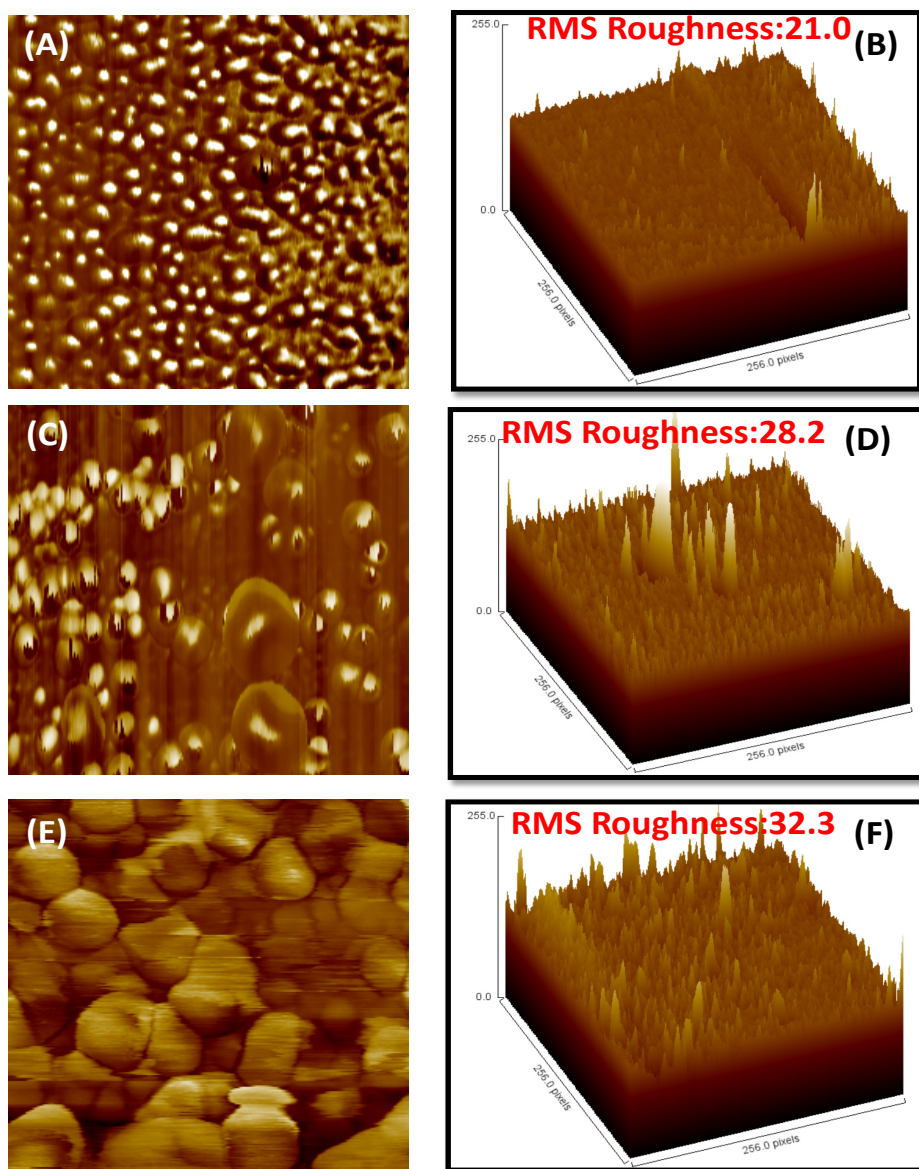
Fig. 5. AFM images for (A & B) CdS 5 minutes, (C & D) CdS 10 minutes and (E & F) CdS 15 minutes

CONCLUSION

An investigation was carried out on CdS thin films for the formation of polymer nanocomposites. The CdS thin films were synthesized using a chemical bath deposition (CBD) method. This method proves to be cost-effective, time saving and easier to grow CdS thin films. This method allowed us to collect thin films of different thickness with variation in reaction time during synthesis. The structural, morphological, and optical characterization of CdS thin films were carried out using various techniques such as XRD, UV- visible spectroscopy and AFM. XRD confirmed its crystalline nature and the diffraction peaks obtained at specific angles confirmed the cubic structure of CdS. The crystalline size calculated from Debye'- Scherrer equation confirmed the increase in size of nanoparticles with increase in reaction time. Optical characteristics of thin films were measured in the visible region and confirmed the decrease in bandgap with increase in particle size. This blue-shift in absorption edge indicates the quantum size effects as the reaction time increases from 5 minutes to 15 minutes and verifies the results obtained by XRD. AFM provided a topographical view, roughness, uniformity defects and surface profile of the fabricated thin films. It was observed that for the procurement of a monodispersed thin film of good quality, the reaction time in CBD method should be short. Thus, the characterization of thin films by XRD, optical UV-visible spectroscopy and AFM confirmed that the nanoparticles or the thin film obtained after reaction time of 5 minutes can be used for the synthesis of polymer nanocomposites.

REFERENCES

1. N. Qutub, P. Singh, S. Sabir, K. Sagadevan Umar, *Nanomater., * **12** (8), 1355 (2022).
2. B. Yeole, T. Sen, D. Hansora, S. Mishra, *J.Appl. Poly. Sci.*, **32**, 132 (2015).
3. S. Tripathi, R. Kaur, *Opt. Commun.,* **352**, 55 (2015).
4. M.S. Hussien, M.I. Mohammed, I.S. Yahia, *Environ. Sci. Pollut. Res.,* **27**, 45225 (2020).
5. S. Mirsharifi, F. Pakpour, D. Ghanbari, *J. Nanostruct.*, **9**, 112 (2019).
6. A. Kharazmi, E. Saion, N. Faraji, R. M. Hussin, R.M., W.M.M. Yunus, *Radiat. Phys. Chem.*, **97**, 212 (2014).
7. L. Midya, A. S. Patra, C. Banerjee, A. B. Panda, S. Pal, *J. Hazard. Mater.*, **369**, 398 (2019).
8. F. Di Benedetto, A. Camposeo, L. Persano, A. M. Laera, E. Piscopiello, R. Cingolani, L. Tapfer, D. Pisignano, *Nanoscale*, **3** (10), 4234 (2011).
9. V. Mathur, M. Dixit, K. S. Rathore, N. Saxena, K. Sharma, *Front. Chem. Sci. Eng.,* **5**, 258 (2011).
10. R. Premachandran, S. Banerjee, V. John, G. McPherson, J. Akkara, D. Kaplan, *Chem. Mater.,* **9** (6), 1342(1997).
11. K. Singhal, M.G.H. Zaidi, S. Mehtab, R. Saleheen, *Renew. Energ. Sustain. Growth Assess.,* Scrivener Publishing, 305 (2022).
12. S. Jain, S. N. Sharma, M. Kumar, *Phys. E: Low-dimen. Syst. Nanostruct.*, **44** (3), 555 (2011).
13. A. Alipour, M. Mansour Lakouraj, H. Tashakkorian, S*ci. Rep.*, **11** (1), 1(2021).
14. R. Rikhari, B.Saklani, A.Bisht, S. Mehtab, M.G.H. Zaidi, *Sensor Lett.* 17, 511 (2019).
15. J. Koteswararao, S. V. Satyanarayana, G. M. Madhu, V. Venkatesham, *Heliyon*, **5** (6), e01851 (2019).
16. A. Sharma, M. Kaur, B. Bhattacharyya, S. Karuppiah, S. P. Singh, T. Senguttuvan, S. Husale, *AIP Advances*, **5** (4), 047116 (2015).
17. 1. Liu, L. Wang, L., Guan, Z., Liu, Z., Zhu, Y., Tang, A. *J.Mater. Chem. C,* **7** (48), 15285 (2019).
18. P. Rodriguez, N. Munoz-Aguirre, E. S. Martínez, G. Gonzalez, O. Zelaya, J. Mendoza, *Appl. surf. sci.,* **255** (3), 740 (2008).
19. R. Banerjee, R.Jayakrishnan, P. Ayyub, *J. Phys.: Condens. Matter*, **12** (50), 10647 (2000).
20. M. Abd El-Sadek, H. Wasly, K. M. Batoo, *Appl. Phys. A*, **125**, 1 (2019).
21. C. Kittel and P. McEuen, I.t.S.S.P.W., New York, 1996.
22. A. M. Al-Hussam, S. A. Jassim, J. *Assoc. Arab Uni. Basic Appl. Sci.*, **11** (1), 27 (2012).
23. A. Singh, G. Gupta, N. Vijayan, S. N. Sharma, *J. Phys. Chem. Solids,* **122**, 8 (2018).
24. S. G. Kumar, K. K. Rao, *Energ. Environ. Sci.*, **7** (1), 45 (2014).

Interaction parameters and volume phase transition of poly(N-isopropylacrylamide-co-N-tertiarybutylacrylamide-co-acrylamide) hydrogels

R. Kumari[1], S. Shekhar[2*]

[1]Department of Chemistry, Magadh University, Bodhgaya (Bihar), 824234 India
[*]Daudnagar College, Daudnagar (Aurangabad) Bihar, 824113 India

In the present study, poly (NIPAM-co-NTBA-co-AAm) terpolymeric hydrogels have been fabricated with different crosslinking ratios. The average molecular mass between crosslinks (M_c), interaction parameter (χ) and crosslinking density of the hydrogels have been determined from stress-strain measurement. The crosslink density of the network increased with an increase in the crosslinking ratio followed by decreases in the value of M_c. The enthalpic interaction parameter (χ_H) was negative whereas larger entropic interaction parameter (χ_S) was found to be positive and responsible for overall increase in total interaction parameter (χ) with temperature. Partial molar enthalpy of dilution (ΔH_1) and partial molar entropy of dilution (ΔS_1) values are found to be negative which are supportive with hydration of gel with hydrogen bonding as well as hydrophobic interaction.

INTRODUCTION

Poly N-isopropylacrylamide (PNIPAM)-based thermoresponsive hydrogels are found to have many applications including biomedical applications such as controlled drug delivery systems, artificial implants, dialysis membrane, burn dressings and cardiovascular devices [1-5]. Since all of these applications primarily depend on swelling capacities of the hydrogels, the fundamental understanding of swelling properties of the hydrogels with water is extremely important [6-10]. The swelling behavior of the hydrogels has been often described not only by equilibrium swelling but also depending on several factors like crosslinking density, network parameter, temperature, and the physical structure of the gels [11-15]. Also, such types of applications need perfect volume phase transition and sharpness.

The total swelling pressure of the non-ionic hydrogels is contributed by mixing polymer and solvent, as well as elasticity. The hydrogels attain the swelling equilibrium at zero osmotic pressure of the hydrogels [16]. The swelling pressure can be determined by the monomer or comonomer type and the effective crosslink density. The effective number of crosslinks consists of both chemical and physical crosslinks playing an important role in controlling the swelling, as well as mechanical behavior of the hydrogels. The physical crosslinking comprises of entanglements of chain, loose chain ends and tied chains [17]. However, due to moisture sensitivity the evaluation of crosslinking density is very tough *via*

instruments like dynamic mechanical analyzer (DMA) and rheology [18].

The volume phase transition of the hydrogels can be discontinuous or continuous depending on the nature of monomer or comonomer present in the hydrogel and stiffness of hydrogel network [13, 19] The presence of ionized group and stiffness of the polymer network cause an increase in the osmotic pressure required for expansion of the network causing the discontinuous volume change. In the last three decades, the effect of crosslinking density on swelling and mechanical properties of NIPAM-based hydrogels has been reported [14, 15]. Saito and coworkers reported the effect of the amount of the crosslinking agent on the volume phase transition and swelling behavior of PNIPAM [20]. The effect of the concentration of crosslinker on the swelling percentage, interaction parameter etc also reported by Huglin and coworkers [21].

In our earlier study we reported the synthesis of poly (NIPAM-co-NTBA-co-AAm) hydrogels for aqueous protein solution separation process [22]. The purpose of this study is to determine the crosslinking density of poly (NIPAM-co-NTBA-co-AAm) hydrogels by stress-strain experiment and elucidate the effect of crosslinking density on the volume phase transition, as well as the interaction parameter. To our knowledge, no efficient investigations on the effect of crosslinking density on the swelling and phase transition of poly (NIPAM-co-NTBA-co-AAm) hydrogels have been published before.

---

* To whom all correspondence should be sent:
E-mail: ss_chem85@rediffmail.com

In light of this, poly (NIPAM-co-NTBA-co-AAm) hydrogels have been prepared varying the concentration of crosslinking agent and their cross-linking density was determined by using stress-strain measurement. Also, the volume phase transitions and value of interaction parameter of the hydrogels were determined. The novelty of the present study is the literature on NIPAM based terpolymeric hydrogels which have been used for the first time to investigate the effect of the crosslinking density on physicochemical properties.

EXPERIMENTAL

Materials and methods

NIPAM (Acros Organic Chemicals, USA), NTBA (Aldrich, USA) and AAm (Central Drug House Ltd. Co., India) were used without any further purification. The other chemicals N,N-methylene-bisacrylamide (MBA) (Sisco Research Lab, India), ammonium persulfate (APS) (Titan Biotech Ltd. Co., India) and N,N,N,N-tetra-methylene-diamine (TEMED) (Central Drug House Ltd. Co., India) were also used in purchased form. The solvent 1,4-dioxane was purchased from Merck, Germany. Double-distilled water was used to explore the swelling behavior of the hydrogels.

The infrared spectra of the hydrogel samples were recorded on Prestige 21 (Shimadzu, Japan), in DRS mode in the range of 4000–400 cm^{-1}, with 4 cm^{-1} of resolution. Swelling experiment was performed at different constant temperatures and the swelling percentages were determined by equation (1):

$$\% \, Swelling = \frac{m_t - m_d}{m_d} \times 100 \qquad (1)$$

where m_d represents the dry weight of gel and m_t denotes the weight of swollen hydrogel at different time intervals.

The compressive elastic moduli of the equilibrium swollen hydrogels (at 25°C) were determined using a universal tensile machine (UTM, Instron 3360, USA). The compressive stress, (F'/A, force/area) was calculated at constant deformation rate of 1 mm/min. The compression modulus of the hydrogel network can be determined from the slope of the linear plots of compression stress *vs* strain using equation (2):

$$\frac{F'}{A} = -G(\lambda - \lambda^{-2}) \qquad (2)$$

where F' represents applied force, "A" cross-sectional area, "G" compression elastic modulus and λ denote the ratio of deformed length to initial length of the hydrogel, respectively.

Hydrogel preparation

Free radical polymerization was applied to prepare terpolymeric hydrogels using NIPAM, NTBA, and AAm [22] at room temperature. In the process, the monomers NIPAM, NTBA and AAm were dissolved in (10 ml, 1:2 vol) mixture of 1, 4-dioxane and doubly distilled water followed by addition of MBA. After complete mixing the added initiator APS was dissolved completely. After complete dissolution TEMED (0.25 ml aqueous solution) was added and allowed to complete the polymerization for 24 h. The prepared hydrogels were washed 8-10 times in distilled water and 10-12 cycles by SOXHLET extraction with 1,4-dioxane to eliminate the unreacted monomers, linear homopolymers and other chemicals present in the gel. The washed hydrogels were dried at room temperature for 2-4 days and at about 80°C for 48 h till constant weight. The compositions of the poly (NIPAM-co-NTBA-co-AAm) hydrogels are given below (Table 1):

Table 1. The different proportions of monomers and reagents in copolymer composition

NIPAM/NTBA/ AAm (Molar ratio)	MBA (moles) × 10^{-8}	APS (moles) × 10^{-4}	TEMED (20 vol %)	Nomenclature
25/37.5/37.5	0.00649	1.85	0.25	NTA1
25/37.5/37.5	0.0194	1.85	0.25	NTA2
25/37.5/37.5	0.0779	1.85	0.25	NTA3
25/37.5/37.5	0.155	1.85	0.25	NTA4
25/37.5/37.5	0.233	1.85	0.25	NTA5

RESULTS AND DISCUSSION

Fourier transform infrared spectroscopy

The infrared spectra of the fabricated hydrogels are depicted in Fig. 1. The main features of the spectrum are: (a) the bands associated with the polymer network such as the broad band between 3110 cm^{-1} & 3567 cm^{-1}, which is attributed to the presence of the N–H stretching frequency of the amide group, (b) the appearance of a peak related to C=O stretching, asymmetric stretching of COO$^-$ and symmetric stretching of COO$^-$ at 1649 cm^{-1}, 1612 cm^{-1} and 1448 cm^{-1}, respectively, (c) broad band at 2147 cm^{-1}, is assigned to the presence of –C–N group of MBA, NIPAM, NTBA and AAm. Presence of iso-intensity double peaks at 1394 cm^{-1} and 1333 cm^{-1} corresponding to the symmetrical bending vibrations and bimethyl of isopropyl group peak at 1228 cm^{-1} assigned to –C(CH$_3$)$_3$ group.

Network parameters

The theoretical crosslinking density (V_t) of the hydrogels can be expressed in terms of concentration of crosslinking agent (C) and their functionality f:

$$V_t = Cf/2 \qquad (3)$$

In the present case the functionality of the methylenebis acrylamide is taken as '4' and the value of C was calculated from their molar concentration in the feed and density of all the dried hydrogels (1.08 kg/dm).
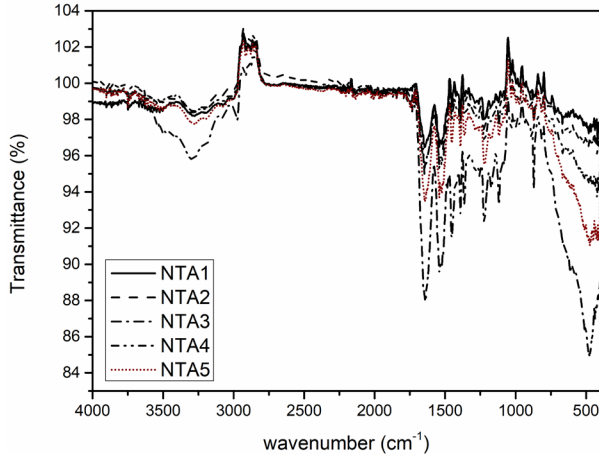
Fig. 1. FTIR spectra of the NTA terpolymer

For compression measurement the cylindrical gels of 1.0 cm in height and 0.8 cm in diameter were swollen in water at 25°C to attain equilibrium. Assuming that the gels swell isotropically, the swelling ratio may be defined as the reciprocal of hydrogel volume fraction was:

$$\frac{V_s}{V_r} = \frac{\vartheta_{2r}}{\vartheta_{2s}} = \left(\frac{d}{d_o}\right)^3 \qquad (4)$$

where ϑ_{2s} and ϑ_{2r} represent the volume fractions of the hydrogels in the equilibrium swollen and relaxed state, respectively. ϑ_{2r} and ϑ_{2s} can be calculated using the following relations:

$$\vartheta_{2r} = C_o \left(\frac{M_o}{\rho_2}\right) \qquad (5)$$

$$\vartheta_{2s} = \vartheta_{2r} \left(\frac{d_o}{d}\right)^3 \qquad (6)$$

Here, C_o represents the initial concentration of monomers, ρ_2 is the density of the dry hydrogels and M_o denotes the molecular weight of repeat unit of the hydrogel network.

Compression (G) moduli were estimated according to:

$$\tau = G(\lambda - \lambda^{-2})$$

where τ denotes the compression stress and the G (modulus) slope of the linear plots of the τ versus $(\lambda - \lambda^{-2})$. The effective crosslinking density, V_e, can be calculated from equation (7):

$$V_e = \frac{G}{RTV_{2s}^{\frac{1}{3}}V_{2r}^{\frac{2}{3}}} \qquad (7)$$

The interaction parameter, χ, can be determined using Flory–Rehner quation8, [16, 23, 24]:

$$\chi = \frac{-\left[ln(1-\vartheta_{2s})+\vartheta_{2s}+V_eV_1\vartheta_{2r}\left\{\left(\vartheta_{2s}/\vartheta_{2r}\right)^{1/3}-\left(\vartheta_{2s}/\vartheta_{2r}\right)\left(\frac{1}{2}\right)\right\}\right]}{\vartheta_{2s}^2} \qquad (8)$$

In the present study, the value of V_t has been found to be increased with increasing crosslinking agent concentration (Table 2). The effective crosslinking density of hydrogels (V_e) a factor determining the polymer network was evaluated by equation 7 on the basis of the modulus. It is found that the effective crosslinking density get increased with moduli G of hydrogels which indicates the enhancement of mechanical strength of hydrogels. These results indicate that along with the degree of crosslinking, microstructure regularity also affects the mechanical properties. Similar type of results was found in literature [13, 25]. Also, it can be observed that the crosslink density of the hydrogel network, as well as the number of elastically effective chains increase with decrease in the value of M_c.

The value of V_e is related to V_t by equation 9 in which the α represents the value of the effective crosslinking without any crosslinking agent [26]. It may be arisen due to crosslinking in γ –irradiation induced synthesis [26]. The parameter β represents the crosslinking efficiency (β=V_e/V_t, when α=0) and

its magnitude which is generally ≤ 1.0 except some cases where $\beta > 1.0$ is reported [27, 28].

$$V_e = \alpha + \beta V_t \tag{9}$$

Figure 2 shows the plots between V_e and V_t according to equation 9 exhibiting linearity for all hydrogels with α=4.16E-05 and β=1.62E-05 which indicates the low crosslinking efficiency of the MBA in the hydrogels. The low crosslinking efficiency of the hydrogels may be attributed to formation of many elastically ineffective hanging chain ends in the hydrogel network [29]. A perfect comparison of the present results cannot be compared with values reported in literatures due to scant value [30] for thermoresponsive hydrogels and nonexistent for the terpolymer considered here. Theoretically the amount of crosslinking agent in the terpolymeric hydrogels calculated at every stage of fractional conversion for each sample is accountable for observed low or high crosslinking efficiency. The relevant reactivity ratios (Q, e) are usually acceptable alternative [26].

Further, the interaction parameter (χ) was found to decrease as MBA content was reduced. Increased crosslinking density decreases the swelling percentage of the hydrogels below the transition temperature. Beyond transition temperature the hydrophobic effect dominates on crosslinking effect on swelling of thermoresponsive hydrogels. χ and T are related in the second-power polynomial: [31]

$$\chi = a_0 + a_1 T + a_2 T^2 \tag{10}$$

where T represents the temperature while the total interaction parameters have enthalpic (χ_H) and entropic (χ_S) contributions [21, 31]. Enthalpic (χ_H) and entropic (χ_S) parameters depend on enthalpy (κ) and entropy (ψ) dilution parameters as $\chi_H = (\kappa)$ and $\chi_S = 0.5 - (\psi)$ [16].

$$\chi_H = -T \frac{d\chi}{dT} = -T(a_1 + 2a_2 T) \tag{11}$$

$$\chi_S = \chi + T \frac{d\chi}{dT} = a_0 + 2a_1 T + 3a_2 T^2 \tag{12}$$

The actual partial molar enthalpy of dilution (H_1) and partial molar entropy of dilution (ΔS_1) can be calculated by:

$$\Delta H_1 = RT\varphi^2 \kappa \tag{13}$$
$$\Delta S_1 = R\phi\psi \tag{14}$$
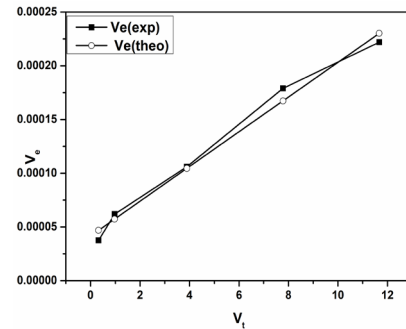
Fig. 2. Plots of theoretical and experimental effective crosslinking density

The plots of χ_H and χ_S *versus* temperature are depicted in Figure 3. The larger positive value of χ_S and smaller negative value of χ_H gives the overall value of χ.

On the basis of the values of χ_H and χ_S for all samples at various temperatures both ΔH_1 and ΔS_1 values are found to be negative. The plots of ΔH_1 and ΔS_1 *versus* temperature T are depicted in Fig. 3. The decrease in entropy favors the swelling of hydrogels *via* hydrophobic hydration and solvation, as well as hydrogen bonding [21]. Also, the reduced enthalpy causes increase in water structuring *via* enhanced hydrogen bonding and negative ΔH.

Overall total interaction parameter χ are found to be increased with increasing the temperature which may be due to the decrease in mixing of polymer chains upon increase in temperature. The mixing of polymeric chain decreases due to release of absorbed water from the network if the temperature of solution increased. Since the amide groups of NIPAM, NTBA and AAm exhibit hydrogen bonding with water molecules below LCST. it indicates that the water molecules absorbed within the hydrogel network interact with the hydrophilic amide groups on the side chains before the hydrophobic hydration. It results into expelling of absorbed water from collapsed hydrogel network causing the increase in total entropy of the hydrogel.

Table 2. Compression (G) modulus, V_e and M_c for NTA copolymers

	Crosslinking ratio	V_t	V_e (mole/m^3)	M_c(kg/mole)	G (Modulus) MPa	χ (at 25°C)
NTA 1	1.6	0.32	3.75E-05	19.2	0.065	0.49
NTA 2	4.8	0.97	6.19E-05	11.7	0.081	0.52
NTA 3	19.4	3.89	0.000106	6.75	0.101	0.57
NTA 4	38.9	7.78	0.000179	4.02	0.236	0.62
NTA 5	58.4	11.67	0.000222	3.23	0.424	0.69
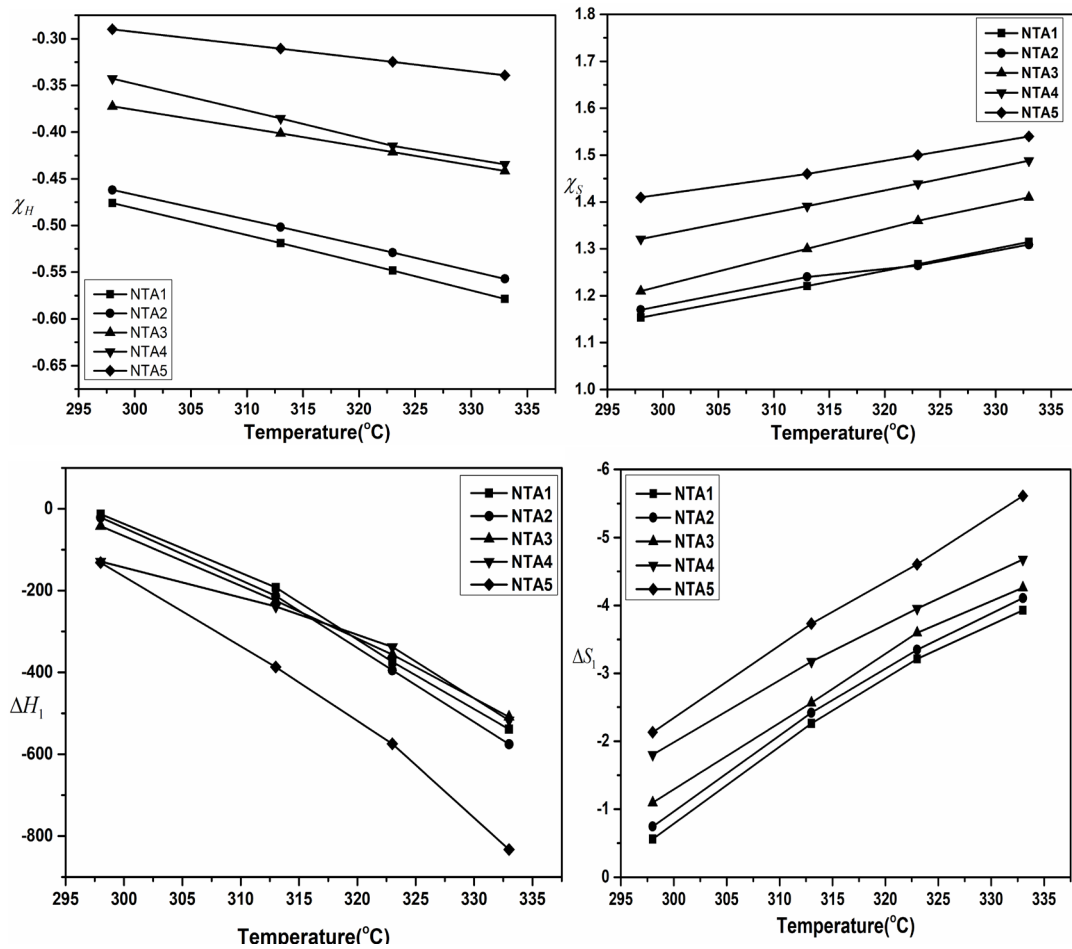
Fig. 3. Plots of χ_H, χ_S, ΔH_1 and ΔS_1 *versus* 1/T for NTH 1, NTH 2, NTH 3, NTH 4 and NTH 5 copolymers

Transition temperature and sharpness of transition

The swelling behavior of the different thermoresponsive hydrogels can be compared with the help of transition temperature and sharpness. Some hydrogels show discontinuous volume transition at specific temperature whereas some shows transition in broad range of temperature [32]. Therefore, it needs to distinguish among broad, gradual and absolute rapid volume change which can be clarified with sharpness. Therefore, the swelling of the hydrogels was normalized with range of temperature used for swelling experiment. The transition temperature of the hydrogel was determined from the inflection point on normalized curve of swelling equilibrium versus temperature (Figure 4) and mentioned in Table 3. The slop of the curve has been used to evaluate the sharpness of transition (Table 3). The transition temperature of

the hydrogels is increased slightly with increasing the crosslinking density of the hydrogel. This may be attributed to the increased stiffness of the hydrogels with increased crosslinking density.
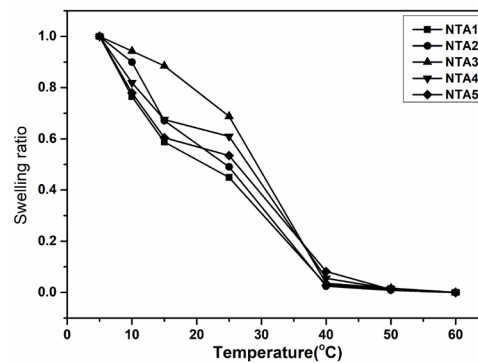
Fig. 4. Normalized swelling equilibrium vs temperature for NTA hydrogels

213

Table 3. The transition temperature and sharpness of the NTA hydrogels.

Sample	Transition Temperature (ºC)	Sharpness (%/ºC)
NTA 1	33±1	2 ±0.028
NTA 2	34±1	3 ±0.033
NTA 3	35±2	2 ±0.032
NTA 4	36±2	2 ±0.035
NTA 5	36±2	2 ±0.033

The results of the effect of temperature on the swelling of hydrogel studied in the temperature range 5–60°C in distilled water (Figure 2) clearly suggest that the equilibrium swelling decreased when temperature is raised, which may be due to the hydrophobic interactions of the polymer hydrophobes at higher temperature proving them as thermoresponsive hydrogels. At all temperatures the equilibrium swelling percentages of the hydrogels were found to increase with decreasing the crosslinking ratio.

CONCLUSIONS

The results, from the compression experiments, exploiting mechanical properties, strongly showed a crosslinking density-dependent behavior. The present work on dependence of cross-linking density allowed shedding light on the swelling equilibria, interaction parameter as well as mechanical strength. The volume phase transition of the hydrogels increased with stiffness of the hydrogels. Also, there was not any significant effect of crosslinking density of hydrogels on their thermoresponsive behavior. The current study demonstrates that the swelling and mechanical properties of the poly (NIPAM-co-NTBA-co-AAm) hydrogels can be controlled effectively by varying the amount of MBA.

REFERENCES

1. X. Xu, Y. Liu, W. Fu, M. Yao, Z. Ding, J. Xuan, D. Li, S. Wang, Y. Xia, Cao M. Meiwen, *Poly.,***12**, 580 (2020).
2. L. Tang, L. Wang, X. Yang, Y. Feng, Y. Lia, W. Feng, *Progress Mater. Sci.* ,**115**, 100702 (2021).
3. P. Joshi, G. Bisht, S. Mehtab, M. G. H. Zaidi, *Mater. Today Chem.*, **62**, 6814 (2022).
4. M. Hamcerencu, J. Desbrieres, M. Popa, G. Riess, *Poly. Bull.,***77**, 741 (2020).
5. N. Rafique, M. Ahmad, M.U. Minhas, S.F. Badshah, N.S. Malik, K.U. Khan, *Poly. Bull.* **79**, 4535 (2021).
6. S. Shekhar, M. Mukherjee, A.K. Sen, *Poly. Bull.,***77**,4355 (2020).
7. S. Shekhar, M. Mukherjee, A.K. Sen, *Poly. Bull.,***78**,5029 (2021)
8. P.Joshi, S. Mehtab, M. G. H. Zaidi, *Bull. Chem. Soc. Jpn*., 95, 855 (2022).
9. J.A. Paulin, J.E. Lopez-Aguilar, B. Fouconnier, R.O. Vargas, F. Lopez-Serrano, *Poly. Bull.***, 79**, 6709 (2022).
10. M. Saidi, A. Dabbaghi, S. Rahmani, *Poly. Bull.*, **77**, 3989 (2020).
11. C.H. Mah, Q.Y. Wu, G.R. Deen, *Polym. Bull.*, **75**, 221 (2018).
12. H. Zhang, X. Huang, J. Jiang, S. Shang, Z. Song, *RSC Adv.*, **7**, 42541 (2017).
13. T. Caykara, S. Kiper, Gokhan Demirel, *J. Appl. Poly. Sci.,***101**, 1756 (2006).
14. G. Hoti, F. Caldera, C. Cecone, R.A. Rubin Pedrazzo, A. Anceschi, S.L. Appleton, M.Y. Khazaei, F. Trotta, *Materials,***14**, 478 (2021).
15. H. Salimi-Kenari, F. Mollaie, E. Dashtimoghadam, M. Imani, B. Nyström, *Carbohydr. Polym.,* **181**,141 (2018).
16. P. J. Flory, Principles of Polymer Chemistry; Cornell University Press, Ithaca, NY, USA, 1953; ISBN 0801401348 (1953).
17. R. Hagen, L. Salman, B. Sternerg, *J. Polym. Sci. B, Polym. Phys.,***34,** , 1997 (1996)
18. Z. Xia, M. Patchan, J. Maranchi, J. Elisseeff, M. Trexler, *J. Appl. Polym. Sci.,* (2012).
19. S. Hirotsu, Y. Hirokawa, T. Tanaka, *J. Chem. Phys.,* 87, 1392 (1987). K. Otake, H. Inomata, M. Konno, S. Saito, *Macromolecules*, **23**, 283 (1990)
20. M.B. Huglin, M M.A.M Rehab, M.B. Zakaria, *Macromolecules,* **19**, 2986 (1986).
21. S. Shekhar, M. Mukherjee, A.K. Sen, *Iran. Polym. J.*, **21(12)**, 895 (2012).
22. C.G. Lopez, W. Richtering, *R. Soc. Chem.*, **13**, 8271 (2017).
23. P.J. Flory, J. Rehner, *J. Chem. Phys.*, **11**, 521 (1943).
24. S.K. Bajpai, S. Singh, *Reactive & Functional Polymers*, **66**, 431 (2006).
25. W. Xue, S. Champ, M. B. Huglin, *Poly.*, **42**, 3665 (2001).
26. M.B. Huglin, MMA-M Rehab, *Poly.*, **28,** 2200 (1987).
27. T. P. Davis, M. B. Huglin, *Macromol. Chem.*, **191**, 331 (1990).
28. J. E. in: Mark, K. Dusek, (ed.), Advance. Poly. Sci., vol. **44**. Berlin, Springer, 1982, p. 1.
29. S. H. Gehrke, M. Palasis, M.K. Akhtar, *Poly. Int.*, **29**, 29 (1992).
30. Th. P. Davis, M. B. Huglin, *Poly.*, **31**, 513 (1990).
31. D. C. Harsh Gehrke, *J. Controll. Rel.*, **17,** 175 (1991).

Efficient removal of Pb^{2+}, Ni^{2+} Cu^{2+}, and Zn^{2+} ions from water using activated soybean seed adsorbent

F. Ummul Khair[1][*], N. Gulrez [1], H. Mohd Kamil[2]

[1]Department of Chemistry, Sir Syed Faculty of Science, Mohammad Ali Jauhar University, Rampur 244901, India
[2]Department of Chemistry, Govt. Raza P.G. College, Rampur 244901 (MJP Rohilkhand University Bareilly) India

Industries often release contaminated water containing various pollutants, including hazardous heavy metals, posing significant risks to the environment. To mitigate these dangers, effective water treatment methods are essential. Adsorption is a well-established, cost-effective process for water treatment. In this research, we investigated the use of activated soybean seed (ASS) as an adsorbent for removing heavy metal ions from waste water. Batch experiments were conducted to assess the efficiency of ASS in removing Pb^{2+}, Ni^{2+} Cu^{2+}, and Zn^{2+}. The study examined the impact of several parameters, such as pH, adsorbent dose, shaking time, shaking speed, temperature, and particle size, on the adsorption rate. The equilibrium data were fitted using the Langmuir, Freundlich, and Temkin adsorption isotherm models, while the kinetic data were analyzed using the pseudo-first-order (PFO) and pseudo-second-order (PSO) kinetic models. To understand the changes occurring during the adsorption process, we characterized the ASS adsorbent before and after adsorption using SEM, XRD, TGA, ICP-MS, and FT-IR spectrometry. This study provides valuable insights into the potential application of activated soybean seed as an effective adsorbent for heavy metal removal from aqueous solutions.

Keywords: Soybean seed, adsorbent, heavy metal, waste water.

INTRODUCTION

Pollution is the presence of unwanted substances, known as pollutants, in the environment, surpassing allowable contaminant limits and negatively impacting all aspects of life. Water contamination arises not only from man-made sources like rapid industrialization and the excessive use of chemicals such as hydrocarbons, heavy metals, chlorinated hydrocarbons, and pesticides, but also from natural factors like geothermal activities, space dust, and volcanic eruptions [1,2]. It is worth noting that man-made sources are the primary contributors to pollution in comparison to natural ones [3]. Heavy metals like As, Cd, Hg, and Pb are well-known for their toxicological manifestations and the harm they can cause [4, 5]. Heavy metals, including As, Cd, Hg, and Pb, pose significant threats to the aquatic environment and the food chain, even at low concentrations [6, 7]. These heavy metals are non-biodegradable, leading to their widespread presence in the environment. Their accumulation can result in various irreversible health effects [8, 9]. Many biological processes, membrane processes, sedimentation, ion-exchange, chemical reduction, electro-despostion, and adsorption have their benefits and application limitations. While the adsorption process is an environmental-friendly [10], low-cost, easy method, effective-purification, and separation technique, used in industry for the removal of contaminated water [11]. This facilitates availability and makes the process cost-effective, as non-living biomass requires no maintenance or nutrient input [12, 13].

The efficient recovery of heavy metals from living biomass is challenging due to their tight binding within the cell structure. As a result, residual soybean biomass serves as a promising adsorbent, benefiting from its abundance and favorable physicochemical properties [12]. This study aims to assess the effectiveness of soybean adsorbents in removing Pb^{2+}, Ni^{2+} Cu^{2+}, and Zn^{2+} ions from aqueous solutions. Batch studies were conducted, exploring various parameters such as adsorbent dose, pH, shaking time, shaking speed, temperature, and particle size, to investigate the adsorption of Pb^{2+}, Ni^{2+} Cu^{2+}, and Zn^{2+} by soybean. The equilibrium data were analyzed using several isothermal models. The research endeavors to evaluate a novel, cost-effective biosorbent suitable for environmental applications.

MATERIALS AND METHODS

Preparation of adsorbent

Soybean seeds were collected from Rajasthan, India, followed by washing with distilled water and

---

sun-drying for about 3-5 days before grinding. Later on seeds were ground into small particles by using a manual grinder then fine particles were classified into three particle sizes: 300 μm, 355 μm and 710 μm. The soybean powder particles were subjected to treatment using NaOH solutions with concentrations of 0.5%, 1%, and 1.5% to create a negative control. Subsequently, the soybean powder slurry obtained was dried in an oven at 75°C for 3 hours and stored in a container for future use. For study the standard stock solution of Pb^{2+}, Ni^{2+} Cu^{2+}, and Zn^{2+} were prepared by dissolving suitable $Pb(CH_3COOH)_2 \cdot 3H_2O$, $CuSO_4 \cdot 5H_2O$, $ZnCl_2$, and $NiCl_2 \cdot 6H_2O$ in distilled water. All chemicals used were analytical reagent grade for the experiments. Distilled water was used for the experiments.

Characterization of ASS adsorbent

The characterization of the treated and untreated ASS was done by using FT-IR, SEM, ICP-MS, XRD, and TGA. Surface morphology and texture of the adsorbent was observed by using SEM and FT-IR analysis was used to determine the functional groups and sites in the ASS at the range of 4000 to 400 cm^{-1}. Structures and phases of before and the after adsorption of ASS adsorbent

surfaces were examined using a XRD at a 2θ diffraction angle of 5° to 80° with the scan rate was 10/min. The characterization of thermal degradation of untreated and treated adsorbent was performed using TGA. The analysis of adsorbent was determined by using ICP-MS.

RESULTS AND DISCUSSION
Characteristics of the adsorbents
Scanning electron microscope analysis

The SEM analysis was used to characterize the surface morphology of the ASS adsorbents before and after the adsorption of metal ions (Figure 1 a-f). The surface of the ASS adsorbent significantly changes after the interaction with metal ions. Prior to adsorption, the ASS exhibited a visibly smooth surface texture with distinct particles of different sizes on its surface. However, after interacting with Pb^{2+}, Ni^{2+} Cu^{2+}, and Zn^{2+} ions, the morphology of the ASS adsorbent underwent a transformation, leading to the presence of rougher stone particles with increased size. This change suggests that Pb^{2+}, Ni^{2+} Cu^{2+}, and Zn^{2+} ions were efficiently absorbed on the ASS surface, indicating the active sites' capacity to adsorb these metal ions to the maximum extent [13,14].
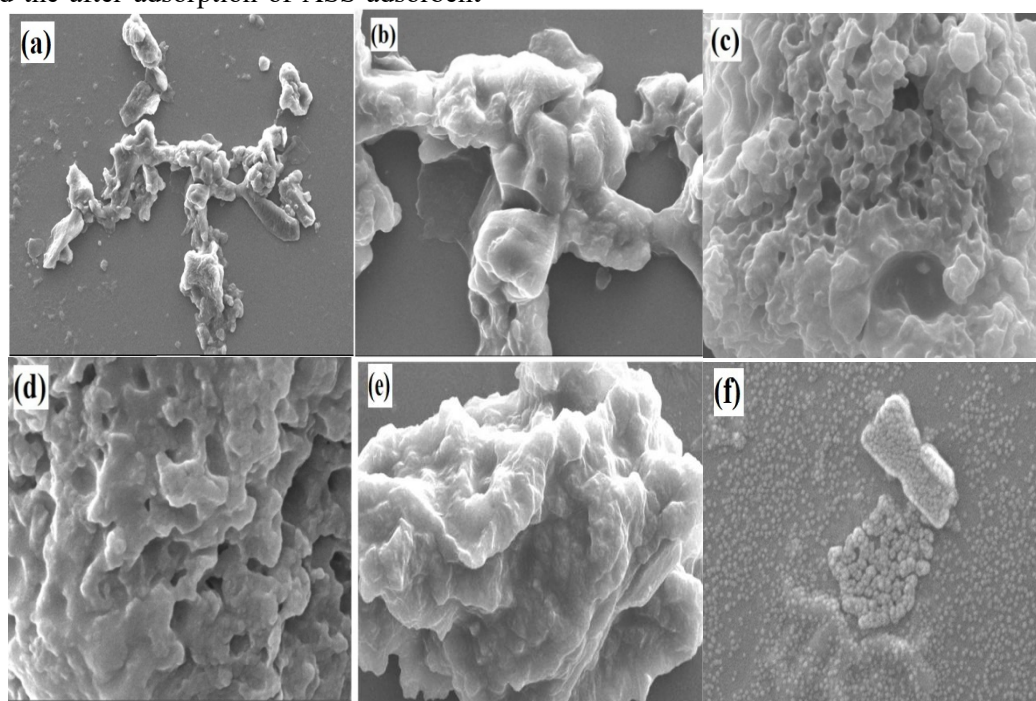
Fig. 1. SEM image of ASS adsorbent (a) & (b) before adsorption (c), (d), (e), (f) after adsorption of Cu^{2+} Pb^{2+}, Zn^{2+} Ni^{2+}

Fourier transform infrared spectroscopy analysis (FTIR)

FTIR analysis was conducted to examine the functional groups present on the surface of the ASS adsorbent before and after the adsorption of heavy metal ions. The analysis also revealed functional groups associated with the binding of metals to the adsorbent (Fig. 2a). The FTIR peaks in cm^{-1} of the ASS sample exhibited a strong and broad band between 3200 and 3500, indicating the presence of the O–H group. Additionally, two adsorption peaks at 2924 and 2856 were assigned to alkyl (-C–H) groups. Other absorption bands were observed at 1746, 1646, and 1454, which corresponded to the stretching vibrations of the carbonyl group (–C=O)

and -C–O from the carboxyl group. The peak at 1540 represented the N-H bending vibration of the amine group, while the C-N stretching was observed at 1247. The C-O stretching vibration was noticed at the 1054 absorption band. Upon adsorption of heavy metal ions, the absorption peaks of the OH group, C-N, and C-O stretch shifted. Specifically, the absorption band of the -OH group changed from 3362 to 3288, 3298, 3392, and 3492 when interacting with Pb^{2+}, Ni^{2+} Cu^{2+}, and Zn^{2+} respectively. Similarly, for the C-N stretching vibration, peaks shifted from 1240 to 1242, 1240, 1244, and 1244 respectively for Pb^{2+}, Ni^{2+} Cu^{2+}, and Zn^{2+}. The FTIR analysis indicated that hydroxyl groups and amine groups serve as major adsorption sites in the ASS adsorbents [13, 15].
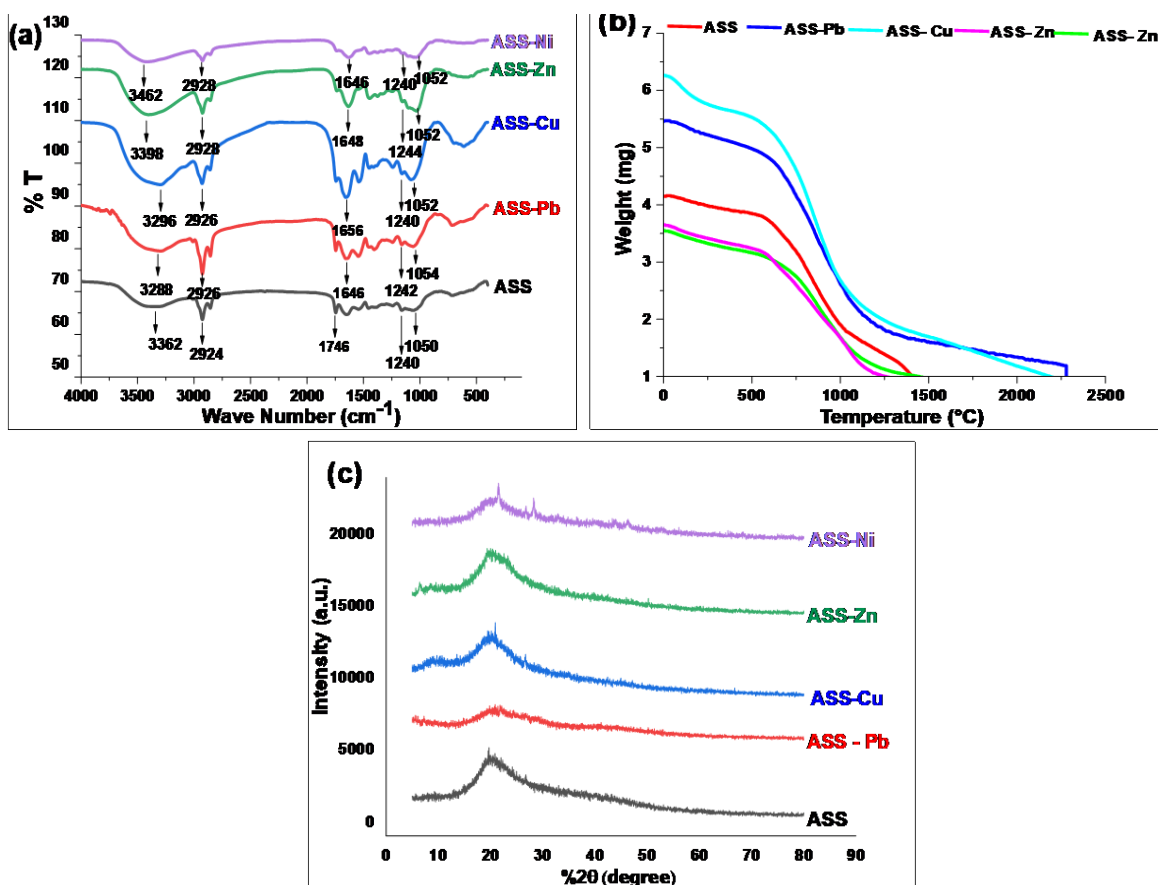
Fig. 2. (a) FT-IR spectra of ASS adsorbent, sample ASS-Pb, ASS-Cu, ASS-Zn and ASS-Ni. (b) TGA for original ASS adsorbent, sample ASS–Pb, ASS–Cu, ASS–Zn and ASS-Ni. (c) XRD for original ASS adsorbent, sample ASS–Pb, ASS–Cu, ASS–Zn and ASS-Ni

Thermogravimetric analysis (TGA)

TGA was employed to study the thermal degradation of the adsorbent before and after metal deposition. This technique allows for the assessment of the material's thermal stability in a controlled atmosphere and measures the rate of weight change

as a function of time and temperature. TGA is commonly used to determine the compositional properties, as well as the thermal and oxidative stability of materials [13]. For the analysis, approximately 5.471 mg samples of the ASS adsorbent were subjected to heating from 30°C to 800°C, with the temperature gradually increased at a

217

rate of 20°C/min (Fig. 2b). The changes in weight loss of the ASS adsorbent concerning temperature and time were observed using TGA.

X-ray diffraction analysis (XRD)

XRD of ASS adsorbent before and after Pb^{2+}, Ni^{2+} Cu^{2+}, and Zn^{2+} adsorption are also analyzed at 2θ at a diffraction angle of 5° to 80°. The scan rate was 10°C/min. This analysis method gave information about the crystal structure of ASS. However, a decrease in peak density after Pb^{2+} adsorption is indicative of the decreasing degree of crystallinity [16]. Fig. 2c shows that there are no significant peaks for Pb^{2+}, Ni^{2+} Cu^{2+}, and Zn^{2+} in the loaded ASS samples, indicating that ASS adsorbent surface is are amorphous before and after adsorption. Amorphous solids are good adsorbents, having more active sites and higher specific surface area. So, ASS was observed to be an effective adsorbent for the adsorption of Pb^{2+}, Ni^{2+} Cu^{2+}, and Zn^{2+} from contaminated water.

Study of pH of metal ion solutions

The value of pH of the solution is important parameter, affecting the adsorption of metal ions by ASS. The pH of metal ion solutions is investigated in the range of 3-8 and pH is adjusted by NaOH and HCl. Elimination efficiency of metal ions is depends on the concentration of hydrogen ions present in an aqueous solution. It was observed for all metal ions studied, the adsorption decreases with decreasing pH beyond 5. The decrease in metal ions adsorption at low pH can be responsible for contesting between metal ions and H^+ ions. Therefore, it is clear from fig. 3a that at a low pH, the adsorption of the studied metal ions is significantly reduced. Though, with a continuous increase in pH, the adsorption rate may decrease due to metal hydroxide formation. So, the optimum pH value of 5 was chosen for further study. According to the results, the removal rate of metal ions increases with increasing pH up to a certain limit, beyond pH 6 the rate of removal of metal ions decreases gradually. It was observed that at lower pH, the active sites were taken by protons on the ASS surface. [3, 16, 17].

Study of adsorbent dose of adsorbent on adsorption

The effect of the adsorbent dose is noteworthy parameter to the adsorption of metal ions from an aqueous solution. This experiment was carried out at different adsorbent doses from 1 to 6 g/100ml, optimal pH (3-6), 4 h shaking speed, and 28 °C temperature (fig. 3b). According to the results, it was found that the rate of adsorption of metal ions

increases by the increase in adsorbent dose due to the presence of active sites for adsorption [13, 15]. The maximum removal of Pb^{2+}, Cu^{2+}, Zn^{2+}, and Ni^{2+} was shown at 4g/100ml by ASS adsorbent from 61.07% to 86.15%, 26.69% to 60.70%, 33.92% to 68.34% and 24.54 % to 69.82%, respectively. Further, the increase ASS adsorbent dose from 4 to 6 g/100ml then the adsorption of the Pb^{2+}, Cu^{2+}, Zn^{2+}, and Ni^{2+} decreased from 86.15% to 85.71%, 60.70% to 59.37%, 68.34% to 58.88% and 24.54% t0 67.24, respectively. This may be due to the overlap of the adsorption site and the crowding of adsorbent particles [3, 18].

Study of the shaking time of the aqueous solution of heavy metal with the ASS adsorbent

In this experiment, the effect of contact time was conducted at 25-28 °C by the different adsorption time from 1 to 4 h (Fig. 3c). The adsorption of metal ions increases with increasing contact time [13] but remained suitable after reaching equilibrium [19]. The maximum adsorption percent of Pb^{2+}, Cu^{2+}, Zn^{2+}, and Ni^{2+} was obtained at a 3h shaking time. Then after a while, it reaches an equilibrium state after which the amount of adsorption does not increase significantly.

Study of the shaking speed of the aqueous solution of heavy metal with the ASS adsorbent

The effect of shaking speed on the removal of metal ions was investigated by ASS adsorbent at different shaking speeds of 220 and 320 rpm. This experiment was carried out at adsorbent doses from 4g/100ml, optimal pH (3-6), and 4h shaking speed. At 220 rpm shaking speed the adsorption of Pb^{2+}, Cu^{2+}, Zn^{2+}, and Ni^{2+} metals were found to be 94.87%, 58.22%, 63.78%, & 76.43%, respectively. However at 320 rpm shaking speed the adsorption of Pb^{2+}, Cu^{2+}, Zn^{2+}, and Ni^{2+} were found to be 78.7%, 51.41%, 59.33% & 54.98%, respectively. Fig. 3d indicates that the percent removal of heavy metal ions increased at decrease in shaking speed and obtained maximum adsorption of metal ions at near 220 rpm. Adsorption of heavy metal ions was found less than optimum at lower and higher shaking speeds. The low shaking speed could not sufficiently disperse the particles in water to provide active binding sites for metal ions adsorption. On the other hand, the high shaking speed strongly dispersed the AAS particles in the water and did not give them enough time to bond with the metal ions.

Study of the temperature of the heavy metal solution with the adsorbent

The adsorption capacity of ASS for removal of metal ions was investigated at the various temperature of 25-50 °C with adsorbent dose 4g (Fig.3e). In addition, temperature directly affects the reaction rate between adsorbate and adsorbent in an aqueous solution during the adsorption process. The diffusion rate of adsorbed molecules increases with increasing temperature from the outer boundary layer to the pores of the adsorbent. This can lead to a decrease in the viscosity of the solution [20]. Maximum adsorption of Pb^{2+}, Cu^{2+}, Zn^{2+}, and Ni^{2+} was observed at 35°C and decreased with a further increase in temperature. This may be due to the deterioration of the solution's ion balance, the destruction of active binding sites in the residual AAS, or the increased tendency to separate metal ions from the solution interface [13]. The mobility of metal ions increases with increased temperature; it is recommended that the adsorption is endothermic in nature [21].
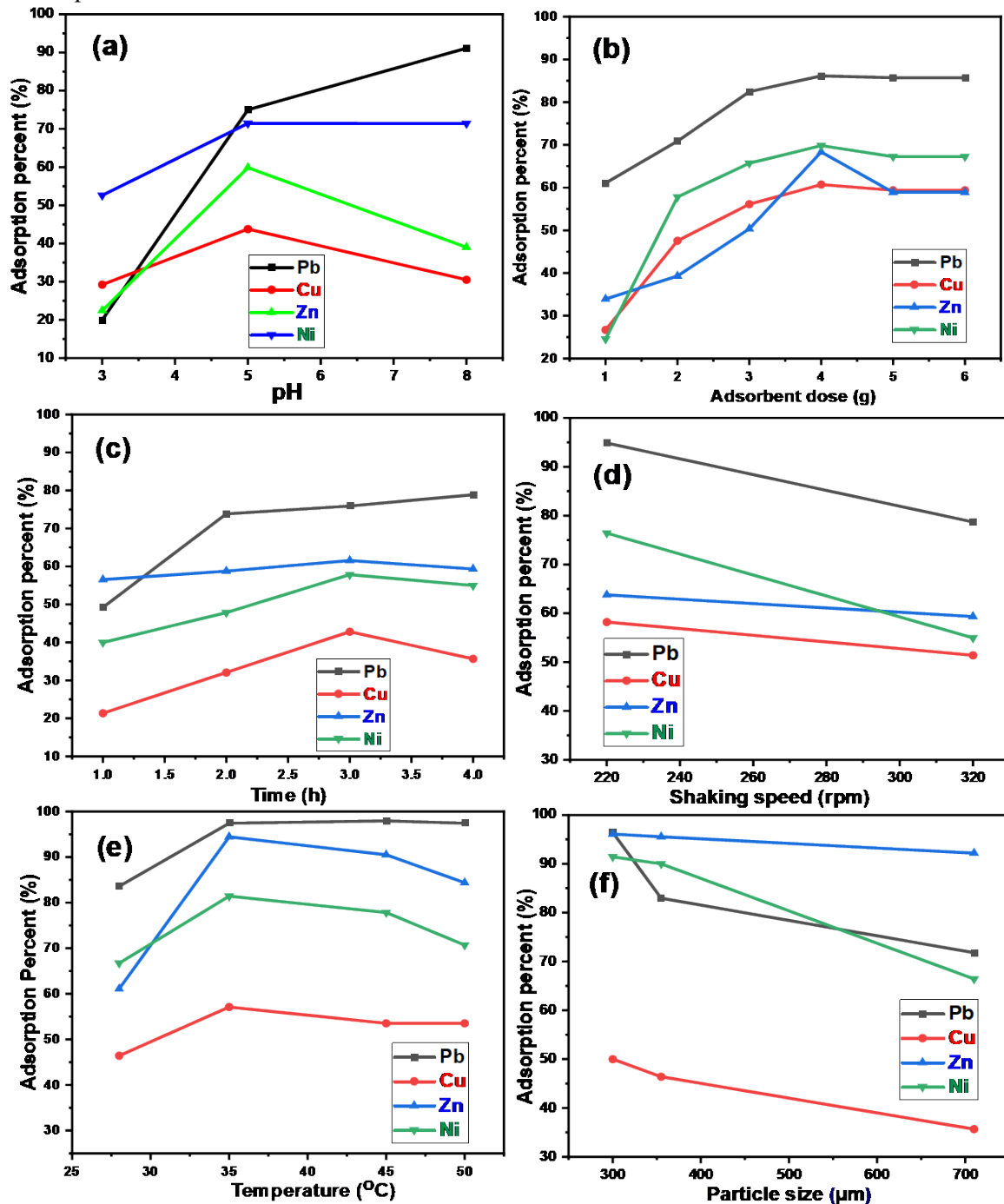
Fig. 3. (a) Effect of pH; (b) Effect of adsorbent dose; (c) Effects of shaking time; (d) Effects of shaking speed; (e) Effects of temperature; (f) Effects of particle size

Study of particle size of adsorbent on adsorption

The effect of adsorption by particle size was studied from several surface areas of various particle sizes of ASS absorbent. The adsorption capacity of ASS for the removal of Pb^{2+}, Cu^{2+}, Zn^{2+}, and Ni^2 was investigated at various particle sizes 300, 355, and 710 μm with adsorbent dose 4g (Fig. 3f). As shown, the adsorption capacity of the heavy metals decreases with increases in the adsorbent particle size from 300μm <710 μm, the percent adsorption of Pb^{2+}, Cu^{2+}, Zn^{2+}, and Ni^{2+} was decreasing from 96.41 to 71.79%, 50 to 35.66%, 96.1 to 92.19% and 91.42 to 66.42%, respectively.

Thermodynamic parameters and temperature distribution

In this study, the effect of temperature on the adsorption of ASS for the removal of metal ions was investigated at 301, 308, 318, and 328K temperatures. The nature of adsorption of exothermic or endothermic, spontaneity, and feasibility was evaluated by thermodynamic parameters of Gibbs energy (ΔG°), entropy (ΔS°), and enthalpy (ΔH°). Values of thermodynamic parameters calculated as a function of temperature changes are given in Table 2. According to this study, the value of ΔS° was found to be positive at tested 301, 308, 318, and 328K temperatures and ΔH° was also found to be positive. The system is endothermic due to the positive value of ΔH°. Adsorption is the spontaneous process or not, dependent on Gibbs energy. The negative value of Gibbs energy indicates, the adsorption process is a spontaneous process.

Ci and Ce are the initial and equilibrium concentrations of metal ions Pb^{2+}, Cu^{2+}, Zn^{2+} and Ni^{2+} (mg/L) respectively in an aqueous solution. m – Mass (g). R is gas constant (8.314 J mol⁻¹ K⁻¹). T is absolute temperature (K).V is volume of heavy metal ion solution. k_d is adsorption affinity. Enthalpy (ΔH), entropy (ΔS). Gibbs free energy (ΔG⁰). k_1 is a PFO rate constant. k_2 is PSO rate constant. K_f is Freundlich isotherm constant. 1/n is the adsorption intensity. qe the amount of adsorbed metal per gram of the ASS adsorbent at equilibrium (mg g⁻¹). 'a' is the equilibrium binding constant and 'b' represents the intensity of adsorption. K_T is Temkin constant. q_{max} is maximum adsorption capacity (mg g⁻¹). K_L is Langmuir isotherm constants (L mg⁻¹). Adsorption of Pb^{2+}, Cu^{2+}, Zn^{2+} and Ni^{2+} are decreased at high temperature and also the value of $ΔG^0$ is decreased with increased temperature

Table 1. Equations used in Pb^{2+}, Cu^{2+}, Zn^{2+}, and Ni^{2+} adsorption isotherm on ASS.

Isotherm	Equation	Equation No.
Adsorption capacity	$q_e = (C_i - C_e)\dfrac{V}{W}$	1
Adsorption yield	$R\% = \dfrac{(Ci - Ce)}{Ci} \times 100$	2
Langmuir	$\dfrac{1}{q_e} = \dfrac{1}{k_L q_{max}}\dfrac{1}{C_e} + \dfrac{1}{q_{max}}$ $R_L = \dfrac{1}{1 + C_i \times K_L}$	3 4
Freundlich	$Log q_e = Log K_f + \dfrac{1}{n} Log C_e$	5
Temkin	$q_e = a + b log C_e$	6
PFO	$\ln(qe - qt) = \ln qe - K_1 t$	7
PSO	$\dfrac{1}{q_t} = \dfrac{1}{k_2 q_e^2} + \dfrac{t}{q_e}$	8
Thermodynamic studies	$ΔG° = -RT\ln Kd$ $\ln K_d = \dfrac{ΔS°}{R} - \dfrac{ΔH°}{RT}$	9 10

Adsorption isotherms and kinetics

The adsorption isotherm model describes the relation between adsorbents and heavy metal ions in the solution at equilibrium state [22]. Pb^{2+}, Cu^{2+}, Zn^{2+} and Ni^{2+} adsorption study was conducted under the most favorable conditions. This study evaluated the adsorption behaviors and efficiency of ASS for Pb^{2+}, Cu^{2+}, Zn^{2+} and Ni^{2+} adsorption with the Langmuir, Freundlich, and Temkin isotherm models (Table 1). In Langmuir isotherm model, there is no interaction between the solute concentrations on the adsorbent surface. In this adsorption isotherm, absorption takes place on a homogeneous surface by monolayer absorption without interaction between adsorbed metal ions [13, 23]. The Freundlich isotherm model is assumed as a heterogeneous adsorbent surface that represents the interaction between the metal ions on the surface of the adsorbent and the metal ions concentration in the liquid [24]. The adsorption rate of heavy metal ions is equal to the rate of desorption of the same heavy metal ions before the adsorption equilibrium occurs [25, 26]. Accordingly, the R^2 value was calculated from experimental data and concluded that Langmuir isotherm was the most favorable model for soybean adsorbent. As the results of the experiment R^2 values occur in Langmuir > Freundlich > Temkin order (fig.4 (a-d)). The data were fitted by the linear form Ce/qe versus Ce, at a concentration range from 0.05 to 2g/l. The qmax and RL were calculated by slope and intercept, respectively. The results obtained with soybean adsorbent are consistent with previous batch adsorption studies [27, 28]. According to this kinetic adsorption model, PFO and PSO were used for Pb^{2+}, Cu^{2+}, Zn^{2+} and Ni^{2+} adsorption (Table 1). The value of coefficients (R^2) is shown in Table 2 with velocity and other constants. According to this study, the correlation coefficients were obtained 0.97294, 0.54588, 0.99674 and 0.97536 for the elimination of Pb^{2+}, Cu^{2+}, Zn^{2+}, and Ni^{2+} from aqueous solution by AAS. The intercept values of the lines drawn in Fig. 5(a-d) were used to determine the adsorption rate.
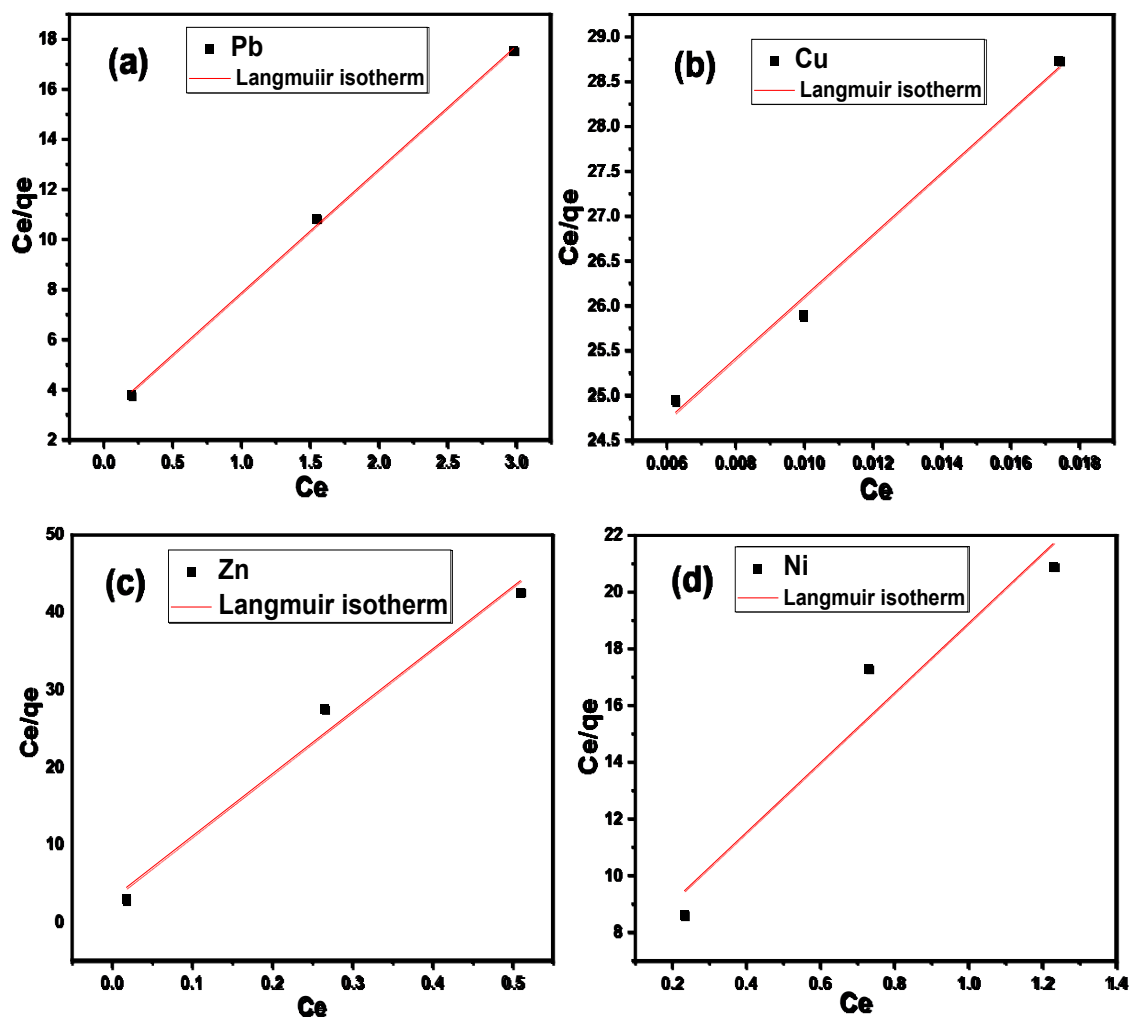
Fig. 4. Langmuir adsorption isotherms of (a) Pb^{2+}; (b) Cu^{2+}; (c) Zn^{2+}; (d) Ni^{2+}

Based on the kinetic studies, it is clear that the rate of adsorption can be well described by a PSO. In other words, the data fit well with the proposed pseudo-quadratic equation. The data also showed that the initial metal ion concentration affected the contact time required to reach equilibrium. The adsorption capacity increases for the highest initial concentrations of metal ions. These results show similarity to previous studies.

Table 2. Equations used in Pb^{2+}, Cu^{2+}, Zn^{2+}, and Ni^{2+} adsorption process on ASS adsorbent.

S.No.	Isotherms	Parameters	Values			
			Pb	Cu	Zn	Ni
1.	Langmuir	q_{max} (mg/g)	0.0698	0.0441	0.3429	0.1516
		K_L (l/mg)	0.0698	0.0001	0.0042	0.0123
		R_L	1.5083	1.000003	1.0027	1.0299
		R^2	0.9976	0.9838	0.9651	0.8915
2.	Freundlich	K_f	0.1121	0.0200	0.013	0.0517
		$1/n$	0.4462	0.8620	0.1816	0.4548
		R^2	0.9852	0.9974	0.9563	0.9681
3.	Temkin	a	0.0919	0.0037	0.001	0.0257
		b	0.2916	77.141	2832.86	3.7892
		R^2	0.6062	0.7072	0.8958	0.9256
4.	PFO	qe	0.3514	0.0350	0.0306	0.1605
		K_1	-0.3452	-0.5098	-0.4185	-0.3093
		R^2	0.7810	0.5833	0.2580	0.5238
5.	PSO	qe	0.15059	0.0002	0.0098	0.0352
		K_2	0.0126	0.000029	0.00016	0.00039
		R^2	0.9673	0.7963	0.9983	0.9753
6.	Thermodynamic studies	$\Delta H°$ (kJ/mol)	68.14	3.70	12.95	4.23
		$\Delta S°$ (J/mol/K)	214.11	14.29	96.29	5.31
		$\Delta G°301$ (kJ/mol)	5.9595	1.1968	8.2867	8.2867
		$\Delta G°308$ (kJ/mol)	1.0197	1.7443	3.6664	5.6610
		$\Delta G°318$ (kJ/mol)	1.4206	0.42934	5.2900	6.4290
		$\Delta G°323$ (kJ/mol)	7.2594	0.2584	7.4805	7.5396
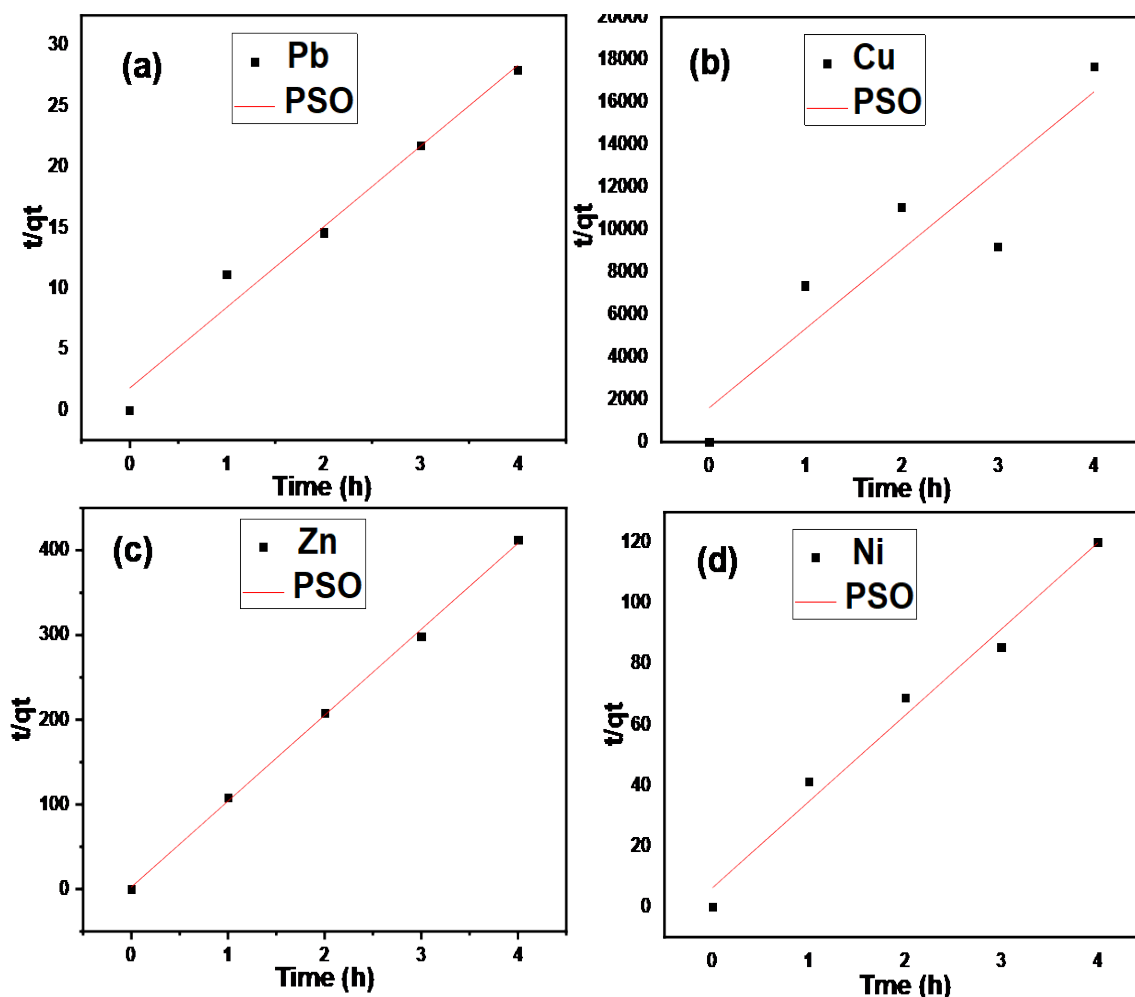
Fig. 5. PSO kinetic model of (a) Pb^{2+}; (b) Cu^{2+}; (c) Zn^{2+}; (d) Ni^{2+}

CONCLUSION

Adsorption shows selectivity and higher efficiency in the elimination of heavy metals and also does not produce any pollutants. It is not only a low-cost but a highly effective process. Results of this study show that ASS can be used as an effective adsorbent for the elimination of Pb^{2+}, Cu^{2+}, Zn^{2+}, and Ni^{2+} metal ions from aqueous solutions. Better efficacy of ASS adsorbent was observed at optimum parameters like adsorbent dose (4g/100ml), pH (5), temperature (35 °C), shaking time (4h), and shaking speed 220 rpm. PFO, PSO, Langmuir, Freundlich and Temkin all adsorption cases studied. But additionally, adsorption data were well-fitted by PSO kinetics and Langmuir isotherm models.

REFERENCES

1. V. Marcano, P. Benitez, E. Palacios-Prü, *Planet Space Sci,* **51**, 159 (2003).
2. A. Blanco, M. Pignata, H. Lascano, M. Salazar, J. Rodriguez. *Env. Sci. Pollut. Res*, **28**, 20624 (2021).
3. T. Mahmudiono, D. Boko.v, G. Widjaja, I. S. Konstantinov, K. Setiyawan, W. K. Abdelbasset, H. S. Majdi, M. M. Kadhim, H. A. Kareem, K. Bansal. *Food Sci. Technol, Campinas*, **42**, e111721 (2022).
4. C. Su, *Environ. Skept. Crit.,* **3**, 24 (2014).
5. A.K. Singh, V. Aggarwal, U. P. Singh, S. Mehtab, *Talanta,* **77**, 718 (2008).
6. A. K. Singh, U. P. Singh, V. Aggarwal, S. Mehtab, *Anal. Bioanal. Chem.*, **391**, 2299 (2008).
7. I. R. Chowdhury, S. Chowdhury, M. A. J. Mazumder, A. Al-Ahmed, *Appl. Water Sci.,* **12**, 185 (2022).
8. M. Tamás, S. Sharma, S. Ibstedt, T. Jacobson, P. Christen, *The National Center for Biotechnology Information (NCBI),* **4**, 252 (2014).
9. P. Tchounwou, C. Yedjou, A. Patlolla, D. Sutton. *Springer, Berlin*, 2012, p. 133.
10. S. P. Mishra, *Biointerface Research in Appl. Chem.*, **12**, 2, 1884 (2022).
11. S. Ai-Asheh, R. Banat, Ai-omari, Duvnjak. *Chemosphere*, **41**, 659 (2000).
12. K. Vijayaraghavan, S. Yun. *Biotechnology Adv* **26**:266 (2008).
13. N. Gaur, A. Kukreja, M. Yadav, A. Tiwar. *Applied Water Science,* **8**, 98 (2018).
14. S. Najiah, M. Yusoff, A. Kamari, W. P. Putra, C. F. Ishak, A. Mohamed, N. Hashim, I. Md Isa, *Studies. Jour. of Env. Protection*, **5**, 289 (2014).

15. F. Zhang, B. Zhang, H. Dandan, W. Lishun, H. Wanguo. *Open Chemistry*, **19**, 726 (2021).
16. X. Wei, L. Hui-Ru, L. Wang, H. Yu-Feng, R. Wang. *Pure Appl. Chem,* (2014).
17. J. A. Torres, F. G. E. Nogueira, M. C. Silva, J. H. Lopes, T. S.Tavares, T. C. Ramalho, *RSC Adv.* **7**, 16460 (2017).
18. S.N. Jain, P.R. Gogate. *J Mol Liq*., **243** (2017).
19. D. Arimurti, E. Heraldy, W. Lestari. in: AIP conference proceedings, Vol 1. AIP Publishing, 2016, p. 030036.
20. L. Khezami, R. Capart. *J. Hazard. Mater.,* **123**, 223 (2005).
21. M. Saleem, T. Pirzada, R. Qadeer. *Colloids Surf. A,* **292**, 246 (2007).
22. Z. Hu, H. Chen, S. Yuan. *J. of Hazardous Materials*, **173**, 292 (2010).
23. A.K. Singh, A.K. Jain, P. Saxena, S. Mehtab, *Electroanalysis,* **18 (12)**, 1186 (2006).
24. A. Heidari, H. Younesi, Z. Mehraban, H. Heikkinen. *International Jour. of Biological Macromolecules*, **61**, 251 (2013).
25. Renu, M. Agarwal, K. Singh. *J Water Reuse Desalin.,* **7(4)**, 387 (2017).
26. A.K. Singh, S. Mehtab, U. P. Singh, V. Aggarwal, *Anal. Bioanal. Chem.,* **388 (8)**, 1867 (2007).
27. A.K. Singh, S. Mehtab, A.K. Jain, *Anal. Chim. Acta* **575 (1)**, 25 (2006).
28. J.S. Yadav, M. Soni, A. Lashkari, *International Refereed Jour. of Eng. and Sci.,* **6**, 30 (2017).

Thermal kinetics of poly(amidoamine) functionalized silica gel

V. K. Singh[1*], M. Musharraf[1], S K Swain[2], R K Dey[3], S. Shekhar[4*]

[1]Department of Chemistry, Teerthanker Mahaveer University, Moradabad, Uttar Pradesh-244001, India
[2] Central Instrumentation Facility, Birla Institute of Technology, Mesra, Ranchi, Jharkhand-835215, India
[3]Department of Chemistry, Central University of Jharkhand, Ranchi, Jharkhand-835205, India
[4]Daudnagar College, Daudnagar (Aurangabad), Magadh University, Bodhgaya, Bihar-824113, India

In the present work, the degradation steps of polyamidoamine (PAA) functionalized silica gel (SiPOLHOM) was investigated under dynamic conditions. The degradation of SiPOLHOM was studied with thermogravimetric analyzer (TGA). The kinetics of degradation process was analyzed by Kissinger method, Flynn–Wall–Ozawa's (FWO) method and deconvolution method. The degradation of SiPOLHOM was explained by two-portion process model (PI-TPPM), according to which the decomposition of PAA moieties takes place in two steps called process 1 and 2. Also, Flynn–Wall–Ozawa's (FWO) method and deconvolution method were used to evaluate the apparent activation energy (Ea).

Keywords: Poly (amido amine), Silica gel, Activation energy, Kinetic triplet, Deconvolution method

INTRODUCTION

Chemically modified silica gels have been paid much attention for adsorption process and other applications [1-6]. Such applications require assessment of thermal properties to understand their structural integrity, functional performance and overall suitability for specific needs. The study of thermal stability is also very crucial while designing materials for high-temperature applications such as adsorption, catalyst supports, thermal barrier coatings and gas separation membranes [7-9]. In the quest for understanding and plan the applications of chemically modified silica gels, the knowledge of thermal decomposition under different conditions may be helpful [10-14]. It enables researchers and engineers to optimize material synthesis with improved process efficiency and enhanced thermal properties. There currently exist many literatures available on degradation kinetics of polymers and composites using different conditions and kinetic models [15-20].

Degradation kinetics of chemically modified silica gels is affected by various factors so it is difficult to reveal their mechanism of decomposition [21-28]. Thermal decomposition generally consists of different steps, and it is challenging to predict a global mechanism to formulate the degradation kinetics. Therefore, some well-known methods were used to study the thermal degradation kinetics. Valuable information regarding characteristics of thermal degradation, i.e., the mechanism of degradation reaction, kinetic triplet, thermal stability

and phase change, can be determined from thermogravimetric analysis (TGA) or differential thermogravimetric (DTG) curves [18, 29]. The kinetic triplet (i.e., E, A, and f(a)-function) offer mathematical description which can be used to generate the parent kinetic data as well as to predict the degradation kinetics beyond the range of experimental temperature [30]. The results of kinetic study can be applicable for development of composite material in industrial purpose [31].

The main goal of present work is to analyze the thermal degradation kinetic of chemically modified silica and evaluate the kinetics triplet using thermogravimetric data. Also, the present work is targeted to reveal the devolatilization kinetics during thermal decomposition of chemically modified silica gels, under dynamic circumstances at different heating rates.

In this context, the present work reveals the investigation results related to thermal analysis of polyamidoamine (PAA) immobilized silica gel. The detailed report on characterization of material & its metal binding behaviors are explored in our earlier work [32].

MATERIALS AND METHODS

Starting materials

All reagents: piperazine (Aldrich), 3-chloropropyltrimethoxysilane (Aldrich) and methylene-bis-acrylamide (Acros) were used without purification. Silica gel (0.063–0.200 mm particle size, 60 Å pore diameter, 2.82 g mL^{-1}

---

pore volume, 422 m^2g^{-1} surface area) was purchased from Fluka. An ultra-pure Milli-Q 18.2 MV system was used to produce doubly distilled water (DDW).
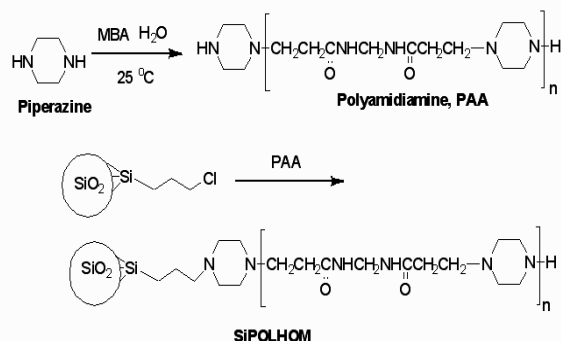
Scheme 1. Synthetic route of poly (amido amine) functionalized silica surface

Material synthesis

The fictionalization of silica surface was done as process adopted by Dey *et al.* [32]. Firstly, preparation of polyamidoamines (PAAs) was done *via* mixing 7.5 g of MBA with 4.4 g of piperazine in deionized water. The resulting suspension was stirred slowly at room temperature for seventy-two hours. Once PAA formed, 2.1 g of organo-functionalized silica (SiCl) was mixed with it. After that 2.0 mL of triethylamine was added to it & the stirring continued for 50 hours at a temperature of 60ºC. The final material SiPOLHOM was filtered, washed with ethanol and dried in vacuum.

Thermal study

The thermogravimetric analysis (TGA) and differential scanning calorimetry (DSC) of the samples were carried out on a TA Instruments, USA;Q10 in argon atmosphere with flow rate of 30 cm^3 s^{-1}, in the range of temperature from room temperature to 1000 °C at the heating rate of 5, 10, 15, 20°C/min, respectively.

Calculation procedure

Thermogravimetric (TG) analysis was used to determine degradation kinetics which can be described with various equations describing degradation mechanisms [18]. The rate of reactions involved during degradation analyzed as a function of the temperature T, and degree of conversion x, which is calculated by:

$$x = \frac{W_0 - W_t}{W_0 - W_f} \qquad (1)$$

where W_0 – weight of sample (gm), W_t – weight of sample at time t, W_f – Final weight of sample.

During degradation the rate of decomposition $\left(\frac{dx}{dt}\right)$ is a function of temperature and weight of the

226

sample while the rate of conversion (x) is assumed to be proportional to the concentration of the sample. Then, the rate of conversion (x) can be given:

$$\frac{dx}{dt} = k(T).f(x) \qquad (2)$$

The apparent activation energy (E_a) may be expressed as the following equation for non-Arrhenius type temperature dependence of reactions,

$$E_a = RT^2 . \frac{dlnk}{dT} = -R . \frac{d\ln k}{d\left(\frac{1}{T}\right)} \qquad (3)$$

leading to Arrhenius equation:

$$k(T) = A.e^{-E_a/RT}.$$

where k(T) represents the rate constant, R denotes the gas constant, and "A" refers to pre-exponential factor [27].

For non-isothermal degradation process linear heating rate H=dT / dt is used to change the variable from time (t) into the temperature (T),

$$H.\left(\frac{dx}{dT}\right) \equiv \left(\frac{dx}{dt}\right) = k(T).f(x) = A.e^{-E_a/RT}.(1-x)^n \qquad (4)$$

Kissinger method

Kissinger method is also called model free method used to determine the kinetic triplet and E_a without knowing the reaction pathway [33]. We can evaluate the E_a using Eq. (4).:

$$ln\left(\frac{H}{T_p^2}\right) \equiv \left(\frac{dx}{dt}\right) = ln\left\{\left(\frac{A.R}{E_a}\right).[-f'_x(x)]\right\}.^{-E_a}/_{RT} \qquad (5)$$

where T_p represents the peak temperature. E_a can be calculated from the slope of the plot of $ln(H/T_p^2)$ verses $1/T_p$. In the present case, $f'_x(x) = -1$ (for first order kinetics) in Eq. (5). In addition, the preexponential factor (A) for degradation process in the case of nth order (when $n \neq 1$), may be calculated based on following equation:

$$A \approx H \cdot A.\exp(\frac{E_a}{RT_p})/RT_p^2$$

FWO method

Flynn–Wall–Ozawa's (FWO) integral isoconversional method is the most commonly used method [34-36] which can be represented as follows:

$$ln\,H = ln[constant.A] - 1.052.\frac{E_a}{RT_p} \qquad (6)$$

ln H was plotted against 1/T, at different heating rates, for the similar value of x considered within 5–95% limits as given in Eq. (6), can be used to calculate E_a. The slope of the plot is utilized to

evaluate the activation energy (slope$=-1.052 \cdot$ (E$_a$ / R)).

Deconvolution method

Linear algorithm model of deconvolution has been applied to extract each process of decomposition rate signal. On the basis of superposition principle, the recorded rate signal is always equal to the signal of every component in its participation proportion (Eq. 7) [29]:

$$\left(\frac{dx}{dT}\right) = \sum_{i=1}^{p} C_i \frac{dx_i}{dt} \tag{7}$$

where C_1, C_2, …, C_p represents constants as weight values and p denotes the number of processes. Applying superposition principle for individual process Eq. (4), can be written as following [29]:

$$\frac{dx}{dt} = \sum_{i=1}^{p} C_i . A_i e^{-E_{a,i}/RT} . (1-x)^{n_i} \tag{8}$$

where E_{ai} represents the apparent activation energy of each process "i", which can be approximated graphically with a Gaussian curve in the following form [29]:

$$\frac{dx_i}{dx} = \frac{1}{\sqrt{2\pi}\sigma_i} . exp\left[-\frac{1}{2} . \frac{(T-T_p)^2}{\sigma_i}\right] \tag{9}$$

where T and T_p represent the independent variable and peak location on the rate curve, respectively, σ_i denotes standard deviation. As a result, assuming linear sum of Gaussian curves approximates whole conversion in thermal decomposition is given as follows:

$$\frac{dx}{dt} = \sum_{i=1}^{p} C_i . \frac{1}{\sqrt{2\pi}} . \frac{1}{\sigma_i} . exp\left[-\frac{1}{2} . \frac{(T-T_p)^2}{\sigma_i}\right] \tag{10}$$

where $C_i . \frac{1}{\sqrt{2\pi}\sigma_i}$ denotes the area of fitted peak.

RESULTS AND DISCUSSION

Thermal degradation

The thermal degradation of SiPOLHOM is shown in Figure 1. It can be observed that material degrade in multiple stages. In the first stage mass loss up to 100°C may be attributed to loss of moisture in the material. In next stage, it can be seen a small weigh down part on the TG graph where weight loss continues up to 600°C due to degradation of PAA chain attached to silica surface. The degradation pattern shown in figure indicates that PAA degrades in multiple scissions. PAA degradation takes place mainly in two regions first from 220-310°C and 2nd from 315-597°C. After 600°C the mass loss rate decreases.

Figure 1. TG curve of SiPOLHOM
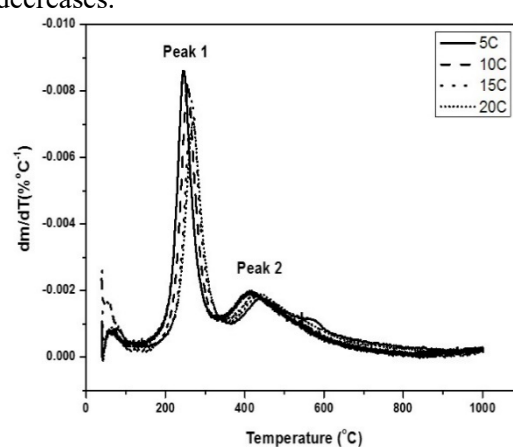
Figure2. DTG curve of SiPOLHOM

The TG and DTG curves of silica supported by PAA obtained at the heating rate of 5, 10, 15 and 20°C are shown in Figures 1 and 2, respectively. The major degradation takes place in the first region ("1") where the majority of PAA was lost. Such region is called an active degradation zone, as major part of PAA decomposed in a sequence manner. In the second region ("2") the rest compound partially decomposed termed as slow decomposition stage.

Figures 1 and 2 refer to process 1 and process 2, respectively. Figure 2 depicts the DTG curve of

SiPOLHOM showing two distinct peaks (marked as peak 1 and peak 2) between 200 and 600 °C. The first peak found between 200–320 °C which can be assigned to the sequenced decomposition of main chain of PAA. The second peak positioned between 340–600°C is due to decomposition of remaining organic part of SiPOLHOM. It can be pointed out that the small peaks become distinct when the rate of heating increased.

Kinetic analysis

Kissinger method

The Kissinger plots obtained using T_p for all processes are depicted in Figure 3 and their kinetics results are presented in Table 1. The value of apparent activation energy (Ea) and pre-exponential factor (A) (Table 1) are found to be different for each process due to the difference in energy required for the decomposition of main chain of PAA (p = 1) and remaining organic part of SiPOLHOM. (p = 2), respectively.

Table 1. Results estimated from the Kissinger method for SiPOLHOM.

Kissinger (peak) analysis	$\ln(H/T_p^2)$ vs. $1/T_p$	
	Process 1	Process 2
E_a (kJ mol^{-1})	4.416	5.660
lnA	-1.62	-1.90
A (min^{-1})	0.197	0.149
RSS	0.00151	0.00135
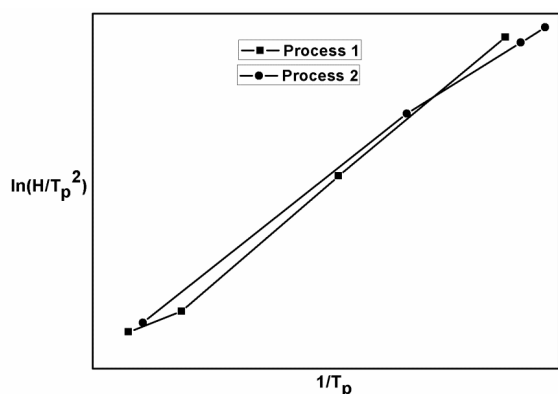
Figure 3. Kissinger plot of SiPOLHOM
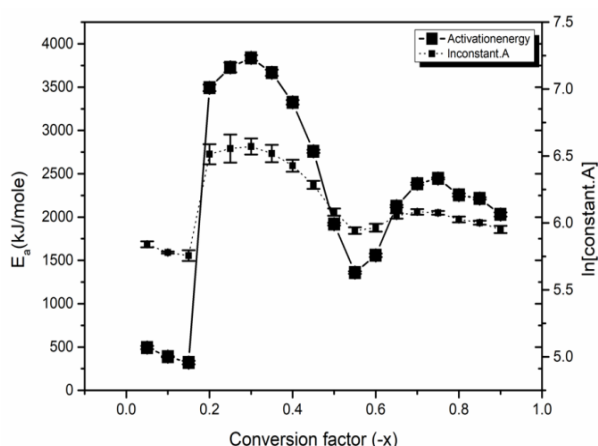
Figure 4. FWO plot of SiPOLHOM

FWO method

The apparent activation energies determined using FWO method are depicted in Figure 4. This

228

provides information about $E_a = E_a(x)$ and iso-conversional intercept (ln [constant · A]) dependency on the fraction of conversion. It is observed that the on the whole decomposition process executed in multi-steps decomposition reactions in which each step reaction contributes partially to the whole reaction mechanism to a dissimilar extent, depending on the process of decomposition [29]. Similar trends were found in case of in E_a and iso-conversional intercept.

The E_a decreased steeply from 493 to 320.9 kJ mol^{-1} between 0.05 and 0.15 of x then it increased up to 3837 kJ mol^{-1} between 0.2 and 0.3 of x. It again found to be decreased to 1359 kJ mol^{-1} in the intervals of x = 0.30–0.55 followed by an increment up to 2445kJ mol^{-1} in the interval of x=0.60-0.75. However, the value of E_a is found to be stable when the value of x lies between 0.75 and 0.90. E_a exhibits lower value at the initial decomposition stage up to x = 0.15, which attributes to loss of water vapor [37]. The major change in E_a when conversion fraction lies between 0.2 and 0.3 for temperature range 200-320°C, may be attributed to major degradation of PAA chain in region ("1") results into peak 1 (Figure 2). The E_a value increased from 1359 kJ mol^{-1} to 2445kJ mol^{-1} when the conversion fraction increased from 0.55 to 0.75, and beyond 0.75, E_a started to decrease (Fig. 5). The changes in the value of E_a happen above 322°C, in region ("2") including peak 2 (Figure 2).

Deconvolution analysis and kinetic parameters

Deconvolution method was applied to separate the individual process of degradation using Gaussian algorithm to rate curves at different heating rates 5, 10, 15 and 20°C min^{-1}, depicted in Figure 5 showing two Gaussian curves corresponding to two core processes. Two peaks, p, have been found except at higher heating rate 20°C min^{-1} where a small peak observed around 80°C. The Gaussian function points of linear combination required value close to the experimental data in rate curve for performing linear deconvolution algorithm.

Gauss curves corresponding to studied processes

The results of the deconvolution method are depicted in Table 2 showing quality of fitting. The heating rate is found to affect the magnitudes of area of each fitted peak ($C_i · [1 / (2\pi)1/2·\sigma_i]$), T_p and standard deviation (σ_i, FWHM), for process 1 and process 2 (Figure 5). Also, it is observed that a small peak appears on increase in rate of heating, 20°C min^{-1}. The degradation rate has been found continuously increased on increasing the rate of

heating of process 1 and process 2 as per result presented in Table 2.

Differential scanning calorimetry

The DSC signatures for SiPOLHOM at the four varied rate of heating can be seen in the curves of Figure 6 with the accompanying data in Table 1. It seems that the heating rate have much effect on the degradation of SiPOLHOM. The temperature at the peak of mass loss occurred at 341°C, 428°C, 482°C, 480°C at the heating rate of 5, 10, 15, 20°C/minute,

respectively, which may be attributed to the removal of the organic moieties. We found a slow and continuous mass loss in the second peak of each curve observed at 673 °C, 754 °C, 803 °C and 801°C with the heating rate of 5, 10, 15, 20°C/minute, respectively. It is due to silanol condensation to stable siloxane, Si–O–Si bonds. The peak of the temperature was found to increase with increase in rate of heating.
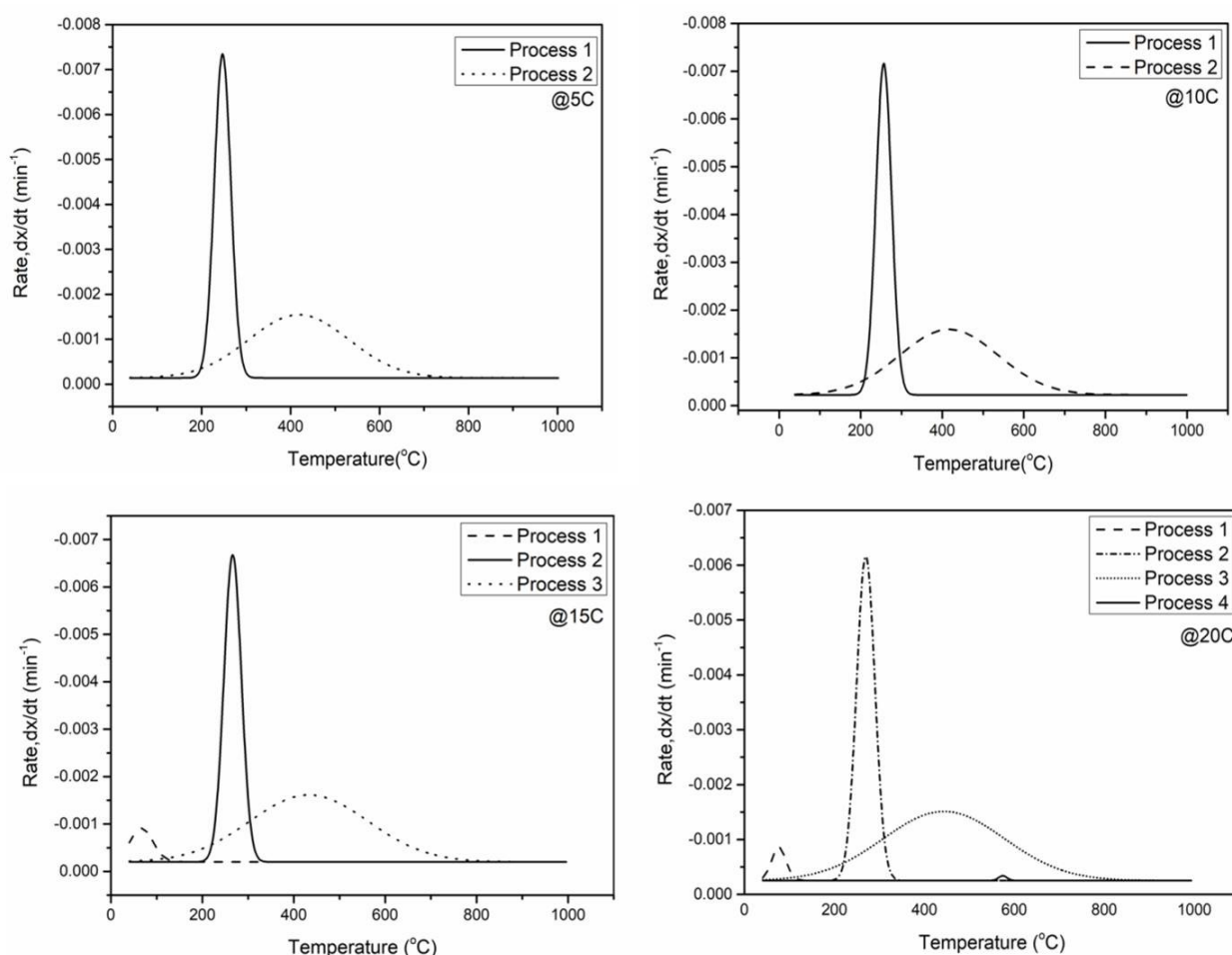
Figure 5. The procedure of deconvolution for the rate pyrolysis curve at 5, 10, 15, 20 °C min^{-1}
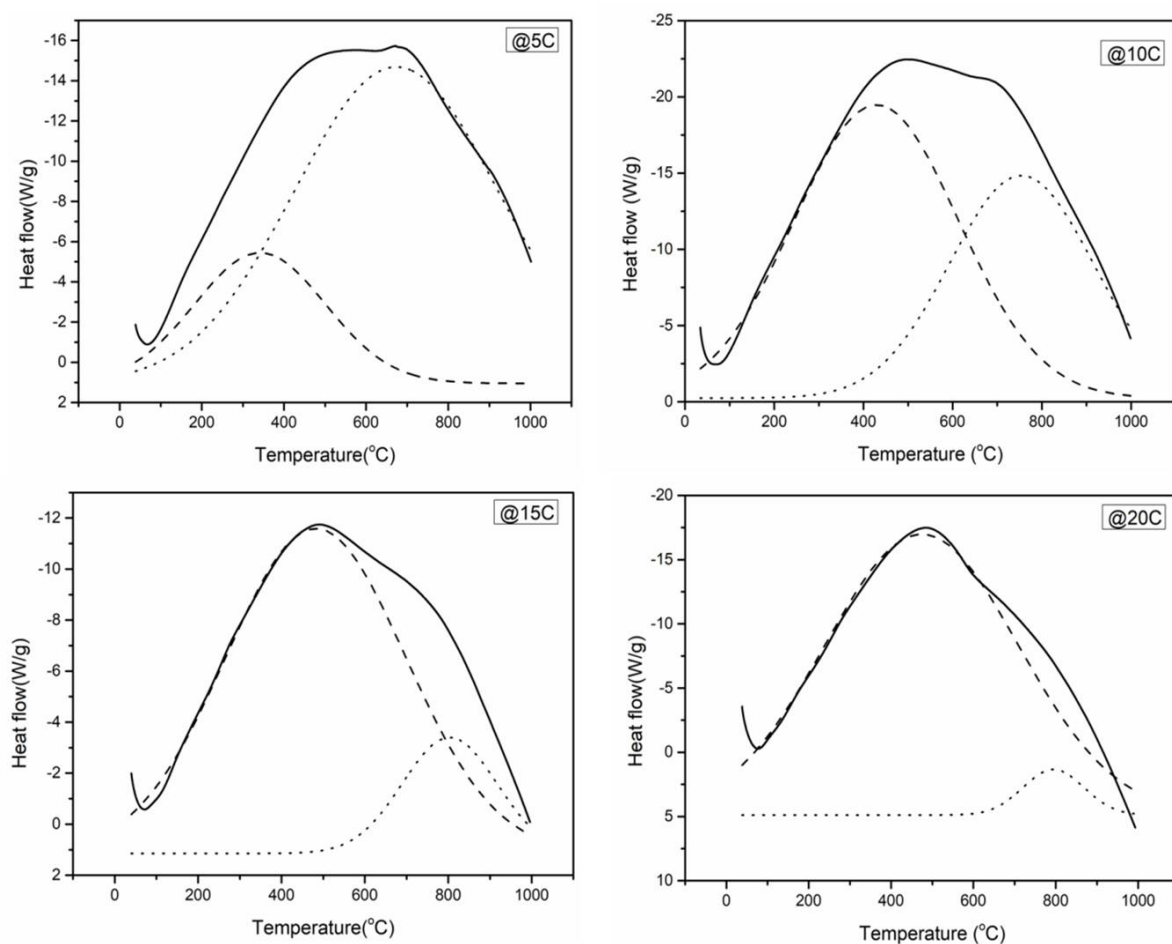
Figure 6. DSC thermogram of SiPOLHOM at a heating rate of 5, 10, 15, and 20 °C min^{-1}

Table 2. Results of deconvolution process for the degradation of SiPOLHOM

		5°C	10°C	15°C	20°C
Process 1	T_p (°C)	**246.8583**	**256.4726**	**266.22528**	**269.7015**
	$C_i \cdot [1/(2\pi)1/2 \cdot \sigma_i]$	-0.33429	-0.3325	-0.30982	-0.29949
	FWHM (°C)	43.57103	45.09463	44.90165	47.75549
	Max. Height (min^{-1})	-0.00721	-0.00693	-0.00648	-0.00589
	σ_i (°C)	43.57103	45.09463	44.90165	47.75549
Process 2	T_p (°C)	**418.3097**	**417.3487**	**432.76337**	**473.303**
	$C_i \cdot [1/(2\pi)1/2 \cdot \sigma_i]$	-0.3973	-0.50627	-0.40364	-0.56287
	FWHM (°C)	265.156	314.4975	284.67853	382.8385
	Max. Height (min^{-1})	-0.00141	-0.00151	-0.00133	-0.00138
	σ_i (°C)	265.156	314.4975	284.67853	382.8385
Process 3					**629.5319**
					0.07625
					193.7139
					3.70E-04
					193.7139
	Reduced χ^2	2.68E-08	1.91E-08	3.66E-08	1.41E-08

CONCLUSIONS

The current work deals with the kinetics of degradation of polyamidoamine (PAA) immobilized silica gel SiPOLHOM, investigated by Kissinger method and Flynn–Wall–Ozawa's (FWO) method. The apparent activation energy (Ea) was calculated by the FWO method and deconvolution method. DSC results reconfirmed the overall degradation

process constitutes two individual processes. The SiPOLHOM may be predicted as materials having potential to be applied in many fields such as adsorption, chromatography, catalysis, etc. This study is the first step towards evaluation of degradation kinetics of SiPOLHOM, keeping in view a commercial application at large scale.

REFERENCES

1. A.Ali, S. Alharthi, B. Ahmad, A. Naz, I. Khan, F. Mabood, *Molecules*, **26**(22), 6885 (2021).
2. Y. Niu, J. Yang, R. Qu, Y. Gao, N. Du, H. Chen, C. Sun, W. Wang, *Ind. Eng. Chem. Res.*, **55**, 3679 (2016).
3. S.S.Nikolića, K. V. Pavlović, M. P. Nikolić, V. V Srdić, M. Šćiban, *Mater. Res.*, 25 (2022).
4. R. K. Dey, U. Jha, T. Patnaik, A. C. Singh, V. K. Singh, *Separat. Sci. Tech.*, **44**(8), 1829 (2009).
5. R.K. Dey, T Patnaik, V.K. Singh, S.K. Swain, M A de Melo, C Airoldi, *Solid State Sci.*, **12**(4), 440 (2010).
6. V. K. Singh, S. Sur, R. Kansal, A. Kumar, P. Rathi, S. Shekhar, *Bull. Pure Appl. Sci. Chem.*, **42**(1), 27 (2023).
7. T. Nguyen, Tu. Hoai D Nguyen, T. T. T. Huynh, M-H D. Dang, L. H. T. Nguyen, T. L. H. Doan, T. P. Nguyen, M. A. Nguyen, P. H. Tran, *RSC Adv.*, **12**, 19741 (2022).
8. J. A. A. Sales, G. C. Petrucelli, F.J.V.E. Oliveira, C. Airoldi, *J. Coll. Int. Sci.*, **297**(1), 95 (2006).
9. R. K. Dey, A.S. Oliveira, T. Patnaik, V. K. Singh, D. Tiwary, C. Airoldi, *J. Sold. State Chem.*, **182** (8), 2010 (2009).
10. P. Ferruti, M. A. Marchisio, R. Duncan, *Macromol. Rapid Commun.*, **23**, 332 (2002).
11. M.A. Kaczorowska, H.J. Cooper, *J. Amer. Chem. for Mass Spectr.*, **20**(4), 674 (2009).
12. R. Smaail, T. Said, E. M. Mohamed, B. Maryse, D. Stéphanie, R. Bertrand, N. M. Yahia, *J. Chem. Eng. Data*, **60**(10), 2915 (2015).
13. A. Bisht, R. Sati, K. Singhal, S. Mehtab, M.G.H. Zaidi, *Advances in Solar Power Generation and Energy Harvesting*, 127 (2020).
14. A Gamal. E.Mostafa, M. M.Hassanien, K. S. Abou-El-Sherbini, V Gorlitz, *Anal. Sci.*, **19**(8), 1151 (2003).
15. S. Mehtab, A. Bisht, R. Sati, K. Singhal, S. Mehtab, M.G.H. Zaidi, *Advances in Solar Power Generation and Energy Harvesting*, 127 (2020).
16. S. Mehtab, M.G.H. Zaidi, R. Kunwar, K. Singhal, T. I. Siddiqui, *Int. J. Polym. Anal. and Charact.*, 1 (2021).
17. D. V. Quang, J. E. Lee, J. K. Kim, Y. N. Kim, G. N. Shao, H. T. Kim, *Powder Tech.*, **235**, 221 (2013).
18. K.-M. Klaudia, P. Kinga, *Polymer Composites with Functionalized Nanoparticles*, 405 (2019).
19. A. Jancirani, V. Kohila, B. Meenarathi, A.Yelilarasi, R. Anbarasan, *Bull. Mater. Sci.*, **39** (7), 1725 (2016).
20. V. Georgieva, D. Zvezdova, L. Vlaev, *Chem. Cent. J.,* 81 (2012).
21. J. B. Dahiya, K. Kumar, M. M. Hagedorn, H. Bockhorn, *Polym. Int.*, **57**(5), 722 (2008).
22. P. Joshi, G. Bisht, S. Mehtab, M.G.H. Zaidi, *Mater. Today Proc.*, **62**(12), 6814 (2022).
23. S. Mehtab, M.G.H. Zaidi, N. Rana, K. Khati, S. Sharma, *Bull. Mater. Sci.*, **45**,162 (2022).
24. B. Charmas, K. Kucio, V. Sydorchuk, S. Khalameida, M. Ziezio, A. Nowicka, *Coll. Interf.*, **3**(1), 1 (2019).
25. M. Karimi, S. Davoudizadeh, S. Bahadorikhalili, K. Khezri, *Int. J. Res. Phys. Chem. Chem. Phys.,* **233**(3), 393 (2019).
26. E. Pakhmutova, Y. Slizhov, *AIP Conf. Proc*, 1899(1) (2017).
27. B. P. Jaroniec, R. K. Gilpin, M. Jaroniec, *The J. Phy. Chem. B*, **101(35)**, 6861 (1997).
28. Y. Fang, W. Yao, J. Guo, X. Gao, *Int. J.of Low-Carb. Tech.*, 7(4), 271 (2012).
29. B. Janković, *Fuel Proc. Techn.,***138**,1 (215).
30. S. Vyazovkin, *J. Thermal and Calor.,* **83**, 45 (2006).
31. L. Vlaev, N. Nedelchev, K. Gyurova, M. Zagorcheva, *J. Anal. Appl. Pyrol.*, **81**(2), 253 (2008).
32. R. K. Dey, T. Patnaik, V. K. Singh, S. K. Swain, C. Airoldi, *App. Surf. Sci.***255**(18), 8176 (2009).
33. H. E. Kissinger, *Anal. Chem.*, **29** (11), 1702 (1957).
34. P. Brachi, F. Miccio, M. Miccio, G. Ruoppolo, *Fuel Process.Tech.,***130,** 147 (2015).
35. J. H. Flynn, L. A. Wall, *J. Res. Natl. Bur. Stand. A Phys. Chem.,* **70A** (6), 487 (1966).
36. T. Ozawa, *Thermochimica Acta*, **355**(1-2), 35 (2000).
37. J. Giuntoli, W. D. Jong, S. Arvelakis, H. Spliethoff, A. H. M. Verkooijen, *J. Anal. And Appl. Pyrol.*, **85**(1-2), 301 (2009).

Facile preparation and characterization of graphite coated magnetite nanoparticles

V. Rani[1]*, I. Joshi[2], P. S. Rawat[3] R. C. Srivastava[4]

[1]Department of Physics, Sri Ram Singh Dhoni Govt. Degree College, Jianti, 263626, Uttarakhand, India
[2] Department of Chemistry, G.B. Pant University of Agriculture & Technology, Pantnagar, 263145, Uttarakhand, India
[3]Department of Physics, SALS, Uttaranchal University, Dehradun,248001, Uttarakhand, India
[4]Department of Physics, G.B. Pant University of Agriculture & Technology, Pantnagar, 263145, Uttarakhand, India

A facile procedure for the preparation of graphite coated magnetite nanoparticles with the size of ~ 12 nm using simple chemical co-precipitation method is reported. The co-existence of both phases in the graphite coated magnetite nanoparticles was confirmed by X-ray diffraction. Scanning electron microscopy was used to express its surface morphology. Fourier transform infrared spectroscopy was used to assure the binding of graphite onto the surface of magnetite nanoparticles. Non-isothermal kinetic parameters were calculated by Coats-Redfern method using thermo-gravimetric analysis curves. DC conductivity was measured by using four probe techniques at room temperature for selected voltage compliances (1V, 10V & 100V). Vibrating sample measurement displayed superparamagnetic behavior with saturation magnetization of graphite coated magnetite nanoparticles was found ~47-54 emu/g. These nanostructures exhibited excellent electrical and magnetic properties which were dependent on the content of the magnetite nanoparticles, making it a promising material for practical applications in biomedical research and nanotechnology.

INTRODUCTION

Magnetic nanoparticles have received growing attention over the decades due to their unique properties and applicatons [1, 2]. These magnetic nanoparticles have tremendous applications in the field of pharmaceuticals, environmental remediation, magnetic resonance imaging, magnetic recording media, data storage, ferro-fluids as well as in various biomedical applications etc. [3-5]. Because of instability and small in particle size, magnetite nanoparticles (MNPs) are difficult to employ for engineering and biomedical applications. MNPs are highly susceptible to oxidant ion when it is exposed to the atmosphere [6]. To overcome this difficulty, several researchers have synthesized magnetic nanoparticles impregnated in a polymer matrix [7]. In addition to inorganic coating, gold [8] and silica [9] with MNPs have been successfully examined as stabilizing shell of magnetic nanoparticles. It was reported that gold shells provide a multifunctional platform for surface modification but it could not protect the magnetic properties due to it grain boundaries. Therefore, new more stable magnetic materials are in demands by industries [10].

Surface functionalization of MNPs is required to improve its physical, chemical and electrical properties for further applications. The carbonaceous fillers to magnetite matrix provide a remarkable feature to the composites [11]. Carbon based magnetic nanocomposites with accurate their components (matrix and filler material) have unique scientific and technological importance [11]. Graphite (GR) and graphene-oxide (GO) are vastly used as fillers in the composite systems [12,13]. Recently, Meysam *et al.* have prepared carbon/magnetite nanocomposites for copper removal [14]. Malhotra *et al.* [15] modified the magnetic nanoparticles by carbon coating for the increment in bio safety. Magnetite/graphite nanocomposites synthesized and characterized by Kusrini *et al.* [16]. The extraordinary properties of the mentioned fillers have enhanced physical, chemical, mechanical, optical and antimicrobial properties of composite system. [17]. GR has recently attracted considerable attention due to its unique atomic arrangement. It has wide applications in chemical sensors, energy storage, optoelectronics and molecular separation [17-19]. GR nano plates in composite form with magnetic matrices can also enhance the mechanical and corrosion resistance properties [20-22].

Graphitic magnetic nanocomposites are highly demanded due to their extensive applications in

---

* To whom all correspondence should be sent:
E-mail: vershachauhan31@gmail.com

various fields such as, microwave absorption [23], electro-magnetic shielding [24], water purification [25], adsorption of heavy metal ion and toxic gases from the environment [26, 27], catalysis [28], sensors [29], drug delivery [30-32], and bio-medical diagnosis [33, 34]. In the present work, we have fabricated graphite coated magnetite nanoparticles (GNPs) with different weight ratios using chemical co-precipitation method. The structural, thermal, electrical and magnetic properties of prepared nanostructures were compared with that of GR and MNPs.

EXPERIMENTAL

Starting materials

Graphite powder (500 μM) was procured from Merck (99.98 %), ferrous chloride ($FeCl_2.4H_2O$), ferric chloride ($FeCl_3.6H_2O$) and ammonia solution were procured from Sd Fine Chemicals India.

Preparation of GNPs

GNPs were prepared through chemical co-precipitation of Fe_3O_4 from a composition of $FeCl_2.4H_2O$ and $FeCl_3.6H_2O$ in 1:2 molar ratio supplemented with varying weight fractions of GR. The weight fractions of Fe (III) to GR was adjusted to 5:1, 8:1, 15:1 to afford the three samples of GNPs. For the preparation of GNPs involving Fe (III): GR (1:5), a suspension of GR (0.1g/dL, 50 mL) in deionized water was subjected to ultrasonic treatment over 45 min with simultaneous feeding of 50 mL a formulation of Fe (III):Fe (II) in 1:0.6 (w/w,50 mL) in deionized water @ 0.1 mL/min at 300K. Chemical co-precipitation of Fe_3O_4 in presence of GR was conducted through addition of ammonia solution (30%,v/v) at 85^0C till rise in pH level of reaction medium to 10.The contents were allowed for stirring @500 rpm over 180 min thereafter cooled to 300K and subsequently centrifuged at ~4000 rpm for 15 min. GNPs settled at the bottom of centrifuge tube were successively washed with deionized water till removal of chloride ions. GNPs were isolated from centrifuge tube through magnetic separation and dried at 400 mmHg/300K. MNPs were also prepared following identical co precipitation method and served as reference for measurement of spectral and electrical, thermal and magnetic properties of GNPs.

Characterization

XRD spectra were recorded on a Bruker D8 Advance spectrophotometer at 30 mA and 40 kV. Average crystallite size (D, nm) were deduced from XRD using Debye Scherrer formula D=$K\lambda/\beta \cos\theta$) using Cu K_α irradiation (λ= 1.54Å) [35-36], where K

is Scherrer constant, β (in radian at full width and half maximum and θ is the angle of diffraction. Scanning electron measurement (SEM) is used to determine the surface morphology. SEM pictures of synthesized samples were taken for a number of magnifications at FEI QUANTA 200HV. Fourier transform infrared (FTIR) spectra were analyzed over Perkin Elmer spectrophotometer in the wave number (cm^{-1}) ranging in 500-4000. Hysteresis curves were recorded over vibrating sample magnetometer model 155 procured from EG & G Princeton Applied Research, at 300K. DC conductivity (σDC) measurements were conducted over disk shaped samples with 1.0 cm diameter and 0.1 cm thickness. For this purpose, specimen was fabricated through compression molding at 10 MPa. σDC data were recorded over Keithley four-point probe arrangement connected with 6221 DC current source and 2182 A nanovoltmeter at 300K. Thermogravimetric curves were recorded over simultaneous thermogravimetric /differential thermal analyzer (TG/DTA) model SII 6300 EXSTAR under progressive heating @ 10°C/ min from ambient temperature to 1000°C in air flow @ 250 mL /min. TG data were used for evaluation of non-isothermal kinetic and thermodynamic parameters of solid state decomposition of GR, MNPs and respective GNPs. Thermal data deduced from TG curve was used for evaluation of activation energy (E_a), pre-exponential factor (A^*), entropy (ΔS), enthalpy (ΔH) and Gibb's free energy (ΔF) pertinent to solid sate decomposition using Coats-Redfern equation [37].

$$\log_{10}\left[\frac{-\log_{10}(1-\alpha)}{T^2}\right] = \log_{10}\frac{AR}{\beta E}\left[1-\frac{2RT}{E}\right] - \frac{E}{2.303RT}$$

where α is the decomposed fraction of material, A^* is pre-exponential factor and R (J mol^{-1} K^{-1}) is the gas constant. E_a and A^* values are calculated from slope and intercept respectively drawn between log [g(α)/T^2] against 1000/T [Fig. 8].

The change in entropy for activation ΔS (J K^{-1} mol^{-1}) was calculated according to the relation: $\Delta S=Rln(Ah/k_B T_S)$, where k_B is the Boltzmann constant, h is the Plank's constant, T_s is the peak temperature deduced from DTA [38, 40].

RESULTS AND DISCUSSION

Microstructure

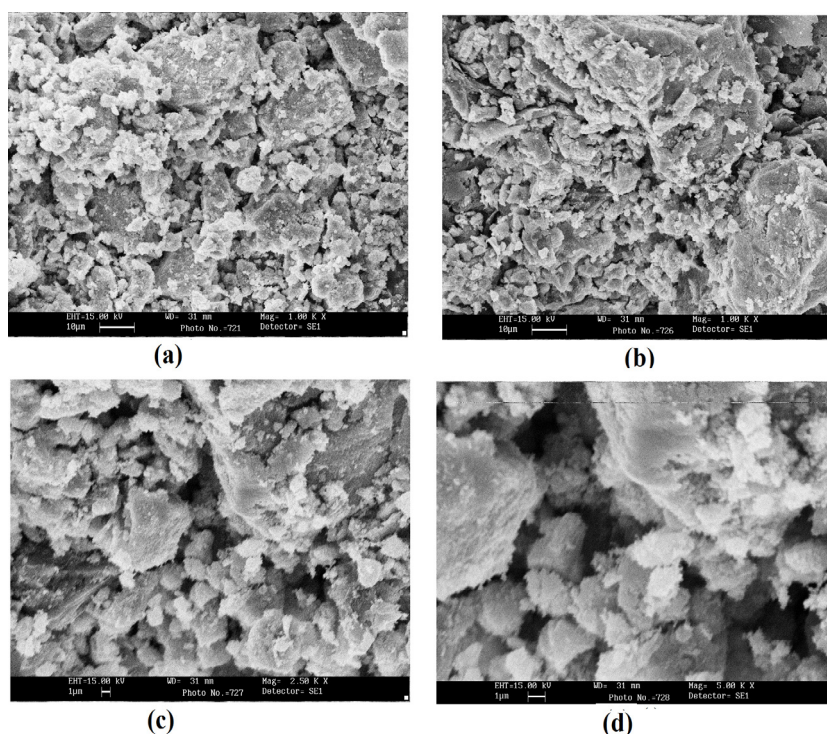The surface characteristics of the MNPs and GNPs were found out by using scanning electron microscopy.

Fig. 1. SEM images for MNPs at 10 µM, 1 kx (a), for GNPs 10 µM, 1 Kx (b), 1 µM, 2.5 Kx (c) 1 µM, 5 Kx (d)
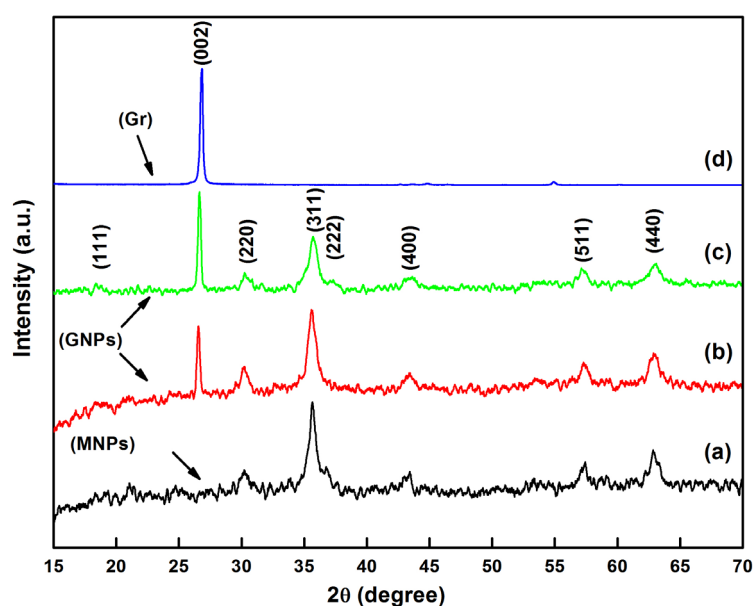

Fig. 2. XRD patterns of (a) MNPs (b) GNPs (I), (c) GNPs (III) and (d) GR**.**

SEM images (Fig. 1 (a) show that MNPs are spherical in shape with a narrow particle size (17.5 nm which is calculated by the Debye–Scherrer formula). Particles agglomeration is indicating a good connectivity between the grains all together. SEM images of GNPs are shown in fig. 1(b-d). It looks like a smoothed sponge-like structure.XRD measurements reveal the co-existence of phases of MNPs and GR in GNPs. The XRD pattern of the GR [fig.2] shows a sharp peak (002) at $2\theta = 26.81^0$ with the interplanar spacing of about 0.33 nm. The absence of any other impurity peak in the XRD of

GR confirms its purity [40-42]. For MNPs, the diffraction peaks at $2\theta =30.30^o$, 35.66^o, 43.35^o, 57.30^o, 63.00^o correspond to (220), (311), (400), (511) and (440) planes respectively. All the diffraction peaks can be identified from the JCPDS card no. 77-1545 [41]. The lattice parameter of MNPs deduced from XRD data was around ~8.36 Å which indicates that the product consists of cubic spinel structure and crystalline single-phase of MNPs. In the XRD patterns of the GNPs the expected diffraction peak at ~26.90º resulted from GR and remaining peaks can be indexed similar to

MNPs. The similar presence of Graphitic peaks in XRD patterns of Iron oxide can be confirmed by other researches too [44-46]. The average crystallite sizes, as calculated from XRD data using Debye Scherer's formula, was ~17 nm and ~12 nm MNPs and GNPs, respectively.

FTIR spectra

Fig. 3 shows the FTIR spectra of GR, MNPs and as-synthesized GNPs. In the spectrum of GR, the characteristic absorption peaks at ~3447.28 cm^{-1} (v-O–H) and ~1628.79cm^{-1}(δ-O–H) attributed the presence of absorbed moisture. It is observed that the peaks in the region about 1520-1600 cm^{-1} assign to the aromatic C=C stretching vibrations and band near 2800-2900cm^{-1} correspond to the aliphatic carbon [34, 35].For the spectra of MNPs and GNPs, the band around 586 cm^{-1} is attributed to the stretching vibration (Fe-O) of the tetrahedral groups and band around 445cm^{-1}is attributed to the octahedral groups [45].The intense broad band at ~3394cm^{-1} and the less intense band at 1624 cm^{-1} are due to stretching vibrations corresponding to -OH. Absorption peak around 2356 cm^{-1} attributes to the traces of absorbed CO$_2$ [48, 49]. The spectra reveals that the C-H and other carbon-based groups are more prominent in MNPs (I) than in MNPs (III) due to high GR content.

Magnetic behavior

Fig. 4 shows the effect of magnetic field on the magnetization (M-H) of MNPs and GNPs. The magnetization was recorded at 300K with the maximum field of 40K Oe.

The samples exhibit immeasurable values of coercive field and remnant magnetization which shows the superparamagnetic nature of all samples [50]. The saturation magnetization of the GNPs (I) and GNPs(III) [~47 emu/g and ~54 emu/g respectively] is smaller than the value of bulk MNPs [~70.5emu/g] [44]. It is observed that saturation magnetization value in GNPs decreases by adding GR into the MNPs [51, 52]. This can be attributed to the small particle size and relatively low amount of MNPs in the GNPs.

DC conductivity

As we know that dc conductivity (σ) measures the ability of substance to conduct electricity [53]. The DC conductivity measurement of samples was investigated under selected voltage compliances (1 V, 10 V, 100 V) at room temperature. The electrical conductivities are shown in Fig 5. As shown in the figure the conductivity of GNPs is much higher than parent MNPs which shows enhanced

semiconducting properties of the synthesized nanostructures.

The DC conductivity of MNPs at 1V shows the value of ~7.45×10^{-4} S/cm which increased to the value ~1.38×10^{-3} S/cm for highest GR doped GNPs i.e., for GNPs (I). The similar trend was observed for 10V and 100V. This indicates the conductive nature of GR. Among the nanocomposites, GNPs (I) shows highest DC conductivity and the value decreases with further addition of MNPs supported to available literature [54]. The higher conductivity of GNPs(I) may be due to the strong interfacial adhesion between the GR and MNPs.

Thermal behavior

Fig. 6 shows TG thermogram of GR, MNPs and GNPs. As shown in figure, GR renders thermall stability in the range of 25^{0}C-102^{0}C. Marginal degradation occurs in ~102^{0}C-570^{0}C range with the ~1.5% weight loss atributes to moiture content [55]. TG onset for all samples attributes to their low thermo-oxidative stability [56-57, 58]. The decomposition of GR started at 102^{0}C. The first decomposition stage occurs in the range of 570^{0}C-722^{0}C associated with weight loss of ~37.4%. The second decomposition stage occurs in the temperature range 742^{0}C-830^{0}C with the weight loss of~56.2% along with DTA signal 79.8 µV at 740^{0}C [Fig. 7].
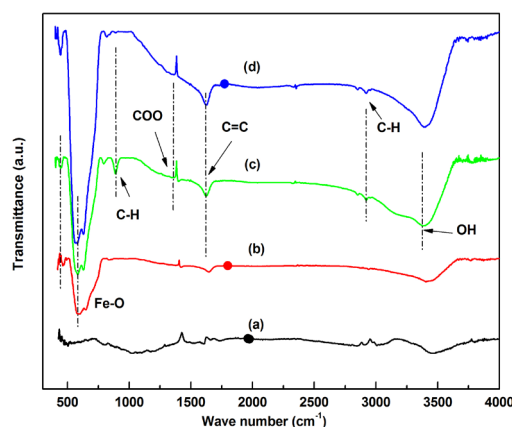
Fig. 3. FTIR spectra of (a) GR, (b) magnetite NPs (c) GNPs (I) and (d) GNPs(III)

Pure MNPs degradation goes in two steps resulting in minor weight loss. The initial weight loss was observed at 102^{0}C due to the loss of water content. Further slight decrement in the weight is due to the phase change of magnetite (Fe$_3$O$_4$) into maghemite (Fe$_2$O$_3$) in the temperature range 200^{0}C-400^{0}C and afterwards above 420^{0}C, there was no weight loss.
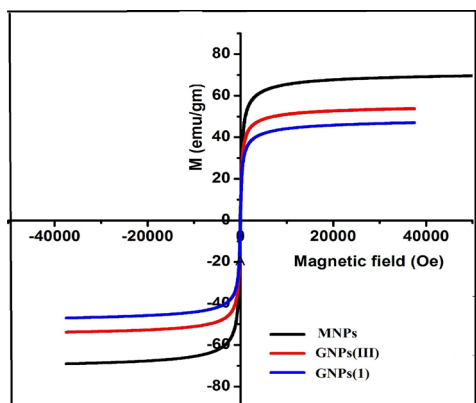
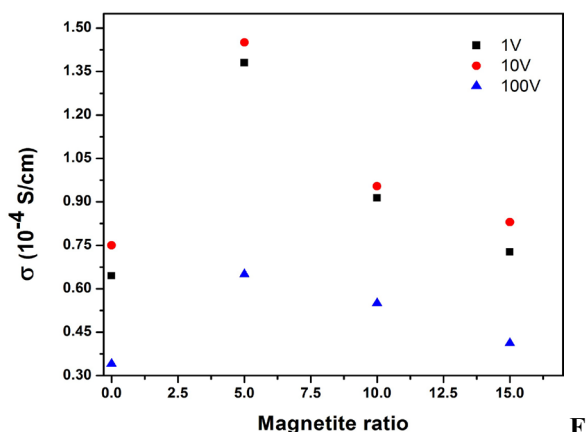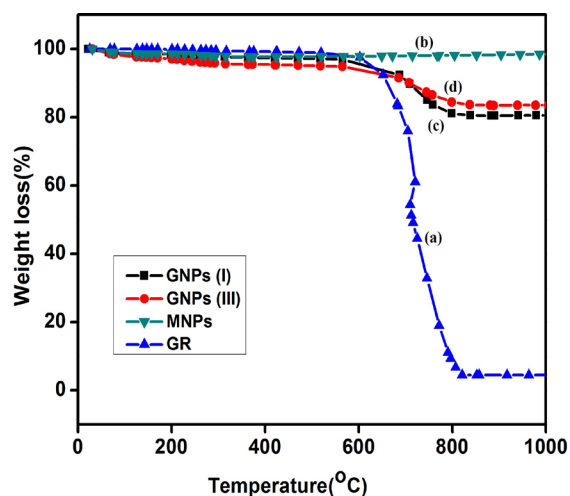**Fig. 4.** Magnetization curve (B-H) for ((a) MNPs (b) and (c) GNPs

Fig. 5. Electrical conductivities of GNPs at different voltage compliances

GNPs undergo similar degradation as that of GR but with higher thermal stability due to the presence of

relatively thermal resistance MNPs. GNPs (III) thus shows more stability than GNPs(I) [56].

Fig. 6. TG curves for (a) GR , (b) MNPs , (c) GNPs (I)

and (d) GNPs (III).

The results of TGA are in agreement with DTA curves which indicate the exothermic peaks nearly at same temperatures. The determined values of activation energies obtained by CR method can be regarded as indicator of the thermo-oxidative stability of samples. The activation energy for GR was at 157.14 kJ/mol relative to ~159.1 kJ/mol for CNTs [59]. The activation energies for MNPs and GNPs are 22.76 kJ/mol and 129.47 kJ/mol respectively along with negative values of entropy (Table 1).

Table I. Kinetic parameters for solid-state thermal decomposition determined using the Coats–Redfern method.

Samples	T (K)	T_S(K)	E (KJmol^{-1})	A (s^{-1})	ΔS (KJmol^{-1}K^{-1})	ΔH (KJmol^{-1})	$\Delta G \times 10^5$ (KJmol^{-1})
GR	844-1100	993	157.14	5.48×10^6	-125.83	149.0	2.72
MNPs	473-673	534	22.76	5.33	-1116.48	18.32	6.14
GNPs(I)	873-1073	987	129.47	2.01×10^5	-153.33	122.43	2.52
GNPs(III)	823-1123	976	98.81	3.92×10^3	-186.01	106.12	2.89
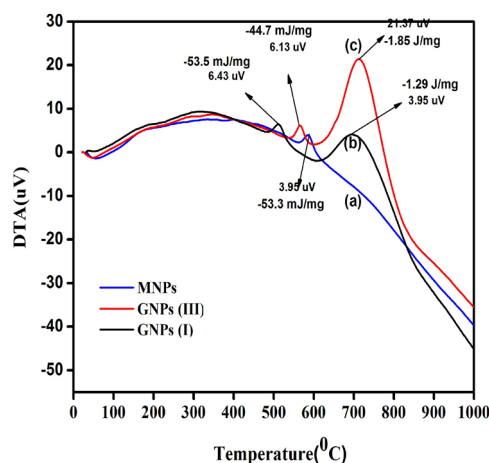
Fig. 7. DTA curves for (a) MNPs (b) and (c) GNPs
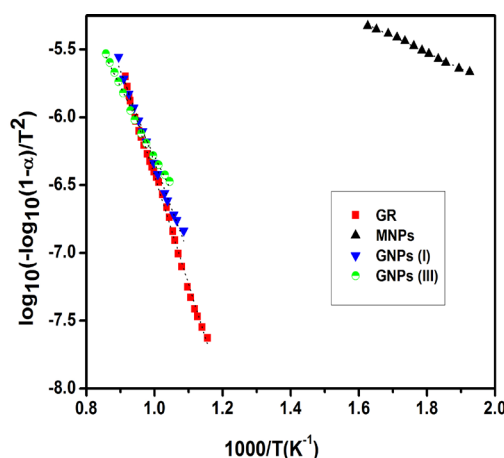
Fig. 8. Coats-Redfern Plots for GR, MNPs and GNPs

CONCLUSION

Graphite coated magnetite nanoparticles with different weight ratios of graphite and magnetite nanoparticles were successfully synthesized by an easy and cost-effective co-precipitation method. The magnetite nanoparticles with the size of ~17 nm were attached with graphite layers. The formation of samples were confirmed by XRD and FTIR studies. Graphite coated nanoparticles showed the different thermal, magnetic and electrical properties than their pristine form which defines the wide applicability of such nanostructures. Thermogravimetric analysis reveals that magnetite nanoparticles can improve thermal stability of graphite in synthesized nanostructures. The graphite coated magnetic nanoparticles with superparamagnetic behavior provide the opportunities for various applications in the fields of biomedicine, bio-material separation and bio-diagnostics, etc.

REFERENCES

1. K. A. Abro, I. Khan, J. F. Gomez-Aguilar, *J. Ther. Anal. and Cal.,* **143**(5), 3633 (2021).
2. P. Kulal, V. Badalamoole, *Int. J. Bio. Macromolecules*, **165**, 542 (2020).
3. N. Ahmadpour, M. H. Sayadi, S. Sobhani, M. Hajiani,. *J. Env. Management*, **271**, 110964 (2020).
4. T. Muraliganth, A. V. Murugan, A. Manthiram, *Chem. Comm.,* **47**, 7360 (2009).
5. A.C.S. Costa, H.P.A. Alves, M. A. Correa, F. Bohn, W. Acchar. *Mat. Chem. and Phys.,* **232**, 1 (2019).
6. D. Padalia, U. C. Johri, M.G.H. Zaidi, *Physical B, Condensed Matter*, **407**, 838 (2012).
7. T. Agarwal, K. A. Gupta, M. G. H. Zaidi, Sarfraz Alam, *Nanoscience & Nanotechnology*, **2**, (2012).
8. L. León Félix, B. Sanz, V. Sebastián, T. E. Torres, M. H. Sousa, J. A. H. Coaquira, M. R. Ibarra , G. F. Goya. *Scientific Reports.*, **9**, 4185 (2019)
9. X. Ni, Z. Zheng, X. Xiao, L. Huang, L. He, *Mat. Chem. and Phys.*, **120** (1), 206 (2010).
10. A. M. Espinoza-Rivas, M. A. Pérez Guzmán, R. Ortega-Amaya, J. Santoyo-Salazar, C. D. Gutiérrez-Lazos, M. Ortega-López. *J. of Nanotech.,* (2016).
11. S. K. Joshi, A. Kumar, M.G.H. Zaidi, *Defense Sci. J.,* **70**(3), 306 (2020).
12. H. Mudila, P. Parashr, H.L. Kapoor, S. Rana, M.G.H. Zaidi, *Electrochim. Acta,* **38**(2), 69 (2020).
13. S. Mahtab, P. Joshi, B. Arya, M.G.H. Zaidi, T. I. Siddiqui. M. *Sci. Res. India*., **17** (1), 8 (2020).
14. M. Shahrashoub, S. Bakhtiari, *Mic. and Meso. M.*, **311**, 110692 (2021).
15. N. Malhotra, G. Audira, J. Chen, P. Siregar, H. Hsu, J. Lee, T. Ger, C. D. Hsiao, *Molecules*, **25**(9), 2256 (2020).
16. E. Kusrini, F. Oktavianto, A. Simanjuntak, G. Pasca , A. Usman, *E3S Web of Con.,* **67**, 03029 (2018).
17. H. Mudila, M.G.H. Zaidi, S. Rana , S. Alam, *Carbon let.* **18**, 43 (2016).
18. H Mudila, M.G.H. Zaidi, S. Rana, V. Joshi, S. Alam. *Int. J. Chem. Anal. Sci.,* **4**(3), 139 (2013).
19. K. Khati, S. Mahtab, M.G.H.Zaidi, I. Joshi, S. Rathore. *Mat. Today.,* **46**(20), 10257 (2020).
20. D. Padalia, U. C. Johri, M.G.H. Zaidi. *Mat. Chem. Phys.,* **169**(89) (2016).
21. B. Wen, X. Zheng. *Composites Sci. and Tech.,* **174**, 68 (2019)
22. A. Jamwal, P. Prakash, D. Kumar, N. Singh, K. K. Sadasivuni, K. Harshit, S. Gupta, P. Gupta. *J of Composite Mat.*, **53**(18), 2545 (2019).
23. X. Huang, J. Zhang, W. Rao, T. Sang, B. Song, C. Wong. *J Alloys and Compounds.*, **662**, 409 (2016).

24. C. K. Madhusudhan, K. Mahendra, B. S. Madhukar, T. E. Somesh, M. Faisal. *Synthetic Metals*, **267**, 116450 (2020)

25. Y. Tian, H. Ma, B. Xing. *Applied Surface Sci.*, **537**, 147995 (2021)

26. R. Foroutan, S. J. Peighambardoust, A. Ahmadi, A. Akbari, S. Farjadfard , B. Ramavandi. *J. of Environ. Chem. Eng.*, **9**(4), 105709 (2021)

27. Y. N. Zhang, Q. Niu, X. Gu, N. Yang, G. Zhao. *Nanoscale.*, **11**(25), 11992 (2019)

28. M. Ahmadi, F. Ghanbari. *Mat. Res. Bulletin.*, **111**, 43 (2019)

29. S. Mehtab, M.G.H. Zaidi, P. Bhatt, P. Joshi, T.Agarwal. *Portugaliae Electrochemica Acta.*, **40**(3),209 (2022).

30. G. Bisht, M.G.H. Zaidi, S. Rayamajhi. *Int. J of Polymeric Mat. and Polymeric Biomat*., **66**(14), 708 (2017).

31. G. Bisht, M.G.H.Zaidi. *Drug Delivery and Translational Res.,* **5**, 268 (2015).

32. G. Bisht , M.G.H. Zaidi, *Int. J of Biomedical Material Res.*, **2**(1),1(2014).

33. C. Xiong, X. Lin, H. Liu, M. Li, B. Li, S. Jiao, W. Zhao, C. Duan, L. Dai, Y. Ni. *J. of the Electrochemical Society*, **166**(16), 3965 (2019).

34. S. Abazari, A. Shamsipur, H. R. Bakhsheshi-Rad, S. Ramakrishna, F. Berto. *Metals.*, **10**(8), 1002 (2020).

35. L. V. Azaroff. McGraw-Hill: New York, NY, USA, 1970.

36. V. S. Vinila, I. Jayakumari. *Micro and Nano Technologies*, 319 (2022).

37. A.W. Coats, J. P. Redfern. *Nature*. **68**,201(1964).

38. G. Zheng, J.Wu, W. Wang, C. Pan. *Carbon.,***42**(14), 2839 (2004).

39. V. Rani, R. C. Srivastava, H. M. Agarwal, M.G.H. Zaidi. *Mat. Today: Proc.,* **4** (9), 9471 (2017).

40. P. S. Rawat, R. C. Srivastava, G. Dixit, K. Asokan. *Vacuum.*, **182**, 109700 (2020).

41. Mu Q, Sun Y, Guo A, Yu X, Xu X, Cai A, X. Wang. *Mater Res Express* **6**(9), 950 (2019).

42. R. Madhuvilakku., Y. K. Yen, W. M. Yan, G.W. Huang. *ACS omega*, 7 (18), 15936 (2022).

43. F. Moniriya, S. J. Sabounchei, A. Yousefi, O. Akhavan, *J. Nanoparticle Res.,* **23**(8), 1(2021).

44. J. Sun, L. L.i, R. Yu, X. Ma, S. Jin, K. Chen, Q. Shu. *Molecules*, **25**(13):3044 (2020).

45. C. Li, B. Xie, D. Chen, J. Chen, W. Li , Z.Chen, Y. Long. *Energy.*, **166**, 246(2019).

46. A. T. Ubando, W. H. Chen, H. C. Ong. *Energy*, **180**, 968 (2019).

47. S. M. Fotukian, A. Barati, M. Soleymani, A. M. Alizadeh. *J Alloys and Compounds*, **816**, 152548 (2020).

48. H. Jiang, Y. Cao, F. Zeng, Z. Xie, F. He, *J of Nanomaterials*,1 (2021)

49. S. Park, C. Raj, J. Manikandan, R. Kim, K. H. Yu. *Bulletin of Korean Chemical Society*, **41** (8), 856 (2020).

50. B. S. Damasceno, A. F. V. da Silva, A. C. V. de Araújo. *J Environmental Chemical Engineering*, **8**(5), 103994 (2020).

51. H. Xiang, G. Ren, Y. Zhong, X. Yang, D. Xu, Z. Zhang, X. Wang. *Mater. Res. Express.,* **8**(2), 025016 (2021).

52. M. S. Raghu, K. Y. Kumar, M. K. Prashanth, B. P. Prasanna, R. Vinut, C. P. Kumar. *J Water Process Engineering,* **17**, 22 (2017).

53. Q. C. Bracamonte, M.Y. Pedram, H. A. Bolados. *Polymers.*, **14**, 4266 (2022)

54. Y. Zhao, L. Liu, J. Han, W. Wu, G. Tong. *J Alloys and Compounds.*, **728**, 100 (2017)

55. M.G.H. Zaidi, D. Sharma, N. Bhullar, V. Agarwal, S. Alam, A. Kumar Rai, R.P. Pant, J. Nanostr. Poly. & Nanocom., **6**(4): 103 (2010).

56. M.G.H. Zaidi, P.L. Sah, S. Alam, A. K. Rai, J. Exp. Nanosci., **4** (1): 55 (2009).

57. P.Joshi, G. Bisht, S. Mehtab, M.G.H. Zaidi. *Materials Today: Proc.,* **62** (12), 6814 (2022)

58. S. Ratkovic, N. Peica, C. Thomsen, D.B Bukur, G.Boskovic .**115**,1477. (2014).

59. S. Panic, E. Kiss, G. Boskovic. *Reaction Kinetics, Mechanisms and Catalysis.*, **115**, 93 (2015).

Fabrication and performance evaluation of calcium bentonite-reinforced epoxy composites

V. Saxena*, U. Sharma, S. Jaiswal, P. K. Jayasawal, R. Patel

Department of Mechanical Engineering, Mahatma Jyotiba Phule, Rohilkhand University, Bareilly (U.P.), 243001 India

In this study, bentonite-reinforced epoxy composites (ECs) were fabricated from different epoxy resins using a common amine functional hardener**.** Composite material is fabricated by two methods. One consists of epoxy (poly-epoxides) and hardener and the other consists of epoxy resin specimen mixed with HY 951 hardener. In the present work, composite material was fabricated by using unfilled epoxy resin and calcium bentonite-filled epoxy resin mixed with HY-951 hardener. ECs are known for their low cost, good properties, exceptional strength, super adhesion and good heat and weight resistance. The present experimental study focuses on the analysis of the material characteristics of unfilled epoxy resin and calcium bentonite-filled epoxy resin. The study revealed that tensile strength of calcium bentonite-filled epoxy resin is higher than that of unfilled epoxy resin. The energy absorbed by calcium bentonite-filled epoxy resin is greater than unfilled epoxy resin when performed by Izod test.

Keywords: Epoxy resins, calcium bentonite, epoxy composites, mechanical properties

INTRODUCTION

Bentonite is a clay mineral composed of two tetrahedral silica sheets and an octahedral aluminum sheet [1]. Natural calcium bentonite contains very low exchangeable sodium and large exchangeable calcium, although the proportions vary from one bentonite to another. It has a very low concentration of calcium **(**usually ≤0.5%) and has almost no pH value difference compared to salts (sodium, calcium), thus makes a small amount of grain distiller due to its low viscosity, but unfortunately is not very effective at protein removal [2]. Generally speaking, bentonite is usually formed by the erosion of volcanic ash in the presence of water.

Bentonite is a significant type of impure clay, characterized by its aluminum phyllosilicate adsorbent properties. It usually contains montmorillonite, arranged with gibbsite layers interspersed between silica layers, forming the basic structural unit (see Fig. 1).
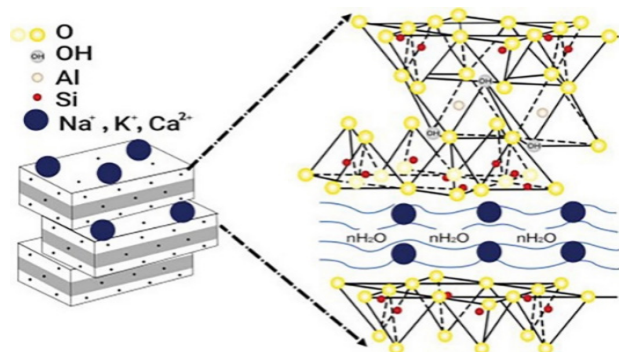
Fig. 1. Structure of bentonite

Replacements primarily occur within the octahedral layer (Mg^{2+}, Fe^{2+}) and, to a lesser extent, between the silicate layers (Al^{3+}/Si^{4+}). The composition of the clay is mainly attributed to the hydroxyl-alumino silicate structure. The crystal framework of clays is formed through the interaction between tetrahedral layers of silica and alumina octahedral sheets. Within their structure, partial exchange of Al^{3+} cations by Mg^{2+} or Fe^{2+} takes place, and this is balanced by the inclusion of metals such as Na, K, Mg, or Ca. The cation exchange capacity of the studied organoclays varies, depending on the type of organic counter-ions used [1].

In their study, Wang *et al*. conducted research on the preparation and properties of a bentonite-modified epoxy sheet molding compound. They reported that the inclusion of 1.5% BS (bentonite) in the BS/ESMC composite resulted in the highest recorded values for tensile strength, flexural strength, and impact strength, measuring 77.68 MPa, 230.75 MPa, and 108.07 MPa, respectively. Compared to the 0% bentonite/ESMC composite, the inclusion of bentonite increased the tensile strength, flexural strength, and impact strength by 24.15%, 26.56%, and 51.33%, respectively [3].

According to the study conducted by Jassim *et al*., the use of bentonite (a locally sourced raw material) in the preparation of ceramic bodies led to the formation of highly basic phases, namely mullite and cordierite, as confirmed by X-ray diffraction results [4].

* To whom all correspondence should be sent:
E-mail: vishal.saxena@mjpru.ac.in

Zimou *et al*. discovered that under pore water pressure conditions, the cyclic resistance of grouted specimens consisting solely of epoxy resin was found to be negligible.

However, the incorporation of 2.5% and 5% bentonite led to a significant increase in the cyclic strength of most of the grouted specimens [5].

In their investigation, T. Benelli *et al*. studied the preparation of two distinct organoclays obtained by modifying natural bentonite with nitrogen-based organic compounds, specifically BFTDA and APUA. These organoclays were subsequently utilized in the preparation of epoxy resin-based nanocomposites. The results showed that the incorporation of nanofillers did not have any adverse impact on the mechanical properties of the obtained nanocomposites [6].

Rubehghani *et al*. discovered that the energy absorption resulting from ballistic impact and the extent of damage were superior in composites containing cellulosic fibers compared to those with mineral fibers. The highest absorbed energy of ballistic impact (60.7 J) and the smallest damaged area (10.7 cm^2) were achieved when the composite included the highest concentration of cellulosic fibers (0.5%) and nano-bentonite (0.2%) [7]. In their research, Arif *et al*. examined the influence of BT (presumably bentonite) on the microstructure and physical behavior of SCs (likely referring to a specific material or composite). The results indicated that SCs exhibited a porous morphology, and the electrical percolation threshold was observed at 1.0 wt.% of BT. Additionally, the density and hydrophobicity of SCs increased progressively, with the highest values recorded at 2.0 wt.% of BT [8].

The study conducted by Jaidi *et al*. presents an eco-friendly approach for dispersing MWCNTs (multi-walled carbon nanotubes) into epoxy with the assistance of SCC (self-compacting concrete). This method led to the creation of CECs (carbon nanotube-epoxy composites) with enhanced dispersion and improved physical properties [9].

Jaidi *et al*. conducted a study on the wear behavior of EFNCs (presumably epoxy-ferrite nano-composites) and observed that it increased with the particle size of ferrite nanoparticles across all combinations of hydraulic end load and disc speeds [10].In their research, Jaidi *et al*. investigated the impact of PMMA (poly (methyl methacrylate)) mass uptake on various properties of E/PMMA blends. They found that PMMA mass uptake led to significant improvements in compression strength and resistance against thermo-oxidation. However, it resulted in a simultaneous decrease in Rockwell hardness (R scale), Charpy impact, and tensile strength of the E/PMMA blends. Furthermore, the incorporation of PMMA increased the thermo-oxidative stability, thermal properties, and char yield of all E/PMMA blends studied [11].

The researchers characterized the network structure of bentonite in both deionized water and salt water with calcium ions. The study found that the stability of the structure exhibited an initial increase followed by a decrease as the concentration of calcium ions increased. In deionized water, platelets were formed in an E-F mode, which then developed into E-E associations and denser aggregates with the gradual rise in calcium ion concentration. Moreover, the size of the network structure initially increased but subsequently slightly decreased. The findings of this study can serve as a useful guideline for controlling clay minerals in flotation processes [12].

MATERIAL AND METHOD

Materials

CY-230 epoxy resins, hardener HY-951, epoxy resin specimen, bentonite powder. The epoxy resins used for fabrication of composite have a density of 1.2 g/cm^3 and epoxy equivalent of 500 g/eq epoxy, respectively, whereas the density of hardener of HY 951 is 1.19 g/cm^3. Further, for the fabrication of the composite material a suitable particle size of bentonite powder is taken ranging from 0.8 μm to 2000 μm.

Fabrication of EC

Fabrication of ECs includes two types of casting. One consists of epoxy and hardener and the other consists of epoxy resin specimen mixed with HY-951 hardener.

Calculations

The calculation below gives the composition of material by first calculating its volume as 230.01 cm^3 using the dimension of length, breadth, and height. The density of the material is then calculated as 1.15 g/cm^3, which is used to find its mass as 264.51 g. subtracting the mass of 0.5% ferrite (1.32 g) and 9% hardener (21.05 g) gives the mass of the remaining epoxy as242.14 g.

Thus, the final composite of the material consists of 242.14g of epoxy resin, 21.05 g of hardener, and 1.32 g of ferrite.

Volume = L×B×H = 10.2×20.5×1.1 = 230.01 cm^3, density = M/V, therefore M = V×d =230.01×1.15 =264.51g, 0.5% ferrite 1.32 g, remaining volume = 264.51- 1.32 = 263.19 g, 9% hardener 21.05 g. Thus, the remaining epoxy = 263.19-21.05 = 242.14 g; the composition becomes:

epoxy resin - 242.14 g, hardener - 21.05 g and ferrite - 1.32 g.

Fabrication of epoxy resin specimen

First, we take the mould and pour the decided quantity of epoxy resin inside the mould and fill it with the given quantity and then pour the given quantity of hardener inside the mould. And then we heat the material for 1 hour at a temperature of 100 degrees Celsius.

After heating the material at 100 degrees Celsius for one hour, we take the material and stir it here for some time so that the material mixes itself homogeneously towards the whole composition.

The preparation process involves stirring and mixing the material at a specific temperature, after which it is poured into the mould and left undisturbed for a minimum of 24 hours. During this period, the material solidifies, allowing the specimen to be removed from the mould. Based on the calculations provided, the required amount of epoxy resin for the specimen is 242.14 g, while the necessary quantity of hardener is 21.05 g.

Fabrication of ECs material

First, we take the mould and pour the decided quantity of epoxy resin inside the mould and fill the mould with the given quantity and then pour the given quantity of hardener inside the mould. And then we heat the material for 1 hour at a temperature of 100 degree Celsius.

After heating the material at 100 degrees Celsius for one hour, we take the material and stir it here for some time so that the material mixes itself homogeneously towards the whole composition, now we stir it well so that its temperature falls. We stir it till the temperature reaches 45 degrees. And now we take the HY 951 hardener and put it inside the resin material and stir it well so that it mixes homogeneously. And then we pour the material inside the mould.

Araldite CY-230 is a liquid solvent-free epoxy resin. The treatment takes place at atmospheric pressure and at room temperature after adding the hardener. Usually, there is little healing of the contractions which can reduce more because of this bio-particles, China clay, etc. The addition of fillers is such that resin can be easily discolored. Mechanical, electrical properties and excellent

resistance to chemical attack and atmosphere of fully cured composite are outstanding.

Fig. 2. Prepared mould
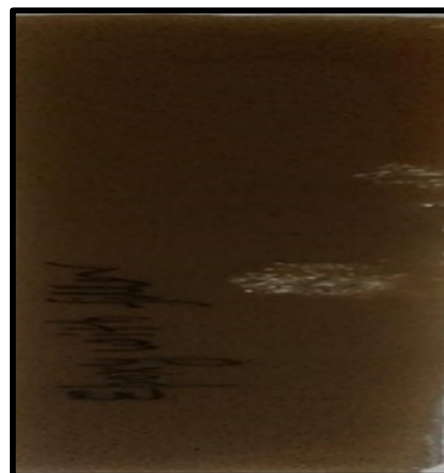
Fig. 3. Composite of epoxy resins and bentonite hardener

CY-230 epoxy resins (poly-epoxides)

Table 1 shows the physical and chemical properties of CY-230 rubber. It is a plastic condensation product bisphenol-A and epichlorohydrin, yellow-brown, odorless, tasteless and non-toxic. It has a viscosity of 1350-2000 mPa * s and specific gravity 1.1-1.2 g / cm^3 at 25 ° C. Epoxy content 4.20-4.35 eq / kg, flash point 160°. The resin appears to be a clear liquid.

Table 1. Physical and chemical properties of CY-230

Resin (Araldite CY-230)			
Physical properties		Yellow-brown, odorless, tasteless and completely nontoxic	
Chemical properties		Plasticized condensation product of bisphenol-A and epichlorohydrin.	
Viscosity at 25°C	ISO 2555	mPa*s	1350-2000
Specific gravity at 25°C	ISO 1675	g/cm³	1.1- 1.2
Appearance	Visual		Clear liquid
Epoxy content	ISO 3001	Eq/kg	4.20 -4.35
Flash point	DIN 51758	°C	160

Table 2. Chemical properties of HY- 951

Viscosity at 25°C	ISO 12058	mPa*s	10-20
Specific Gravity at 20°C	ISO 1675	g/cm³	0.98
Appearance	Visual		Clear liquid
Flash point	DIN 51758	°C	110
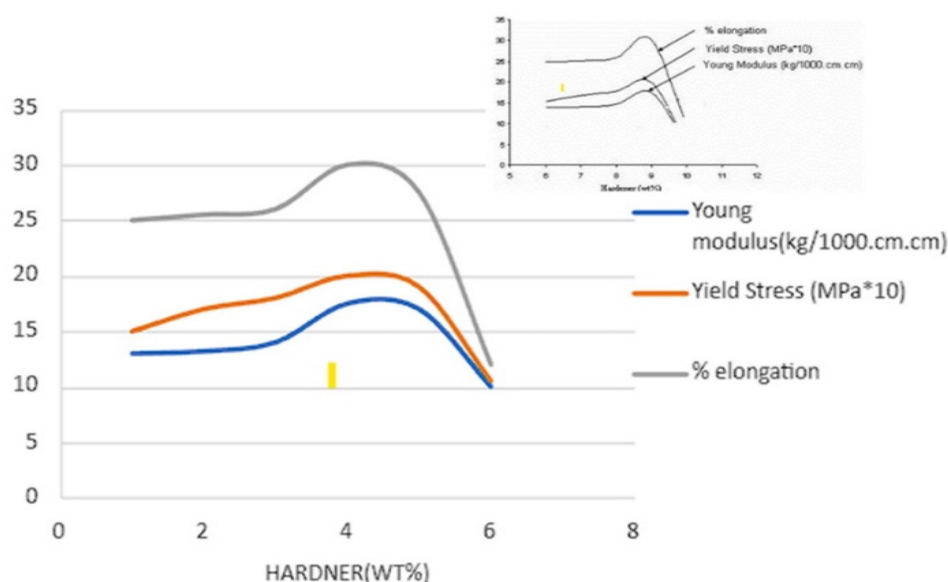
Fig. 4. Effect of wt.% of hardener HY951 on mechanical properties

Hardener HY-951

Araldite HY951 is an unfilled epoxy casting resin system known for its outstanding electrical properties and its ability to accommodate a high number of fillers.

Table 2 outlines the chemical properties of HY-951. The viscosity at 25°C, as determined by the ISO 12058 standard, ranges from 10 to 20 MPa*s. The specific gravity at 20°C, measured according to the ISO1675 standard, is 0.98 g/cm³. HY-951 appears as a clear liquid, as determined by visual inspection. The flash point of HY-951, measured using the DIN 51758 standard, is 110°.

RESULTS AND DISCUSSION

Hardener HY-951

Figure 4 illustrates the correlation between the concentration of HY-951 and three mechanical properties: Young's modulus, yield stress, and % elongation. The graph shows the change in these properties as the concentration of HY-951 varies, with maximum & minimum values of 30 & 12 for % elongation, 20 & 11 MPa*10 for yield stress, & 17.5 &10 Kg/1000*cm^2 for Young's modulus, respectively.

Results of unfilled epoxy resin tension test

Ultimate tensile strength (UTS) is a measure of the stress applied to a sample up to failure (fracture). provides important information on tensile properties, including yield point, tensile strength, and yield strength. The tensile strength of unfilled epoxy and calcium bentonite-filled epoxy composites was determined with a 100 kn universal testing machine of the transfer control type at a constant speed of 0.5 mm/min. Tensile stress-strain curves of unfilled epoxy resin (10% by weight HY-951 hardener and CY-230 resin) and calcium bentonite composite material provides some insight about material characteristics.

It is embedded in Fig. 5 that the material breaks at 12.5% strain and 0.045 KN/mm² stress with respect to strain. Its stress is greater than that of epoxy with hardener [13].

Maximum force: 4.815 kN; displacement at maximum force: 6.210 mm; maximum displacement: 7.480 mm; tensile strength: 0.048 kN/mm²; elongation: 5.000 %; reduction in area: 0.100 %.
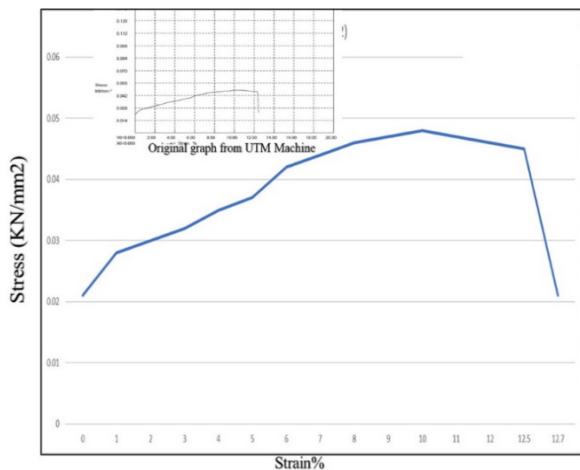
Fig. 5. Stress-strain graph of unfilled epoxy resin

Results of bentonite-filled epoxy resin tension test

In the tension test of epoxy resin filled with bentonite, the material's breaking point was observed to increase compared to the unfilled epoxy resin, making it suitable for high-tension applications. Figure 6 illustrates the behavior of the bentonite-filled epoxy, showing a breaking point at 8.20% strain and 53 MPa stress concerning strain.

Our research paper identified that the maximum tensile strength of the bentonite-filled epoxy was achieved at 1.5% bentonite content, measuring 77.68 MPa.

This represented a significant increase of 24.15% compared to the unmodified epoxy. However, in our specific study, the tensile strength

was determined to be 53 MPa for the given composition [3]. Its stress is greater than epoxy $CaCO_3$nano cubes/epoxy composites and $CaCO_3$ nanorods/epoxy composites with hardener [14].
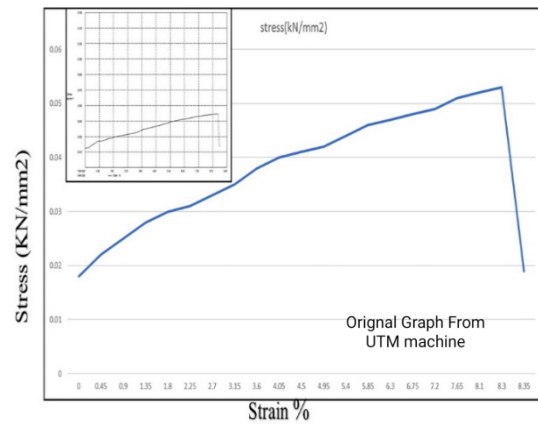
Fig. 6. Stress-strain graph of filled epoxy resin

Maximum force: 5.215 kN; displacement at maximum force: 8.420 mm; max. Displacement: 8.530 mm; tensile strength: 0.052 kn/mm²; elongation: 10.000 %; reduction in area: 1.000 %.

Impact test

The impact strength of epoxy resin and its composite specimens was tested using an impact testing machine. The apparatus consists of a pendulum whose mass is known and whose length falls from a certain height and strikes material samples drawn. The difference in energy transferred to the material can be determined by comparison of the height of the attacker before and after the break (energy absorbed in the punch). Therefore, Table 3 shows that calcium bentonite-filled epoxy has higher impact strength compared to calcium bentonite filled epoxy, clear epoxy. For example, an unprescribed epoxy resin has energy of 2.5 joules, calcium bentonite-filled epoxy. Resin energy absorbed is 3.8 joules. Therefore, we see that the energy absorption of epoxy resin filled with calcium bentonite increases.

Therefore, calcium bentonite filled with epoxy can be used in applications where strength is more important.

Table. 3. Energy absorbed by the specimen in Joule during Izod test

Unfilled Epoxy Resin	2.5
Calcium Bentonite filled Epoxy Resin	3.8

CONCLUSION

Bentonite composite is made with the help of

243

CY-230 epoxy resins (poly-epoxides), hardener HY-951 and bentonite powder. We made two types of composites- unfilled epoxy resin and calcium bentonite filled epoxy resin. We found that the tensile strength test and energy storage test is best performed by the bentonite-filled epoxy resin. Tensile strength test was performed on calcium bentonite filled epoxy resin and energy absorbed by specimen during Izod test was determined. Same test was performed on the unfilled epoxy resin and energy absorbed by specimen during Izod test was determined.

So, we conclude that calcium bentonite-filled epoxy resin is best at maximum tensile stress and toughness.

REFERENCES

1. P. Pourhakkak, M. Taghizadeh, A. Taghizadeh, M. Ghaedi, Adsorbent, Elsevier, Payame Noor University, Tehran, Iran, **33**, 71 (2021).
2. J. Moreno, R. Peinado, *Enolog. Chem.*, **27**, 323 (2012).
3. J. Wang, Z. Deng, Z. Huang, Z. Li, J. Yue, *e-Poly.,***21**, 309 (2021).
4. K. A. Jassim, M. A. N. Thejeel, E. M. T. Salman, S. H. Mahdi. *Engy. Proceed.*, **119**, 670 (2017).
5. C. A. Anagnostopoulos, T. Chrysanidis, M. Zimou, M. Rapo. *J. Appl. Sci. Engin. Technol.*, **16**, 15 (2019).
6. T. Benelli, E. D. Angelo, L. Mazzocchetti, F. Saraga, L. Sambria, M. C. Franchinia, L. Giorginia. *AIP Conf.Proceed.,***1736**, 020142 (2016).
7. A. Keshaavarz, H. J. Torshizi, F. Mohamad Kazemi, M. Koosha, *Iran. J. Wood Paper Sci. Res.,***33**, 347 (2018).
8. M. Arif, S. Mehtab, A. Misra, M. G. H. Zaidi, *Mater. Today Proceed.*, **47**, 4210 (2021).
9. M. G. H. Zaidi, S. K. Joshi, M. Kumar, D. Sharma, A. Kumar, S. Alam, P. L. Sah, *Carbon Lett.*, **14**, 218 (2013).
10. M. G. H. Zaidi, P. L. Sah, S. Alam, A. K. Rai. *J. Exp. Nanosci.*, **4**, 55 (2009).
11. M. G. H. Zaidi, N. Bhullar, V. P. Singh, P. L. Sah, S. Alam, R. Singh. *J. Appl. Polymer Sci.*, **103**, 303 (2007).
12. S. Du, T. Peng, S. Song, G. Gu, Y. Wang. *Minerals Engine.,* **189**, 107724 (2022).
13. Yohanes, I. Sidharta, A. S. Pramono, K. Varian. IOP *Conf. Ser. Mater. Sci. Eng.*, **12**, 1034012162 (2021).
14. G. Yang, Y. J. Heo, S. J. Park. *Processes,***7**, 178 (2019).
15. K. J. Narayana, R. G. Burela, *Mater. Today, Proceed.*, **5**, 5580 (2018).
16. M. K. Egbo. *J. King Saud Univ. – Eng. Sci.,***33**, 557 (2021).
17. Q. U. Ain, U. Rasheed, M. Yaseen, H. Zhang, Z. Tong. *J. Hazard. Mater.*, **397**, 122758 (2020).
18. A. B. M. Supian, M. Jawaid, B. Rashid, H. Fouad, N. Saba, H. N. Dhakal, R. Khiari, *J. Mater. Res. Technol.,***15**, 1330 (2021).
19. S. G. Ranjbar, G. Roudini, F. Barahuie, *J. Engy. Stor.*, **27**, 101168 (2020).
20. D. K. Rajak, D. D. Pagar, R. Kumar, C. I. Pruncu, *J. Mater. Res. Tech.*, **8**, 6354 (2019).
21. J. He, J. Shi, X. Cao, Y. Hu. *Adv. Civil Engin.*, **23**, 1 (2018).
22. F. L. Jin, X. Li, S. J. Park. *J. Ind. Engin. Chem.*, **29**, 1 (2015).

Performance of rocket nozzle with polymer material and its numerical analysis

V. Saxena[*], K. K. Soni, D. Kumar, P. Patel, B. P. Singh

Mahatma Jyotiba Phule Rohilkhand University, Bareilly, 243001, India

Polymer material modeling is an effective tool for optimizing rocket nozzle design and improving its performance. It provides a means of predicting the behavior of the nozzle under different operating conditions, enabling the evaluation of different polymer materials that can be used in nozzle construction. It also allows for the optimization of nozzle design through the analysis of various parameters, such as shape, thickness, and material composition. Polyimide and polyether ether ketone (PEEK) are excellent materials for use in modeling rocket nozzle design and manufacture. The use of these materials can result in high-quality rocket nozzles that can withstand the rigors of spaceflight. In this study, we will study the rocket nozzle performance by using ANSYS software with polymer materials.

INTRODUCTION

Rocket nozzles are key components of rockets, as they regulate the flow of exhaust gases during propulsion. The creation of a high-quality rocket nozzle requires the use of materials that can withstand high temperatures and pressures. A nozzle is a tool used to simultaneously manipulate a fluid flow's direction and properties. When it leaves or enters a closed chamber or conduit, it is generally employed to boost velocity [1]. A nozzle is a tool used to change the properties of a fluid flow as it leaves (or enters) a closed chamber, notably to enhance velocity. In order to direct or modify the flow of a fluid, nozzles are frequently pipes or tubes with different cross-sections (liquid or gas). Nozzles are widely employed to adjust the stream's pressure, mass, direction, speed, and/or other characteristics. The energy from burning fuel combined with the inducted air in a jet exhaust generates a net thrust. This heated air is sent into a propelling nozzle at high speed, greatly boosting its kinetic energy. A nozzle's main function is to increase a fluid's kinetic energy while decreasing its pressure and internal energy. Nozzles are also used to increase the velocity of fluid and maximize the thrust. When the mixture of fuel and propellant is burned in a combustion chamber, nozzles are typically pipes or tubes with various cross-sectional areas that can be used to adjust fluid flow. These devices are regularly employed to control flow, speed, direction, and mass [2].

Polymer materials offer several advantages such as flexibility, durability, and minimal thermal expansion which make them ideal for designing high-performance nozzles. These simulations exhaust gases through nozzle geometries and variations in polymer composition, enabling precise optimization of nozzle design to achieve maximum thrust at different altitudes and velocities. Polyimide is an excellent material for use in the fabrication of nozzle components that require a high level of durability and resistance to high temperatures. PEEK, on the other hand, can be used in the manufacture of nozzle components that require a high level of mechanical and thermal properties [3-5].

EXPERIMENTAL

Numerical consideration and methodology

The hyperbolic nature of the Euler equations in supersonic flow means that only upstream conditions can affect the flow. The nozzle flow field in this situation can be calculated using the MOC (method of characteristics). This technique is most frequently used in rocket nozzles to generate nozzle shapes and assess loads and performances. Furthermore, wave-free parallel flow in the test section at the specified Mach number is crucial for supersonic convergent diverging nozzle. [6, 7]. The shortest length L for shock-free, isentropic flow is depicted. If the contour is created within a length smaller than L, shocks will form inside the nozzle.

Computational model

This issue examines the air and combustible gas flow along the turbojet engine's inlet and exhaust passages. Convergent exhaust nozzles and divergent inlets are used. The analysis also displays the mole fractions of each species. Define material attributes and enable physical modeling.

* To whom all correspondence should be sent:
E-mail: vishal.saxena@mjpru.ac.in

1. Specify the domain as being two-dimensional, and leave the default (segregated) solver in place.

2. Turn on the k-epsilon turbulence model.

3. Enable the exchange and reaction of chemical species.

4. Make the field variable initial.

5. Enable residual plotting throughout the computation.

RESULTS AND DISCUSSION

How are nozzles designed?

To design a rocket nozzle using polyimide and PEEK, several factors are considered. These include the shape and dimensions of the nozzle, the combustion properties of the fuel used, and the environmental conditions in which the nozzle will operate. The shape and dimensions of the nozzle are crucial factors in determining the thrust and efficiency of the propulsion system. The combustion properties of the fuel used will determine the temperature and pressure in the combustion chamber, which will affect the durability of the nozzle. The environmental conditions in which the nozzle will operate will affect the overall performance of the propulsion system [8].

There are a few variables that affect how a nozzle is designed, including the amount of thrust it should generate, exit velocity, pressure at the engine's exit and mass flow rate. To comprehend the phenomenon of subsonic flow through a rocket engine nozzle at various divergence angles, a CFD analysis of the nozzle was performed. The governing equations were solved using the finite-volume approach in the ANSYS fluent® program employing a two-dimensional axis-symmetric model for the analysis. Various techniques, including the analytical method and experimental methods including prototypes, can be used to solve engineering problems [9]. It's a really challenging and complicated analytical process. Here, analysis was done on divergent-angle nozzles, resulting in changes to the external diameters 32, 34, 40, 44, 50, and 55.

CFD have shown to be a useful technique for getting reliable solution over mentioned restrictions. The trend of several flow parameters is also studied in this work. After that, when the flow begins to diverge, it isentropic and expands until it achieves supersonic velocity, but the ratio of the area at the neck to the area at the exit determines the Mach number.

When the gases expand in the diverging portion, their pressure and temperature also decrease [10]. The expanding process led to this. The quantity of

thrust that should be produced, the engine's exit velocity, the pressure there, and the engine's mass flow rate are all factors that affect the nozzle design. The speed of sound at exit depends on exit temperature. Every one of these flow variables is impacted by the rocket design. A rocket is bulky; a nozzle is little [11].

Software used

The programme we employed to create several nozzle types is known as ANSYS Fluent 2021 R1. There are five components to it: geometry, mesh, setup, solution, and result. The geometry section defines the nozzle's dimensions in 2D before converting them to 3D. While working with geometry in the past, extra caution should be used since if it is not appropriately defined, we won't find the needed solutions.

1. To ensure proper heat distribution, the 3D nozzle is further separated into pieces in the mesh section.

2. We include various materials and boundary conditions in the setup and solution parts. Then computations are performed and iterations are performed.

3. The results section, as the name suggests, has a number of contours, including pressure, velocity, kinetic energy, temperature, etc.

Plotted are the key points: The necessary dimensions must first be created using the provided coordinate points. Producing edges: To construct edges, join these focal points together, we must be considering how important it is to the process, make sure the appropriate key points are connected with one another. Creating faces: The generated 2D figure does not provide enough thickness to be transformed into a 3D figure.

Procedure for analysis

Meshing: We now close the geometry part and launch the mesh section. We divide the figure into various components in the mesh portion, and then accurately size & mesh each piece [12]. Put together the required mesh (Fig. 3).

Applying boundary conditions: We define the boundary conditions specified above, such as temperature, inlet pressure, outlet pressure, and viscosity set to Sutherland technique, in the setup and solution phase because results are precise and plausible.

We will turn on the energy calculations, choose air as the material, and determine its ideal density [13]. Finally, we'll perform calculations and iterations (Figs. 4 and 5).
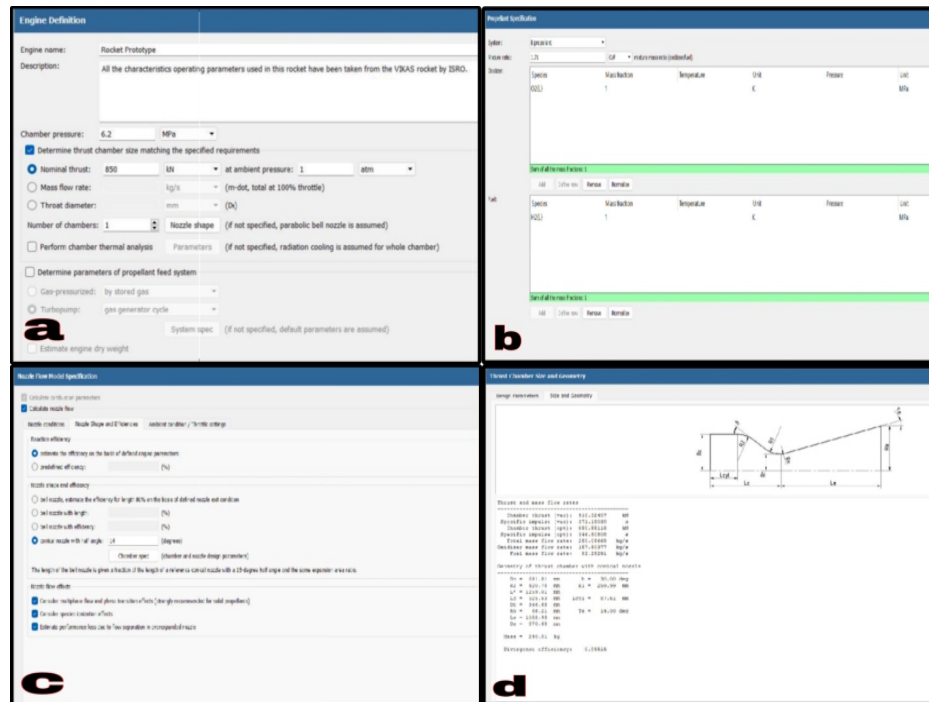
Fig. 1.(a) designing of rocket nozzle using engine definition, (b) propellant specification, (c) nozzle flow model specifications, (d) size and geometry output.
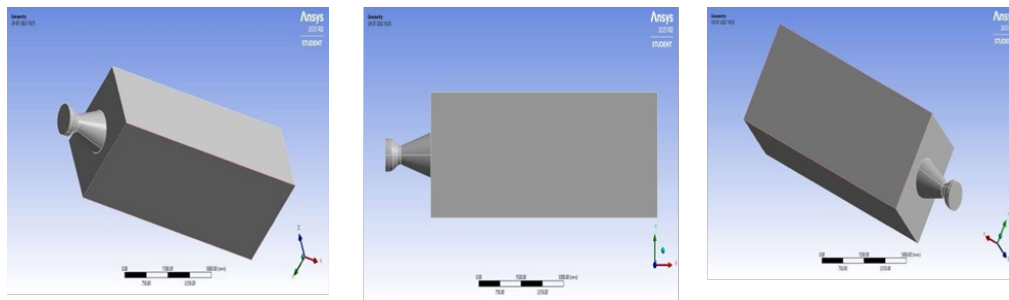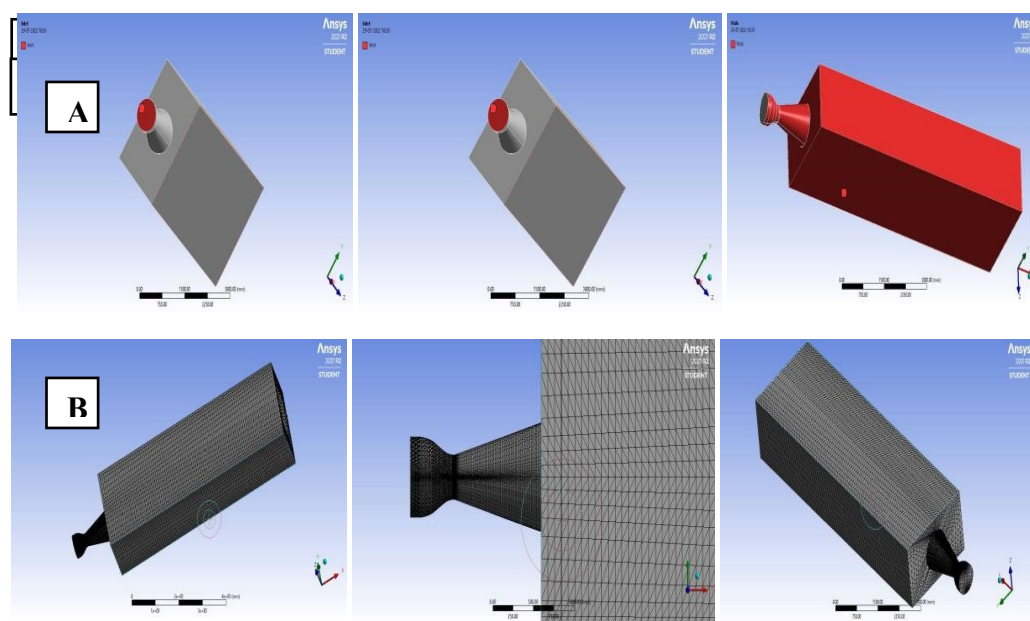

Fig. 2. Designing of nozzle

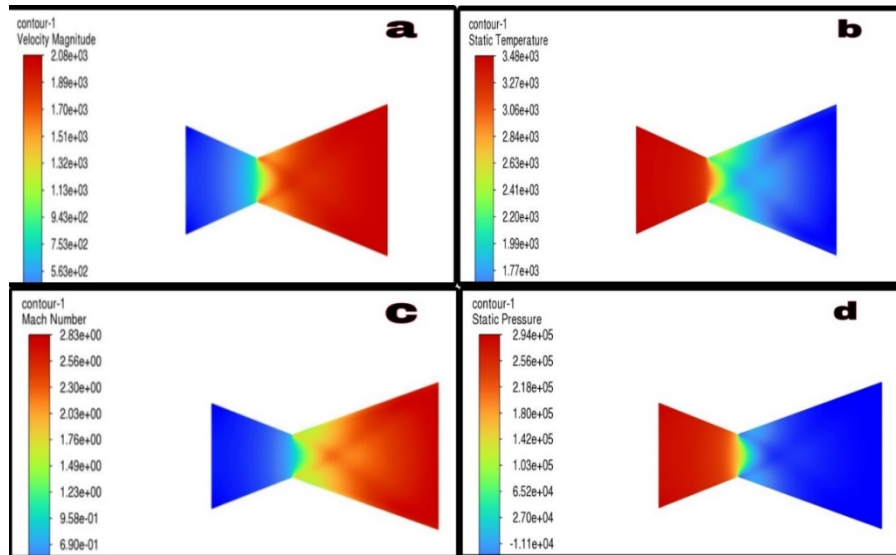**Fig. 3.** (A) Named selection in ANSYS mechanical (B) Meshing in ANSYS mechanical

247

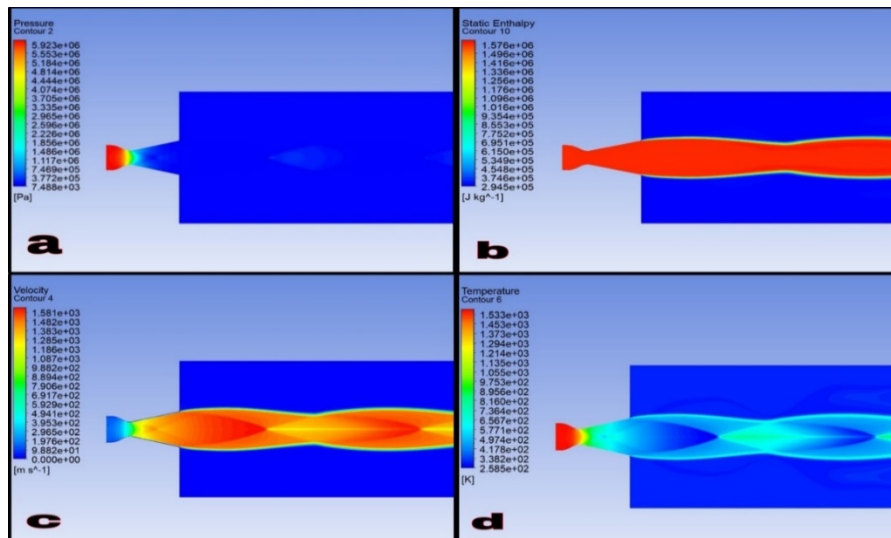**Fig.4.**(a) velocity distribution, (b) temperature distribution, (c) mach number variation, (d) static pressure contour

Fig. 5.(a) Pressure contours in far field, (b) Enthalpy contours in far field, (c) Velocity contours in far field, (d) Temperature contours in far field.

Table 1. Results of the conical conventional nozzle

Nozzle type	Average velocity
Conical nozzle	906e+02
Bell nozzle	882e+02
Dual bell nozzle	917e+02

Table 2. Dimensions and boundary conditions for the bell nozzle

Nozzle type	Exit velocity
Conical nozzle	2.18e+05
Bell nozzle	2.56e+05
Dual bell nozzle	2.70e+04

ANSYS software does the CFD analysis of various nozzles to determine the mass's temperature, velocity, and other characteristics as it passes through various-sized nozzles, as well as forms. We consider fluid to be compressible, so the energy approach is activated as well as calculations based on density. The K-epsilon-2 equation model is chosen. The turbulent kinetic energy and turbulent dissipation rate are both selected to be second-order upwind [14].

CONCLUSION

In this review, we have observed that polymer material modeling and simulation is critical in the design of rocket nozzles. Accurate modeling of the thermal behavior and mechanical properties of polymers under extreme conditions is crucial in ensuring optimal performance of rocket nozzles. Multi-scale modeling approaches that account for the polymer's microstructure, chemical composition,

and mechanical properties are required to accurately model polymer materials. Advances in polymer material modeling and simulation will lead to the development of more efficient and reliable rocket propulsion systems that can take us to new heights in space exploration. Future work on the design, analysis and simulation of the rocket propulsion system would be CFD calculations, heat transfer calculations and material choices for the nozzle.

REFERENCES

1. A. T. Bolson, *J. Fluids Eng.,* **96**(2), 21 (1974).
2. B. P. Krushna, *Int. J. Res. Eng. Technol.,* **2** (3), 412 (2013).
3. T. Benson, *Nat. Aeron. Space Admin.* (2013).
4. G.V.R. Rao, *J. Jet Propul.,* **28** (6), 377 (1958).
5. J. M. Farley, C. E. Campbell, *Nat. Aeron. Space Admin.* (1960).
6. P. Sajesh, M. Sajesh, *Int. J. Eng. Sci.*, **2** (2),196 (2013).
7.   K. Kuo, R. Houim, in: 47th AIAA/ASME/SAE /ASEE. *Joint Propul. Conf. Exhibit.,* **23** (5), 5608 (2011).
8. Davydenko, *Aerosp. Sci. Technol.,***11** (5), 55 (2007).
9. Hagemann, *J. Propul. Power,* **14**(3), 620(1998).
10. M. Frey, Hageman, *J. Propul. Power,* **15**(2), 225 (1999).
11. Hagemann, *Adv. Nozzle Concepts Future Rocket Eng. Appl.*, **4** (5), 3 (2002).
12. D. R. Bartz, *Adv. Heat Transfer*, **2** (1), 43 (1965).
13. R. A. Signorelli, J. R. Johnston. *Nat. Aeron. Space Admin.* 0050 (1963).
14. Shaffer, T. Peter, *Therm. Shock Resis. Refract. Ind. Res.*, **5**(5),36 (1963).

An overview of macrolactone in polymer synthesis

M. Tiwari, A. K. Srivastava, V. K. Mishra*

Department of Basic Sciences and Humanities, Pranveer Singh Institute of Technology Kanpur-209305, India

The article uniquely describes the ring-opening polymerization (ROP) of macrolactones. Nature is the source of information, naturally occurring macrolides could assist in monomers design and synthesis. The available approaches in the synthesis of medium-sized amphidinolides Qalong with their retrosynthetic analysis are presented. The analogues of naturally occurring biologically relevant macrolactone could be the ideal monomers for chiral polyesters for various applications.

Keywords: Macrolactones, macrolides, amphidinolides, polyolefins, polyester

INTRODUCTION

The polyolefins demand remained at 146.99 million tons in 2020 and is expected to reach at 250.43 million Tons by 2030.The polyolefins business is highly dependent on the petroleum industry. Polyolefins are not biodegradable and cause a major issue to the environment, especially to marine life [1]. Therefore, an alternative to polyolefins is needed. Two approaches could be used in the replacement of polyolefins. First, by replacing the monomer source by finding a way to monomers from feedstocks. In this regard, biopolyethylene has already been developed [2]. The other approach could be to find the way in which the properties and cost of existing polymers match the production of renewable sources. To obtain high molecular weight polymer by polycondensation reactions is challenging. The material of high molecular weight obtained from lactones *via* ring-opening polymerization (ROP) showed polyethylene-like properties [3]. In 2010, polyethylene-like polyesters have been reported through methoxy carbonylation of unsaturated fats followed by polycondensation [4]. The scope of polymers is steadily increasing in biomedical applications [5].

The polyolefins demand remained at 146.99 million tons in 2020 and is expected to reach 250.43 million tons by 2030. The polyolefins business is highly dependent on the petroleum industry. Polyolefins are not biodegradable and cause a major issue to the environment, especially to marine life [1]. Therefore, an alternative to polyolefins is needed. Two approaches could be used in the replacement of polyolefins. First, by replacing the monomer source by finding a way to monomers from feedstocks. In this regard, biopolyethylene has already been developed [2]. The other approach could be to find the way in which the properties and cost of existing polymers match the production of renewable sources. To obtain high molecular weight polymer by polycondensation reactions is challenging. The material of high molecular weight obtained from lactones via Ring-opening polymerization (ROP) showed polyethylene-like properties [3]. In 2010, polyethylene-like polyesters have been reported through methoxy carbonylation of unsaturated fats followed by polycondensation [4]. The scope of polymers is steadily increasing in biomedical applications [5] in the body. In implants, the material should not degrade at all inside the body, ultrahigh molecular weight polyethylene is used in implants because of very high relative resistance. The implant lifetime is quite high, though there are issues in wear resistance that needs improvement [6]. Radiation postprocessing has shown in the improvement of material [7]. Aliphatic polyesters are broadly used in biomedical and drug applications since they keep up with suitable synthetic, thermal, and mechanical properties and are often biodegradable and biocompatible [8]. There are various lactones which have been polymerized to get the polymers for various applications. And the optically active polymers keep a place in macromolecules because of their diverse applications. The optical rotation of polymer obtained from (R)-(+)-2-methyl-2-ethyl-3-propiothiolactone showed an increase in the optical rotation compared to small molecules, suggesting polymers have a rigid structure in the chain [9]. For intravenous applications, the polymer particles are specially adequately little (around 100 nm), and a tight safeguarding layer of poly(ethylene glycol)

* To whom all correspondence should be sent:
E-mail: vivekcbmr@gmail.com

ended up avoiding immunoresponse ("secrecy particles") and to extended circulation time [10]. There are various methods of ring opening polymerization of macrolactones.

Enzymatic Ring Opening Polymerization of Macrolactones

The enzyme-mediated production of polymers *via* ring lactone ring-opening polymerization is gaining an impetus. The enzymatic reactions are green reactions and provide a synthetically versatile tool for regio- and enantioselective polymers. They produce high selectivity and are environmentally friendly. The enzymatic reactions usually take place in water. The use of organic solvent offers various advantages over the aqueous media, it increases the thermal stability of enzymes and increases solubility of a range of substrates. And does not require adjustment of pH [11]. The direct enzymatic polymerization of emulsions comprising lactone nanodroplets addresses a new and helpful pathway for the combination of biodegradable polymer nanoparticles, where the compound structure and sub-atomic weight can differ in a specifically. Oligoesters totally end-covered with an alkene or diene gathering can likewise be ready by this strategy. These structure blocks broaden polyester application as they permit to grant further developed biodegradability to both siloxane and gum chemistry [12].
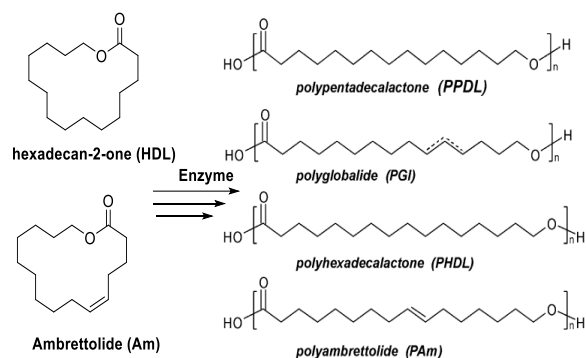
Figure 1. Enzymatic polymerization of macrolactones.

The polymers obtained from pentadecalactone, hexadecalactone, and their unsaturated analogues ambrettolide and globalide are potential biomaterials. By enzymatic ring-opening polymerization, these monomers can lead to high molecular weight materials. All these polymers are nontoxic estimated by a MTT measure for metabolic cell movement of a 3T3 mouse fibroblast cell line. The polymers are exceptionally translucent with a melting point of around 95 °C for the saturated polymers and a little lower for the unsaturated polymers (46-55 °C). It

seems polymers are stable once generated because degradation was not observed under hydrolytic and enzymatic conditions. The unsaturated polymers could be crosslinked under the melt to obtain fully amorphous transparent material [13]. Albertsson *et al*. have reported enzymes as catalysed miniemulsion polymerization of PDL and HDL [14].

Acid Catalyzed Ring Opening Polymerization:

The polymer micro-nanoparticles dispersion in the water called polymer latexes, is an example of sustainable polymer science since water is safe and environmentally benign solvent. It is easy to process latexes for various applications. They are synthesized by free radical polymerization. Nonetheless, somewhat recently the development of miniemulsion polymerization has stretched out the creation of latexes to polymers which might be incorporated by polycondensation or catalytic polymerization processes prompting new kinds of polymer latexes.

A few endeavors have been conveyed to combine polyester latexes by a buildup of hydrophobic alcohols and dicarboxylic acids. In those works, Landfester and others utilized dodecylbenzene sulphonic acid (DBSA) which went about as impetuses and surfactant. The miniemulsion polymerization of macrolactones involving natural acids follows ring opening polymerization (ROP) [15]. It has been observed that polymerization at 80 ºC leads to full transformations and relatively lower polymerization time. This polymerization results in high molecular weight compounds (>10.000 g/mol). Increasing the strength of acid also increases the catalytic effect. The acid-catalyzed miniemulsion polymerization of macrolactones follows a condensation mechanism limiting the molecular weight of polymer latex [16].

ORGANOCATALYZED RING OPENING POLYMERIZATION

Organocatalyzed ring-opening polymerization of little and medium ring-sized cyclic esters, for instance, lactides, valerolactone, or caprolactone have been considered while macrocyclic lactones (macrolactones) polymerization is still in its earliest phases of studies. Metal-catalyzed ROP of lactones is an especially effective strategy to create polymers of high molecular weight, low polydispersity, and with controlled microstructure [17]. The work on lactide and ε-caprolactone has provided a mechanistic understanding of ROP [18]. The main driving force of ROP proceeding is the ring strain. Thusly, as the ring strain diminishes with expanding lactone size decreases ROP. Exceptionally productive metal-catalyzed ROP of macrolactones was reported by

Meulen *et al.* [19]. The avocation behind this is that the ROP part of these macrolactones differs from the approach to the acting of pretty much nothing or medium size cyclic lactones. Generally, the assistance of the ring sort of little lactone monomers coordinates the primary stimulus for ring-opening polymerization. In any case, the huge ring size of macrolactones is connected with low ring strain, and in this manner, polymerization reactions are driven generally by entropy. This is the explanation, a set number of catalysts have been strong for the mix of polyesters from macrolactones when appeared differently in relation to little lactones, for instance, ε-caprolactone what's more, consequently, two or three reports have been dispersed state of the art about the association of polyesters from gigantic lactones, for instance, ω-pentadecalactone (PDL) or 16-hexadecalactone (HDL)[20]. The ring-opening polymerization of macrolactones (C15-C23) empowers the creation of long-chain aliphatic polyesters which are glasslike polymers with liquefying temperatures going from 98-106 °C. The polymerization of ω-pentadecalactone (C15), nonadecalactone (C19) and tricosalactone (C23) was investigated by Myers *et al.* utilizing yttrium phosphasalen catalyst [21].

Bioactive Natural Macrolactones

Among nature's creation, macrolides are versatile and exciting natural products due to their diverse biological activities such as antibiotic, cytotoxic, or antiangiogenic. Several macrolides and polyketides have been isolated from symbiotic marine dinoflagellates [22]. Many of them show potent cytotoxicity against murine lymphoma L1210 cells. The smallest macrolactones are 8-membered (octalactins-1-2) and biggest vary upto 60-membered (quinolidomicins) (Figure 2). Erythromycin (**1**) a macrolide isolated in 1952 is widely used to treat bacterial infections, and because of its safety and efficacy, it is still a preferred therapeutic agent for the treatment of respiratory infections. Apoptolidin a 20-membered macrolide, selectively induces apoptosis in rat glia cells transformed with adenovirus E1A oncogene in the presence of normal cells and inhibits the mitochondrial F_0F_1-ATPase [23]. Actin-binding marine macrocyclic lactones, and benzolactone enamides are also possessing potent antitumor activity.
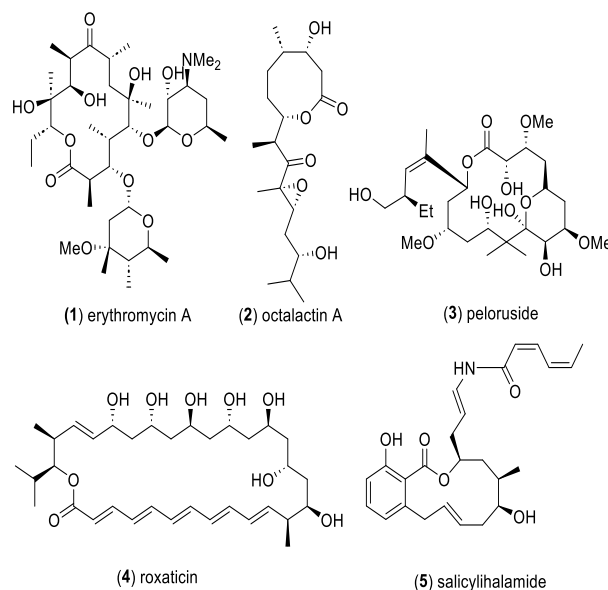
Figure 2. Examples of naturally occurring macrolactones.

A marine microorganism such as bacteria, cyanobacteria, or dinoflagellates produces toxins for their defense mechanism. That is the main source of fish and algal poisoning. Though these poisons in microgram scale can kill a person but if used in medically administered could be useful for treatment of many fatal diseases such as cancer. Many bioactive substances isolated from marine invertebrates such as sponges, tunicates, and so on have proved to be essential tools in biology for example, neurotoxins like maitotoxins helped to understand the molecular basis of cellular excitability [24]. Biologically significant secondary metabolites isolated from symbiotic marine dinoflagellates *Amphidinium* sp. called as Amphidinolides. Amp B (**6**) increased the ATPase activity of myofibrils and natural actomyosin, resulting increased in contractile responses of myofilaments. Amp H (**7**) is a novel F-actin stabilizer that covalently binds on actin [25]. It stabilizes actin similar to phalloidin (**9**) but the Amp-H-binding does not compete with phalloidin-binding to F-actin [26].

Amphidinolide W (**8**) and Q (**10**) both are 12-membered macrolides and exhibit cytotoxicity against murine lymphoma L1210 cells. Amp W is quite unique as it is the first and only macrolide in its family without an exomethylene unit.

amphidinolide B (6)

amphidinolide H (7)

amphidinolide Q (10)

amphidinolide W (8)

phalloidin (9)

Figure 3. Structures of the 12-membered amphidinolides Q (1), W (2) and the 26-membered amphidinolide H (3).

The C9-C16 moiety of amphidinolide W compares to that of C6-C15 of amp H, which was disconnected from strain Y-42, recommending that amphidinolide W might be biogenetically connected with amphidinolide H. As of late four new polyketides, amphidinins C-F have been separated from *Amphidinium* sp of dinoflagellates [27]. They showed antimicrobial activity against bacteria and/ or fungi. Amphidinin D and F are the first glycosides related to amphidinolides. Spectral data led that amphidinins C-F are 4,5-seco-analogues of amp Q [27]. Cancer is an epidemic, related to abnormal growth of tissues. There are several techniques to treat cancer such as surgery, radiotherapy, immunotherapy, chemotherapy, etc. [28]. In chemotherapy the treatment is done by the use of a pharmaceutical product. It was found that some amphidinolides exhibits very high cytotoxicity. In this article we will discuss about the synthesis, medium sized macrolactone Amphidinolide Q known so far.

SYNTHESIS OF MEDIUM SIZED CHIRAL MACROLACTONE

The structure of amphidinolide-Q was elucidated by NMR spectroscopy and could be proved by synthesis [29]. The retrosynthesis proposed by Hangyou *et al.* is outlined in Scheme-1. Amphidinolide Q (10) was disconnected at the lactone bond; *seco*-acid 11 was derived from ketone 2-3 and aldehyde 2-2 *via* condensation. The key aldehyde 12 containing four stereocenters was prepared from iodide 14 *via* Myers alkylation and

Julia coupling of sulfone 15 with aldehyde 16 could furnish iodide 14.

amphidinolide Q (10)

R = TIPS
11

12   13   14
R = MOM

TIPSO   SO₂Ph +   OBOM
15   16

Scheme 1. Retrosynthetic plan for the synthesis of Am-phidinolide Q by Hangyou *et al*.

The aldehyde obtained from alcohol (R)-2-methyl-3-((triisopropylsilyl)oxy)propan-1-ol was transformed into β-hydroxy sulfone *via* Julia coupling with sulfone 2-6, which after oxidation and reductive removal of the sulfone moiety provide ketone **17** [30]. The compound **17** on reduction produced a racemic alcohol (**18&19**). The configuration of alcohols was deduced by a modified Mosher's ester analysis [31].

The exomethylene function was installed to **18** by a Wittig reaction followed by Appel reaction to achieve iodide **14**. The opposite end functionalization of diastereomer **19** produces desired fragment. Myers alkylation of iodide **14** with propionamide derivative essentially produces a single diastereocenter (C7) [32].

TIPSO   OH   NaBH₄, MeOH   18 (37%)

17

19 (32%)

20: R = (R)-MTPA   21: R = (S)-MTPA

Scheme 2. Δδ Values [Δδ (in ppm) = δ$_S$–δ$_R$] obtained for (S)- and (R)-MTPA ester at C11 (2-13 and 2-14, respectively) of alcohol 2-11.

KHMDS mediated aldol reaction of the aldehyde (**13**) and ketone (**12**) produced β-hydroxy ketone. That after Luche reduction of ketone produced a diastereomeric mixture of allyl alcohol. Pinnick oxidation of the aldehyde to *seco*-acid **11**, followed by Yamaguchi

macrolactonization and TBAF mediated cleavage of silyl ether furnished amp Q.
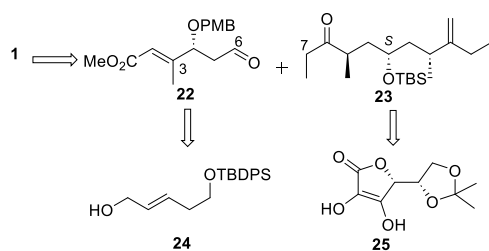
Scheme 3. Retrosynthetic plan for the synthesis of Amphidinolide Q by Nishiyama *et al.*

The synthetic strategy described by Nishiyama *et al.* (Scheme 3) outlines the possibility of constructing amp Q by joining segment **22** and **23** followed by macrolactonization [33]. The synthesis of fragment **22** began with the epoxidation of alcohol **24** obtained from 1,3-propanediol. *E*-selective methylation of the propiolic ester part using a PhS group as an auxiliary [34], afforded the α,β-unsaturated ester **22**. The synthesis of ethyl ketone **23** was initiated from the ascorbic acid derivative. Ascorbic acid derivative (**25**) was cleaved, oxidized to corresponding carboxylic acid. The introduction of the Evans auxiliary in acid, followed by methylation leads to the C9 stereocenter. Parikh-Doering oxidation and a Horner-Wadsworth-Emmons reaction and after routine functional group manipulation and Peterson's olefination introduced the *exo*-methylene function [35]. The Aldol reaction of both fragments **22** and **23** under acidic condition gave undesirable elimination whereas under basic conditions the reaction suffered from moderate yield [33]. Moreover, the keto function at C8 still has to be removed. The retrosynthetic approach Mishra *et al.* followed is shown in Scheme 4. They have envisioned to fragment the seco-acid **11**. Into two unequal size fragment considering the aldehyde function *a,b*-unsaturated aldehyde **25** and ketone **26**. The *meso*-diol **28** was converted to alcohol via enzyme-mediated desymmetrization as key step [36]. Chain extension on the derived tosylate led to nitrile **29** [37]. Further the nitrile was reduced to aldehyde using DIBAL-H, following the reaction with lithium trimethylsilylacetylide led the delivery of propargylic alcohol **31** as a mixture of C11 diastereomers. That on, after oxidation with Dess-Martin periodinane, followed to reduction with a Noyori transfer hydrogenation using (*R,R*)-Ru catalyst, produced essentially one diastereomer[38]. Further steps, continuing with the synthesis, to chain extension with *S*-ethyl 2-(triphenyl-λ⁵-phosphanylidene) ethanethioate gave unsaturated thioester **32** [39].
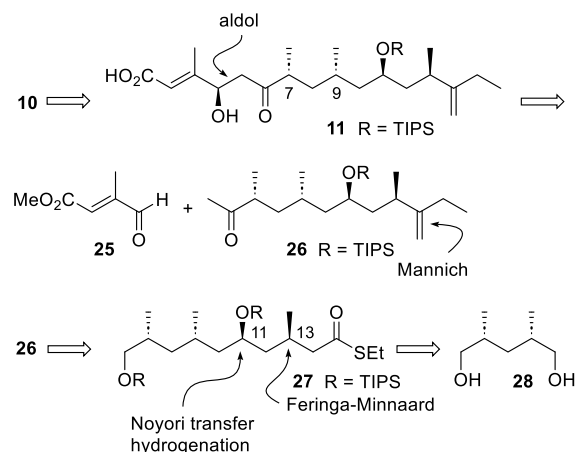
Scheme 4. Retrosynthetic plan for the synthesis of Amphidinolide Q by Mishra *et al.*

The asymmetric methyl cuprate additionin presence of (*R*)-Tol-BINAP provided thioester (C6-C15 fragment) on gram scale. Further, chemical transformation led to seco-acid [40-42].
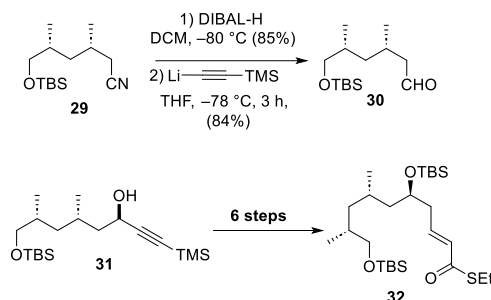
Scheme 5. Conversion of nitrile 29 to thioester 32.

CONCLUSION

In conclusion, the demand for polyethylene is rising day by day and the disclosure of sustainable sources is demanding. Macrolactones are natural compounds, their polymerization could give a material with comparable properties to polyethylene. To plan different polymers for various applications, the idea of monomers is necessary. Various macrolactones could give idea on monomers. Biologically relevant macrolactones have been explored along with the various approaches of ring opening polymerization of macrolactones. The idea on various monomers will open a new dimension in polymer synthesis and in the application such as drug delivery, implants, and tissue engineering. The retrosynthetic analysis and their synthesis will trigger in the discovery of new monomers for chiral polymers. The enzyme-catalyzed uncontrolled polymerization issue was handled using metal catalyzed controlled ring opening polymerization.

REFERENCES

1. (a) Dautel, S. L. *Golden Gate Univ. L. J.*, **181** (2001). (b) Berton, J. *San Francisco Chronicle*, **W-8** (2007). (c) Lovett, R. A. *National Geographic News* March 2 (2010).

2. M.McCoy, *Chem. Eng. News.*, **88**, 11 (2010).

3. (a) Skoglund, P.; Fransson, A. *Polymer*, **39**, 1899 (1998). (b) Gazzano, M.; Malta, V.; Focarete, M. L.; Scandola, M.; Gross, R. A. *J. Polym. Sci., Part B: Polym. Phys.*, **41**, 1009 (2003).

4. Quinzler, D.; Mecking, S. *Angew. Chem., Int. Ed.*, 49, 4306 (2010).

5. (a) Griffith, L. G. *Acta Materialia*, **48**, 263 (2000). (b) Kulshrestha, A. S., Mahapatro, A., *Eds.; ACS Symposium Series***977**; *American Chemical Society: Washington, DC* (2008).

6. Affatato, S.; Zavalloni, M.; Taddei, P.; Di Foggia, M.; Fagnano, C.; Viceconti, M. *Tribol. Int.*, **41**, 813 (2008).

7. Kurtz, S. M.; Muratoglu, O. K.; Evans, M.; Edidin, A. A. *Biomaterials*, **20**, 1659 (1999).

8. (a) McGinty, D.; Letizia, C. S.; Api, A. M., *Food and Chemical Toxicology*, **49**, S193-S201 (2011). (b) Grammer, K., *Ethology and Sociobiology*, **14** (3), 201 (1993). (c) Wilson, J. A.; Ates, Z.; Pflughaupt, R. L.; Dove, A. P.; *Progress in Polymer Science*,**91**, 29 (2019).

9. Jerman, B.; Fles, D. *J. Polym. Sci.*, **14**, 1117 (1976).

10. (a) R. Gref, A. Domb, P. Quellec, T. Blunk, R. H. Muller, J. M. Verbavatz, R. Langer, *Adv. Drug Delivery Rev.*, **16**, 215 (1995). (b) S. Stolnik, S. E. Dunn, M. C. Garnett, M. C. Davies, A. G. A. Coombes, D. C. Taylor, M. P. Irving, T. F. Tadros, S. S. Davis, L. *Illum, Pharm. Res.*, **11**, 1800 (1994).

11. (a) Zaks, A.; Klibanov, A. M. *J. Am. Chem. Soc.*, **106**, 2687 (1984). (b) Wilson, W. K.; Baca, S. B.; Barber, Y. J.; Scallen, T. J.; Morrow, C. J. *J. Org. Chem.*, **48**, 3960 (1983).

12. Taden, A.; Anotnietti, M.; Landfester, K. *Macromol. Rapid Commun.*, **24**, 512 (2003).

13. van der Meulen, I.; de Geus, M.; Antheunis, H.; Deumens, R.; Joosten, E. A. J.; Koning, C. E.; Heise, A. *Biomacromolecules*, **9** (12), 3404 (2008).

14. Målberg S, Finne-Wistrand A, Albertsson A-C*Polymer*; **51**, 5318 (2010).

15. (a) Barrère M, Landfester K. Polyester synthesis in aqueous miniemulsion. *Polymer.*; **44**, 2833 (2003). b) Takasu T, Takemoto A, Hirabayashi T, *Biomacromolecules*; **7**(1), 6 (2006)

16. Pascual, A.; Leiza, J. R.; Mecerreyes, D*., European Polymer Journal*, **49** (6), 1601 (2013).

17. (a) Handbook of Ring-Opening Polymerization; Dubois, P., Coulembier, O., Raquez, J.-M., *Eds.; Wiley-VCH: Weinheim, 2009.* (b) Dechy-Cabaret, O.; Martin-Vaca, B.; Bourissou, D. *Chem. Rev.*, **104**, 6147 (2004). (c) Wheaton, C.; Hayes, P. G.; Ireland, B. J. *Dalton Trans.*, 4832 (2009). (d) Kricheldorf, H. R. *Chem. Rev.*, **109**, 5579 (2009).

18. (a) Clark, L.; Cushion, M. G.; Dyer, H. E.; Schwarz, A. D.; Duchateau, R.; Mountford, P. *Chem. Commun.*, **46**, 273 (2010). (b) Dyer, H. E.; Huijser, S.; Susperregui, N.; Bonnet, F.; Schwarz, A.; Duchateau, R.; Maron, L.; Mountford, P. *Organometallics*, **29**, 3602 (2010).

19. van der Meulen, I.; Gubbels, E.; Huijser, S.; Sablong, R.; Koning, C. E.; Heise, A.; Duchateau, R., *Macromolecules*, **44** (11), 4301 (2011).

20. (a) Bourissou D, Vaca B-M, Dumitrescu A, Graullier M, Lacombe F. *Macromolecules*; **38**, 9993 (2005). (b) Makiguchi K, Satoh T, Kakuchi T. *Macromolecules*; 44, 1999 (2010). (c) Oshimura M, Tang T, Takasu A. *Journal of Polymer Science Part A: Polymer Chemistry*; **49**, 1210 (2011).

21. D. Myers, Witt, T.; Cyriac, A.; Bown, M.; Mecking, S. Williams, C. K., *Polymer Chemistry*, **8** (37), 5780 (2017).

22. (a) Kobayashi, J.-i.; Kubota, T. *J. Nat. Prod.* 2007, **70**, 451 (2007); (b) Kobayashi, J.-i. *J. Antibiot.*, 61, 271 (2008); a) Kobayashi, J.-i.; Ishibashi, M. *Chem. Rev.*, **93**, 1753 (1993); (b) Kobayashi, J.-i.; Ishibashi, M. *Heterocycles*, **44**, 543 (1997); (c) Chakraborty, T. K.; Das, S. *Curr. Med. Chem.: Anti-Cancer Agents*, **1**, 131 (2001).

23. Daniel, P. T.; Koert, U.; Schuppan, J. *Angew. Chem. Int. Ed.*45, 872 (2006); *Angew. Chem.*, **118**, 886 (2006).

24. (a) Takahashi, M.; Ohizumi, Y.; Yasumoto, T. J. *Biol. Chem.*, **257**, 7287 (1982); (b) Ohizumi, Y.; Yasumoto, T. *Br. J. Pharmacol.*, **79**, 3 (1983); (c) Ohizumi, Y.; Kajiwara, A.; Yasumoto, T. *J. Pharmacol. Exp. Ther*, **227**, 199 (1983).

25. Usui, T.; Kazami, S.; Dohmae, N.; Mashimo, Y.; Kondo, H.; Tsuda, M.; Terasaki, G. A.; Ohashi, K.; Kobayashi, J.-i; Osada, H. *Chem. Biol.*, **11**, 1269 (2004).

26. Saito, S-y.; Feng, J.; Kira, A.; Kobayashi, J-i.; Ohizumi, Y. *Biochem. Biophys. Res. Commun.*, **320**, 961 (2004).

27. Kubota T, Iwai T, Sakai K, Gonoi T, Kobayashi J. *Org. Lett.*, **16**(21), 5624 (2014).

28. Pucci C, Martinelli C, Ciofani G. *E Cancer Medical Science*, **13**, 961 (2019).

29. (a) Kobayashi, J.-i.; Takahashi, M.; Ishibashi, M. *Tetrahedron Lett.*, **37**, 1449 (1996); (b) Takahashi, Y.; Kubota, T.; Fukushi, E.; Kawabata, J.; Kobayashi, J.-i. *Org. Lett.*, **10**, 3709 (2008).

30. (a) Ohtawa, M.; Ogihara, S.; Sugiyama, K.; Shiomi, K.; Harigaya, Y.; Nagamitsu, T.; Ojmura, S. *J. Antibiot.*, **62**, 289 (2009). (b) Komatsu, K.; Tanino, K.; Miyashita, M. *Angew. Chem., Int. Ed.*, **43**, 4341 (2004).

31. Ohtani, I.; Kusumi, T.; Kashman, Y.; Kakisawa, H. *J. Am. Chem. Soc.*, **113**, 4092 (1991).

32. Myers, A. G.; Yang, B. H.; Chen, H.; McKinstry, L.; Kopecky, D. J.; Gleason, J. L. *J. Am. Chem. Soc.*, **119**, 6496 (1997).

33. Kawa, K.; Hara, A., Ishikawa, Y.; Nishiyama, S. *Molecules*, **16**, 5422 (2011).

34. Hollowood, C. J.; Yamanoi, S.; Ley, S.V. *Org. Biomol. Chem.*, **1**, 1664 (2003).

35. Dias, L.C.; Melgar, G.Z.; Jardim, L.S.A. *Tetrahedron Lett.*, **46**, 4427 (2005).

36. (a) Tsuji, K.; Terao, Y.; Achiwa, K. *Tetrahedron Lett.*, **30**, 6189 (1989). (b) Fujita, K.; Mori, K. *Eur. J. Org. Chem.*, 493 (2001). (c) Prusov, E.; Röhm, H.; Maier, M. E. *Org. Lett.*, **8**, 1025 (2006). (d) Dash, U.; Sengupta, S.; Sim, T. *Eur. J. Org. Chem.* 3963 (2015).

37. Hoffmann, R. W.; Schopfer, U.; Müller, G.; Brandl, T. *Helv. Chim. Acta*, **85**, 4424 (2002).

38. Matsumura, K.; Hashiguchi, S.; Ikariya, T.; Noyori, R. *J. Am. Chem. Soc.*, **119**, 8738 (1997). (b) Marshall, J. A.; Eidam, P.; Schenck, H. *Org. Synth.*, **84**, 120 (2007).

39. Keck, G. E.; Boden, E. P.; Mabury, S. A. *J. Org. Chem.*, **50**, 709 (1985).

40. (a) Ruiz, B. M.; Geurts, K.; Fernandez-Ibanez, M. A.; ter Horst, B.; Minnaard, A. J.; Feringa, B. L. *Org. Lett.*, 9, 5123 (2007). (b) López, F.; Minnaard, A. J.; Feringa, B. L. *Acc. Chem. Res.*, **40**, 179 (2007).

41. Wang, S.-Y.; Loh, T.-P. *Chem. Commun.*, **46**, 8694 (2010).

42. Mishra, V. K.; Ravikumar, P. C.; Maier, M. E. *J. Org. Chem.*, **81** (20), 9728 (2016).

Performance of rGO/V$_2$O$_5$ as a heterogeneous catalyst for oxidation of methyl phenyl sulfide

N. S. Karki[1], M. Bisht[1]*, A. Sharma[2], H. Mudila[2], M. K. Pal[3]

[1]Department of Chemistry, L.S.M.G.P.G.C., Pithoragarh-262502, India
[2]Department of Chemistry, Lovely Professional University, Phagwara-144411, India
[3] Departments of Microbiology, Graphic Era (Deemed to be University), Dehradun, India

rGO/V$_2$O$_5$ heterogeneous catalyst was prepared by *ex-situ* method and was used for oxidation of methyl phenyl sulfide to produce methyl phenyl sulfoxide and methyl phenyl sulfone. The individual components (rGO and V$_2$O$_5$) and the composites (all ratios of rGO:V$_2$O$_5$) were analyzed by FTIR, XRD, TGA and SEM. The percent conversion and catalytic effect were studied *via* GC and TLC. The rGO:V$_2$O$_5$ in 2:1 ratio was found to give the best result (88.3% conversion); the effect of the amount of oxidizing agent was also determined which shows that with increasing concentration of H$_2$O$_2$ the % conversion was also increased.

Keywords: rGO, V$_2$O$_5$, catalyst, percent conversion, oxidation

INTRODUCTION

Catalysts were always in demand to enhance the product yield and minimize the requirement for reagents. Apart from the above benefits a catalyst also curtails the issue of excessive use of hazardous reagents. Various catalysts are considered in a particular reaction due to their specific advantages, including selectivity, stability, and reusability. Several effective homogeneous and heterogeneous catalysts have been introduced to meet ecological demands. Out of the numerous catalysts used in various reactions graphene (or reduced graphene, rGO) finds its explicit position. Since its introduction rGO had been employed in numerous applications including catalysis. The properties of rGO such as 2D flat extended surface area, highly reduced band gap, and chemical, mechanical and thermal stability confer specific features to rGO to be employed as a promising catalyst for several reactions [1]. Cuni *et al.* 2021 employed rGO as a carbo-catalyst for the dehydrogenation of N-heterocycles, this catalyst was found to generate an appreciable yield with excellent reusability and stability for the next eight experiments [2]. Ruthenium-supported rGO was used for the generation of hydrogen from ammonia decomposition, The optimal catalytic performance was observed with 2.5:10 of Ru:rGO composition where 96% of ammonia was converted [3]. rGO had not only been used as an individual potent catalyst, but studies also show that rGO, due to its tuneable electrical and physical properties, had been proven a

fine catalytic support material for TMOs, thus generating high catalytic surfaces for catalyzing chemical reactions. Askari *et al.* 2022, show the oxidation reaction of methanol by using rGO binary TMO (MnCo$_2$O$_4$/NiCo$_2$O$_4$) catalyst [4]. rGO/Co$_3$O$_4$ nanocomposites had been introduced as a catalyst for oxygen evolution by Abidat *et al.* 2019 [5]. The current article represents an attempt to use rGO/V$_2$O$_5$ in varying compositions to oxidize methyl phenyl sulfide to methyl phenyl sulfone. The compositions were characterized via FTIR, XRD, SEM, and TGA-DSC for their respective chemical and physical properties. The catalytic response of the rGO/V$_2$O$_5$ was studied *via* gas chromatography (GC).

EXPERIMENTAL

Material and method

Conc. sulfuric acid (H$_2$SO$_4$, 98%), hydrochloric acid (HCl, 35.4%), hydrogen peroxide (H$_2$O$_2$, 30%), potassium permanganate (KMnO$_4$), graphite, acetonitrile (ACN), methyl phenyl sulfide, and V$_2$O$_5$ were purchased from Loba Chemie Pvt. Ltd.

Preparation of GO and rGO

rGO was prepared from GO, produced from graphite *via* Modified Hummer's process. In this method, graphite (5g) was taken in a vessel, to which conc. H$_2$SO$_4$ (75 ml) was supplied slowly while maintaining a temperature of 0-5°C. Then KMnO$_4$ (15 g) was slowly added to the reaction mixture. The resulting mixture was continuously stirred for the next 2 h at 5±1°C. After this, the reaction mixture

---

was allowed to come to room temperature with continuous stirring for the next ½ h. Further, the reaction temperature was allowed to increase to 98°C by the addition of 200 ml deionized water and keeping the reaction mixture at constant stirring for the next 45 min. Now to the reaction mixture deionized water (140 ml) and H_2O_2 (30 wt. %, 20 ml) were supplied which resulted in the formation of GO (yellow-brown precipitate). The latter was separated by vacuum filtration and washed with 100 ml of aqueous HCl (5%). The obtained solid material was then dried at 60°C in a vacuum oven [6].

The GO synthesized was reduced to rGO using ascorbic acid as a reducing agent, for the process GO (1 g) was dispersed in deionized water (400 ml) to which ascorbic acid (10 g) was slowly added and was stirred for the next 2 h at 60±1 °C. A black slurry was obtained after the above-mentioned time, which was centrifuged and was further supplied with H_2O_2 (30 wt. %, 10-20 ml) and stirred for ½ h at 60±1 °C to remove excess reducing agent. The final product was then repeatedly washed with ethanol and water and then dried in a vacuum oven [6].

Preparation of rGO/V₂O₅ composite

Solvothermal method was employed for the preparation of rGO/V₂O₅ composites in varying ratios of 1:1, 1:2, and 2:1. In this *ex-situ* method rGO was added with the requisite amount of V_2O_5 and was further stirred for 1 h at room temperature. These various compositions were further sonicated for ½ h for better insertion of the V_2O_5 into the layers of rGO. The final product was separated by centrifugation and was dried.

RESULTS AND DISCUSSION

Fourier transform infrared (FTIR) spectroscopy

The FTIR spectra of all samples were recorded on a Diamond ATR detector Perkin Elmer spectrometer in the range of 400 to 4000 cm⁻¹. The FTIR spectrum of GO shows a peak at 1063 cm⁻¹ due to C-O stretching. A C-O-C bending peak was detected at 1224.85 cm⁻¹, a C=C stretching peak at 1623 cm⁻¹ and an intense C=O peak at 1700 cm⁻¹. A broad peak at ~3342.37 cm⁻¹ was observed related to OH stretching vibrations and absorbed moisture. Peaks observed in GO were found to get less intense or removed in the FTIR spectra of rGO. The broad peak of -OH was nearly lost signifying the reduction of GO to rGO (Fig. 1). A peak near 1600 cm⁻¹ demonstrates the presence of a C=C stretching peak of benzene while a peak at 1066 cm⁻¹ shows C-O stretching [7]. For V_2O_5, peaks at 513.35 and 464 cm⁻¹ were attributed to the presence of symmetric and asymmetric stretching of coordinated oxygens.

258

Peaks at 830.23 cm⁻¹ denote the vibrations of bridged oxygen (V-O-V), while a peak related to V=O was observed near 1003 cm⁻¹ (Fig. 1) [8]. In the FTIR of rGO/V₂O₅ (2:1) peaks related to O-H and CO stretching were observed at 3318 and 1211 cm⁻¹, respectively. A peak for rGO representing C=C stretching was observed at 1560 cm⁻¹. The peak observed near 1003 cm⁻¹ shows stretching vibrations for terminal bonds of oxygen (V=O) (Fig. 1).
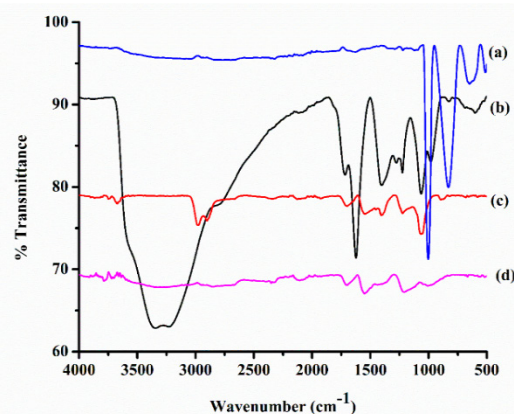
Fig. 1. FTIR spectra of (a)V₂O₅; (b) GO; (c) rGO; (d) rGO:V₂O₅ (2:1)

X-ray diffraction (XRD) analysis

XRD was used for the determination of the morphology of all samples by Bruker AXS D8 Advance A25-X1-1A2Z2C4B0. All spectra were recorded in a 2θ range of 10 to 70°, with λ=1.54 Å at 25°C. For GO at 2θ =10.5° a sharp peak is observed which is considered to be characteristic of GO (Fig. 2a). In the XRD pattern of rGO, the peak at 2θ =10.5° disappeared due to GO reduction. Peaks at 23° and 43° clearly signify the reduction of GO to rGO. Fig. 2b demonstrates the XRD of V_2O_5, the orthorhombic phase of V_2O_5 is mentioned by the peaks present at 16°, 20°, 22°, and 31°, the sharp peaks represent the crystalline nature of the metal oxide [9]. In Fig. 2c, all peaks related to rGO were intensified due to the presence of V_2O_5 in the matrix [10].

Thermogravimetric analysis (TGA)

TGA analysis was carried out a Perkin Elmer thermal analyzer. The temperature ranged from 50 to 550°C in inert conditions (N_2 flow) with a heating rate of 10ºC/min. The TGA curves of rGO, V_2O_5, and the composite are represented in Fig. 3. TGA curve of rGO was found to be stable due to less oxygenated functional groups. Up to 200°C, there is around 20% weight loss attributed to loss of moisture and volatile components, from 200 to 400°C a 41% weight loss is attributed to the loss of CO_2 and CO. In the case of V_2O_5 slight loss (15.4%)

is reduced up to 200°C, which increased to 37% from 200 to 400°C and increases to 44.37% reaching 550°C. For the composite (rGO/V$_2$O$_5$), up to 200°C the weight loss was 7%, which increased to 24% when reaching 400°C, and maximum mass loss (33.7%) was recorded till 550°C [8, 10].

Scanning electron microscopy (SEM)

The morphological study of the gold-coated composite (rGO/V$_2$O$_5$) was carried out by FESEM: JSM-7610F-Plus (Figs. 4a and 4b). rGO was found to show a flaky structure, and V$_2$O$_5$ particles were found to show bead-like shapes due to agglomeration on the surface of rGO [11].
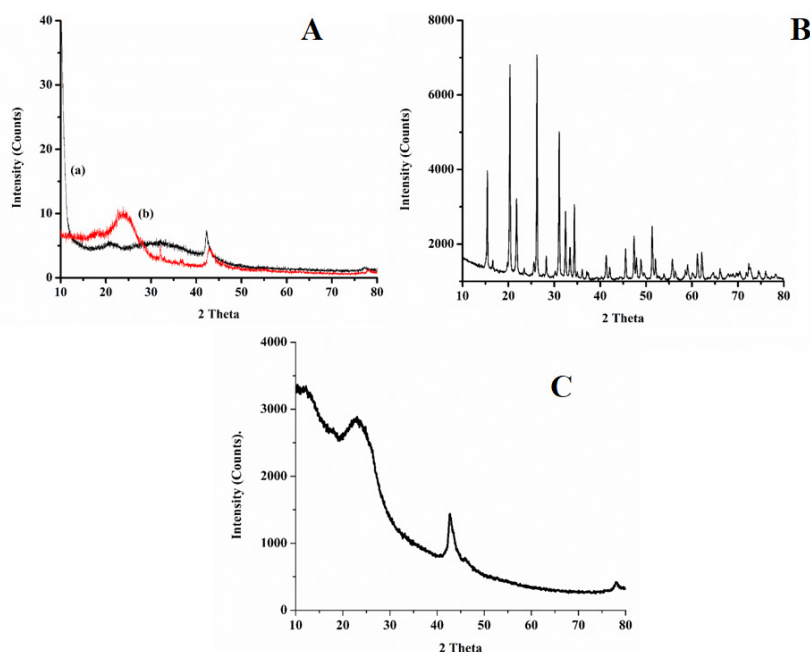
Fig. 2. XRD pattern of (A) GO and rGO: (B) V$_2$O$_5$; (C) rGO/V$_2$O$_5$
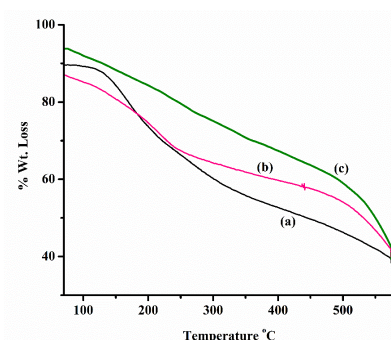
Fig. 3. TGA curves of (a) rGO; (b) V$_2$O$_5$: and (c) rGO/V$_2$O$_5$
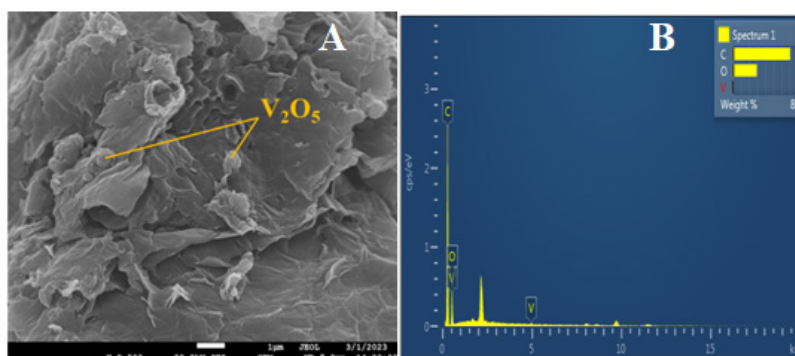
Fig. 4(a) SEM of rGO/V$_2$O$_5$; **(b)**EDX spectra of rGO/V$_2$O$_5$
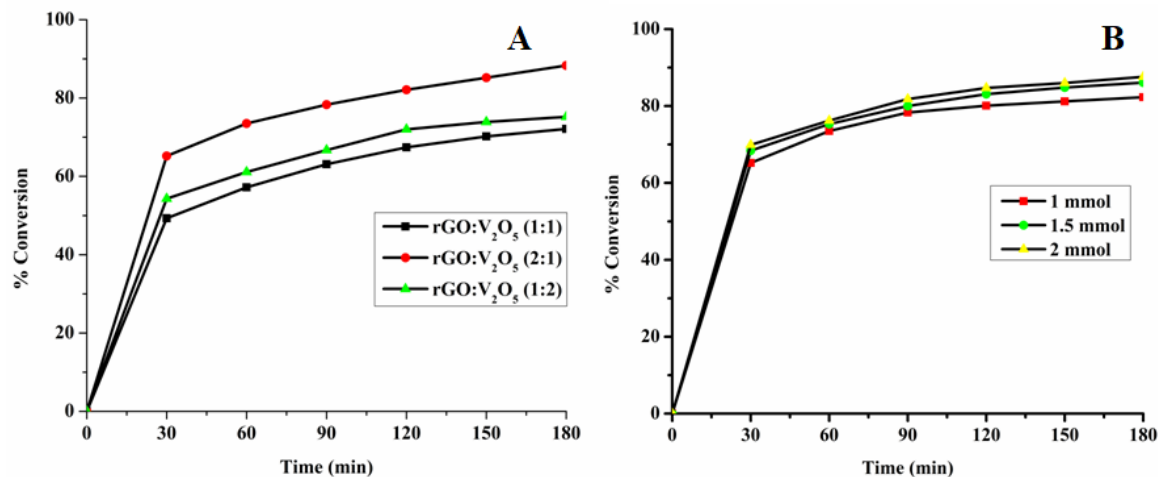
Figure 5. Role of (A) catalyst ratio and (B) catalyst (rGO:V$_2$O$_5$ in 2:1) concentration on the % conversion of reactant to the product after regular intervals

Oxidation studies

Methyl phenyl sulfide (thioanisole, 1 mmol) was oxidized to methyl phenyl sulfoxide and methyl phenyl sulfone, when reacted to H$_2$O$_2$ (1 mmol) in ACN (10 ml) at room temperature in the presence of a catalyst (rGO/V$_2$O$_5$, 5 mg) in 1:1, 2:1, 1:2 ratio, respectively. Product samples were taken every ½ h (30, 60, 90, 120, 150, and 180 min). The results were analyzed through TLC and GC. The sulfur present in the reagent is an electron-rich species and produces sulfoxide and sulfone products by undergoing electrophilic oxidation. The ratio of the catalyst is important to determine the amount of the product. It was found that the 2:1 rGO: V$_2$O$_5$ was the best to generate the maximum yield among all three ratios (Fig. 5a). The effect of the varying amount of oxidant (H$_2$O$_2$, 1, 1.5, and 2 mmol) on the % conversion was also studied by stabilizing the rGO:V$_2$O$_5$ in 2:1 ratio. It was found that with increasing ratio of oxidant in the reaction site the % conversion also increased (Fig. 5b).

CONCLUSIONS

rGO/V$_2$O$_5$ heterogenous catalyst was prepared by *ex-situ* method and was used for oxidation of methyl phenyl sulfide to produce methyl phenyl sulfoxide and methyl phenyl sulfone. The rGO:V$_2$O$_5$ in 2:1 ratio was found to have the best result (88.3% conversion). The effect of amount of oxidising agent was also determined which shows that with

increasing concentration of H$_2$O$_2$ the % conversion increased.

Conflict of interest*: The authors declared no conflicts of interest.*

REFERENCES

1. H. Sachdeva, *De Gruyter,* **9**, 515 (2020).
2. A. M. Cuni, D. V. Espinosa, S. Martín, H. García, J. A. Mata. *ACS Cat.,* **11 (23)**, 14688 (2021).
3. M. Pinzón, O.A. García, A.R. de la Osa, A. de Lucas-Consuegra, P. Sánchez, A. Romero, *Sus. Chem. Phar.,* **25** (2022).
4. M. B. Askari, S. Azizi, M. T. T. Moghadam, M. Seifi, S. M. Rozati, A. Di Bartolomeo, *Nanomat.,* **12**, 4072 (2022).
5. I. Abidat, E. Cazayus, L. Loupias, C. Morais, C. Comminges, T.W. Napporn, D. Portehault, O. Durupthy, A. S. Mamede, C. Chanéac, J. F. Lamonier, A. Habrioux, K. B. Kokoh, *J. Electrochem. Soc.,* **166 (4)** (2019).
6. A. T. Habte, D.W. Ayele, *Adv. Mat. Sci. and Eng.*, **2019**, 1 (2019).
7. R. Maharsi, A. Arif, T. Ogi, H. Widiyandari, F. Iskandar, *RSC Adv.,* **9(48),** 27896 (2019).
8. J. R. Xavier, *Pol. Bull.,* **78**, 5713 (2021).
9. K. S. Prasad, C. Shivamallu, G. Shruthi, M. Prasad, *Chem. Select*, **3(13)**, 3860 (2018).
10. D. Bhardwaj, S. Sangwan, S. A. Shivashankar, A. M. Umarji, *Bull. of Mat. Sci.,* **45**, 135 (2022).
11. T. Tene, G.U. Tubon, M. Guevara, R. Molina, F. Veltri, M. Arias, L. Caputi, C.V. Gomez, *Nanomat.*, **10(2)**, 279 (2020).

Evaluation of properties of native and modified phyto-polymer, starches of *Curcuma angustifolia* and development of polymeric films

N. Singh[1*], N. Rai[1], V. Gupta[2]

[1]*Tropical Forest Research Institute, Jabalpur (M.P.)-482001*
[2]*Faculty of Science, Department of Chemistry, Motherhood University, Roorkee*

In the present study, polysaccharide- starch of *Curcuma angustifolia* was isolated and modified by chemical reactions-acetylation, hydroxy-propylation and carboxy-methylation. The acetyl, hydroxypropyl, carboxylmethyl groups percentage and degree of substitution (DS) for acetylated, hydroxypropylated and caboxymethylated starches of *C. angustifolia* were determined 6.89%, 0.28%, 0.06%, and 0.04, 1.30 ,0.75, respectively. The introduction of carboxymethyl group significantly increase the swelling power and solubility while gelatinization temperature was reduced to 68.70^0C in modified starch in comparison to native (97.03^0C) starch of *C. angustifolia*. Similarly, examination of water absorption capacity showed increasing trend in modified starches. The suspensions from native and modified starches were prepared and polymeric films were developed utilizing glycerol as plasticizer. The casted films thickness varied between 0.040-0.160 mm. The mechanical properties of different polymeric blends showed wide variation (81.1-427.5 kgf/cm^2). The maximum tensile strength showed in acetylated modified blend (427.5 kgf/cm^2) and PVOH blend *C. angustifolia* (391.79 kgf/cm^2) while the polymeric film blend with native potato starch, prepared for comparison, showed minimum tensile strength (81.1 kgf/cm^2).

Keywords: *Curcuma angustifolia,* Starch, Modified starches, Acetylation, Hydroxypropylation, Carboxymethylation, Polymeric films, Tensile strength.

INTRODUCTION

Synthetic non-degradable petrochemical-based polymers poses one of the greatest threats to ecology today as they remain more or less unchanged in landfills even after a period of five decades. This alarming situation necessitates the investigations of viable alternatives or complements to synthetic petro- based chemicals with the aim to reduce their applications. Polysaccharides, i.e., starch and cellulose are the potential renewable raw material, available in plants as stored food, abundantly distributed in forests and can be converted into biodegradable eco-friendly products products by some chemical modification or processing directly [1]. Various work has been done on bioplastic synthesis by cassava, corn, sugar palm, jack fruit seed starch, potato, pea, wheat gluten, tamarind seed and banana peel [2-10].

Curcuma angustifolia Roxb. ('Tikhur') belongs to the family of Zingiberaceae. It occurs in central India, West Bengal, Madras provenances and lower parts of Himalayan ranges as associate of *Shorea robusta*. The plant resembles to *C. Longa* with stout root stock, globose tubers at the ends of the fibrous roots. The rhizomes are collected by the tribals in winter season and used for extraction of starch for edible purposes. In this study, for the first time the modification of *C. angustifolia* starch through introduction of acetyl, hydroxypropyl and carboxymethyl groups was undertaken and utilized in the development of ecofriendly films.

MATERIAL AND METHODS

Isolation and purification of polysaccharides.

The tubers of *C. angustifolia* species were collected from the Achanakmar, Dhamtari forest area in Chattisgargh and extracted by a standard method [11]. Acetylation, hydroxypropylation and carboxymethylation products of different starches were prepared and the degree of substitution was determined according to standard procedure [12, 13]. Physico-chemical properties of native and modified starches were assessed as follows.

Color, pH value and density measurement

Color of the starches was determined by visual color appearance. A 20 % w/v dispersion of the native and modified starches was shaken in water for 5 min and pH of water phase was determined using a digital pH meter. The density of starches from different species was determined by the specific gravity method and calculated by using the formula:

Density (g/ml)=   W1 /[(W1 +W2) – W3)] D1
where, W1 =weight of starch, D1 = density of

---

* To whom all correspondence should be sent:
E-mail: singhn@icfre.org

xylene, W2 = weight of bottle with xylene, W3 = weight of bottle with starch.

Swelling power, solubility and water absorption capacity (WBC)

The swelling power and solubility of starches were determined according to the standard method [14]. 0.5g of starch was taken in 20 ml of distilled water in pre-weighed centrifuge tubes and content was kept on water bath with shaking for half an hour at different temperatures, i.e., 60, 70, 80, and 90ºC. The supernatant was collected and poured into a dish to analyze solubility and put in an oven at 130ºC. The moisture content in the precipitate was assessed as follows: 1 g sample was dissolved in 10ml solvent (water, dimethyl sulfoxide (DMSO), chloroform, toluene, acetic acid, ethanol, ethyl acetate, propanol-2, butanol, diethyl ether, acetonitrile, 1N alkali, 1N acid, tetrahydrofuran (THF) and the solubility pattern was assessed. The WAC of each native and modified starch was determined by dissolving 1 g starch in 10 ml distilled water and centrifuged at 2000 rpm for 10 min. The supernatant was decanted and the final sample weight (Wf) was determined. The WAC (expressed in grams of H_2O absorbed per gram) was calculated after centrifugation [14]:

$$WBC = (Wo - Wf) / Wo$$

where: Wo = sample weight (g), Wf = final sample weight after centrifugation (g).

Gelatinization temperature was determined with the help of a microscope using Congo red dye [15].

Stability and clarity of starch pastes

Stability and clarity of native and modified starch pastes were determined at 4^0C; 0.2 g of starch sample were taken in screw cap-tubes with 5 ml of water and kept in a boiling water bath for 30 min. The % T (Transmittance) was determined at 650 nm against a water blank on a spectrophotometer after cooling to room temperature, and was recorded after 24, 48 and 72 h [16].

Microscopy

A starch dispersion was stirred using a wire loop and was transferred onto a microscope slide. Leica-1000× advanced research scanning electron microscope (SEM) facility was availed from Sophisticated test and Instrumentation Centre, Cochin University, Kochi, Kerala).

Development of polyfilms

Filmogenic suspensions of unmodified and acetylated, hydroxypropylated and carboxymethylated starches of *C. angustifolia* were used for film development adding glycerol as plasticizer (10:1). The starch:water (1:20) suspension was gelatinized. After completion of gelatinization, plastisizer and other additives (10:1) were added under constant stirring for 10 minutes. The additives chitosan, bentonite, mucilage, lignin extract and polyvinyl alcohol were used to check the compatibility. The films were prepared by a casting technique, 20 g suspensions were poured into 15 cm petri dishes, dried at room temperature and cured in an oven at 100^0C to constant weight.

Thickness and film appearance

Thickness of the films was determined using a digital coating thickness gauge. Randomly ten measurements were taken at different points of the film specimen. Homogeneity and appearance of the films were examined by visual observation and by SEM with a JEOL JSM 6360 electron microscope (Japan). The film solubility and opacity were determined [17].

Mechanical properties

The tensile strength of polymeric films (sized 12 × 2 cm^2) was measured by using an Instron Universal Testing machine by adopting IS 2508 method.

Statistical analysis

The results were statistically analyzed using SPSS Version 14 (SPSS Inc., Chicago, III., USA)

RESULTS AND DISCUSSION

Total starch content of *C. angustifolia* was estimated as 38.11% and the color of the starch was white. Variation in starch shapes and size is shown in SEM (Fig.5). The shapes of *C. angustifolia* starch were rounded, oval to elliptical, round, oblong, triangular and asymmetrical, granule length varied between 16.36-48.18 μm (mean 34.62 μm) and width between 20.90 to 40.91 μm (mean 27.49 μm). The starches of *C. zedoaria* and *C. malabarica* showed elliptical shape and granular size of 14-46 μm and 1.6-4.2 μm [18]. *Canna edulis* starch also showed granular shape as starch of *C. angustifolia,* while granule size similar to the starch of *Amorphophallus paeoniifolius* (Dennst.) Nicolson (Elephant foot yam) and *Pachyrrhizus erosus* (Yam bean) [19, 20].

Chemical modification of starches and their characterization

The acetyl, hydroxypropyl, carboxyl groups % and the degree of substitution (DS) for acetylated, hydroxypropylated and caboxymethylated starches of *C. angustifolia* were determined as 6.89%, 0.28%, 0.06%,and 0.04, 1.30, 0.75, respectively.

Solubility and swelling power of native and modified starches

Modification of starches showed changes in solubility behavior. The hydroxypropylated and acetylated starches were insoluble in acetone, tetrahydrofuran (THF), cold water while carboxymethylated starches was found to be soluble in cold water or in water-miscible solvents. All modified starches showed a significantly higher % light transmittance when compared to unmodified ones. The results also revealed that the % light transmittance of all modified starches was reduced with the duration of storage (24 to 72 h). The effect of acetylation on paste clarity has been widely exported for various types of starch [21, 22]. Figs. 1 and 2 depict the changes in swelling power and solubility % of native and modified starches of *C. angustifolia* with respect to different temperatures (40°C, 50°C 60°C, 70°C, 80°C and 90 °C). The increase in solubility and swelling values was observed in all types of modified starches when temperature increased. Carboxymethylation significantly increases the swelling power and solubility of modified starches of *C. angustifolia*. At 40°C, maximum solubility of 5.46% was observed in carboxymethylated starches, in comparison to acetylated and hydroxypropylated starches while native starch was found to be insoluble.

Table 1. Density, pH, water absorption capacity and gelatinization temperature of native and modified starches

Species	Density (g/ml)	pH	Gelatinization temperature(^{0}C)	Water absorption capacity (g/g)
C.angustifilia (CA)	1.46±0.00	7.30±0.011	97.03±0.00	1.93 ±0.01
AcCA	1.45 ±0.03	4.06±0.02	81.90±0.42	1.86 ±0.04
HPCA	1.42 ±0.06	9.60±0.01	75.20±0.69	2.68 ±0.20
CMCA	1.12 ±0.09	3.65±0.03	68.70±0.49	3.48±0.03

Values are the mean of three replicates±standard deviation
Ac-acetylated, HP- hydroxypropylated, CM-carboxymethyl, CA-*C. angustifolia*

Stability and clarity of starch pastes
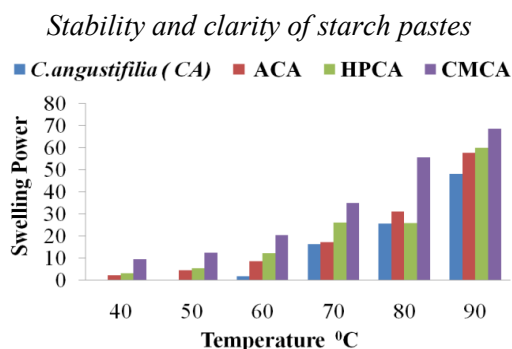
Fig. 1. Swelling power of *C.angustifolia* native and modified starches

Fig. 2. *C. angustifolia* native and modified starches solubility % at different temperatures

Results of starch paste clarity/% transmittance (T) behavior of native and modified starch are depicted in Fig. 3. Modification improved the paste clarity of the starches as shown by an increase in % light transmittance. All modified starches showed a significantly higher % light transmittance when compared to the native starch. The % light transmittance of modified starches were found to be reduced with duration of storage. Maximum paste clarity (9.889% T) was observed in *C. angustifolia* native starch (Fig. 3) which was reduced to 1.578 % T after 72 h.

Fig. 3. Impact of storage time on light transmittance (%) of native and modified *C. angustifolia* starch pastes

Water absorption capacity (WAC)

All modified starches showed significantly higher values in comparison to native starch. Results for water absorption capacity (Table 1) of native and modified starches showed significant variation in binding ability of different starch. Similar behavior was observed in starches of other species, this difference in WAC of different species may be due to the difference in amylose/amylopectin percentage and difference in chain length distribution [23]. Introduction of hydroxypropyl group through hydroxypropylation increases the WAC of modified starch which considerably enhances applicability for different industrial use. It is reported that WAC of starch increased with increase in temperature with the addition of more hydrophilic groups [24]. This property of a particular starch may be potentially useful for different industrial purposes.

Modification of starch showed an increase in solubility and swelling properties. The increase in swelling power and solubility for an acetylated starch of *C. angustifolia was* consistent with observations made by other researchers [21, 22, 25]. This tendency in the present study is in reasonably good agreement with the findings in previous studies with acetylated and hydroxylpropylated potato starches [26, 27]. It is observed that CMS granules readily swelled, even at 40°C, compared with f native starch of *C. angustifolia*.

Development of biofilms and their properties

The thickness of films varied from 0.040 to 0.160 mm. Uniform, transparent, translucent, and flexible films were obtained and they were easily removed after drying. The upper side of the film was observed duller while other side was shiny (Fig.4). The acetylated and hydroxypropylated starches showed good characteristics to form films, they were more transparent and easily removed from the cast plate while carboxymethylated starch blends were not found suitable for film preparation. The dried bentonite- and lignin-blended films appeared pale yellow in color. No pores or cracks were observed in films prepared with lignin and bentonite with *C. angustifolia* starches (native and modified).

Film opacity and swelling %

Opacity is an important characteristic of the film. Transparent films showed low absorption values. Table 2 indicates the opacity results of different blends. Phytopolymer-starch has received considerable attention because of its biodegradable nature and abundant availability, as well as low cost [28-30]. The acetylated and hydroxypropylated starches were more transparent, having good characteristics and were easily removed from the plate. Filmogenic suspension containing carboxymethylated starches was difficult to handle in casting technique of film preparation. Blending polysaccharides with other polymers, *i.e.* chitosan and polyvinyl alcohol, improved mechanical properties and applications of starches. The surface morphology of different blends was found to different and showed different transparency and opacity. *Curcuma* starches, polyvinyl alcohol and chitosan were found to be compatible. Starch-based films incorporated with lignin, chitosan, bentonite were compact, flexible and translucent in comparison to native starch-based film. The results revealed that use of other polymers with starch could be beneficial for cost reduction and also improve properties in comparison to native and modified starches of species. The chemical structure and physical characteristics of the polymers were changed due to blending. Polymer blending offers wide possibilities of preparing cheap biodegradable materials with potential mechanical properties. SEMs studies revealed the compatibility with different additives.
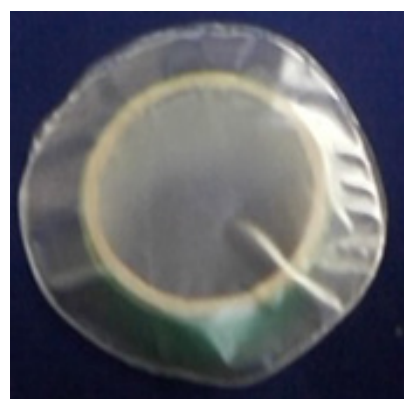
Fig. 4. Polymeric film

Table 2. Physico-chemical characteristics of native and modified starch films

Film composition	Swelling %			Film opacity [AU nm]	Tensile strength (kgf/cm^2)
	Water	Hexane	Oil		
Ac.CA+P	0.05	Resistive	0.00	100	427.5
HPCA +P	2.41	Resistive	0.42	35.48	310.29
CA+B+P	0.56	Resistive	0.00	0.00	159.41
Ac.CA+B+P	0.45	Resistive	0.04	0.00	143.32
HPCA+B+P	0.00	Resistive	0.01	0.00	177.89
CA+CHI+P+Ac	0.24	Resistive	0.00	100	202.69
AcCA+PVOH	0.00	Resistive	0.03	100	391.79
CA+CHI+B+P	0.04	Resistive	0.24	0.00	127.92
CA- *C. angustifolia*, Ac- acetylated, B-bentonite, P-plasticizer, HP-hydroxypropylated, CHI-chitosan, PVOH-polyvinyl alcohol					

(a)   **(b)**   **(c)**
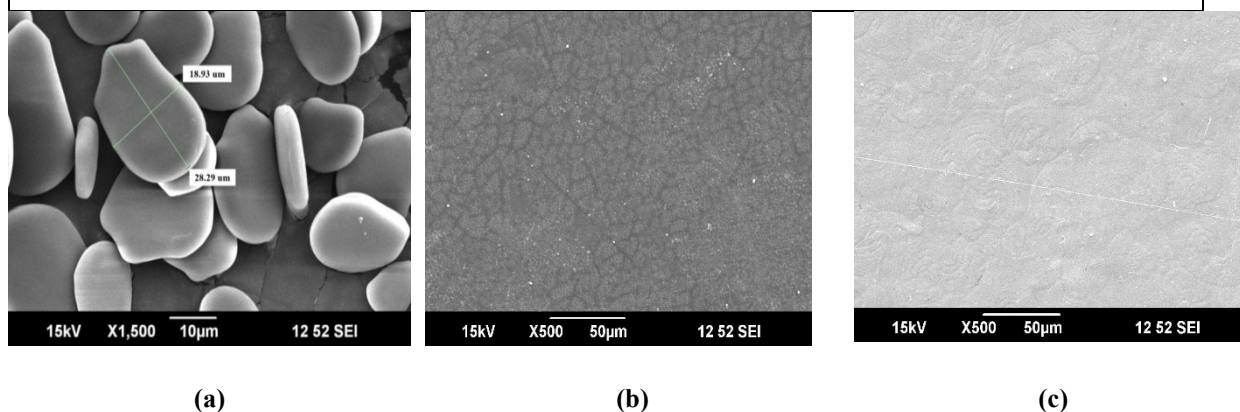
Fig. 5. SEM of granules of *C. angustifolia* (a), modified *C. angustifolia* starch blended film (b) and starch and chitosan blended film (c).

Mechanical analysis of starch-based polyfilms

The native and modified starches blended films tensile strength is depicted in Table 2. Results revealed that the starch modification and different additives showed differences in mechanical properties-tensile strength of polysaccharide films. The films thickness varied between 0.040-0.160 mm. The acetylated *C. angustifolia* blend showed maximum tensile strength (427.5kgf/cm^2), followed by modified *C. angustifolia* and PVOH blend (391.79 kgf/cm^2).

Microscopic studies

The SEM of modified *C. angustifolia*: plasticizer blend, and polyvinyl alcohol:mucilage blends has shown particulate morphology. SEM of the surfaces of the acetylated *C. angustifolia* and plasticizer blend is shown in Fig.6b. The appearance of film is smooth, homogeneous, exhibit characteristic patterns on the film surface. These patterns represent the withered ghost granules of starch. The surface of starch and chitosan blend film (Fig. 6c) showed a continuous matrix without cracks with good structural integrity. It was flat and compact with very sparsely distributed small particles without any phase separation.

CONCLUSIONS

Non-degradable and carcinogenic nature of synthetic polymers are posing great threat to environment and human health. This study shows that the use of polysaccharides from non-conventional sources for the development of environmentally friendly polymer products has broad applicability. This study confides on the isolation and modification of *C. angustifolia* starch into acetylated, hydroxypropylated and carboxy methylated products. The starch content of *Curcuma angustifolia* was estimated as 38.11%. Scanning electron microscopy of starch showed round, oval to elliptical, oblong, triangular and asymmetrical shapes, while mean granule length and width were observed 34.62 μm and27.49 μm, respectively.

The acetyl, hydroxypropyl, carboxyl group % and degree of substitution (DS) for acetylated, hydroxypropylated and caboxymethylated starches of *C. angustifolia* were determined to be 6.89% , 0.28%, 0.06%, and 0.04, 1.30,0.75, respectively. The introduction of acetyl, hydroxypropyl and carboxymethyl groups severely affects the properties of native starches. It reveals that this species may be the potential source of starches for

industrial use. The good swelling power makes it a promising pharmaceutical incipient. The modification of starch with the introduction of hydrophobic and hydrophilic groups improves the properties of starch and biofilms, and shows that *C. angustifolia* starches hold great potential for commercial utilization.

The films thickness varied betwen 0.040-0.160 mm. The acetylated *C. angustifolia* blend showed maximum tensile strength (427.5 kgf/cm^2), followed by modified *C. angustifolia* and PVOH blend (391.79 kgf/cm^2). The results indicate that composition of native and modified starch of *C angustifolia* with other synthetic and natural polymers improves the strength of biofilms and thus may be useful for different purposes. The use of underutilized phytopolymer sources offers tremendous possibilities of preparing inexpensive ecofriendly materials with potential mechanical and thermal properties. The applicability of *C. angustifolia* starch polymer may be further explored in the preparation of super-absorbent hydrogels, flocculants, adhesives, and pharmaceuticals for drug release, etc.

REFERENCES

1. I. U. Agbo, G. E. Odo, *Bio – Research,* **8**,593 (2010).
2. C. L. Luchese, J. C. Spada, I. C. Tessaro, *Ind. Crops Prod.*, **109**, 619 (2017).
3. M. I. J. Ibrahim, S. M. Sapuan, E. S. Zainudin, M. Y. M. Zuhri. *J. Biol. Macromol.*, **139**, 596 (2019).
4. R.A. Ilyas, S. M. Sapuan, M. R. Ishak, E. S. Zainudin. *J. Adv. Res. Fluid Mech. Therm. Sci.*, **51**, 234 (2018).
5. N. A. Shahrim, N.N.S.A. Rani, N. Sarifuddin, H.H.M. Zaki, A.Z.A. Azhar, in: *Proc. of AMCT,* 2017, p.571.
6. K.K. Dash, N.A. Ali, D. Das, D. Mohanta, *Int. J. Biol. Macromol.,***139**, 449 (2019).
7. X. Li, C. Qiu , N. Ji, C. Sun , L. Xiong , Q. Sun, *Carbohydr. Polym.,***121,** 155 (2015).
8. S. Hemsri, K. Grieco, A. D. Asandei, R. S. Parnas, *Compos. Part A Appl. Sci. Manuf.*, **43**, 1160 (2012).
9. A. V. Kiruthika, T. R. K. Priyadarzini, K. Veluraja, *Fibers Polym.,* **13**, 51 (2012).
10. N. F. K. Sultan, W. L. W. Johari, *BSTR*. **5**, 12 (2017).
11. F. C. F. Galvez, A. V. A. Resurreccion, *J. Food Process. Preserv.,* **17**, 93 (1993).
12. T. Whisler, in: W. W. Cooper, H. J. Leavitt, M. W. Shelly (eds.), New Perspectives in Organization Research, New York, John Wiley & Sons, 1964, p. 314.
13. O. B. Wurzburg, in: Methods in Carbohydrate Chemistry. Whistler, R.L., Smith, R.J. Wolfrom, M.L. (eds.), Academic Press; New York 1964, p. 240.
14. T. J. Schoch, in: R.L. Whistler, M.L. Wolfrom (eds.), Methods in Carbohydrate Chemistry: Starch. vol. 4. p. 157. New York and London: Academic Press, 1964.
15. T. J. Schoch, E. C. Maywald, *Anal. Chem.*, **28**, 382 (1956).
16. S. A. S. Craig, C. C. Maningat, P. A. Seib, R. C. Hoseney, *Cereal Chemistry*, **66**, 173 (1989).
17. N. Gontard, S. Guilbert, J. L. Cuq, *J. Food Sci.,***58**, 206 (1992).
18. A. N. Jyoti, S. N. Moorthy, B. Vimala, *Intern. J. Food Prop.*, **6**,135 (2003).
19. J. L.Forsyth, S. G. Ring, T. R. Noel, R. Parker, P. Cairns*, J. Agric. Food Chem.,* **50**, 361 (2002).
20. A. Rani, H. Chawhaan, *Indian J. Nat. Prod. Resour.*, **3**(3), 407 (2012)
21. J. Singh, L. Kaur, N. Singh, *Starch*, **56**, 586 (2004).
22. O. S. Lawal, *Carbohydr. Res.*, **339**, 2673 (2004).
23. F. Aryee, I., Oduro, W. Ellis, J. Afuakwa, *Food Control.*, **17**, 916 (2006).
24. P. Zhang, R. Whistler, J. BeMiller, B. Hamaker, *Carbohydr. Polym.,* **59**, 443 (2005).
25. K. O. Adebowale, O.S. Lawal, *J. Sci. Food Agric.*, **83**, 1541 (2003).
26. L. Kaur, N. Singh, J. Singh, *Carbohydr. Polym.,* **55**, 211 (2004).
27. K.J. Shon, B. Yoo, *Starch,* **58**, 177 (2006).
28. I. Arvanitoyannis, A. Nakayama, S. I. Aiba, *Carbohydr. Polym.,* **36**, 105 (1998).
29. M. A. Garcia, M. N. Martino, N. E. Zaritzky, *Starch/Stärke,* **52**, 118 (2000).
30. Z. Liu, in: J. J. Han (ed.), Innovations in food packagings*,* Elsevier, Amsterdam. The Netherlands, 2005, p. 318.

Responsive PNIPAM coated Au core-shell nanoparticle for optical sensing

S. Faujdar[1], P. Pathania[2*], A. Preet[2], J. Katyal[1]

[1] *Department of Physics, Amity Institute of Applied Science, Amity University, Noida 201301, India*

[2] *Department of Applied Sciences, Galgotias College of Engineering and Technology, Greater Noida, 201306, India*

In this work, we analyze the optical properties of responsive poly (N-isopropylacrylamide) (PNIPAM) coated plasmonic Au core-shell nanoparticle for sensing application. With external chemical or physical stimuli, the responsive PNIPAM polymeric layer exhibits unique properties like variation of solvent concentration, density and subsequently a change in refractive index (RI). Mie theory-based calculation modeled the change in the position of the localized surface plasmon resonance (LSPR) peak with linear change in refractive index of PNIPAM-coated Au nanosystem with external stimuli like change in salt concentration in water, temperature, pH, etc. It paves the way for designing efficient PNIPAM-coated Au-based refractive index-based system for bio/chemical sensing/detection. We theoretically report the sensitivity (S) equal to ~65.8 nm/RIU and the corresponding figure of merit (RIU/nm) is~ 3.6×10^2 RIU/nm. Present investigation can lead to the realization of efficient bio/chemical sensors and light harvesting structures/devices.

Keywords: Plasmonics; Surface Plasmon; Sensor; PNIPAM; Core-Shell Nanoparticle;

INTRODUCTION

Sub-wavelength light-matter interaction and corresponding plasmonic excitation has unfolded new and interesting avenues for advanced research due to formation of localized surface plasmons in metallic nanoparticles [1]. Nanosystems based on plasmonic nanoparticles possess the potential of achieving subwave length confinement below diffraction limit [2-4]. It can subsequently lead to the realization of ultrasensitive bio/chemical sensors, medical diagnostics, metamaterials, imaging, spectroscopy, lensing, lasing, fast optical switches, highly coherent nanolasers [5-10], etc. The key properties of nanoparticle-based plasmonic systems like resonant wavelength, scattering efficiency, absorption efficiency, and electric field/ intensity enhancement can be controlled through size, shape and material of nanoparticles [11]. The optical response of nanoparticles-based plasmonic system is mainly characterized by: (I) dielectric function, (II) the spectral range in which LSPRs can be excited, (III) peak value and FWHM of resonance. Conventionally, noble metals (e.g., silver, gold, aluminum, copper, etc.) have been the primary and most widely employed plasmonic materials for plasmonic-based systems and components operating in visible and IR region [11]. Due to the substantial progress in synthesis, designing, and characterization tools for concentric core-shell nanoparticles, these particles are being widely investigated and finding diverse applications. The polarization-independent tunable core shell nanoparticle system which consists of the core and shell/cladding geometry, has the innate capacity to fine-tune the resonance peak's spectral characteristics through altering the relative sizes of the core and shell [12]. Owing to the better tunability of resonance wavelength, and controllability of optical properties, core-shells have found applications in SERS, refractive index-based sensing, optical switching, lasing, etc. This shows that plasmonic nanostructures and systems contain the core-shell nanoparticle as a crucial component for bio-molecular sensing [13]. In recent years, unique optical properties of gold-coated responsive polymer hybrid plasmonic-based systems, play an important role in engineering of photonic materials and plasmonic (active) metamaterials in a variety of applications, including sensing, detection, plasmon-enhanced optical spectroscopic readout, etc. [14, 15].Gold-coated 8-nm thick responsive polyaniline (PANI) shell exhibits plasmon resonance peak wavelength shift by 107 nm due to modulation of refractive index at the interface of core (gold)–shell (polymer) system [16]. Wu and coworkers investigated a PNIPAM shell (thickness=2.6 nm) -coated core gold nanoparticle (diameter =14.8 nm) for "calorimetric temperature sensor and temperature switchable catalyst" [17]. Miller and Lazarides demonstrated the LSPR peak position's sensitivity for Au nanoparticles and core shell of various shapes and sizes with variations in the

---

refractive index in dielectric environment [18]. The responsive polymer-coated plasmonic nanostructures can change their atomic configuration and subsequently their characteristics in the presence of external stimuli, e,g., pH, ions, temperature, light, electric or magnetic field, or biochemical agents [19-23]. The thermo-responsive polymers are the most frequently used materials for both *in vivo* and *in vitro* bio-medical applications. The responsive polymer-coated Au hybrid nanostructure like core shell, nanocages, nanostar, are used successfully in chemo-photothermal therapy of breast cancer cells, and photochemotherapy of pancreatic cancer with gemcitabine [24, 25]. The chemical synthesis of spherical gold nanoparticles with a diameter of 15 to 50 nm in 100 nm coated thick PNIPAM-based hydrogel shell was used to detune the LSPs on collapse of PNIPAM in dynamic light scattering studies [26].The most recent developments in the use of such responsive plasmonic nanomaterials are discussed, with a focus on plasmonic bio/chemical sensing which makes use of refractometric measurements, plasmon-enhanced optical spectroscopy readout, optically driven miniature soft actuators, and light-powered micromachines that operate in a setting similar to biological systems [27]. In the literature it is found that the LSPR resonant peak's position varies with the responsive PNIPAM shell characteristics (from swollen to collapsed) due to the surrounding physical and chemical environment. The PNIPAM microgels coupled with gold nanoparticles were used as plasmonic sensor components in a smart wearable device that enables naked-eye reading of temperature changes in contact with skin [28]. LSPs supported by a single metallic nanoparticle can be activated by altering the sensitive hydrogel shell's surrounding refractive index. The local rise in the refractive index caused by the collapse of the hydrogel shell next to the metallic core often causes resonant excitation of LSPs to red-shift to longer wavelengths. It is evident that sensitivity of the LSPR to the dielectric environment grows linearly with the position of the LSPR [21]. We present the Mie theory-based investigation of optical (extinction cross-section) properties of the gold/core-PNIPAM /shell-based plasmonic system. In this work, we investigate and optimize the sensing parameters of Au-coated responsive PNIPAM plasmonic system for sensing/detection.

THEORY

The schematic diagram of the core–shell nanoparticle is shown in Fig. 1 with geometrical parameter (a) of metal Au core having permittivity ε_1 radius R_1, and polymeric PNIPAM shell having permittivity ε_2 and radius R_2, ingrained in a medium of permittivity ε_m. The optical response of nanoparticles is modeled using wavelength-dependent dielectric function of plasmonic Au material. The plasmonic system is exposed to uniform electric field directed along +Z direction.
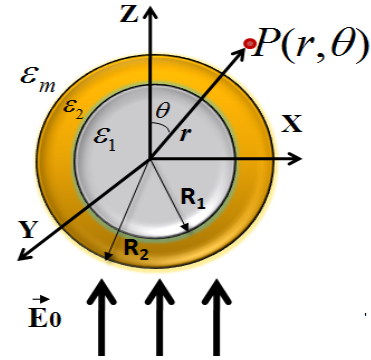
Figure 1. The schematic diagram shows a spherical Au metallic core of radius R_1 with frequency/wavelength dependent dielectric function ε_1 covered by polymeric PNIPAM shell of radius R_2 with dielectric function ε_2 ingrained in a medium having dielectric constant ε_m. The excitation of localized plasmon modes of gold modifies the electric field near the nanoparticle.

The incident electromagnetic waves are expanded in partially spherical waves using vector spherical harmonics. Solving Maxwell's equation and using boundary condition in each layer of core-shell nanoparticle to calculate the Mie coefficients a_l and b_l of the scattered and interior waves is described in the form of Bessel's and Hankel's functions as shown below [29]:

$$a_l = \frac{\psi_l(x_2)[\psi_l'(f_2x_2) - A_l\chi_l'(f_2x_2)] - m_2\psi_l'(x_2)[\psi_l(f_2x_2) - A_l\chi_l(f_2x_2)]}{\xi_l(x_2)[\psi_l'(f_2x_2) - A_l\chi_2'(f_2x_2)] - m_2\xi_l'(f_2)[\psi_l(f_2x_2) - A_l\chi_l(f_2x_2)]}$$

$$b_l = \frac{f_2\psi_l(x_2)[\psi_l'(f_2x_2) - B_l\chi_l'(f_2x_2)] - \psi_l'(x_2)[\psi_l(f_2x_2) - B_l\chi_l(f_2x_2)]}{f_2\xi_l(x_2)[\psi_l'(f_2x_2) - B_l\chi_l'(f_2x_2)] - \xi_l'(x_2)[\psi_l(f_2x_2) - B_l\chi_l(f_2x_2)]}$$

where the unknown coefficients are:

$$A_l = \frac{f_2\psi_l(f_2x_l)[\psi_l'(f_2x_l)] - f_l[\psi_l'(f_2x_l)\psi_l(f_1x_l)]}{[f_2\chi_l(f_2x_l)\psi_l'(f_1x_l)] - f_l\chi_l'(f_2x_l)\psi_l(f_1x_l)]}$$

$$B_l = \frac{f_2\psi_l(f_1x_l)[\psi_l'(f_2x_l)] - f_l[\psi_l'(f_2x_l)\psi_l(f_1x_l)]}{[f_2\psi_l'(f_2x_l)\psi_l(f_1x_l)] - f_l\psi_l'(f_2x_l)\chi_l(f_2x_l)]}$$

where f_1 and f_2 are the relative refractive indices of the core and clad/shell with respect to ingrained medium, $x_l = kR_l, x_2 = kR_2$ are the size parameters.

The Recatti Bessel functions written in terms of Bessel function are:

$$\psi_l(x) = xj_l, \chi_l(x) = -xy_l, \xi_l(x) = xh_l.$$

When the optimized Mie coefficients are known, the extinction efficiency, scattering efficiency, and absorption efficiency of the system are calculated using equation (1) [29]:

$$Q_{ext} = \frac{2}{x^2}\sum_{l=1}^{\infty}[2l+1]\text{Re}(a_l + b_l)$$
$$Q_{sca} = \frac{2}{x^2}\sum_{l=1}^{\infty}[2l+1](|a_l|^2 + |b_l|^2) \qquad (1)$$
$$Q_{abs} = Q_{ext} - Q_{sca}$$

In order to validate the present theoretical calculations, we reproduced a result reported in ref. [13] using our developed Matlab code. The calculated extinction cross-section Au-based core-shell [13] nanoparticle of different sizes [($R_1 = 2$ nm, $R_2 = 4$ nm), ($R_1 = 8$ nm, $R_2 = 10$ nm), ($R_1 = 15$ nm, $R_2 = 17$ nm)] embedded in air is presented in Fig. 2. The calculated spectral variation data using Mie theory-based calculations are shown as solid lines and corresponding circles are taken from ref. [12]. An excellent match between present calculations and those published in literature validates our theoretical method (MATLAB code).
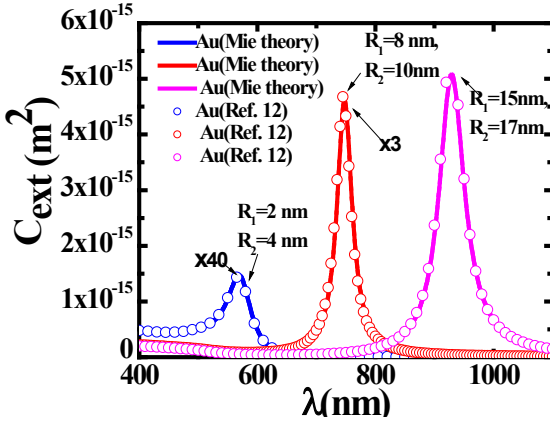
Figure 2. Calculated (solid line) extinction cross-section (C_{ext}) for core (silica)/ shell (gold) nanoparticle based on Mie theory. The results reported in ref. [12] are also shown (open circles) for the validation purpose. The dielectric constant of silica core is ε_2=2.04. An excellent match validates the approach used for present investigations.

RESULTS AND DISCUSSION

This section presents the results of theoretical investigations of Au-coated poly (N-isopropylacrylamide) (PNIPAM) core-shell nanoparticle-based nanosystems embedded in water (refractive index 1.33) using Mie theory.The radius

(R_1) of the inner gold core is taken as 5 nm and the thickness of surrounding polymeric shell (R_2) is 2 nm. The refractive index of Au is adopted from Palik's experimentally fitted data [13]. The optimized parameter (χ) models the effective quality of the solvent in the polymer layer which controls the volume fraction and strength of the polymer interaction forces [21]. The film is considered as inhomogeneous only in the radial coordinate. The optimized linear-dependent refractive index of the polymeric shell at 2 nm thickness coated in 5 nm gold core is taken from ref. [21]. The radial-dependent refractive index(n_p) of the polymer layer of thickness 2 nm coated at core Au radius 5 nm is modeled as 1.34 ($\chi = 2.0k_BT$), 1.37 ($\chi = 1.2k_BT$), 1.43 ($\chi = 0.8k_BT$), 1.48 ($\chi = 0.0k_BT$) and at polymer collapse the correspong refractive index is 1.52 [20]. Au-PNIPAM core shell nanosystem is kept in water as a surrounding medium having refractive index of 1.33. The change in external stimuli like temperature, pH, salt concentration, etc., leads to a change in χ from good solvent ($\chi = 0 k_BT$) to poor solvent ($\chi = 2 k_BT$) responsible for polymer collapse, corresponding to an increase in the average polymer volume fraction with decrease in film thickness. The calculated extinction efficiency (normalized extinction cross-section) is shown in Fig. 3.
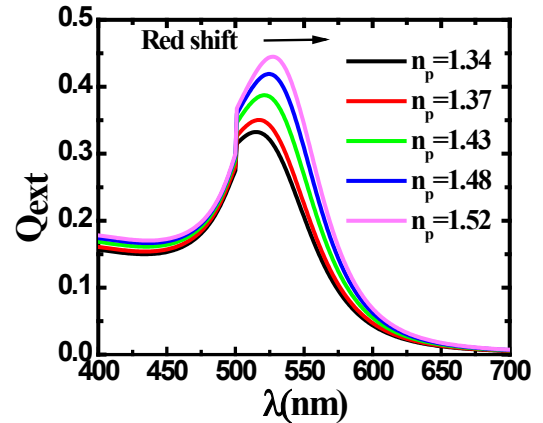
Figure 3. Calculated extinction efficiency (normalized cross-section) for 5 nm gold core coated with responsive PNIPAM outer shell thickness of 2 nm. As the concentration of solvent PNIPAM change with external stimuli there will change in the refractive index leading to red shift in the resonant peak. The surrounding medium refractive index will be 1.33 (water). The optimized linear dependent refractive index of the polymeric shell at 2 nm thick coated in 5nm gold core is taken from ref.[21].

The normalized extinction cross-section (absorption and scattering) at swollen state with optimized refractive index (n_p=1.34) is 0.332 with corresponding resonating peak wavength of 515 nm.

This evidences that the extinction efficiency (scattering and absorption) spectra show a resonant behavior by virtue of occurrence of localized surface plasmon resonance at resonant wavelength (λ_R) =515 nm, 517 nm, 521 nm and 525 nm for an optimized refractive index of 1.34 ($\chi = 2.0k_BT$), 1.37 ($\chi = 1.2k_BT$), 1.43 ($\chi = 0.8k_BT$), 1.48 ($\chi = 0.0k_BT$), respectively and corresponding magnitudes of extinction efficiency of 0.332, 0.351, 0.38 and 0.41, respectively. It is found that there will be a red shift in the resonant peak with increase in refractive index of polymer shell layer with change in the external physical and chemical enviroment/stumuli.The variation of resonant peak wavelength as the soft shell evolves from a swollen ($\chi = 2.0k_BT$) to a collapsed state ($\chi = 0.0k_BT$) with optimized refractive index is well suitable for refractive index-based sensing/detection.The performance of the sensor is analyzed through sensing parameters: (I) quality factor (QF) of extinction resonance peak, (II) sensitivity (S) and (III) figure of merit (FOM). The sensitivity (S) of the sensor is calculated as the rate of shift of resonant peak wavelength with the variation in the refractive index (n_p) of shell medium, and the same is mathematically written as [30]:

$$S(nm/RIU) = d\lambda_R / dn_p \qquad (2)$$

(a)
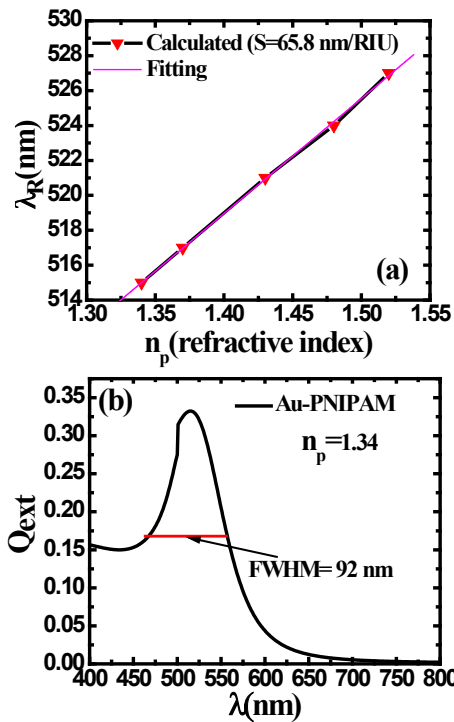
Figure 4. (a) Calculated dependence of the resonant wavelength $(\lambda_R(nm))$ on the refractive index (n_p) of the responsive shell medium PNIPAM. **(b)** Full width half

maximum at the resonant peak is calculated as 92 nm at n_p =1.34 ($\chi = 2.0k_BT$).

The calculated sensitivity (S) using eqution 3 is 65.8 nm/RIU, shown in Fig. 4(a).The resonant peak at swollen state (n_p =1.34) is optimized with resonant wavelength (λ_R) 515 nm and the corrosponding calculated full width at half maximum (FWHM) is 92 nm, shown in Fig. 4(b). The quality factor of the resonant peak is calculated as the ratio of resonant wavelength of peak to the full width at half maximum of the resonant peak as [30]:

$$QF = \frac{\lambda_R}{FWHM} \qquad (3)$$

This suggests that the resonant peak with smaller full width half maximum corresponds to a higher quality factor of the sensor.The figure of merit (FOM) is defined in terms of quality factor of the extinction resonant peak and the coresponding sensitivity. It is a comprehensive parameter to evaluate the performance of a plasmonic sensor, expressed as [30]:

$$FOM(RIU/nm) = QF \times S \qquad (4)$$

The calculated figure of merit (FOM) using equation 4 is $\sim 3.6 \times 10^2$ RIU/nm. Overall, the present work suggests that the responsive polymer-based plasmonic system provides an efficient refractive index-based sensing machanism for external physical and chemical stumuli.

SUMMARY

In this work we assessed the bio/chemical sensing characteristics of an Au-coated PNIPAM-based plasmonic nano system. The theoretically estimated sensitivity (S) in the present work is 65.8 nm/RIU and the optimized figure of merit is $\sim 3.6 \times 10^2$ RIU/nm. It is evident that bio/chemical sensors with high sensitivity and figure of merit can be developed by employing plasmonic modes in an Au-PNIPAM based system. The availability of hybrid responsive polymer-based plasmonic nanosystem can open the door for advanced applications.

REFERENCES

1. N. Jiang, X. Zhuo, J. Wang, *Chem. Rev.,* **118**, 3054 (2018).
2. R. P. Feynman, *Engineering and Science*, **5**, 22 (1960).

3. W. L. Barnes, A. Dereux, T. W. Ebbesen, *Nature*, **424**, 824 (2003).
4. E. Ozbay, *Science,* **311**, 189 (2006).
5. M. S. Shishodia, P. V. V. Jayaweera, S. G. Matsik, A. G. U. Perera, H. C. Liu, M. Buchanan, *Photonics and Nanostructures: Fundam. Appl.,* **9**, 95 (2011).
6. P. Pathania, M. S. Shishodia, *Plasmonics*, **16**, 2717 (2021).
7. P. Pathania, M. S. Shishodia, *Plasmonics*, **14**, 1435 (2019).
8. M. S. Shishodia, P. Pathania, *Phys. Plasmas,* **25**, 042101 (2018).
9. S. Faujdar, P. Pathania, *Materials Today: Proceedings ,***57**, 2295 (2022).
10. M. S. Shishodia, A. G. U. Perera, *J. Appl. Phys.* **109**, 043108 (2011).
11. J. Katyal, R. Soni, *Plasmonics*, **9**, 1171(2014).
12. R. D. Averitt, S. L. Westcott, N. J. Halas, *JOSA A*, **16**, 10 (1999).
13. K. Tanabe, *J. Phys. Chem.,* **C112**, 15721 (2008).
14. Tao Ding, J. J. Baumberg, *Nanoscale Adv.*, **2**, 1410 (2020).
15. J. F. Herrmann, F. Kretschmer, S. Höppener, C. Höppener, U. S. Schubert, *Small*, **13,** 39 (2017).
16. J.-W. Jeon, J. Zhou, J. A. Geldmeier, J. F. Ponder, Jr., M. A. Mahmoud, M. El-Sayed, J. R. Reynolds, V. V. Tsukruk, *Chem. Mater.* **28**, 7551 (2016)
17. S. Wu, L. Lei, Y. Xia, S. Oliver, Y. Xia, X. Chen, C. Boyer, Z. Nie, S. Shi, *Polym. Chem*., **12**, 6903 (2021).
18. M. M. Miller, A. A. Lazarides, *J. Phys. Chem. B*, **109,** 21556 (2005).
19. R. S. Lee, Y. T. Huang, W. H Chen, *J. Appl. Polym. Sci.,* **118**, 1634 (2010).
20. E. S. Gill, S. M. Hudson, *Prog. Polym. Sci.* **29**, 1173 (2004).
21. M. Tagliazucchi, M. G. Blaber, G. C. Schatz, E. A. Weiss, I. Szleifer, *ACS Nano*, **6**, 8397 (2012).
22. F. D Jochum, P. Theato, *Chem. Commun.,* **46**, 6717 (2010).
23. M. Emamzadeh, G. Pasparakis, *Sci. Rep.*,**11**, 9404 (2021).
24. A. Pakravan, M. Azizi, F. Rahimi, F. Bani, F. Mahmoudzadeh, R. Salehi, M. Mahkam, *Cancer Nanotechnology*, **12**, 1 (2021).
25. B. Jeon, A. Gutowska,*Trends in Biotechnology*, **20**, 305 (2002).
26. N. Carl, J. Sindram, M. Gallei, S. U. Egelhaaf, M. Karg, *Phys. Rev. E.,* **100**, 052605 (2019).
27. F. Diehl, S. Hageneder, S. Fossati, S. K. Auer, J. Dostalek, U. Jonasl, *Chem. Soc. Rev.*, **51**, 3926 (2022).
28. A. Choe, J. Yeom, R. Shanker, M. P. Kim, S. Kang , H. Ko, *NPG Asia Mater.*, **10**, 912 (2018).
29. C. F. Bohren, D. R. Huffman, Wiley, New York, 1983.
30. Y .Tao, Z .Guo, A .Zhang, J. Zhang, B.Wang, S. Qu, *Opt. Commun*., **349**, 193 (2015).

BULGARIAN CHEMICAL COMMUNICATIONS

Instructions about Preparation of Manuscripts

General remarks: Manuscripts are submitted in English by e-mail or by mail (in duplicate). The text must be typed double-spaced, on A4 format paper using Times New Roman font size 12, normal character spacing. The manuscript should not exceed 15 pages (about 3500 words), including photographs, tables, drawings, formulae, etc. Authors are requested to use margins of 3 cm on all sides. For mail submission hard copies, made by a clearly legible duplication process, are requested. Manuscripts should be subdivided into labelled sections, e.g. **Introduction, Experimental, Results and Discussion**, *etc*.

The title page comprises headline, author's names and affiliations, abstract and key words.

Attention is drawn to the following:

a) **The title** of the manuscript should reflect concisely the purpose and findings of the work. Abbreviations, symbols, chemical formulas, references and footnotes should be avoided. If indispensable, abbreviations and formulas should be given in parentheses immediately after the respective full form.

b) **The author**'s first and middle name initials, and family name in full should be given, followed by the address (or addresses) of the contributing laboratory (laboratories). **The affiliation** of the author(s) should be listed in detail (no abbreviations!). The author to whom correspondence and/or inquiries should be sent should be indicated by asterisk (*).

The abstract should be self-explanatory and intelligible without any references to the text and containing not more than 250 words. It should be followed by key words (not more than six).

References should be numbered sequentially in the order, in which they are cited in the text. The numbers in the text should be enclosed in brackets [2], [5, 6], [9–12], etc., set on the text line. References, typed with double spacing, are to be listed in numerical order on a separate sheet. All references are to be given in Latin letters. The names of the authors are given without inversion. Titles of journals must be abbreviated according to Chemical Abstracts and given in italics, the volume is typed in bold, the initial page is given and the year in parentheses. Attention is drawn to the following conventions:

a) The names of all authors of a certain publications should be given. The use of "*et al.*" in the list of references is not acceptable.

b) Only the initials of the first and middle names should be given.

In the manuscripts, the reference to author(s) of cited works should be made without giving initials, e.g. "Bush and Smith [7] pioneered...". If the reference carries the names of three or more authors it should be quoted as "Bush *et al*. [7]", if Bush is the first author, or as "Bush and co-workers [7]", if Bush is the senior author.

Footnotes should be reduced to a minimum. Each footnote should be typed double-spaced at the bottom of the page, on which its subject is first mentioned.

Tables are numbered with Arabic numerals on the left-hand top. Each table should be referred to in the text. Column headings should be as short as possible but they must define units unambiguously. The units are to be separated from the preceding symbols by a comma or brackets.

Note: The following format should be used when figures, equations, *etc*. are referred to the text (followed by the respective numbers): Fig., Eqns., Table, Scheme.

Schemes and figures. Each manuscript (hard copy) should contain or be accompanied by the respective illustrative material as well as by the respective figure captions in a separate file (sheet). As far as presentation of units is concerned, SI units are to be used. However, some non-SI units are also acceptable, such as °C, ml, l, etc.

The author(s) name(s), the title of the manuscript, the number of drawings, photographs, diagrams, etc., should be written in black pencil on the back of the illustrative material (hard copies) in accordance with the list enclosed. Avoid using more than 6 (12 for reviews, respectively) figures in the manuscript. Since most of the illustrative materials are to be presented as 8-cm wide pictures, attention should be paid that all axis titles, numerals, legend(s) and texts are legible.

The authors are asked to submit **the final text** (after the manuscript has been accepted for publication) in electronic form either by e-mail or mail on a 3.5'' diskette (CD) using a PC Word-processor. The main text, list of references, tables and figure captions should be saved in separate files (as *.rtf or *.doc) with clearly identifiable file names. It is essential that the name and version of

the word-processing program and the format of the text files is clearly indicated. It is recommended that the pictures are presented in *.tif, *.jpg, *.cdr or *.bmp format, the equations are written using "Equation Editor" and chemical reaction schemes are written using ISIS Draw or ChemDraw programme.

The authors are required to submit the final text with a list of three individuals and their e-mail addresses that can be considered by the Editors as potential reviewers. Please, note that the reviewers should be outside the authors' own institution or organization. The Editorial Board of the journal is not obliged to accept these proposals.

EXAMPLES FOR PRESENTATION OF REFERENCES

REFERENCES

1. D. S. Newsome, *Catal. Rev.–Sci. Eng.*, **21**, 275 (1980).
2. C.-H. Lin, C.-Y. Hsu, *J. Chem. Soc. Chem. Commun.*, 1479 (1992).
3. R. G. Parr, W. Yang, Density Functional Theory of Atoms and Molecules, Oxford Univ. Press, New York, 1989.
4. V. Ponec, G. C. Bond, Catalysis by Metals and Alloys (Stud. Surf. Sci. Catal., vol. 95), Elsevier, Amsterdam, 1995.
5. G. Kadinov, S. Todorova, A. Palazov, in: New Frontiers in Catalysis (Proc. 10th Int. Congr. Catal., Budapest, 1992), L. Guczi, F. Solymosi, P. Tetenyi (eds.), Akademiai Kiado, Budapest, 1993, Part C, p. 2817.
6. G. L. C. Maire, F. Garin, in: Catalysis. Science and Technology, J. R. Anderson, M. Boudart (eds), vol. 6, Springer-Verlag, Berlin, 1984, p. 161.
7. D. Pocknell, *GB Patent* 2 207 355 (1949).
8. G. Angelov, PhD Thesis, UCTM, Sofia, 2001.
9. JCPDS International Center for Diffraction Data, Power Diffraction File, Swarthmore, PA, 1991.
10. CA **127**, 184 762q (1998).
11. P. Hou, H. Wise, *J. Catal.*, in press.
12. M. Sinev, private communication.
13. http://www.chemweb.com/alchem/articles/1051611477211.html.